



UNIVERSITAT DE
BARCELONA

COUPY coumarins as privileged scaffolds for the development of novel targeted fluorophores and metalbased PDT anticancer agents

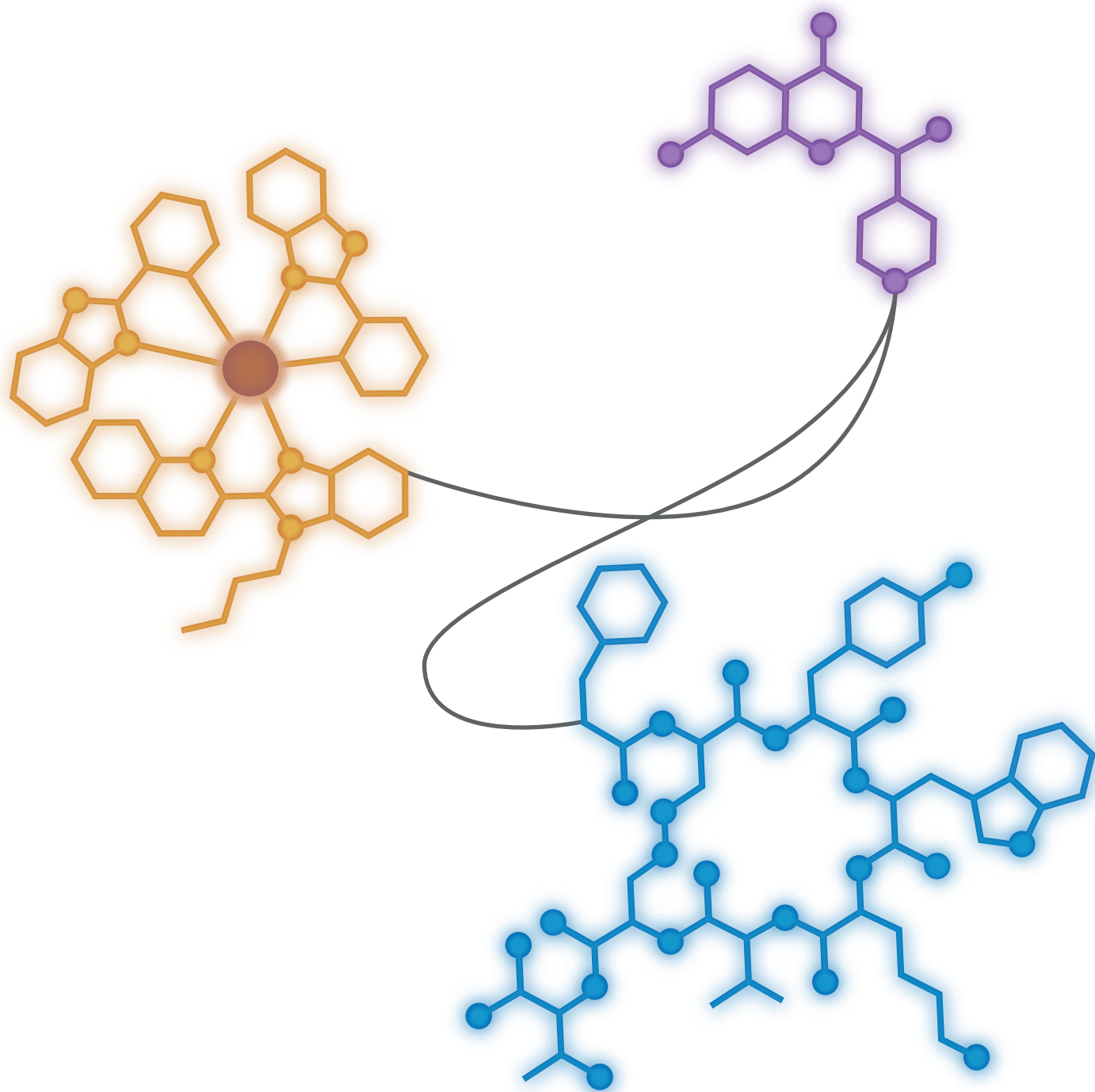
Anna Rovira Vidal

ADVERTIMENT. La consulta d'aquesta tesi queda condicionada a l'acceptació de les següents condicions d'ús: La difusió d'aquesta tesi per mitjà del servei TDX (www.tdx.cat) i a través del Dipòsit Digital de la UB (diposit.ub.edu) ha estat autoritzada pels titulars dels drets de propietat intel·lectual únicament per a usos privats emmarcats en activitats d'investigació i docència. No s'autoritza la seva reproducció amb finalitats de lucre ni la seva difusió i posada a disposició des d'un lloc aliè al servei TDX ni al Dipòsit Digital de la UB. No s'autoritza la presentació del seu contingut en una finestra o marc aliè a TDX o al Dipòsit Digital de la UB (framing). Aquesta reserva de drets afecta tant al resum de presentació de la tesi com als seus continguts. En la utilització o cita de parts de la tesi és obligat indicar el nom de la persona autora.

ADVERTENCIA. La consulta de esta tesis queda condicionada a la aceptación de las siguientes condiciones de uso: La difusión de esta tesis por medio del servicio TDR (www.tdx.cat) y a través del Repositorio Digital de la UB (diposit.ub.edu) ha sido autorizada por los titulares de los derechos de propiedad intelectual únicamente para usos privados enmarcados en actividades de investigación y docencia. No se autoriza su reproducción con finalidades de lucro ni su difusión y puesta a disposición desde un sitio ajeno al servicio TDR o al Repositorio Digital de la UB. No se autoriza la presentación de su contenido en una ventana o marco ajeno a TDR o al Repositorio Digital de la UB (framing). Esta reserva de derechos afecta tanto al resumen de presentación de la tesis como a sus contenidos. En la utilización o cita de partes de la tesis es obligado indicar el nombre de la persona autora.

WARNING. On having consulted this thesis you're accepting the following use conditions: Spreading this thesis by the TDX (www.tdx.cat) service and by the UB Digital Repository (diposit.ub.edu) has been authorized by the titular of the intellectual property rights only for private uses placed in investigation and teaching activities. Reproduction with lucrative aims is not authorized nor its spreading and availability from a site foreign to the TDX service or to the UB Digital Repository. Introducing its content in a window or frame foreign to the TDX service or to the UB Digital Repository is not authorized (framing). Those rights affect to the presentation summary of the thesis as well as to its contents. In the using or citation of parts of the thesis it's obliged to indicate the name of the author.

COUPY COUMARINS AS PRIVILEGED SCAFFOLDS FOR THE DEVELOPMENT OF NOVEL TARGETED FLUOROPHORES AND METAL-BASED PDT ANTICANCER AGENTS



Anna Rovira Vidal



UNIVERSITAT DE
BARCELONA

Programa de Doctorat de Química Orgànica

**COUPY coumarins as privileged scaffolds for the
development of novel targeted fluorophores and metal-
based PDT anticancer agents**

Doctoral Thesis submitted by

Anna Rovira Vidal

Supervised by

Dr. Vicente Marchán Sancho

Departament de Química Inorgànica i Orgànica

Secció de Química Orgànica

Facultat de Química

Universitat de Barcelona

Barcelona, November 2022



UNIVERSITAT DE
BARCELONA

This thesis was performed from October 2017 until November 2022 in the Section of Organic Chemistry of the Department of Inorganic and Organic Chemistry of the University of Barcelona. The work has been carried out with the financial support of the “Ministerio de Ciencia e Innovación” (Projects CTQ2017-84779-R and PID2020-117508RB-I00) and with the support of a fellowship from the University of Barcelona (“ajuts de personal investigador predoctoral en formació” - APIF).

Agraïments

Aquesta Tesis no hagués estat possible sense el recolzament de moltes persones, que o m'han acompanyat durant tota aquesta aventura, o s'han unit en diferents etapes. En les següents línies m'agradaria agrair a cada una d'elles haver-hi format part.

Primerament agrair-te Vicente per donar-me aquesta oportunitat i per brindar-me la teva confiança des del primer moment en que em vas proposar aquest projecte, la veritat és que aquesta aventura va començar gràcies a tu. Gràcies per transmetrem els teus coneixements, guiar-me i estar allà sempre que ho he necessitat.

Gràcies també a Ignacio, Núria i Joaquim per tots els bons consells que m'heu donat durant aquests anys.

I would like to thank Pablo and his amazing research group for the warmth and kindness they showed me from the very beginning of my Stay at the University of Zurich. During my time there, it was mainly thanks to Sarah that I was able to learn new concepts and techniques, thanks for helping me whenever I needed, I really miss our couch time. Agrair-te també a tu Carla, per fer-me sentir com a casa en una ciutat a 1000 km de Catalunya. Thanks to each of you for your time, energy, and expertise: Doro, Krzysztof, Annabell, Hen, Juan, Set, Adam, Salome and Lea. I'm really looking forward to our next Apéro.

I would also like to thank my amazing roommates in Zurich, you definitely made this experience unforgettable. Thanks to Kili for helping me when I needed, to Manu for showing me the beauty of Zurich with our publibike tours, and to Eemeli for being my perroo partner and Eurovision specialist. Y sin duda lo mejor que me llevo de esta experiencia eres tú, gracias Urs por creer siempre en mí, por ayudarme cuando más lo he necesitado, y por aguantarme en mis momentos de estrés. No tengo duda de que nos esperan cosas increíbles juntos.

També vull donar les gràcies a tots els meus companys de laboratori. Marta, no hauria pogut tenir millor companya de laboratori durant aquests anys. Gràcies per tots els bons moments viscuts en el laboratori 500, que es va convertir en la nostra segona casa, per tots els riures, i per les llargues tardes treballant vitrina amb vitrina mentre reflexionàvem sobre la vida. Sergi, gràcies pels bons moments i ajudar-me sempre que ho he necessitat. Davor, tot i que has estat poc temps, amb el teu sentit de l'humor has deixat petjada en el grup. Tomeu, moltes gràcies per fer-me l'inici d'aquesta etapa més fàcil i divertida. Joaquin, gràcies per ajudar-me quan ho he necessitat, sobretot en aquest final de tesis. Albert, gràcies per ajudar-me des del principi i introduir-me en aquest projecte. I

finalment vull agrair a tots els estudiants que m'han ajudat i que han passat pel laboratori en diferents moments: Nicole, Joan, Míriam i Marina.

No em podria oblidar dels meus companys de departament, sens dubte sense vosaltres no hauria estat el mateix. Moltes gràcies per tots els bons moments, els dinars, les barbacoes, les activitats amb la colla, sopars de Nadal,... Roberto, Marina, Miquel, Marina, Héctor, Júlia, Macarena, Fernanda, Marc, Ari y Saj.

Agrair als meus companys de pis, Marina, Stuart i Roberto, gràcies per ser la meva família a Barcelona. Ha estat un plaer tenir-vos al meu costat en aquesta etapa. La Tesis no hagués estat el mateix sense les nits de pizza/sushi de la Yen al sofà, els jocs de taula que tant em costaven d'entendre, o els diumenges de pel·lícula i manta.

Roberto, gràcies per acompanyar-me tots aquests anys, sens dubte aquesta experiència no hagués estat el mateix sense tu, i sé que m'emporto amb mi un gran amic per tota la vida, tot i que no estiguem a la mateixa ciutat. Trobaré a faltar moltes coses que no cabrien en aquest full, però algunes d'elles són: totes les nits rient de qualsevol frase o vídeo sense sentit, els nostres sopars a les 7 de la tarda, els diumenges de sofà i Tiktok amb el Lima sobre les cames, els dies de la quarantena anant a caminar per Barcelona, la introducció al CrossFit, anar a prendre una cervesa en qualsevol terrassa, tots els Glovo que hem demanat, o simplement anar a fer la compra junts. Moltes gràcies per tot!

No em podria oblidar tampoc de les meves amigues de la Uni, i els amics del poble per tots els bons moments durant aquest temps.

Finalment voldria agrair a la meva família tot el recolzament durant aquests anys, gràcies per confiar en mi i ajudar-me sempre que ho he necessitat. I Daniel, moltes gràcies per aquesta meravellosa portada.

*"Nothing in life is to be feared. It is only to be understood. Now is
the time to understand more, so that we may fear less."*

— **Marie Curie**

Thesis outline

This Thesis is structured as a compendium of publications, being organized around three published articles, one manuscript under preparation (see below), together with the corresponding supplementary materials, and one section describing additional non-published results. The Thesis contains a General Introduction, presented as a summary/review of the state-of-the-art of the antecedents related to the main Objectives proposed in this research project regarding the use of targeting organic fluorophores for bioimaging applications, as well as of metal complexes for anticancer photodynamic therapy. Immediately after the Results and Discussion section, which has been organized in two chapters that include the four publications as well as additional non-published results, the Conclusions section can be found. Finally, according to the guidelines of the University of Barcelona for Thesis presented as a compendium of publications, a summary of the main results of the Thesis written in Spanish is provided.

List of publications:

- Publication A. **Rovira, A.**; Pujals, M.; Gandioso, A.; López-Corrales, M.; Bosch, M.; Marchán, V. Modulating photostability and mitochondria selectivity in far-red/NIR emitting coumarin fluorophores through replacement of pyridinium by pyrimidinium. *J. Org. Chem.* **2020**, *85*, 6086-6097.
- Publication B. **Rovira, A.**; Gandioso, A.; Goñalons, M.; Galindo, A.; Massaguer, A.; Bosch, M.; Marchán, V. Solid-phase approaches for labeling targeting peptides with far-red emitting coumarin fluorophores. *J. Org. Chem.* **2019**, *84*, 1808–1817.
- Publication C. Novohradsky, V.; **Rovira, A.**; Hally, C.; Galindo, A.; Viguera, G.; Gandioso, G.; Svitelova, M.; Bresolí-Obach, R.; Kostrhunova, H.; Markova, L.; Kasparkova, J.; Nonell, S.; Ruiz, R.; Brabec, V.; Marchán, V. Towards novel photodynamic anticancer agents generating superoxide anion radicals: a cyclometalated Ir^{III} complex conjugated to a far-red emitting coumarin. *Angew. Chem. Int. Ed.* **2019**, *58*, 6311-6315.
- Publication D. **Rovira, A.**; Ortega-Forte, E.; Hally, C.; Jordà, M.; Viguera, G.; Bosch, M.; Nonell, S.; Ruiz, J.; Marchán, V. Exploring structure-activity relationships in photodynamic therapy anticancer agents based on Ir(III)-COUPY conjugates. *Manuscript under preparation*.

Non-published results:

- Chapter IIc. **Rovira, A.** *et al.* Development of a new photosensitizer based on the conjugation of a NIR-emitting COUPY dye to a cyclometalated Ru(II) polypyridyl complex.

TABLE OF CONTENTS

Abbreviations and acronyms	1
Introduction and objectives	7
1. Cancer: an overview.....	9
2. Organic fluorophores in cancer imaging and therapy	11
2.1 Fluorescence spectroscopy in bioscience	11
2.2 Fluorescence principles	12
2.2.1 Jablonski diagram	12
2.2.2 Photophysical properties of organic fluorophores	13
2.3 Long-lived fluorescent organic probes.....	15
2.3.1 UV-excitabile fluorophores	16
2.3.2 Visible light-NIR-excitabile fluorophores.....	17
2.4 Coumarin-based fluorescent probes for bioimaging applications	20
2.4.1 General overview of the coumarin scaffold	20
2.4.2 Synthesis of coumarin-based fluorophores	21
2.4.2.1 Modification of the 3-position in the coumarin scaffold.....	22
2.4.2.2 Modification of the 4-position in the coumarin scaffold.....	24
2.4.2.3 Fused coumarin dyes	25
2.4.2.4 Hybrid dyes between coumarins and other fluorophores	27
2.4.2.5 2-Extended coumarin dyes: COUPY dyes	28
2.5 Targeted approaches in cancer imaging and therapy	34
2.5.1 Ligand-targeted drug delivery: an overview	34
2.5.2 Targeting ligands based on receptor-binding peptides	37
2.5.3 Targeted fluorophores for cancer imaging and fluorescent-guided surgery	40
2.6 Photodynamic therapy (PDT).....	46

2.6.1 Photosensitizers (PS).....	48
2.6.2 Light source	48
2.6.3 PDT mechanism of action	50
2.6.4 Clinically-approved PSs for cancer therapy	51
2.6.5 Advantages and challenges of PDT treatment.....	54
2.6.6 Photosensitizers based on organic fluorophores.....	55
3. Metal-based anticancer drugs in conventional chemotherapy and photodynamic therapy.....	57
3.1 Metal complexes in conventional chemotherapy.....	57
3.1.1 Platinum(II) and platinum(IV) anticancer complexes	57
3.1.1.1 Mechanism of action of Pt-based anticancer drugs.....	59
3.1.1.2 Resistance to cisplatin	61
3.1.2 Ruthenium(II) anticancer complexes	62
3.1.2.1 Ru-based anticancer agents in clinical trials.....	63
3.1.2.2 Mechanism of action of Ru(II) anticancer complexes	63
3.1.2.3 Ruthenium(II) polypyridyl complexes	66
3.1.3 Iridium(III) complexes	69
3.1.3.1 Cyclometalated iridium(III) complexes.....	70
3.2 Photosensitizers based on metal complexes	72
3.2.1 Ruthenium(II) polypyridyl complexes as PDT agents.....	72
3.2.2 Iridium(III) complexes as PDT agents.....	78
4. Objectives	85
5. References	93

Results and Discussion	111
Chapter I: Development of novel coumarin-based COUPY fluorophores for bioimaging applications.....	113
6. Chapter Ia. Publication A: Modulating photostability and mitochondria selectivity in far-red/NIR emitting coumarin fluorophores through replacement of pyridinium by pyrimidinium. (A. Rovira <i>et al. J. Org. Chem.</i> 2020 , 85, 6086–6097)	115
7. Chapter Ib. Publication B: Solid-phase approaches for labeling targeting peptides with far-red emitting coumarin fluorophores. (A. Rovira <i>et al. J. Org. Chem.</i> 2019 , 84, 1808–1817)	167
Chapter II: Conjugation of COUPY fluorophores to Ir(III) and Ru(II) complexes for anticancer photodynamic therapy	209
8. Chapter IIa. Publication C: Towards novel photodynamic anticancer agents generating superoxide anion radicals: a cyclometalated Ir ^{III} complex conjugated to a far-red emitting coumarin. (V. Novohradsky <i>et al. Angew. Chem. Int. Ed.</i> 2019 , 58, 6311 –6315)	211
9. Chapter IIb. Publication D: Exploring structure–activity relationships in photodynamic therapy anticancer agents based on Ir(III)-COUPY conjugates. (A. Rovira <i>et al. Manuscript under preparation</i>).....	259
10. Chapter IIc. Non-published results: Development of a new photosensitizer based on the conjugation of a NIR-emitting COUPY dye to a cyclometalated Ru(II) polypyridyl complex.	343
Conclusions	363
Summaries	369
Resumen del capítulo I	371
Resumen del capítulo II	403

Abbreviations and acronyms

5-ALA	5-Aminolevulinic acid
A	Adenine
A17	Breast cancer cell line
A2780	Human ovarian cancer cell line
A2780CisR	Cisplatin-resistant ovarian cancer cell line
A549	Human non-small cell lung cancer cell line
A549R	Cisplatin-resistant human non-small cell lung cancer cell line
ACN	Acetonitrile
ATP	Adenosine triphosphate
ATP7	Copper-transporting P-type ATPase
AZB	Aza-BODIPY
ben	Benzene group
bip	Biphenyl group
Boc	<i>tert</i> -Butyloxycarbonyl
BODIPY	Boron-dipyrromethene
br	Broad signal
CML	Chronic myeloid leukemia
COX-2	Cyclooxygenase 2
CRT	Cyclic peptide CRTIGPSVC
CTR1	Copper transport protein
CuAAC	Cu(I)-catalyzed azide–alkyne cycloaddition
CURL	Compartment for uncoupling of receptor and ligand
CV	Cresyl violet
Cy	Cyanine
cym	Methylisopropylbenzene group
Cyto C	Cytochrome complex
d	Doublet

DAPI	4',6-Diamidino-2-phenylindole
DCM	Dichloromethane
dd	Doublet of doublets
ddd	Doublet of doublet of doublets
dha	Dihydroanthracene group
DHR123	Dihydrorhodamine 123
DIPC	<i>N,N'</i> -Diisopropylcarbodiimide
DIPEA	<i>N,N</i> -Diisopropylethylamine
DMEM	Dulbecco modified eagle medium
DMF	<i>N,N</i> -Dimethylformamide
DMSO	Dimethylsulfoxide
DNA	Deoxyribonucleic acid
DPBS	Dulbecco's phosphate-buffered saline
dt	Doublet of triplets
DTPA	Diethylenetriaminepentaacetic acid
EDG	Electron-donating group
EDT	Ethane-1,2-dithiol
EGF	Epidermal growth factor
en	Ethylenediamine
EPR	Permeability and retention effect
ER	Endoplasmic reticulum
ERS	Endoplasmic reticulum stress
ESI-MS	Electrospray ionization mass spectra
EWG	Electron-withdrawing group
FCS	Fetal calf serum
FDA	Food and drug administration
FGS	Fluorescence-guided surgery
FIR	Far-infrared
Fmoc	9-Fluorenylmethoxycarbonyl

FRET	Förster-type resonance energy-transfer
G	Guanine
GBM	Intracranial glioblastoma
GnRH	Gonadotropin-releasing hormone
GSH	Glutathione
HAS	Human serum albumin protein
HATU	1-[Bis(dimethylamino)methylene]-1H-1,2,3-triazolo[4,5-b]pyridinium 3-oxide hexafluorophosphate
HBIND	H-bond-induced nonradiative decay
HCT116	Human colon cancer cell line
HeLa	Human cervical carcinoma cell line
HepG2	Human liver cancer cell line
HL-60	Human promyelocytic leukemia cells
hmb	Hexamethylbenzene
HOBt	Hydroxybenzotriazole
HPD	Hematoporphyrin derivative
HPLC	High-performance liquid chromatography
HPLC-MS	High-performance liquid chromatography-mass spectrometry
HR	High resolution
HT29	Human colorectal adenocarcinoma cell line
ICG	Indocyanine green
ICP-MS	Inductively-coupled plasma mass spectrometry
ICT	Intramolecular charge transfer
IMC	Indomethacin
ISC	Intersystem crossing
K562	Human erythroleukemic cell line
K562/A02	Human leukemic cell line
LED	Light-emitting diode
LW	Lawesson's reagent

Lys	Lysine
m	Multiplet
m/z	Mass to charge ratio
MB	Methylene blue
MCF-7	Breast cancer cell line
MCF7/ADM	Doxorubicin-resistant breast cancer cell line
MDA-MB-231	Breast cancer cell line
MG-63	Human osteosarcoma cell line
MIR	Mid-infrared
mRNA	Messenger ribonucleic acid
NADH	Nicotinamide adenine dinucleotide
NER	Nucleotide excision repair machinery
NHC	N-heterocyclic carbene
NIR	Near-infrared region
NMIBC	Non-muscle-invasive bladder cancer cell line
NMR	Nuclear magnetic resonance
NOESY	Nuclear overhauser enhancement spectroscopy
NSCLC	Non-small cell lung cancer
PANC-1	Epithelioid carcinoma cell line
PBS	Phosphate Buffered Saline
PDT	Photodynamic therapy
PEG	Polyethylene glycol
Phe	Phenylalanine
PI	Phototoxic/Phototherapeutic index
PLK1	Polo-like kinase 1
PpIX	Protoporphyrin IX
ppm	Part per million
PS	Photosensitizer
q	Quartet

qt	Quintuplet
RB	Rose bengal
RES	Reticuloendothelial system
RGD	Arginylglycylaspartic acid
Rho	Rhodamine
ROS	Reactive oxygen species
RT	Room temperature
s	Singlet
S ₀	Singlet electronic ground state
S ₁	First singlet excited state
SBE13	Polo-like kinase 1 inhibitor
SCLC	Small cell lung cancer
Ser	Serine
SK-MEL-28	Melanoma cell line
SOC	Spin-orbital coupling
SOD	Superoxide dismutase
SPPS	Solid-phase peptide synthesis
SRBAC	Sulforhodamine B acid chloride
SST	Somatostatin
SSTR	Somatostatin receptor
SW480	Human colon adenocarcinoma cell line
t	Triplet
T ₁	Triplet excited states
T47D	Human breast cancer cell line
TFA	Trifluoroacetic acid
Thr	Threonine
TICT	Twisted intramolecular charge-transfer formation
TIS	Triisopropylsilane
TLC	Thin-layer chromatography

TMS	Tetramethylsilane
TPP	Tetraphenylporphyrin
TPPS	Meso-tetra(4-sulfonatophenyl)porphyrin
Trp	Tryptophan
Trt	Trityl
Tyr	Tyrosine
UV	Ultraviolet
Val	Valine
VIP	Vasoactive intestinal peptide

General Introduction and Objectives

1. Cancer: an overview

In recent decades, cancer has become one of the leading causes of death worldwide and an obstacle to increasing life expectancy in all regions of the world and regardless the level of human development. There were an estimated 19.3 million new cancer cases worldwide and nearly 10 million cancer deaths only in the year 2020. An estimated 28.4 million new cancer cases are expected to occur in 2040, increasing by a 47% the number of cases in 2020 (Figure 1).¹

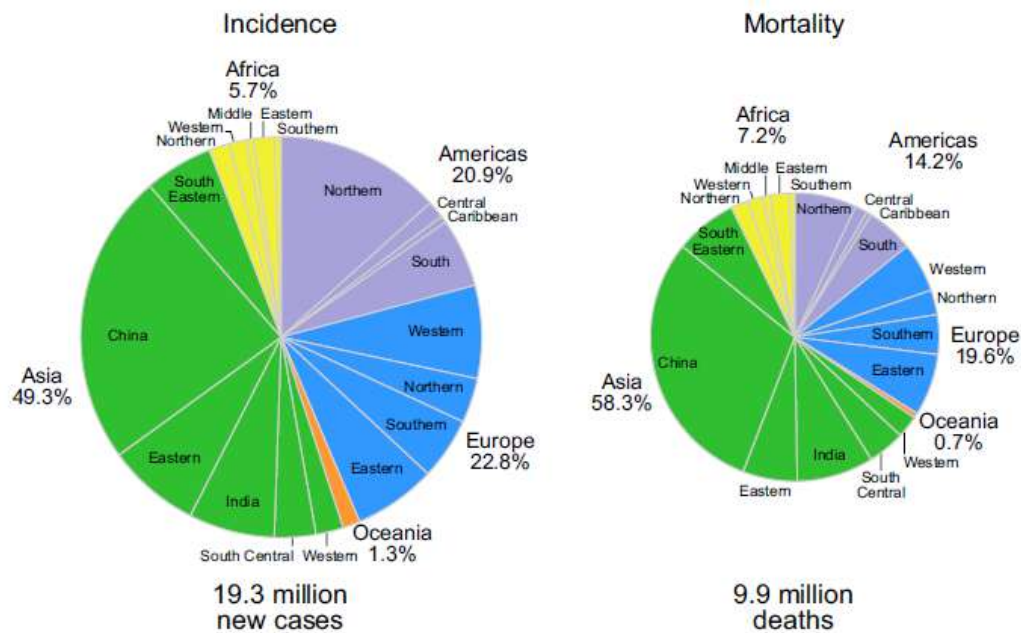


Figure 1. Distribution of cancer cases and deaths by world area in 2020 for both sexes. Adapted with permission from reference [1].

Cancer can be defined as a disease in which abnormal cells divide without control invading the nearby tissues and spreading to other parts of the body through the blood and lymph systems in a process named metastasis.² The large number of different cancer types creates the need of a global effort to control the disease. To date, there are four main approaches to treat cancer: surgery, chemotherapy, radiotherapy, and immunotherapy. Nowadays, a conventional therapeutic treatment consists of a combination of some of these techniques starting with the removal of the tumor by surgery, which is usually followed by the treatment of the patient with chemotherapy, radiotherapy, or immunotherapy. Despite the great success achieved in recent years with such therapeutic approaches, there are still some important problems that must be solved such as the appearance of severe adverse effects, drug resistance, relapses, and the occurrence of metastasis. In addition, one of the major problems of current chemotherapeutic drugs, either metallodrugs or organic-based anticancer agents, is the lack of selectivity that impacts healthy tissues, which might lead to severe systemic toxicity.^{3,4}

To address the abovementioned issues, specifically the high systemic toxicity and the lack of tumor selectivity of conventional chemotherapeutic drugs, numerous research efforts have been focused in recent years on developing novel anticancer strategies based on drug targeting as well as on controlling the release of the active drug at the tumor site. Targeted drug delivery in oncology consists of using a bioactive compound that targets specific receptors, antigens or enzymes that are overexpressed on tumor cells. Hence, targeted approaches require the therapeutic drug to be conjugated to a targeting ligand through a suitable linker.^{5,6}

In recent years, light has been also positioned as an ideal tool both in cancer diagnosis and therapy owing to its outstanding properties. In consideration of that, in the following sections of this thesis we have focused on the use of fluorescent probes based on organic molecules both for the detection and treatment of cancer.

On the one hand, since an early detection is probably the main factor that can contribute to the reduction of the mortality associated to some types of cancer, there is an actual need for developing novel diagnostic techniques. **Fluorescence imaging** exhibits some advantages over other techniques in terms of safety and resolution of cancer detection, including real time monitoring, minimal invasiveness, and accessibility without tissue destruction.^{7,8} For this reason, we will focus on low molecular-weight fluorescent probes operating in the far-red and near-infrared (NIR) region (650-900 nm) of the electromagnetic spectrum since the use of this non-toxic and highly penetrating radiation is appropriate for clinical purposes.⁹ Ideally, such fluorophores should be capable of undergoing structural modifications to tune their photophysical and physicochemical properties on demand, as well as to facilitate conjugation with a wide variety of targeting ligands (e.g. peptides, proteins, folic acid, etc.).

On the other hand, **photodynamic therapy (PDT)**, although it is still considered an emerging technique, it offers several appealing advantages for cancer treatment such as selectivity, noninvasiveness, and few adverse side effects. PDT is based on the administration of a non-toxic photosensitizing agent to the patients that, upon exposure to a light source of a specific wavelength, induces oxidative damage to the target cells.¹⁰ In this context, in the following sections we will also discuss the improvements that organic fluorophores and transition metal complexes can offer to cancer phototherapy.

2. Organic fluorophores in cancer imaging and therapy

2.1. Fluorescence spectroscopy in bioscience

Fluorescence spectroscopy has become an indispensable tool in several areas related to medical sciences. The combination between fluorescence and optical microscopy has led to great advances in detecting species in *in vitro* assays and also has allowed the visualization of intracellular structures even in live cells and tissue sections. Medical imaging is based on the creation of visual representations of the inside of the human body that can render precise information for clinical diagnosis.

There are three characteristics of the fluorescence phenomenon that make it particularly useful for accurate tumor diagnosis. Firstly, (i) it is important to mention the extraordinary sensitivity that fluorescence offers due to the high efficiency in which light can be detected. Indeed, the sensitivity of fluorescence only competes with that of radioisotope-based methods; however, the harmlessness of light makes fluorescence much more attractive. Secondly, (ii) it is easy to reach a spatial resolution of around 1 μm in the wavelength range of visible light with simple optical microscopes. Finally, (iii) the timescale of light emission is fast (nano-microseconds), allowing to motorize in real time events that are rapidly changing.¹¹

On account of the three key features of fluorescence explained above, luminescent imaging has gained great interest in recent years. The rapid development of luminescence imaging microscopes and the large number of emissive probes available such as organic fluorophores, transition-metal complexes, lanthanide chelates, nanoparticles and fluorescent proteins make possible the visualization of physiological processes at cellular and molecular levels.¹²

2.2. Fluorescence principles

2.2.1. Jablonski diagram

Luminescence can be defined as the spontaneous emission of light from a molecule that takes place from an electronically excited state. There are two types of luminescence processes depending on the nature of the excited state: fluorescence and phosphorescence. During the fluorescence process a molecule in a singlet electronic ground state (S_0) absorbs a photon of suitable energy promoting an electron to a higher energy orbital, which relax quickly to the first singlet excited state (S_1). Therefore, fluorescence emission results from the return of the molecule to the ground state from the lowest energy vibrational state of S_1 by emission of a photon. However, the decay of the excited state can also occur in a nonradioactive manner. Meanwhile, in a phosphorescence process molecules undergo a spin conversion from S_1 to the first triplet state T_1 through an intersystem crossing process (ISC). The decay from the triplet state to the singlet ground state results in phosphorescence emission. In general, molecules with heavy atoms in their structure facilitate intersystem crossing leading to phosphorescence emission. The photophysical processes related to fluorescence and phosphorescence are typically illustrated in a Jablonski diagram (**Figure 2**).¹³

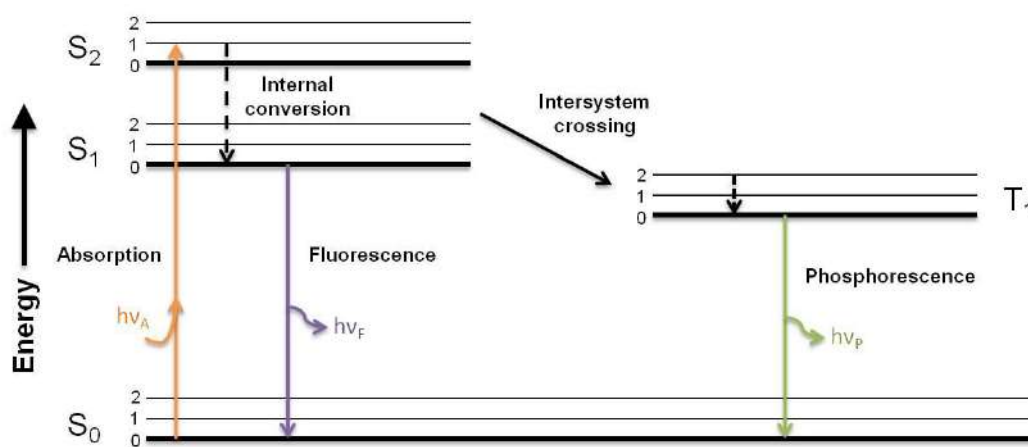


Figure 2. Simplified Jablonski diagram illustrating the processes of fluorescence and phosphorescence.

In a typical Jablonski diagram the ground state is described as S_0 and the first and second electronic states as S_1 and S_2 , respectively. Every electronic energy state has a number of vibrational energy levels, described as 0, 1, 2, etc. The vertical lines illustrate the transitions between states by light absorption. Absorption and emission occur mainly from molecules with the lowest vibrational energy.

2.2.2. Photophysical properties of organic fluorophores

A typical absorption and emission spectrum of a fluorophore is illustrated in **Figure 3**. The maximum absorption wavelength (λ_{max}) is based on the difference in energy between the ground state and the higher energy levels in the Jablonski diagram. The extinction coefficient (ϵ) shows the absorptivity of a compound at its maximum absorption wavelength (λ_{max}) according to the Beer-Lambert law. The maximum emission wavelength (λ_{em}) is always higher (lower in energy) than the maximum absorption wavelength. The difference between λ_{max} and λ_{em} is known as Stokes' shift, which can be influenced by several factors, such as the solvent, excited-state reactions, and energy transfer. Fluorescent molecules with small Stokes' shifts can undergo self-quenching due to energy transfer and, consequently, it is important to develop new dyes with large Stokes' shifts.

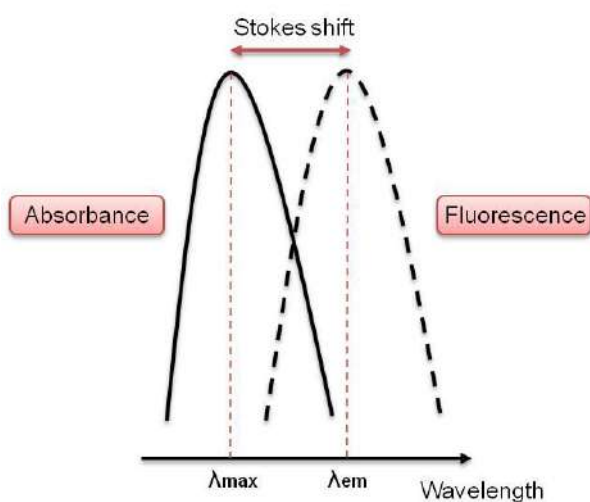


Figure 3. Representation of a typical absorption and emission spectrum.

In bioimaging applications, the detection of luminescence signals depends on several factors such as intensity, wavelength, lifetime, and polarization. The intensity reflects the localization and concentration of a fluorophore allowing thus to create images. The wavelength is characteristic of each fluorescent probe and, depending on the structure of the compound, different luminescence colors can be displayed, which can also be useful in multicolor imaging. As shown in **Figure 4**, consecutive to the visible region of the electromagnetic spectrum, there is the IR region, which is divided into three subregions, near-infrared (NIR), mid-infrared (MIR) and far-infrared (FIR). The far-red to NIR light offers suitable characteristics for imaging applications *in vivo* and, for this reason, dyes which are operative in this region of the electromagnetic spectrum, known as the phototherapeutic window (650-900 nm), have recently attracted attention especially in fields related to biomedicine. The advantages of far-red to NIR emitting fluorophores include minimal autofluorescence interference, deep tissue penetration and reduced light scattering. In addition, longer wavelengths minimize the photodamage to living cells compared to UV and blue light.¹⁴⁻¹⁷

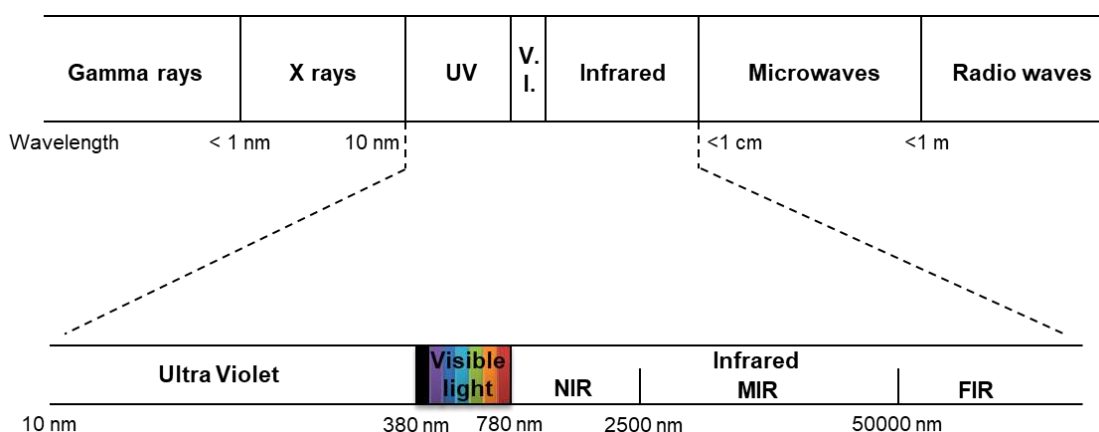


Figure 4. Simplified representation of the electromagnetic spectrum.

Another relevant characteristic of a fluorophore is the luminescence lifetime which is the average time that a fluorophore remains in its excited state before returning to the ground state. This lifetime, named with the Greek letter τ , is characteristic of each compound. The use of long-lived fluorophores for bioimaging applications allows minimal autofluorescence interference. In this context, transition metal complexes and lanthanides are known to exhibit long luminescence lifetime due to the spin-forbidden nature of their luminescence. In addition, some organic compounds can also exhibit long luminescence lifetimes suitable for bioimaging applications.

Along with the luminescence lifetime, quantum yield (Φ) is probably the most important parameter of a fluorophore. Quantum yield represents the ratio of the number of emitted photons relative to the number of absorbed photons and, consequently, fluorophores with largest luminescent quantum yields will display brightest emissions.

2.3. Long-lived fluorescent organic probes

Organic compounds that contain conjugated systems are commonly emissive because of the $\pi - \pi^*$ transitions. **Figure 5** shows the basic structure of some representative fluorophores that are commonly used in bioimaging applications. Organic fluorophores with separated electron donor and acceptor groups can emit from a charge-transfer state.¹⁵

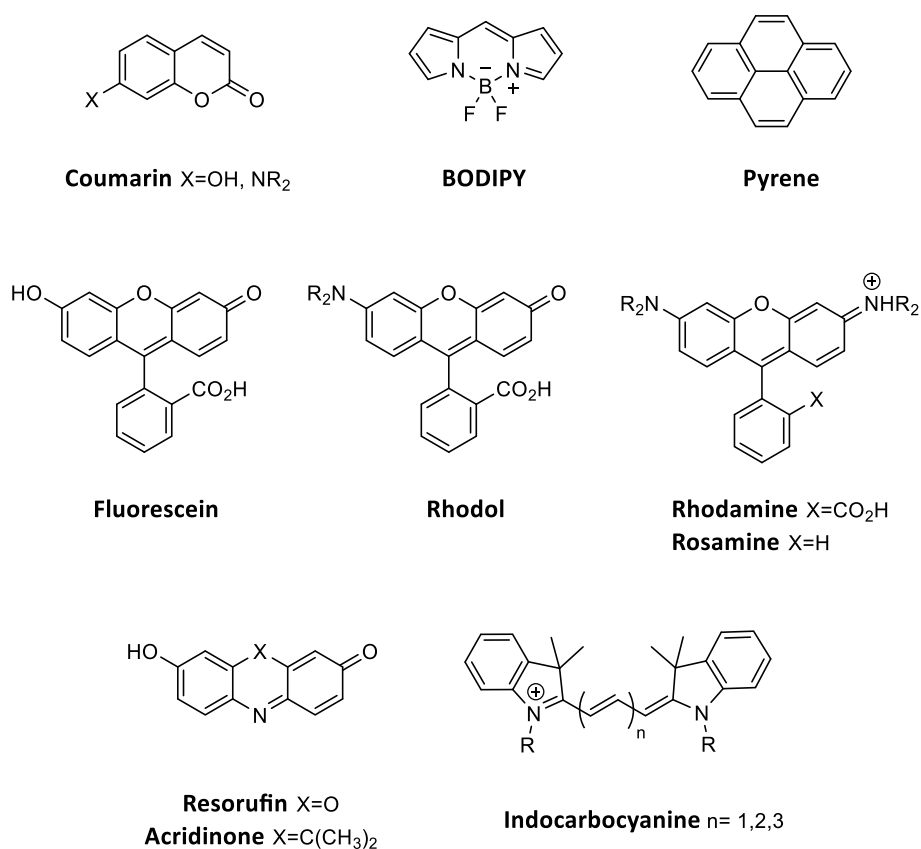


Figure 5. Core structures of some common organic fluorescent probes.

The aim of the development of new organic fluorophores has been always focused on achieving optimal photophysical properties for bioimaging applications, such as high quantum yields, brightness, or long luminescent lifetimes. In addition, as previously stated, fluorophores that emit at longer wavelengths, particularly in the phototherapeutic window, are especially useful due to several appealing features of the light in this region of the electromagnetic spectrum, including deep tissue penetration, minimal autofluorescence, and low light scattering. Naturally, there are other properties of a fluorophore that must be also considered such as water solubility, tendency to aggregation, photostability, toxicity, and synthetic accessibility. In the following sections, we will introduce the main classes of small organic fluorescent probes based on the core structures shown in **Figure 5**, as well as the modifications that have been carried out for developing novel fluorophores with improved photophysical and physicochemical properties.

2.3.1. UV-excitable fluorophores

Pyrene consists of four benzene rings fused in a cyclic aromatic hydrocarbon structure. The main scaffold of pyrene (**Figure 6, A**) absorbs UV light ($\lambda_{\text{abs}} = 340 \text{ nm}$) and emits at $\lambda_{\text{em}} = 376 \text{ nm}$ with a very small Stokes' shift and a quantum yield equal a $\Phi_{\text{F}} = 0.75$ in methanol. Pyrene also exhibits a long-lived excited state ($\tau > 100 \text{ ns}$).^{18–20} Molecules derived from pyrene have been also used as fluorescent probes with a spectrum sensitive to the polarity of its environment.

The coumarin scaffold is a privileged scaffold in organic chemistry since it can be found in a large variety of biologically active natural products, pharmacological agents, dyes, agrochemicals, polymeric and optoelectronic materials.²¹ The structure of coumarins can be modified at various points with different types of substituents, thus influencing their biological activity. A characteristic coumarin fluorophore is 7-hydroxy-4-methylcoumarin (**Figure 6, B**), which absorbs UV light ($\lambda_{\text{abs}} = 360 \text{ nm}$) and emits blue light ($\lambda_{\text{em}} = 450 \text{ nm}$) with a fluorescent quantum yield $\Phi_{\text{F}} = 0.63$ in PBS.²² Coumarin derivatives have been the basis for many fluorescent dyes and sensors and, for this reason, the chemistry of coumarins continues to be exploited to prepared novel probes.²³

There are several other small heterocyclic molecules that have been used as fluorescent probes with UV or near-UV excitation. For example, the fluorophores based on indoles and imidazole structures, such as 4',6-diamidino-2-phenylindole (**DAPI**, **Figure 6, C**) which binds to DNA ($\lambda_{\text{abs}} = 358$ nm and a $\lambda_{\text{em}} = 461$ nm and $\Phi_{\text{F}} = 0.34$ in PBS).²⁴ Another fluorophore that absorbs in this region is called Bimane (pyrazolo[1,2-a]pyrazole-1,7-dione) (**Figure 6, D**), which exhibits a $\lambda_{\text{abs}} = 390$ nm and a $\lambda_{\text{em}} = 450$ nm and a quantum yield $\Phi_{\text{F}} = 0.3$ in aqueous solution. Cascade Yellow dye is a good example (**Figure 6, E**) of an organic fluorophore with large Stokes' shift ($\lambda_{\text{abs}} = 409$ nm and a $\lambda_{\text{em}} = 559$ nm and $\Phi_{\text{F}} = 0.56$ in aqueous solution).^{18,23}

2.3.2. Visible light-NIR-excitable fluorophores

Among organic fluorophores, fluorescein (**Figure 6, F**) is widely employed both as a fluorescent probe and for labelling biomolecules in modern biochemical, biological, and medicinal research due to a high intensity emission peak, high molar absorption coefficient and good quantum yield in aqueous media. The dianion form is the most fluorescent form with $\lambda_{\text{abs}} = 490$ nm, $\lambda_{\text{em}} = 514$ nm and a quantum yield of $\Phi_{\text{F}} = 0.95$ in aqueous solution.^{18,23,25}

Rhodamines are amino analogues of fluorescein that belong to the xanthene class of dyes. Rhodamine fluorophores have wide utility as fluorescent probes owing to high brightness, excellent photostability, low pH sensibility and tunable photophysical properties through substitution. The simplest structure of this class of fluorophores is rhodamine 110 (Rh₁₁₀, **Figure 6, G**), which exhibits fluorescein-like spectral properties since it absorbs in the green region ($\lambda_{\text{abs}} = 496$ nm) and emits in the yellow one ($\lambda_{\text{em}} = 517$ nm) with a $\Phi_{\text{F}} = 0.92$ in aqueous solution.^{18,20,23}

Boron-dipyrromethene (BODIPY) dyes exhibit high fluorescence quantum yields, high absorption coefficients, insensitivity of the spectral properties to environment and an excellent stability. However, they have relatively small Stokes' shifts. BODIPY scaffold has been used to synthesize several fluorescent probes for bioimaging applications as well as for photodynamic therapy. The simplest BODIPY scaffold (**Figure 6, H**) operates on the visible light region ($\lambda_{\text{abs}} = 505$ nm, $\lambda_{\text{em}} = 511$ nm, $\Phi_{\text{F}} = 0.94$ in methanol). Another important characteristic of this scaffold is the tunability of the absorption maximum wavelength by using suitable substitutions.^{18,20,23}

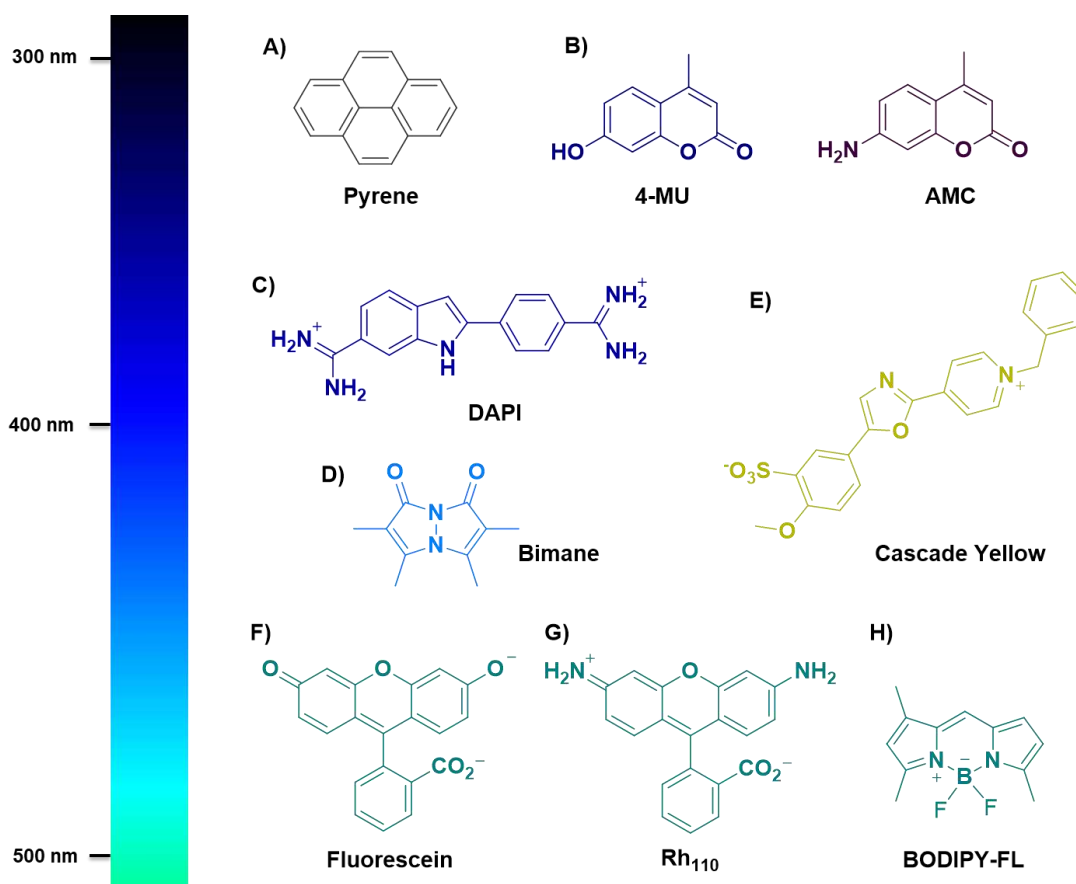


Figure 6. Examples of some representative types of organic fluorophores absorbing in the 300-500 nm region. The color of each structure represents its maximum emission wavelength (λ_{em}).

Oxazines and acridinones are analogues of xanthene-based fluorescein and rhodamines. The oxazine nitrogen in the ring scaffold induces a large bathochromic shift. The main characteristics of this type of dyes are red-shifted spectra and sensitivity to the polarity of the medium. The simplest oxazine dye, Resorufin (**Figure 7, A**), exhibits maximum absorption wavelength at $\lambda_{abs} = 550$ nm and emission at $\lambda_{em} = 585$ nm and a $\Phi_F = 0.74$ in basic aqueous solution.^{18,20,23}

The general structure of cyanines contains two aromatic nitrogenated heterocyclic rings connected by a polymethine bridge (*i.e.*, $R_2N-(CH=CH)_n-CH=N^+R_2$). Key features of this class of dyes include large extinction coefficients, strong fluorescence, and easily tunable structures. The most known cyanine dyes are the CyDye fluorophores, which are based on a sulfoindocyanine structure. The name of these compounds is related to the number of carbon atoms connecting the two nitrogen centers. In general, an increase in the length of the polymethine chain provides fluorophores with longer absorption and emission wavelengths.

Cy3 (**Figure 7, B**), a trimethine cyanine, exhibits a maximum absorption at $\lambda_{\text{abs}} = 554$ nm, emission at $\lambda_{\text{em}} = 568$ nm and $\Phi_{\text{F}} = 0.14$ in PBS. Cy5 (**Figure 7, C**) has longer absorption and emission wavelengths ($\lambda_{\text{abs}} = 652$ nm, $\lambda_{\text{em}} = 672$ nm) and a similar quantum yield $\Phi_{\text{F}} = 0.18$ in PBS. Continuing this trend, Cy7 (**Figure 7, D**) exhibits both absorption and emission on the NIR region ($\lambda_{\text{abs}} = 755$ nm, $\lambda_{\text{em}} = 788$ nm) but a lower quantum yield $\Phi_{\text{F}} = 0.02$ in PBS. The CyDye are used as biomolecular labels and as standard fluorophores for microarrays and other analysis.^{18,23}

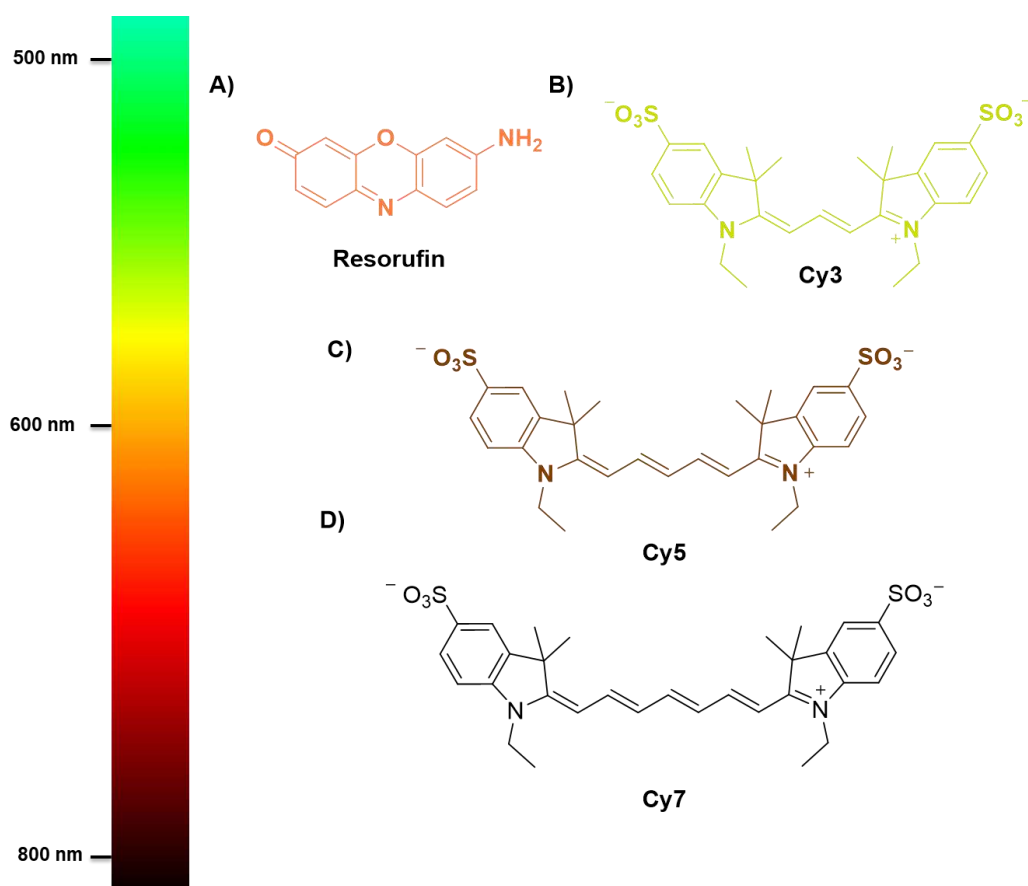


Figure 7. Structure of some representative types of organic fluorophores absorbing in the 500-800 nm region. The color of each structure represents its maximum emission wavelength (λ_{em}).

A special effort has been focused in recent years on the development of novel fluorescent probes based on organic fluorophores for biological and biomedical applications. The reason relies on the fact that most dyes derived from the conventional core scaffolds do not operate in the phototherapeutic window and exhibit non-optimal photophysical, and/or physicochemical properties such as small Stokes' shifts, poor photostability, low aqueous solubility, and tend to form aggregates due to their large size and structural complexity.

2.4. Coumarin-based fluorescent probes for bioimaging applications

2.4.1. General overview of the coumarin scaffold

Coumarins, also known as benzopyran-2-one, consist of a large class of molecules found in the plant kingdom. They belong to the flavonoid class of plant secondary metabolites, generally associated with low toxicity. Coumarins are present in several essential oils such as cinnamon bark oil, cassia leaf oil and lavender oil. They are also found in some fruits and green tea. Although coumarins are widely distributed in all parts of a plant, they are found in higher levels in the fruits, followed by the roots, stems and leaves.^{26,27}

Coumarins have been traditionally used in popular medicine all over the world. The simplest coumarin, shown in **Figure 8, A**, was first isolated in 1820 from Tonka beans, the seeds from a flowering tree known as *Dipteryx odorata*. Several coumarin derivatives synthesized by modifying the structure of this coumarin show different pharmacological activities, making them ideal as potential drugs candidates. For example, the anticoagulants Warfarin (**Figure 8, B**) and Acenocoumarin (**Figure 8, C**), and the choloretics Armillarisin A (**Figure 8, D**) and Hymecromone (**Figure 8, E**).²¹ Other relevant examples are furanocoumarins such as Psoralen (**Figure 8, F**), which are used for the treatment of several skin diseases with light such as vitiligo.²⁸

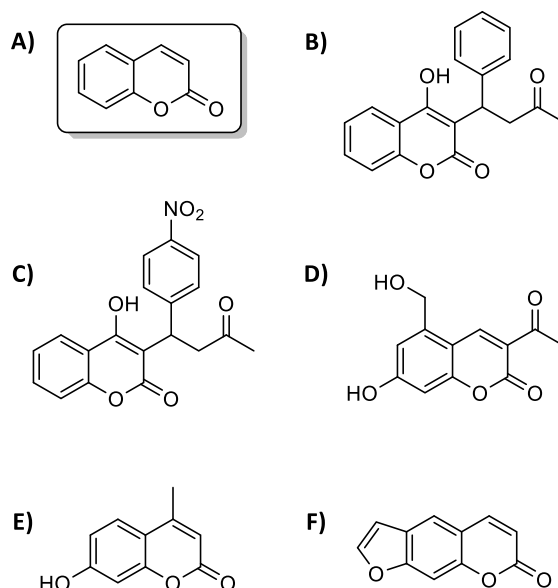


Figure 8. Structures of some coumarin-based drugs: A) Coumarin, B) Warfarin, C) Acenocoumarin, D) Armillarisin A, E) Hymecromone and (F) Psoralen.

Depending on their core structure, coumarins can exhibit several different pharmacological activities: antibacterial, antitubercular, antifungal, antiviral, antimutagenic, antioxidant, scavenging of reactive oxygen species (ROS), anti-inflammatory, antithrombotic, anticancer, and anticoagulant.²¹ In addition, coumarin-based derivatives are used in food additives, cosmetics, perfume fixatives, pesticides, odor maskers in paints and rubbers, and odor stabilizers in tobacco.²⁹

2.4.2. Synthesis of coumarin-based fluorophores

As previously stated, the two-ring coumarin scaffold is formed by the fusion of a pyran ring and benzene. Hence, the coumarin system contains a characteristic lactone group at positions 1 and 2, and the six hydrogen atoms from C-3 to C-8 can be properly substituted. In particular, the substitution at positions C3, C4, C6 and C7 have been widely studied. In the Nature, the common groups present at position C7 are hydroxyl or amino groups.²⁹

The coumarin structure exhibits a great charge transfer due to a planar structure that provides this compound with excellent photophysical properties. The benzene ring in the unsubstituted coumarin structure acts as a donor while the pyrone ring acts as an acceptor. The weak charge transfer created by these two moieties lead to an absorption and emission maxima of 280 nm and 330 nm in acetonitrile, respectively. Even though this unsubstituted coumarin scaffold is poorly fluorescent, the substitution of the hydrogens at some key positions is known to increase the fluorescence, leading to coumarin dyes with improved photophysical properties, including high fluorescence quantum yield and relatively large Stokes' shift.

In recent years, a lot of efforts have been dedicated to the improvement of the photophysical properties of the coumarin structure, mainly to red-shift absorption and emission maximum wavelengths. The incorporation of electron-donating groups at positions 6 or 7 (e.g., alkoxy, hydroxyl or dialkylamino) partnering with electron-withdrawing groups at position 3 or 4 (e.g., CF₃, carboxylic acid, esters, aldehyde, and ketone) to create a strong push-pull effect, can red-shift the absorption and the emission spectra of the resulting coumarin derivatives (**Figure 9**).²⁹

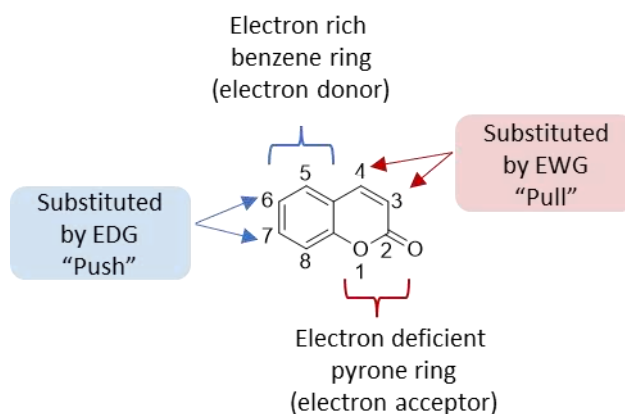


Figure 9. Representation of the push-pull effect over the coumarin scaffold.

2.4.2.1. Modification of the 3-position in the coumarin scaffold

Until now, the main efforts have been focused on synthesizing pull-push fluorophores based on coumarins by modifying the 3-position of the coumarin scaffold through the introduction of suitable substituents. Indeed, the modification of the 3-position of the coumarin scaffold with an appropriate donor group at position 7 is one of the simplest ways to red-shift the absorption and emission spectra of the coumarin derivatives. There are numerous possibilities of modifying the 3-position of the coumarin scaffold, depending on the length and the type of the groups incorporated.

Branco *et al.* reported a series of 7-substituted and 3-extended coumarin-styryl and coumarin-vinyl derivatives. Some representative examples of this novel class of coumarin dyes are represented in **Figure 10** (compounds **1**, **2**, **3** and **4**). They observed that the fluorescence properties of the coumarin derivatives were strongly dependent on the electron-donating and the electron-withdrawing ability of the substituents. The more conjugated styryl derivatives had a stronger absorption and emission red-shift compared with the respective vinyl derivatives. In addition, the introduction of a *p*-nitro group in the 3-styryl moiety had a considerable effect on the fluorescence properties. In the case of **4**, the fluorescence quantum yield was very low ($\Phi_F = <0.01$) and the emission occurred above 800 nm, due to a strong charge transfer between the *N,N*-dialkylamino group and the nitro group. All the photophysical properties of coumarins **1-4** are summarized in **Table 1**.³⁰

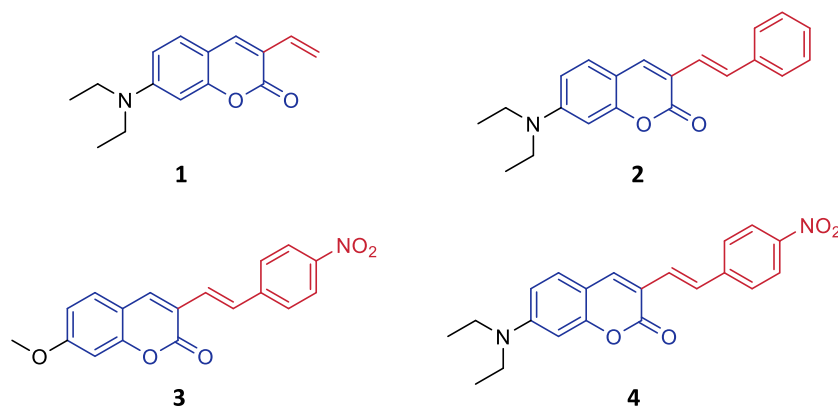


Figure 10. Structure of 7-substituted coumarin-based 3-extended styryl and vinyl dyes.

Kanetkar *et al.* reported the synthesis of a series of novel coumarin derivatives by extending the π -system through the incorporation of other small groups via the 3-position of the coumarin scaffold. In general, small sized fluorophores exhibit some advantages in biological applications since a low molecular weight allows a better cell permeability. As an example, the absorption spectra of the acetyl coumarin **5** (**Figure 11**) showed an absorption maximum at 474 nm and an emission maximum at 601 nm, with a high quantum yield of 0.54. The same group also reported a series of 3-extended coumarin-chalcone dyes. Such coumarin-chalcone derivatives, compounds **6-8** (**Figure 11**), showed longer absorption and emission maxima compared to the acetyl coumarin **5** precursor, with absorption maxima around 505 nm and emission maxima between 615 nm and 635 nm. However, these novel fluorophores exhibit low fluorescence quantum yields.^{31,32}

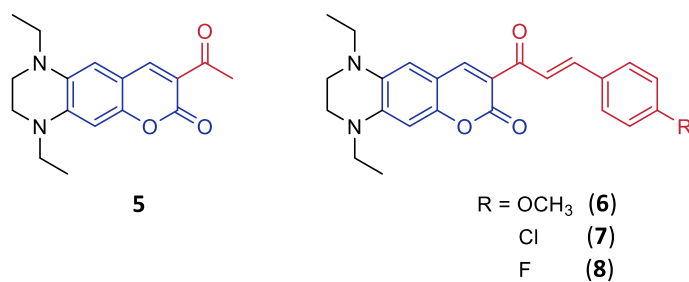


Figure 11. Structures of 3-extended coumarin derivatives **5-8**.

Table 1. Photophysical properties of 3-extended coumarin dyes **1-8**.

Compound	λ_{max} (nm)	λ_{em} (nm)	Stokes' shift (nm)	Φ_{F}	Solvent	Ref.
1	400	470	70	0.98	Acetonitrile	30
2	421	477	56	0.85	Acetonitrile	30
3	392	610	218	0.24	Acetonitrile	30
4	459	>800	>341	<0.01	Acetonitrile	30
5	474	601	127	0.56	Chloroform	31,32
6	502	635	133	0.39	Chloroform	31,32
7	508	615	107	0.30	Chloroform	31,32
8	509	617	108	0.34	Chloroform	31,32

2.4.2.2. Modification of the 4-position in the coumarin scaffold

The modification of the C4 position in the coumarin skeleton is also known to strongly alter its photophysical properties. In general, coumarin absorption and emission spectra undergo a strong red-shift with the addition of an electron-withdrawing group at the 4-position. For example, a 24 nm and 56 nm red-shift of the absorbance and emission maxima wavelength, respectively, was found for the 4-trifluoromethylcoumarin (**11**) compared to the 4-methylcoumarin (**10**) analog. By contrast, the presence of EDG groups at C4 position of the coumarin scaffold, induces a slight blue-shift in the absorption and emission maxima. For example, the 4-methylcoumarin (**10**) exhibits a 5 nm and 11 nm blue-shift of the λ_{abs} and λ_{em} , respectively, in comparison with the non-substituted coumarin (**9**). Pandey *et al.* studied the photophysical properties of coumarins with several C4 substituents, including H- (**9**), CH₃- (**10**), CF₃- (**11**), Ph- (**12**), COOEt- (**13**), CONH₂- (**14**), CONHMe- (**15**), and CONHPh- (**16**) (Table 2).³³

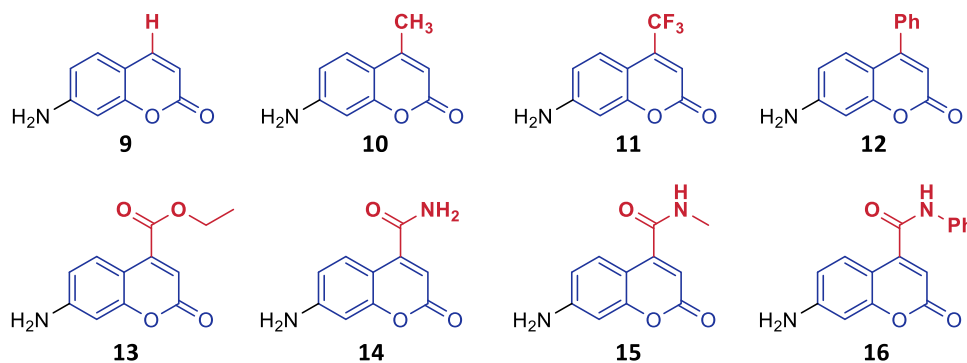
**Figure 12.** Structures of 4-extended coumarin derivatives **9-16**.

Table 2. Photophysical properties of 4-extended coumarin dyes **9-16**.

Compound	λ_{max} (nm)	λ_{em} (nm)	Stokes' shift (nm)	Solvent	Ref.
9	352	463	111	Water	33
10	347	452	105	Water	33
11	371	508	136	Water	33
12	358	509	151	Water	33
13	377	566	189	Water	33
14	364	567	203	Water	33
15	362	552	190	Water	33
16	362	398, 560	36, 198	Water	33

2.4.2.3. Fused coumarin dyes

Fusion is another common strategy for red-shifting the absorption and emission maxima of coumarin derivatives. There are different fusion approaches depending on the bond through which the additional ring is fused to the coumarin core. Ahn *et al.* synthesized a benzo-fused coumarin, compound **17** (**Figure 13**), which shows an absorption maximum of 487 nm and an emission maximum of 633 nm with a quantum yield of 0.12.³⁴

Recently, Zhang *et al.* described a series of novel naphthalene-fused coumarin dyes, compounds **18-22** (**Figure 13**). Taking the non-substituted coumarin **23** ($\lambda_{\text{abs}} = 418$, $\lambda_{\text{em}} = 488$ nm, $\Phi_{\text{F}} = 0.35$) as a reference, a significant bathochromic shift was observed when the phenyllynyl group was added to the coumarin scaffold, especially for **22** ($\lambda_{\text{abs}} = 519$, $\lambda_{\text{em}} = 671$ nm). In addition, a significant increase in the emission quantum yield was observed when a cyano group was introduced at the 3-position of the coumarin skeleton (**18**, $\Phi_{\text{F}} = 0.80$).³⁵

Traven *et al.* reported the synthesis of a series of novel furo[3,2-c] and thieno[3,2-c] coumarin derivatives, compounds **24-27** (**Figure 13**). The absorption and emission bands of thieno[3,2-c] coumarin derivatives were red-shifted compared to the equivalent furo[3,2-c] coumarin derivatives. The photophysical properties of fluorophores **17-27** are described in **Table 3**.³⁶

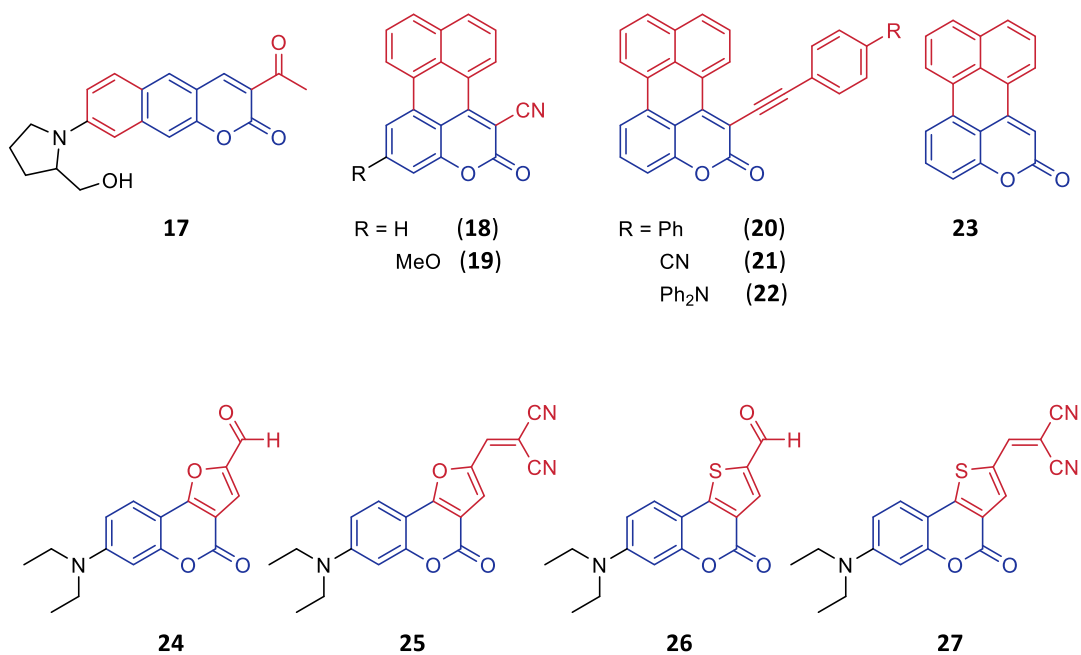


Figure 13. Examples of fused coumarin dyes.

Table 3. Photophysical properties of fused coumarin dyes **17-27**.

Compound	λ_{max} (nm)	λ_{em} (nm)	Stokes' shift (nm)	Φ_{F}	Solvent	Ref.
17	487	633	146	0.12	PBS	34
18	464	546	82	0.80	DMF	35
19	449	528	79	0.36	DMF	35
20	473	589	116	0.24	DMF	35
21	472	583	111	0.23	DMF	35
22	519	617	98	0.21	DMF	35
23	418	488	70	0.35	DMF	36
24	390	500	110	0.72	DMF	36
25	494	641	147	0.15	DMF	36
26	436	515	79	0.45	DMF	36
27	514	647	133	0.31	DMF	36

2.4.2.4. Hybrid dyes between coumarins and other fluorophores

Liu *et al.* synthesized new fluorescent dyes with deep-red fluorescence by hybridizing coumarin and pyronin moieties. Interestingly, the introduction of a hydrophilic group like carboxylic acid was found to enhance the solubility of the dyes. Such coumarin-pyronin derivatives, **28** and **29** (**Figure 14**), exhibit promising absorption and emission wavelengths with reasonable quantum yields ($\lambda_{\text{abs}} = 593$, $\lambda_{\text{em}} = 644$ nm, $\Phi_{\text{F}} = 0.24$).³⁷

Romieu *et al.* reported the synthesis of coumarin-rhodamine hybrids, **30-32** (**Figure 14**), that also exhibited interesting photophysical properties. Such coumarin derivatives had an intense absorption band with a maximum located in the 598-617 nm range and an intense emission peak with a maximum around 635-675 nm, with acceptable quantum yields in acetonitrile, between 0.18-0.58.³⁸

Kele *et al.* synthesized two coumarin-cyanine dyes, **33** and **34** (**Figure 14**), which presented water solubility and membrane permeability. These coumarin-cyanine derivatives were excitable in the visible region of the electromagnetic spectrum with emission maxima located in the far-red.³⁹

Xie *et al.* reported a near-infrared coumarin-BODIPY dye, compound **35** (**Figure 14**), with an absorption wavelength maximum of 623 nm and an emission maximum at 665 nm with a fluorescence quantum yield of 0.32 in chloroform.⁴⁰ All the photophysical properties of compounds **28-35** are summarized in **Table 4**.

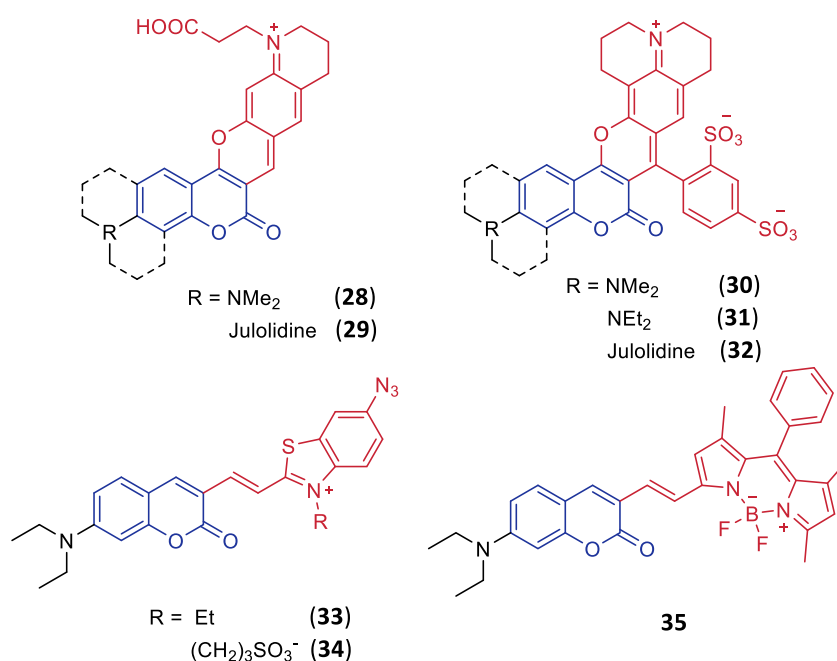


Figure 14. Structures of some hybrid dyes between coumarins and other fluorophores.

Table 4. Photophysical properties of coumarin derivatives **28-35**.

Compound	λ_{max} (nm)	λ_{em} (nm)	Stokes' shift (nm)	Φ_{F}	Solvent	Ref.
28	593	644	51	0.24	Acetonitrile	37
29	593	643	50	0.21	Acetonitrile	37
30	598	635	34	0.58	Acetonitrile	38
31	602	635	33	0.58	Acetonitrile	38
32	617	675	58	0.18	Acetonitrile	38
33	563	661	98	0.32	DMSO	39
34	565	676	111	0.27	DMSO	39
35	623	665	42	0.32	chloroform	40

2.4.2.5. 2-Extended coumarin dyes: COUPY dyes

The lactone function of the coumarin scaffold can also be modified to red-shift its absorption and emission maximum. However, this modification has not been explored extensively despite its great potential. Two of the reported approaches that result in a significant red-shift are the thionation of the carbonyl group (**37**, **Figure 15**), and the extension of the conjugation at position 2 with a dicyanomethylene group (**38**, **Figure 15**). As described by Fournier *et al.* compounds **36-38** were functionalized at position 4 of the coumarin moiety with an ester bond, being useful for synthesizing coumarin-based caging groups that can be removed with visible light.⁴¹

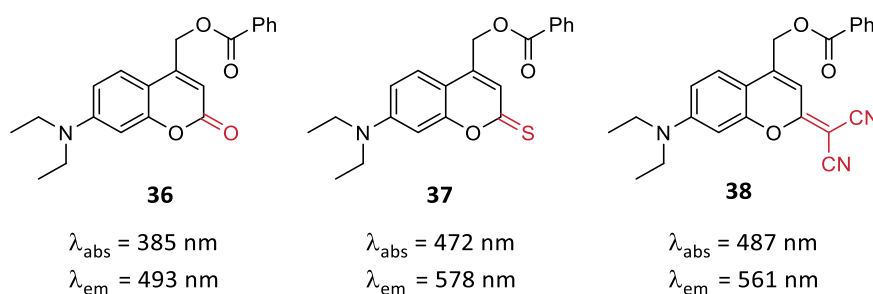
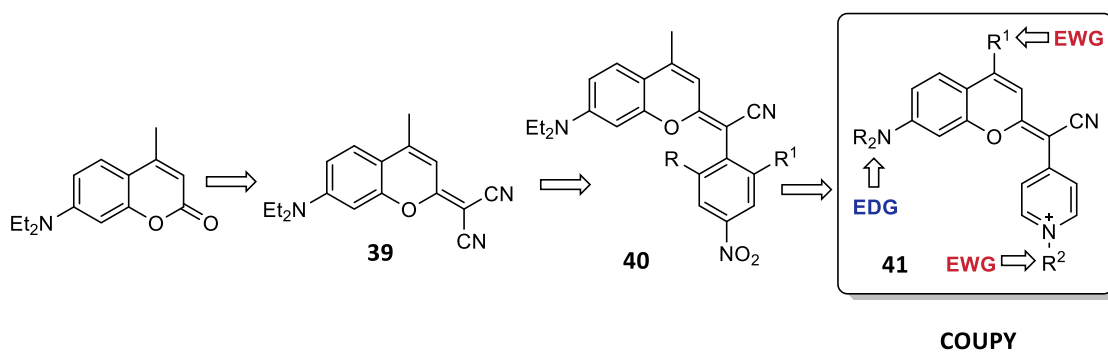


Figure 15. Examples of the modifications of the lactone function of the coumarin scaffold described by Fournier and co-workers through the incorporation of thiocarbonyl or dicyanomethylene groups.

In this context, our group has focused in recent years research efforts on the development of novel coumarin derivatives through the modification of the lactone function with appropriate groups with the aim of improving their photophysical and physicochemical properties. First, we reported the synthesis of coumarin derivatives in which one cyano group in coumarin **39** (**Scheme 1**)⁴² was replaced by a phenyl ring containing strong electron-withdrawing groups to increase the push-pull effect of the fluorophore (**40**, **Scheme 1**). However, the incorporation of nitro groups was found to have a negative effect on the fluorescence of the chromophores.⁴³

Based on the previous results, we decided to synthesize new coumarin derivatives in which one cyano group in coumarin **39** (**Scheme 1**) was replaced by an electron-deficient pyridine heterocycle (**41**, **Scheme 1**). This modification increases the π -conjugation and the push-pull character of the chromophore, resulting in a red-shift in the absorption and emission spectra, especially when the pyridine heterocycle was *N*-alkylated. This novel family of push-pull fluorophores based on coumarin scaffolds was named COUPY.⁴⁴

The photophysical properties of COUPY dyes can be selectively tuned by the suitable combination of *N*-alkylating groups and the substituent at position 4. As an example, COUPY dyes **42-45** (**Figure 16**) exhibit interesting photophysical properties including, emission in the far-red to NIR region, large Stokes' shifts, moderate-to-high fluorescence quantum yields and high photostability. All the photophysical properties of COUPY dyes **42-45** are summarized in **Table 5**.⁴⁴



Scheme 1. Design of the new coumarin-based fluorophores developed by Marchán group (COUPY dyes).

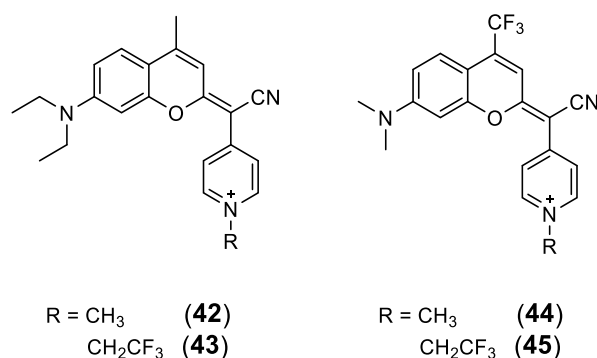


Figure 16. Examples of some representative COUPY fluorophores.

Table 5. Photophysical properties of some representative COUPY dyes.

Compound	λ_{max} (nm)	λ_{em} (nm)	Stokes' shift (nm)	Φ_{F}	Solvent	Ref.
42	548	609	61	0.18	Acetonitrile	44
43	567	636	69	0.12	Acetonitrile	44
44	569	668	99	0.023	Acetonitrile	44
45	597	689	92	0.12	Acetonitrile	44

After demonstrating the promising photophysical properties of COUPY dyes, we investigated their potential applications for cellular imaging. The cellular uptake of COUPY coumarins was studied in HeLa cells by confocal microscopy by irradiation with a yellow light laser ($\lambda_{\text{ex}} = 561$ nm). After incubation for 20 minutes, fluorescence was clearly observed in different cellular organelles, confirming an efficient uptake by the cells. In general, COUPY dyes accumulate in mitochondria and nucleoli and, to a lesser extent in intracellular vesicles (**Figure 17**). In addition, the higher red-shifted absorption of coumarin **45** allowed the visualization after irradiation with a red light laser ($\lambda_{\text{ex}} = 633$ nm).

Co-localization experiments with mitochondria and nucleoli specific markers confirmed the subcellular localization of COUPY dyes (**Figure 18**). These results are consistent with previous findings that report that pyridinium-containing positively charged fluorophores accumulate mainly in mitochondria.⁴⁴

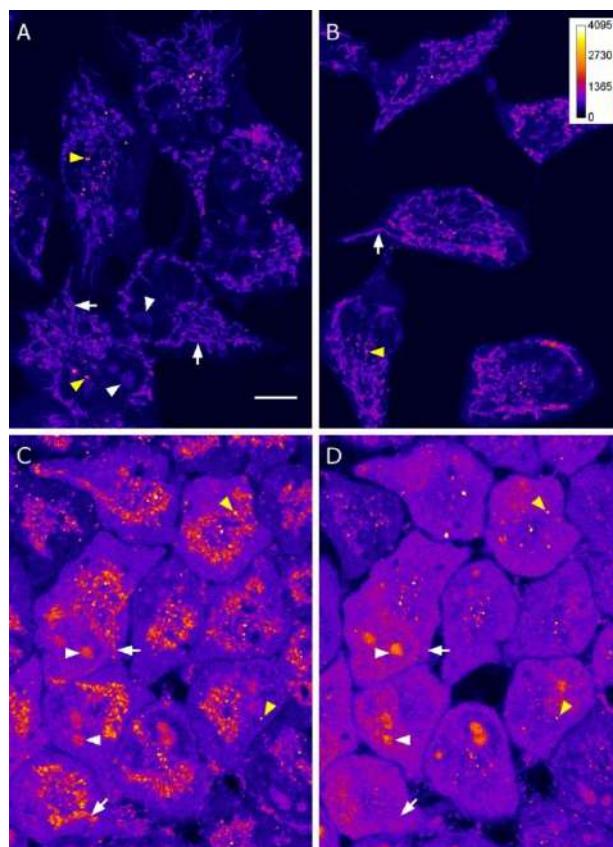


Figure 17. Cellular uptake of coumarin **42**. HeLa cells incubated with **42** for 20 min at 37°C: A) 0.5 μM , B) 1.0 μM , C) and (C and D) 2 μM . D) same cells as in C after 3 min of 561 nm laser irradiation. White arrows point out mitochondria, white arrowheads nucleoli, and yellow arrowheads vesicle staining. Adapted with permission from reference [44].

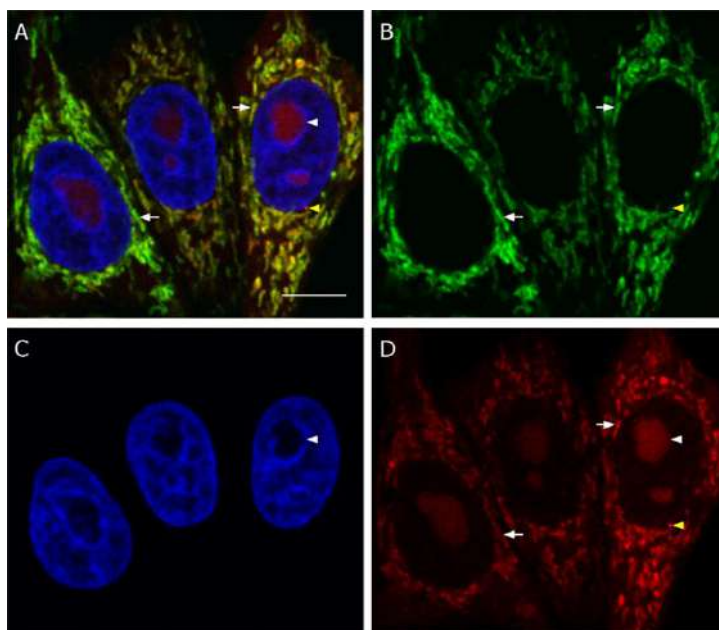


Figure 18. HeLa cells incubated with coumarin **42** (0.5 μM , red), Mitotracker Green FM (0.1 μM , green), and Hoechst 33342 (1 $\mu\text{g}/\text{mL}$, blue). (A) Overlay of the three staining images. (B, C, and D) Mitotracker Green FM, Hoechst 33342, and coumarin **42** staining, respectively. Adapted with permission from reference [44].

With the aim of improving the photophysical properties of COUPY dyes, we investigated the effect of the replacement of the electron-donating *N,N*-dialkyl group at the 7 position of the coumarin scaffold with azetidine, a four-membered cyclic amine. This replacement in conventional fluorophores is known to increase the fluorescent quantum yield (Φ_{F}) in polar solvents.⁴⁵ In addition, the introduction of a cyclic amine has been demonstrated to suppress the twisted intramolecular charge-transfer formation (TICT), which is one of the most common nonradioactive de-excitation pathways found in fluorophores with *N,N*-dialkyl fragments. Based on these precedents, we synthesized and photophysically characterized four azetidinyll analogues of our original COUPY fluorophores (**46-49**, **Figure 19**).⁴⁶

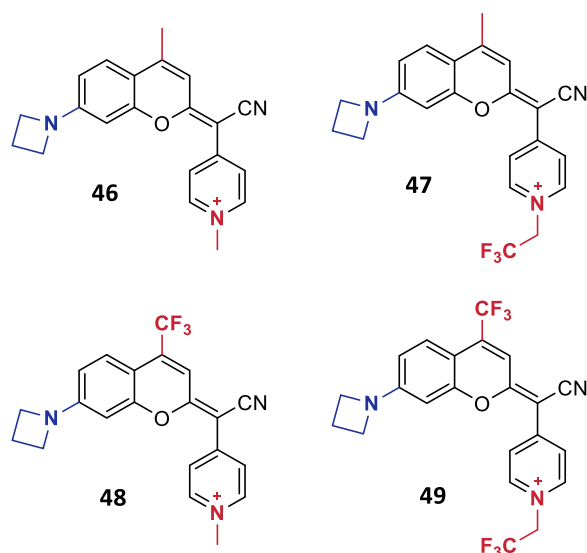


Figure 19. Structures of 7-azetidinyl COUPY fluorophores.

As shown in **Table 6**, the replacement of the *N,N*-dialkylamino group with azetidine led to a slight blue-shift in the absorption spectra of **46-49** in polar solvents indicating that their ground state is more polar than the excited state when compared with *N,N*-dialkylamino COUPY fluorophores. On the other hand, azetidinyl substitution did not considerably alter the emission wavelength, leading to large Stokes' shifts in polar solvents compared with their parent COUPY dyes. Azetidinyl substitution also led to a clear improvement of the photostability of the fluorophores, however, the Φ_F were not significantly modified in aqueous media, contrary to previously reported observations in other fluorophores.

Table 6. Photophysical properties of 7-azetidinyl-COUPY dyes.

Compound	λ_{\max} (nm)	λ_{em} (nm)	Stokes' shift (nm)	Φ_F	Solvent	Ref.
46	541	605	64	0.21	Acetonitrile	46
47	561	627	66	0.03	Acetonitrile	46
48	567	661	94	0.02	Acetonitrile	46
49	602	681	79	0.063	Acetonitrile	46

2.5. Targeted approaches in cancer imaging and therapy

2.5.1. Ligand-targeted drug delivery: an overview

Nowadays, the use of suitable therapeutic agents in medicine is highly compromised by the capacity to be specifically delivered to the diseased cells in front of the healthy ones.⁴⁷ The design of efficient and safe methods for delivering drugs to specific areas of the body that require intervention offers a good opportunity to improve the therapeutic outcome. In this context, drug targeting is gaining attention as an active area of research,⁴⁸ in which a suitable bioactive molecule must be conjugated to a targeting ligand that shows higher affinity for pathologic cells compared to healthy cells. In this context, the conjugation of specific targeting ligands to bioimaging or anticancer agents represents a promising strategy for improving the on-site delivery, which results in a better tumor detection, as well as in the reduction of the adverse effects typically associated to conventional chemotherapy.⁴⁹

Hence, one of the most common approaches for designing a therapeutic or bioimaging agent with high specificity for diseased cells consists of linking it to a targeting ligand that is able to selectively deliver the therapeutic payload to the desired pathologic cells (**Figure 20**). Once the bioactive molecule is chosen, a wide kind of targeting moieties can be used such as small molecules, antibodies, small protein scaffolds, peptides, and oligonucleotides. In general, ligand-targeted drug conjugates include the targeting moiety linked to the therapeutic payload via a suitable spacer that might also contain a cleavable linker.⁵⁰

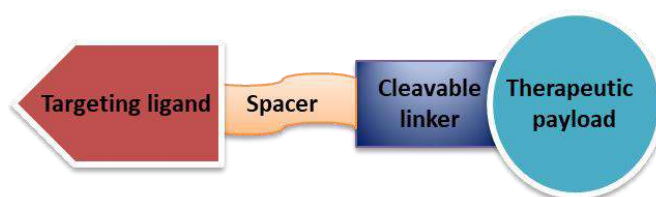


Figure 20. Schematic representation of a ligand-targeted drug conjugate.

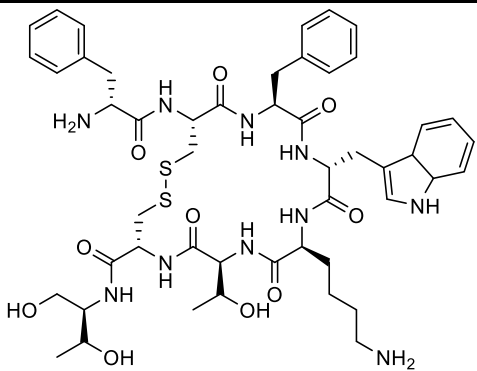
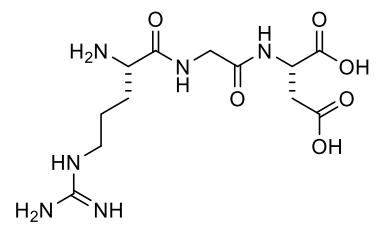
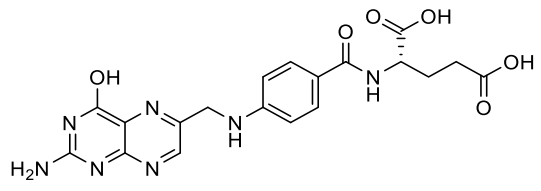
Following this design strategy, the safety and efficacy of a ligand-targeted drug conjugate can be maximized by optimizing the two parts separately without modifying the properties of the other part. In the process of designing an optimal ligand-targeted drug conjugate, the following elements must be properly chosen and optimized: i) a disease-specific receptor, ii) a suitable targeting ligand, iii) a spacer and cleavable linker, and iv) an optimal payload.

In general, targeted-receptors must be overexpressed in the pathologic cells to ensure an efficient and specific uptake of the conjugate in front of the healthy cells. Another important parameter is the level of receptor expression in the diseased cells since sufficient receptors must be present to enable delivery of the desired therapeutic quantities of the drug.⁵¹

A targeting ligand must have high binding affinity for its receptor in order to achieve specificity in the drug delivery process. Hence, the effective dose of a ligand-targeted drug conjugate depends on both the potency of the therapeutic payload and the affinity and specificity of the ligand for the receptor. When designing a targeted drug delivery strategy, factors such as binding affinity, size and the functional group availability for the easy conjugation to the therapeutic payload must be taken into account. There is a wide variety of targeting ligands that can be used in active targeted drug delivery for cancer imaging and therapy ranging from proteins (e.g., antibodies, growth factors, and transferrin), peptides (e.g., cyclic RGD and octreotide), aptamers (e.g., A10 and AS1411), polysaccharides (e.g., hyaluronic acid), and small biomolecules (e.g., folic acid and galactose) (**Table 7**).

The linkers or spacers are located between the targeting ligand and its payload with the purpose of minimizing the possible steric interferences from the drug cargo that could modify the affinity of the ligand for its receptor, as well as to improve the pharmacokinetics and pharmacodynamics of the resulting ligand-targeted drug conjugate. For these reasons, several elements such as the size, length, hydrophilicity, etc. must be considered for optimal drug performance when choosing a linker. When using cleavable linkers, the therapeutic payload must remain attached to the linker during the circulation of the drug in the body but must be cleaved once the conjugate is internalized into the diseased cell.⁵²

Table 7. Examples of targeting ligands used in active targeted drug delivery for cancer imaging and therapy.

Targeted receptor	Targeting ligand	Structure of targeting ligand	ref
Somatostatin receptors	Octreotide peptide		53
$\alpha\beta3$ and $\alpha\beta5$ Integrins	RGD peptide		54
Folate receptor	Folic acid		55

2.5.2. Targeting ligands based on receptor-binding peptides

In recent years, it has been demonstrated that peptide receptors can be used as efficient targets for developing novel anticancer strategies, since they are overexpressed in certain tumors. Some regulatory peptides such as somatostatin, gonadotropin-releasing hormone (GnRH), vasoactive intestinal peptide (VIP), and neurotensin have membrane-bound receptors in several different types of tumors. The use of peptides as carriers offers several advantages such as high tissue permeability and affinity for their receptors, minimal side effects, rapid clearance from the body and an easy synthesis.^{56,57}

Somatostatin (SST) is a cyclic peptide containing a disulfide bond between the cysteine residues at positions 3 and 14 (**Figure 21**). Native somatostatin has two biologically active forms: a tetradecapeptide (SST-14) and a 28-amino acid peptide (SST-28).⁵³ Somatostatin and its analogues exhibit a strong growth inhibition effect on various tumors, which is related to a high binding affinity for somatostatin receptors located on the tumor cell-membrane (SST1, SST2, SST3, SST4 and SST5). The most frequent receptor subtypes found on tumor cells are SST2 and SST5. SST functions include the inhibition of endocrine and exocrine secretions via the activation of five G-protein-coupled receptors, while in central nervous system, SST acts as a neurotransmitter/neuromodulator by regulating motor and cognitive functions.^{53,57-59}

The large number of physiological functions that somatostatin performs makes this peptide an ideal candidate for the treatment of numerous human diseases. However, the lack of selectivity and the very short half-life in blood circulation (>3 min) of this hormone has prompted the development of analogues with the aim of overcoming some of these problems. The main strategy in the synthesis of SST analogues consists of keeping the essential tetrapeptide segment Phe⁷, Trp⁸, Lys⁹, and Thr¹⁰, together with the incorporation of amino acid residues that form a disulfide bond or an amide linkage to stabilize the β turn of the essential residues of the pharmacophore sequence. Following this strategy, several SST analogues have been synthesized, improving the specificity and metabolic stability in comparison with the original SST-14 (**Figure 21**).^{53,58}

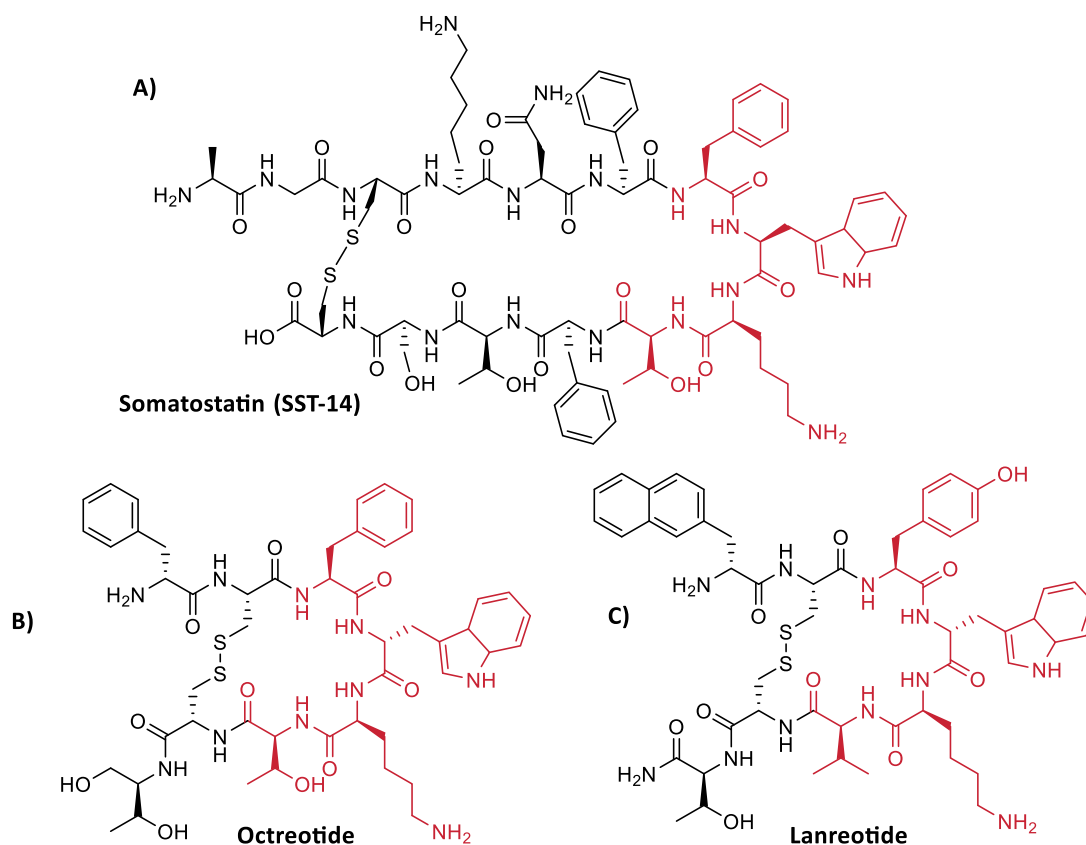


Figure 21. Structures of A) somatostatin 14 (SST-14) and of two of the more representative analogs developed, B) octreotide and C) lanreotide.

The first analogue based on SST-14 to enter in clinical use was the cyclooctapeptide analogue named octreotide (or SMS-201-995), which contains a C-terminal diol. Octreotide has been used in clinical practice since 1983 for the treatment of hormone-producing pituitary, pancreatic, and intestinal tumors. Octreotide and its analogue lanreotide are both approved for the treatment of GH-secreting pituitary adenomas.^{58,60}

However, since the disulfide bridge is susceptible to be attacked by endogenous reducing enzymes or by nucleophilic and basic agents, more robust octreotide derivatives have been developed in recent years. For example, dicarba-analogs of octreotide, where the disulfide bond is replaced by a CH₂-CH₂ linkage, have been described to have good binding affinity and high specificity for the sst5 receptor. In addition, it is known that constrained carba-tethers in cyclic peptides can stabilize helices or β -turns.⁶¹

On the other hand, as it will be discussed in detail in **Section 3**, organometallic complexes are promising anticancer drug candidates and, consequently, conjugation of receptor-binding peptides to metal-based anticancer drugs offers a good opportunity in cancer therapy.⁶² Marchán *et al.* conjugated Ru(II) arene complexes to dicarba analogues of octreotide (**A**, **Figure 22**), and demonstrated high anticancer activity in cancer cells overexpressing somatostatin receptors.⁶³ Fish *et al.* conjugated a stable organometallic aqua complex, [Cp*⁺Rh(H₂O)₃](OTf)₂, to the tyrosine amino acid in octreotide peptide (**B**, **Figure 22**), and demonstrated that the conjugation did not affect the reactivity of the drug, leading to growth inhibition activity toward several cancer cell lines.⁶⁴

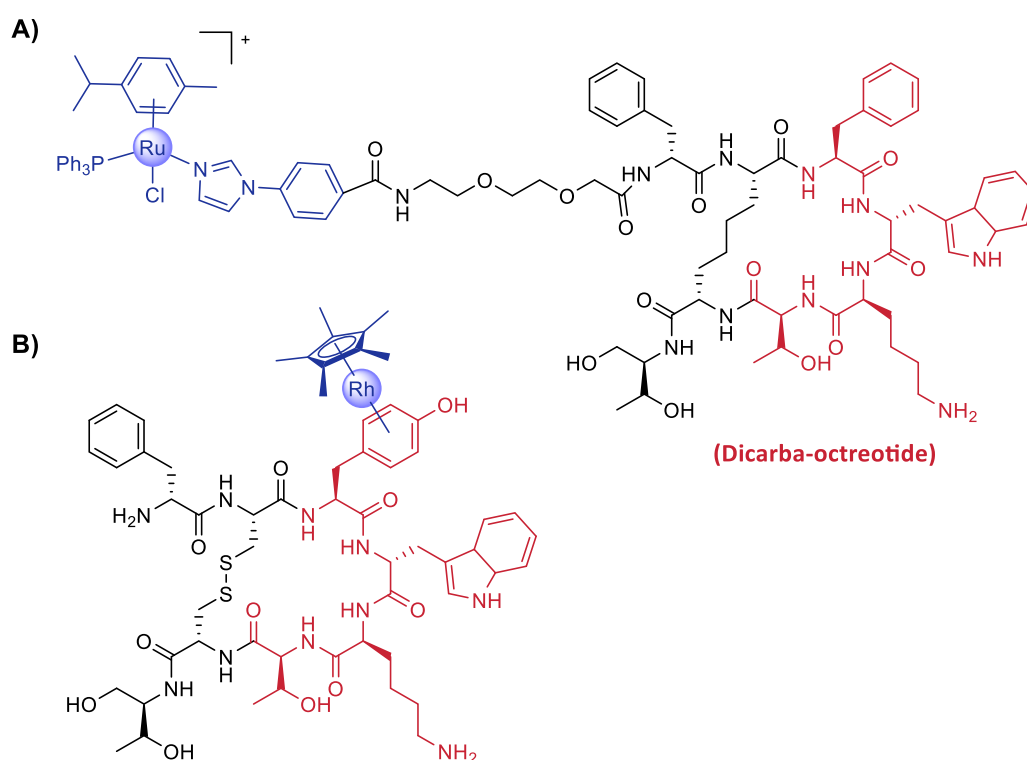


Figure 22. Structure of two examples of metallo-drug-peptide conjugates. A) Conjugation of a dicarba analogue of octreotide to a Ru(II) arene complex. B) Conjugation of octreotide to an organometallic Rh(III) complex.

2.5.3. Targeted fluorophores for cancer imaging and fluorescent-guided surgery

Despite the different types of imaging technologies currently available (e.g., magnetic resonance imaging, ultrasound or computed tomography and positron emission tomography), fluorescence imaging exhibits several advantages, such as high spatial and temporal resolution, great sensitivity, non-damaging, quick response, and low economic cost. In fact, fluorescence imaging is a promising technique that is currently transforming the manner surgeries are conducted through the identification of tumor structures, lymph nodes and cancer in real time during the surgical procedure.^{15,65} In clinical trials, ligand-targeted imaging agents are also used for detecting tumors and selecting patients for ligand-targeted therapies, using then a therapeutic agent as the payload.^{50,66}

The most important applications of targeted fluorophores include tumor diagnosis, targeted therapy, and fluorescence-guided surgery (FGS).⁶⁵ Fluorescence-guided imaging involves the administration of the fluorescent probe followed by imaging at the optimal time to get the best signal to noise contrast. Fluorophores with absorption and emission within the far-red and NIR region of the electromagnetic spectrum (650-900 nm) are especially advantageous owing to their depth-penetration range compared to fluorophores that operate at shorter wavelengths. In addition, in *in vivo* experiments the background fluorescence is highly minimized in the NIR region. Hence, the FGS process starts with the administration of a NIR fluorescent contrast agent via an intravenous, topical or intraparenchymal pathway. During surgery, the contrast agent is visualized using a specific NIR fluorescence imaging system depending on the type of surgery (e.g., above the surgical area for open surgeries or covered inside a fiberscope for minimal invasiveness and robotic surgeries). The systems must be equipped with appropriate NIR excitation light, collection optics, filtration, and a camera sensitive to NIR fluorescence emission light. Sensing devices can measure the difference between excited and emitted light and display it on a monitor in real time.^{67,68} In summary, the FGS instrumentation is composed of three essential parts: (i) an excitation source responsible for exciting the fluorescent probe, (ii) a collection source that collects the fluorophore emission wavelengths while discarding other light, and (iii) a display that provides a real-time monitoring of the surgical field. The contrast agents can be used in several forms, including free dyes, dyes conjugated to targeting ligands or encapsulated in nanoparticles.⁶⁹

At present, most of the fluorescent probes approved for cancer imaging are based on non-receptor-targeted fluorophores, such as indocyanine green (ICG), 5-aminolevulinic acid (5-ALA), and methylene blue (MB) (**Figure 23**). Despite the fact that some of these organic dyes accumulate in certain specific tissues (e.g., 5-ALA), the lack of tissue selectivity remains a main drawback, and for this reason, cancer imaging research has largely been focused on the development of receptor-targeted fluorescent probes which include, as previously stated in **Section 2.5.1** three different parts: the targeting ligand, which is the recognition group, the fluorophore, and the linker. Ideally, a receptor-targeted fluorescent probe should exhibit high specificity and binding affinity towards the target tissue, as well as a rapid clearance from the non-target sites.^{15,65}

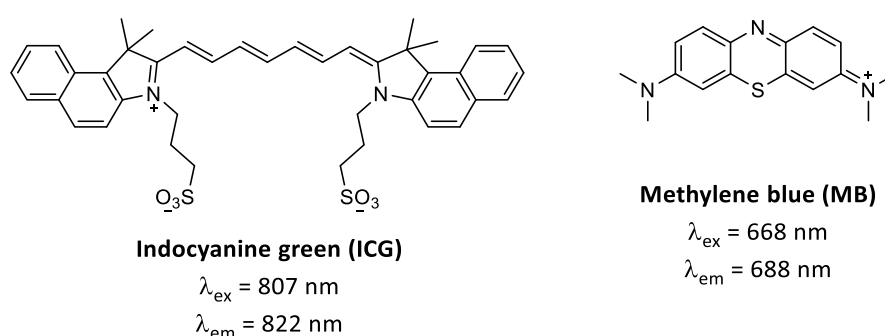


Figure 23. Structures of clinically-approved fluorophores for cancer imaging.

As previously stated in **Section 2.3.2**, some cyanine dyes exhibit absorption and emission in the NIR region making them ideal for the *in vivo* imaging of tumors. Liu *et al.* synthesized a folate receptor-targeted NIR fluorescent probe, fPI-01 (**Figure 24**), by linking the recognition group (folic acid) and the cyanine derivative (ICG) through a PEG-bis-amine linker. Tumor tissue was recognized about 2 h after probe administration.⁷⁰

Ni *et al.* described a transferrin receptor 1 (TfR1)-targeted NIR fluorescent probe, Cy5-CRT (**Figure 24**), based on the conjugation of the TfR1-targeted peptide CRTIGPSVC (CRT) and the cyanine derivative Cy5. Cy5-CRT accumulated in intracranial glioblastoma (GBM) tissues enabling fluorescence-guided GBM removal.⁷¹

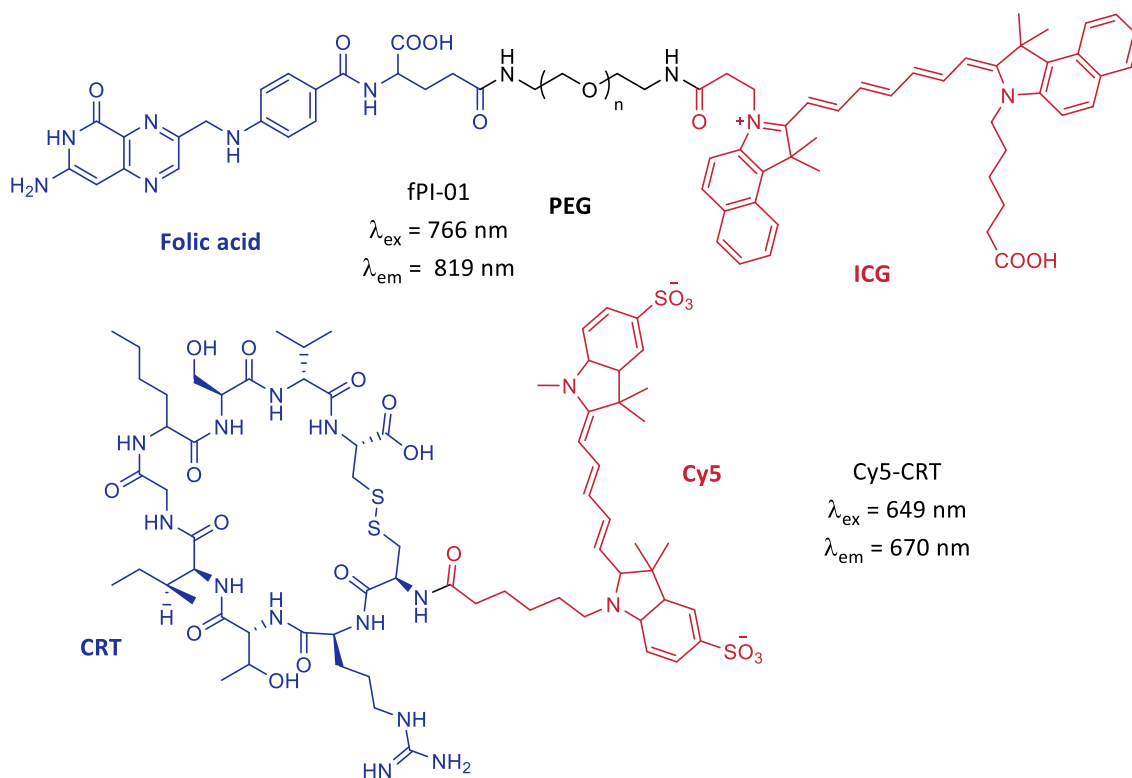


Figure 24. Structures of targeted cyanine-based fluorescent probes.

As it has been stated in the previous section, somatostatin receptor (SSTR) targeted fluorescent probes have been developed for cancer imaging applications, basically through the attachment of a fluorescent dye to octreotide or its analogues. Licha *et al.* designed two SSTR-targeted fluorescent probes by conjugation cyanine dyes to the *N*-terminal amino group of octreotate (**Figure 25**). Octreotate is a somatostatin analogue that is closely related to octreotide. The compounds exhibited absorption and fluorescence emission in the far-red and NIR region and moderate quantum yields ($\lambda_{\text{abs}} = 648 \text{ nm}$, $\lambda_{\text{em}} = 670 \text{ nm}$ and $\Phi_{\text{F}} = 0.20$ for the indodicarbocyanine conjugate, and $\lambda_{\text{abs}} = 748 \text{ nm}$, $\lambda_{\text{em}} = 780 \text{ nm}$ and $\Phi_{\text{F}} = 0.10$ for the indotricarbocyanine conjugate in PBS).⁷² Then, they reported *in vivo* imaging of mouse SSTR2 tumor model using the indotricarbocyanine conjugate. Between 3 and 24 h after the injection of the compound, the tumor fluorescence was more than three times higher than that of normal tissues.⁷³

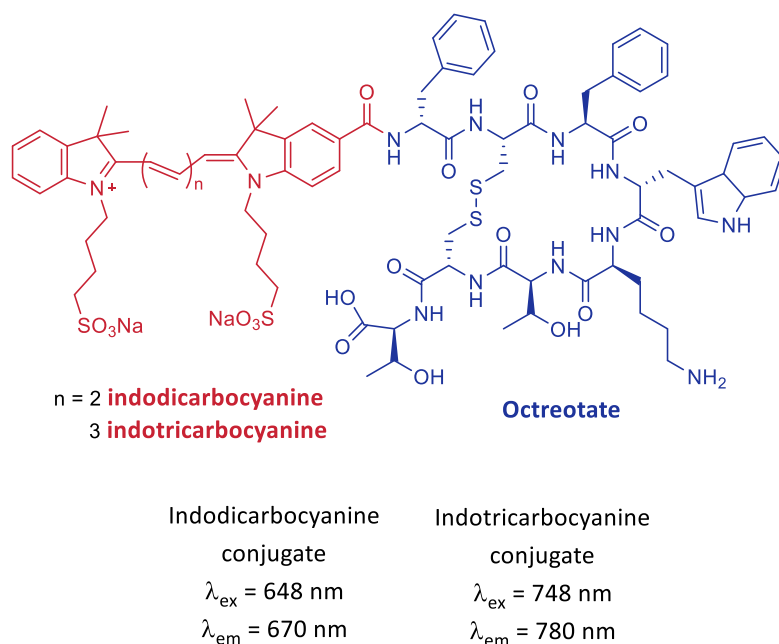


Figure 25. Structures of SSTR-targeted cyanine-based fluorescent probes.

Chen *et al.* reported a conjugate between a RGD peptide c(RGDyK) and a NIR fluorescent dye (Cy5.5) that specifically targeted integrin receptor $\alpha_v\beta_3$ both in cell culture and in living subjects (**Figure 26**). The binding affinity of Cy5.5-RGD conjugate for integrin $\alpha_v\beta_3$ was carried out using $\alpha_v\beta_3$ positive U87MG glioblastoma cells ($\text{IC}_{50} = 42.9 \text{ nM}$). The absorbance and emission characteristics of Cy5.5-RGD conjugate was found identical to those of free Cy5.5.⁷⁴

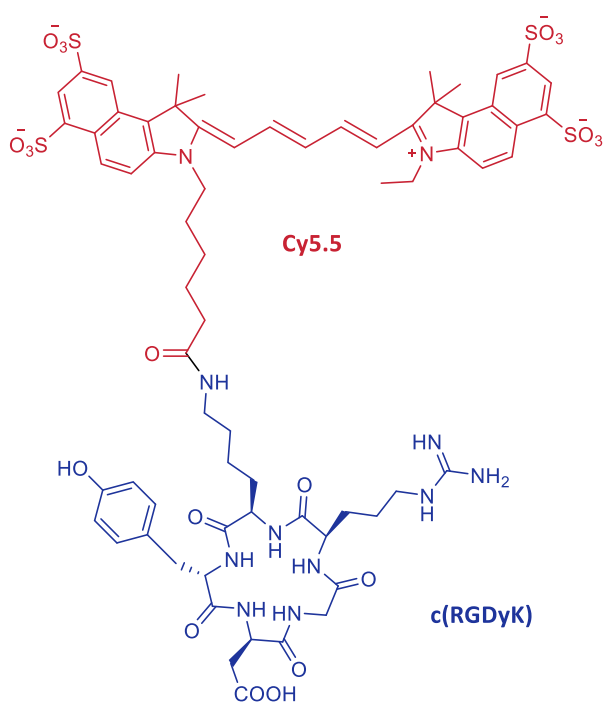


Figure 26. Structure of Cy5.5-RGD conjugate.

BODIPY dyes are also a good choice for the synthesis of receptor-targeted fluorescent probes since some of them can emit in the NIR region (**Section 2.3.2**). Since cyclooxygenase 2 (COX-2) is overexpressed in several cancer cells (e.g., ovarian cancer, gastric cancer, and breast cancer) at the initial phases of the tumor as well as in cancer metastasis,⁶⁵ Pewklang *et al.* focused on the synthesis of a COX-2-targeted NIR fluorescent probe, AZB-IMC2 (**Figure 27**), by linking an aza-BODIPY derivative to the ligand indomethacin (IMC) via the azidotriethylene glycol linker. AZB-IMC2 exhibited high selectivity towards cancer cells where COX-2 is overexpressed after 3 h incubation.⁷⁵

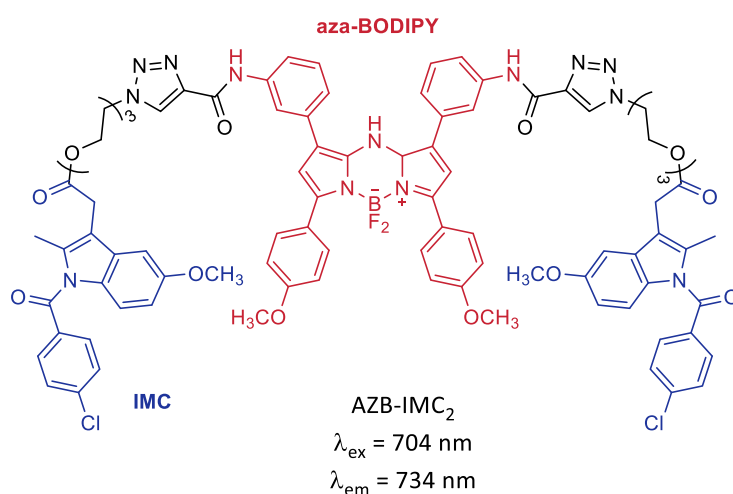


Figure 27. Structure of BODIPY-based fluorescent probe targeting COX-2.

Although rhodamine dyes exhibit some promising properties such as good water solubility, high fluorescence quantum yield and photobleaching resistance, the main drawback is that their absorption and emission wavelengths are below 600 nm. For this reason, rhodamine dyes need to be derivatized in order to be used for deep-tissue imaging applications. For example, Numasawa *et al.* reported a folate receptor-targeted far-red fluorescent probe, FolateSiR-1 (**Figure 28**), which was synthesized by the conjugation between a Si-rhodamine fluorophore and folic acid through a tripeptide linker. The *in vivo* experiments allowed to clearly visualize tumors within less than 30 min after probe injection.⁷⁶

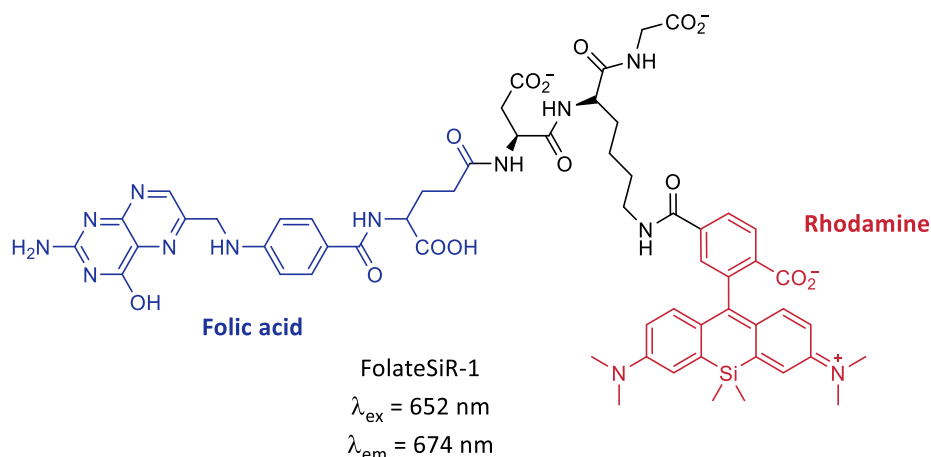


Figure 28. Structure of a Rhodamine-based fluorescent probe.

Mier *et al.* developed Tyr³-octreotide and Tyr³-octreotate scaffolds conjugated with or without linkers to different rhodamine derivatives (e.g., rhodamine B isothiocyanate, rhodamine 101, sulforhodamine 101, and sulforhodamine B acid chloride). An *in vitro* competition assay revealed that all of the fluorescent conjugates exhibited relatively high affinity for the SSTR with IC₅₀ ranging from 0.72 nM to 89 nM. The conjugation between sulforhodamine B (SRBAC) and Tyr³-octreotate (**Figure 29**) through a pentapeptide spacer, exhibited a lower IC₅₀ value (0.72 nM) than octreotide (2.78 nM).⁷⁷

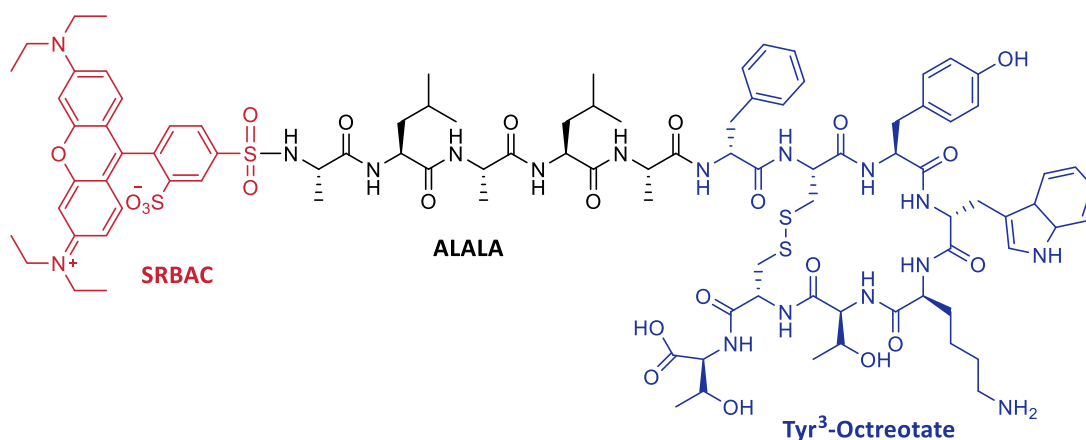


Figure 29. Structure of SRBAC-ALALA-Tyr³-Octreotate conjugate.

Similarly to rhodamine dyes, coumarin fluorophores exhibit great photophysical and physicochemical properties (see **Section 2.4**). However, the emission wavelength of conventional coumarins is located below 520 nm. Hot *et al.* synthesized a polo-like kinase 1 (PLK1)-targeted dye (**Figure 30**) by connecting SBE13 (PLK1 inhibitor) to a far-red emitting coumarin derivative. Polo-like kinase 1 (PLK1) is significantly expressed during cell division, thus making it a potential marker for tumor diagnosis. The fluorescent probe was effectively used for imaging PLK1-upregulated tumors with remarkable signal-to-background ratios.⁷⁸

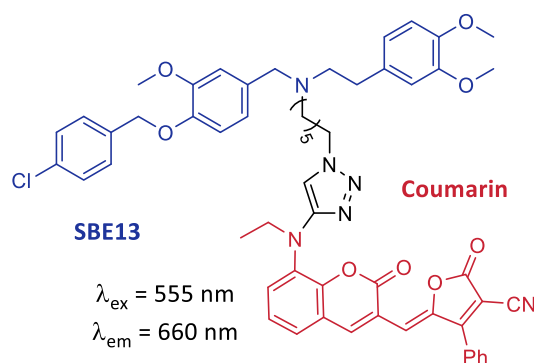


Figure 30. Structure of coumarin-based fluorescent probe.

2.6. Photodynamic therapy (PDT)

Organic fluorophores, such as BODIPYs, cyanines, naphthalimides, rhodamines and coumarins (**Section 2.3**), can be designed not only for precise diagnosis but also for the treatment of cancer with photodynamic therapy.⁷⁹ Among all the available cancer treatments, PDT has emerged in the past few decades as a promising non-invasive oncotherapy modality which requires light triggering.^{80,81} In fact, the use of light as a therapy dates back more than three thousand years ago since ancient Egyptian, Indian and Chinese civilizations used it to treat several skin diseases such as vitiligo. The history of PDT started in 1900 when Oscar Raab reported that a combination of acridine and light was toxic to paramecium (**Figure 31**).⁸²

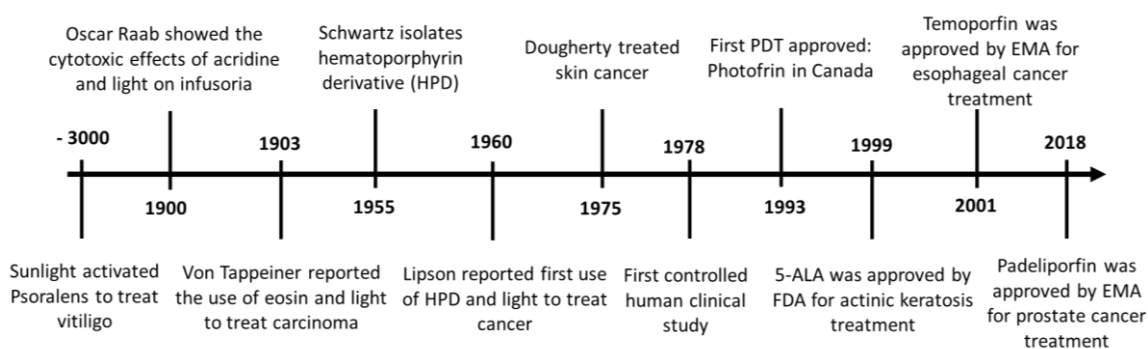


Figure 31. Historical development of PDT.^{83,84}

PDT involves three essential non-toxic components: a photosensitizer (PS), light, and oxygen. The combination of the three components triggers the generation of highly cytotoxic reactive oxygen species (ROS) that damage biomolecules (e.g., proteins, nucleic acids) and cell organelles, and finally lead to cell death. Three interrelated mechanisms originate the antitumor effect of PDT: (1) phototoxicity on cancer cells, (2) damage to the tumor vasculature, and (3) production of an inflammatory reaction that can activate the immune system. The contribution of each mechanism depends on the type and dose of the PS, the total light dose and the time between its exposure and the administration of the PS, the concentration of oxygen in the tumor, and probably other factors.⁸⁵

In general, the profile of a PDT treatment, shown in **Figure 32**, starts with the injection of a non-toxic dose of a photosensitizer into the blood circulatory system. The PS can be distributed in a non-specific way into the whole body, or ideally in a specific target tissue. After the proper incubating time, which can oscillate between 5 min to 24 h depending on the PS, the tumor is irradiated with light of a specific wavelength. The exposure to light can be used for a therapeutic effect as well as for tumor detection using fluorescence-guided surgical techniques. The use of light in a specific area offers the possibility for a precise and selective cancer treatment.^{86,87}

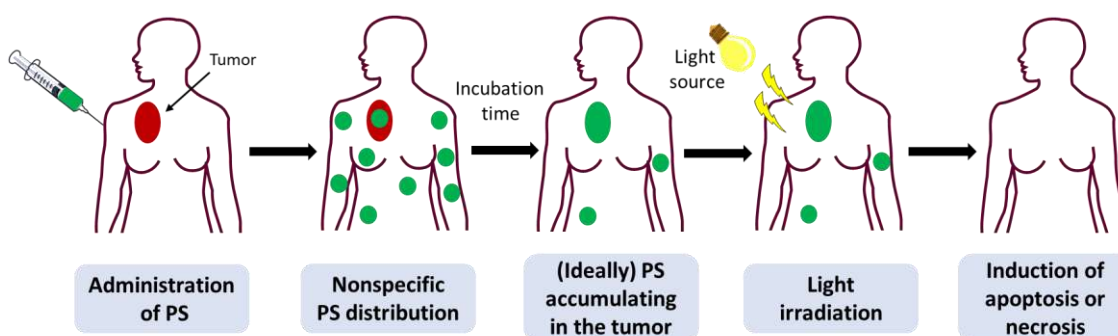


Figure 32. Schematic representation of the profile of a PDT treatment. Adapted with permission from reference [86].

2.6.1. Photosensitizers (PS)

The selection of the PS is crucial for an effective therapy with PDT. An ideal PS should be a single molecule with good storage stability and low manufacturing costs. The PS should be excited by light of a range of wavelengths between 650 and 900 nm. As previously stated (**Section 2.2.2**), this specific window, from far-red to NIR, will be the optimal for PDT propose because the light exhibits higher tissue penetration capacity. Importantly, the PS agent must be non-cytotoxic to the cells in the dark and, consequently, a high phototoxic index (PI), which is calculated as the ratio between dark and light toxicity, is highly desired. PI is an important value that is commonly used to rank photosensitizers for clinical uses in photodynamic therapy.

Another factor to be considered is the incubation time of the PS, which is usually relatively long. However, some studies suggest that a better tumor response can be achieved by using shorter incubation times because light exposure can produce vascular damage if the PS remains for a long time in the blood vessels. For some types of cancer, a marked inflammatory response and necrotic cell death is preferred, whereas for other types of cancer, such as brain tumors where swelling is undesirable, it is more suitable apoptosis and less inflammation. Finally, the phenomenon known as photobleaching in which the PS is destroyed upon light irradiation exposure, was first thought to be undesirable but some reports suggest that it is a good way to avoid overtreatment by destroying the PS.^{10,85}

In summary, an ideally photosensitizer should meet several requirements including chemical stability, water solubility, lack of dark cytotoxicity, high quantum yields of reactive oxygen species generation, tumor selectivity, rapid clearance from patient and absorption in the far-red to NIR region for a deeper tissue penetration.⁸⁷

2.6.2. Light source

Ideally, a PDT treatment should only affect the tumor and not damage healthy tissues. For this reason, the selection of the wavelength of the light to be applied is an important factor to be considered and that it is directly related to the location, size, shape and depth of the tumor, the absorption and emission spectra of the PS, and the cost. Shorter wavelengths, in the blue to green region of the electromagnetic spectrum, penetrate slightly through tissues, while longer wavelengths, in the far-red to NIR region, penetrate more deeply favoring to reach deeper or larger tumors while minimizing photodamage (**Figure 33**). In fact, long exposure to short wavelengths irradiation can gravely damage cells by inducing undesired photochemical reactions.⁸⁸ On the other hand, longer wavelengths, between 900-1200 nm, might not have enough energy to induce a PDT reaction.^{85,86}

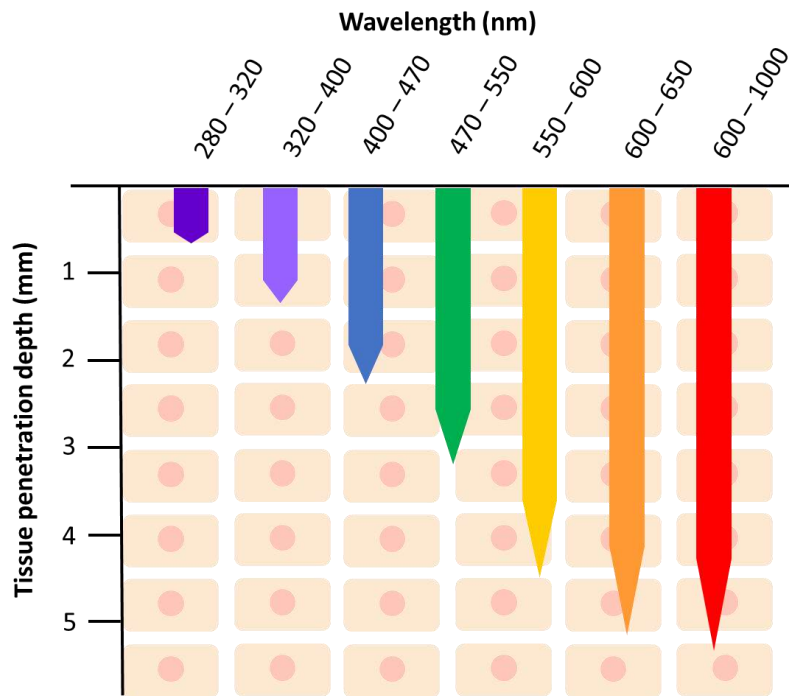


Figure 33. Light penetration depth at various wavelengths in skin tissue. Adapted with permission from reference [88].

In addition, the four main factors of the light source that will determine the clinical efficacy of a PDT treatment are: (1) the total light dose, (2) light exposure time, (3) light delivery method, and (4) the fluence rate of the light. As the source of light for PDT, either lasers or incandescent light sources have been used and showed similar effectiveness. Diode laser lights are a good choice for PDT because they are cost-efficient, small, simple to use, automatized and have a long operational life. They can also be attached to fibers to treat tumors in the urinary bladder and the digestive tract. Light-emitting diodes (LEDs), also used in PDT, have a reasonable narrow spectra and high fluence rates.⁸⁵

2.6.3. PDT mechanism of action

The PDT process starts with the absorption of a photon by the PS followed by various competing reactions leading to the oxidation and degradation of vital biomolecules and cell organelles. The overall mechanism of action of PDT involves several stages which can be illustrated in the Jablonski diagram (see **Section 2.2.1**). First, after the absorption of light, an electronically excited state of the PS is initially populated, generally the singlet excited state (S_1) whose lifetimes are in a nanosecond range. Then, the lowest excited singlet state S_1 can either rapidly go back to its ground state via fluorescence emission (or through non-radiative decay), or be stabilized through a nonradiative intersystem crossing (ISC) in which the triplet state of the PS is populated via $S_1 \rightarrow T_1$ (**Figure 34**). Because of the longer lifetimes of the T_1 species, around the micro- to millisecond range, they can participate in photodynamic reactions. The PDT effect is based on the transference of energy, electrons or protons from the triplet excited state of the photosensitizer to other molecules, including organic substrates or molecular oxygen, which trigger the generation of ROS through type I or type II processes, leading at the end to cytotoxicity.^{81,87,89}

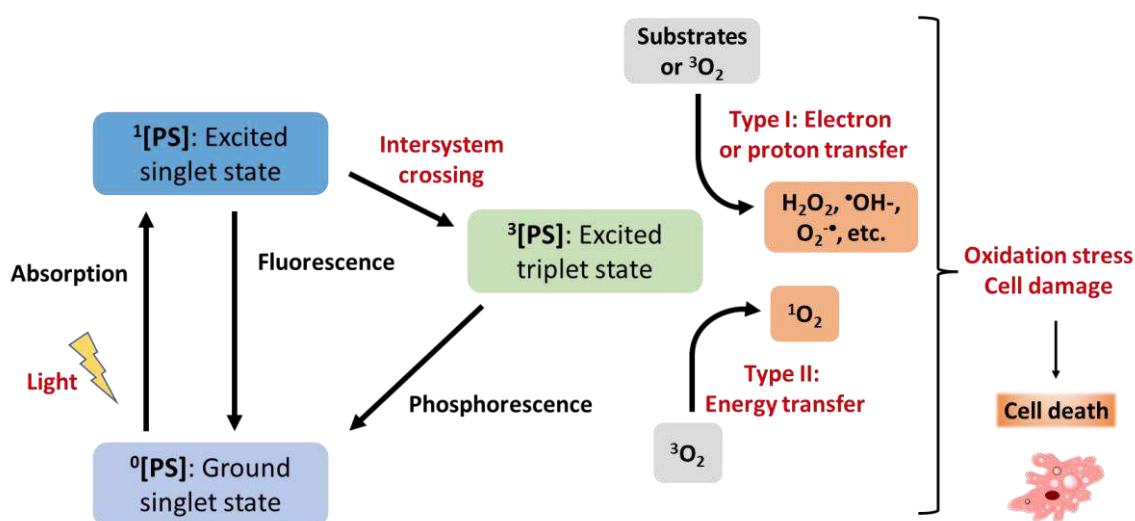


Figure 34. Simplified overview of the PDT mechanism of action.

Type I reactions require electron or proton transfer between the T_1 of the PS and the substrate molecules to generate radical ions and free radicals. These radicals react with oxygen and produce highly reactive oxygenated products such as superoxide anion radicals ($O_2^{\bullet-}$) or hydroxyl radicals (OH^{\bullet}). In type II process, the excited triplet state of the PS interacts with the ground-state molecular oxygen (3O_2), which involves an energy transfer, to transform it into a highly reactive singlet oxygen species (1O_2). Although type II mechanism is the main pathway for most of the clinically approved PSs, both mechanisms, type I and II, cause oxidative biological damage to target tissues in an irreversible way and lead to cell death.^{81,87}

It is worth nothing that the environment in which solid tumors grow is generally devoid of oxygen (hypoxic conditions), which seriously reduces the effectiveness of oxygen-dependent PSs. Since type II photodynamic reactions need an aerobic microenvironment to produce cytotoxic 1O_2 , PSs that can react with biomolecules to produce oxygenated products (e.g., $O_2^{\bullet-}$, OH^{\bullet} , and H_2O_2) via type I PDT mechanisms may allow to partially overcome this problem. Hence, given the promising perspectives of type I PDT, there is an increasing need of developing novel type I photosensitizers.^{89,90}

2.6.4. Clinically-approved PSs for cancer therapy

The first photosensitizer clinically used for the treatment of cancer was a mixture of porphyrins named hematoporphyrin derivative (HPD), which in a purified form, later became known as Photofrin®. Even though this porphimer sodium has some disadvantages such as a low absorbance at 630 nm and skin photosensitivity, to date, Photofrin® is the only PS that has been approved all over the world for cancer therapy. The compounds 5-aminolevulinic acid (Ameluz®, Levulan®) and methyl 5-aminolevulinate (Metvix®, Metvixia®), precursors for the synthesis of protoporphyrin IX (PpIX), are clinically approved worldwide for the treatment of basal cell carcinoma except in the United States where it is only approved for actinic keratosis. Apart from these PSs, there are also other PSs approved only in certain countries, which are summarized in **Table 8**. It is worth nothing that most of the clinically approved photosensitizers are based on a tetrapyrrolic structural core, which determines their properties as photosensitizers. The most common drawbacks of such conventional PSs are poor water solubility, poor photostability, poor selectivity for cancer cells, and slow clearance from the patient, which causes sensitivity, as well as difficult synthesis.^{83,85,86}

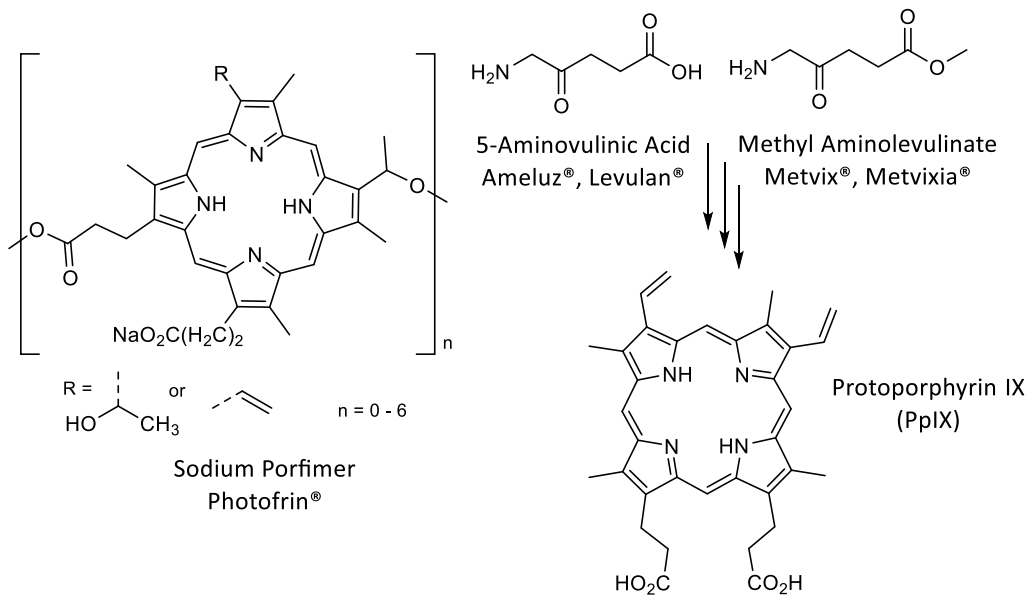


Figure 35. Structure of some PSs clinically approved for PDT.

Table 8. Clinically approved PSs for cancer therapy.⁸⁶

Chemical name	Generic name	Structure	Country	Type of cancer treated
Sodium porfimer	Photofrin®	Porphyrin	Worldwide	Oesophageal, endobronchial and lung cancer (gastric cancer in Japan, bladder cancer in Canada)
5-Aminolevulinic acid	Ameluz®, Levulan®	Porphyrin precursor	Worldwide	Basal cell carcinoma, squamous cell carcinoma
Methyl 5-aminolevulinate	Metvix®, Metvixia®	Porphyrin precursor	Worldwide	Basal cell carcinoma
Temoporfin	Foscan®	Chlorin	EU	Head and neck squamous cell carcinoma
LUZ111	Redaporfin®	Bacteriochlorin	EU	Head and neck cancer
Talaporfin	Laserphyrin®	Chlorin	Japan	Glioblastoma, lung cancer
chlorin mixture: 80% chlorin e6, 15% chlorin p6, 5% purpurin	Radachlorin®	Chlorin	Russia	Basal cell carcinoma

2.6.5. Advantages and challenges of PDT treatment

Compared to conventional cancer treatments (e.g., chemotherapy, surgery or radiotherapy), PDT offers several advantages: (1) it is less invasive than surgery, (2) side effects last for a shorter period of time compared with chemotherapy or radiotherapy, (3) PDT is a highly selective technique because PSs only work after light irradiation in the target area, thus minimizing systemic toxicity, (4) compared to radiotherapy, PDT can be repeated several times in the specific area, (5) apart from destroying the tumor, PDT also destroys the vasculature related to the tumor, (6) PDT can be combined with other cancer treatments, (7) PDT can be applied to overcome the resistance phenomenon, and (8) it generally costs less than the other treatments.

However, PDT has also some disadvantages or limitations that need to be addressed: (1) PDT is not useful for combating metastases, because the effect only takes place in the specific irradiated area and it is impossible the whole body irradiation with proper light intensity, (2) the penetration depths of the light used in PDT are relatively small, thus making difficult to reach deep tumors, (3) most of the PDT treatments require a certain level of oxygen in the tumors and therefore hypoxic deep-seated tumors are more difficult to be treated with this technique.^{10,81}

Table 9. Advantages and disadvantages of Photodynamic Therapy.¹⁰

PDT advantages	PDT disadvantages
- Reduced adverse effects	
- Non-invasiveness treatment	- An effective treatment depends on the correct light delivery to the tumor
- Selectivity	- The presence of oxygen in the tissue is crucial for PDT.
- Short treatment time	
- Can be applied several times at the same place	- It is not possible to treat metastatic cancers
- No scar after healing	- Photosensitivity after treatment
- Lower costs than other treatments	

2.6.6. Photosensitizers based on organic fluorophores

Organic fluorophores have been extensively studied for the synthesis of efficient PDT photosensitizers. The synthesis of heavy-atom-free PSs has been focused on improving their ISC characteristics. An ideal organic PS should absorb light of long wavelengths, from the visible to the NIR region, and have a large molar extinction coefficient. In addition, optimal luminescent properties can be exploited to combine real-time monitoring and PDT treatment. The most studied PSs based on organic fluorophores include porphyrins, cyanines, BODIPYs, naphthalimides, and coumarins.⁹¹

Porphyrins, containing a cyclic tetrapyrrole scaffold linked by conjugated chains and a cavity in the center are, as previously indicated, the most common photosensitizers in clinical applications. Porphyrins can also be used as theranostic agents by combining bioimaging and cancer therapy, owing to strong absorption and emission bands, long-lived triplet excited states, and ROS generation via either type I or type II processes under light irradiation.^{81,91} Xodo *et al.* synthesized a family of alkyl porphyrins, being compound **50 (Figure 36)** a representative example, with capacity to target mRNA and induce its breakdown upon photoirradiation. Such alkyl porphyrins enter the pancreatic cells via endocytosis and passive diffusion and accumulate in the cytoplasm. The compounds generate ROS in pancreatic cancer cells upon photoirradiation.⁹²

As described in **Sections 2.3.2** and **2.5.3**, cyanines exhibit great photophysical properties and low toxicity, which makes them interesting compounds for bioimaging applications. Recently, some studies have also explored the use of cyanines as PSs in PDT. Song *et al.* reported a water-soluble NIR aminocyanine fluorophore (**51, Figure 36**) that shows a long triple state lifetime, high singlet oxygen quantum yield and low cytotoxicity in the dark, thus making it a potential compound for PDT therapy.⁹³

BODIPY-based photosensitizers can be developed through the introduction of halogen atoms such as bromide or iodine within the scaffold structure with the aim of enhancing the production of ¹O₂. Yan *et al.* described a pyrrole substituted iodinated BODIPY (**52, Figure 36**) with a strong NIR absorption and emission, good singlet oxygen quantum yield and IC₅₀ values in the micromolar range.⁹⁴

Coumarin scaffolds have also attracted recently attention as PSs in PDT due to their excellent chemical and photophysical properties. Li *et al.* designed a series of coumarin-based PSs with an absorption band in the red range and emission in the NIR region with large Stokes' shifts, around 100 nm. Coumarin derivative **53 (Figure 36)** could easily enter the cell and accumulate in the mitochondria, leading to efficient PDT effect for living cells.⁹⁵

Very recently, Marchán and collaborators have described a detailed structure-activity relationship study to investigate the potential applications of COUPY coumarins, previously introduced in **Section 2.4.2.5**, as PSs in PDT. This study allowed the identification of new PSs based on COUPY scaffolds which exhibited effective *in vitro* anticancer activities upon visible-light irradiation in both normoxia and hypoxia (phototherapeutic indexes up to 71) and minimal toxicity toward normal cells. Compounds **54-56** represented in **Figure 36** are some examples of these PSs based on COUPY coumarins.⁹⁶

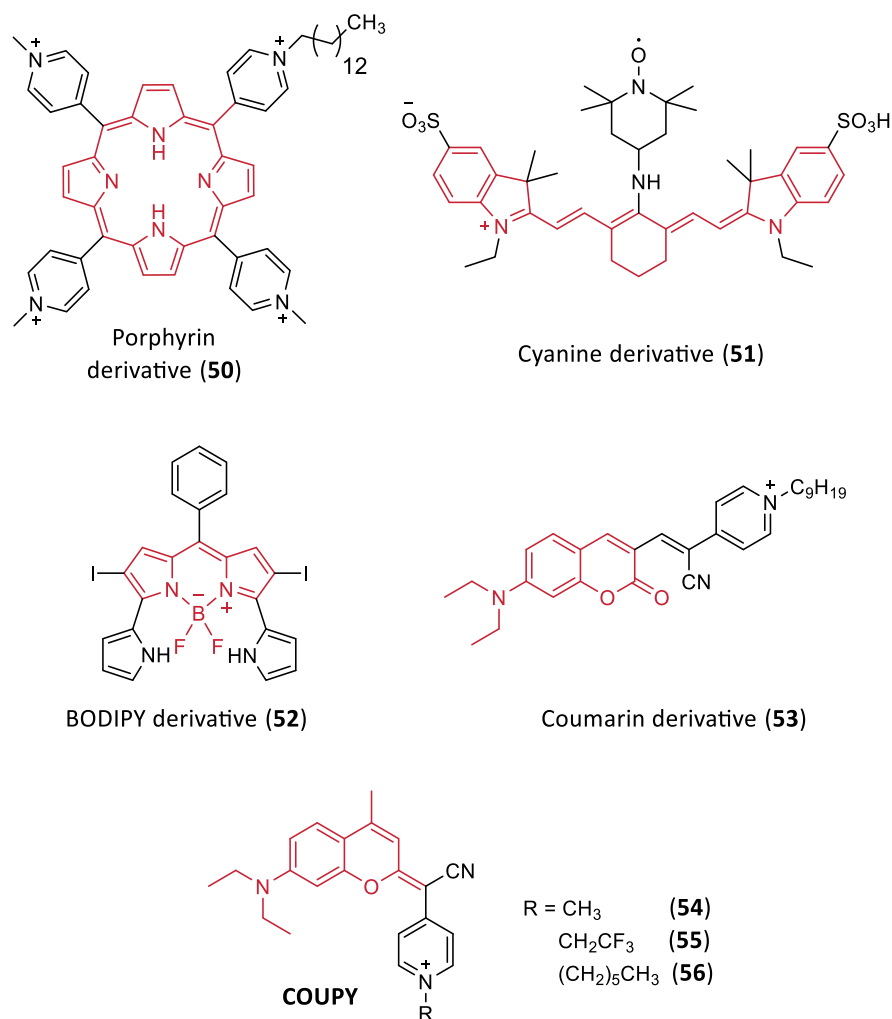


Figure 36. Structures of some organic fluorophores used as PSs in PDT.

3. Metal-based anticancer drugs in conventional chemotherapy and photodynamic therapy

Transition metal complexes, including coordination complexes and organometallic structures, are great gaining interest in the medicinal field. Their unique characteristics such as their variable number of oxidation states, coordination motifs, and geometries, offers a wide spectrum of structural and chemical possibilities to be exploited for biomedical applications. Despite metal-containing compounds have long been used in the medicinal field, their enormous potential as anticancer agents was only revealed after the discovery of the biological activity of cisplatin, described in the next section. Although, a lot of efforts have been dedicated to the development of new platinum-based anticancer agents, there are some problems related to this type of metallodrugs, that led researchers to explore alternative approaches based on other transition metals, such as Ru(II) and Ir(III).⁹⁷

On the other hand, several basic needs of modern PDT, already introduced in **Section 2.6**, can be fulfilled owing to the characteristic properties of transition metal complexes, which makes them attractive candidates to develop new PSs. Their excellent photophysical and photochemical properties, including large quantum yields for triplet-state formation, offer a good opportunity to design PSs with enhanced properties and alternative mechanisms of action compared to organic photosensitizers (**Section 2.6.6**). The most studied transition metal complexes as PSs are based on Pt(IV), Ru(II), and Rh(III), followed more recently by Ir(III) and finally Os(II).⁸³

In this chapter, after describing the successful history of cisplatin in oncological chemotherapy, we will introduce some other clinically-approved platinum anticancer drugs and discuss other emerging anticancer agents based on metals other than platinum such as ruthenium and iridium. Finally, we will briefly discuss the applications of Ru(II) and Ir(III) complexes in anticancer PDT.

3.1. Metal complexes in conventional chemotherapy

3.1.1. Platinum(II) and platinum(IV) anticancer complexes

Platinum anticancer agents have a key role in the field of medicinal inorganic chemistry, being cisplatin a reference compound worldwide for the treatment of numerous types of cancers, including ovarian, lung, testicular, bladder, head and neck, melanoma, lymphomas, and several others. Cisplatin was first described in 1845 by an Italian chemist Michele Peyrone but it was not until 1965 when a biophysical chemist, Dr. Barnett Rosenberg, discovered accidentally its ability of inhibiting cell division.⁹⁸

At present, there are only three **Pt(II) complexes** approved worldwide for cancer treatment in humans: cisplatin, carboplatin and oxaliplatin. Additionally, there are three more approved only for the use in specific countries: nedaplatin, lobaplatin and heptaplatin (**Figure 37**). Even though cisplatin was first used as anticancer agent more than 40 years ago, platinum complexes are still the most widely used drugs in cancer therapy.⁹⁹

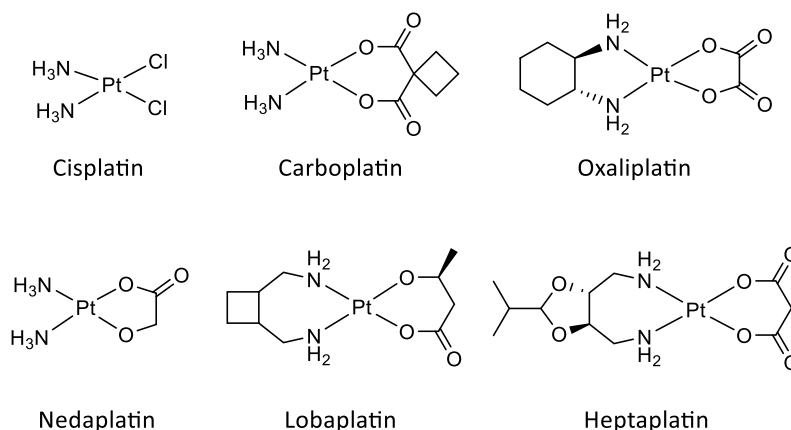


Figure 37. Chemical structures of clinically approved platinum(II) anticancer agents.

Carboplatin can be administrated at higher doses than cisplatin because is less toxic and induces fewer side effects. The cyclobutanedicarboxylate group is a bad leaving group leading to slow substitution reactions, which results in an overall low cytotoxic effect. However, carboplatin is only active in the same kind of tumors than cisplatin and also exhibits similar resistant problems. By contrast, oxaliplatin exhibits better properties against resistant tumors, and it is used for colon cancer treatment since 1996. The increased lipophilicity provided by 1,2-diamminocyclohexane ligand results in a greater influx of the drug through the cell membrane. The higher cellular uptake and the formation of different of platinum-DNA adducts is highly beneficial for overcoming cisplatin resistance.⁹⁸

Although nedaplatin has similar anticancer activity than cisplatin, it is 10 times more soluble in water and less toxic for the kidneys and the gastrointestinal system than the parent drug. However, it can cause thrombocytopenia and is crossresistant with cisplatin. Nedaplatin has been only approved in Japan for some specific cancers including esophageal cancer and head and neck cancers. By contrast, heptaplatin exhibits higher anticancer activity, lower toxicity, and higher solubility than cisplatin. Currently heptaplatin is under clinical trials and it has been only approved by Korea for the treatment of gastric cancer. Lobaplatin is approved in China for treating chronic myelogenous leukemia, and it has passed phase II trials in several countries for the treatment of various types of cancer. However, it causes anemia, leucopenia, nausea, and vomiting.⁹⁸

Table 10. Clinically approved Pt(II)-anticancer drugs.

Pt (II) Drug	Year of approval	Country approved	Type of cancer treated
Cisplatin	1978	Worldwide	Testicular, ovarian, bladder, melanoma, NSCLC, lymphomas, Myelomas cancer
Carboplatin	1989	Worldwide	Ovarian, retinoblastomas, neuroblastomas, nephroblastomas, brain tumor, head and neck, cervix, testis, breast, lung, bladder cancer
Oxaliplatin	1996	Worldwide	Colon cancer
Nedaplatin	1995	Japan	NSCLC, SCLC, oesophageal cancer, head and neck cancers
Lobaplatin	1999	Korea	Advanced gastric cancer
Heptaplatin	2010	China	CML, SCLC, inoperable metastatic breast cancer

3.1.1.1. Mechanism of action of Pt-based anticancer drugs

The mechanism of action of platinum-based anticancer drugs involves four steps: (i) cellular uptake, (ii) aquation/activation, (iii) DNA binding, and (iv) cellular processing of Pt-DNA lesions, which leads to either apoptosis or cell survival.⁹⁹

Cisplatin is administered intravenously as a saline solution to the patient. In the bloodstream the drug remains neutral and unchanged because the concentration of chloride is high.⁹⁸

The cellular uptake combines both passive diffusion through the plasma and active transport mediated by membrane proteins. The small size of cisplatin and its planar geometry can favor the passive diffusion. However, cisplatin uptake has been also related to expression levels of copper transport CTR1, suggesting that the active transport might be the predominant mechanism of internalization.^{98,99}

Inside the cell the concentration of chloride in the cytoplasm is relatively low and cisplatin is activated by the replacement of one of the two chlorido ligands by a water molecule. Once inside the nucleus, the cationic monoaquated platinum complex, *cis*-[Pt(NH₃)₂Cl(H₂O)]⁺, is a potent electrophile that can react with the nitrogen donor atoms of nucleic acids because water is a good leaving group, being the N7 position of the imidazole ring of guanine and adenine nucleobases in DNA the preferred site to be attacked. Cisplatin forms different types of adducts with DNA bases. First, cisplatin forms monofunctional adducts with DNA, and then, the free chloride ligand is replaced by a second guanine nucleobase either in the same strand or in a different one forming a cross-link (**Figure 38**). The predominant crosslinks are intrastrand 1,2-(GpG) followed by 1,2-(ApG). These adducts are able to induce cell apoptosis by impeding vital cellular processes such as DNA replication and transcription.^{98–100}

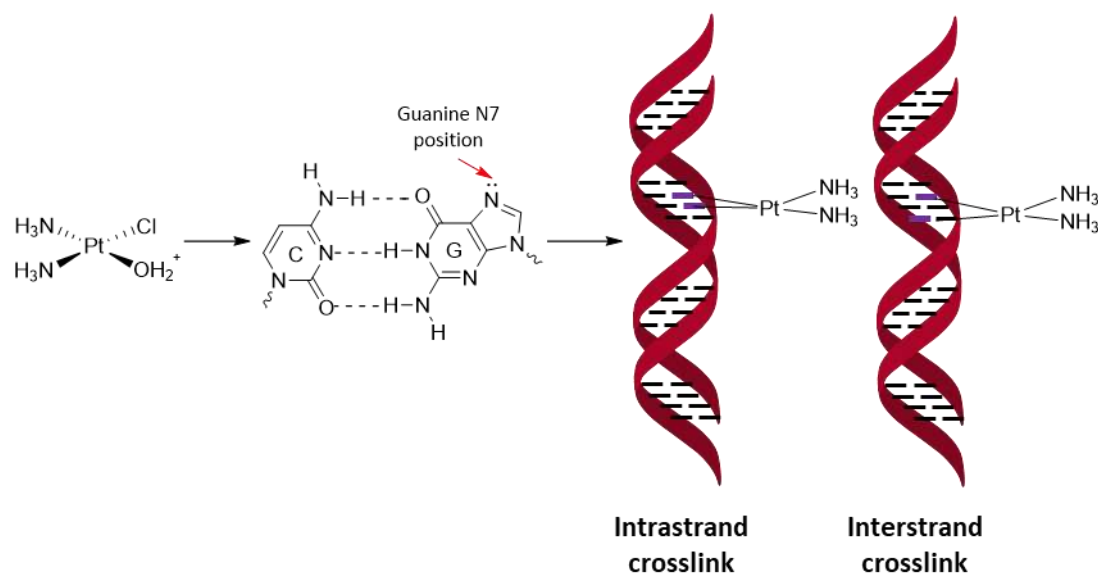


Figure 38. Examples of cisplatin adducts with DNA. Adapted with permission from reference [100].

3.1.1.2. Resistance to cisplatin

In general, many tumors exhibit resistance to cisplatin, either intrinsically or acquired during the administration of the drug. The main resistance mechanisms involve a decrease in the membrane transport of cisplatin, an increase of the DNA repair by the nucleotide excision repair machinery (NER), an increase in the cytoplasmic detoxification and an increased tolerance to DNA damage.

During the circulation of cisplatin through the bloodstream, peptides and proteins present in the blood are known to bind to it, especially those containing thiol groups, causing the deactivation of the major part of the administered drug. The most important biomolecules that bind to platinum complexes are human serum albumin protein (HAS) and glutathione (GSH) tripeptide.

Once inside the cell, cisplatin can also be deactivated in the cytoplasm upon binding with glutathione and metallothioneins. For example, the complex formed between cisplatin and glutathione is excreted by a GS-conjugated export pump.

After the formation of the cisplatin-DNA adducts, nucleotide excision repair machinery (NER) can remove DNA lesions by reconstituting the gene integrity. Hence, an overexpression of NER in cancer cells leads to resistance to cisplatin by repairing DNA lesions perfectly.

The resistance phenomenon toward cancer cells, which obviously depends on the type of cancer, has become one of the most important drawbacks of cisplatin therapy. For this reason, many efforts have been dedicated to the development of novel platinum anticancer drugs, either Pt(II) or Pt(IV) complexes, with the aim of reducing both toxic side effects and inherent or acquired resistance.

Among **Pt(IV) complexes** described so far as potential anticancer agents, some of them have exhibited sufficient anticancer activity to enter clinical trials: iproplatin, satraplatin and tetraplatin (**Figure 39**). Pt(IV) complexes can be considered prodrugs and, consequently, need to be reduced to the Pt(II) form to show anticancer activity. Although none of the Pt(IV) complexes that have entered clinical trials have shown a significantly improved activity compared to cisplatin, Pt(IV) complexes offer a great potential in terms of reduced toxicity and improved bioavailability. However, one of the main problems related to these prodrugs is a premature activation by the reduction of the Pt(IV) complex in the bloodstream.¹⁰¹

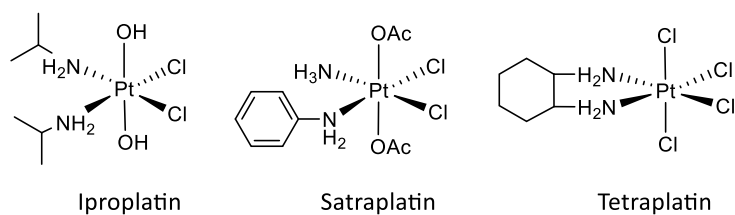


Figure 39. Structure of Pt(IV) complexes that have entered clinical trials.

Although iproplatin exhibits lower toxicity and higher solubility compared to cisplatin, it was abandoned after phase I trials because of poor activity. Tetraplatin was also abandoned after phase I because of the appearance of neurotoxic side effects. Finally, satraplatin, the first orally active platinum, is under phase II trials.¹⁰²

3.1.2. Ruthenium(II) anticancer complexes

The important limitations of Pt-based anticancer drugs (e.g., toxicity, poor selectivity and chemoresistance) prompted researchers to explore the development of safer metal-based chemotherapeutic agents with improved properties. Among all of the metal complexes investigated until now, ruthenium-based compounds are currently of great interest in the diagnosis and treatment of cancer, thus being a valuable alternative to Pt(II)-based anticancer drugs.¹⁰³

Ruthenium has three important chemical and biochemical properties that makes this metal highly suitable for medical applications: (i) slow ligand-exchange kinetics, (ii) existence of several oxidation states and, (iii) iron mimicking ability in binding to biomolecules.¹⁰⁴

(i) The aquation reaction in cisplatin in which one of the chlorido ligands is replaced by a water molecule inside the cells takes approximately 2 hours.⁹⁹ However, this ligand-exchange kinetics in many other coordination compounds falls in the order of microseconds to seconds. By contrast, Ru(II) complexes have similar ligand-exchange reactions kinetics than Pt(II) complexes, mimicking the time scale for many cell division processes.

(ii) Ruthenium is a transition metal of group 8 and, consequently, has three accessible oxidation states (II, III and IV) under physiological conditions, although the reduced state is considered to be more reactive. The ruthenium ion is hexacoordinated with octahedral coordination geometries in all oxidation states. In addition, the redox potential of ruthenium can be tuned by modifying the coordination environment. This property is very useful for improving drug selectivity and, for example, ruthenium-based drugs can be administered as the relatively inert Ru(III) complex, which will be activated in the desired place by reduction.

(iii) The ability of ruthenium for mimicking iron in binding to serum transferrin and albumin seems to be one of the main reasons that accounts for the reduced cytotoxicity of Ru-based drugs compared with platinum complexes. Since cancer cells require more iron for dividing rapidly, they overexpress transferrin receptors on the cell surface resulting in an increased accumulation of ruthenium complexes when compared to healthy cells.

3.1.2.1. Ru-based anticancer agents in clinical trials

Despite the large number of Ru-based anticancer agents developed until now, none of them have succeeded to pass clinical trials. The first ruthenium complex ever introduced in clinical trials as an anticancer agent was NAMI-A. However, the unexpected low therapeutic efficacy of the treatment resulted in the failure of the clinical investigations.^{105,106}

Then, KP1019 entered the clinical trials, however it was not soluble enough making its sodium salt KP1339 a better choice, that is being evaluated at present in clinical trials.^{105,107}

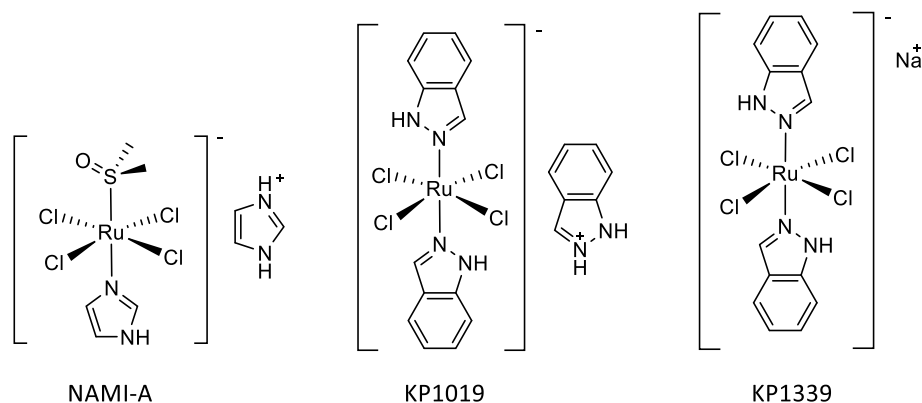


Figure 40. Examples of ruthenium(III) complexes in clinical trials.

3.1.2.2. Mechanism of action

The cellular uptake of Ru(II) complexes can take place through several mechanisms, including passive diffusion, facilitated diffusion, active transport, and endocytosis (**Figure 41**).¹⁰⁸ Although the mechanism of action of ruthenium complexes is not completely clear, they tend to accumulate in four different organelles: mitochondria, nucleus, lysosomes, and endoplasmic reticulum, being DNA and proteins the two main targets.^{105,109}

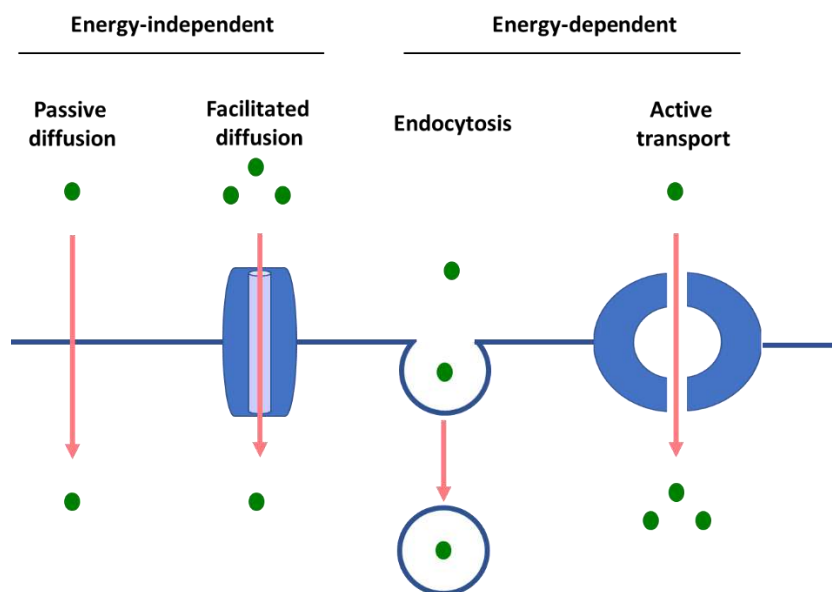


Figure 41. Representation of the different cellular uptake mechanisms for Ru complexes. Adapted with permission from reference [108].

For a better comprehension of the mechanism of action of ruthenium complexes as anticancer agents, it is important to know how they interact with the two main targets, DNA and proteins:¹⁰⁵

- Numerous ruthenium complexes are known to bind selectively to DNA. There are two different binding modes between ruthenium complexes and DNA which involve (i) covalent binding, which is irreversible and forms Ru-DNA adducts, similar to those produced by cisplatin; and (ii) non-covalent binding, which is a reversible process and includes intercalation, electrostatic binding, and groove binding.
- Although DNA is considered the main target for ruthenium complexes, some proteins such as protein kinases have also been found to be a target. In general, binding of ruthenium complexes to the active site of a protein occurs through interaction with the active ligands.

The induction of cell death by ruthenium complexes can take place through different mechanisms, being apoptosis the main cell death mechanism. Apoptosis can be activated in cells by a mitochondria-dependent pathway (intrinsic) or by a death receptor-dependent pathway (extrinsic). The intrinsic pathway can be activated by DNA damage and also by endoplasmic reticulum stress (ERS) and oxidative stress. Subsequently, the mitochondria releases cytochrome c, thus activating the apoptotic protease and other proteins that participate in the apoptosis mechanism (**Figure 42**). It has also been demonstrated that ruthenium complexes can induce autophagy and necrosis. Autophagy is a self-degradative process that plays an important role in removing aggregated proteins and damaged organelles. Unlike apoptosis and autophagy, necrosis starts with an early permeabilization of the plasma membrane, causing swelling to the cell and leaking of the intracellular content into the extracellular medium.^{105,110}

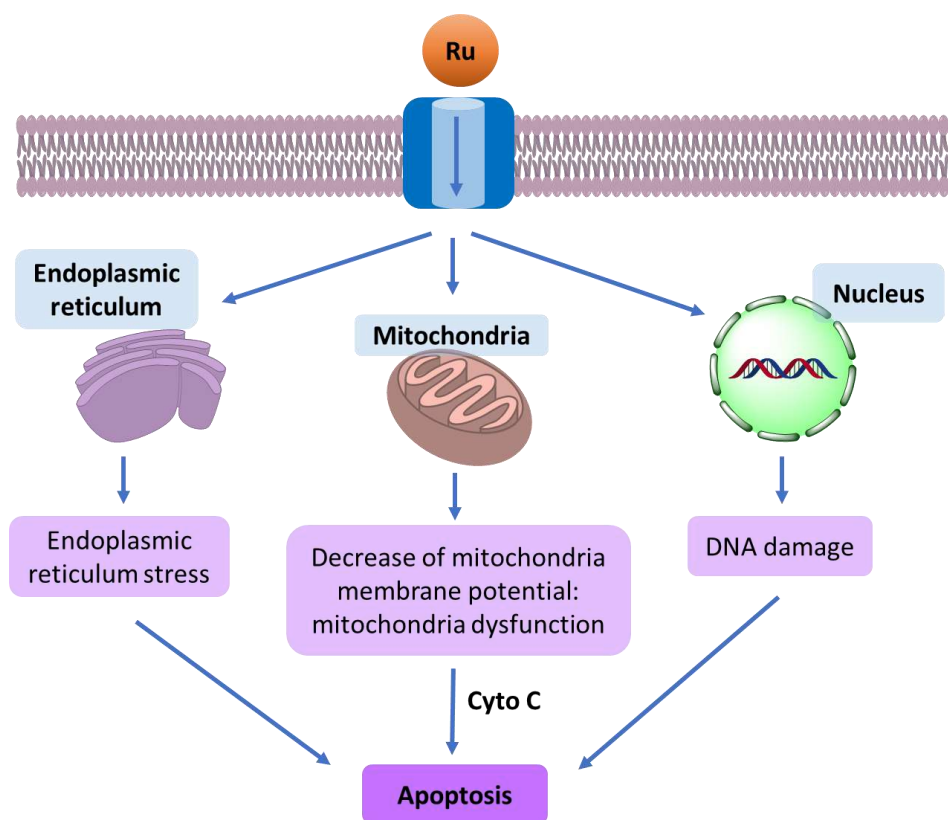


Figure 42. Schematic representation of the targets and the mechanisms of action of ruthenium complexes used as anticancer drugs. Adapted with permission from reference [109].

3.1.2.3. Ruthenium(II) polypyridyl complexes

Ruthenium(II) polypyridyl complexes have gained much attention over last decades in biomedical applications since they exhibit unique photophysical, physicochemical and biological properties. Their great reactivity, specific binding to DNA, high chemical stability and photostability and redox chemistry make them promising anticancer drug candidates. Ruthenium(II) polypyridyl complexes are kinetically inert and usually have an hexacoordinated octahedral structure.^{105,111,112}

Ruthenium(II) polypyridyl complexes are typically coordinated to *N,N*-chelating ligands such as bipyridine, 1,10-phenanthroline and their derivatives. These type of complexes, also known as tris(polypyridyl) complexes, are cationic, lipophilic and have an octahedral geometry. The cellular uptake, the intracellular localization, the lipophilicity, and the cytotoxicity of ruthenium(II) complexes are determined by their ligands. Dwyer *et al.* developed a first series of Ru(II) polypyridyl complexes and demonstrated that the biological activity can change depending on the enantiomer of the ruthenium(II) complex (**Figure 43**).^{105,113}

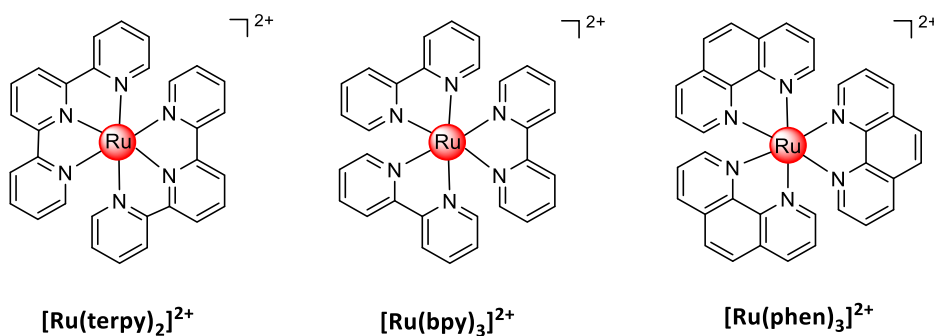


Figure 43. Ru(II) polypyridyl complexes synthesized by Dwyer *et al.*¹¹³

Zeng *et al.* demonstrated that the chirality can also determine the intracellular localization and the anticancer activity of the complexes. The isomer of the chiral Ru(II) complex L-**57** was located in the cell nucleus, while the D-**57** isomer was mainly located in the cytoplasm. The *in vitro* and *in vivo* cytotoxicity of the complexes showed that L-**57** slightly inhibited the growth of MDA-MB-231 breast cancer cells in comparison with D-**57**, which had no significant cytotoxicity against MDA-MB-231 cancer cell.¹¹⁴

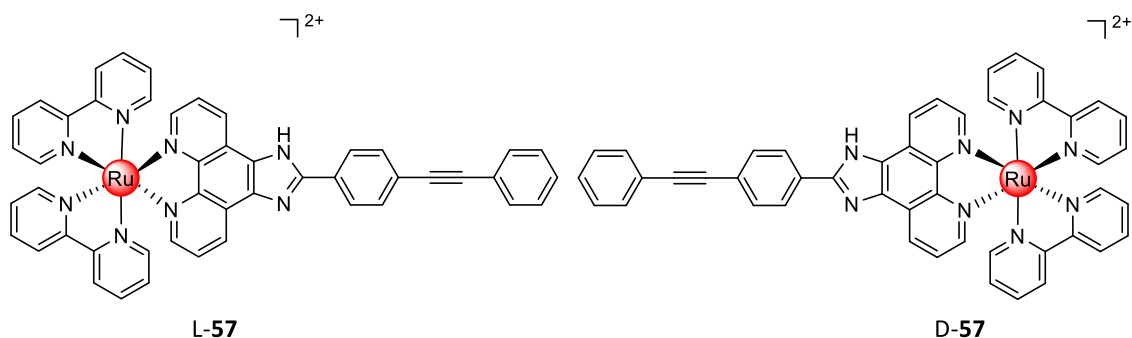


Figure 44. Chemical structures of chiral Ru(II) complexes L-57 and D-57.

Liu *et al.* synthesized compounds **58** and **59** (Figure 45), two novel Ru(II) polypyridyl complexes that enter HeLa cells via an energy-dependent mechanism and accumulate first in lysosomes, but then escape to the nuclei inducing cell apoptosis by inhibiting DNA transcription and translation. It was also demonstrated that the complexes were able to induce mitochondria-mediated apoptosis in HeLa cells through the activation of initiator caspase-9.¹¹⁵ Similar Ru(II) polypyridyl complexes were synthesized by Chen's group, such as complex **60** (Figure 45) that exhibits anticancer activity against MG-63 osteosarcoma and induces mitochondria-mediated apoptosis in cells.¹¹⁶

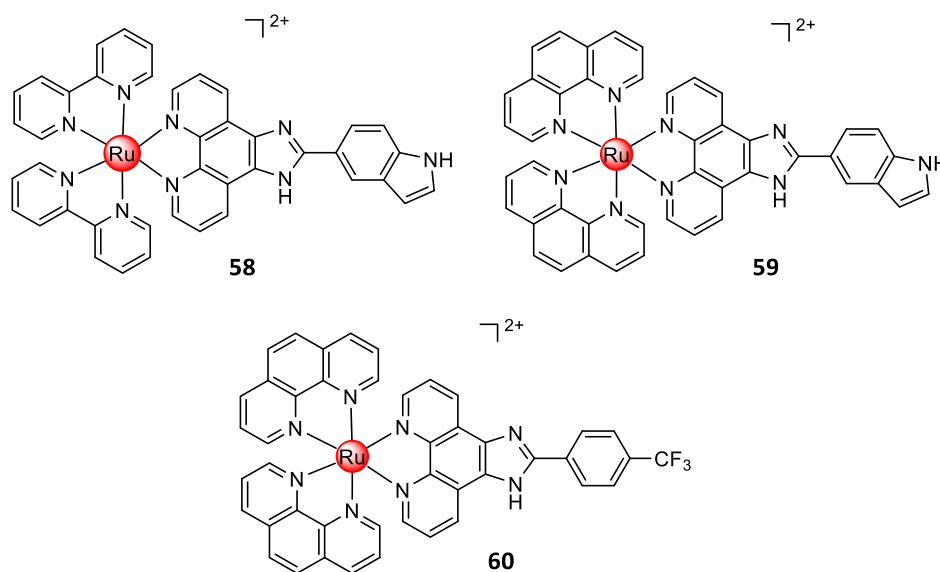


Figure 45. Structures of ruthenium(II) polypyridyl complexes 58-60.

Cyclometalated ruthenium(II) complexes contain *N,C*-chelating ligands. The Ru-C bond is shorter than Ru-N, thus conferring the cyclometalated complexes with higher stability. Interestingly, Chao *et al.* studied the different anticancer activities between coordinatively saturated polypyridyl and cyclometalated ruthenium(II) complexes (**Figure 46**). The cytotoxicity of cyclometalated Ru(II) complexes was nearly an order of magnitude higher than that of cisplatin in cancer cells, while the Ru(II) polypyridyl analogues were found inactive. The greater lipophilicity and cellular uptake, the ability to target the nucleus and the high DNA binding affinity of cyclometalated ruthenium(II) polypyridyl complexes contribute to the improvement of the anticancer activity.¹¹⁷

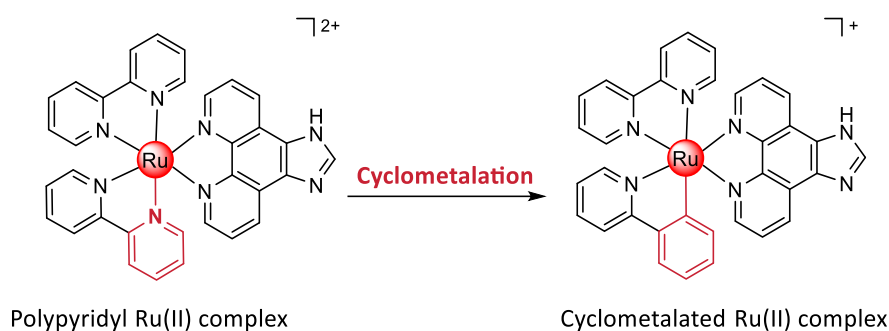


Figure 46. Structures of a Ru(II) polypyridyl complex and its cyclometalated analogue.

Peña *et al.* and Chao *et al.* synthesized a series of cyclometalated Ru(II) complexes (**61**, **62**, **63** and **64**, **Figure 47**) with similar cytotoxicity than cisplatin in HeLa cells. Compound **63** (**Figure 47**) was 6 times more active than cisplatin causing loss of the mitochondrial membrane potential. Increasing the volume of the chelating ligand led to lower IC₅₀ values in HeLa cells due to the stronger interactions with DNA.^{118,119} Later, novel bistridentate ruthenium(II) complexes with anthraquinone substituents as functional ligands were synthesized, being **65** (**Figure 47**) the most effective against hypoxic HeLa cancer cells. This complex had a 46-fold better activity than cisplatin, and accumulated in the mitochondria and the nucleus, inducing the apoptosis via several pathways including DNA and mitochondrial damage.¹²⁰

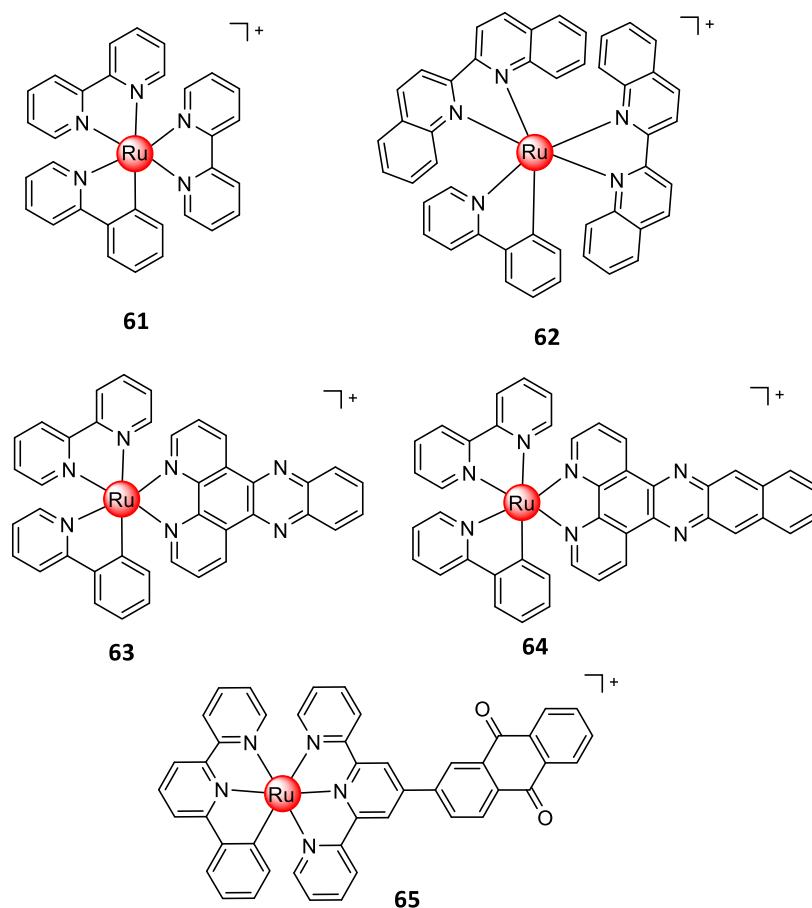


Figure 47. Structures of cyclometalated Ru(II) polypyridyl complexes **61-65**.

3.1.3. Iridium(III) complexes

In recent years, many research efforts have been focused on the development of other metal ions-based complexes with anticancer activity. Even though organoiridium chemistry needs to be further explored, iridium(III) complexes are becoming promising anticancer scaffolds. Iridium is a third-row metal ion which was discovered in 1803 as an impurity in platinum. It has several oxidation states (I, III and IV), coordination numbers (mainly 4 and 6) and coordination geometries.

The first iridium compound investigated as an anticancer agent was based on an Ir(I) complex with square-planar geometry similar to that of cisplatin. However, the +3 oxidation state is much more stable and iridium(III) complexes exhibit many interesting properties that make them ideal as anticancer agents, including high water solubility and relatively accessibility. In addition, the ligands enable fine tuning of the chemical and photophysical properties of iridium(III) complexes. However, the mechanism of action of Ir(III) complexes have only been barely investigated.^{121,122}

3.1.3.1. Cyclometalated iridium(III) complexes

Octahedral Ir(III) cyclometalated complexes containing N^N and N^C chelating ligands have appealing photophysical and biological properties. These complexes are kinetically inert, and their cytotoxicity depends on the cellular uptake efficiency and the composition of the chelating ligands.¹²³

Some cyclometalated iridium(III) complexes can target DNA or inhibit specific proteins.¹²⁴ For example, Pandey *et al.* synthesized a new Ir(III) complex **66 (Figure 48)** which effectively intercalates with DNA. They also demonstrated that **66** binds to the human serum albumin (HSA) protein through the hydrophobic residues located within the subdomain IIA cavity.¹²⁵

As previously stated, mitochondria is one of the main targets for the design of new anticancer agents because these organelles are essential for cellular energy production and participate in many other cellular activities such as the production of ROS. Interestingly, many Ir(III) complexes tend to accumulate in mitochondria, increasing the generation of ROS, which leads to the depolarization of the mitochondrial membrane potential.¹²⁴ Wang *et al.* synthesized the cyclometalated iridium(III) complex **67 (Figure 48)** that has anticancer activity against MDA-MB-231 human breast cancer cells. The complex accumulates in the mitochondria and induces apoptosis through a mitochondria-mediated apoptotic pathway.¹²⁶

Mao *et al.* described a new Ir(III) cyclometalated complex **68 (Figure 48)** with potential anticancer activity. Their compound exhibits activity against human lung adenocarcinoma A549 cells and accumulate specifically in the mitochondria. Mechanistic studies showed that the complex induced loss of mitochondrial membrane potential, inhibition of mitochondrial respiration and an elevation of the generation of ROS leading to apoptosis and/or autophagy.¹²⁷ Recently, Mao's group has reported a novel cyclometalated iridium(III) complex, compound **69 (Figure 48)**, used as anion transporter for cancer therapy. The complex accumulates in lysosomes and exhibits higher activity compared to cisplatin towards different cancer cells lines (HeLa, lung adenocarcinoma A549, cisplatin-resistant A549R, human hepatoma HepG2 and human metastatic breast cancer MDAMB-231). The mechanism of cell death seems to be related to the generation of ROS which triggers apoptosis.¹²⁸

Theranostic anticancer agents are also promising candidates for chemotherapy due to the ability of combining real-time monitoring and anticancer properties. Mao *et al.* synthesized a mitochondria-targeted cyclometalated iridium(III) complex appended with a coumarin moiety (**70**). Their compound (**Figure 48**) showed higher activity than cisplatin in several cancer cells, including cisplatin resistant A549 cells. Simultaneously, the morphological changes in mitochondria could be monitored due to the theranostic character of the anticancer agent.¹²⁹

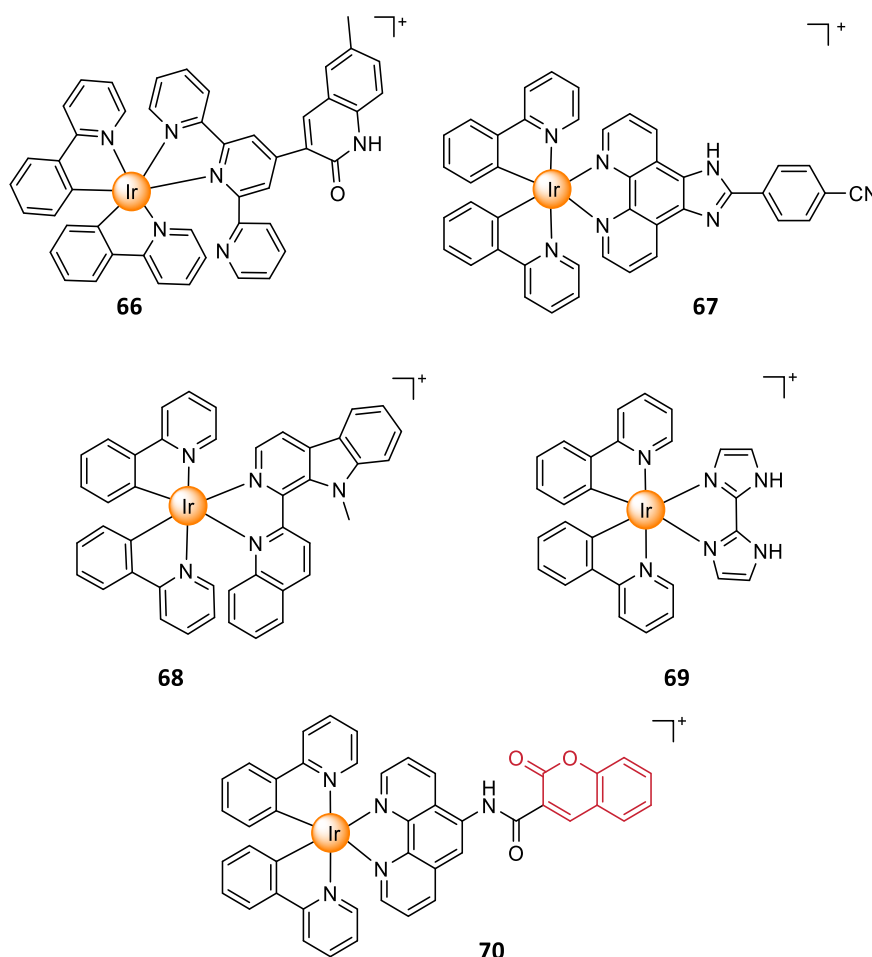


Figure 48. Chemical structures of cyclometalated Ir(III) complexes **66-70**.

Ruiz *et al.* described a series of luminescent cyclometalated iridium(III) antitumor agents containing a benzimidazole N^N ligand with an ester group as a handle for further functionalization (**71-72**, **Figure 49**). These compounds showed very high cytotoxicity towards A2780 cells, A2780cis cells, breast tumor cell lines MDA-MB-231 and MFC-7. Confocal luminescent imaging experiments showed that the complexes were located in the actin cortex predominantly.¹³⁰

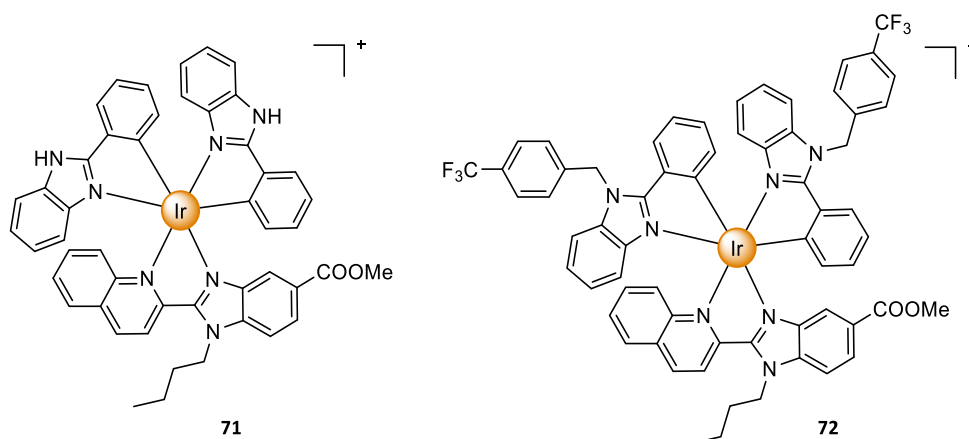


Figure 49. Structures of cyclometalated Ir(III) complexes **71-72**.

3.2. Photosensitizers based on metal complexes

As previously introduced in **Section 2.6**, PDT is a promising modality for the treatment of cancer and, consequently, the development of novel photosensitizers with improved properties has become an important research topic in the medicinal field. In such a context, transition metal complexes have attracted great interest in recent years as promising photosensitizers for PDT applications. The heavy atom effect of metal complexes mediates strong spin-orbital coupling (SOC), which increases the lifetime of the triplet excited state (T_1), thereby providing more time to interact with the ground-state molecular oxygen (3O_2). As a consequence, high singlet oxygen quantum yields can be obtained with metal complexes. In addition, PSs based on metal complexes exhibit several attractive photophysical properties, including large Stokes' shifts and a higher photostability compared with PSs based on conventional organic fluorophores.⁹¹

3.2.1. Ruthenium(II) polypyridyl complexes as PDT agents

The use of ruthenium(II) complexes as photosensitizers in PDT has been explored by several research groups due to their favorable chemical and photophysical properties. Ru(II) complexes exhibit long excited-state lifetimes and large quantum yields for the triplet-state formation. As described in **Section 3.1.2**, these complexes usually have an hexacoordinated octahedral structure, and their properties can be easily modified through the appropriate selection of ligands that better suit the needs of PDT. Some of the properties that can be fine-tuned through the modification of the ligands include aqueous solubility, cellular uptake efficiency, charge distribution, and targeting ability.⁴

In this context, it is worth noting that McFarland and coworkers reported the first Ru(II)-based photosensitizer, TLD1433, a Ru(II) polypyridyl complex (**Figure 50**), to enter human clinical trials for the treatment of non-muscle invasive bladder cancer (NMIBC) with PDT. Some studies suggest that the polythiophene ligand in the complex could be the responsible for the generation of ROS by both type I and type II PDT mechanisms.^{4,83,131}

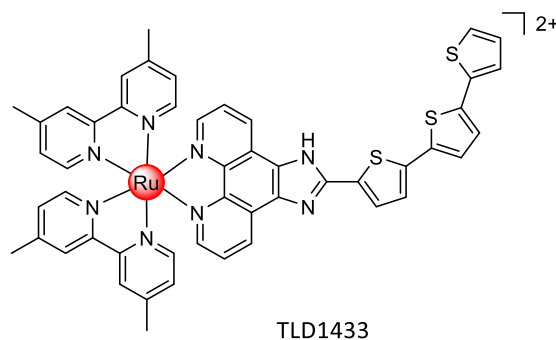


Figure 50. Structure of ruthenium-based PS TLD1433.

However, despite of this success, most PSs based on Ru(II) complexes still have some drawbacks, such as activation with shorter wavelengths of light (e.g., UV or blue light) and low photoactivity under low oxygen concentration, thus limiting their use for treating deep-seated or large hypoxic tumors. To overcome some of these problems, Gasser *et al.* reported a long wavelength absorbing Ru(II) polypyridine complex (**73, Figure 51**) that produces phototoxicity with very low IC₅₀ values, in the micromolar to nanomolar range, upon 510, 540, or 595 nm irradiation. Specifically, it was found to localize in the cytoplasm of HeLa cells disturbing the mitochondrial respiration and glycolysis processes.¹³²

Williams *et al.* designed a new Ru(II) complex (**74, Figure 51**) that could be efficiently taken up into cells via an energy dependent mechanism due to the presence of the lipophilic aromatic pdppz ([2,3-h]dipyrido[3,2-a:2',3'-c]phenazine) ligand. The complex was localized in several organelles including mitochondria, lysosomes, and ER. The Ru(II) complex **74** was found nontoxic to HeLa cells in the dark; however, upon visible light irradiation showed significant photoactivity with low micromolar IC₅₀ values. It was also demonstrated that upon light activation, the complex induces DNA photocleavage and caspase-dependent and ROS-dependent apoptosis.¹³³

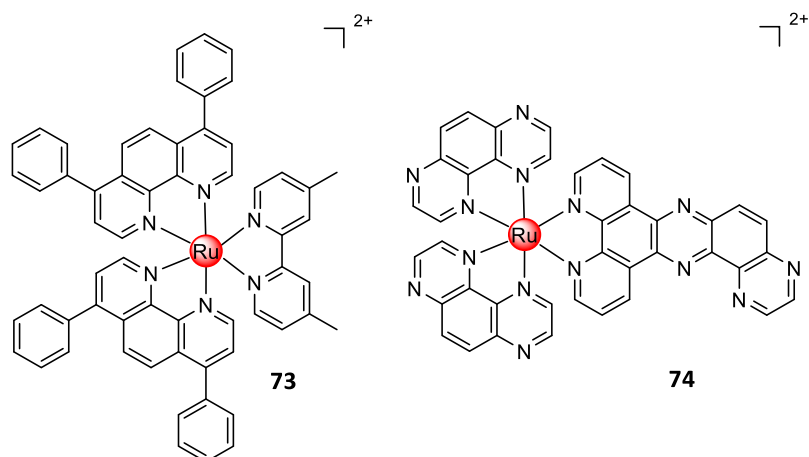


Figure 51. Structures of Ru(II) polypyridyl PSs **73** and **74**.

Ru(II) complexes containing tridentate ligands are hardly studied for PDT applications since they usually exhibit low quantum yields and very short excited-state lifetimes, thus not being able to generate ROS. However, Glazer *et al.* described bis-tridentate Ru(II) complexes with applicability in PDT by modifying the photophysical properties through the inclusion of N-heterocyclic carbene (NHC) ligands (**75-77**, **Figure 52**). The NHC Ru(II) complexes were found to have superior excited-state lifetimes, $^1\text{O}_2$ production, and photocytotoxicity than the corresponding terpyridine Ru(II) complexes analogues $[\text{Ru}(\text{tpy})_2]^{2+}$.¹³⁴

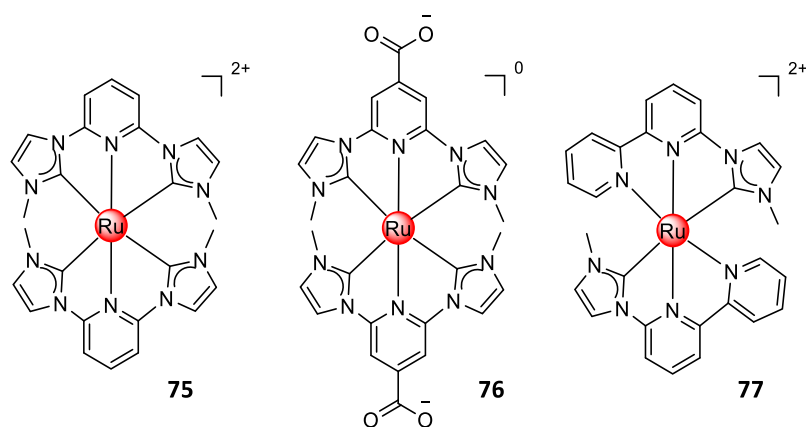


Figure 52. Structures of NHC Ru(II) complexes **75-77**.

Common fluorophores can be efficiently excited to the triplet excited state, via the heavy atom effect which improves the ISC processes. In this context, BODIPY derivatives have been described as efficient triplet PSs when conjugated to heavy transition metal complexes, thus being useful for PDT treatments.⁸¹ Zhao *et al.* synthesized a BODIPY-containing Ru(II) polypyridyl complex, compound **78** (**Figure 53**), that showed a strong absorption in the visible region. Although the fluorescence of the BODIPY ligand was almost entirely quenched, conjugate **78** exhibited room temperature phosphorescence and a long triple excited state upon visible light excitation with an efficient singlet oxygen quantum yield ($\Phi_{\Delta}=0.93$).¹³⁵

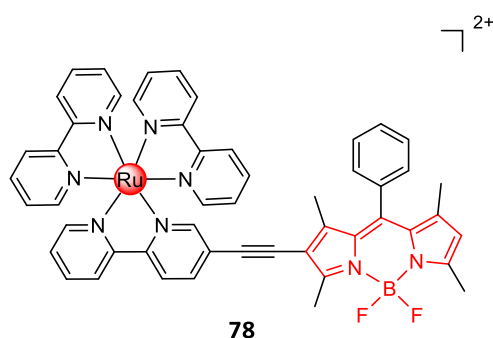


Figure 53. Structures of Ru(II) based PSs **78**.

McFarland *et al.* investigated the influence of increasing the π -conjugation of the cyclometalating ligand on the photophysical properties and cytotoxic activity of four Ru(II) complexes (compounds **79-82**, **Figure 54**). Three of the Ru(II) compounds derived from the smallest C^N ligands (compounds **79-81**), were found highly cytotoxic to cancer cells in the dark, and light activation did not significantly increase the toxicity. Remarkably, the complex incorporating the most π -expansive cyclometalating ligand, compound **82**, exhibited no cytotoxicity in the dark but was found highly phototoxic to cancer cells, with high PI values (>1.400 in SK-MEL-28 cells and >410 in HL-60 cells).¹³⁶

Recently, McFarland's group also described a new family NIR-absorbing PSs based on a Ru(II) tris-heteroleptic scaffold [Ru(NNN)(NN)(L)]Cl_n. As an example of this family of NIR-PSs, compound **83** (**Figure 54**) was the most efficient producer of ¹O₂ ($\Phi_{\Delta} = 93\%$ with excitation at 630 nm, and $\Phi_{\Delta} = 86\%$ with excitation at 753 nm). Compound **83** was found highly phototoxic toward several melanoma cell lines and, as an example, it exhibited relatively high PI values in SK-MEL-28 under different light treatments (PI = 360 with visible light, PI = 132 with 633 nm light and, PI = 67 with 733 nm light).¹³⁷

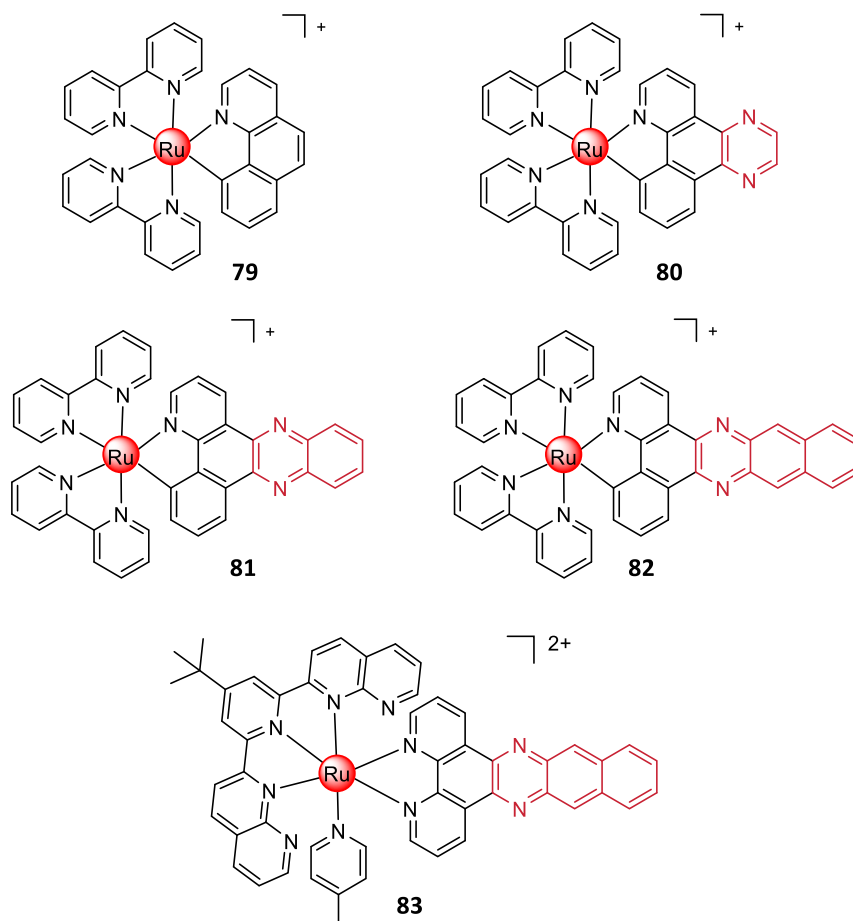


Figure 54. Ru(II) complexes studied by McFarland's group.

As previously stated (**Section 2.6**), to date most reported photosensitizers generate ROS via the type II process, which strongly depends on the oxygen concentration. However, as tumors tend to grow in an exaggerated way, a common feature is a low level of oxygen, which produces an hypoxic tumor microenvironment and, as a consequence it limits the phototoxic potential of a wide range of PSs. Hence, it is important to develop type I PSs, which are less oxygen-dependent and generate other ROS than singlet oxygen. Huang *et al.* reported a coumarin-modified cyclometalated Ru(II) polypyridyl PS, compound **84** (**Figure 55**), which exhibits a stronger absorption band in the visible region than the equivalent coumarin-free complex. This compound exhibited an excellent PDT effect under normoxia and especially under hypoxia. The good results under hypoxia were attributed to the formation of highly oxidative hydroxyl radicals (OH[•]) via an electron transfer from the excited PS to substrates upon light irradiation.¹³⁸ Recently, Zhao *et al.* described a type I PS based on a triphenylamine-modified Ru(II) complex (**85**, **Figure 55**), which efficiently produced superoxide anions (O₂^{•-}) and hydroxyl radicals (OH[•]).¹³⁹

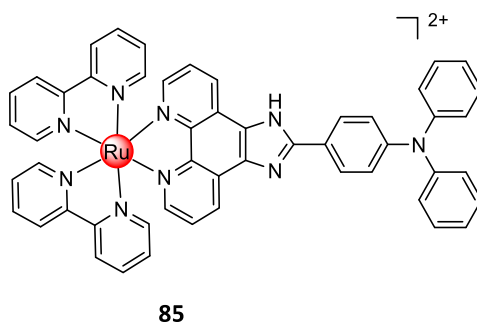
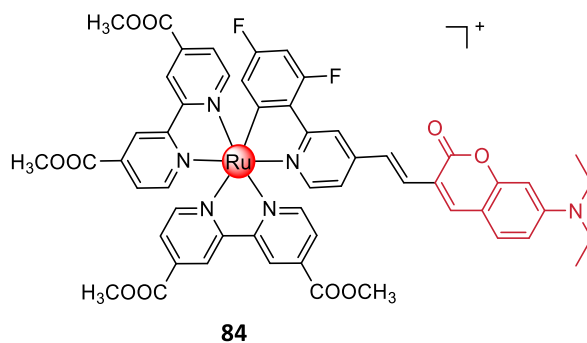


Figure 55. Structure of Ru(II) complexes **84-85**.

Ruiz *et al.* described a family of Ru(II) polypyridyl complexes which act as green light activatable photosensitizers (PSs). The most active complexes were **86** and **87** (**Figure 56**) which exhibited high PI values under hypoxia conditions (PI > 750 for **86** and PI > 550 for **87**) in HeLa cells. Under normoxia, H₂O₂ was found to be the main photogenerated species by the complexes; however, under hypoxia, **86** and **87** generated H₂O₂ and also O₂^{•-}.¹⁴⁰

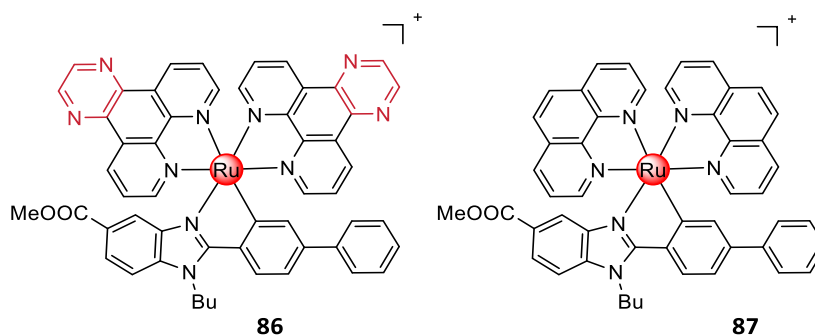


Figure 56. Structures of Ru(II) complexes **86-87**.

3.2.2. Iridium(III) complexes as PDT agents

Although iridium(III) complexes have shown excellent anticancer activities and a great potential to overcome cisplatin drawbacks (see **Section 3.1.3**), they remain in the early stages to become optimal photosensitizers for PDT. However, cyclometalated Ir(III) complexes possess several excellent photophysical and photochemical properties required for PDT treatment such as large Stokes' shifts, high phosphorescent quantum yields, a great capability of color-tuning, high singlet oxygen quantum yields, and high photostability. In additions, all of these properties can be also tuned by modifying the coordination ligands.^{4,81}

Sun *et al.* described a tricationic bis(terpyridine) Ir(III) complex **88** (**Figure 57**) which exhibits a broad absorption band in the visible region which is extended to the NIR region. The presence of the pyrenyl moiety, a strong donor group, at the position 4 of the terpyridine ligand, was observed to be the responsible to increase the lifetime of the lowest triplet excited state leading to a higher generation of singlet oxygen ($\Phi_{\Delta} = 0.81$). Complex **88** showed a good phototoxicity toward SK-MEL-28 and MCF-7 cells *in vitro*, and additionally could also inhibit tumor growth after 12 days of PDT treatment *in vivo*.¹⁴¹ Mao *et al.* designed an Ir(III)-nitroxide cyclometalated complex (**89**, **Figure 57**) that acted as a mitochondria-targeted PS for PDT with high phototoxicity and selectivity for cancer cells. Upon light irradiation, the Ir(III) complex caused mitochondrial dysfunction and, in addition, it also allowed a real-time monitoring of the morphological changes of mitochondria, being useful as a PDT theranostic agent.¹⁴²

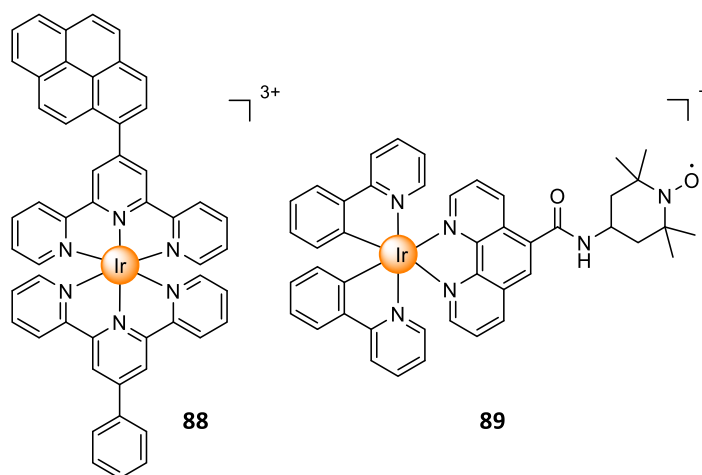


Figure 57. Structure of Ir(III) based PSs **88** and **89**.

As described in **Section 2.3**, Rhodamine is a common organic dye used in bioimaging applications due to its great properties such as high photostability, excellent fluorescent quantum yields and long excitation and emission wavelengths.⁸¹ Wong *et al.* reported a family of photosensitizers based on the combination of rhodamine dye and a luminescent Ir(III) complex, being compound **90**, represented in **Figure 58**, a representative example. The combination of both moieties increased the selectivity of the conjugate for the mitochondria. Complex **90** showed selectivity for cancer cells, low dark cytotoxicity, high molar absorptivity, and high photostability.¹⁴³

Ortiz *et al.* reported new PSs based on the combination of a cyclometalated Ir(III) complex with a BODIPY moiety. They demonstrated that a direct attachment of the BODIPY dye to the acetylacetonate ligand of the Ir(III) complex, for example compound **91** (**Figure 58**), led to an improvement of the required properties for PDT, including low dark cytotoxicity, high photocytotoxicity and efficient singlet oxygen generation upon visible-light irradiation ($\Phi_{\Delta} = 0.86$).¹⁴⁴

Zhao *et al.* designed a coumarin-modified Ir(III) complex, compound **92** (**Figure 58**), which shows an intense absorption band in the visible region compared with the very weak band for the parent cyclometalated Ir(III) complex. The compound showed a long-lived triplet excited states, which allowed to enhance the production of singlet oxygen.¹⁴⁵

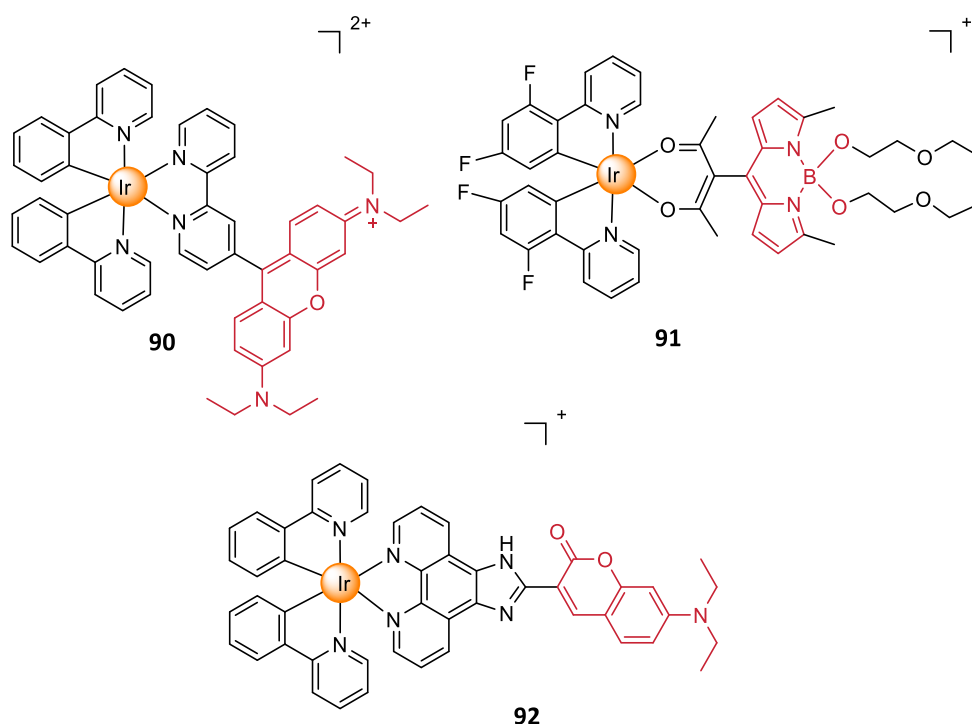


Figure 58. Structure of rhodamine-based, BODIPY-based and coumarin-based Ir(III) complex PSs, **90**, **91** and **92** respectively.

With the aim of extending the absorption of Ir(III) complexes to the phototherapeutic window, Zhao's group synthesized four styryl-BODIPY-containing heteroleptic C^N Ir(III) complexes (**93-96**, **Figure 59**) which showed absorption in the far-red and NIR region (wavelengths from 644 nm to 729 nm), NIR luminescent (700–800 nm), and long-lived triplet excited states (92.5–156.5 μs). The conjugates were designed by connecting the two moieties through a C≡C bond, with the aim of inducing efficient ISC. Interestingly, the quantum yield of ¹O₂ generation in MeOH:H₂O (4:1) for **93** and **94** were 70% and 35%, respectively; however, **95** and **96** did not show ¹O₂ production. The authors suggested that the failure of **95** and **96** to produce singlet oxygen in aqueous solution may be caused by the quenching of the triplet states by the intramolecular charge transfer (ICT).¹⁴⁶

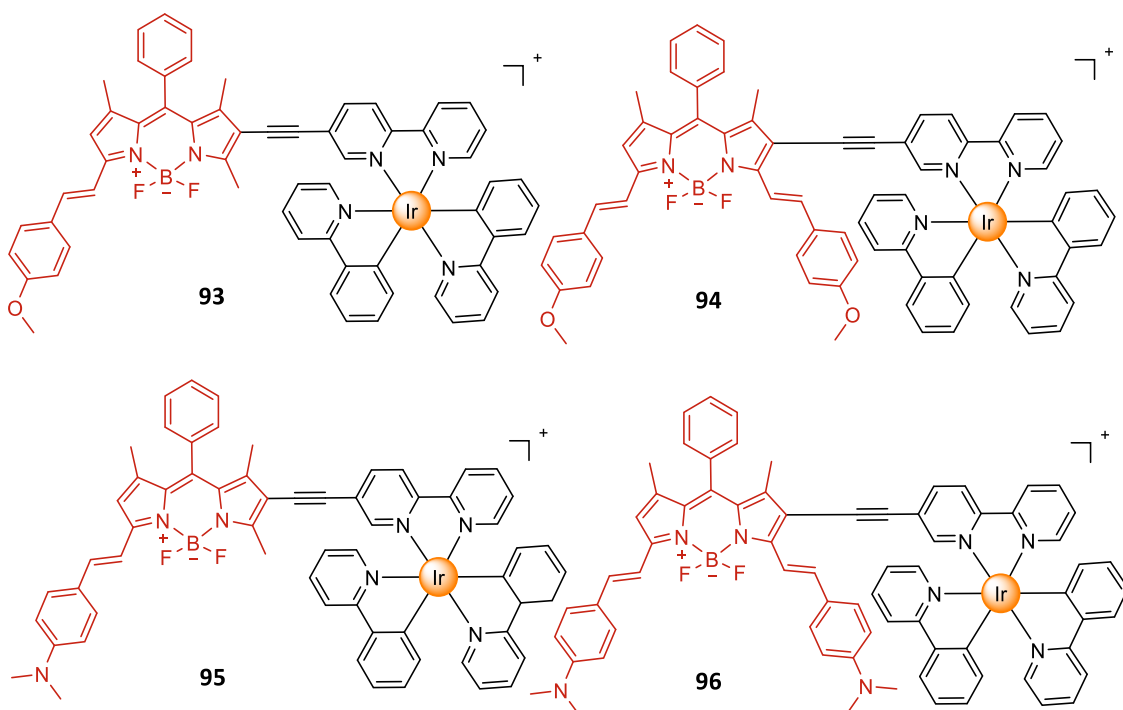


Figure 59. BODIPY-based Ir(III) complexes synthesized by Zhao's group.

In view of the difficulties associated to the treatment of hypoxic tumors, there is an increasing interest in developing type I PSs based on iridium(III) complexes. Elias *et al.* developed an Ir(III) based complex able to oxidize biomolecules under hypoxic conditions via type I processes. The Ir(III) complex (**97**, **Figure 60**), which accumulates in mitochondria, induces rapid apoptotic cell death upon light excitation. The complex **97** combines a low singlet oxygen quantum yield and the ability to induce type I oxygen-independent processes. In addition, the destruction of a 3D tumor spheroids was achieved at a concentration of 20 μM.¹⁴⁷

The groups of Gasser, Sadler and Chao described a highly oxidative mitochondria-targeted Ir(III) photocatalyst (**98**, **Figure 60**) with high phototoxicity towards both normoxic and hypoxic cancer cells. Complex **98** photocatalytically oxidizes NADH (an important coenzyme in living cells) generating NAD• radicals in biological conditions. **98** was highly photostable with a long phosphorescence lifetime. Upon irradiation, complex **98** induces NADH depletion and perturbs electron transfer pathways in mitochondria by reduction of cytochrome c, inducing redox imbalance and leading to apoptotic cancer cell death.¹⁴⁸

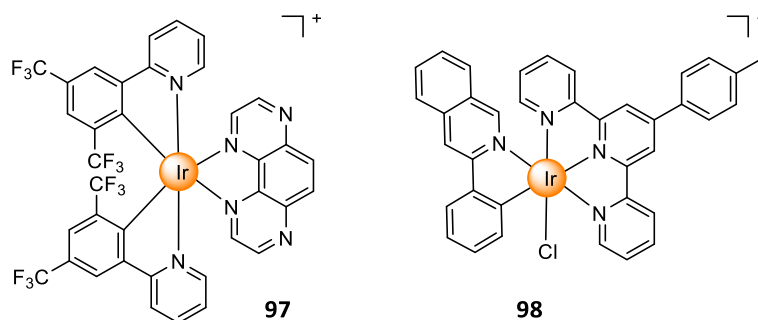


Figure 60. Structure of Ir(III) complexes **97-98** used as type I PDT agents.

Directing the intracellular targeting of a PS can also make a difference in hypoxic PDT. Huang *et al.* evaluated the PDT efficacies under hypoxic conditions of two biscyclometalated Ir(III) complexes (**99** and **100**, **Figure 61**) which presented different organelle-targeting abilities and specifically accumulated in the mitochondria and lysosomes of living cells, respectively. The mitochondria-targeting compound **99** exhibited an enhanced therapeutic effect compared to the lysosome-targeted PDT agent. The authors suggested that the mitochondria-targeted PS inhibited mitochondrial respiration, producing higher levels of intramitochondrial oxygen, which is beneficial for PDT in hypoxic tumor cells.¹⁴⁹

Similarly, He's group reported two new benzothiophenylisoquinoline(btiq)-derived cyclometalated Ir(III) complexes (**101-102**, **Figure 61**). Compound **101** bearing a mitochondria-targeting triphenyl phosphite (TPP) group was designed for mitochondria accumulation. The complexes demonstrated a type I PDT process and caused photoinduced ferroptosis in hypoxic tumor cells. Interestingly, under photoirradiation and in hypoxic conditions, the mitochondria-targeting Ir(III) complex **101**, caused mitochondria membrane potential collapse, ATP production suppression and induced cell apoptosis. The synergetic effect of ferroptosis and apoptosis caused by **101** led to a better PDT effectivity compared to **102** in inhibiting MCF-7, PANC-1 and MDA-MB-231 cells under hypoxia.¹⁵⁰

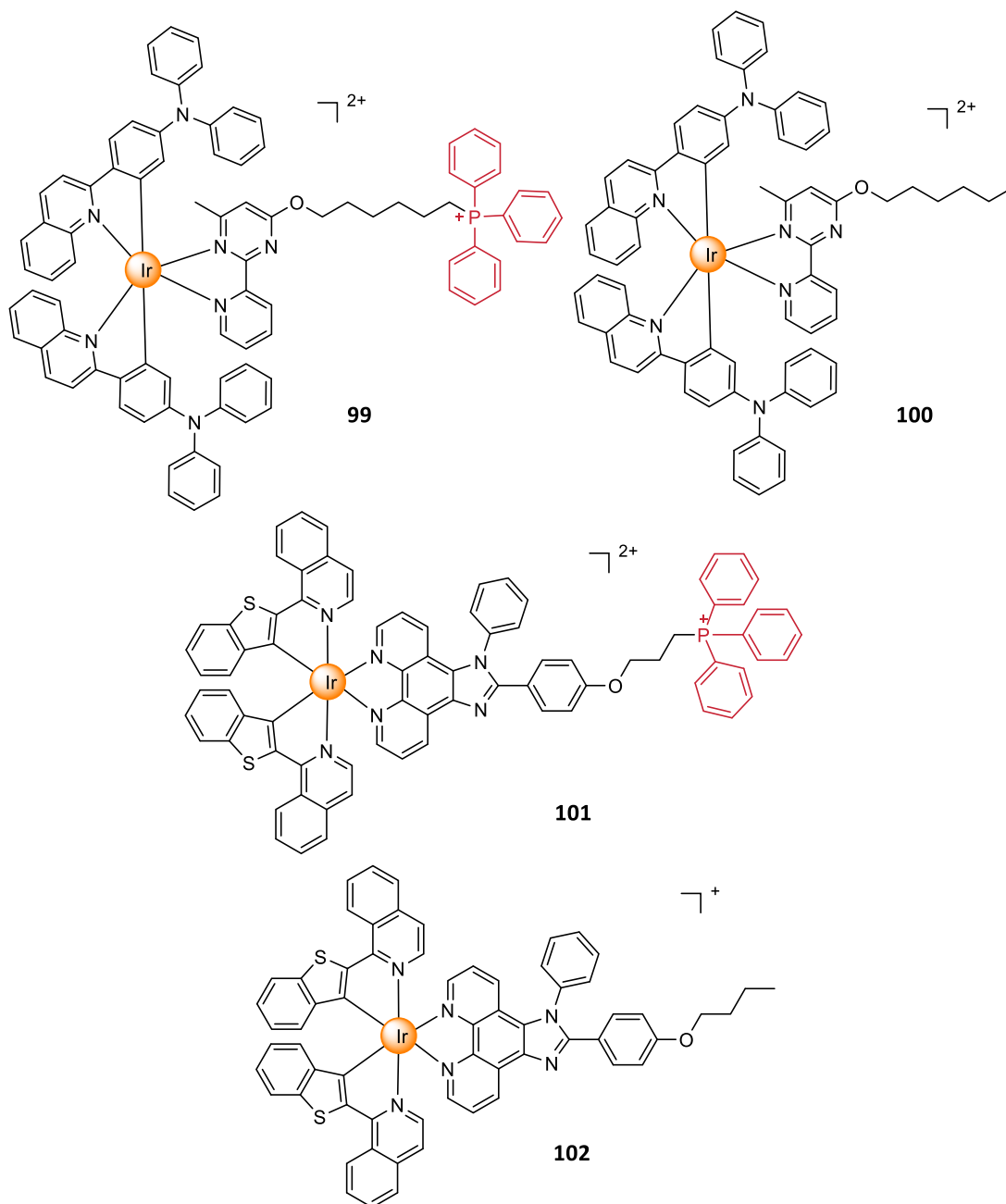


Figure 61. Structures of cyclometalated Ir(III) complexes **99-102**.

Espino *et al.* described new Ir(III) biscyclometalated complexes with the formula $[\text{Ir}(\text{C}^{\wedge}\text{N})_2(\text{N}^{\wedge}\text{N}')]\text{Cl}$ (**Figure 62**), where $\text{N}^{\wedge}\text{N}'$ ligands contain a carboxamide-substituted benzimidazole fragment and thiazolyl (**103**) or pyridyl (**104**) rings. The UV-vis spectra of the complexes showed strong absorption bands in the UV region 250-315 nm and emission maxima between 450-605 nm. All complexes generated $^1\text{O}_2$ in aerated solutions upon irradiation. The efficacy of these Ir(III) complexes for cancer PDT was explored in PC-3 prostate cancer cells. All compounds were moderately cytotoxic in the dark but their photoactivity was markedly increased upon blue light irradiation (EC_{50} values of 2.7 and 2.4 μM for **103** and **104**, respectively). The complexes were efficiently taken up by cells through endocytosis and accumulated in mitochondria, where after irradiation the membrane potential was altered, thus compromising mitochondrial function and activating cell death by apoptosis.¹⁵¹

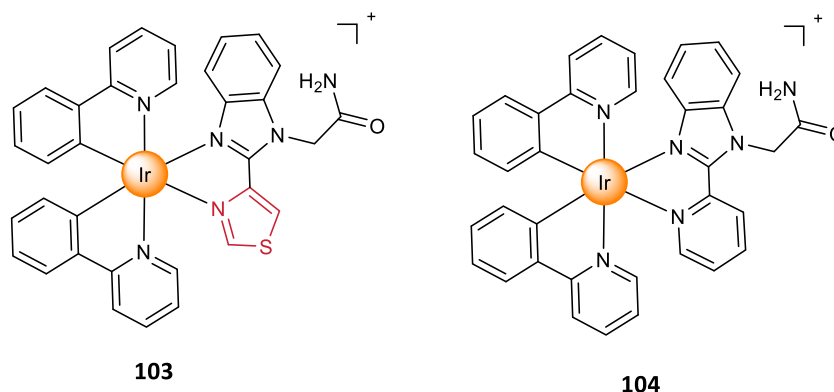


Figure 62. Structures of cyclometalated Ir(III) complexes **103-104**.

Brabec and Ruiz studied the cytotoxicity in cancer cells of five biscyclometalated Ir(III) complexes (**105-109**, **Figure 63**) presenting different degrees of conjugation on the polypyridyl ligand. The less lipophilic complexes, **105** and **106**, exhibited the highest toxicity in A2780, HeLa, and MCF-7 cancer cells, and they were found more efficient than platinum-based drugs. It was demonstrated that the Ir(III) complexes kill cancer cells by targeting endoplasmic reticulum and by inhibiting protein translation. Importantly, the cytotoxic effect could be potentiated by more than two orders of magnitude upon irradiation with visible light ($\lambda = 420$ nm), which was attributed to intracellular ROS generation.¹⁵²

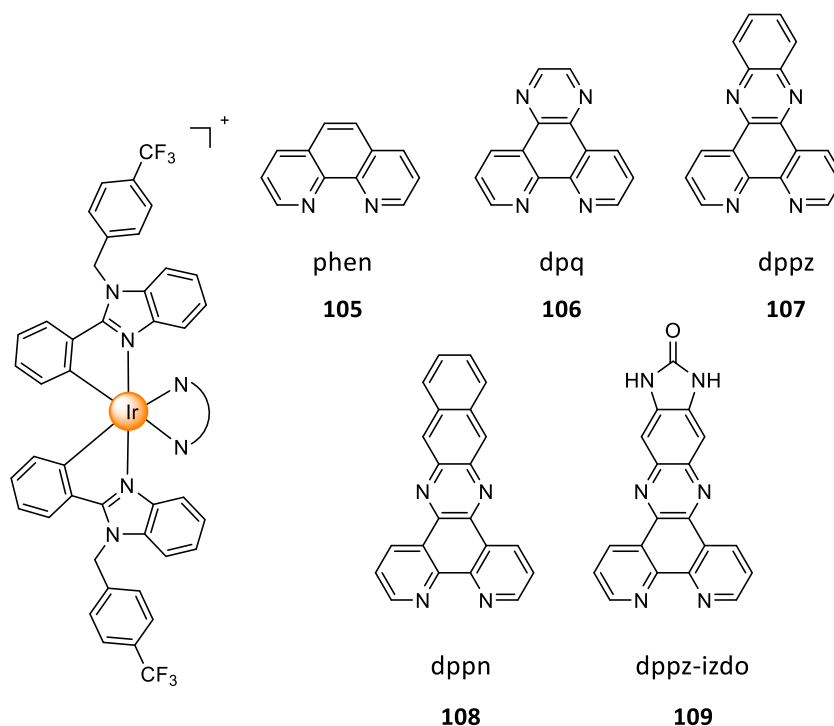


Figure 63. Structures of Ir(III) complexes developed by Brabec and Ruiz's groups.

Qin *et al.* developed an iridium complex (**110**, **Figure 64**), containing a β -carboline alkaloid ligand, which was found cytotoxic under dark conditions (IC_{50} values of around $1 \mu M$) against several cancer cell lines. Markedly, the anticancer activity was significantly improved in the presence of blue light (425 nm) with a PI value of 120. Complex **110** induced an increase in intracellular ROS levels, reduction in ATP production, mitochondrial DNA damage and an increase in lipid peroxidation levels.¹⁵³

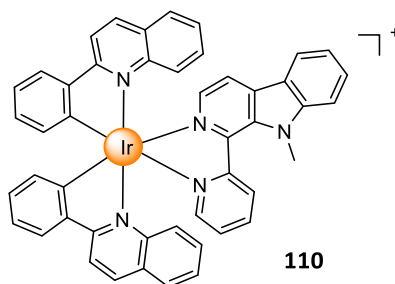


Figure 64. Structure of Ir(III) complex described by Qin *et al.*

4. Objectives

The general objective of this Thesis was to develop novel far-red to NIR-emitting organic fluorophores based on the COUPY coumarin scaffold with enhanced photophysical and physicochemical properties for fluorescence imaging, as well as to investigate their conjugation to receptor-binding peptides for tumor targeting, and to metal complexes for PDT applications. Targeted-fluorescent imaging agents are promising tools for cancer detection since they provide a noninvasive way for recognizing cancer cells with high sensitivity and specificity. In addition, the conjugation of small organic fluorophores and metal complexes offers a good opportunity to develop novel luminescent PDT anticancer agents with innovative mechanisms of action by taking advantage of their well-established photophysical properties and anticancer activities, respectively.

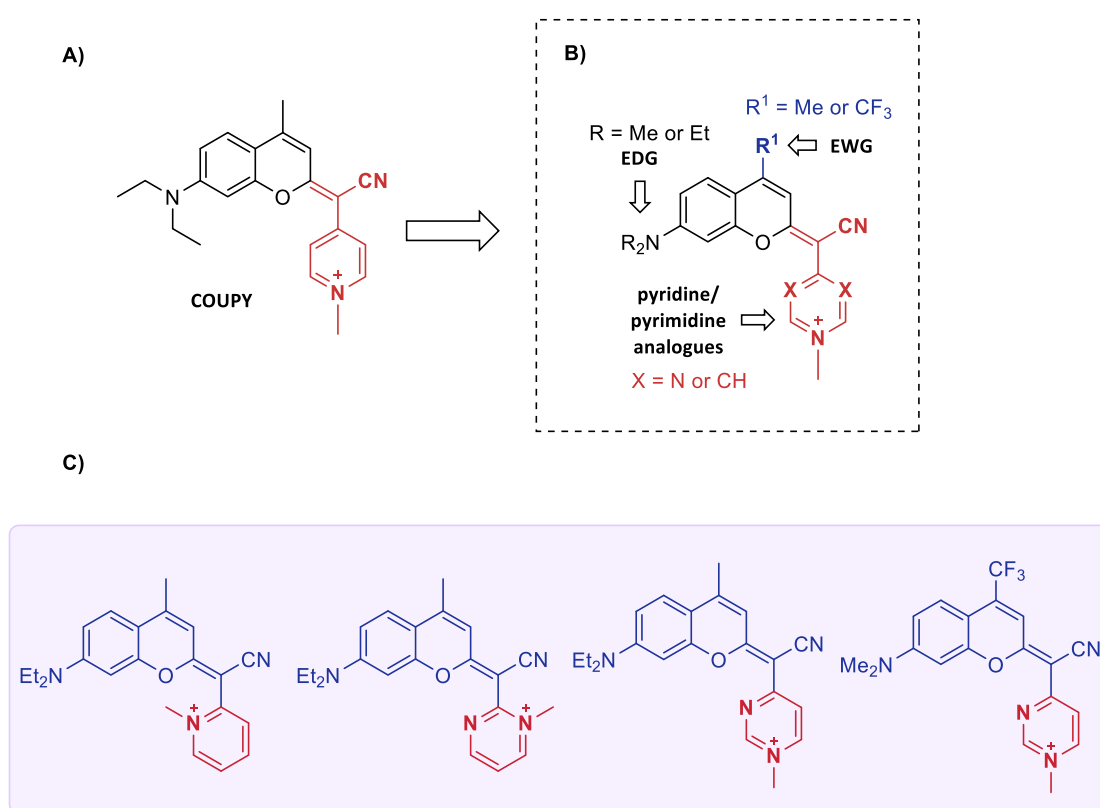
Specifically, the following two main goals were proposed:

1. Development of novel coumarin-based COUPY fluorophores for bioimaging applications.

Nowadays, far-red and NIR fluorescent dyes are essential tools in fluorescence imaging since they can offer accurate images of targeted tissues. For this reason, there is a need for developing novel fluorescent probes based on small organic molecules for clinical applications. In this context, ligand-targeted fluorescent probes operating in the phototherapeutic window (650 – 900 nm) are particularly useful for cancer diagnosis, as well as for guiding surgical procedures in fluorescence-guided surgery.

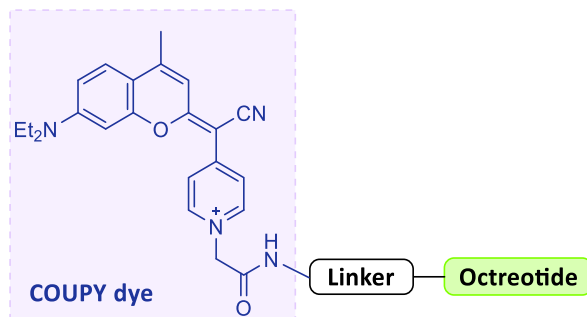
In our research group, we have developed a new class of low molecular weight coumarin-based fluorophores, named COUPY, in which the carbonyl group of the electron-withdrawing lactone in conventional coumarins was replaced by a cyano(4-pyridinium)methylene moiety (**A**, **Scheme 2**) with the aim of increasing the push-pull character of the chromophores. COUPY dyes exhibit several interesting photophysical properties, including emission in the far-red/NIR region, large Stokes' shifts, high photostability, and moderate to high brightness. In addition, COUPY fluorophores show excellent cell membrane permeability and accumulate selectively in mitochondria and nucleoli.

Based on these antecedents, the first main goal of this Thesis was to design new COUPY derivatives to establish additional structure-photophysical property relationships. In our group, we had previously investigated how the photophysical properties of COUPY dyes can be modified through the introduction of electron-withdrawing groups either at the 4-position of the coumarin skeleton or via *N*-alkylation of the pyridine heterocycle. In addition, the effect of replacing the electron-donating *N,N*-dialkylamino group at the 7-position by azetidino was also studied. In this work, we will investigate how the replacement of the *para*-pyridinium moiety in the original COUPY fluorophores with different nitrogenated heterocycles, partnering with two different substituents at the 4-position of the coumarin skeleton (**B, Scheme 2**), influences both the photophysical properties of the compounds and the subcellular accumulation.



Scheme 2. (A) Structure of a representative COUPY dye. (B) Rational design of the new coumarin-based fluorophores developed in this work. (C) Structure of the COUPY fluorophores synthesized in this work.

As previously mentioned, the use of targeted fluorescent probes has become increasingly important in biomedicine since they can provide precise and specific information on the diagnosis of cancer. For this purpose, in order to overcome some of the limitations of conventional organic dyes, such as poor specificity for cancer cells, we will explore the conjugation of COUPY dyes to targeting ligands based on octreotide (**Scheme 3**), a FDA-approved cyclooctapeptide with a high affinity and specificity towards somatostatin subtype 2 receptor (SSTR2), which is overexpressed in several types of malignant cells.



Scheme 3. Schematic representation of the approach used for labeling a peptide with a COUPY dye.

This first main goal can be divided in the following specific objectives:

- 1.1 To design, synthesize and characterize novel coumarin-based COUPY fluorophores by replacing the *para*-pyridinium moiety with several heterocycles, including *ortho*- and *para*-pyrimidinium substitution (**C**, **Scheme 2**).
- 1.2 To study the photophysical properties (absorption and emission spectra, molar absorption coefficients (ϵ), fluorescence quantum yields (Φ_F) and photostability) of the newly synthesized COUPY derivatives in several solvents of different polarities and compare with those of the parent *para*-pyridine-containing coumarins.
- 1.3 To investigate the cellular uptake of the compounds in living HeLa cells by using confocal microscopy and compare with that of the parent COUPY fluorophores.
- 1.4 To perform colocalization experiments with specific organelle markers and determine the subcellular localization of COUPY dyes.
- 1.5 To design, synthesize and characterize conjugatable versions of COUPY fluorophores incorporating the required functional groups for enabling conjugation to octreotide peptide.

- 1.6 To synthesize COUPY-octreotide conjugates following a stepwise Fmoc/tBu solid-phase peptide strategy by labelling octreotide on the solid support with the appropriate COUPY derivatives, either via amide-bond formation or by Cu(I)-catalyzed azide-alkyne cycloaddition reactions (**Scheme 3**).
- 1.7 To study the photophysical properties (absorption and emission spectra, molar absorption coefficients (ϵ), and fluorescence quantum yields (Φ_F)) of COUPY-octreotide conjugates in aqueous solution and compare with those of their respective coumarin precursors.
- 1.8 To investigate the cellular uptake of a representative COUPY-octreotide conjugate by confocal microscopy in SSTR2-overexpressing HeLa cells and compare with that of two octreotide derivatives labelled with two commercially available fluorophores, 5(6)-carboxyfluorescein and a rhodamine dye (Atto-Rho12).

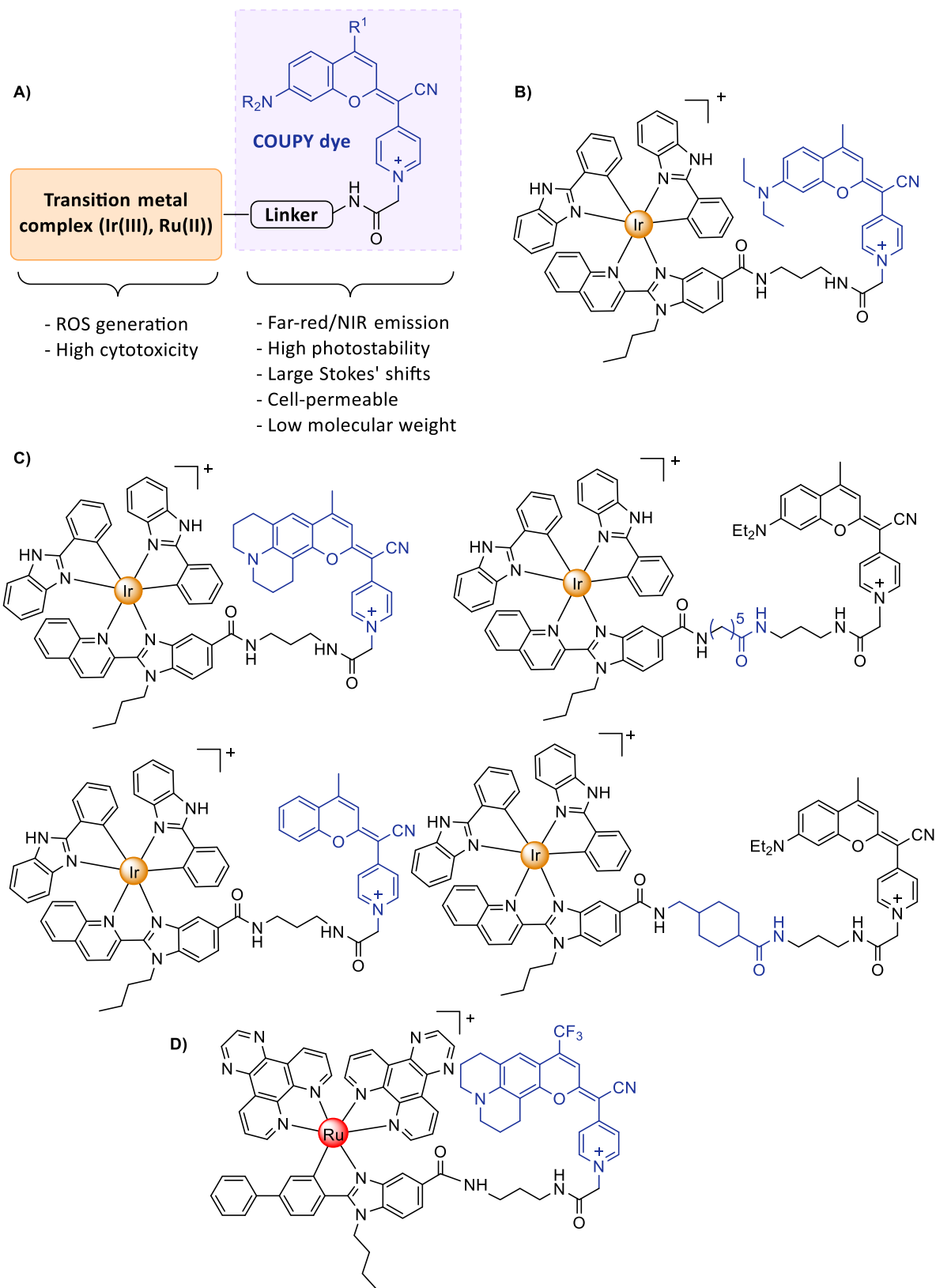
The results concerning the objectives 1.1 - 1.4 regarding the synthesis and characterization of the new COUPY fluorophores (**C**, **Scheme 2**) and the study of their photophysical properties and cellular uptake in living HeLa cells are described in the publication A (A. Rovira *et al. J. Org. Chem.* **2020**, 85, 6086–6097) of Chapter Ia.

The synthesis and characterization of COUPY-octreotide conjugates (**Scheme 3**) (objectives 1.5 - 1.8) can be found in the publication B (A. Rovira *et al. J. Org. Chem.* **2019**, 84, 1808–1817) of Chapter Ib.

2. Conjugation of COUPY fluorophores to Ir(III) and Ru(II) complexes for anticancer photodynamic therapy.

PDT is a promising medical technique for the treatment of cancer since it offers several advantages compared to conventional oncological approaches, including selectivity, noninvasiveness, and few adverse side effects. However, the efficacy of a PDT treatment depends on the selection of a suitable PS, that should be nontoxic in the dark, but produce extensive phototoxicity after irradiation with light of a range of wavelengths between 650-900 nm for an optimal tissue penetration and minimal photodamage. Moreover, an ideal PS should exhibit tumor selectivity and high quantum yield of ROS generation, both of singlet oxygen and of Type I ROS to allow the treatment of deep-seated hypoxic tumors. In this regard, although metal complexes are considered promising PDT agents since they can efficiently generate ROS under visible light irradiation, they use to exhibit high dark cytotoxicity.

To address some of these issues, the second main goal of this Thesis was focused on the development of novel PSs based on the conjugation of COUPY dyes and metal complexes, with the aim of combining the excellent photophysical properties of organic fluorophores and the well-known anticancer activities of transition metal complexes (**A**, **Scheme 4**).



Scheme 4. (A) General structure of a PS based on the conjugation of a COUPY dye and a transition metal complex. (B) Ir(III)-COUPY conjugate described in Publication C. (C) Ir(III)-COUPY conjugates described in Publication D. (D) Ru(II)-COUPY conjugate described in Chapter IIc.

This second main goal can be divided into the following specific objectives:

- 2.1 To design, synthesize and characterize a conjugatable version of a COUPY dye containing a linker with a free primary amino group.
- 2.2 To design, synthesize and characterize a novel PS agent by conjugating a far-red emitting COUPY fluorophore to a highly potent cyclometalated Ir(III) complex bearing a carboxylic acid group (**B, Scheme 4**).
- 2.3 To study the photophysical and photochemical properties (absorption and emission spectra, molar absorption coefficient (ϵ), fluorescence or phosphorescence quantum yield (Φ_F/Φ_P), fluorescence or phosphorescence lifetime (τ_F/τ_P), singlet oxygen quantum yield (Φ_Δ) and superoxide generation) and photostability of the Ir(III)-COUPY conjugate in several solvents of different polarities and viscosities and compare with those of the unconjugated moieties (Ir(III) complex and COUPY fluorophore).
- 2.4 To investigate the cellular uptake and Ir accumulation of the Ir(III)-COUPY conjugate in HeLa cells by confocal microscopy and ICP-MS, respectively.
- 2.5 To study the *in vitro* antitumor activity of the Ir(III)-COUPY conjugate in HeLa cells both in the dark and after irradiation with visible light, either with blue (420 nm) or green light (550 nm), in normoxic and hypoxic conditions. To identify the specific ROS involved in cell death.
- 2.6 To design, synthesize and characterize a series of new COUPY derivatives incorporating different structural modifications within the coumarin skeleton and their corresponding conjugatable versions.
- 2.7 To synthesize and characterize new Ir(III)-COUPY conjugates combining the parent cyclometalated Ir(III) complex and several COUPY derivatives connected through flexible or rigid linkers (**C, Scheme 4**) to investigate how the structural modifications within the COUPY scaffold and the linker influence the photophysical, photochemical and biological properties of the resulting PSs compared with the parent Ir(III)-COUPY conjugate.
- 2.8 To study the photophysical and photochemical properties (absorption and emission spectra, molar absorption coefficients (ϵ), fluorescence or phosphorescence quantum yields (Φ_F/Φ_P), fluorescence or phosphorescence lifetime (τ_F/τ_P), singlet oxygen quantum yields (Φ_Δ) and superoxide generation) of the new Ir(III)-COUPY conjugates along with the new COUPY dyes in several solvents of different polarity and compare with those of the original Ir(III)-COUPY conjugate.

- 2.9 To investigate the cellular uptake and Ir accumulation of the new Ir(III)-COUPY conjugates in HeLa cells by confocal microscopy and ICP-MS, respectively.
- 2.10 To study the photocytotoxicity of the new Ir(III)-COUPY conjugates upon green light irradiation (520 nm) towards cervix and melanoma cancer cells in normoxic conditions, and towards ovarian cancer cells in both normoxic and hypoxic conditions.
- 2.11 To design, synthesize and characterize a novel PS agent based on the conjugation of a NIR-emitting COUPY fluorophore to a cyclometalated Ru(II) polypyridyl complex (**D, Scheme 4**).
- 2.12 To study the photophysical and photochemical properties (absorption and emission spectra, fluorescence quantum yield (Φ_F), singlet oxygen quantum yield (Φ_Δ) and superoxide generation) of the new Ru(II)-COUPY conjugate along with the NIR-emitting COUPY dye.
- 2.13 To investigate the cellular uptake of the Ru(II)-COUPY conjugate in HeLa cells by confocal microscopy.
- 2.14 To study the photocytotoxicity of the new Ru(II)-COUPY conjugate upon irradiation with red light (633 nm) towards cervix cancer cells in normoxic conditions.

The results concerning the synthesis, characterization and biological evaluation of the first Ir(III)-COUPY conjugate (**B, Scheme 4**) are reported in the publication C (V. Novohradsky *et al. Angew. Chem. Int. Ed.* **2019**, 58, 6311-6315) of Chapter IIa.

The synthesis and characterization of the four Ir(III)-COUPY conjugates (**C, Scheme 4**) for establishing structure-activity relationships and the investigation how the structural modifications within the COUPY scaffold influence the photophysical, photochemical and biological properties of the resulting PSs are described in the publication D (A. Rovira *et al. Manuscript under preparation*) of Chapter IIb.

The synthesis, characterization and preliminary biological evaluation of the new Ru(II)-COUPY conjugate (**D, Scheme 4**) are described in Chapter IIc (non-published results).

5. References

- (1) Sung, H.; Ferlay, J.; Siegel, R. L.; Laversanne, M.; Soerjomataram, I.; Jemal, A.; Bray, F. Global Cancer Statistics 2020: GLOBOCAN Estimates of Incidence and Mortality Worldwide for 36 Cancers in 185 Countries. *CA: Cancer J. Clin.* **2021**, *71*, 209–249. <https://doi.org/10.3322/caac.21660>.
- (2) Singh, Y.; Palombo, M.; Sinko, P. Recent Trends in Targeted Anticancer Prodrug and Conjugate Design. *Curr. Med. Chem.* **2008**, *15*, 1802–1826. <https://doi.org/10.2174/092986708785132997>.
- (3) Holohan, C.; van Schaeybroeck, S.; Longley, D. B.; Johnston, P. G. Cancer Drug Resistance: An Evolving Paradigm. *Nat. Rev. Cancer* **2013**, *13*, 714–726. <https://doi.org/10.1038/nrc3599>.
- (4) Wu, Y.; Li, S.; Chen, Y.; He, W.; Guo, Z. Recent Advances in Noble Metal Complex Based Photodynamic Therapy. *Chem. Sci.* **2022**, *13*, 5085–5106. <https://doi.org/10.1039/d1sc05478c>.
- (5) Kratz, F.; Müller, I. A.; Ryppa, C.; Warnecke, A. Prodrug Strategies in Anticancer Chemotherapy. *ChemMedChem.* **2008**, *3*, 20–53. <https://doi.org/10.1002/cmdc.200700159>.
- (6) Mahato, R.; Tai, W.; Cheng, K. Prodrugs for Improving Tumor Targetability and Efficiency. *Adv. Drug Deliv. Rev.* **2011**, *63*, 659–670. <https://doi.org/10.1016/j.addr.2011.02.002>.
- (7) Fass, L. Imaging and Cancer: A Review. *Mol. Oncol.* **2008**, *2*, 115–152. <https://doi.org/10.1016/j.molonc.2008.04.001>.
- (8) Zhu, S.; Tian, R.; Antaris, A. L.; Chen, X.; Dai, H. Near-Infrared-II Molecular Dyes for Cancer Imaging and Surgery. *Adv. Mater.* **2019**, *31*, 1–25. <https://doi.org/10.1002/adma.201900321>.
- (9) Hong, G.; Antaris, A. L.; Dai, H. Near-Infrared Fluorophores for Biomedical Imaging. *Nat. Biomed. Eng.* **2017**, *1*, 1–22. <https://doi.org/10.1038/s41551-016-0010>.
- (10) Calixto, G. M. F.; Bernegossi, J.; de Freitas, L. M.; Fontana, C. R.; Chorilli, M. Nanotechnology-Based Drug Delivery Systems for Photodynamic Therapy of Cancer: A Review. *Molecules* **2016**, *21*, 1–18. <https://doi.org/10.3390/molecules21030342>.

- (11) Baggaley, E.; Weinstein, J. A.; Williams, J. A. G. Lighting the Way to See inside the Live Cell with Luminescent Transition Metal Complexes. *Coord. Chem. Rev.* **2012**, *256*, 1762–1785. <https://doi.org/10.1016/j.ccr.2012.03.018>.
- (12) Zhang, K. Y.; Yu, Q.; Wei, H.; Liu, S.; Zhao, Q.; Huang, W. Long-Lived Emissive Probes for Time-Resolved Photoluminescence Bioimaging and Biosensing. *Chem. Rev.* **2018**, *118*, 1770–1839. <https://doi.org/10.1021/acs.chemrev.7b00425>.
- (13) Lakowicz, J. R. Principles of Fluorescence Spectroscopy, 3rd Edition, Joseph R. Lakowicz, Editor; **2006**. <https://doi.org/10.1007/978-0-387-46312-4>.
- (14) Escobedo, J. O.; Rusin, O.; Lim, S.; Strongin, R. M. NIR Dyes for Bioimaging Applications. *Curr. Opin. Chem. Biol.* **2010**, *14*, 64–70. <https://doi.org/10.1016/j.cbpa.2009.10.022>.
- (15) Zhang, R. R.; Schroeder, A. B.; Grudzinski, J. J.; Rosenthal, E. L.; Warram, J. M.; Pinchuk, A. N.; Eliceiri, K. W.; Kuo, J. S.; Weichert, J. P. Beyond the Margins: Real-Time Detection of Cancer Using Targeted Fluorophores. *Nat. Rev. Clin. Oncol.* **2017**, *14*, 347–364. <https://doi.org/10.1038/nrclinonc.2016.212>.
- (16) Owens, E. A.; Henary, M.; El Fakhri, G.; Choi, H. S. Tissue-Specific Near-Infrared Fluorescence Imaging. *Acc. Chem. Res.* **2016**, *49*, 1731–1740. <https://doi.org/10.1021/acs.accounts.6b00239>.
- (17) Haque, A.; Faizi, M. S. H.; Rather, J. A.; Khan, M. S. Next Generation NIR Fluorophores for Tumor Imaging and Fluorescence-Guided Surgery: A Review. *Bioorg. Med. Chem.* **2017**, *25*, 2017–2034. <https://doi.org/10.1016/j.bmc.2017.02.061>.
- (18) Lavis, L. D.; Raines, R. T. Bright Ideas for Chemical Biology. *ACS Chem. Biol.* **2008**, *3*, 142–155. <https://doi.org/10.1021/cb700248m>.
- (19) Karpovich, D. S.; Blanchard, G. J. Relating the Polarity-Dependent Fluorescence Response of Pyrene to Vibronic Coupling. Achieving a Fundamental Understanding of the Py Polarity Scale. *J. Phys. Chem.* **1995**, *99*, 3951–3958. <https://doi.org/10.1021/j100012a014>.
- (20) Jiao, Y.; Zhu, B.; Chen, J.; Duan, X. Fluorescent Sensing of Fluoride in Cellular System. *Theranostics* **2015**, *5*, 173–187. <https://doi.org/10.7150/thno.9860>.
- (21) Stefanachi, A.; Leonetti, F.; Pisani, L.; Catto, M.; Carotti, A. Coumarin: A Natural, Privileged and Versatile Scaffold for Bioactive Compounds. *Molecules* **2018**, *23*, 250–284. <https://doi.org/10.3390/molecules23020250>.

- (22) Sun, W. C.; Gee, K. R.; Haugland, R. P. Synthesis of Novel Fluorinated Coumarins: Excellent UV-Light Excitable Fluorescent Dyes. *Bioorg. Med. Chem. Lett.* **1998**, *8*, 3107–3110. [https://doi.org/10.1016/S0960-894X\(98\)00578-2](https://doi.org/10.1016/S0960-894X(98)00578-2).
- (23) Lavis, L. D.; Raines, R. T. Bright Building Blocks for Chemical Biology. *ACS Chem. Biol.* **2014**, *9*, 855–866. <https://doi.org/10.1021/cb500078u>.
- (24) Cosa, G.; Focsaneanu, K.-S.; McLean, J. R. N.; McNamee, J. P.; Scaiano, J. C. Photophysical Properties of Fluorescent DNA-Dyes Bound to Single- and Double-Stranded DNA in Aqueous Buffered Solution. *Photochem. Photobiol.* **2001**, *73*, 585–599. [https://doi.org/10.1562/0031-8655\(2001\)0730585PPOFDD2.0.CO2](https://doi.org/10.1562/0031-8655(2001)0730585PPOFDD2.0.CO2).
- (25) Yan, F.; Fan, K.; Bai, Z.; Zhang, R.; Zu, F.; Xu, J.; Li, X. Fluorescein Applications as Fluorescent Probes for the Detection of Analytes. *TrAC - Trends Anal. Chem.* **2017**, *97*, 15–35. <https://doi.org/10.1016/j.trac.2017.08.013>.
- (26) Jain, P. K.; Joshi, H. Coumarin: Chemical and Pharmacological Profile. *J. Appl. Pharm. Sci.* **2012**, *2*, 236–240. <https://doi.org/10.7324/JAPS.2012.2643>.
- (27) Sun, X. Y.; Liu, T.; Sun, J.; Wang, X. J. Synthesis and Application of Coumarin Fluorescence Probes. *RSC Adv.* **2020**, *10*, 10826–10847. <https://doi.org/10.1039/c9ra10290f>.
- (28) Tasior, M.; Kim, D.; Singha, S.; Krzeszewski, M.; Ahn, K. H.; Gryko, D. T. π -Expanded Coumarins: Synthesis, Optical Properties and Applications. *J. Mater. Chem. C* **2015**, *3*, 1421–1446. <https://doi.org/10.1039/c4tc02665a>.
- (29) Sharma, S. J.; Sekar, N. Deep-Red/NIR Emitting Coumarin Derivatives - Synthesis, Photophysical Properties, and Biological Applications. *Dyes Pigm.* **2022**, *202*, 110306–110364. <https://doi.org/10.1016/j.dyepig.2022.110306>.
- (30) Gordo, J.; Parola, A. J.; Lima, C.; Branco, P. S. Convenient Synthesis of 3-Vinyl and 3-Styryl Coumarins. *Org. Lett.* **2011**, *13*, 5112–5115. <https://doi.org/10.1021/ol201983u>.
- (31) Jagtap, A. R.; Satam, V. S.; Rajule, R. N.; Kanetkar, V. R. The Synthesis and Characterization of Novel Coumarin Dyes Derived from 1,4-Diethyl-1,2,3,4-Tetrahydro-7-Hydroxyquinoxalin-6-Carboxaldehyde. *Dyes Pigm.* **2009**, *82*, 84–89. <https://doi.org/10.1016/j.dyepig.2008.11.007>.

- (32) Jagtap, A. R.; Satam, V. S.; Rajule, R. N.; Kanetkar, V. R. Synthesis of Highly Fluorescent Coumarinyl Chalcones Derived from 8-Acetyl-1,4-Diethyl-1,2,3,4-Tetrahydro-7H-Pyrano[2,3-g]Quinoxalin-7-One and Their Spectral Characteristics. *Dyes Pigm.* **2011**, *91*, 20–25. <https://doi.org/10.1016/j.dyepig.2011.01.011>.
- (33) Singh, S.; Begoyan, V. v.; Tanasova, M.; Waters, K.; Seel, M.; Pandey, R. Coumarins: Spectroscopic Measurements and First Principles Calculations of C4-Substituted 7-Aminocoumarins. *J. Phys. Org. Chem.* **2018**, *31*, 1–9. <https://doi.org/10.1002/poc.3852>.
- (34) Jun, Y. W.; Sarkar, S.; Singha, S.; Reo, Y. J.; Kim, H. R.; Kim, J. J.; Chang, Y. T.; Ahn, K. H. A Two-Photon Fluorescent Probe for Ratiometric Imaging of Endogenous Hypochlorous Acid in Live Cells and Tissues. *Chem. Commun.* **2017**, *53*, 10800–10803. <https://doi.org/10.1039/c7cc05834a>.
- (35) Li, C.; Wang, D.; Xue, W.; Peng, J.; Wang, T.; Zhang, Z. Synthesis and Photophysical Properties of Vertically π -Expanded Coumarins. *Dyes Pigm.* **2021**, *186*, 108956–108964. <https://doi.org/10.1016/j.dyepig.2020.108956>.
- (36) Akchurin, I. O.; Yakhutina, A. I.; Bochkov, A. Y.; Solovjova, N. P.; Medvedev, M. G.; Traven, V. F. Novel Push-Pull Fluorescent Dyes – 7-(Diethylamino)Furo- and Thieno[3,2-c]Coumarins Derivatives: Structure, Electronic Spectra and TD-DFT Study. *J. Mol. Struct.* **2018**, *1160*, 215–221. <https://doi.org/10.1016/j.molstruc.2018.01.086>.
- (37) Li, Q.; Liu, W.; Wu, J.; Zhou, B.; Niu, G.; Zhang, H.; Ge, J.; Wang, P. Deep-Red to near-Infrared Fluorescent Dyes: Synthesis, Photophysical Properties, and Application in Cell Imaging. *Spectrochim. Acta A Mol Biomol. Spectrosc.* **2016**, *164*, 8–14. <https://doi.org/10.1016/j.saa.2016.03.042>.
- (38) Chevalier, A.; Renard, P. Y.; Romieu, A. Straightforward Access to Water-Soluble Unsymmetrical Sulfoxanthene Dyes: Application to the Preparation of Far-Red Fluorescent Dyes with Large Stokes' Shifts. *Chem. Eur. J.* **2014**, *20*, 8330–8337. <https://doi.org/10.1002/chem.201402306>.
- (39) Eördögh, Á.; Steinmeyer, J.; Peewasan, K.; Schepers, U.; Wagenknecht, H. A.; Kele, P. Polarity Sensitive Bioorthogonally Applicable Far-Red Emitting Labels for Postsynthetic Nucleic Acid Labeling by Copper-Catalyzed and Copper-Free Cycloaddition. *Bioconjug. Chem.* **2016**, *27*, 457–464. <https://doi.org/10.1021/acs.bioconjchem.5b00557>.

- (40) Zhang, Y.; Song, N.; Li, Y.; Yang, Z.; Chen, L.; Sun, T.; Xie, Z. Comparative Study of Two Near-Infrared Coumarin-BODIPY Dyes for Bioimaging and Photothermal Therapy of Cancer. *J. Mater. Chem. B* **2019**, *7*, 4717–4724. <https://doi.org/10.1039/c9tb01165j>.
- (41) Fournier, L.; Aujard, I.; le Saux, T.; Maurin, S.; Beaupierre, S.; Baudin, J. B.; Jullien, L. Coumarinylmethyl Caging Groups with Redshifted Absorption. *Chem. Eur. J.* **2013**, *19*, 17494–17507. <https://doi.org/10.1002/chem.201302630>.
- (42) Gandioso, A.; Palau, M.; Nin-Hill, A.; Melnyk, I.; Rovira, C.; Nonell, S.; Velasco, D.; García-Amorós, J.; Marchán, V. Sequential Uncaging with Green Light Can Be Achieved by Fine-Tuning the Structure of a Dicyanocoumarin Chromophore. *ChemistryOpen* **2017**, *6*, 375–384. <https://doi.org/10.1002/open.201700067>.
- (43) Gandioso, A.; Contreras, S.; Melnyk, I.; Oliva, J.; Nonell, S.; Velasco, D.; García-Amorós, J.; Marchán, V. Development of Green/Red-Absorbing Chromophores Based on a Coumarin Scaffold That Are Useful as Caging Groups. *J. Org. Chem.* **2017**, *82*, 5398–5408. <https://doi.org/10.1021/acs.joc.7b00788>.
- (44) Gandioso, A.; Bresolí-Obach, R.; Nin-Hill, A.; Bosch, M.; Palau, M.; Galindo, A.; Contreras, S.; Rovira, A.; Rovira, C.; Nonell, S.; Marchán, V. Redesigning the Coumarin Scaffold into Small Bright Fluorophores with Far-Red to Near-Infrared Emission and Large Stokes Shifts Useful for Cell Imaging. *J. Org. Chem.* **2018**, *83*, 1185–1195. <https://doi.org/10.1021/acs.joc.7b02660>.
- (45) Grimm, J. B.; English, B. P.; Choi, H.; Muthusamy, A. K.; Mehl, B. P.; Dong, P.; Brown, T. A.; Lippincott-Schwartz, J.; Liu, Z.; Lionnet, T.; Lavis, L. D. Bright Photoactivatable Fluorophores for Single-Molecule Imaging. *Nat. Methods* **2016**, *13*, 985–988. <https://doi.org/10.1038/nmeth.4034>.
- (46) Gandioso, A.; Palau, M.; Bresolí-Obach, R.; Galindo, A.; Rovira, A.; Bosch, M.; Nonell, S.; Marchán, V. High Photostability in Nonconventional Coumarins with Far-Red/NIR Emission through Azetidinylation. *J. Org. Chem.* **2018**, *83*, 11519–11531. <https://doi.org/10.1021/acs.joc.8b01422>.
- (47) Ashley, E. A. Towards Precision Medicine. *Nat. Rev. Genet.* **2016**, *17*, 507–522. <https://doi.org/10.1038/nrg.2016.86>.
- (48) Muro, S. Challenges in Design and Characterization of Ligand-Targeted Drug Delivery Systems. *J. Control. Release* **2012**, *164*, 125–137. <https://doi.org/10.1016/j.jconrel.2012.05.052>.
- (49) Srinivasarao, M.; Low, P. S. Ligand-Targeted Drug Delivery. *Chem. Rev.* **2017**, *117*, 12133–12164. <https://doi.org/10.1021/acs.chemrev.7b00013>.

- (50) Srinivasarao, M.; Galliford, C. v.; Low, P. S. Principles in the Design of Ligand-Targeted Cancer Therapeutics and Imaging Agents. *Nat. Rev. Drug Discov.* **2015**, *14*, 203–219. <https://doi.org/10.1038/nrd4519>.
- (51) Caplan, M. R.; Rosca, E. V. Targeting Drugs to Combinations of Receptors: A Modeling Analysis of Potential Specificity. *Ann. Biomed. Eng.* **2005**, *33*, 1113–1124. <https://doi.org/10.1007/s10439-005-5779-1>.
- (52) Zhong, Y.; Meng, F.; Deng, C.; Zhong, Z. Ligand-Directed Active Tumor-Targeting Polymeric Nanoparticles for Cancer Chemotherapy. *Biomacromolecules* **2014**, *15*, 1955–1969. <https://doi.org/10.1021/bm5003009>.
- (53) Barbieri, F.; Bajetto, A.; Pattarozzi, A.; Gatti, M.; Würth, R.; Thellung, S.; Corsaro, A.; Villa, V.; Nizzari, M.; Florio, T. Peptide Receptor Targeting in Cancer: The Somatostatin Paradigm. *Int. J. Pept.* **2012**, *2013*, 1–20. <https://doi.org/10.1155/2013/926295>.
- (54) Wang, F.; Li, Y.; Shen, Y.; Wang, A.; Wang, S.; Xie, T. The Functions and Applications of RGD in Tumor Therapy and Tissue Engineering. *Int. J. Mol. Sci.* **2013**, *14*, 13447–13462. <https://doi.org/10.3390/ijms140713447>.
- (55) Zwicke, G. L.; Mansoori, G. A.; Jeffery, C. J. Utilizing the Folate Receptor for Active Targeting of Cancer Nanotherapeutics. *Nano Rev.* **2012**, *3*, 18496–18507. <http://dx.doi.org/10.3402/nano.v3i0.18496>.
- (56) Reubi, J. C. Peptide Receptors as Molecular Targets for Cancer Diagnosis and Therapy. *Endocr. Rev.* **2003**, *24*, 389–427. <https://doi.org/10.1210/er.2002-0007>.
- (57) Mezo, G.; Manea, M. Receptor-Mediated Tumor Targeting Based on Peptide Hormones. *Expert Opin. Drug Deliv.* **2010**, *7*, 79–96. <https://doi.org/10.1517/17425240903418410>.
- (58) Patel, Y. Somatostatin and Its Family of Receptors. *Front. Neuroendocrinol.* **1999**, *20*, 157–198. <https://doi.org/10.1006/frne.1999.0183>.
- (59) Talme, T.; Ivanoff, J.; Hägglund, M.; Van Neerven, R. J. J.; Ivanoff, A.; Sundqvist, K. G. Somatostatin Receptor (SSTR) Expression and Function in Normal and Leukaemic T-Cells. Evidence for Selective Effects on Adhesion to Extracellular Matrix Components via SSTR2 and/or 3. *Clin. Exp. Immunol.* **2001**, *125*, 71–79. <https://doi.org/10.1046/j.1365-2249.2001.01577.x>.
- (60) Froidevaux, S.; Eberle, A. N. Somatostatin Analogs and Radiopeptides in Cancer Therapy. *Biopolymers – Pept. Sc.* **2002**, *66*, 161–183. <https://doi.org/10.1002/bip.10256>.

- (61) Addona, D. D.; Carotenuto, A.; Novellino, E.; Piccand, V.; Reubi, J. C.; Cianni, A. di; Gori, F.; Papini, A. M.; Ginanneschi, M. Novel Sst 5 -Selective Somatostatin Dicarba-Analogues: Synthesis and Conformation - Affinity Relationships. *J. Med. Chem.* **2008**, *51*, 512–520. <https://doi.org/10.1021/jm070886i>.
- (62) Albada, B.; Metzler-Nolte, N. Organometallic-Peptide Bioconjugates: Synthetic Strategies and Medicinal Applications. *Chem. Rev.* **2016**, *116*, 11797–11839. <https://doi.org/10.1021/acs.chemrev.6b00166>.
- (63) Barragan, F.; Carrion-Salip, D.; Goomez-Pinto, I.; Gonzalez-Canto, A.; Sadler, P. J.; Llorens, R. de; Moreno, V.; Gonzalez, C.; Massaguer, A.; Marchan, V. Somatostatin Subtype - 2 Receptor-Targeted Metal-Based Anticancer Complexes. *Bioconjug. Chem.* **2012**, *23*, 1838–1855. <https://doi.org/10.1021/bc300173h>.
- (64) Albada, H. B.; Wieberneit, F.; Dijkgraaf, I.; Harvey, J. H.; Whistler, J. L.; Stoll, R.; Metzler-Nolte, N.; Fish, R. H. The Chemoselective Reactions of Tyrosine-Containing G-Protein-Coupled Receptor Peptides with [Cp*Rh(H₂O)₃](OTf)₂, Including 2D NMR Structures and the Biological Consequences. *J. Am. Chem. Soc.* **2012**, *134*, 10321–10324. <https://doi.org/10.1021/ja303010k>.
- (65) Zhang, Y.; Li, S.; Zhang, H.; Xu, H. Design and Application of Receptor-Targeted Fluorescent Probes Based on Small Molecular Fluorescent Dyes. *Bioconjug. Chem.* **2021**, *32*, 4–24. <https://doi.org/10.1021/acs.bioconjchem.0c00606>.
- (66) Bai, M.; J. Bornhop, D. Recent Advances in Receptor-Targeted Fluorescent Probes for In Vivo Cancer Imaging. *Curr. Med. Chem.* **2012**, *19*, 4742–4758. <https://doi.org/10.2174/092986712803341467>.
- (67) Vahrmeijer, A. L.; Hutteman, M.; van der Vorst, J. R.; van de Velde, C. J. H.; Frangioni, J. v. Image-Guided Cancer Surgery Using near-Infrared Fluorescence. *Nat. Rev. Clin. Oncol.* **2013**, *10*, 507–518. <https://doi.org/10.1038/nrclinonc.2013.123>.
- (68) Mieog, J. S. D.; Achterberg, F. B.; Zlitni, A.; Hutteman, M.; Burggraaf, J.; Swijnenburg, R. J.; Gioux, S.; Vahrmeijer, A. L. Fundamentals and Developments in Fluorescence-Guided Cancer Surgery. *Nat. Rev. Clin. Oncol.* **2022**, *19*, 9–22. <https://doi.org/10.1038/s41571-021-00548-3>.
- (69) Olson, M. T.; Ly, Q. P.; Mohs, A. M. Fluorescence Guidance in Surgical Oncology: Challenges, Opportunities, and Translation. *Mol. Imaging. Biol.* **2019**, *21*, 200–218. <https://doi.org/10.1007/s11307-018-1239-2>.

- (70) Liu, F.; Deng, D.; Chen, X.; Qian, Z.; Achilefu, S.; Gu, Y. Folate-Polyethylene Glycol Conjugated near-Infrared Fluorescence Probe with High Targeting Affinity and Sensitivity for in Vivo Early Tumor Diagnosis. *Mol. Imaging Biol.* **2010**, *12*, 595–607. <https://doi.org/10.1007/s11307-010-0305-1>.
- (71) Ni, X. R.; Zhao, Y. Y.; Cai, H. P.; Yu, Z. H.; Wang, J.; Chen, F. R.; Yu, Y. J.; Feng, G. K.; Chen, Z. P. Transferrin Receptor 1 Targeted Optical Imaging for Identifying Glioma Margin in Mouse Models. *J. Neuro-oncol.* **2020**, *148*, 245–258. <https://doi.org/10.1007/s11060-020-03527-3>.
- (72) Licha, K.; Hassenius, C.; Becker, A.; Henklein, P.; Bauer, M.; Wisniewski, S.; Wiedenmann, B.; Semmler, W. Synthesis, Characterization, and Biological Properties of Cyanine-Labeled Somatostatin Analogues as Receptor-Targeted Fluorescent Probes. *Bioconjug. Chem.* **2001**, *12*, 44–50. <https://doi.org/10.1021/bc000040s>.
- (73) Becker, A.; Hassenius, C.; Licha, K.; Ebert, B.; Sukowski, U.; Semmler, W.; Wiedenmann, B.; Grötzinger, C. Receptor-Targeted Optical Imaging of Tumors with near-Infrared Fluorescent Ligands. *Nat. Biotechnol.* **2001**, *19*, 327–331. <https://doi.org/10.1038/86707>.
- (74) Cheng, Z.; Wu, Y.; Xiong, Z.; Gambhir, S. S.; Chen, X. Near-Infrared Fluorescent RGD Peptides for Optical Imaging of Integrin $\text{Av}\beta 3$ Expression in Living Mice. *Bioconjug. Chem.* **2005**, *16*, 1433–1441. <https://doi.org/10.1021/bc0501698>.
- (75) Pewklang, T.; Chansaenpak, K.; Lai, R. Y.; Noisa, P.; Kamkaew, A. Aza-BODIPY Probe for Selective Visualization of Cyclooxygenase-2 in Cancer Cells. *RSC Adv.* **2019**, *9*, 13372–13377. <https://doi.org/10.1039/c9ra01948k>.
- (76) Numasawa, K.; Hanaoka, K.; Saito, N.; Yamaguchi, Y.; Ikeno, T.; Echizen, H.; Yasunaga, M.; Komatsu, T.; Ueno, T.; Miura, M.; Nagano, T.; Urano, Y. A Fluorescent Probe for Rapid, High-Contrast Visualization of Folate-Receptor-Expressing Tumors In Vivo. *Angew. Chem. Int. Ed.* **2020**, *59*, 6015–6020. <https://doi.org/10.1002/anie.201914826>.
- (77) Mier, W.; Beijer, B.; Graham, K.; Hull, W. E. Fluorescent Somatostatin Receptor Probes for the Intraoperative Detection of Tumor Tissue with Long-Wavelength Visible Light. *Bioorg. Med. Chem.* **2002**, *10*, 2543–2552. [https://doi.org/10.1016/S0968-0896\(02\)00114-1](https://doi.org/10.1016/S0968-0896(02)00114-1).

- (78) Hou, J. T.; Ko, K. P.; Shi, H.; Ren, W. X.; Verwilt, P.; Koo, S.; Lee, J. Y.; Chi, S. G.; Kim, J. S. PLK1-Targeted Fluorescent Tumor Imaging with High Signal-to-Background Ratio. *ACS Sens.* **2017**, *2*, 1512–1516. <https://doi.org/10.1021/acssensors.7b00544>.
- (79) Correia, J. H.; Rodrigues, J. A.; Pimenta, S.; Dong, T.; Yang, Z. Photodynamic Therapy Review: Principles, Photosensitizers, Applications, and Future Directions. *Pharmaceutics* **2021**, *13*, 1–16. <https://doi.org/10.3390/pharmaceutics13091332>.
- (80) Guo, Z.; Park, S.; Yoon, J.; Shin, I. Recent Progress in the Development of Near-Infrared Fluorescent Probes for Bioimaging Applications. *Chem. Soc. Rev.* **2014**, *43*, 16–29. <https://doi.org/10.1039/c3cs60271k>.
- (81) Pham, T. C.; Nguyen, V. N.; Choi, Y.; Lee, S.; Yoon, J. Recent Strategies to Develop Innovative Photosensitizers for Enhanced Photodynamic Therapy. *Chem. Rev.* **2021**, *121*, 13454–13619. <https://doi.org/10.1021/acs.chemrev.1c00381>.
- (82) Felsher, D. W. Cancer Revoked: Oncogenes as Therapeutic Targets. *Nat. Rev. Cancer* **2003**, *3*, 375–380. <https://doi.org/10.1038/nrc1070>.
- (83) Monroe, S.; Colón, K. L.; Yin, H.; Roque, J.; Konda, P.; Gujar, S.; Thummel, R. P.; Lilge, L.; Cameron, C. G.; McFarland, S. A. Transition Metal Complexes and Photodynamic Therapy from a Tumor-Centered Approach: Challenges, Opportunities, and Highlights from the Development of TLD1433. *Chem. Rev.* **2019**, *119*, 797–828. <https://doi.org/10.1021/acs.chemrev.8b00211>.
- (84) Gunaydin, G.; Gedik, M. E.; Ayan, S. Photodynamic Therapy for the Treatment and Diagnosis of Cancer—A Review of the Current Clinical Status. *Front. Chem.* **2021**, *9*, 1–26. <https://doi.org/10.3389/fchem.2021.686303>.
- (85) Agostinis, P.; Berg, K.; Cengel, K. A.; Foster, T. H.; Girotti, A. W.; Gollnick, S. O.; Hahn, S. M.; Hamblin, M. R.; Juzeniene, A.; Kessel, D.; Korbelik, M.; Moan, J.; Mroz, P.; Nowis, D.; Piette, J.; Wilson, B. C.; Golab, J. Photodynamic Therapy of Cancer: An Update. *CA: Cancer J. Clin.* **2011**, *61*, 250–281. <https://doi.org/10.3322/caac.20114>.
- (86) Karges, J. Clinical Development of Metal Complexes as Photosensitizers for Photodynamic Therapy of Cancer. *Angew. Chem. Int. Ed.* **2022**, *61*, 1–9. <https://doi.org/10.1002/anie.202112236>.

- (87) Yano, S.; Hirohara, S.; Obata, M.; Hagiya, Y.; Ogura, S. ichiro; Ikeda, A.; Kataoka, H.; Tanaka, M.; Joh, T. Current States and Future Views in Photodynamic Therapy. *J. Photochem. Photobiol.* **2011**, *12*, 46–67. <https://doi.org/10.1016/j.jphotochemrev.2011.06.001>.
- (88) Ruggiero, E.; Alonso-De Castro, S.; Habtemariam, A.; Salassa, L. Upconverting Nanoparticles for the near Infrared Photoactivation of Transition Metal Complexes: New Opportunities and Challenges in Medicinal Inorganic Photochemistry. *Dalton Trans.* **2016**, *45*, 13012–13020. <https://doi.org/10.1039/c6dt01428c>.
- (89) Chen, D.; Xu, Q.; Wang, W.; Shao, J.; Huang, W.; Dong, X. Type I Photosensitizers Revitalizing Photodynamic Oncotherapy. *Small* **2021**, *17*, 2006742–2006742. <https://doi.org/10.1002/sml.202006742>.
- (90) Wang, Y.; Shi, X.; Fang, H.; Han, Z.; Yuan, H.; Zhu, Z.; Dong, L.; Guo, Z.; Wang, X. Platinum-Based Two-Photon Photosensitizer Responsive to NIR Light in Tumor Hypoxia Microenvironment. *J. Med. Chem.* **2022**, *65*, 7786–7798. <https://doi.org/10.1021/acs.jmedchem.2c00141>.
- (91) Zhao, X.; Liu, J.; Fan, J.; Chao, H.; Peng, X. Recent Progress in Photosensitizers for Overcoming the Challenges of Photodynamic Therapy: From Molecular Design to Application. *Chem. Soc. Rev.* **2021**, *50*, 4185–4219. <https://doi.org/10.1039/d0cs00173b>.
- (92) Ferino, A.; Nicoletto, G.; D’Este, F.; Zorzet, S.; Lago, S.; Richter, S. N.; Tikhomirov, A.; Shchekotikhin, A.; Xodo, L. E. Photodynamic Therapy for Ras-Driven Cancers: Targeting G-Quadruplex RNA Structures with Bifunctional Alkyl-Modified Porphyrins. *J. Med. Chem.* **2020**, *63*, 1245–1260. <https://doi.org/10.1021/acs.jmedchem.9b01577>.
- (93) Jiao, L.; Song, F.; Cui, J.; Peng, X. A Near-Infrared Heptamethine Aminocyanine Dye with a Long-Lived Excited Triplet State for Photodynamic Therapy. *Chem. Commun.* **2018**, *54*, 9198–9201. <https://doi.org/10.1039/c8cc04582h>.
- (94) Ruan, Z.; Miao, W.; Yuan, P.; Le, L.; Jiao, L.; Hao, E.; Yan, L. High Singlet Oxygen Yield Photosensitizer Based Polypeptide Nanoparticles for Low-Power Near-Infrared Light Imaging-Guided Photodynamic Therapy. *Bioconjug. Chem.* **2018**, *29*, 3441–3451. <https://doi.org/10.1021/acs.bioconjchem.8b00576>.

- (95) Zhao, N.; Li, Y.; Yin, W.; Zhuang, J.; Jia, Q.; Wang, Z.; Li, N. Controllable Coumarin-Based NIR Fluorophores: Selective Subcellular Imaging, Cell Membrane Potential Indication, and Enhanced Photodynamic Therapy. *ACS Appl. Mater. Interfaces* **2020**, *12*, 2076–2086. <https://doi.org/10.1021/acsami.9b18666>.
- (96) Ortega-Forte, E.; Rovira, A.; Gandioso, A.; Bonelli, J.; Bosch, M.; Ruiz, J.; Marchán, V. COUPY Coumarins as Novel Mitochondria-Targeted Photodynamic Therapy Anticancer Agents. *J. Med. Chem.* **2021**, *64*, 17209–17220. <https://doi.org/10.1021/acs.jmedchem.1c01254>.
- (97) Bruijninx, P. C.; Sadler, P. J. New Trends for Metal Complexes with Anticancer Activity. *Curr. Opin. Chem. Biol.* **2008**, *12*, 197–206. <https://doi.org/10.1016/j.cbpa.2007.11.013>.
- (98) Ghosh, S. Cisplatin: The First Metal Based Anticancer Drug. *Bioorg. Chem.* **2019**, *88*, 102925–102945. <https://doi.org/10.1016/j.bioorg.2019.102925>.
- (99) Johnstone, T. C.; Suntharalingam, K.; Lippard, S. J. The Next Generation of Platinum Drugs: Targeted Pt(II) Agents, Nanoparticle Delivery, and Pt(IV) Prodrugs. *Chem. Rev.* **2016**, *116*, 3436–3486. <https://doi.org/10.1021/acs.chemrev.5b00597>.
- (100) Kelland, L. The Resurgence of Platinum-Based Cancer Chemotherapy. *Nat. Rev. Cancer* **2007**, *7*, 573–584. <https://doi.org/10.1038/nrc2167>.
- (101) Hall, M. D.; Hambley, W. Platinum (IV) Antitumour Compounds: Their Bioinorganic Chemistry. *Coord. Chem. Rev.* **2002**, *232*, 49–67. [https://doi.org/10.1016/S0010-8545\(02\)00026-7](https://doi.org/10.1016/S0010-8545(02)00026-7).
- (102) Lucaciu, R. L.; Hangan, A. C.; Sevastre, B.; Oprean, L. S. Metallo-Drugs in Cancer Therapy: Past, Present and Future. *Molecules* **2022**, *27*, 6485–6514. <https://doi.org/10.3390/molecules27196485>.
- (103) Riccardi, C.; Musumeci, D.; Trifuoggi, M.; Irace, C.; Paduano, L.; Montesarchio, D. Anticancer Ruthenium(III) Complexes and Ru(III)-Containing Nanoformulations: An Update on the Mechanism of Action and Biological Activity. *Pharmaceuticals* **2019**, *12*, 1–46. <https://doi.org/10.3390/ph12040146>.
- (104) Antonarakis, Emmanuel S.; Emadi, A. Ruthenium-Based Chemotherapeutics: Are They Ready for Prime Time? *Cancer Chemother. Pharmacol.* **2010**, *66*, 1–9. <https://doi.org/10.1007/s00280-010-1293-1>.

- (105) Zeng, L.; Gupta, P.; Chen, Y.; Wang, E.; Ji, L.; Chao, H.; Chen, Z. S. The Development of Anticancer Ruthenium(II) Complexes: From Single Molecule Compounds to Nanomaterials. *Chem. Soc. Rev.* **2017**, *46*, 5771–5804. <https://doi.org/10.1039/c7cs00195a>.
- (106) Alessio, E. Thirty Years of the Drug Candidate NAMI-A and the Myths in the Field of Ruthenium Anticancer Compounds: A Personal Perspective. *Eur. J. Inorg. Chem.* **2017**, *2017*, 1549–1560. <https://doi.org/10.1002/ejic.201600986>.
- (107) Levina, A.; Crans, D. C.; Lay, P. A. Advantageous Reactivity of Unstable Metal Complexes: Potential Applications of Metal-Based Anticancer Drugs for Intratumoral Injections. *Pharmaceutics* **2022**, *14*, 1–22. <https://doi.org/10.3390/pharmaceutics14040790>.
- (108) Gill, M. R.; Thomas, J. A. Ruthenium(II) Polypyridyl Complexes and DNA - From Structural Probes to Cellular Imaging and Therapeutics. *Chem. Soc. Rev.* **2012**, *41*, 3179–3192. <https://doi.org/10.1039/c2cs15299a>.
- (109) Lin, K.; Zhao, Z. Z.; Bo, H. ben; Hao, X. J.; Wang, J. Q. Applications of Ruthenium Complex in Tumor Diagnosis and Therapy. *Front. Pharmacol.* **2018**, *9*, 1–10. <https://doi.org/10.3389/fphar.2018.01323>.
- (110) Tan, C. P.; Lu, Y. Y.; Ji, L. N.; Mao, Z. W. Metallomics Insights into the Programmed Cell Death Induced by Metal-Based Anticancer Compounds. *Metallomics* **2014**, *6*, 978–995. <https://doi.org/10.1039/c3mt00225j>.
- (111) Li, S.; Xu, G.; Zhu, Y.; Zhao, J.; Gou, S. Bifunctional Ruthenium(II) Polypyridyl Complexes of Curcumin as Potential Anticancer Agents. *Dalton Trans.* **2020**, *49*, 9454–9463. <https://doi.org/10.1039/d0dt01040e>.
- (112) Rilak Simović, A.; Masnikosa, R.; Bratsos, I.; Alessio, E. Chemistry and Reactivity of Ruthenium(II) Complexes: DNA/Protein Binding Mode and Anticancer Activity Are Related to the Complex Structure. *Coord. Chem. Rev.* **2019**, *398*, 1–26. <https://doi.org/10.1016/j.ccr.2019.07.008>.
- (113) Dwyer, F. P.; Gyarfas, E. C.; Rogers, W. P.; Koch J. H. Biological Activity of Complex Ions. *Nature* **1952**, *170*, 190–191. <https://doi.org/10.1038/170190a0>.
- (114) Zeng, Z. P.; Wu, Q.; Sun, F. Y.; Zheng, K. di; Mei, W. J. Imaging Nuclei of MDA-MB-231 Breast Cancer Cells by Chiral Ruthenium(II) Complex Coordinated by 2-(4-Phenylacetylenophenyl)-1H-Imidazo[4,5f][1,10]Phenanthroline. *Inorg. Chem.* **2016**, *55*, 5710–5718. <https://doi.org/10.1021/acs.inorgchem.6b00824>.

- (115) Yu, Q.; Liu, Y.; Xu, L.; Zheng, C.; Le, F.; Qin, X.; Liu, Y.; Liu, J. Ruthenium(II) Polypyridyl Complexes: Cellular Uptake, Cell Image and Apoptosis of HeLa Cancer Cells Induced by Double Targets. *Eur. J. Med. Chem.* **2014**, *82*, 82–95. <https://doi.org/10.1016/j.ejmech.2014.05.040>.
- (116) Du, Y.; Fu, X.; Li, H.; Chen, B.; Guo, Y.; Su, G.; Zhang, H.; Ning, F.; Lin, Y.; Mei, W.; Chen, T. Mitochondrial Fragmentation Is an Important Cellular Event Induced by Ruthenium(II) Polypyridyl Complexes in Osteosarcoma Cells. *ChemMedChem.* **2014**, *9*, 714–718. <https://doi.org/10.1002/cmcd.201300379>.
- (117) Huang, H.; Zhang, P.; Chen, H.; Ji, L.; Chao, H. Comparison Between Polypyridyl and Cyclometalated Ruthenium (II) Complexes: Anticancer Activities Against 2D and 3D Cancer Models. *Chem. Eur. J.* **2015**, *21*, 715–725. <https://doi.org/10.1002/chem.201404922>.
- (118) Peña, B.; David, A.; Pavani, C.; Baptista, M. S.; Pellois, J. P.; Turro, C.; Dunbar, K. R. Cytotoxicity Studies of Cyclometallated Ruthenium(II) Compounds: New Applications for Ruthenium Dyes. *Organometallics* **2014**, *33*, 1100–1103. <https://doi.org/10.1021/om500001h>.
- (119) Huang, H.; Zhang, P.; Yu, B.; Chen, Y.; Wang, J.; Ji, L.; Chao, H. Targeting Nucleus DNA with a Cyclometalated Dipyrindophenazineruthenium(II) Complex. *J. Med. Chem.* **2014**, *57*, 8971–8983. <https://doi.org/10.1021/jm501095r>.
- (120) Zeng, L.; Chen, Y.; Huang, H.; Wang, J.; Zhao, D.; Ji, L.; Chao, H. Cyclometalated Ruthenium(II) Anthraquinone Complexes Exhibit Strong Anticancer Activity in Hypoxic Tumor Cells. *Chem. Eur. J.* **2015**, *21*, 15308–15319. <https://doi.org/10.1002/chem.201502154>.
- (121) Lo, K. K. W.; Zhang, K. Y. Iridium(III) Complexes as Therapeutic and Bioimaging Reagents for Cellular Applications. *RSC Adv.* **2012**, *2*, 12069–12083. <https://doi.org/10.1039/c2ra20967e>.
- (122) Caporale, C.; Massi, M. Cyclometalated Iridium(III) Complexes for Life Science. *Coord. Chem. Rev.* **2018**, *363*, 71–91. <https://doi.org/10.1016/j.ccr.2018.02.006>.
- (123) Liu, Z.; Sadler, P. J. Organoiridium Complexes: Anticancer Agents and Catalysts. *Acc. Chem. Res.* **2014**, *47*, 1174–1185. <https://doi.org/10.1021/ar400266c>.
- (124) Konkankit, C. C.; Marker, S. C.; Knopf, K. M.; Wilson, J. J. Anticancer Activity of Complexes of the Third Row Transition Metals, Rhenium, Osmium, and Iridium. *Dalton Trans.* **2018**, *47*, 9934–9974. <https://doi.org/10.1039/c8dt01858h>.

- (125) Mukhopadhyay, S.; Singh, R. S.; Paitandi, R. P.; Sharma, G.; Koch, B.; Pandey, D. S. Influence of Substituents on DNA and Protein Binding of Cyclometalated Ir(III) Complexes and Anticancer Activity. *Dalton Trans.* **2017**, *46*, 8572–8585. <https://doi.org/10.1039/c7dt01015j>.
- (126) Wang, J.; Hou, X.; Zhao, Z.; Bo, H.; Chen, Q. A Cyclometalated Iridium(III) Complex That Inhibits the Migration and Invasion of MDA-MB-231 Cells. *Inorg. Chem. Commun.* **2016**, *67*, 40–43. <https://doi.org/10.1016/j.inoche.2016.02.018>.
- (127) He, L.; Wang, K. N.; Zheng, Y.; Cao, J. J.; Zhang, M. F.; Tan, C. P.; Ji, L. N.; Mao, Z. W. Cyclometalated Iridium(III) Complexes Induce Mitochondria-Derived Paraptotic Cell Death and Inhibit Tumor Growth: In Vivo. *Dalton Trans.* **2018**, *47*, 6942–6953. <https://doi.org/10.1039/c8dt00783g>.
- (128) Chen, M. H.; Zheng, Y.; Cai, X. J.; Zhang, H.; Wang, F. X.; Tan, C. P.; Chen, W. H.; Ji, L. N.; Mao, Z. W. Inhibition of Autophagic Flux by Cyclometalated Iridium(III) Complexes through Anion Transportation. *Chem. Sci.* **2019**, *10*, 3315–3323. <https://doi.org/10.1039/C8SC04520H>.
- (129) Ye, R. R.; Tan, C. P.; Ji, L. N.; Mao, Z. W. Coumarin-Appended Phosphorescent Cyclometalated Iridium(III) Complexes as Mitochondria-Targeted Theranostic Anticancer Agents. *Dalton Trans.* **2016**, *45*, 13042–13051. <https://doi.org/10.1039/c6dt00601a>.
- (130) Yellol, J.; Pérez, S. A.; Yellol, G.; Zajac, J.; Donaire, A.; Viguera, G.; Novohradsky, V.; Janiak, C.; Brabec, V.; Ruiz, J. Highly Potent Extranuclear-Targeted Luminescent Iridium(III) Antitumor Agents Containing Benzimidazole-Based Ligands with a Handle for Functionalization. *Chem. Commun.* **2016**, *52*, 14165–14168. <https://doi.org/10.1039/c6cc07909a>.
- (131) McFarland, S. A.; Mandel, A.; Dumoulin-White, R.; Gasser, G. Metal-Based Photosensitizers for Photodynamic Therapy: The Future of Multimodal Oncology? *Curr. Opin. Chem. Biol.* **2020**, *56*, 23–27. <https://doi.org/10.1016/j.cbpa.2019.10.004>.
- (132) Karges, J.; Heinemann, F.; Jakubaszek, M.; Maschietto, F.; Subecz, C.; Dotou, M.; Vinck, R.; Blacque, O.; Tharaud, M.; Goud, B.; Viñuelas Zahlnos, E.; Spingler, B.; Ciofini, I.; Gasser, G. Rationally Designed Long-Wavelength Absorbing Ru(II) Polypyridyl Complexes as Photosensitizers for Photodynamic Therapy. *J. Am. Chem. Soc.* **2020**, *142*, 6578–6587. <https://doi.org/10.1021/jacs.9b13620>.

- (133) Cloonan, S. M.; Elmes, R. B. P.; Erby, M.; Bright, S. A.; Poynton, F. E.; Nolan, D. E.; Quinn, S. J.; Gunnlaugsson, T.; Williams, D. C. Detailed Biological Profiling of a Photoactivated and Apoptosis Inducing Pdppz Ruthenium(II) Polypyridyl Complex in Cancer Cells. *J. Med. Chem.* **2015**, *58*, 4494–4505. <https://doi.org/10.1021/acs.jmedchem.5b00451>.
- (134) Ryan, R. T.; Stevens, K. C.; Calabro, R.; Parkin, S.; Mahmoud, J.; Kim, D. Y.; Heidary, D. K.; Glazer, E. C.; Selegue, J. P. Bis-Tridentate N-Heterocyclic Carbene Ru(II) Complexes Are Promising New Agents for Photodynamic Therapy. *Inorg. Chem.* **2020**, *59*, 8882–8892. <https://doi.org/10.1021/acs.inorgchem.0c00686>.
- (135) Wu, W.; Sun, J.; Cui, X.; Zhao, J. Observation of the Room Temperature Phosphorescence of Bodipy in Visible Light-Harvesting Ru(II) Polyimine Complexes and Application as Triplet Photosensitizers for Triplet-Triplet-Annihilation Upconversion and Photocatalytic Oxidation. *J. Mater. Chem. C* **2013**, *1*, 4577–4589. <https://doi.org/10.1039/c3tc30592a>.
- (136) Sainuddin, T.; McCain, J.; Pinto, M.; Yin, H.; Gibson, J.; Hetu, M.; McFarland, S. A. Organometallic Ru(II) Photosensitizers Derived from π -Expansive Cyclometalating Ligands: Surprising Theranostic PDT Effects. *Inorg. Chem.* **2016**, *55*, 83–95. <https://doi.org/10.1021/acs.inorgchem.5b01838>.
- (137) Lifshits, L. M.; Roque, J. A.; Konda, P.; Monro, S.; Cole, H. D.; von Dohlen, D.; Kim, S.; Deep, G.; Thummel, R. P.; Cameron, C. G.; Gujar, S.; McFarland, S. A. Near-Infrared Absorbing Ru(II) Complexes Act as Immunoprotective Photodynamic Therapy (PDT) Agents against Aggressive Melanoma. *Chem. Sci.* **2020**, *11*, 11740–11762. <https://doi.org/10.1039/d0sc03875j>.
- (138) Lv, Z.; Wei, H.; Li, Q.; Su, X.; Liu, S.; Zhang, K. Y.; Lv, W.; Zhao, Q.; Li, X.; Huang, W. Achieving Efficient Photodynamic Therapy under Both Normoxia and Hypoxia Using Cyclometalated Ru(II) Photosensitizer through Type I Photochemical Process. *Chem. Sci.* **2018**, *9*, 502–512. <https://doi.org/10.1039/c7sc03765a>.
- (139) Liu, X.; Li, G.; Xie, M.; Guo, S.; Zhao, W.; Li, F.; Liu, S.; Zhao, Q. Rational Design of Type I Photosensitizers Based on Ru(II) Complexes for Effective Photodynamic Therapy under Hypoxia. *Dalton Trans.* **2020**, *49*, 11192–11200. <https://doi.org/10.1039/d0dt01684e>.
- (140) Ballester, F. J.; Ortega, E.; Bautista, D.; Santana, M. D.; Ruiz, J. Ru(II) Photosensitizers Competent for Hypoxic Cancers via Green Light Activation. *Chem. Commun.* **2020**, *56*, 10301–10304. <https://doi.org/10.1039/d0cc02417a>.

- (141) Liu, B.; Monro, S.; Li, Z.; Javed, M. A.; Ramirez, D.; Cameron, C. G.; Colón, K.; Roque, J.; Kilina, S.; Tian, J.; Mcfarland, S. A.; Sun, W. New Class of Homoleptic and Heteroleptic Bis(Terpyridine) Iridium(III) Complexes with Strong Photodynamic Therapy Effects. *ACS Appl. Bio. Mater.* **2019**, *2*, 2964–2977. <https://doi.org/10.1021/acsabm.9b00312>.
- (142) Jing, Y.; Cao, Q.; Hao, L.; Yang, G. G.; Hu, W. L.; Ji, L. N.; Mao, Z. W. A Self-Assessed Photosensitizer: Inducing and Dual-Modal Phosphorescence Imaging of Mitochondria Oxidative Stress. *Chem. Commun.* **2018**, *54*, 271–274. <https://doi.org/10.1039/c7cc07797a>.
- (143) Liu, C.; Zhou, L.; Wei, F.; Li, L.; Zhao, S.; Gong, P.; Cai, L.; Wong, K. M. C. Versatile Strategy to Generate a Rhodamine Triplet State as Mitochondria-Targeting Visible-Light Photosensitizers for Efficient Photodynamic Therapy. *ACS Appl. Mater. Interfaces* **2019**, *11*, 8797–8806. <https://doi.org/10.1021/acsami.8b20224>.
- (144) Palao, E.; Sola-Llano, R.; Tabero, A.; Manzano, H.; Agarrabeitia, A. R.; Villanueva, A.; López-Arbeloa, I.; Martínez-Martínez, V.; Ortiz, M. J. AcetylacetonateBODIPY-Biscyclometalated Iridium(III) Complexes: Effective Strategy towards Smarter Fluorescent Photosensitizer Agents. *Chem. Eur. J.* **2017**, *23*, 10139–10147. <https://doi.org/10.1002/chem.201701347>.
- (145) Sun, J.; Zhao, J.; Guo, H.; Wu, W. Visible-Light Harvesting Iridium Complexes as Singlet Oxygen Sensitizers for Photooxidation of 1,5-Dihydroxynaphthalene. *Chem. Commun.* **2012**, *48*, 4169–4171. <https://doi.org/10.1039/c2cc16690a>.
- (146) Majumdar, P.; Yuan, X.; Li, S.; le Guennic, B.; Ma, J.; Zhang, C.; Jacquemin, D.; Zhao, J. Cyclometalated Ir(III) Complexes with Styryl-BODIPY Ligands Showing near IR Absorption/Emission: Preparation, Study of Photophysical Properties and Application as Photodynamic/Luminescence Imaging Materials. *J. Mater. Chem. B* **2014**, *2*, 2838–2854. <https://doi.org/10.1039/c4tb00284a>.
- (147) Bevernaegie, R.; Doix, B.; Bastien, E.; Diman, A.; Decottignies, A.; Feron, O.; Elias, B. Exploring the Phototoxicity of Hypoxic Active Iridium(III)-Based Sensitizers in 3D Tumor Spheroids. *J. Am. Chem. Soc.* **2019**, *141*, 18486–18491. <https://doi.org/10.1021/jacs.9b07723>.
- (148) Huang, H.; Banerjee, S.; Qiu, K.; Zhang, P.; Blacque, O.; Malcomson, T.; Paterson, M. J.; Clarkson, G. J.; Staniforth, M.; Stavros, V. G.; Gasser, G.; Chao, H.; Sadler, P. J. Targeted Photoredox Catalysis in Cancer Cells. *Nat. Chem.* **2019**, *11*, 1041–1048. <https://doi.org/10.1038/s41557-019-0328-4>.

- (149) Lv, W.; Zhang, Z.; Zhang, K. Y.; Yang, H.; Liu, S.; Xu, A.; Guo, S.; Zhao, Q.; Huang, W. A Mitochondria-Targeted Photosensitizer Showing Improved Photodynamic Therapy Effects Under Hypoxia. *Angew. Chem. Int. Ed.* **2016**, *55*, 9947–9951. <https://doi.org/10.1002/anie.201604130>.
- (150) Yuan, H.; Han, Z.; Chen, Y.; Qi, F.; Fang, H.; Guo, Z.; Zhang, S.; He, W. Ferroptosis Photoinduced by New Cyclometalated Iridium(III) Complexes and Its Synergism with Apoptosis in Tumor Cell Inhibition. *Angew. Chem. Int. Ed.* **2021**, *60*, 8174–8181. <https://doi.org/10.1002/anie.202014959>.
- (151) Zafon, E.; Echevarría, I.; Barrabés, S.; Manzano, B. R.; Jalón, F. A.; Rodríguez, A. M.; Massaguer, A.; Espino, G. Photodynamic Therapy with Mitochondria-Targeted Biscyclometallated Ir(III) Complexes. Multi-Action Mechanism and Strong Influence of the Cyclometallating Ligand. *Dalton Trans.* **2022**, *51*, 111–128. <https://doi.org/10.1039/d1dt03080a>.
- (152) Pracharova, J.; Viguera, G.; Novohradsky, V.; Cutillas, N.; Janiak, C.; Kostrhunova, H.; Kasparkova, J.; Ruiz, J.; Brabec, V. Exploring the Effect of Polypyridyl Ligands on the Anticancer Activity of Phosphorescent Iridium(III) Complexes: From Proteosynthesis Inhibitors to Photodynamic Therapy Agents. *Chem. Eur. J.* **2018**, *24*, 4607–4619. <https://doi.org/10.1002/chem.201705362>.
- (153) Qin, W. W.; Pan, Z. Y.; Cai, D. H.; Li, Y.; He, L. Cyclometalated Iridium(III) Complexes for Mitochondria-Targeted Combined Chemo-Photodynamic Therapy. *Dalton Trans.* **2020**, *49*, 3562–3569. <https://doi.org/10.1039/d0dt00180e>.

Results and Discussion

Chapter I

Development of novel coumarin-based COUPY
fluorophores for bioimaging applications

6. Chapter Ia. Publication A

Modulating photostability and mitochondria selectivity in far-red/NIR emitting coumarin fluorophores through replacement of pyridinium by pyrimidinium.

(A. Rovira *et al.* *J. Org. Chem.* **2020**, *85*, 6086–6097)

Modulating Photostability and Mitochondria Selectivity in Far-Red/NIR Emitting Coumarin Fluorophores through Replacement of Pyridinium by Pyrimidinium

Anna Rovira, Miriam Pujals, Albert Gandioso, Marta López-Corrales, Manel Bosch, and Vicente Marchán*



Cite This: *J. Org. Chem.* 2020, 85, 6086–6097



Read Online

ACCESS |



Metrics & More



Article Recommendations



Supporting Information

ABSTRACT: Mitochondrial dysfunction has been associated with several human pathological conditions, including cancer, aging, and neurodegenerative diseases. Thus, the availability of selective fluorescent probes for mitochondria could play an important role in the future for monitoring cellular functions and disease progression. In this work, we have studied how the photophysical properties and subcellular accumulation of nonconventional coumarin-based COUPY fluorophores can be fine-tuned through replacement of the *para*-pyridinium moiety with several heterocycles. Among them, *ortho,para*-pyrimidinium substitution provided novel fluorophores with suitable photophysical properties for bioimaging applications, including emission in the far-red to NIR region, large Stokes' shifts, and high photostability. Furthermore, the compounds exhibited excellent cell membrane permeability in living cells and a higher selectivity for mitochondria compared with the parent COUPY fluorophores. Overall, these results provided useful insights into the development of novel mitochondria-targeted fluorescent probes based on small organic molecules, since higher selectivity for this organelle can be achieved through the replacement of conventional N-alkylated pyridinium moieties by the corresponding N-alkylated-*ortho,para*-pyrimidinium counterparts.



INTRODUCTION

Fluorescence imaging in combination with organic fluorophores has become a powerful tool for understanding biological events at a molecular level. In this context, the use of fluorescent probes with operability in the less energetic far-red and near-infrared (NIR) region of the electromagnetic spectrum offers several appealing features for *in vivo* imaging applications, such as increased tissue penetration depth and minimal autofluorescence interference from natively occurring biomolecules.¹ For this reason, recent efforts have been devoted to the development of novel organic chromophores operating in the phototherapeutic window with optimal photophysical (e.g., long-wavelength absorption and emission, brightness, large Stokes' shifts, and photostability) and physicochemical (e.g., aqueous solubility, good cell permeability, and target specificity) properties. Ideally, such fluorescent compounds should be based on chemically stable, low molecular weight scaffolds amenable to smart and simple structural modifications to fine-tune the abovementioned properties and to facilitate conjugation to targeting ligands.² Besides biocompatibility, an ideal fluorophore should permit the interrogation of intracellular architectures and dynamics without disturbing and compromising the integrity of the cellular target.³

Mitochondria are involved in many key cellular processes, including ATP synthesis, calcium signaling, and redox

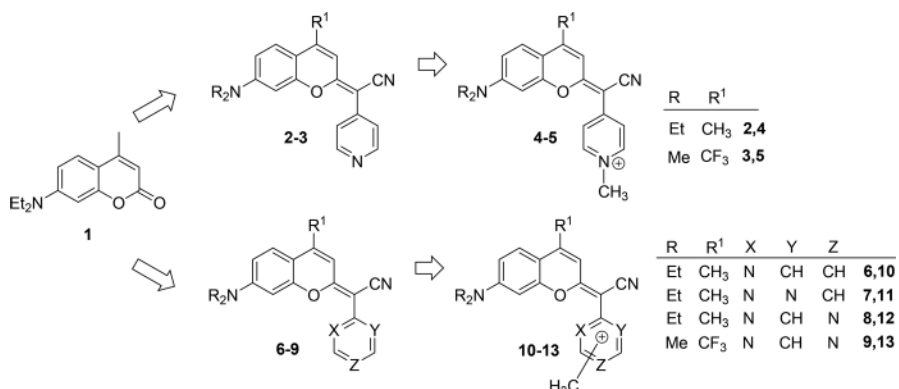
homeostasis.⁴ Mitochondrial dysfunction has been associated with a wide range of human pathological conditions, such as cancer disease, aging, and metabolic and neurodegenerative diseases.⁵ Thus, the availability of fluorescent dyes that can selectively stain mitochondria opens the door to monitoring cellular functions and disease progression by studying mitochondrial morphology and mitophagy.⁶ Among fluorescent mitochondrial probes described to date, some of them intrinsically target this organelle such as some cyanine derivatives (e.g., IR-780 and MHI-148) and some rhodamines (Rhodamine 123).⁷ Another approach to achieve mitochondria selectivity consists of incorporating lipophilic positively charged moieties such as triphenylphosphonium or pyridinium groups, which exploit the negative potential across the outer and inner mitochondrial membrane.⁸ In this context, anticancer mitochondria-targeted fluorescent molecules are considered attractive theranostic agents.⁹ Similarly, mitochondria-targeted photocages based on organic chromophores

Received: March 3, 2020

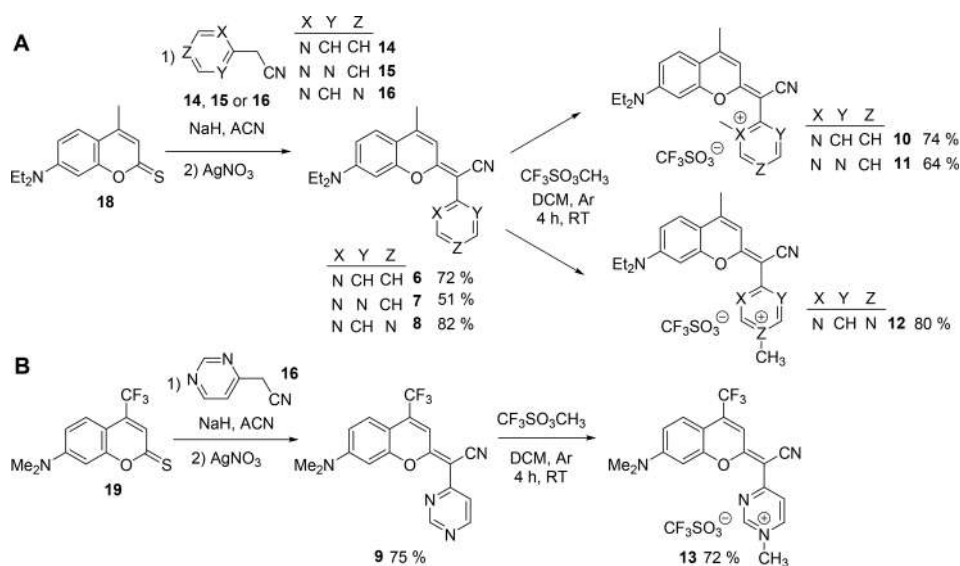
Published: April 2, 2020



Scheme 1. Rational design of novel COUPY fluorophores



Scheme 2. Synthesis of COUPY scaffolds (6–9) and the corresponding N-methylated dyes (10–13)



provide a powerful method for releasing bioactive compounds within this organelle.¹⁰

In our laboratory, we have recently described a new class of coumarin-based chromophores in which the carbonyl group of the electron-withdrawing lactone in conventional coumarin **1** was replaced by the cyano(4-pyridine)methylene moiety (e.g., compounds **2** and **3**; see Scheme 1) with the aim of increasing the push-pull character of the π -delocalized system.¹¹ N-Alkylation of the pyridine heterocycle provides low molecular weight fluorophores, nicknamed COUPYs, with several attractive characteristics, including emission in the far-red/NIR region, large Stokes' shifts, and good brightness.¹¹ Moreover, COUPY dyes (e.g., see compounds **4** and **5** in Scheme 1 as representative examples) exhibited moderate to good aqueous solubility and excellent cell membrane permeability and accumulated preferentially in two specific cellular compartments, the mitochondria and nucleoli. After the discovery of this promising fluorescent platform, we have initiated a systematic study to unveil the principles governing the structure-photophysical property relationships (SPPR) of COUPY dyes, which are necessary to design new fluorescent probes as per need. Compared with conventional coumarins (e.g., **1**), the molecular framework of COUPY scaffolds offers several advantages for carrying out a systematic SPPR study. Indeed, we have found that absorption and emission maxima

can be red-shifted through the incorporation of strong electron-withdrawing groups like CF₃ either at the 4-position or via N-alkylation of the pyridine heterocycle,¹¹ while photostability can be increased through replacement of the electron-donating *N,N*-dialkyl groups (e.g., NMe₂ or NEt₂) at position 7 with azetidine.¹² In addition, conjugatable versions of COUPY dyes can be easily obtained by incorporation of suitable functional groups (e.g., carboxylic acid, amino, azide, or alkyne) via N-alkylation of the pyridine moiety. Such COUPY derivatives allowed us to label receptor-binding peptides on a solid phase by using efficient click chemistry methodologies¹³ and to develop novel photosensitizers for photodynamic anticancer therapy via conjugation to cyclometalated Ir(III) complexes.¹⁴

On the basis of all these precedents, in this work we focused on investigating how the modification of the pyridine moiety in COUPY chromophores could influence the photophysical properties and subcellular accumulation of the compounds. With this idea in mind, herein we describe the synthesis and characterization of four analogues (compounds **10–13**, Scheme 1) of our original COUPY dyes (**4** and **5**). Surprisingly, the replacement of the *para*-pyridine heterocycle by *ortho*-pyridine (**10**) or *ortho,ortho*-pyrimidine (**11**) had a negative effect on the spectroscopic properties of the compounds since both absorption and emission were blue-

shifted. By contrast, the incorporation of *ortho,para*-pyrimidine (12 and 13) led to highly photostable fluorophores with improved photophysical properties compared with that of the parent compounds, including emission in the far-red to NIR region and large Stokes's shifts. Furthermore, high cell permeability was retained in both *ortho,para*-pyrimidine-containing dyes and a higher selectivity for mitochondria of HeLa cells was achieved. Overall, these results provided new insights into the design and optimization of mitochondria-targeted fluorescent probes.

RESULTS AND DISCUSSION

Design, Synthesis, and Characterization of COUPY Dyes. COUPY dyes 10–13 were synthesized by following our previously described methodology for the parent dyes (4 and 5), which is based on the reaction of a thiocoumarin precursor with suitable heteroarylacetonitrile derivatives followed by N-methylation of the pyridine or pyrimidine moieties (Scheme 2). First, thiocoumarin 18¹⁵ was reacted with 2-(pyridin-2-yl)acetonitrile (14), 2-(pyrimidin-2-yl)acetonitrile (15), or 2-(pyrimidin-4-yl)acetonitrile (16) in the presence of NaH followed by AgNO₃ treatment, which afforded COUPY scaffolds 6, 7, and 8, respectively, after purification by silica column chromatography with moderate to good yields (51–82%). Similarly, coumarin 9 was obtained by condensation of thiocoumarin 19¹¹ with 16 (yield 75%). All the compounds were fully characterized by reversed-phase high-performance liquid chromatography (HPLC) (Figure S1), HR ESI-MS, and ¹H, ¹⁹F (only in the case of 9), and ¹³C NMR.

It is worth noting that ¹H–¹H NOESY experiments (Figure 1 and Figures S2–S5) account for the existence of two species in equilibrium in solution because of the rotation around the exocyclic C=C bond, which reproduces the behavior previously found in the parent COUPY scaffolds (compounds 2 and 3, Scheme 1).¹¹ As shown in Figure 1, chemical

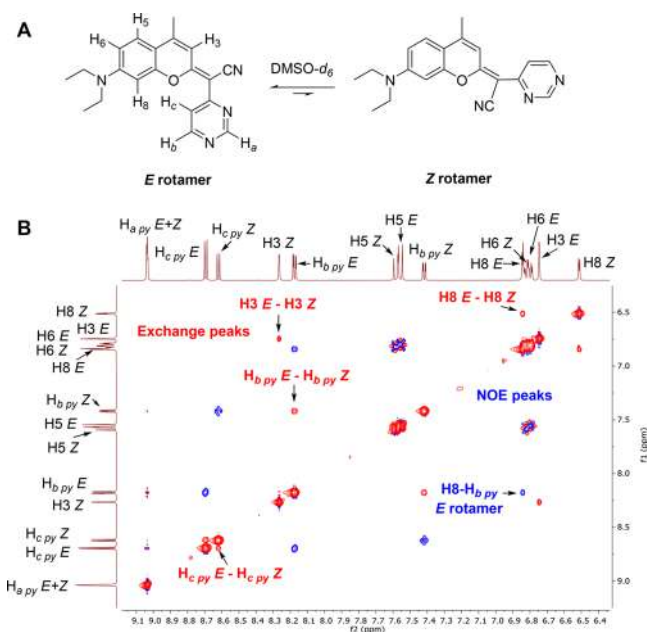


Figure 1. (A) Structures of the *E* and *Z* rotamers of coumarin 8. (B) Expansion of the 2D NOESY spectrum ($t_m = 500$ ms, 25 °C) of 8 in DMSO- d_6 showing NOE cross-peaks and exchange cross-peaks between rotamer resonances of the same sign as the diagonal.

exchange cross-peaks between the resonances of *E* and *Z* rotamers were observed in the 2D NOESY spectrum of coumarin 8. In the case of coumarins 6, 8, and 9, the two rotamers were present in a ~60:40 ratio according to the integration of the ¹H NMR spectrum, the *E* rotamer being the major species. This is in contrast with the *para*-pyridine-containing coumarins 2 and 3 in which the *E/Z* ratio was ~90:10. Surprisingly, the *Z* rotamer was the major species in solution (95%) in the COUPY scaffold containing the *ortho,ortho*-pyrimidine heterocycle (7), which was confirmed by the existence of a NOE cross-peak between the proton at position 3 of the coumarin moiety and the proton at the *ortho* position of the pyrimidine ring (Figure S3). It is worth noting that in all of the COUPY scaffolds the chemical shift of H3 appears at higher δ in the *Z* isomer (e.g., 8.18 ppm in 7 and 8.26 ppm in 8) than in the *E* isomer (e.g., 6.70 ppm in 7 and 6.75 ppm in 8).

Next, we synthesized the corresponding N-methylated pyridinium (10) and pyrimidinium (11–13) dyes by reaction with methyl trifluoromethanesulfonate in DCM at room temperature.¹¹ The four new coumarin derivatives were isolated after silica column chromatography as reddish-orange (10 and 11), purple (12), and dark blue (13) solids (yields 64–80%), and their purity was assessed by reversed-phase HPLC (Figure S1). Characterization was carried out by HR ESI-MS and 1D and 2D NMR spectroscopy. As expected, methylation occurred at the less sterically hindered nitrogen in the *ortho,para*-pyrimidine derivatives (12 and 13) according to NOESY NMR characterization, and in all cases the *E* rotamer was the major species in solution (Figures S6–S9).

Photophysical Characterization of COUPY Fluorophores. Having at hand COUPY dyes 10–13, we investigated the effect of replacing the *para*-pyridine moiety in the parent fluorophores (4 and 5) by the *ortho*-pyridine or *ortho,ortho*- or *ortho,para*-pyrimidine on the spectroscopic and photophysical properties of the compounds with the aim of establishing new SPPR. Although water or phosphate buffered saline (PBS) is often used to evaluate the usefulness of a new fluorophore within a spectroscopy cuvette, the heterogeneity and complexity of the cellular environment cannot be accurately described by using a simple aqueous buffer.¹⁶ For this reason, we decided to register the UV–vis absorption and emission spectra in four solvents of different polarities (PBS buffer pH 7.4, EtOH, ACN, and DCM; Figure 2 and Figures S10–S17) to get some

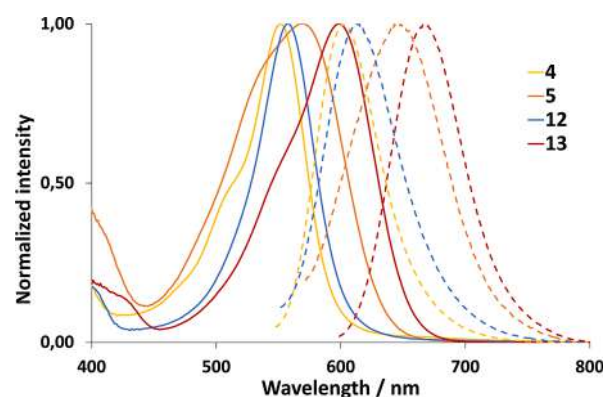


Figure 2. Comparison of the normalized absorption (solid lines) and fluorescence (dotted lines) spectra of COUPY dyes (compounds 4, 5, 12, and 13) in EtOH.

Table 1. Photophysical Data of the Coumarin Derivatives 4 and 5 and 10–13 in Different Solvents

compd.	X, Y, Z	solvent	λ_{abs} (nm) ^a	ϵ (M ⁻¹ cm ⁻¹) ^b	λ_{em} (nm) ^c	Stokes shift (nm) ^d	Φ_{F} ^e
4	CH, CH, N	PBS	545	34,000	604	59	0.12
		EtOH	552	59,000	603	51	0.45
		ACN	548	75,000	609	61	0.18
		DCM	569	67,000	607	38	0.70
10	N, CH, CH	PBS	502	25,000	583	81	0.01
		EtOH	515	31,000	592	77	0.02
		ACN	505	26,000	589	84	0.02
		DCM	543	36,000	594	51	0.20
11	N, N, CH	PBS	525	37,000	561	36	0.01
		EtOH	528	59,000	564	36	0.11
		ACN	526	23,000	575	49	0.02
		DCM	551	45,000	565	14	0.02
12	N, CH, N	PBS	557	56,000	628	71	0.01
		EtOH	558	58,000	615	57	0.13
		ACN	557	50,000	621	64	0.10
		DCM	575	73,000	618	43	0.11
5	CH, CH, N	PBS	568	14,000	660	92	0.02
		EtOH	568	20,000	648	80	0.05
		ACN	569	47,000	668	99	0.02
		DCM	600	34,000	657	57	0.05
13	N, CH, N	PBS	600	35,000	673	73	0.02
		EtOH	598	58,000	667	69	0.08
		ACN	597	42,000	674	77	0.10
		DCM	624	60,000	663	39	0.41

^aWavelength of the absorption maximum. ^bMolar absorption coefficient at λ_{max} . ^cWavelength of the emission maximum upon excitation at a wavelength 20 nm below λ_{max} . ^dStokes' shift. ^eFluorescence quantum yields (Φ_{F}) were measured by a comparative method using cresyl violet in ethanol ($\Phi_{\text{F,Ref}} = 0.54$) as a reference for compounds 4, 5, 12, and 13. Fluorescein dissolved in aqueous sodium hydroxide (0.1 M; $\Phi_{\text{F,Ref}} = 0.92$) was used as a reference in the case of compounds 10 and 11.¹⁷

insights into the photophysical behavior of the compounds in polar and less-polar environments. As shown in Table 1, the photophysical properties of coumarins 10–13 were compared with those of the parent compounds 4 and 5¹¹ to facilitate the establishment of SPPR.

All the new compounds exhibited an intense absorption band in the visible region of the electromagnetic spectrum, with the absorption maxima ranging from 502 nm (10) to 600 nm (13) in aqueous solution (PBS pH 7.4) and from 543 nm (10) to 624 nm (13) in DCM. To our surprise, the absorption maximum of coumarin 10 was significantly blue-shifted with respect the reference compound 4 (e.g., compare $\lambda_{\text{abs}} = 515$ and 543 nm for 10 and $\lambda_{\text{abs}} = 552$ and 569 nm for 4 in EtOH and DCM, respectively). Although not as pronounced as in the case of 10, a similar trend was found in *ortho,ortho*-pyrimidine-containing coumarin (11) since its absorption maximum was also blue-shifted (18–24 nm depending on the solvent) with respect 4. By contrast, a slight red shift was found in the absorption maximum of the *ortho,para*-pyrimidine-containing coumarin 12 (12 nm in PBS and 6 nm in DCM). This red-shift was considerably larger in the 4-CF₃ analogue (e.g., compare $\lambda_{\text{abs}} = 600$ nm for 13 and $\lambda_{\text{abs}} = 568$ nm for 5 in PBS). As previously observed with the first generation of COUPY dyes,^{11,12} 10–13 showed negative solvatochromism since the

absorption maxima was blue-shifted with increasing polarity of the solvent (e.g., compare the λ_{abs} of 10–13 in DCM with the corresponding values in aprotic (ACN) and protic (EtOH) polar solvents). Moreover, the molar absorption coefficients of the two derivatives containing the *ortho,para*-pyrimidine moiety were similar to or even higher than those of their respective parent dyes, especially in the 4-CF₃ analogue (e.g., compare $\epsilon = 58$ mM⁻¹ cm⁻¹ for 13 and $\epsilon = 20$ mM⁻¹ cm⁻¹ for 5 in EtOH).

The emission maxima of coumarins 10 and 11 were also blue-shifted both in polar and less-polar solvents with respect coumarin 4 (e.g., $\lambda_{\text{em}} = 564$ nm for 11 and $\lambda_{\text{em}} = 603$ nm for 4 in EtOH), which reproduces the effect of replacing *para*-pyridine by *ortho*-pyridine or *ortho,ortho*-pyrimidine moieties on the compounds' absorption maxima. By contrast, the emission maxima of COUPY dyes containing the *ortho,para*-pyrimidine moiety was red-shifted with respect to that of their parent compounds (11–24 nm in 12 and 6–19 nm in 13), especially in polar solvents. As a consequence, COUPY dyes 12 and 13 showed emission in the far-red to NIR region (Figure 2 and Figures S10–S17), the emission maximum in polar media being particularly appealing in the case of the 4-CF₃ fluorophore ($\lambda_{\text{em}} = 673$ nm for 13 in PBS). Interestingly, coumarin 12 exhibited larger Stokes' shifts than its parent dye

4 in all the solvents evaluated, while the replacement of *para*-pyridine by *ortho,para*-pyrimidine in 5 led to slightly lower values. Nevertheless, the Stokes' shifts of 12 and 13 in polar solvents are sufficiently large (e.g., 71 and 73 nm in PBS, respectively) to avoid the light reabsorption problems typically found in bioimaging applications.¹

As shown in Table 1, compounds 10 and 11 exhibited very weak fluorescence in all the solvents investigated. By contrast, fluorescence quantum yields for coumarin 13 were much higher than those of the parent compound 5, especially in less-polar solvents (e.g., 0.41 and 0.05 in DCM, respectively). This tendency was reversed in the case of the 4-CH₃ analogue since the Φ_F for 12 was smaller compared with that of 4 (e.g., 0.11 and 0.70 in DCM, respectively). Both *ortho,para*-pyrimidine-containing compounds exhibited moderate fluorescence quantum yields in polar protic solvents ($\Phi_F = 0.13$ for 12 and $\Phi_F = 0.08$ for 13 in EtOH).

Finally, the photostability of the most promising coumarins (12 and 13) was investigated in PBS buffer (pH 7.4) under green LED irradiation (Figure 3 and Figure S18). As shown in

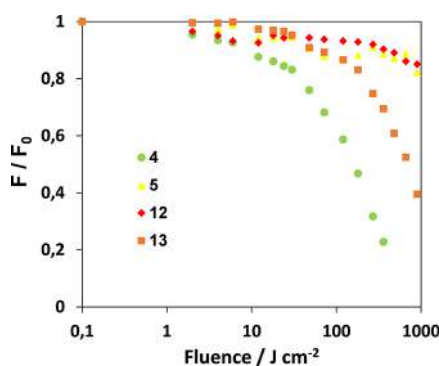


Figure 3. Fluorescence bleaching of COUPY dyes (4, 5, 12, and 13) in PBS buffer pH 7.4 (5 μ M) irradiated with green light (505 nm, 100 mW/cm²).

Figure 3, the replacement of pyridine in coumarin 4 with *ortho,para*-pyrimidine had a positive effect on the photostability of the resulting fluorophore (12). By contrast, coumarin 13 was found less photostable than its parent compound 5 and coumarin 12, which indicates that replacement of the CH₃ group at the 4-position with CF₃ in *ortho,para*-pyrimidine-containing COUPY dyes does not lead to an improvement of the overall photostability of the compounds. Nevertheless, it is worth noting that the two new pyrimidine-containing COUPY dyes were found photostable up to light fluences larger than 1000 J/cm² (12) and 200 J/cm² (13), which are more than 50- and 10-fold, respectively, higher than those typically used in imaging experiments with living cells.

In summary, all these observations allowed us to establish some SPPR. First, replacement of *para*-pyridine in COUPY dyes with *ortho*-pyridine or *ortho,ortho*-pyrimidine moieties had a negative effect on the spectroscopic properties of the fluorophores since both absorption and emission maxima were blue-shifted. Moreover, compounds 10 and 11 were found to be weakly fluorescent and their extinction coefficients were smaller than those of the parent coumarin 4. By contrast, the photophysical properties of COUPY dyes were clearly improved when *para*-pyridine was replaced with *ortho,para*-pyrimidine. On the one hand, both absorption and emission

maxima were red-shifted with respect to that of the parent compounds, especially in polar protic solvents. Indeed, the incorporation of the second nitrogen atom in the pyridine moiety in 5 caused a red shift of the absorption (32 nm) and emission (12 nm) bands in PBS pH 7.4 in the resulting coumarin 13 when compared with the parent compound. Very interestingly, the emission of 13 was extended beyond 750 nm (Figure 2), which would facilitate *in vivo* imaging. Although the incorporation of the *ortho,para*-pyrimidine moiety caused a slight decrease in the fluorescence quantum yields of the compounds (e.g., compare Φ_F of 4 and 12), the combination of this heterocycle with the CF₃ group at position 4 seems to compensate for this phenomenon, leading to moderate Φ_F values in protic and aprotic polar solvents (0.08–0.13) in the case of compound 13.

Fluorescence Imaging of COUPY Dyes in Living Cells. Taking into account the large photostability and the photophysical properties of the two *ortho,para*-pyrimidine-containing COUPY dyes (12 and 13), we decided to evaluate their usefulness as fluorescent probes in a more realistic situation (e.g., in living cells). As previously stated, the heterogeneous environment of an organic fluorophore within a cell or within a specific cellular organelle might be considerably different than the homogeneity of a solution in a spectroscopy cuvette. In fact, the presence of biomolecules such as proteins and lipids or the interaction with the components of cellular membranes might provide the fluorescent probe with an environment less hydrophilic than expected, thereby modifying the key parameters for bioimaging applications such as brightness.

The cellular uptake of 12 and 13 was first investigated in living HeLa cells (2 μ M, 30 min incubation) by using confocal microscopy and compared with that of the *para*-pyridine-containing coumarins (compounds 4 and 5, respectively). Irradiation was carried out with a yellow light laser ($\lambda_{ex} = 561$ nm) in the case of 4-CH₃ coumarins (4 and 12), while the higher red-shift absorption of the 4-CF₃ compounds (5 and 13) allowed the use of a red one ($\lambda_{ex} = 633$ nm). As shown in Figure 4, in all cases the fluorescence signal was clearly observed inside the cell, which confirms that the excellent cellular uptake of the parent COUPY dyes was retained after replacement of pyridine with pyrimidine. In addition, it is worth noting that no cell toxicity was observed during these studies. The overall pattern of staining (but not the relative fluorescence intensity between organelles; see below for a discussion) of pyrimidine-containing coumarins (12 and 13) was similar to that found with the parent fluorophores (4 and 5), suggesting accumulation in mitochondria, nucleoli and, to a lesser extent, in intracellular vesicles, mostly lysosomes. Colocalization experiments with two specific markers for labeling mitochondria (MitoTracker Green FM, MTG) and lysosomes (LysoTracker Green FM, LTG) confirmed the subcellular localization of the compounds.

As shown in Figure 5, the distribution of the fluorescence emission of the compounds was similar to that of MitoTracker Green FM, which confirmed accumulation into the mitochondria. Pearson's and Manders' (M_1 and M_2) coefficients were used to measure the degree of colocalization.^{11,12,18} On the one hand, Pearson's coefficients of 0.86 (12) and 0.87 (13) confirmed a clear correlation between the coumarin signals and MTG (Pearson's coefficients ranging from -1 to +1, +1 being the indicator of a perfect match). Such coefficients were higher than those obtained for the parent COUPY dyes (0.65 for 4 and 0.73 for 5), indicating a better correlation between

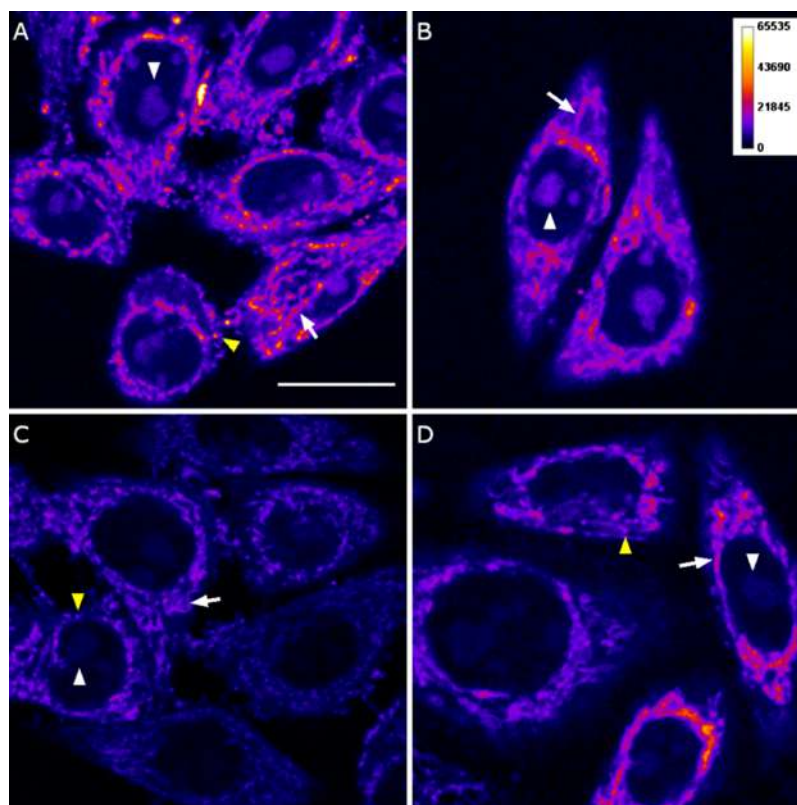


Figure 4. Cellular uptake of COUPY fluorophores (A) 4, (B) 5, (C) 12, and (D) 13. Single confocal planes of HeLa cells incubated with the compounds ($2 \mu\text{M}$, 30 min, 37°C). White arrows point out mitochondria, white arrowheads nucleoli, and yellow arrowheads stained vesicles. Scale bar: $20 \mu\text{m}$. All images are at the same scale as (A) and color coded using the Fire lookup table from Fiji (intensity calibration bar is showed in (B)).

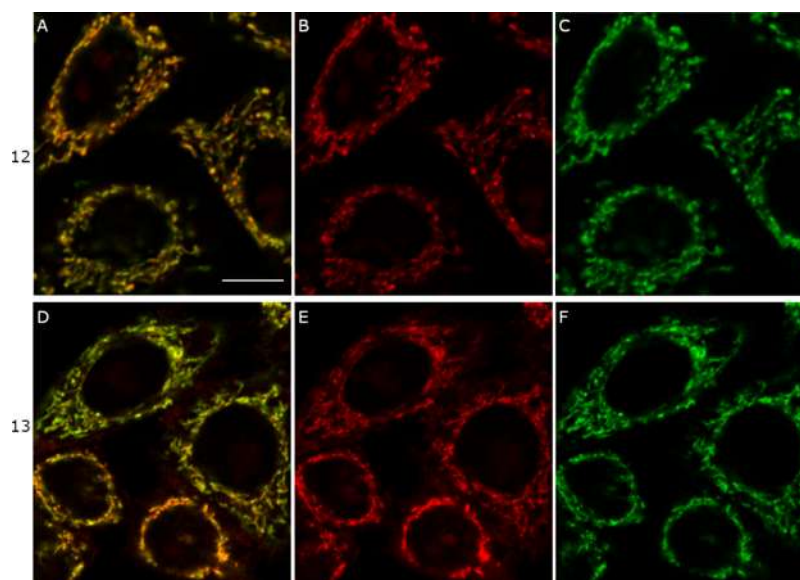


Figure 5. Colocalization studies with COUPY dyes 12 (top) and 13 (bottom) and MitoTracker Green FM. Single confocal plane of HeLa cells incubated with 12 or 13 ($2 \mu\text{M}$, red) and MitoTracker Green FM ($0.1 \mu\text{M}$, green). (A, D) Overlay of the two staining. (B, E) coumarin 12 and 13 signal, respectively. (C, F) MitoTracker Green FM signal. Scale bar: $10 \mu\text{m}$. All images are at the same scale as (A).

pyrimidine-containing coumarins and MTG. On the other hand, the Manders' coefficients (which ranges from 0 to 1, determining the intensities of one channel colocalizing with the other) also confirmed that 12 and 13 were mainly placed in the mitochondria. The degree of colocalization of 12 over MTG (M_1 coefficient) was 0.40, whereas that of MTG over 12 (M_2

coefficient) was 0.73. These values indicate that there is more MTG signal colocalizing with 12 than 12 colocalizing with MTG. The localization of the coumarin probe in other organelles such as nucleoli and intracellular vesicles accounts for the differences in both Manders' coefficients. It is worth noting that smaller values for M_1 (0.28) and M_2 (0.68) were

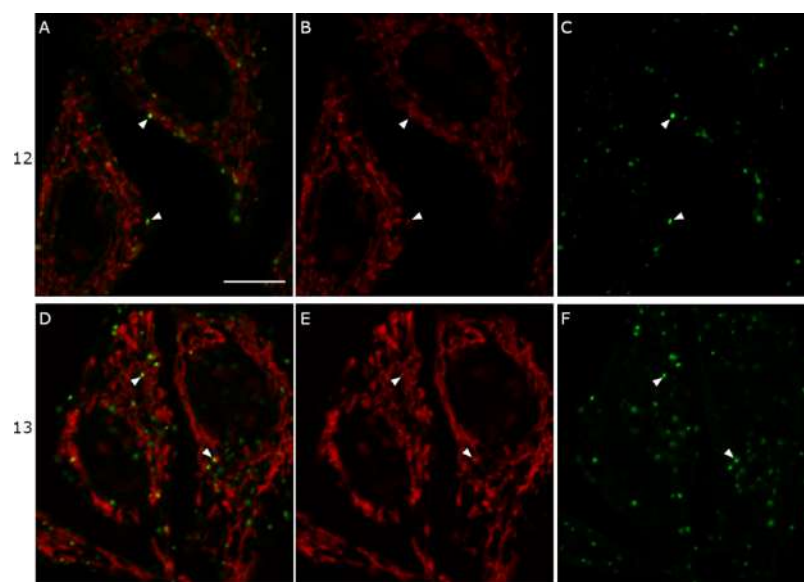


Figure 6. Colocalization studies with COUPY dyes and LysoTracker Green FM. Single confocal plane of HeLa cells incubated with coumarins **12** and **13** ($2\ \mu\text{M}$, red) and LysoTracker Green FM ($0.2\ \mu\text{M}$, green). (A, D) Overlay of the two staining. (B, E) coumarins **12** and **13** signal. (C, F) LysoTracker Green FM staining. White arrowheads point out COUPY dye vesicles colocalized with LysoTracker staining. Scale bar: $10\ \mu\text{m}$. All images are at the same scale as (A).

obtained in the case of the parent coumarin **4**, which indicates that the signal from the fluorophore that colocalizes with MTG is higher in the case of pyrimidine-containing coumarin (**12**) than in the pyridine analogue (**4**), thereby suggesting a higher preference for mitochondria. Although not as pronounced, a similar trend was found for coumarins **13** ($M_1 = 0.19$ and $M_2 = 0.86$) and **5** ($M_1 = 0.18$ and $M_2 = 0.76$).

As previously observed with the parent fluorophores,¹² colocalization experiments with LTG (Figure 6) confirmed that most of the fluorescence observed in intracellular vesicles along the cytoplasm was associated with lysosome accumulation (Pearson's coefficients being equal to 0.52 (**12**) and 0.49 (**13**) on average). The smaller Mander's coefficients for the colocalization of the compounds over LTG ($M_1 = 0.02$ for **12** and **13**) and of LTG over the coumarins ($M_2 = 0.45$ for **12** and 0.62 for **13**) in the colocalization experiment with LTG compared with MTG might be explained by a reduced affinity of COUPY dyes for lysosome and/or by lower abundance of this organelle in cells compared with mitochondria.

Very interestingly, the nucleoli inside the nuclei was much less intensely stained in compounds **12** and **13** than in the parent coumarins: compare in Figure 4 panels (C) (**12**) and (D) (**13**) with panels (A) (**4**) and (B) (**5**), respectively. As shown in Figure 7, measurement of the mean fluorescence intensity both in the mitochondria and nucleoli confirmed this

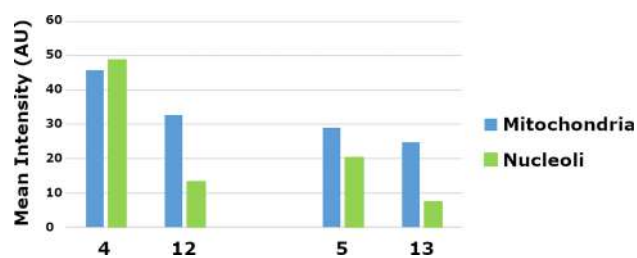


Figure 7. Graph of COUPY dyes **4**, **5**, **12**, and **13** vs mean intensity (Arbitrary Units) at the mitochondria and nucleoli.

observation. Indeed, the mean intensity for mitochondria and nucleoli was quite similar in the parent coumarins **4** and **5**, whereas the mean intensity for nucleoli staining was considerably reduced in case of the pyrimidine analogues **12** and **13**. These results are in line with the higher M_1 coefficients measured in colocalization experiments with MTG and indicate that replacement of *para*-pyridine by *ortho,para*-pyrimidine in COUPY dyes caused an increase in the selectivity of the compounds toward mitochondria.

Finally, the photostability of coumarins **12** and **13** was evaluated in a more realistic situation and compared with that of the parent compounds (**4** and **5**, respectively). For this purpose, living HeLa cells were incubated at $37\ ^\circ\text{C}$ with the compounds and irradiated continuously with the laser beam of the confocal microscope ($\lambda_{\text{ex}} = 561\ \text{nm}$ at $4.32\ \mu\text{W}$ for **4** and **12**, and $\lambda_{\text{ex}} = 633\ \text{nm}$ at $10.2\ \mu\text{W}$ for **5** and **13**) and images were acquired with an interval time of 0.42 s for 4.5 min. As shown in Figures S19 and S20, the overall fluorescence signal was significantly decreased in all the cases. In good agreement with the photobleaching studies (Figure 3), the *ortho,para*-containing coumarin **12** was found to be slightly more photostable than its parent compound (**4**), while this trend was found to be opposite in the case of the 4-CF₃-containing compounds. Nevertheless, it is worth noting that the laser power used in the photobleaching experiments was much higher than the one used during the conventional observation (0.3 and $1.7\ \mu\text{W}$ with 561 and 633 nm lasers, respectively), which confirms a good photostability and applicability of these molecules for imaging living cells by using fluorescence microscopy.

CONCLUSIONS

In summary, in this manuscript we have investigated how the photophysical properties and subcellular accumulation of coumarin-based COUPY fluorophores can be fine-tuned through replacement of the *para*-pyridine moiety with different heterocycles (*ortho*-pyridine and *ortho,ortho*- or *ortho,para*-pyrimidine), with the aim of establishing new SPPR. COUPY

dyes **10–13** were easily obtained from cheap, commercially available compounds in three linear synthetic steps, the reaction of thiocoumarins with suitable heteroarylacetonitrile derivatives followed by N-methylation of the pyridine or pyrimidine moieties being the key steps. Very interestingly, the photophysical properties of the new fluorophores were strongly influenced by these modifications. On the one hand, the replacement of the *para*-pyridine moiety with *ortho*-pyridine (**10**) or *ortho,ortho*-pyrimidine (**11**) had a negative effect on the spectroscopic properties of the dyes since both absorption and emission were blue-shifted, leading to weakly fluorescent compounds. On the other hand, the absorption and emission maxima of *ortho,para*-pyrimidine-containing fluorophores (**12–13**) were red-shifted with respect to the parent compounds, particularly in polar solvents. Besides emission in the far-red to NIR region, the newly synthesized fluorophores exhibited other appropriate characteristics for bioimaging applications such as large Stokes' shifts and high photostability. Furthermore, coumarins **12** and **13** retained the excellent cell permeability of COUPY dyes but exhibited a higher preference for mitochondria. Overall, these results provide useful indications for the development of novel mitochondria-targeted fluorescent probes based on small organic compounds since we have demonstrated that the selectivity for this organelle can be improved through the replacement of the N-alkylated pyridinium moieties by the corresponding N-alkylated *ortho,para*-pyrimidinium counterparts.

EXPERIMENTAL SECTION

Materials and Methods. Unless otherwise stated, common chemicals and solvents (HPLC grade or reagent grade quality) were purchased from commercial sources and used without further purification. Aluminum plates coated with a 0.2 mm-thick layer of silica gel 60 F₂₅₄ were used for thin-layer chromatography (TLC) analysis, whereas flash column chromatography purification was carried out using silica gel 60 (230–400 mesh). Reversed-phase HPLC analyses were carried out on a Jupiter Proteo C₁₈ column (250 × 4.6 mm, 90 Å 4 μm, flow rate: 1 mL/min) using linear gradients of 0.1% formic acid in H₂O (A) and 0.1% formic acid in ACN (B). NMR spectra were recorded at 25 °C in a 400 MHz spectrometer using the deuterated solvent as an internal deuterium lock. The residual protic signal of chloroform or DMSO was used as a reference in ¹H and ¹³C NMR spectra recorded in CDCl₃ or DMSO-*d*₆, respectively. Chemical shifts are reported in parts per million (ppm) in the δ scale, coupling constants in Hz, and multiplicity as follows: s (singlet), d (doublet), t (triplet), q (quartet), qt (quintuplet), m (multiplet), dd (doublet of doublets), dq (doublet of quartets), br (broad signal), etc. The proton signals of the *E* and *Z* rotamers were identified by simple inspection of the ¹H spectrum and the rotamer ratio was calculated by peak integration. 2D-NOESY spectra were acquired in DMSO-*d*₆ with a mixing time of 500 ms, either at 298 K or 350 K. Electrospray ionization mass spectra (ESI-MS) were recorded on an instrument equipped with a single quadrupole detector coupled to an HPLC, and high-resolution (HR) ESI-MS on a LC/MS-TOF instrument.

Synthesis of Pyrimidin-Acetonitrile Derivatives. 2-(Pyrimidin-2-yl)acetonitrile (**15**). A solution of KCN (0.63 g, 9.70 mmol) in DMSO (5 mL) was slowly added to a solution of 2-(chloromethyl)pyrimidine (0.5 g, 3.89 mmol) in DMSO (4 mL). The reaction mixture was stirred overnight at 35 °C with a hot plate magnetic stirrer. After addition of 50 mL of K₂CO₃ (10%), the aqueous phase was extracted with diethyl ether (10 × 30 mL). The combined organic fractions were dried over anhydrous Na₂SO₄, filtered, and evaporated under reduced pressure. The crude product was purified by column chromatography (silica gel, 0–15% ethyl acetate in DCM) to give 84 mg of colorless oil (yield 19%). TLC: *R*_f (ethyl acetate/DCM 1:1) 0.44. ¹H NMR (400 MHz, CDCl₃, δ (ppm)): 8.74 (2H, d, *J* = 5.1

Hz), 7.29 (1H, t, *J* = 5.1 Hz), 4.11 (s, 2H). ¹³C{¹H} NMR (101 MHz, CDCl₃, δ (ppm)): 161.4, 158.0, 120.3, 116.1, 28.6. LRMS (ESI-TOF) (*m/z*): [M + H]⁺ Calcd for C₆H₆N₃, 120.06; found, 119.90.

2-(Pyrimidin-4-yl)acetonitrile (**16**). A modified method was followed to synthesize compound **16**.¹⁹

(*E,N,N*-Dimethyl-2-(pyrimidin-4-yl)ethen-1-amine (**17**)). 4-Methylpyrimidine (10 g, 106 mmol) and 1,1-dimethoxy-*N,N*-dimethylmethanamine (38 g, 319 mmol) were dissolved in 50 mL of anhydrous DMF. The solution was heated at 140 °C with a hot plate magnetic stirrer for 24 h. The crude product was evaporated under reduced pressure to provide **17** as brown oil, which was used without further purification. TLC: *R*_f (DCM/MeOH 9:1) 0.50. ¹H NMR (400 MHz, CDCl₃, δ (ppm)): 8.73 (1H, s), 8.21 (1H, d, *J* = 5.6 Hz), 7.76 (1H, d, *J* = 13 Hz), 6.71 (1H, dd, *J* = 5.6, 1.6 Hz), 4.99 (1H, d, *J* = 13 Hz), 2.95 (6H, s).

2-(Pyrimidin-4-yl)acetonitrile (**16**). A solution of hydroxylamine-*O*-sulfonic acid (7.31 g, 57.5 mmol) in Milli-Q water (100 mL) was added to the crude product **17**, and the reaction mixture was heated at 50 °C with a hot plate magnetic stirrer for 45 min. Then, the mixture was cooled at 0 °C and saturated NaHCO₃ was added until basic pH, and the aqueous phase was extracted with ethyl acetate (6 × 200 mL). The combined organic phases were dried over anhydrous Na₂SO₄, filtered, and evaporated under reduced pressure. The brown oil was purified by column chromatography (silica gel, 0–25% ethyl acetate in DCM) to give 1.46 g of a yellow solid (yield 11%). TLC: *R*_f (ethyl acetate/DCM 1:1) 0.34. ¹H NMR (400 MHz, CDCl₃, δ (ppm)): 9.20 (1H, s), 8.80 (1H, d, *J* = 5.2 Hz), 7.51 (1H, d, *J* = 5.2 Hz), 3.94 (2H, s). ¹³C{¹H} NMR (101 MHz, CDCl₃, δ (ppm)): 159.3, 159.2, 158.3, 119.7, 115.5, 26.5. LRMS (ESI-TOF) (*m/z*): [M + H]⁺ Calcd for C₆H₆N₃, 120.06; found, 119.90.

Synthesis of COUPY Scaffolds (6–9). 2-(Cyano(2-pyridine)methylene)-7-(*N,N*-diethylamino)-4-methyl-coumarin (**6**). 7-(*N,N*-Diethylamino)-4-methyl-2-thiocoumarin **18** (0.25 g, 1.01 mmol), 2-(pyridin-2-yl)acetonitrile **14** (0.24 g, 2.02 mmol), and NaH (60% dispersion in mineral oil, 0.36 g, 9 mmol) were dissolved in anhydrous acetonitrile (15 mL) and the mixture was stirred for 2 h under an argon atmosphere at room temperature and protected from light. Then, AgNO₃ (0.34 g, 2.02 mmol) was added and the resulting mixture was stirred for 2 h under Ar at room temperature. The crude product was evaporated under reduced pressure and purified by column chromatography (silica gel, 0–25% ethyl acetate in DCM) to give 240 mg of an orange solid (yield 72%). TLC: *R*_f (ethyl acetate/DCM 1:1) 0.90. ¹H NMR (400 MHz, DMSO-*d*₆, δ (ppm)): (*E* + *Z* rotamers) 8.56 (1H, *m*), 8.13 (0.6H, dt, *J* = 8.2, 0.8 Hz), 7.82 (1.4H, *m*), 7.46 (1.4H, *m*), 7.18 (1H, *m*), 6.70 (1H, dd, *J* = 9.0, 2.4 Hz), 6.65 (1.2H, *m*), 6.42 (0.4H, d, *J* = 2.4 Hz), 3.46 (4H, q, *J* = 7.2 Hz), 2.35 (1.8H, d, *J* = 0.8 Hz), 2.32 (1.2H, d, *J* = 0.8 Hz), 1.14 (6H, *m*). ¹³C{¹H} NMR (101 MHz, DMSO-*d*₆, δ (ppm)): (*E* + *Z* rotamers) 163.2, 161.8, 154.0, 153.8, 152.7, 152.0, 150.6, 150.5, 149.0, 148.8, 144.6, 144.0, 137.1, 136.8, 126.0, 125.9, 121.8, 121.2, 120.7, 120.2, 119.6, 119.3, 110.8, 110.4, 109.8, 109.2, 109.1, 96.7, 96.1, 85.3, 81.0, 44.0, 43.8, 18.5, 18.0, 12.4. HRMS (ESI-TOF) (*m/z*): [M + H]⁺ Calcd for C₂₁H₂₂N₃O, 332.1763; found, 332.1759. Analytical HPLC (30–100% B in 30 min, formic acid additive): *R*_t = 15.2 min.

2-(Cyano(2-pyrimidine)methylene)-7-(*N,N*-diethylamino)-4-methyl-coumarin (**7**). 7-(*N,N*-Diethylamino)-4-methyl-2-thiocoumarin **18** (0.25 g, 1.01 mmol), 2-(pyrimidin-2-yl)acetonitrile **15** (0.24 g, 2.02 mmol), and NaH (60% dispersion in mineral oil, 0.36 g, 9 mmol) were dissolved in anhydrous acetonitrile (15 mL) and the mixture was stirred for 2 h under an argon atmosphere at room temperature and protected from light. Then, AgNO₃ (0.34 g, 2.02 mmol) was added and the resulting mixture was stirred for 2 h under Ar at room temperature. The crude product was evaporated under reduced pressure and purified by column chromatography (silica gel, 0–10% ethyl acetate in DCM) to give 171 mg of an orange solid (yield 51%). TLC: *R*_f (ethyl acetate/DCM 1:1) 0.63. ¹H NMR (400 MHz, DMSO-*d*₆, δ (ppm)): (major rotamer) 8.74 (2H, d, *J* = 4.8 Hz), 8.18 (1H, s), 7.53 (1H, d, *J* = 9.0 Hz), 7.17 (1H, t, *J* = 4.8 Hz), 6.76 (1H, dd, *J* = 9.0, 2.4 Hz), 6.46 (1H, d, *J* = 2.4 Hz), 3.47 (4H, q, *J* = 7.2 Hz), 2.39 (3H, s), 1.15 (6H, t, *J* = 6.9 Hz). ¹³C{¹H} NMR (101

MHz, DMSO- d_6 , δ (ppm)): (major rotamer) 166.6, 162.9, 157.0, 154.1, 150.9, 146.6, 126.3, 118.4, 116.6, 110.5, 109.9, 109.7, 96.0, 82.5, 44.1, 18.7, 12.4. HRMS (ESI-TOF) (m/z): $[M + H]^+$ Calcd for $C_{20}H_{21}N_4O$, 333.1715; found, 333.1710. Analytical HPLC (30–100% B in 30 min, formic acid additive): $R_t = 21.2$ min.

2-(Cyano(4-pyrimidine)methylene)-7-(*N,N*-diethylamino)-4-methyl-coumarin (8). 7-(*N,N*-Diethylamino)-4-methyl-2-thiocoumarin **18** (0.25 g, 1.01 mmol), 2-(pyrimidin-4-yl)acetonitrile **16** (0.24 g, 2.02 mmol), and NaH (60% dispersion in mineral oil, 0.36 g, 9 mmol) were dissolved in anhydrous acetonitrile (15 mL) and the mixture was stirred for 2 h under an argon atmosphere at room temperature and protected from light. Then, $AgNO_3$ (0.34 g, 2.02 mmol) was added and the resulting mixture was stirred for 2 h under Ar at room temperature. The crude product was evaporated under reduced pressure and purified by column chromatography (silica gel, 0–25% ethyl acetate in DCM) to give 275 mg of an orange solid (yield 82%). TLC: R_f (ethyl acetate/DCM 1:1) 0.50. 1H NMR (400 MHz, DMSO- d_6 , δ (ppm)): (*E* + *Z* rotamers) 9.04 (1H, m), 8.69 (0.6H, d, $J = 5.6$ Hz), 8.62 (0.4H, d, $J = 5.6$ Hz), 8.26 (0.4H, d, $J = 0.8$ Hz), 8.18 (0.6H, dd, $J = 5.6, 1.6$ Hz), 7.59 (0.4H, d, $J = 9.2$ Hz), 7.56 (0.6H, d, $J = 8.8$ Hz), 7.42 (0.4H, dd, $J = 5.6, 1.6$ Hz), 6.81 (1.6H, m), 6.75 (0.6H, d, $J = 0.8$ Hz), 6.51 (0.4H, d, $J = 2.8$ Hz), 3.49 (4H, m), 2.43 (1.2H, d, $J = 1.2$ Hz), 2.42 (1.7H, d, $J = 1.2$ Hz), 1.16 (6H, t, $J = 7.0$ Hz). $^{13}C\{^1H\}$ NMR (101 MHz, DMSO- d_6 , δ (ppm)): (*E* + *Z* rotamers) 165.5, 165.2, 160.3, 159.1, 158.1, 157.6, 156.9, 156.7, 154.2, 151.2, 151.0, 148.5, 147.6, 126.5, 126.4, 118.6, 118.4, 117.5, 116.9, 116.7, 110.6, 110.4, 110.3, 110.2, 109.2, 96.6, 95.8, 82.8, 78.5, 44.1, 43.9, 18.8, 18.2, 12.4, 12.3. HRMS (ESI-TOF) (m/z): $[M + H]^+$ Calcd for $C_{20}H_{21}N_4O$, 333.1715; found, 333.1709. Analytical HPLC (30–100% B in 30 min, formic acid additive): $R_t = 17.5$ min.

2-(Cyano(4-pyrimidine)methylene)-7-(*N,N*-dimethylamino)-4-trifluoromethyl-coumarin (9). 7-(*N,N*-Dimethylamino)-4-trifluoromethyl-2-thiocoumarin **19** (0.25 g, 0.92 mmol), 2-(pyrimidin-4-yl)acetonitrile **16** (0.22 g, 1.83 mmol), and NaH (60% dispersion in mineral oil, 0.33 g, 8.25 mmol) were dissolved in anhydrous acetonitrile (15 mL) and the mixture was stirred for 2 h under an argon atmosphere at room temperature and protected from light. Then, $AgNO_3$ (0.31 g, 1.83 mmol) was added and the resulting mixture was stirred for 2 h under Ar at room temperature. The crude product was evaporated under reduced pressure and purified by column chromatography (silica gel, 0–10% ethyl acetate in DCM) to give 248 mg of a red solid (yield 75%). TLC: R_f (ethyl acetate/DCM 1:1) 0.30 and 0.64. 1H NMR (400 MHz, DMSO- d_6 , δ (ppm)): (*E* + *Z* rotamers) 9.17 (0.55H, d, $J = 1.2$ Hz), 9.15 (0.45H, d, $J = 1.2$ Hz), 8.83 (0.55H, d, $J = 5.6$ Hz), 8.78 (0.45H, d, $J = 5.6$ Hz), 8.74 (0.45H, s), 8.28 (0.55H, dd, $J = 5.6, 1.6$ Hz), 7.56 (0.45H, dd, $J = 5.6, 1.6$ Hz), 7.44 (1H, m), 7.03 (0.55H, s), 7.00 (0.55H, d, $J = 2.8$ Hz), 6.87 (1H, m), 6.64 (0.45H, d, $J = 2.4$ Hz), 3.13 (3.3H, s), 3.11 (2.7H, s). $^{13}C\{^1H\}$ NMR (101 MHz, DMSO- d_6 , δ (ppm)): (*E* + *Z* rotamers) 163.3, 162.6, 158.7, 158.3, 157.9, 157.7, 157.6, 154.6, 154.5, 153.7, 153.6, 125.3, 118.8, 117.9, 117.4, 116.8, 111.0, 110.9, 110.8, 110.7, 110.7, 110.5, 110.4, 110.4, 103.5, 102.5, 98.1, 97.4, 89.7, 89.5, 85.2, 39.7. ^{19}F NMR (376 MHz, DMSO- d_6 , δ (ppm)): (*E* + *Z* rotamers) -63.0 (1.35F, s), -63.1 (1.65F, s). HRMS (ESI-TOF) (m/z): $[M + H]^+$ Calcd for $C_{18}H_{14}F_3N_4O$, 359.1114; found, 359.1112. Analytical HPLC (30–100% B in 30 min, formic acid additive): $R_t = 22.8$ min.

Synthesis of COUPY Fluorophores (10–13). **2-(Cyano(1-methyl(2-pyridin-1-ium)methylene)-7-(*N,N*-diethylamino)-4-methyl-coumarin triflate (10).** Methyl trifluoromethanesulfonate (47.5 μ L, 0.42 mmol) was added to a solution of 2-(cyano(2-pyridine)methylene)-7-(*N,N*-diethylamino)-4-methyl-coumarin **6** (70 mg, 0.21 mmol) in DCM (30 mL) under an argon atmosphere. The mixture was stirred for 4 h at room temperature and protected from light. The reaction mixture was evaporated under reduced pressure and purified by column chromatography (silica gel, 0–3% MeOH in DCM) to give 77 mg of a red solid (yield 74%). TLC: R_f (DCM/MeOH 9:1) 0.35. 1H NMR (400 MHz, 77 $^\circ$ C, DMSO- d_6 , δ (ppm)): 9.02 (1H, d, $J = 6.4$ Hz), 8.53 (1H, td, $J = 7.6, 1.2$ Hz), 8.26 (1H, d, $J = 8.0$ Hz), 8.00 (1H, td, $J = 7.6, 1.2$ Hz), 7.59 (1H, d, $J = 9.2$ Hz), 6.83 (1H, dd, $J = 9.2, 2.4$ Hz), 6.62 (1H, br s), 6.51 (1H, br s), 4.28

(3H, s), 3.46 (4H, q, $J = 7.2$ Hz), 2.43 (3H, s), 1.15 (6H, t, $J = 7.2$ Hz). $^{13}C\{^1H\}$ NMR (101 MHz, 77 $^\circ$ C, DMSO- d_6 , δ (ppm)): 165.6, 153.9, 151.2, 149.3, 147.8, 147.1, 144.6, 130.5, 126.2, 125.3, 120.5 (q, $J = 323$ Hz, Tf), 116.5, 110.3, 109.4, 108.0, 96.2, 71.0, 46.0, 43.7, 17.6, 12.0. ^{19}F NMR (376 MHz, DMSO- d_6 , δ (ppm)): -77.8 (3F, s). HRMS (ESI-TOF) (m/z): $[M]^+$ Calcd for $C_{22}H_{24}N_3O$, 346.1914; found, 346.1911. Analytical HPLC (30–100% B in 30 min, formic acid additive): $R_t = 5.5$ min.

2-(Cyano(1-methyl(2-pyrimidin-1-ium)methylene)-7-(*N,N*-diethylamino)-4-methyl-coumarin triflate (11). Methyl trifluoromethanesulfonate (47.5 μ L, 0.42 mmol) was added to a solution of 2-(cyano(2-pyrimidine)methylene)-7-(*N,N*-diethylamino)-4-methyl-coumarin **7** (70 mg, 0.21 mmol) in DCM (30 mL) under an argon atmosphere. The mixture was stirred for 4 h at room temperature and protected from light. Then, an additional amount of methyl trifluoromethanesulfonate (47.5 μ L, 0.42 mmol) was added to the reaction mixture and was stirred for 2 h. The reaction mixture was evaporated under reduced pressure and purified by column chromatography (silica gel, 0–4% MeOH in DCM) to give 66 mg of an orange solid (yield 64%). TLC: R_f (DCM/MeOH 9:1) 0.31. 1H NMR (400 MHz, DMSO- d_6 , δ (ppm)): 9.28 (1H, dd, $J = 4.2, 2.0$ Hz), 9.16 (1H, dd, $J = 6.6, 1.8$ Hz), 7.91 (1H, dd, $J = 6.4, 5.6$ Hz, 1H), 7.70 (1H, d, $J = 9.2$ Hz), 7.06 (1H, s), 6.94 (1H, dd, $J = 9.2, 2.8$ Hz), 6.70 (1H, d, $J = 2.8$ Hz), 4.14 (3H, s), 3.50 (4H, q, $J = 7.2$ Hz), 2.49 (3H, s), 1.15 (6H, t, $J = 7.2$ Hz). $^{13}C\{^1H\}$ NMR (101 MHz, DMSO- d_6 , δ (ppm)): 162.9157.6, 154.7, 154.6, 152.5, 151.8, 127.1, 120.7 (q, $J = 323$ Hz, Tf), 118.7, 116.8, 111.6, 110.4, 109.2, 96.0, 73.4, 46.5, 44.2, 18.5, 12.3. ^{19}F NMR (376 MHz, DMSO- d_6 , δ (ppm)): -77.8 (3F, s). HRMS (ESI-TOF) (m/z): $[M]^+$ Calcd for $C_{21}H_{23}N_4O$, 347.1866; found, 347.1865. Analytical HPLC (30–100% B in 30 min, formic acid additive): $R_t = 5.1$ min.

2-(Cyano(1-methyl(4-pyrimidin-1-ium)methylene)-7-(*N,N*-diethylamino)-4-methyl-coumarin triflate (12). Methyl trifluoromethanesulfonate (47.5 μ L, 0.42 mmol) was added to a solution of 2-(cyano(4-pyrimidine)methylene)-7-(*N,N*-diethylamino)-4-methyl-coumarin **8** (70 mg, 0.21 mmol) in DCM (30 mL) under an argon atmosphere. The mixture was stirred for 4 h at room temperature and protected from light. The reaction mixture was evaporated under reduced pressure and purified by column chromatography (silica gel, 0–2% MeOH in DCM) to give 83 mg of a violet solid (yield 80%). TLC: R_f (DCM/MeOH 9:1) 0.28. 1H NMR (400 MHz, 77 $^\circ$ C, DMSO- d_6 , δ (ppm)): 9.11 (1H, m), 8.53 (1H, dd, $J = 7.6, 2.0$ Hz), 8.00 (1H, d, $J = 7.6$ Hz), 7.84 (1H, d, $J = 9.2$ Hz), 7.60 (1H, br s), 7.09 (1H, dd, $J = 9.2, 2.4$ Hz), 6.89 (1H, d, $J = 2.4$ Hz), 4.02 (3H, s), 3.60 (4H, q, $J = 7.2$ Hz), 2.63 (3H, s), 1.23 (6H, t, $J = 7.2$ Hz). $^{13}C\{^1H\}$ NMR (101 MHz, DMSO- d_6 , δ (ppm)): 167.3, 163.4, 155.6, 155.5, 152.7, 152.2, 147.5, 127.5, 120.7 (q, $J = 323$ Hz, Tf), 117.4, 114.8, 113.1, 111.5, 110.7, 95.9, 44.4, 42.5, 18.9, 12.4. ^{19}F NMR (376 MHz, DMSO- d_6 , δ (ppm)): -77.8 (3F, s). HRMS (ESI-TOF) (m/z): $[M]^+$ Calcd for $C_{21}H_{23}N_4O$, 347.1866; found, 347.1866. Analytical HPLC (30–100% B in 30 min, formic acid additive): $R_t = 5.4$ min.

2-(Cyano(1-methyl(4-pyrimidin-1-ium)methylene)-7-(*N,N*-dimethylamino)-4-trifluoromethyl-coumarin triflate (13). Methyl trifluoromethanesulfonate (47.3 μ L, 0.40 mmol) was added to a solution of 2-(cyano(4-pyrimidine)methylene)-7-(*N,N*-dimethylamino)-4-trifluoromethyl-coumarin **9** (70 mg, 0.20 mmol) in DCM (30 mL) under an argon atmosphere. The mixture was stirred for 4 h at room temperature and protected from light. The reaction mixture was evaporated under reduced pressure and purified by column chromatography (silica gel, 0–2% MeOH in DCM) to give 75 mg of a blue solid (yield 72%). TLC: R_f (DCM/MeOH 9:1) 0.48. 1H NMR (400 MHz, 77 $^\circ$ C, DMSO- d_6 , δ (ppm)): 9.40 (1H, s), 8.81 (1H, dd, $J = 7.4, 1.8$ Hz), 8.21 (1H, br s), 7.65 (1H, dq, $J = 9.2, 2.0$ Hz), 7.13 (1H, dd, $J = 9.2, 2.6$ Hz), 7.01 (1H, br s), 4.13 (3H, s), 3.22 (6H, s). $^{13}C\{^1H\}$ NMR (101 MHz, 77 $^\circ$ C, DMSO- d_6 , δ (ppm)): 166.8, 163.2, 158.8, 156.0, 155.4, 154.5, 153.1, 152.4, 136.7 (q, $J = 32$ Hz), 125.4, 124.9, 121.5 (q, $J = 277$ Hz), 120.5 (q, $J = 323$ Hz), 116.6, 115.6, 113.3, 109.7, 108.4, 107.7, 101.5, 97.7, 97.2, 43.0, 40.0. ^{19}F NMR (376 MHz, DMSO- d_6 , δ (ppm)): -63.1 (3F, s), -77.8 (3F, s). HRMS (ESI-TOF) (m/z): $[M]^+$ Calcd for $C_{19}H_{16}F_3N_4O$, 373.1271;

found, 373.1274. Analytical HPLC (30–100% B in 30 min, formic acid additive): $R_t = 5.1$ min.

Photophysical Characterization of the Compounds. Absorption spectra were recorded on a Jasco V-730 spectrophotometer at room temperature. Molar absorption coefficients (ϵ) were determined by direct application of the Beer–Lambert law, using solutions of the compounds in each solvent with concentrations ranging from 10^{-6} to 10^{-5} M. Emission spectra were measured on a Photon Technology International (PTI) fluorimeter. Fluorescence quantum yields (Φ_F) were measured by a comparative method using Cresyl Violet in ethanol ($\Phi_{F,Ref} = 0.54$) as a reference for compounds 4, 5, 12, and 13. Fluorescein dissolved in aqueous sodium hydroxide (0.1 M; $\Phi_{F,Ref} = 0.92$) was used as a reference in the case of compounds 10 and 11.¹⁷ Then, optically matched solutions of the compounds and CV were prepared and fluorescence spectra were recorded. The absorbance of the sample and reference solutions was set below 0.1 at the excitation wavelength and Φ_F was calculated using the following eq 1:

$$\Phi_{F,Sample} = \frac{Area_{Sample}}{Area_{Ref}} \times \left(\frac{\eta_{Sample}}{\eta_{Ref}} \right)^2 \times \Phi_{F,ref} \quad (1)$$

where $Area_{Sample}$ and $Area_{Ref}$ are the integrated fluorescence for the sample and the reference and η_{Sample} and η_{Ref} are the refractive index of the sample and reference solutions, respectively. The uncertainty in the experimental value of Φ_F has been estimated to be approximately 10%.

Photostability studies were performed by monitoring fluorescence bleaching of a 5 μ M PBS solution (pH 7.4) of the compounds at 37 °C irradiated with a high power 505 nm LED (100 mW/cm²). Fluorescence intensity values were recorded at $t = 0$ (F_0) and after different irradiation times (F).

Cell Culture and Treatments. HeLa cells were maintained in DMEM (Dulbecco's Modified Eagle Medium) containing high glucose (4.5 g/L) and supplemented with 10% fetal calf serum (FCS) and 50 U/mL penicillin–streptomycin. For cellular uptake experiments and posterior observation under a microscope, cells were seeded on glass-bottom dishes (P35G-1.5-14-C, Mattek). The cells were incubated for 30 min at 37 °C with COUPY dyes (4, 5, 12, or 13, 2 μ M) in supplemented DMEM, 24 hours after cell seeding. Then, the cells were washed three times with DPBS (Dulbecco's phosphate buffered saline, pH 7.0–7.3) to remove the excess fluorophores and kept in low glucose DMEM without phenol red for fluorescence imaging.

For colocalization experiments with MitoTracker Green FM, HeLa cells were treated with COUPY dyes (2 μ M) and MitoTracker Green FM (0.1 μ M) for 30 min at 37 °C in nonsupplemented DMEM. After removal of the medium and washing three times with DPBS, cells were kept in low glucose DMEM without phenol red for fluorescence imaging.

For colocalization experiments with LysoTracker Green FM and Hoechst 33342, HeLa cells were treated with COUPY dyes (2 μ M) and LysoTracker Green FM (0.2 μ M) for 30 min at 37 °C in nonsupplemented DMEM. After removal of the medium and washing three times with DPBS, the cells were incubated for 10 min at 37 °C with Hoechst 33342 (1 μ g/mL) in supplemented DMEM. Finally, the cells were washed and kept in low glucose DMEM without phenol red for fluorescence imaging.

Fluorescence Imaging. All microscopy observations were performed using a Zeiss LSM 880 confocal microscope equipped with a 405 nm laser diode, an argon-ion laser, a 561 nm laser, and a 633 nm laser. The microscope was also equipped with a Heating Insert P S (Pecon) and a 5% CO₂ providing system. Cells were observed at 37 °C using a 63 \times 1.2 glycerol immersion objective. Coumarins 4 and 12 were excited using the 561 nm laser and detected from 570 to 670 nm. Coumarins 5 and 13 were excited using the 633 nm laser and detected from 643 to 758 nm. In colocalization studies, MitoTracker Green FM and LysoTracker Green were observed using the 488 nm laser line of the argon-ion laser, whereas the 405 nm laser diode was used for observing Hoechst 33342.

Bleaching experiments were performed at 37 °C by continuous image acquisition with an interval time of 0.42 s for 4.5 min. Coumarins 4 and 12 were bleached using the 561 nm laser at 4.32 μ W and coumarins 5 and 13 were bleached with the 633 nm laser at 10.2 μ W.

Image processing and analysis was performed using Fiji.²⁰

Intensity Measurement. The nuclei and coumarin channels were processed by median filtering (radius = 2), Gaussian filtering (sigma = 2), and background subtraction (rolling ball radius = 300). The mean intensity in the nucleoli was measured in the maximum intensity projection of the processed coumarin image after manually drawing ROIs around each nucleoli. The intensity measurement in mitochondria needed further processing. First, the nuclei were segmented using the Intermodes algorithm,²¹ and the resulting binary image was processed by filling holes and opening operations. Then the binary image of the nuclei was subtracted to the processed coumarin image to get rid of any nuclear signal. After the subtraction, the coumarin staining channel was projected with the maximum intensity and the mitochondria were segmented using the Phansalkar algorithm (radius = 5).²² The binary image of the mitochondria was used as a mask to obtain the coumarin signal in the mitochondria and then measure its mean intensity.

Bleaching Analysis. Images were first processed by median filtering (radius = 1) and background subtraction (rolling ball radius = 50). Then, an ROI was manually drawn around each cell and in the background to measure the mean intensity along time. Intensity normalization was performed using the following eq 2:

$$\text{Normalized intensity} = \frac{\text{Cell}(t) - \text{Backg}(t)}{\text{Cell}(0) - \text{Backg}(0)} \quad (2)$$

where $\text{Cell}(t)$ is the mean intensity in a cell at t time, $\text{Cell}(0)$ is the mean intensity in that cell at the beginning of the experiment, $\text{Backg}(t)$ is the mean intensity in the background at t time, and $\text{Backg}(0)$ is the mean intensity in the background at the beginning of the experiment. After intensity normalization, the time at which the intensity dropped to half the initial one (t_{50}) was obtained. Differences between the different t_{50} of coumarin 4 and 12 were tested with Student's t-test.

Colocalizations Coefficients. The MitoTracker or LysoTracker and coumarin channels were processed by median filtering (radius = 1), Gaussian filtering (sigma = 1), and background subtraction (rolling ball radius = 300). Colocalization coefficients were measured using the JaCoP plugin¹⁷ on the different stacks of images ($n = 4$) with each stack containing 3–5 cells. The threshold for the coumarin channel was set to include the signal in the mitochondria, nucleoli, and vesicles. The threshold for the MitoTracker or LysoTracker channels was set to specifically select mitochondria and lysosomes, respectively.

■ ASSOCIATED CONTENT

Supporting Information

The Supporting Information is available free of charge at <https://pubs.acs.org/doi/10.1021/acs.joc.0c00570>.

Copies of HPLC traces and UV–vis absorption and fluorescence emission spectra of the compounds; additional fluorescence imaging studies; and 1D NMR (¹H, ¹³C, and ¹⁹F), MS, and selected 2D NMR spectra (PDF).

■ AUTHOR INFORMATION

Corresponding Author

Vicente Marchán – *Departament de Química Inorgànica i Orgànica, Secció de Química Orgànica, IBUB, Universitat de Barcelona, E-08028 Barcelona, Spain*; orcid.org/0000-0002-1905-2156; Email: vmarchan@ub.edu

Authors

Anna Rovira – Departament de Química Inorgànica i Orgànica, Secció de Química Orgànica, IBUB, Universitat de Barcelona, E-08028 Barcelona, Spain

Miriam Pujals – Departament de Química Inorgànica i Orgànica, Secció de Química Orgànica, IBUB, Universitat de Barcelona, E-08028 Barcelona, Spain

Albert Gandioso – Departament de Química Inorgànica i Orgànica, Secció de Química Orgànica, IBUB, Universitat de Barcelona, E-08028 Barcelona, Spain

Marta López-Corrales – Departament de Química Inorgànica i Orgànica, Secció de Química Orgànica, IBUB, Universitat de Barcelona, E-08028 Barcelona, Spain

Manel Bosch – Unitat de Microscòpia Òptica Avançada, Centres Científics i Tecnològics, Universitat de Barcelona, E-08028 Barcelona, Spain

Complete contact information is available at:

<https://pubs.acs.org/10.1021/acs.joc.0c00570>

Notes

The authors declare no competing financial interest.

ACKNOWLEDGMENTS

This work was supported by funds from the Spanish Government (MCIU/AEI/FEDER, UE; grant CTQ2017-84779-R) and the Generalitat de Catalunya (2017 DI 072). The authors acknowledge the helpful assistance of Dr. Francisco Cárdenas (NMR) and Dr. Irene Fernández and Laura Ortiz (MS) from CCiTUB. A.R. and A.G. were recipient fellows of the University of Barcelona.

REFERENCES

- (1) (a) Lavis, L. D.; Raines, R. T. Bright Ideas for Chemical Biology. *ACS Chem. Biol.* **2008**, *3*, 142–155. (b) Yuan, L.; Lin, W.; Zheng, K.; He, L.; Huang, W. Far-red to near infrared analyte-responsive fluorescent probes based on organic fluorophore platforms for fluorescence imaging. *Chem. Soc. Rev.* **2013**, *42*, 622–661. (c) Lavis, L. D.; Raines, R. T. Bright Building Blocks for Chemical Biology. *ACS Chem. Biol.* **2014**, *9*, 855–866. (d) Zheng, Q.; Juette, M. F.; Jockusch, S.; Wasserman, M. R.; Zhou, Z.; Altman, R. B.; Blanchard, S. C. Ultra-stable Organic Fluorophores for Single-molecule Research. *Chem. Soc. Rev.* **2014**, *43*, 1044–1056. (e) Zheng, Q.; Lavis, L. D. Development of photostable fluorophores for molecular imaging. *Curr. Opin. Chem. Biol.* **2017**, *39*, 32–38. (f) Freidus, L. G.; Pradeep, P.; Kumar, P.; Choonara, Y. E.; Pillay, V. Alternative Fluorophores Designed for Advanced Molecular Imaging. *Drug Discovery Today* **2018**, *23*, 115–133.
- (2) (a) Srinivasarao, M.; Galliford, C. V.; Low, P. S. Principles in the design of ligand-targeted cancer therapeutics and imaging agents. *Nat. Rev. Drug Discov.* **2015**, *14*, 203–219. (b) Zhang, R. R.; Schroeder, A. B.; Grudzinski, J. J.; Rosenthal, E. L.; Warram, J. M.; Pinchuk, A. N.; Eliceiri, K. W.; Kuo, J. S.; Weichert, J. P. Beyond the margins: realtime detection of cancer using targeted fluorophores. *Nat. Rev. Clin. Oncol.* **2017**, *14*, 347–364. (c) Gao, M.; Yu, F.; Lv, C.; Choo, J.; Chen, L. Fluorescent chemical probes for accurate tumor diagnosis and targeting therapy. *Chem. Soc. Rev.* **2017**, *46*, 2237–2271.
- (3) Alamudi, S. H.; Chang, Y.-T. Advances in the design of cell-permeable fluorescent probes for applications in live cell imaging. *Chem. Commun.* **2018**, *54*, 13641–13653.
- (4) Apostolova, N.; Blas-García, A.; Esplugues, J. V. Mitochondria sentencing about cellular life and death: a matter of oxidative stress. *Curr. Pharm. Des.* **2011**, *17*, 4047–4060.
- (5) (a) Modica-Napolitano, J. S.; Singh, K. K. Mitochondrial dysfunction in cancer. *Mitochondrion* **2004**, *4*, 755–762. (b) Lin, M. T.; Beal, M. F. Mitochondrial dysfunction and oxidative stress in

neurodegenerative diseases. *Nature* **2006**, *443*, 787–795. (c) Sun, N.; Youle, R. J.; Finkel, T. The Mitochondrial Basis of Aging. *Mol. Cell* **2016**, *61*, 654–666. (d) Hou, X.-S.; Wang, H.-S.; Mugaka, B. P.; Yang, G.-J.; Ding, Y. Mitochondria: promising organelle targets for cancer diagnosis and treatment. *Biomater. Sci.* **2018**, *6*, 2786–2797.

(6) Hu, F.; Cai, X.; Manghnani, P. N.; Kenry, K.; Wu, W.; Liu, B. Multicolor monitoring of cellular organelles by single wavelength excitation to visualize the mitophagy process. *Chem. Sci.* **2018**, *9*, 2756–2761.

(7) (a) Wang, Y.; Liu, T.; Zhang, E.; Luo, S.; Tan, X.; Shi, C. Preferential accumulation of the near infrared heptamethine dye IR-780 in the mitochondria of drug-resistant lung cancer cells. *Biomaterials* **2014**, *35*, 4116–4124. (b) Yang, X.; Shi, C.; Tong, R.; Qian, W.; Zhou, H. E.; Wang, R.; Zhu, G.; Cheng, J.; Yang, V. W.; Cheng, T.; Henary, M.; Strekowski, L.; Chung, L. W. K. Near IR Heptamethine Cyanine Dye-Mediated Cancer Imaging. *Clin. Cancer Res.* **2010**, *16*, 2833–2844. (c) Johnson, L. V.; Walsh, M. L.; Chen, L. B. Localization of mitochondria in living cells with rhodamine 123. *Proc. Natl. Acad. Sci. U. S. A.* **1980**, *77*, 990–994.

(8) (a) Zhang, W.; Kwok, R. T. K.; Chen, Y.; Chen, S.; Zhao, E.; Yu, C. Y. Y.; Lam, J. W. Y.; Zheng, Q.; Tang, B. Z. Real-time monitoring of the mitophagy process by a photostable fluorescent mitochondrion-specific bioprobe with AIE characteristics. *Chem. Commun.* **2015**, *51*, 9022–9025. (b) Xu, W.; Zeng, Z.; Jiang, J.-H.; Chang, Y.-T.; Yuan, L. Discerning the Chemistry in Individual Organelles with Small-Molecule Fluorescent Probes. *Angew. Chem. Int. Ed.* **2016**, *55*, 13658–13699. (c) Sung, J.; Lee, Y.; Cha, J.-H.; Park, S. B.; Kim, E. Development of fluorescent mitochondria probe based on 1,2-dihydropyrrolo[3,4-b]indolizine-3-one. *Dyes Pigm.* **2017**, *145*, 461–468. (d) Zielonka, J.; Joseph, J.; Sikora, A.; Hardy, M.; Ouari, O.; Vasquez-Vivar, J.; Cheng, G.; Lopez, M.; Kalyanaraman, B. Mitochondria-Targeted Triphenylphosphonium-Based Compounds: Syntheses, Mechanisms of Action, and Therapeutic and Diagnostic Applications. *Chem. Rev.* **2017**, *117*, 10043–10120.

(9) (a) Wu, S.; Cao, Q.; Wang, X.; Cheng, K.; Cheng, Z. Design, synthesis and biological evaluation of mitochondria targeting theranostic agents. *Chem. Commun.* **2014**, *50*, 8919–8922. (b) Luo, S.; Tan, X.; Fang, S.; Wang, Y.; Liu, T.; Wang, X.; Yuan, Y.; Sun, H.; Qi, Q.; Shi, C. Mitochondria-Targeted Small-Molecule Fluorophores for Dual Modal Cancer Phototherapy. *Adv. Funct. Mater.* **2016**, *26*, 2826–2835. (c) Gao, P.; Pan, W.; Li, N.; Tang, B. Fluorescent probes for organelle-targeted bioactive species imaging. *Chem. Sci.* **2019**, *10*, 6035–6071.

(10) (a) Wagner, N.; Stephan, M.; Höglinger, D.; Nadler, A. A Click cage: Organelle-specific uncaging of lipid messengers. *Angew. Chem. Int. Ed.* **2018**, *57*, 13339–13343. (b) Kand, D.; Pizarro, L.; Angel, I.; Avni, A.; Friedmann-Morvinski, D.; Weinstain, R. Organelle-targeted BODIPY photocages: Visible-light-mediated subcellular photorelease. *Angew. Chem. Int. Ed.* **2019**, *58*, 4659–4663.

(11) Gandioso, A.; Bresolí-Obach, R.; Nin-Hill, A.; Bosch, M.; Palau, M.; Galindo, A.; Contreras, S.; Rovira, A.; Rovira, C.; Nonell, S.; Marchán, V. Redesigning the coumarin scaffold into small bright fluorophores with far-red to near-infrared emission and large Stokes shifts useful for cell imaging. *J. Org. Chem.* **2018**, *83*, 1185–1195.

(12) Gandioso, A.; Palau, M.; Bresolí-Obach, R.; Galindo, A.; Rovira, A.; Bosch, M.; Nonell, S.; Marchán, V. High photostability in nonconventional coumarins with far-red/NIR emission through azetidyl substitution. *J. Org. Chem.* **2018**, *83*, 11519–11531.

(13) Rovira, A.; Gandioso, A.; Goñalons, M.; Galindo, A.; Massaguer, A.; Bosch, M.; Marchán, V. Solid-phase approaches for labeling targeting peptides with far-red emitting coumarin fluorophores. *J. Org. Chem.* **2019**, *84*, 1808–1817.

(14) Novohradsky, V.; Rovira, A.; Hally, C.; Galindo, A.; Viguera, G.; Gandioso, A.; Svitelova, M.; Bresolí-Obach, R.; Kosthunova, H.; Markova, L.; Kasparkova, J.; Nonell, S.; Ruiz, J.; Brabec, V.; Marchán, V. Towards novel photodynamic anticancer agents generating superoxide anion radicals: A cyclometalated Ir(III) complex conjugated to a far-red emitting coumarin. *Angew. Chem., Int. Ed.* **2019**, *58*, 6311–6315.

(15) (a) Gandioso, A.; Palau, M.; Nin-Hill, A.; Melnyk, I.; Rovira, C.; Nonell, S.; Velasco, D.; García-Amorós, J.; Marchán, V. Sequential Uncaging with Green Light can be Achieved by Fine-Tuning the Structure of a Dicyanocoumarin Chromophore. *ChemistryOpen* **2017**, *6*, 375–384. (b) Gandioso, A.; Contreras, S.; Melnyk, I.; Oliva, J.; Nonell, S.; Velasco, D.; García-Amorós, J.; Marchán, V. Development of Green/Red-Absorbing Chromophores Based on a Coumarin Scaffold That Are Useful as Caging Groups. *J. Org. Chem.* **2017**, *82*, 5398–5408.

(16) Vakuliuk, O.; Jun, Y. W.; Vygranenko, K.; Clermont, G.; Reo, Y. J.; Blanchard-Desce, M.; Ahn, K. H.; Gryko, D. T. Modified Isoindoleiones as Bright Fluorescent Probes for Cell and Tissue Imaging. *Chem. – Eur. J.* **2019**, *25*, 13354–13362.

(17) (a) Magde, D.; Brannon, J. H.; Cremers, T. L.; Olmsted, J. Absolute luminescence yield of cresyl violet. A standard for the red. *J. Phys. Chem.* **1979**, *83*, 696–699. (b) Würth, C.; Grabolle, M.; Pauli, J.; Spieles, M.; Resch-Genger, U. Relative and absolute determination of fluorescence quantum yields of transparent samples. *Nat. Protoc.* **2013**, *8*, 1535–1550. (c) Brouwer, A. M. Standards for photoluminescence quantum yield measurements in solution (IUPAC Technical Report). *Pure Appl. Chem.* **2011**, *83*, 2213–2228.

(18) Bolte, S.; Cordelières, F. P. A Guided Tour Into Subcellular Colocalization Analysis in Light Microscopy. *J. Microsc.* **2006**, *224*, 213–232.

(19) Hasumi, K.; Sato, S.; Saito, T.; Kato, J.; Shiota, K.; Sato, J.; Suzuki, H.; Ohta, S. Design and synthesis of 5-[(2-chloro-6-fluorophenyl)acetylamino]-3-(4-fluorophenyl)-4-(4-pyrimidinyl)-isoxazole (AKP-001), a novel inhibitor of p38 MAP kinase with reduced side effects based on the antedrug concept. *Bioorg. Med. Chem.* **2014**, *22*, 4162–4176.

(20) Schindelin, J.; Arganda-Carreras, I.; Frise, E.; Kaynig, V.; Longair, M.; Pietzsch, T.; Preibisch, S.; Rueden, C.; Saalfeld, S.; Schmid, B.; Tinevez, J. Y.; White, D. J.; Hartenstein, V.; Eliceiri, K.; Tomancak, P.; Cardona, A. Fiji: an open-source platform for biological-image analysis. *Nat. Methods* **2012**, *9*, 676–682.

(21) Prewitt, J. M. S.; Mendelsohn, M. L. The analysis of cell images. *Ann. N. Y. Acad. Sci.* **1966**, *128*, 1035–1053.

(22) Phansalkar, N.; More, S.; Sabale, A.; Madhuri, J. Adaptive local thresholding for detection of nuclei in diversity stained cytology images. *International Conference on Communications and Signal Processing (ICCSP)* 2011, 218–220, doi: DOI: 10.1109/ICCSP.2011.5739305.

SUPPORTING INFORMATION

Modulating photostability and mitochondria selectivity in far-red/NIR emitting coumarin fluorophores through replacement of pyridinium by pyrimidinium.

Anna Rovira,[†] Miriam Pujals,[†] Albert Gandioso,[†] Marta López-Corrales,[†] Manel Bosch,[‡]
Vicente Marchán*[†]

[†]Departament de Química Inorgànica i Orgànica, Secció de Química Orgànica, IBUB,
Universitat de Barcelona, Martí i Franquès 1-11, E-08028 Barcelona (Spain).

E-mail: vmarchan@ub.edu

[‡]Unitat de Microscòpia Òptica Avançada, Centres Científics i Tecnològics, Universitat de
Barcelona, E-08028 Barcelona (Spain)

Table of contents

1.- Reversed-phase HPLC analysis of COUPY scaffolds (6-9) and dyes (10-13)	S3
Figure S1	
2.- 2D NMR characterization of COUPY scaffolds (6-9)	S4
Figures S2-S5	
3.- 2D NMR characterization of COUPY fluorophores (10-13)	S6
Figures S6-S9	
4.- Photophysical characterization of COUPY dyes (10-13)	S12
Figures S10-S18	
5.- Fluorescence imaging	S17
Figures S19-S20	
6.- ^1H , ^{13}C and ^{19}F NMR spectra and HR ESI-MS of the compounds	S19
Figures S21-S44	

1.- Reversed-phase HPLC analysis of COUPY scaffolds (6-9) and dyes (10-13).

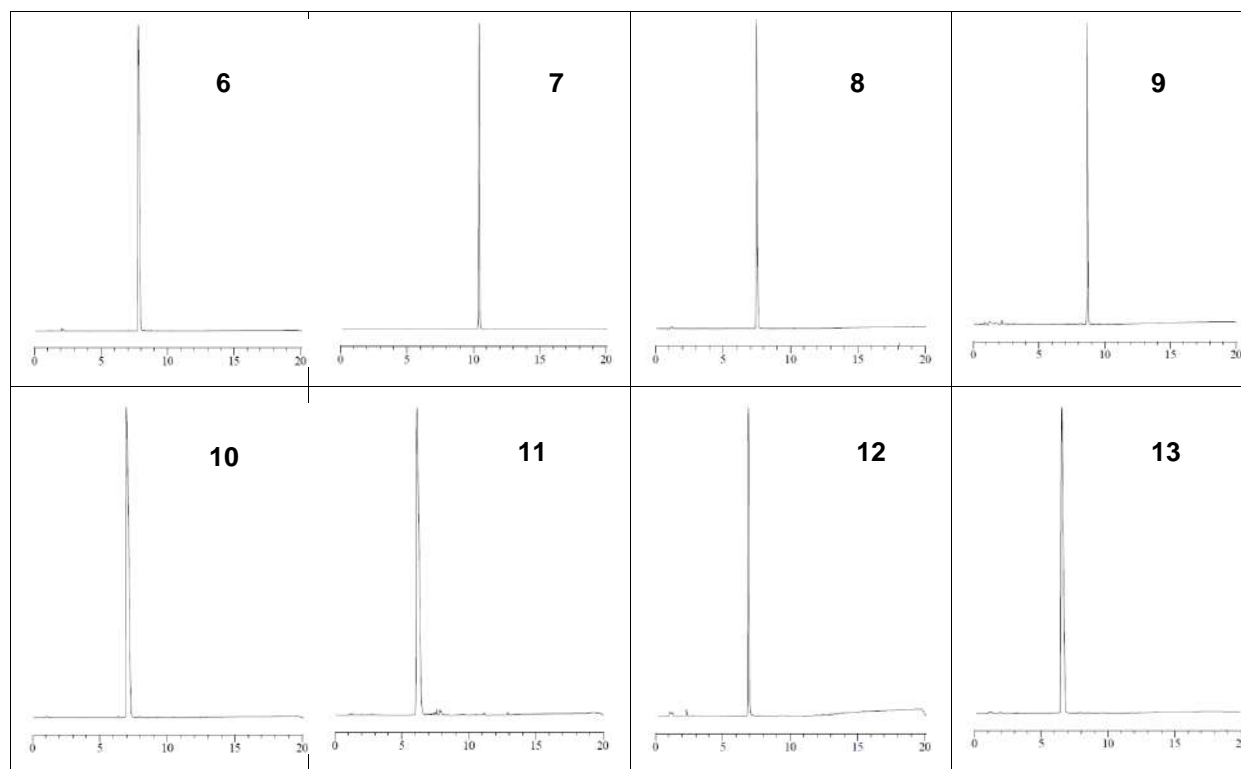


Figure S1. Reversed-phase HPLC traces of COUPY scaffolds (6-9) and dyes (10-13).

2.- 2D NMR characterization of COUPY scaffolds (6-9).

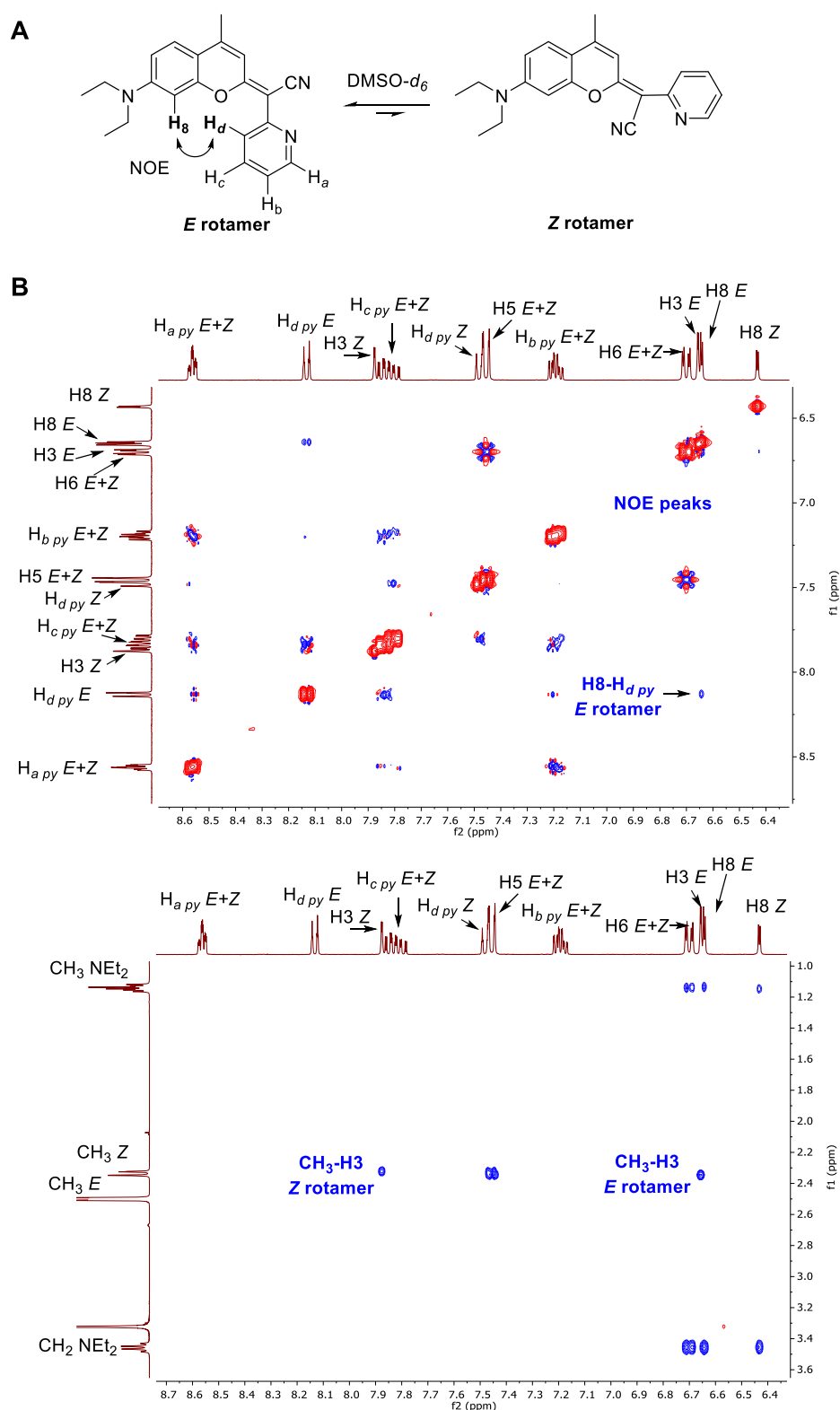


Figure S2. Structure of *E* and *Z* rotamers of coumarin **6** with some diagnostic NOE cross-peaks indicated (A), and expansions of the NOESY spectrum of **6** in DMSO- d_6 at 298 K showing some characteristic NOE cross-peaks (B).

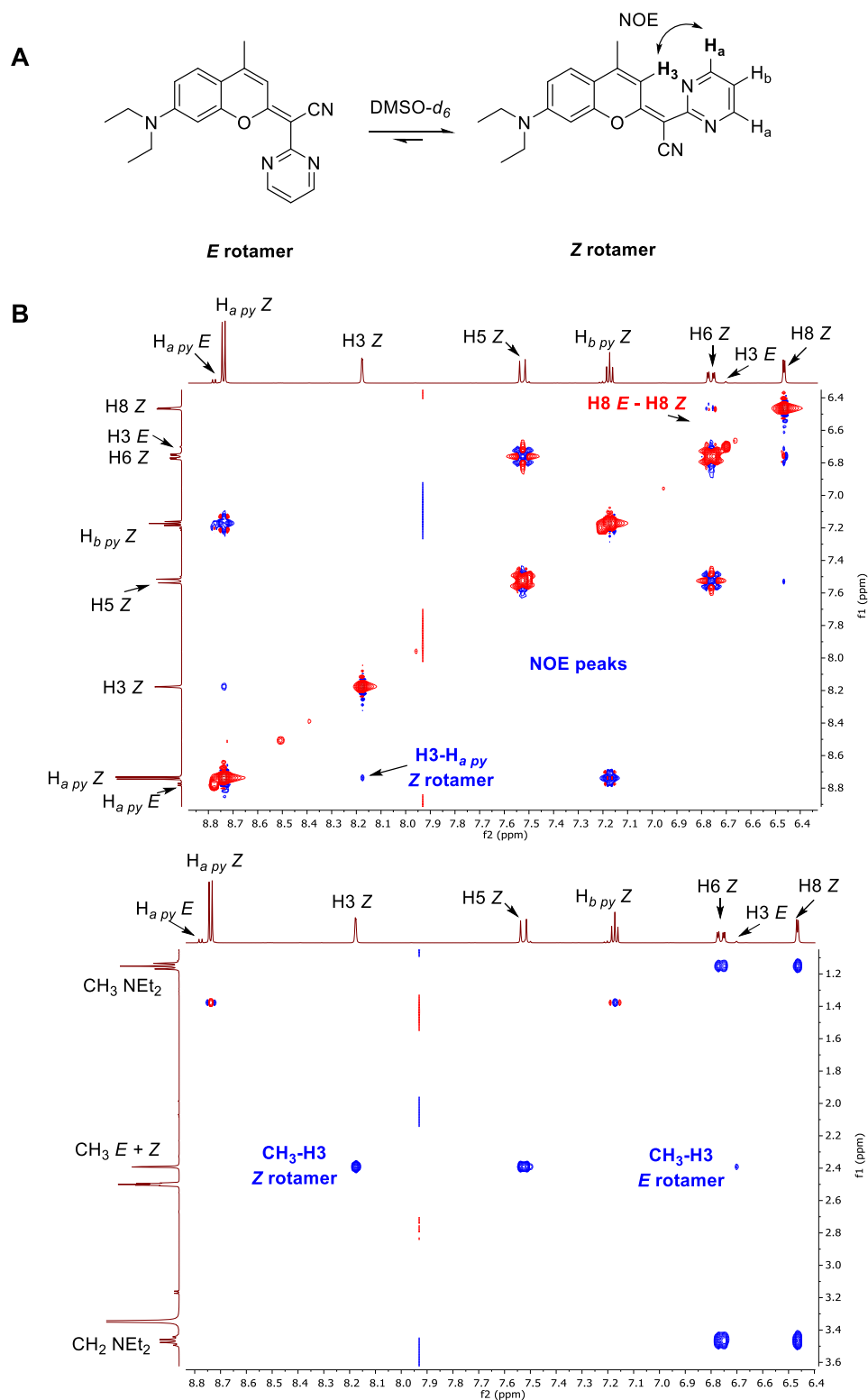


Figure S3. Structure of *E* and *Z* rotamers of coumarin **7** with some diagnostic NOE cross-peaks indicated (A), and expansions of the NOESY spectrum of **7** in DMSO-*d*₆ at 298 K showing some characteristic NOE cross-peaks (B).

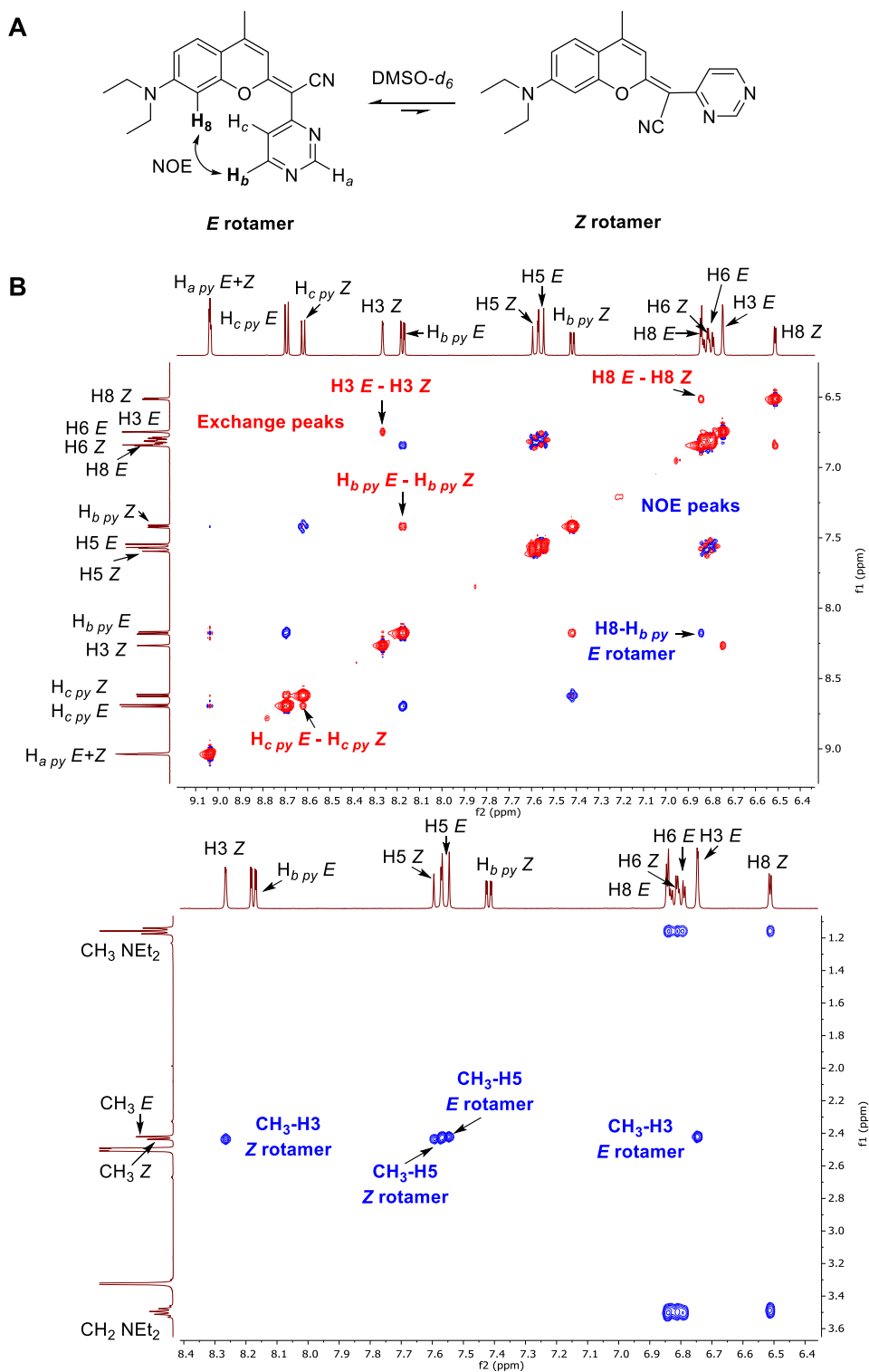


Figure S4. Structure of *E* and *Z* rotamers of coumarin **8** with some diagnostic NOE cross-peaks indicated (A), and expansions of the NOESY spectrum showing some characteristic NOE cross-peaks and exchange cross-peaks between rotamer resonances of the same sign as the diagonal of **8** in DMSO-*d*₆ at 298 K (B).

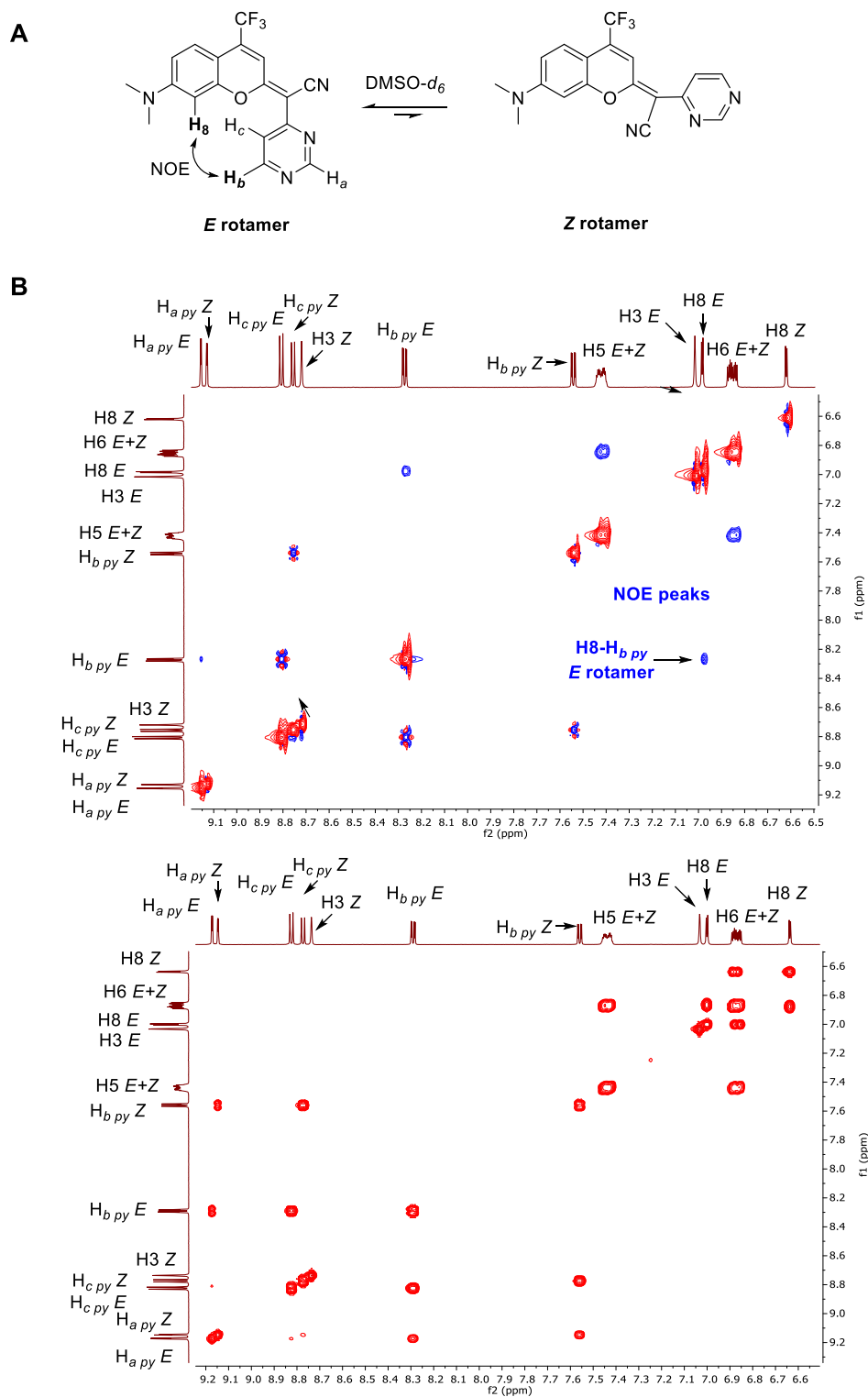


Figure S5. Structure of *E* and *Z* rotamers of coumarin **9** with some diagnostic NOE cross-peaks indicated (A), and expansions of the NOESY spectrum showing some characteristic NOE cross-peaks (top) and of the COSY spectrum (bottom) of **9** in DMSO- d_6 at 298 K (B).

3.- 2D NMR characterization of COUPY fluorophores (10-13).

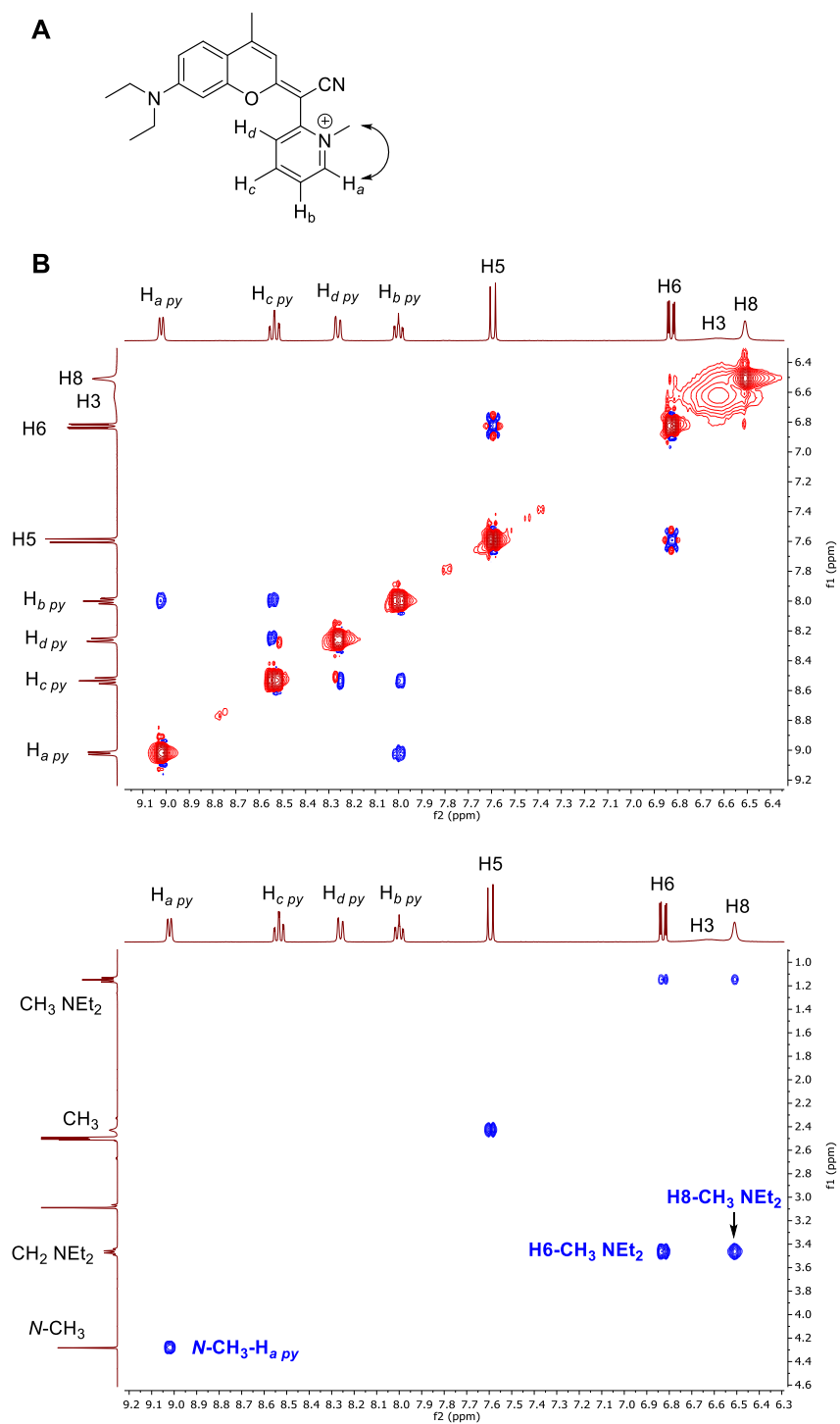


Figure S6. Structure of *E* rotamer of coumarin **10** with some diagnostic NOE cross-peaks indicated (A), and expansions of the NOESY spectrum of **10** in DMSO-*d*₆ at 350 K showing some characteristic NOE cross-peaks (B).

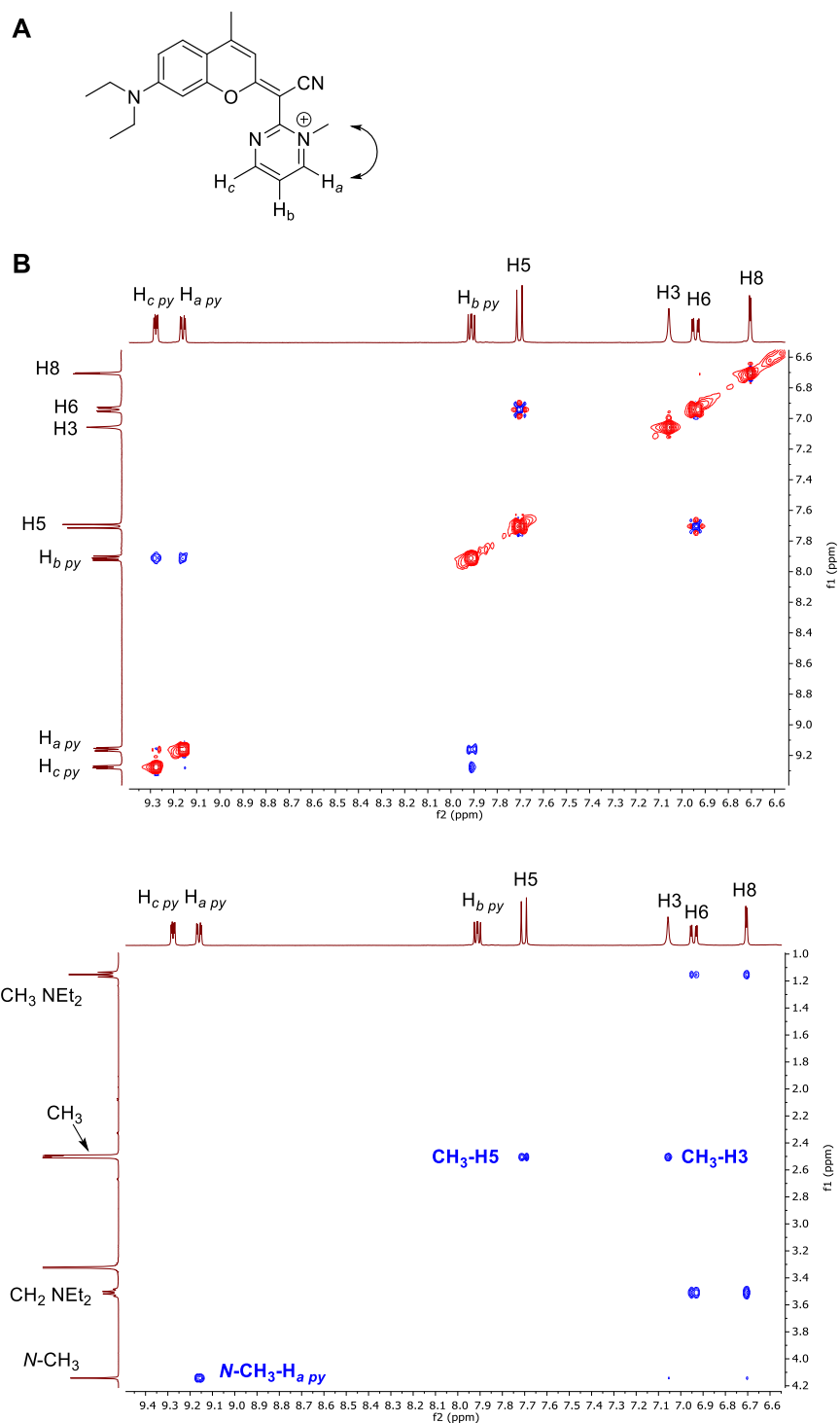


Figure S7. Structure of *E* rotamer of COUPY-caged compound **11** with some diagnostic NOE cross-peaks indicated (A), and expansions of the NOESY spectrum of **11** in DMSO-*d*₆ at 298 K showing some characteristic NOE cross-peaks (B).

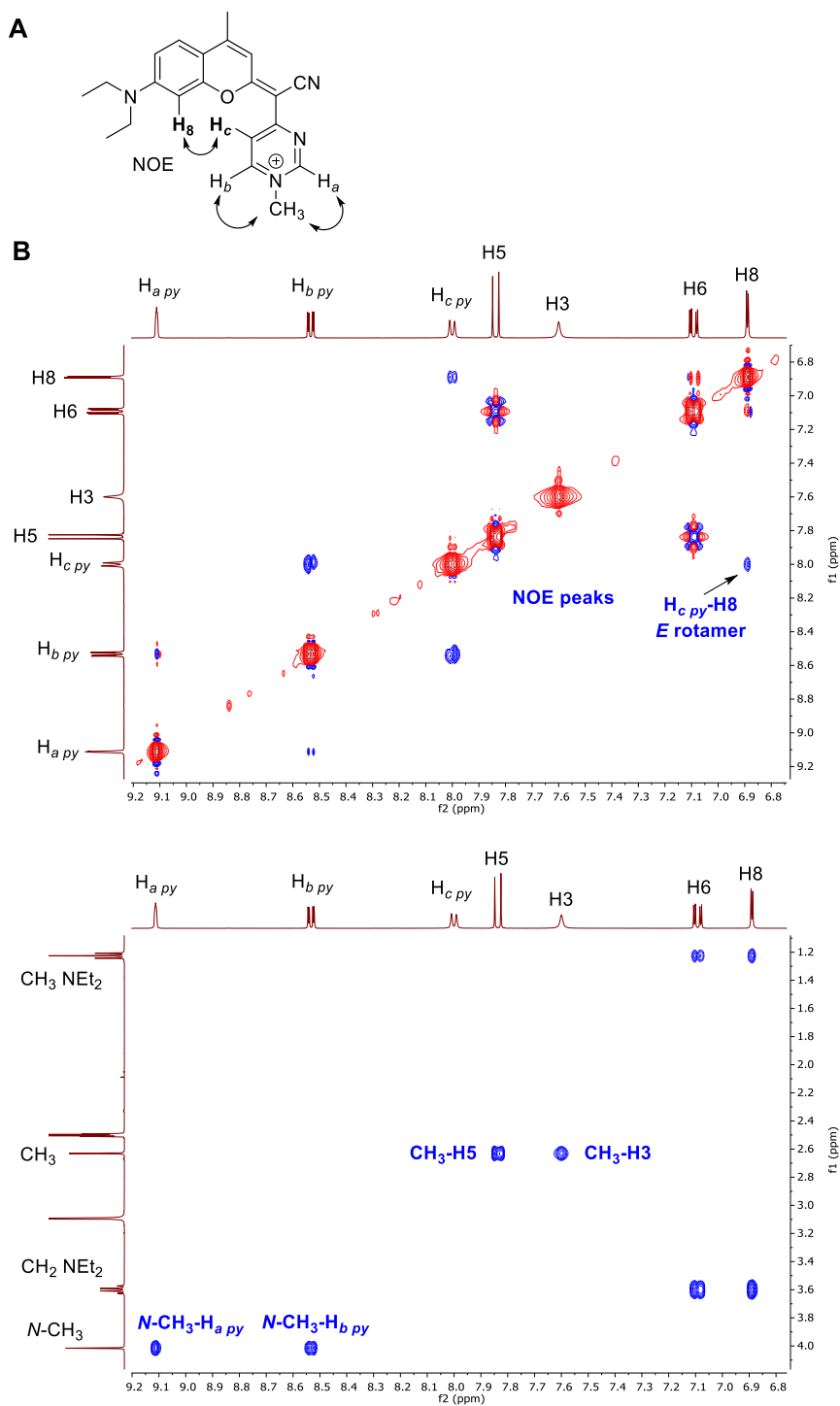


Figure S8. Structure of *E* rotamer of COUPY-caged compound **12** with some diagnostic NOE cross-peaks indicated (A), and expansions of the NOESY spectrum of **12** in DMSO-*d*₆ at 350 K showing some characteristic NOE cross-peaks (B).

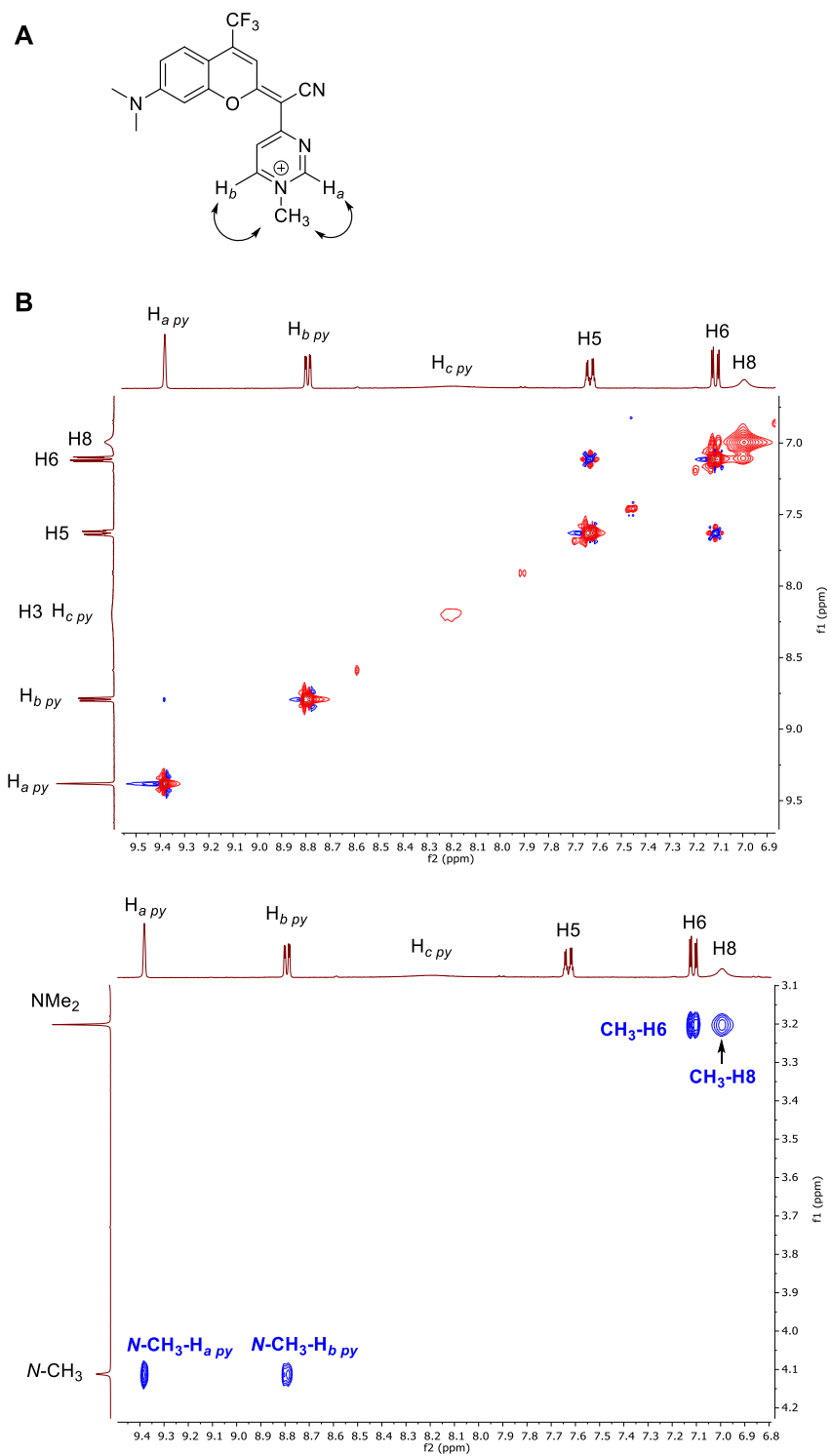


Figure S9. Structure of *E* rotamer of COUPY-caged compound **13** with some diagnostic NOE cross-peaks indicated (A), and expansions of the NOESY spectrum of **13** in DMSO-*d*₆ at 350 K showing some characteristic NOE cross-peaks (B).

4.- Photophysical characterization of COUPY dyes

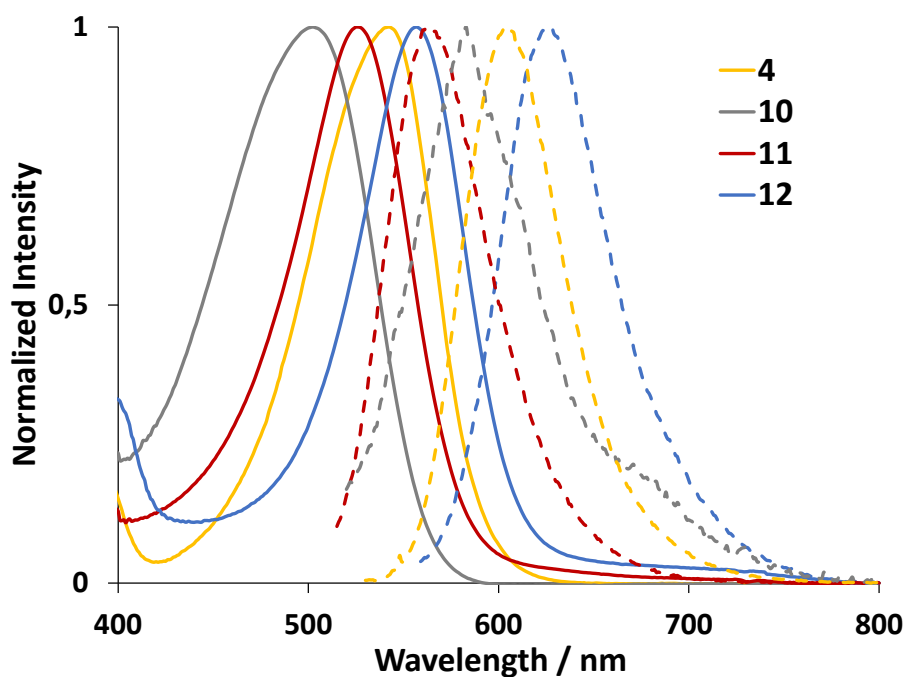


Figure S10. Comparison of the normalized absorption (solid lines) and fluorescence emission (dotted lines) spectra of coumarins **4** and **10-12** in PBS buffer pH 7.4.

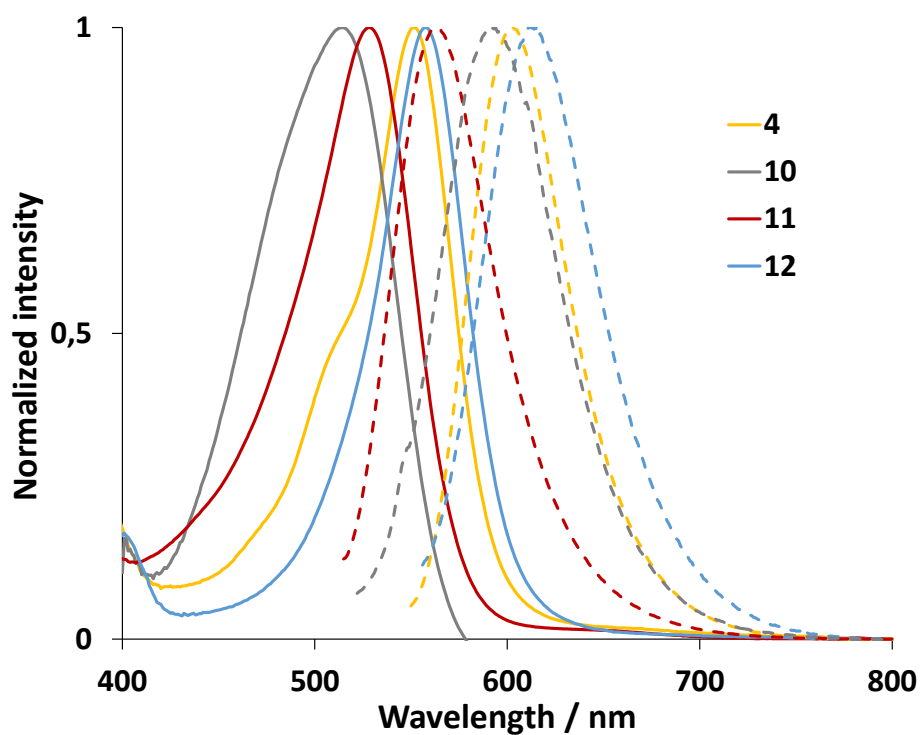


Figure S11. Comparison of the normalized absorption (solid lines) and fluorescence emission (dotted lines) spectra of coumarins **4** and **10-12** in EtOH.

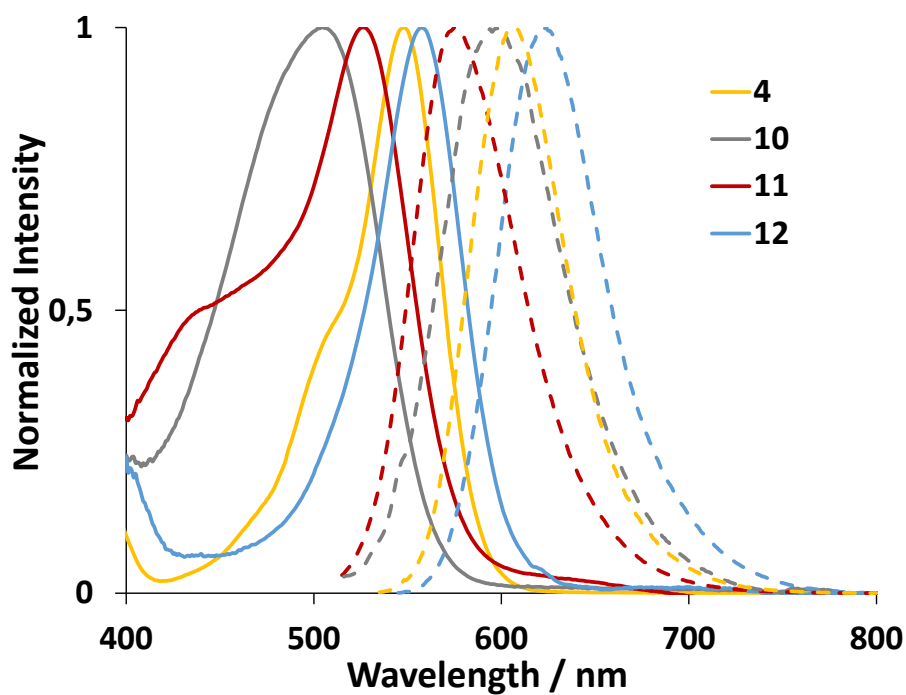


Figure S12. Comparison of the normalized absorption (solid lines) and fluorescence emission (dotted lines) spectra of coumarins **4** and **10-12** in ACN.

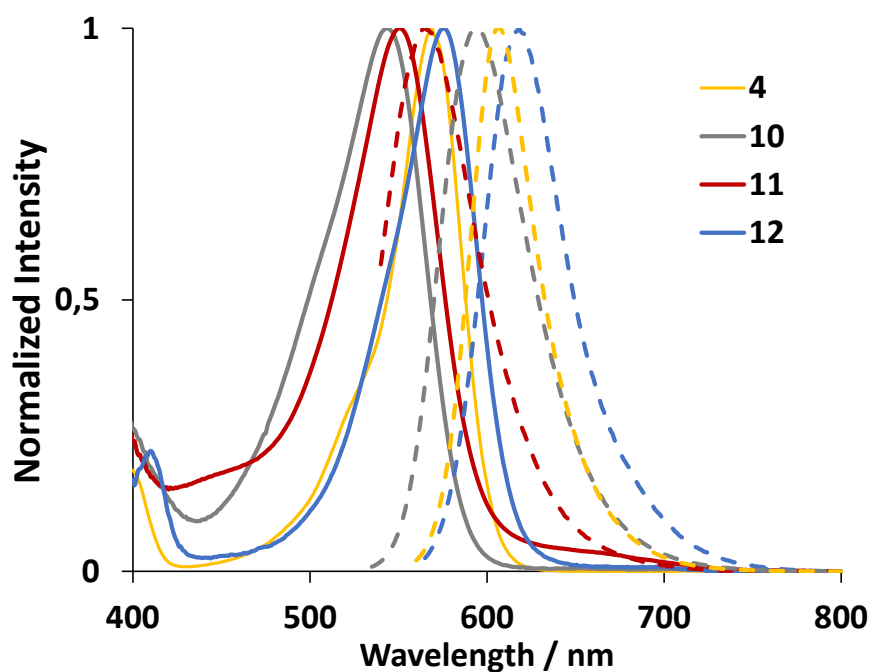


Figure S13. Comparison of the normalized absorption (solid lines) and fluorescence emission (dotted lines) spectra of coumarins **4** and **10-12** in DCM.

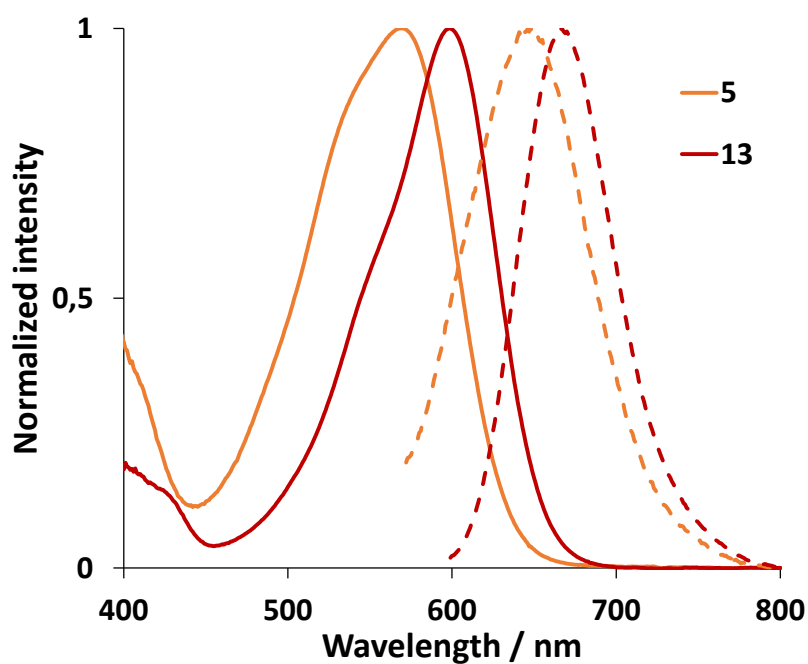


Figure S14. Comparison of the normalized absorption (solid lines) and fluorescence emission (dotted lines) spectra of coumarins **5** and **13** in PBS buffer pH 7.4.

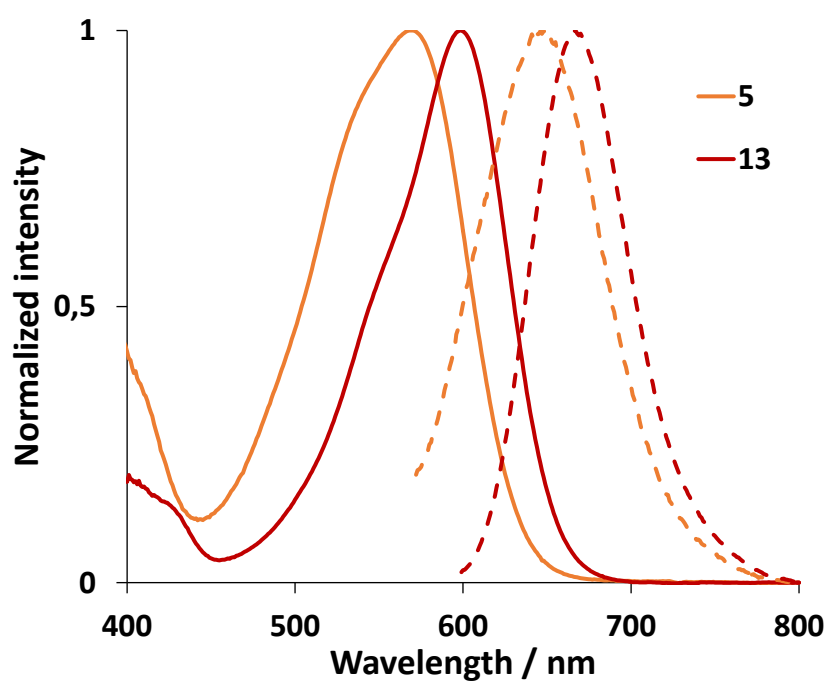


Figure S15. Comparison of the normalized absorption (solid lines) and fluorescence emission (dotted lines) spectra of coumarins **5** and **13** in EtOH.

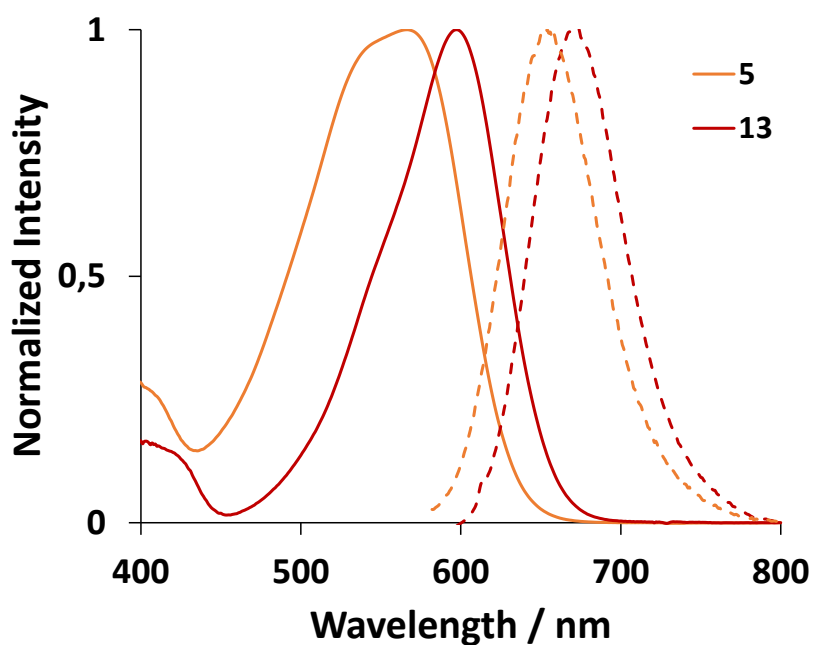


Figure S16. Comparison of the normalized absorption (solid lines) and fluorescence emission (dotted lines) spectra of coumarins **5** and **13** in ACN.

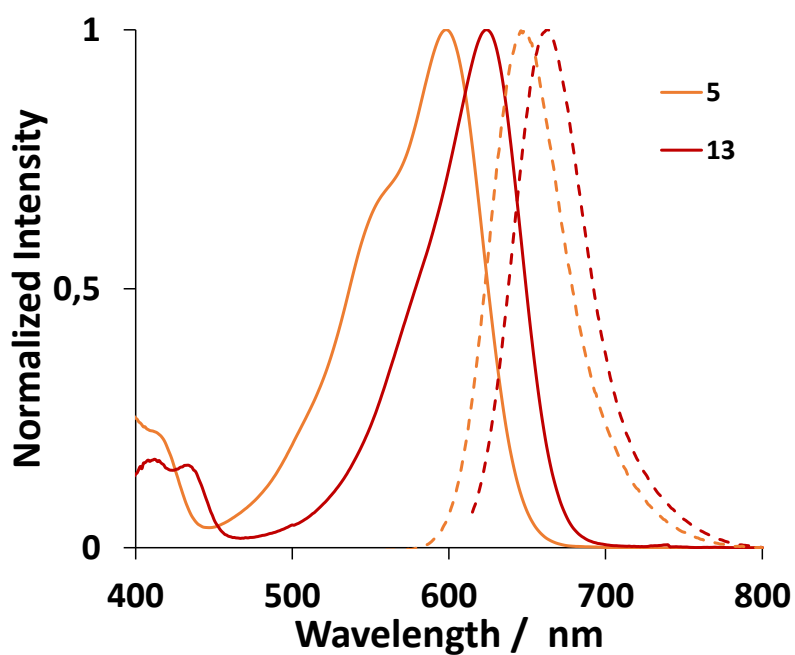


Figure S17. Comparison of the normalized absorption (solid lines) and fluorescence emission (dotted lines) spectra of coumarins **5** and **13** in DCM.

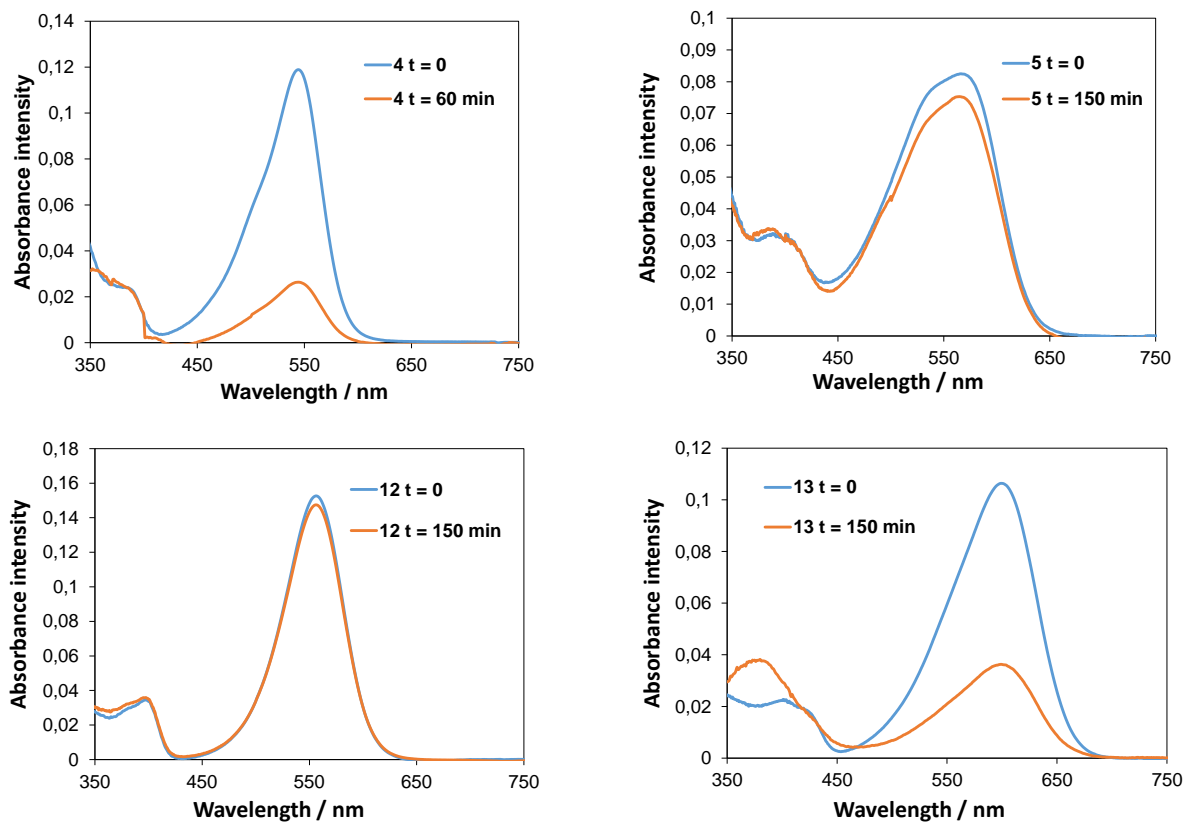


Figure S18. Absorption spectra of COUPY dyes in PBS buffer pH 7.4 (5 μM) at $t = 0$ and after irradiation with green light for 60 min (**4**) or 150 min (**5, 12-13**).

5.- Fluorescence imaging

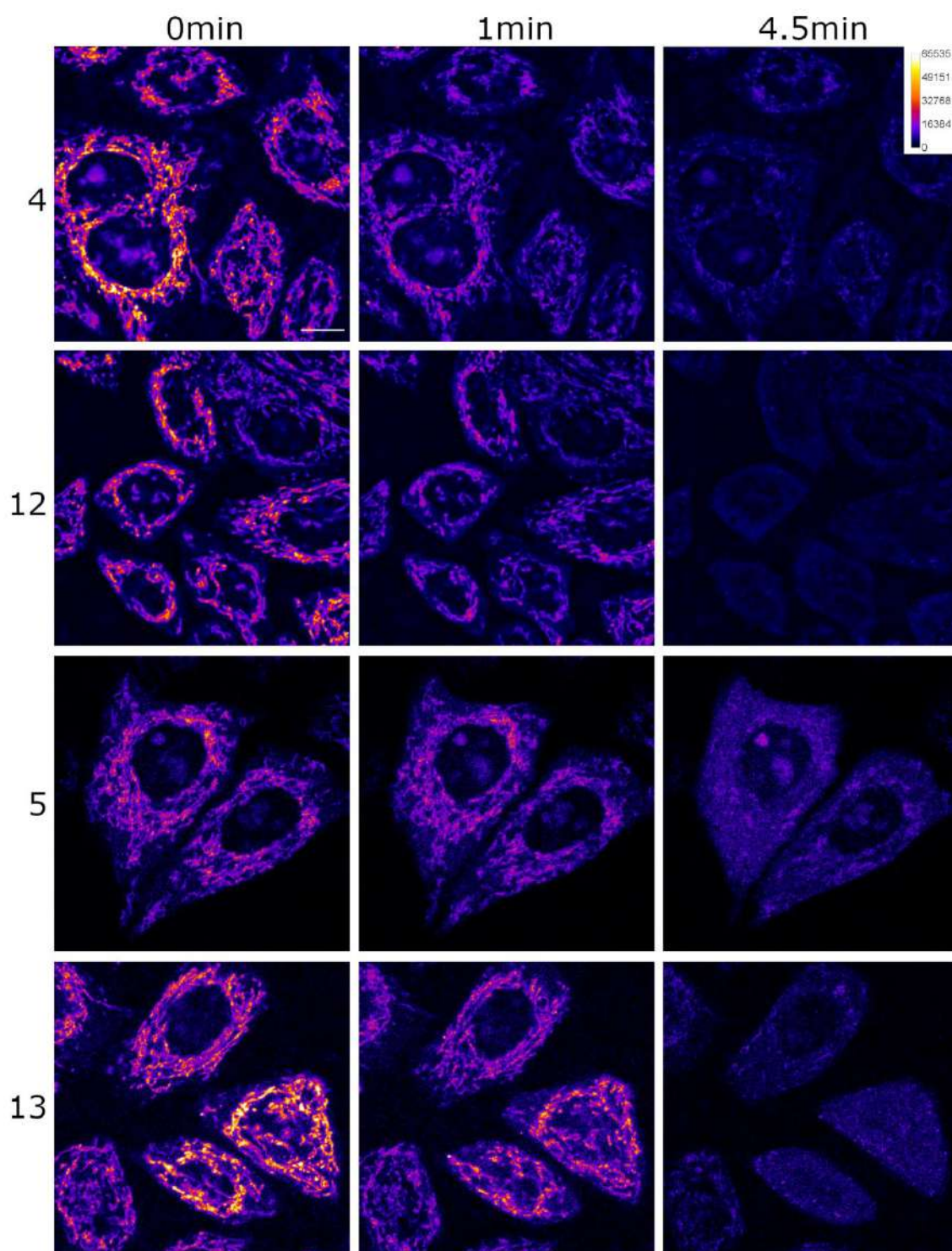


Figure S19. Photostability imaging. Single confocal planes at different time points of image acquisition are shown after incubation of HeLa cells with coumarins **4**, **5**, **12** and **13** (all at 2 μ M) during 30 min at 37 °C. Note that at the end of the bleaching experiment there are some mitochondria and vesicles still visible. Scale bar: 10 μ m. All images are at the same scale. Intensity calibration bar is shown in the upper right corner.

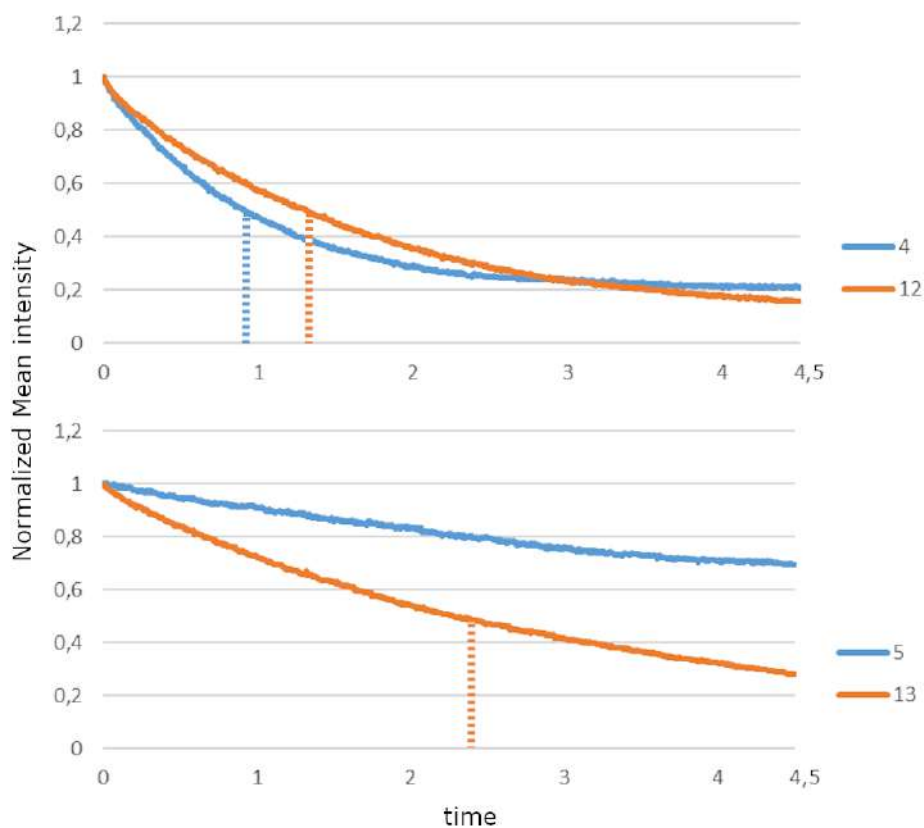


Figure S20. Photobleaching graphs of coumarins **4** vs **12**, and **5** vs **13**. In the upper graph the dotted vertical blue and orange lines indicate the average ($n > 10$ cells) t_{50} time point of coumarin **4** ($t_{50} = 55.63 \text{ sec} \pm 10.4$) and **12** ($t_{50} = 79.93 \text{ sec} \pm 12.28$) respectively. These t_{50} values are statistically different ($p < 0.01$). In the lower graph the dotted vertical orange line indicates the average ($n > 10$ cells) t_{50} time point of coumarin **13** ($t_{50} = 144.11 \text{ sec} \pm 35$). Coumarin **5** did not reach t_{50} under the bleaching conditions.

6.- ^1H , ^{13}C and ^{19}F NMR spectra and HR ESI-MS of the compounds

2-(Pyrimidin-2-yl)acetonitrile (15)

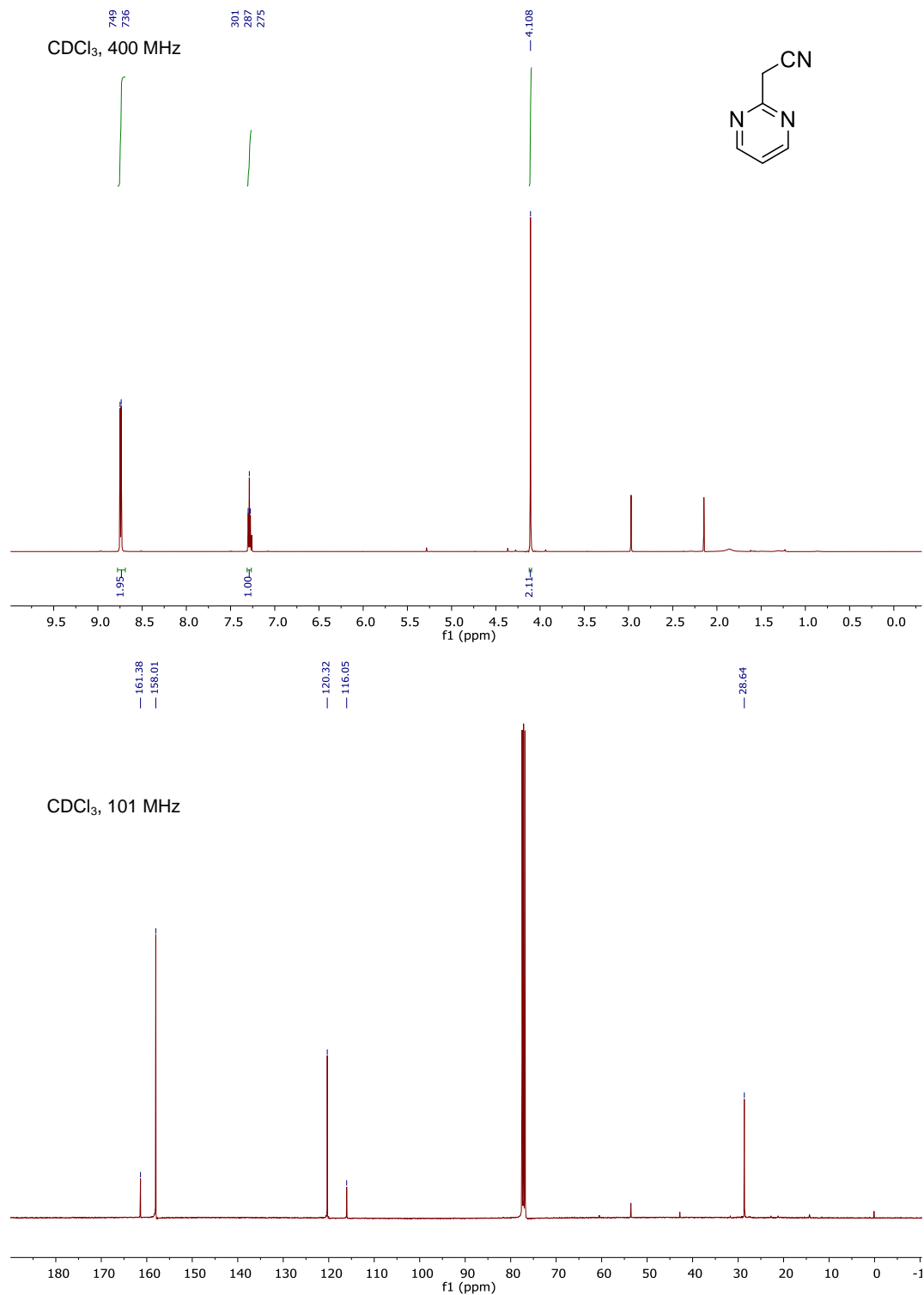


Figure S21. ^1H and ^{13}C NMR spectra of compound **15** in CDCl_3 .

(E)-N,N-Dimethyl-2-(pyrimidin-4-yl)ethen-1-amine (17)

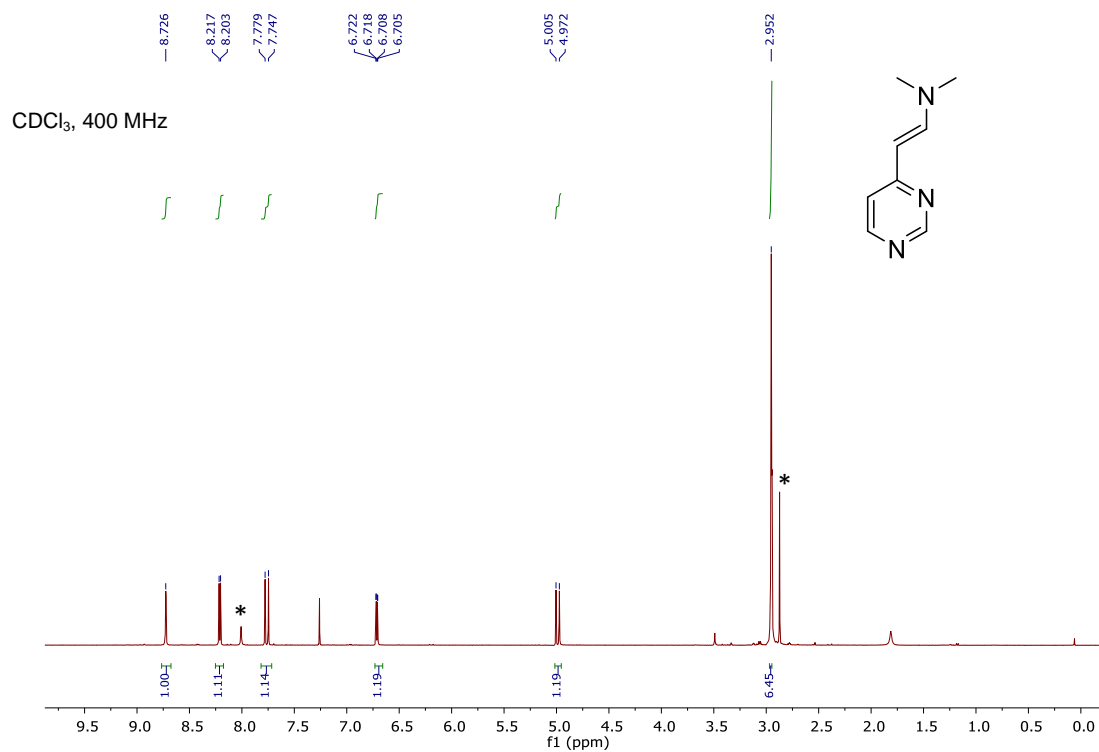


Figure S22. ¹H and ¹³C NMR spectra of compound **17** in CDCl₃ (crude material). *DMF signals.

2-(Pyrimidin-4-yl)acetonitrile (16)

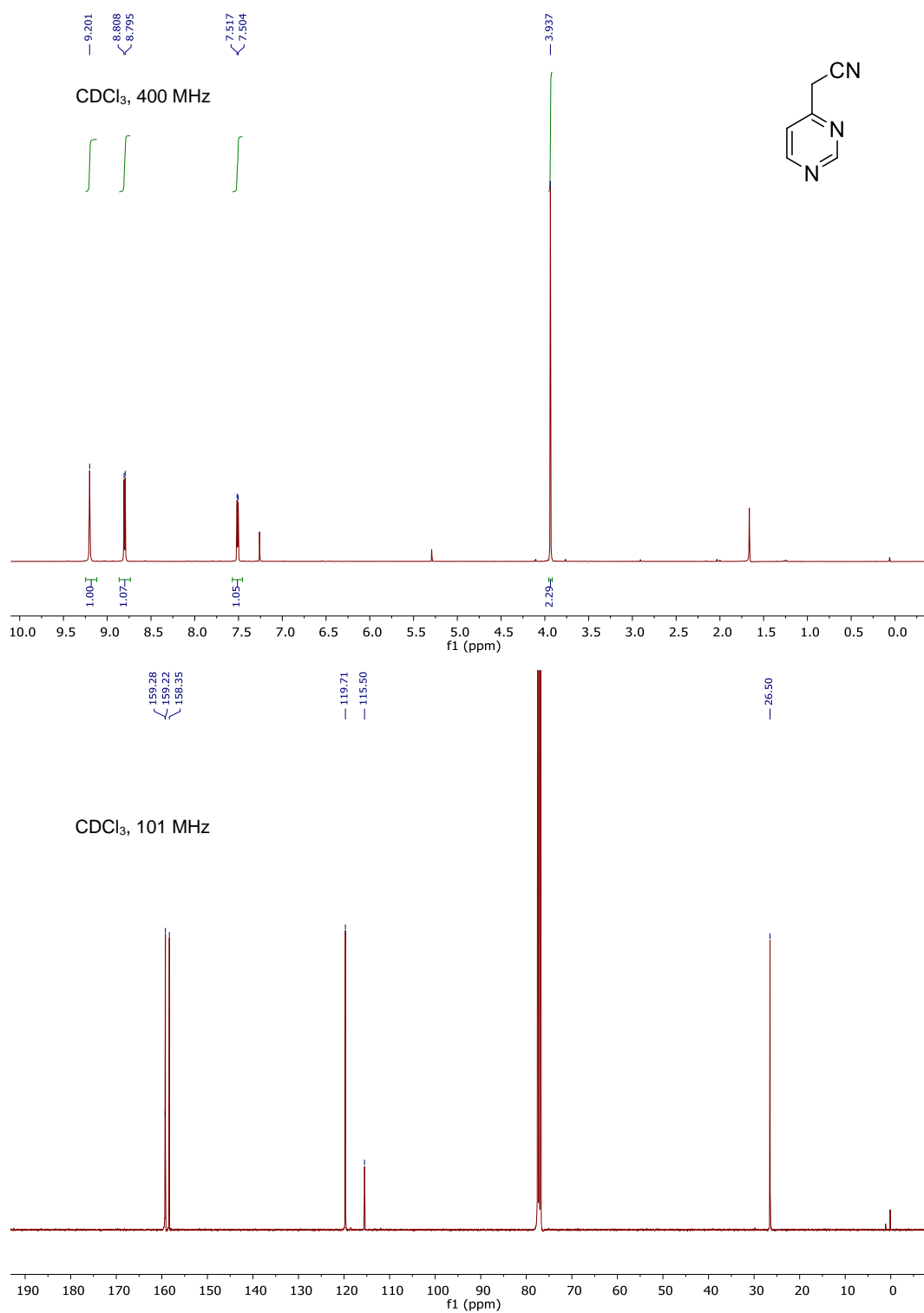


Figure S23. ¹H and ¹³C NMR spectra of compound **16** in CDCl₃.

2-(Cyano(2-pyridine)methylene)-7-(*N,N*-diethylamino)-4-methyl-coumarin (6)

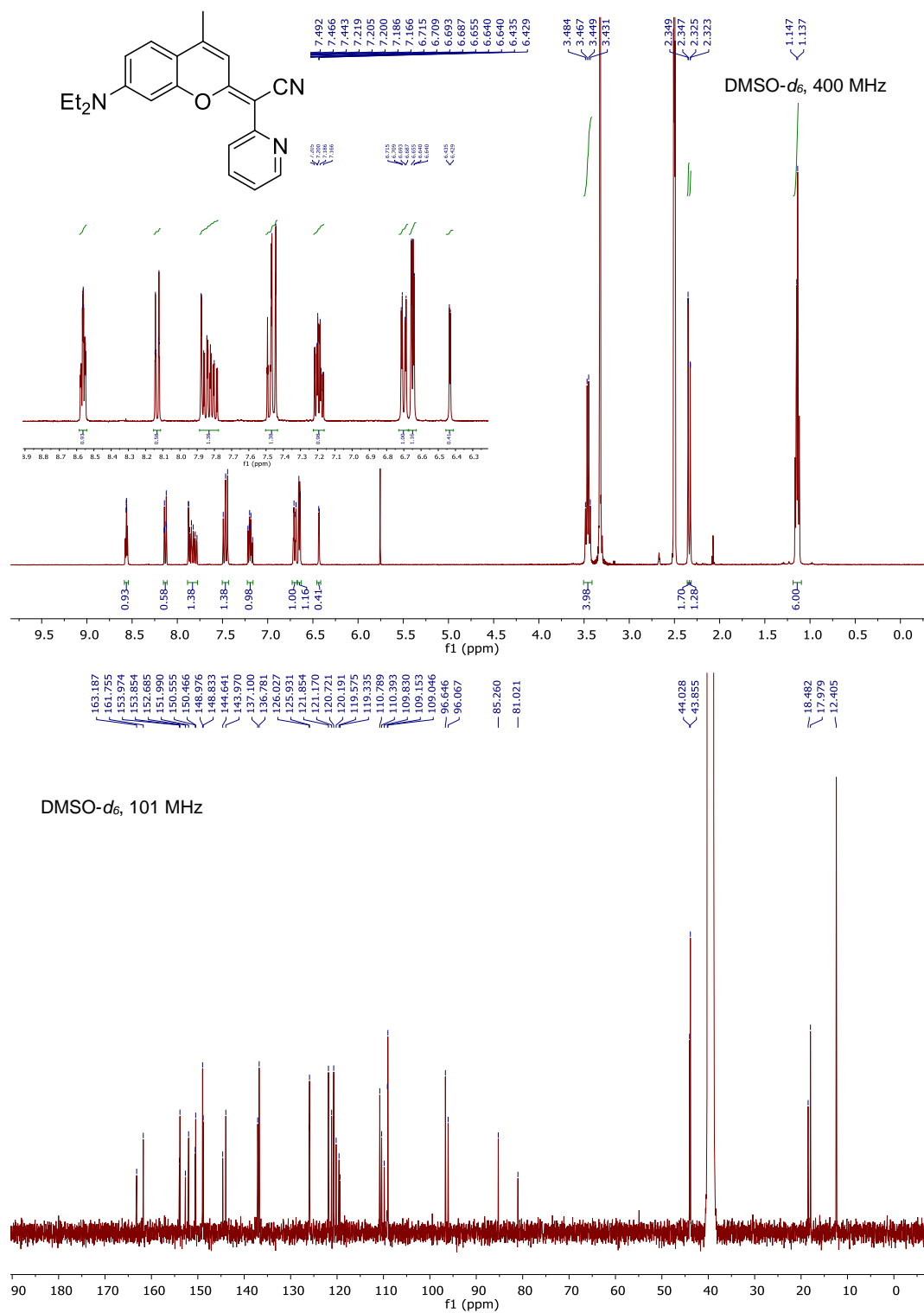


Figure S24. ¹H and ¹³C NMR spectra of compound 6 in DMSO-*d*₆.

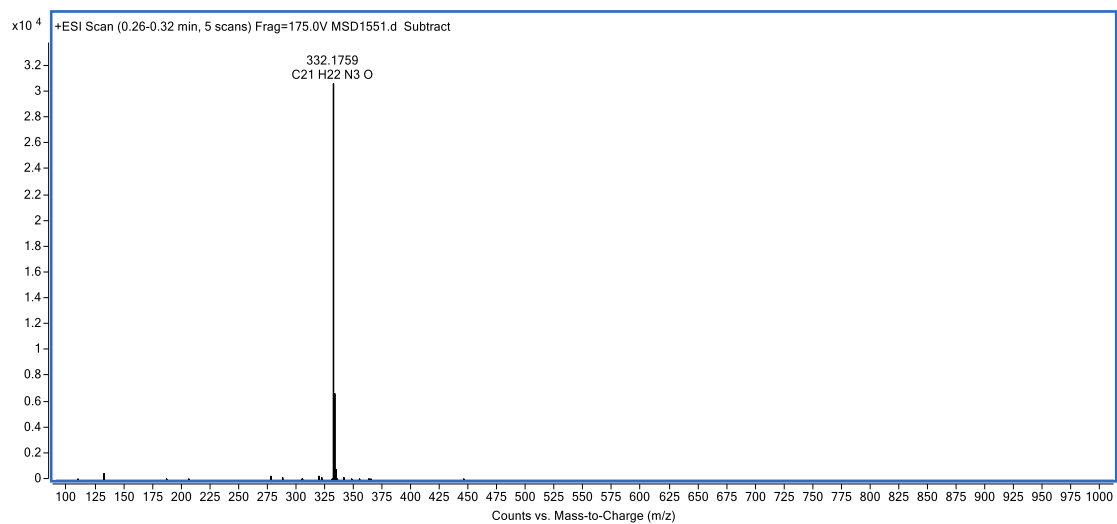


Figure S25. HR ESI-MS spectrum of compound **6**.

2-(Cyano(2-pyrimidine)methylene)-7-(*N,N*-diethylamino)-4-methyl-coumarin (7)

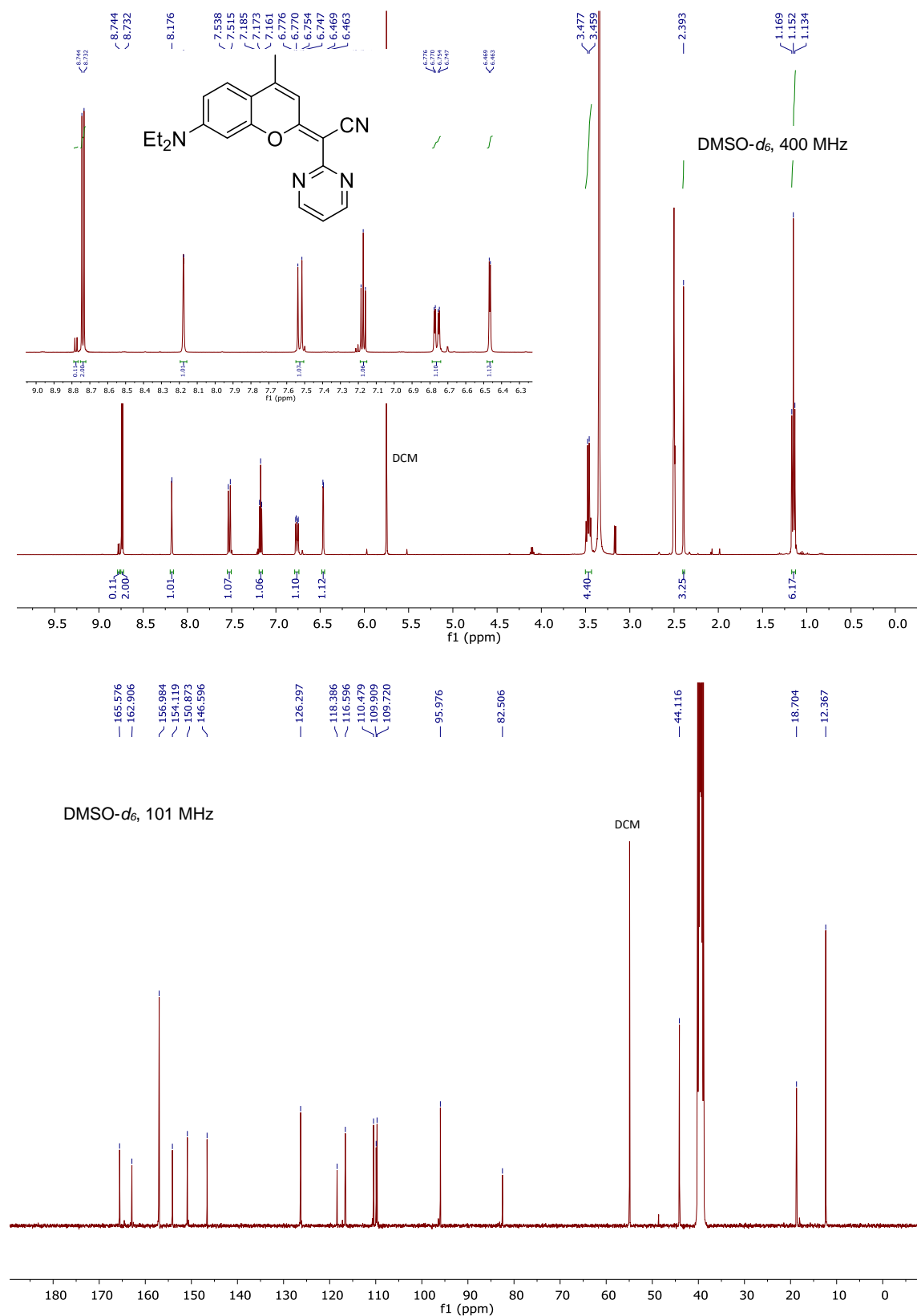


Figure S26. ¹H and ¹³C NMR spectra of compound 7 in DMSO-*d*₆.

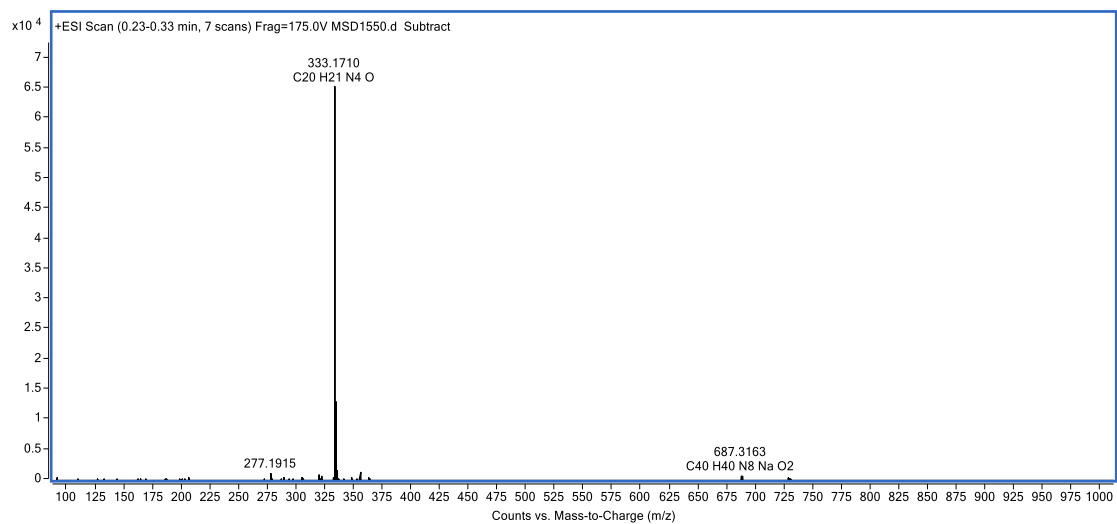


Figure S27. HR ESI-MS spectrum of compound **7**.

2-(Cyano(4-pyrimidine)methylene)-7-(*N,N*-diethylamino)-4-methyl-coumarin (**8**)

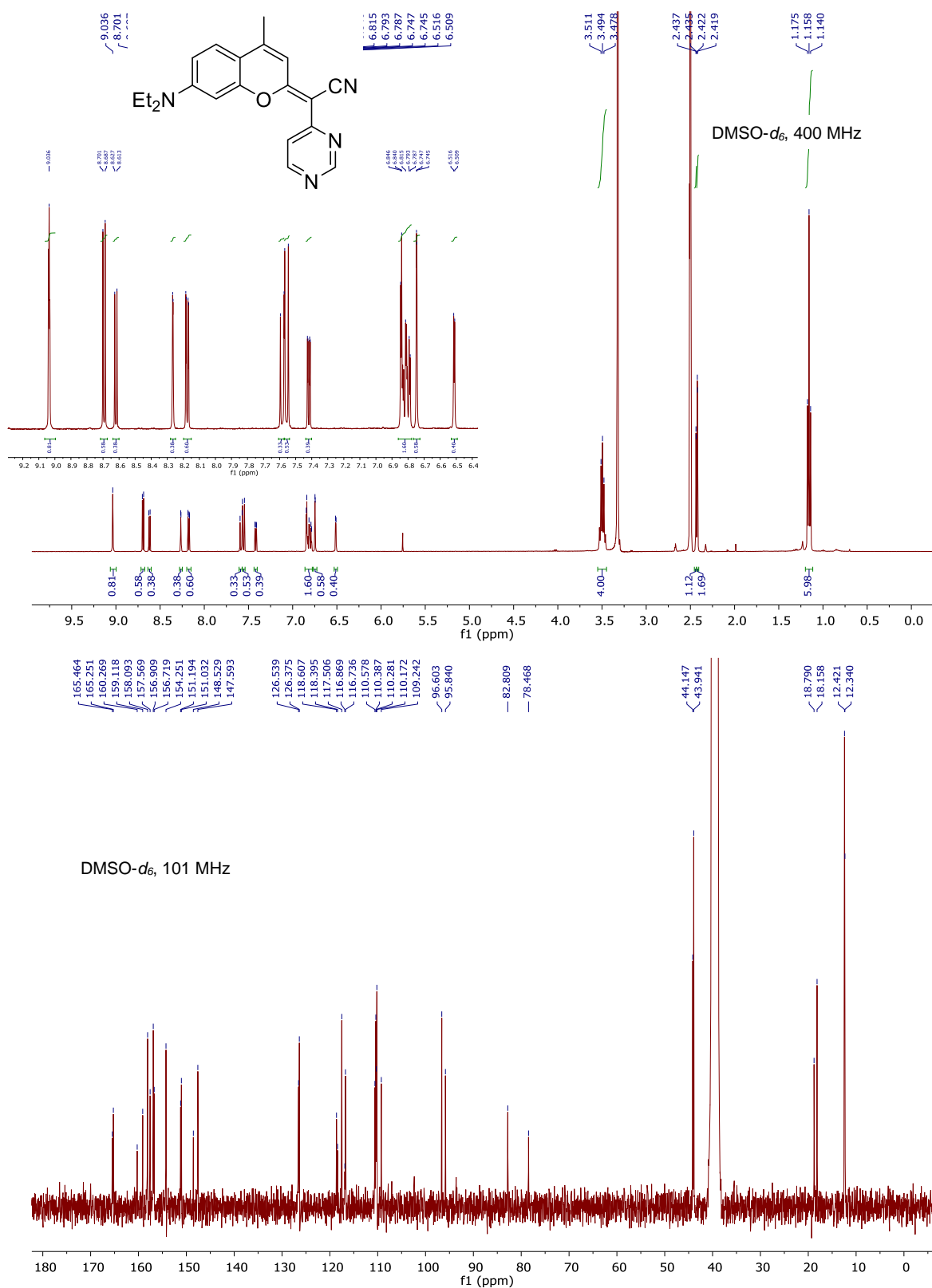


Figure S28. ¹H and ¹³C NMR spectra of compound **8** in DMSO-*d*₆.

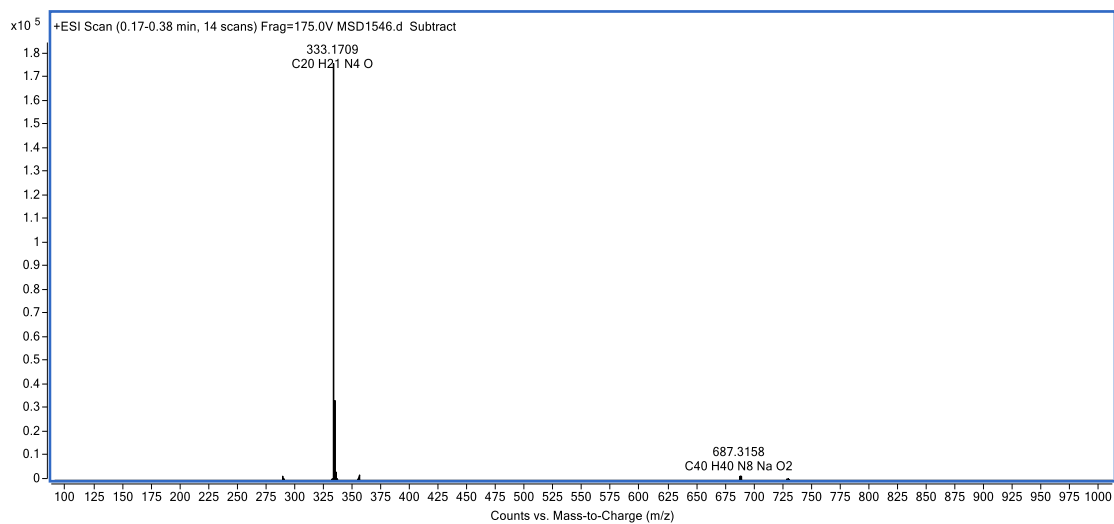


Figure S29. HR ESI-MS spectrum of compound **8**.

2-(Cyano(4-pyrimidine)methylene)-7-(*N,N*-dimethylamino)-4-trifluoromethyl-coumarin (9)

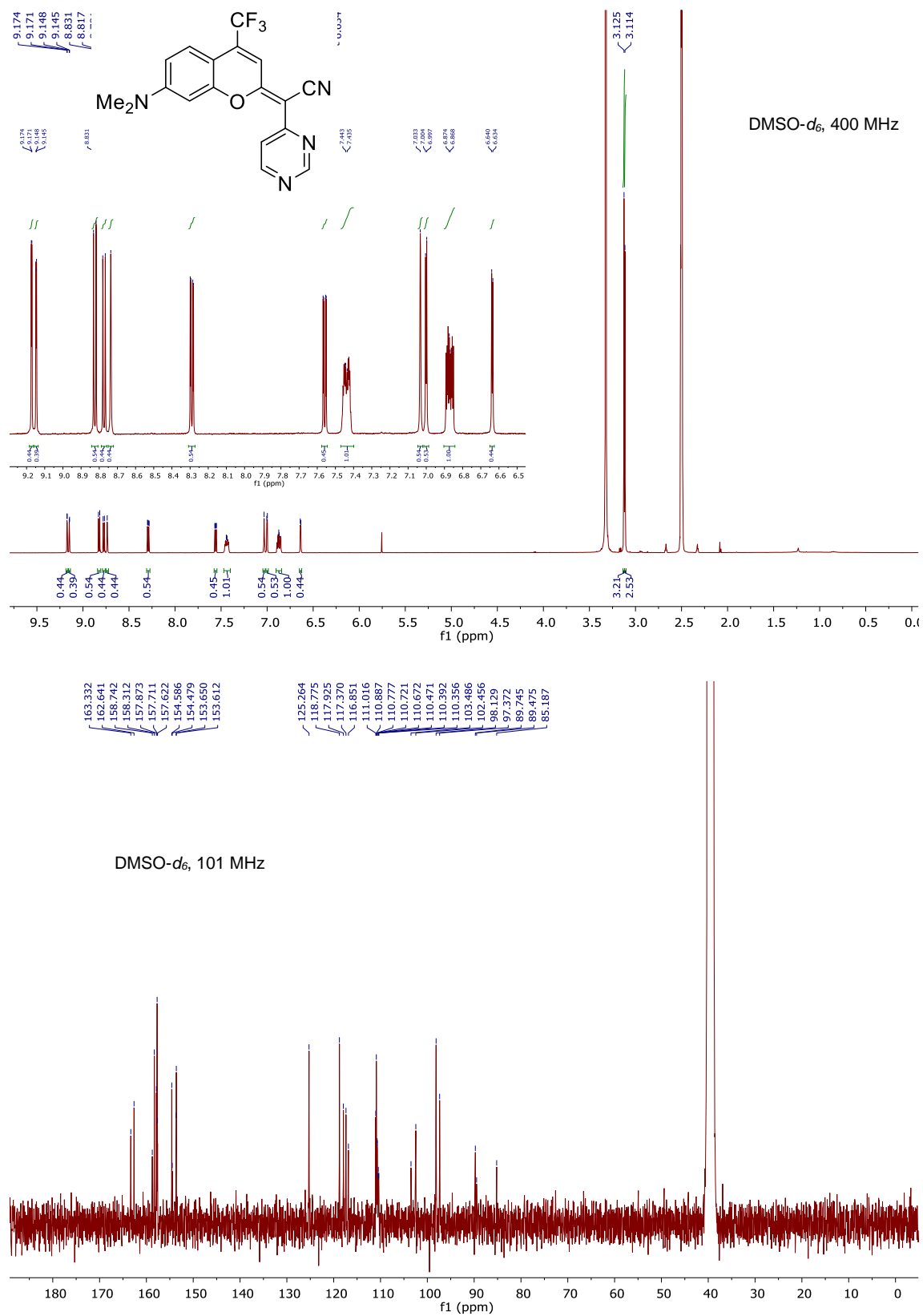


Figure S30. ¹H and ¹³C NMR spectra of compound **9** in DMSO-*d*₆.

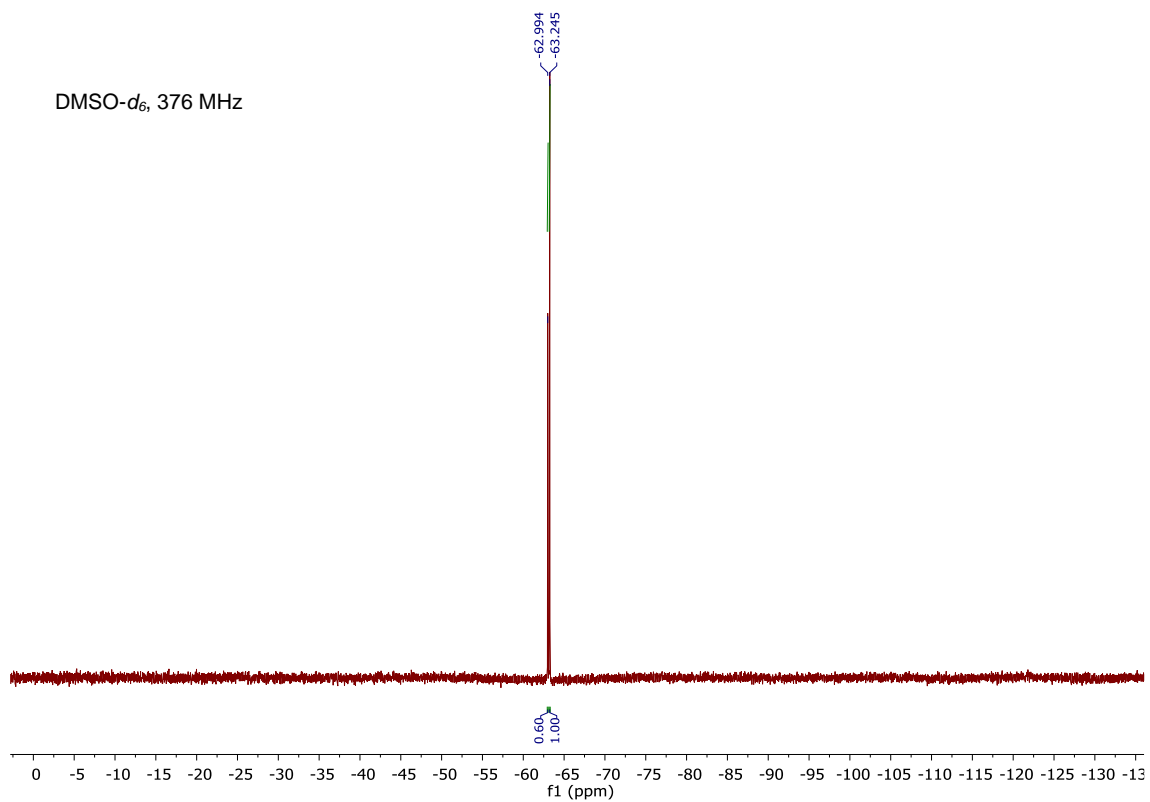


Figure S31. ¹⁹F NMR spectra of compound **9** in DMSO-*d*₆.

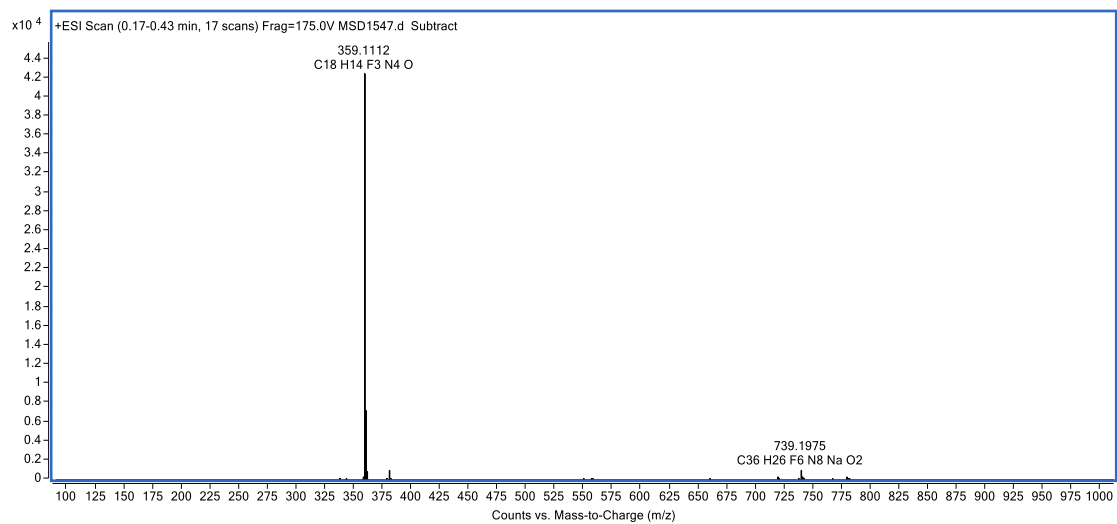


Figure S32. HR ESI-MS spectrum of compound **9**.

2-(Cyano(1-methyl(2-pyridin-1-ium))methylene)-7-(*N,N*-diethylamino)-4-methylcoumarin triflate (10)

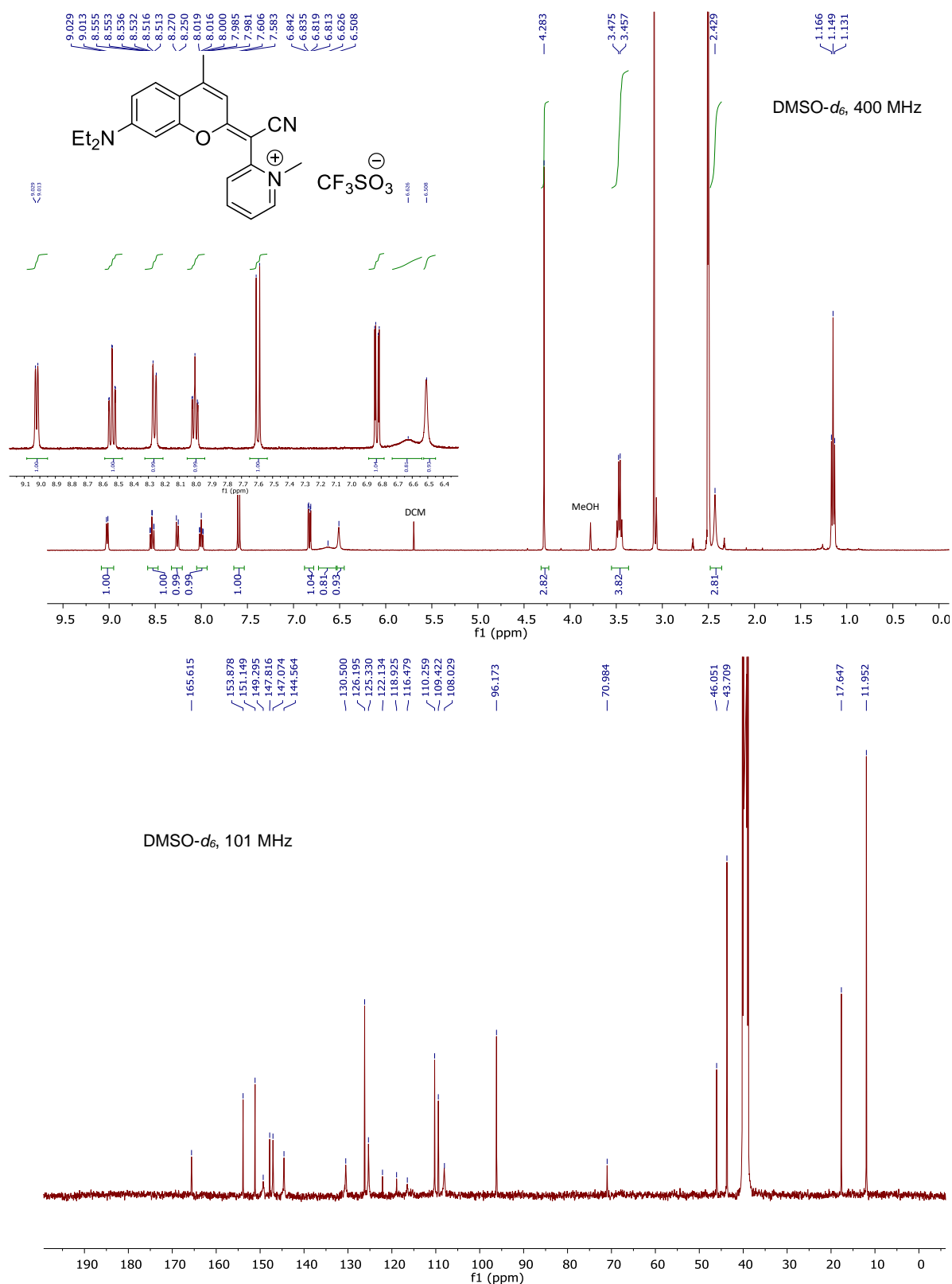


Figure S33. ¹H and ¹³C NMR spectra at 350 K of compound **10** in DMSO-*d*₆.

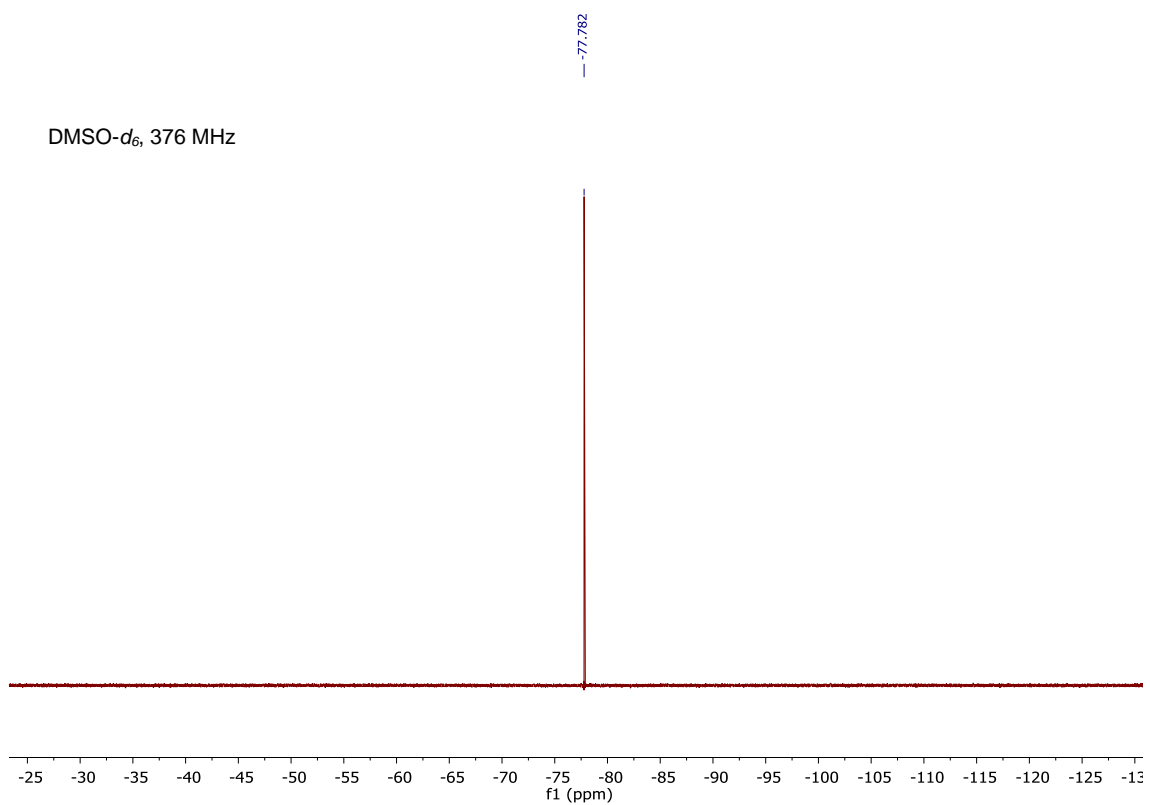


Figure S34. ¹⁹F NMR spectra of compound **10** in DMSO-*d*₆.

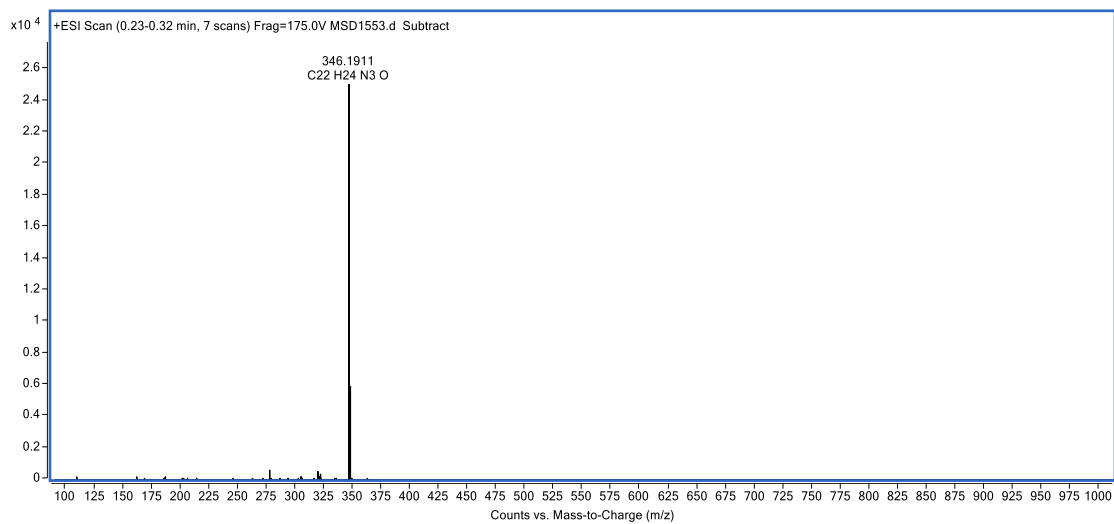


Figure S35. HR ESI-MS spectrum of compound **10**.

2-(Cyano(1-methyl(2-pyrimidin-1-ium))methylene)-7-(*N,N*-diethylamino)-4-methyl-coumarin triflate (11)

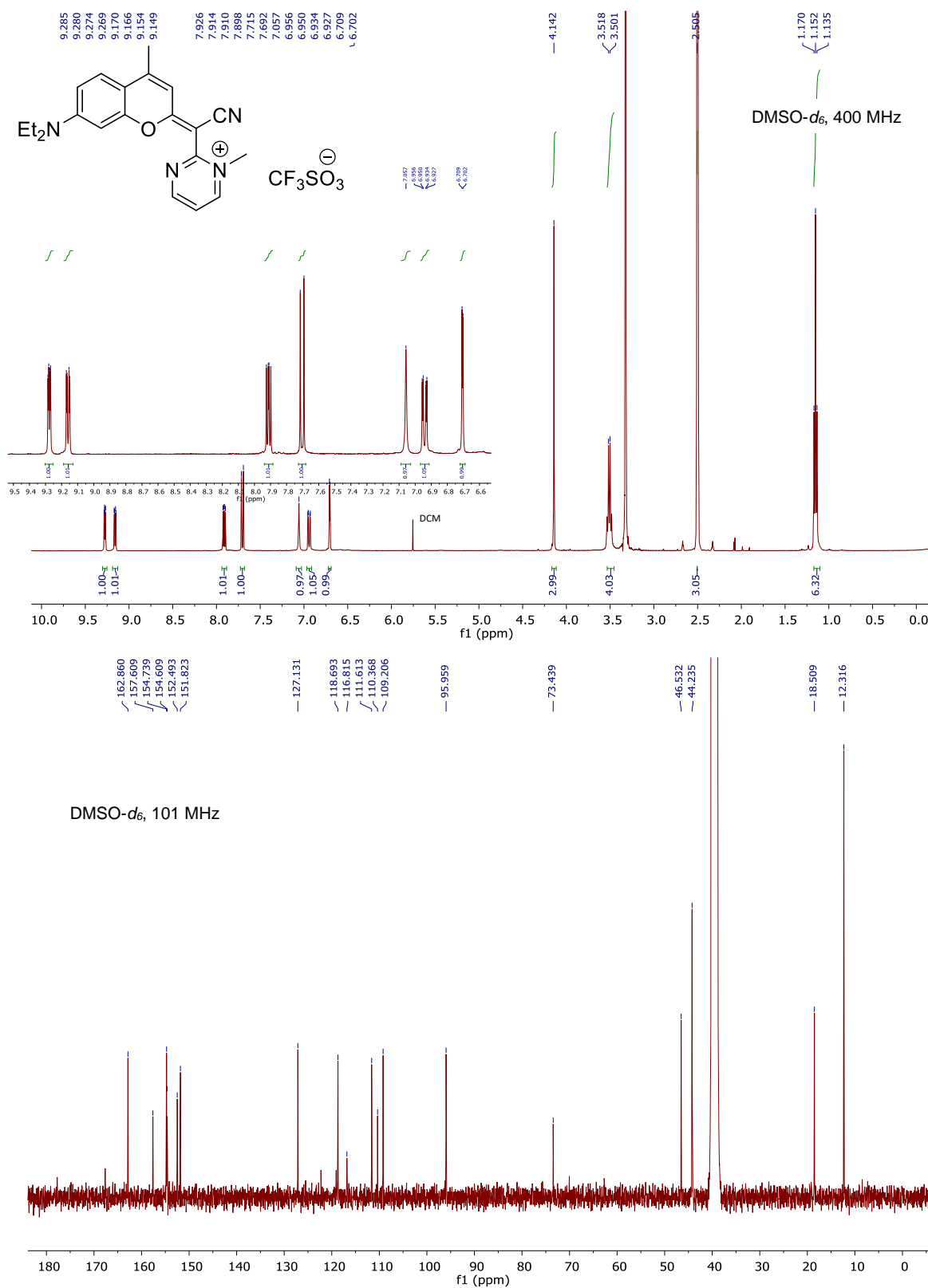


Figure S36. ¹H and ¹³C NMR spectra of compound **11** in DMSO-*d*₆.

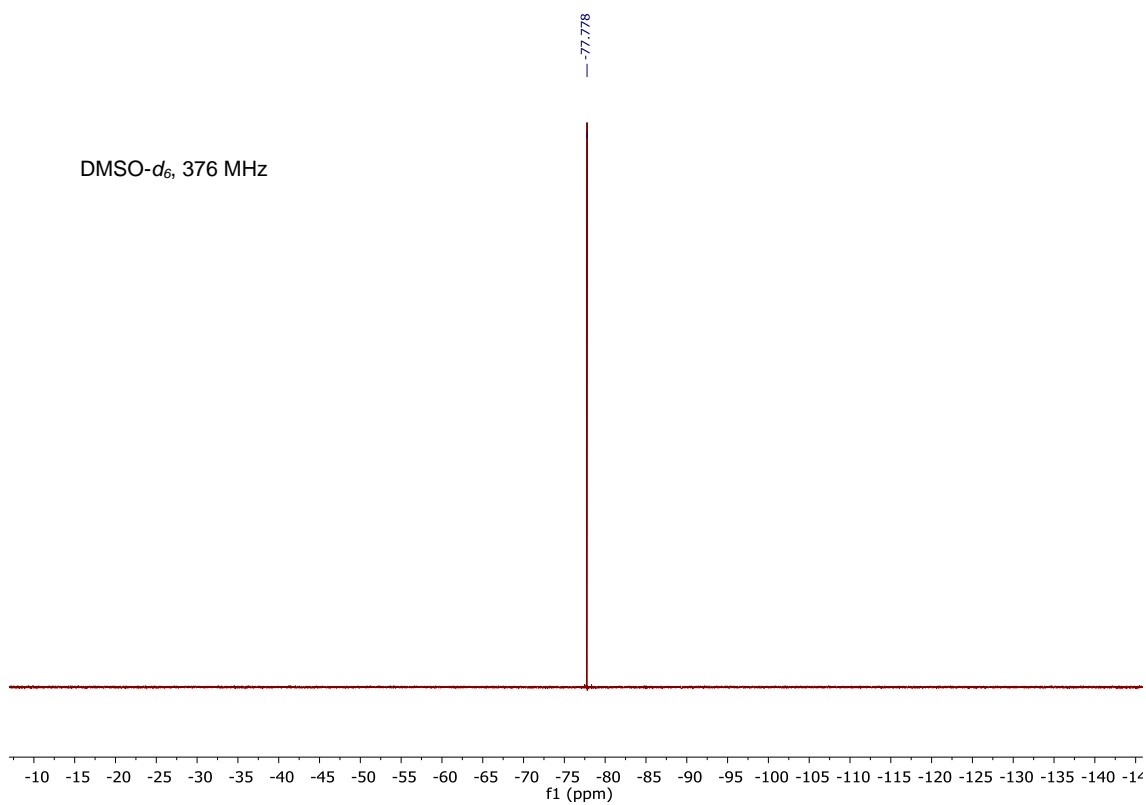


Figure S37. ¹⁹F NMR spectra of compound **11** in DMSO-*d*₆.

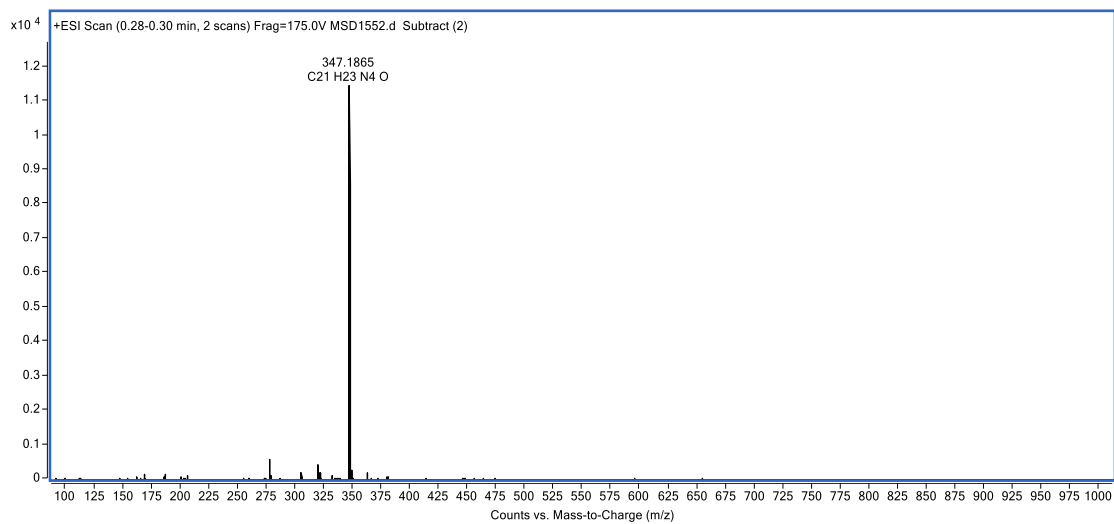


Figure S38. HR ESI-MS spectrum of compound **11**.

2-(Cyano(1-methyl(4-pyrimidin-1-ium))methylene)-7-(*N,N*-diethylamino)-4-methyl-coumarin triflate (12)

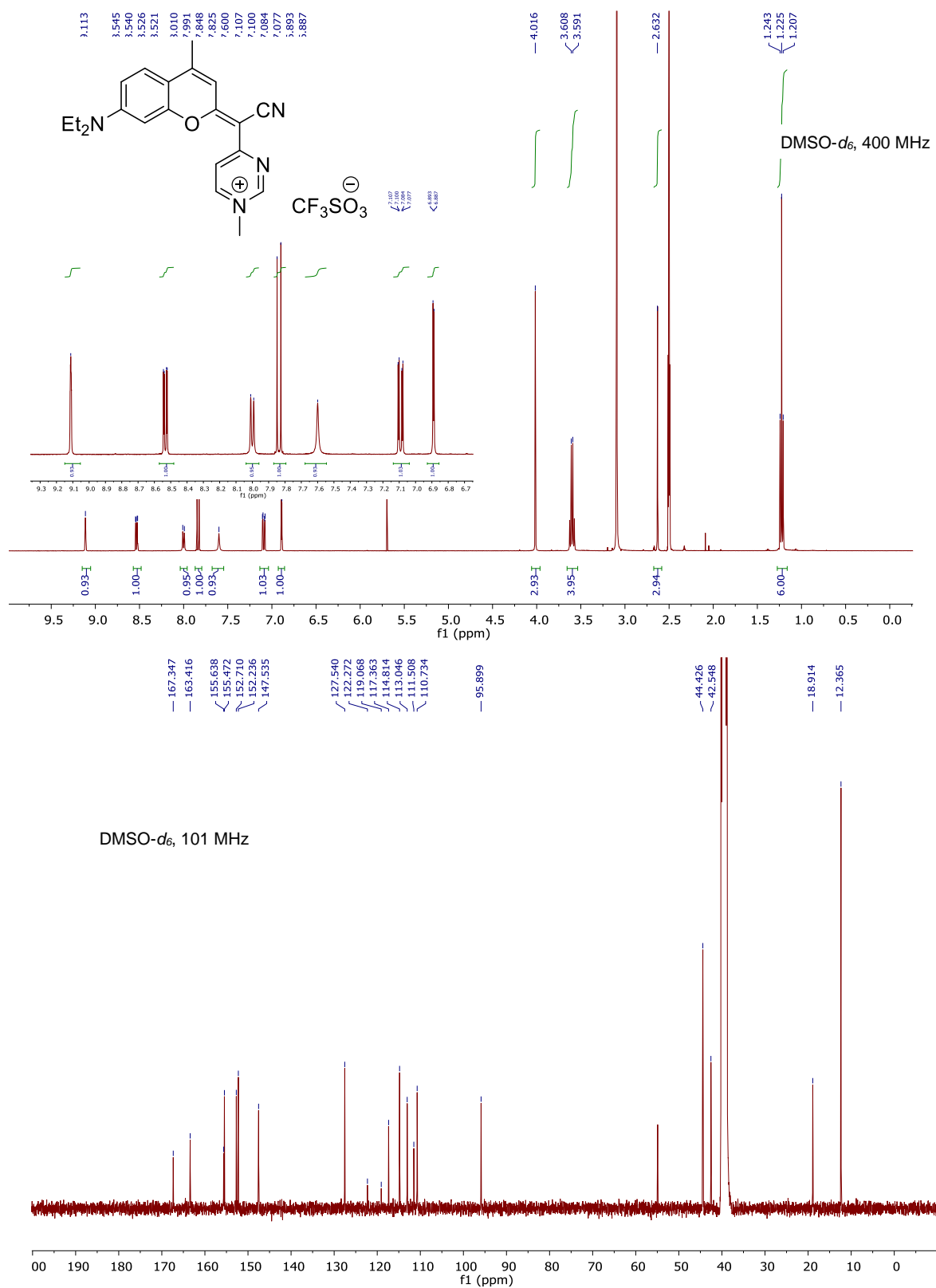


Figure S39. ¹H and ¹³C NMR spectra of compound **11** in DMSO-*d*₆ at 350 K and 298 K, respectively

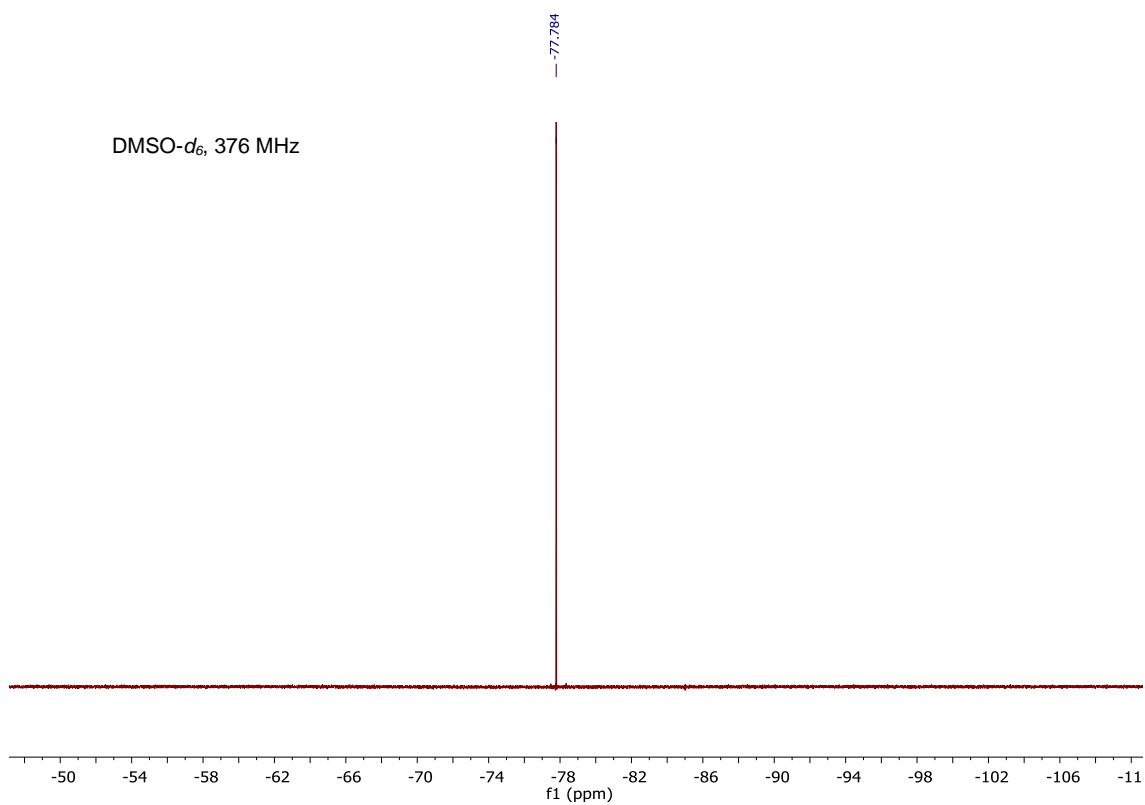


Figure S40. ¹⁹F NMR spectra of compound **12** in DMSO-*d*₆.

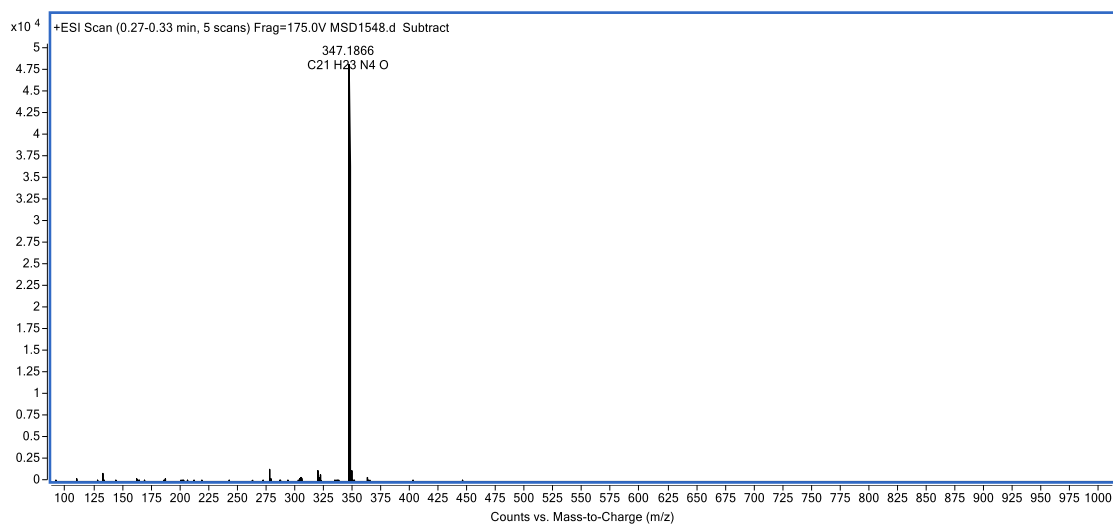


Figure S41. HR ESI-MS spectrum of compound **12**.

2-(Cyano(1-methyl(4-pyrimidin-1-ium))methylene)-7-(*N,N*-dimethylamino)-4-trifluoromethyl-coumarin triflate (13)

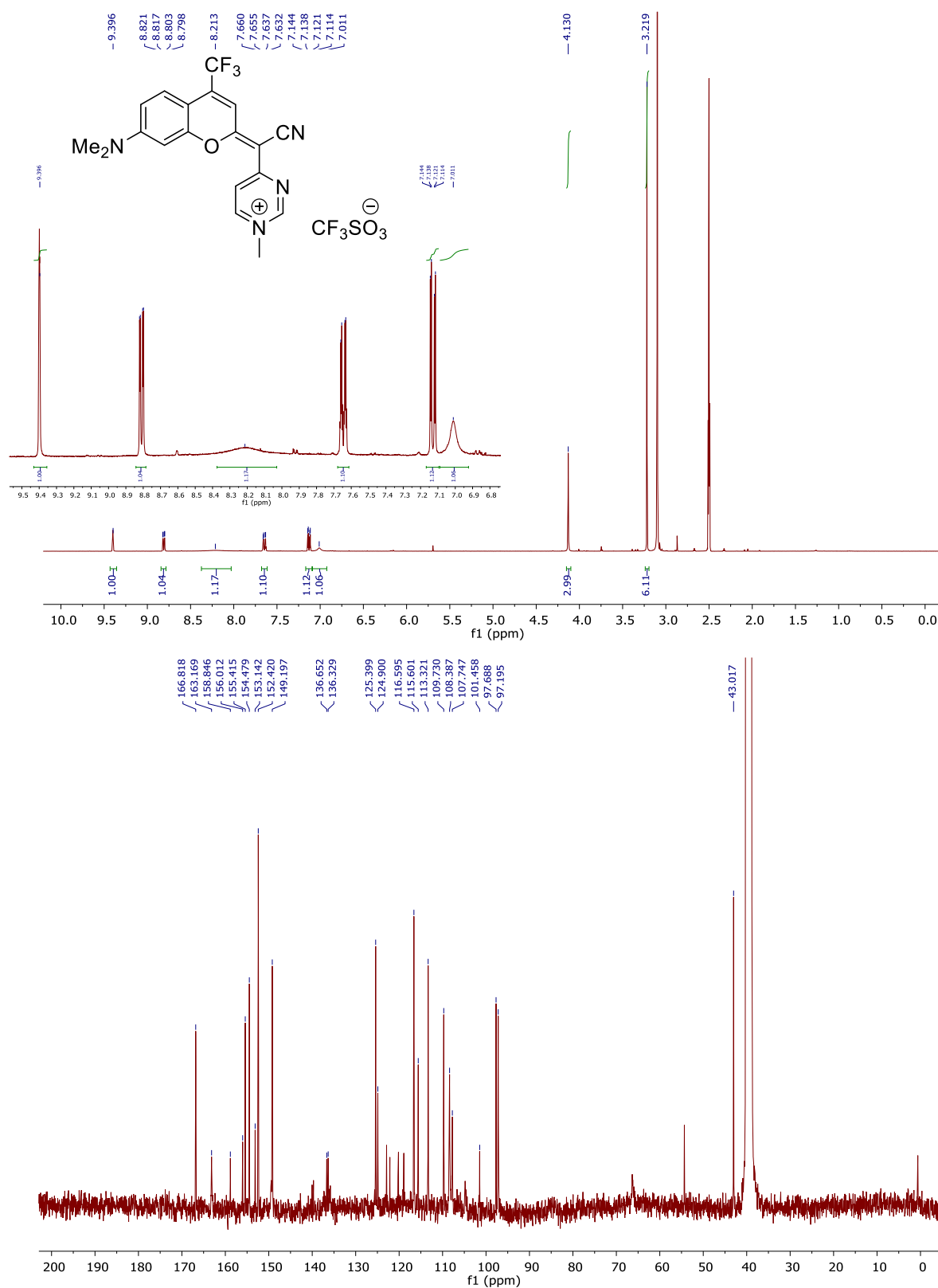


Figure S42. ^1H and ^{13}C NMR spectra at 350 K of compound 13 in $\text{DMSO-}d_6$.

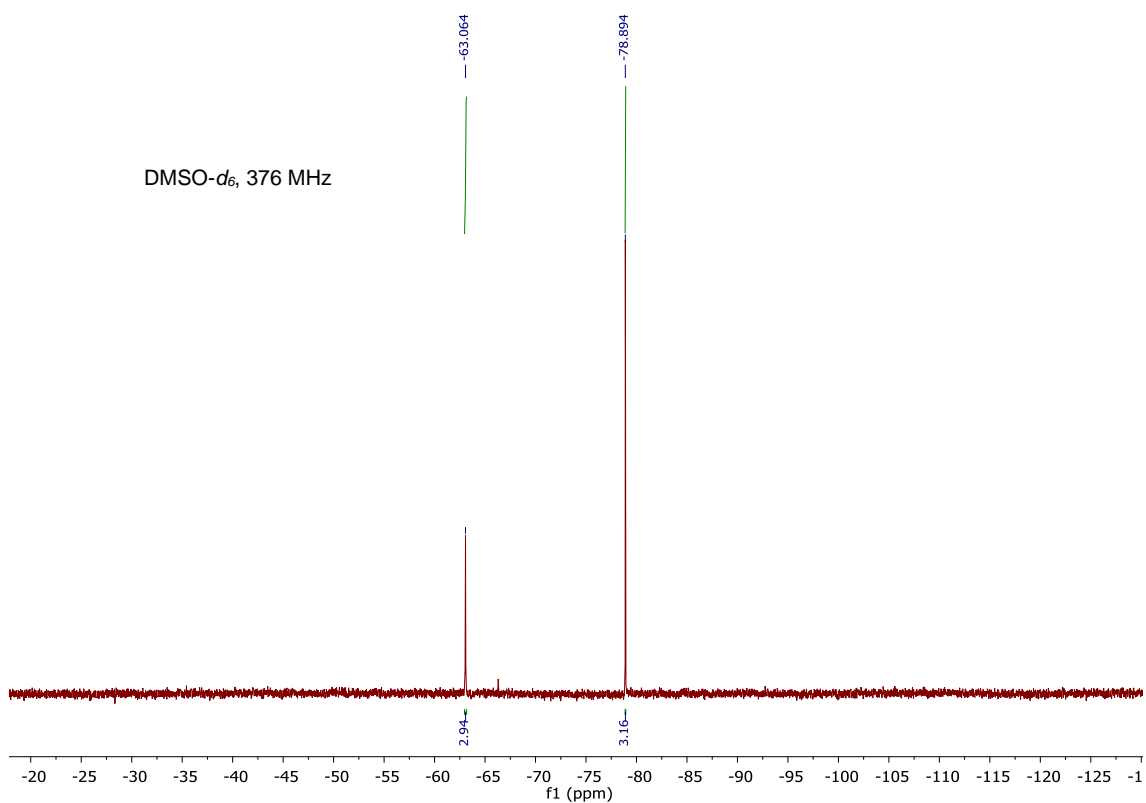


Figure S43. ¹⁹F NMR spectra of compound **13** in DMSO-*d*₆.

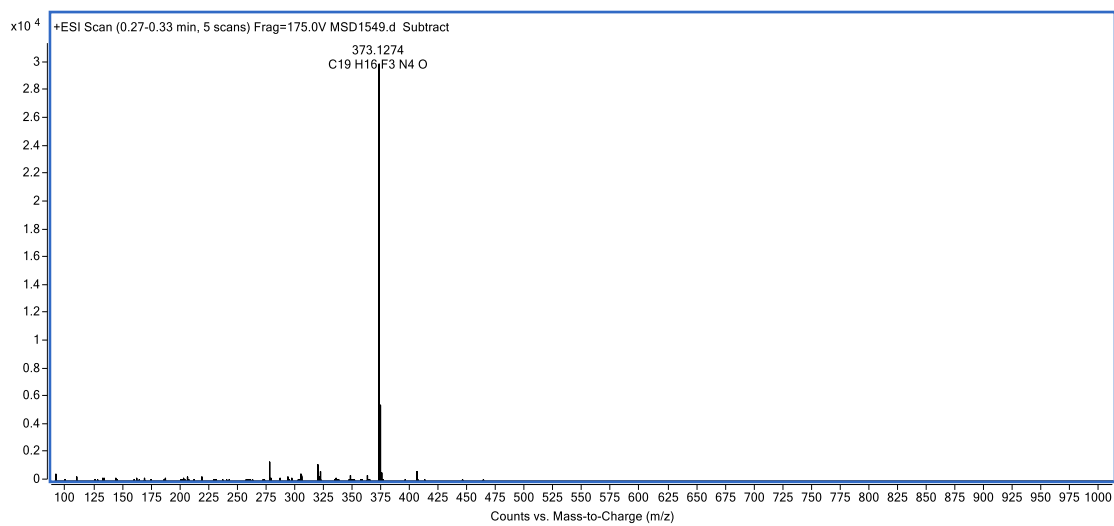


Figure S44. HR ESI-MS spectrum of compound **13**.

7. Chapter Ib. Publication B

Solid-phase approaches for labeling targeting peptides
with far-red emitting coumarin fluorophores.

(A. Rovira *et al.* *J. Org. Chem.* **2019**, *84*, 1808–1817)

Solid-Phase Approaches for Labeling Targeting Peptides with Far-Red Emitting Coumarin Fluorophores

Anna Rovira,^{†,‡} Albert Gandioso,^{†,‡} Marina Goñalons,[†] Alex Galindo,[†] Anna Massaguer,[‡] Manel Bosch,[§] and Vicente Marchán^{*,†}

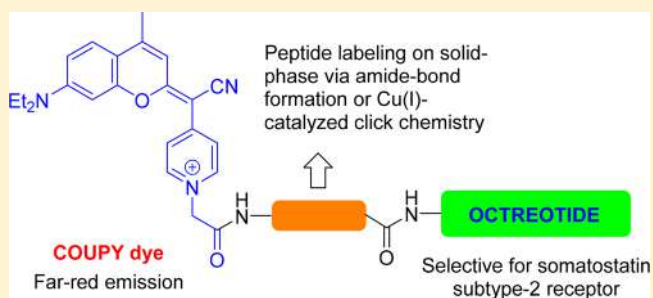
[†]Departament de Química Inorgànica i Orgànica, Secció de Química Orgànica, IBUB, Universitat de Barcelona, Martí i Franquès 1-11, E-08028 Barcelona, Spain

[‡]Departament de Biologia, Universitat de Girona, E-17071 Girona, Spain

[§]Unitat de Microscòpia Òptica Avançada, Centres Científics i Tecnològics, Universitat de Barcelona, E-08028 Barcelona, Spain

Supporting Information

ABSTRACT: Fluorophores based on organic molecules hold great potential for ligand-targeted imaging applications, particularly those operating in the optical window in biological tissues. In this work, we have developed three straightforward solid-phase approaches based on amide-bond formation or a Cu(I)-catalyzed azide–alkyne click (CuAAC) reaction for labeling an octreotide peptide with far-red emitting coumarin-based COUPY dyes. First, the conjugatable versions of COUPY fluorophores incorporating the required functional groups (e.g., carboxylic acid, azide, or alkyne) were synthesized and characterized. All of them were found fully compatible with Fmoc/*t*Bu solid-phase peptide synthesis, which allowed for the labeling of octreotide either through amide-bond formation or by CuAAC reaction. A near quantitative conversion was obtained after only 1 h of reaction at RT when using CuSO₄ and sodium ascorbate independently of the click chemistry approach used (azido-COUPY/alkynyl-peptide resin or alkynyl-COUPY/azido-peptide resin). COUPY-octreotide conjugates were found stable in cell culture medium as well as noncytotoxic in HeLa cells, and their spectroscopic and photophysical properties were found similar to those of their parent coumarin dyes. Finally, the potential bioimaging applications of COUPY-octreotide conjugates were demonstrated by confocal microscopy through the visualization of living HeLa cells overexpressing the somatostatin subtype-2 receptor.



INTRODUCTION

The past few decades have witnessed an impressive growth in the development of novel therapeutic and diagnostic technologies against cancer. In this context, receptors overexpressed on cancer cells have been exploited to selectively deliver a large variety of cytotoxic drugs with the aim of minimizing toxic side-effects associated with chemotherapy. Ligand-targeted imaging agents also offer great potential in the early detection of cancerous cells, as well as in fluorescence-guided surgery (FGS), which allows for resection of solid tumors after illumination of malignancies directly in the operating room.¹ Recent advances in fluorophore chemistry and knowledge of targetable receptors have led to the clinical testing of several targeted fluorophores for intraoperative cancer detection and FGS.^{1b,2}

Owing to the potential of fluorophores based on organic molecules in ligand-targeted imaging applications, it is urgent to develop novel low molecular-weight fluorescent probes operating in the far-red and near-infrared (NIR) region, since only the use of nontoxic and high tissue-penetrating radiation will guarantee clinical translation in the next years.³ Ideally, such fluorophores should be amenable to smart structural

modifications to tune, on demand, photophysical and physicochemical properties, as well as to facilitate conjugation to a broad variety of targeting ligands (e.g., peptides, proteins, folic acid, monoclonal antibodies (mAb), etc.) by using efficient and chemoselective conjugation chemistries. Although many times forgotten, the biological properties of a targeting ligand should not be impaired by the fluorescent tag. This issue is particularly problematic in the case of short peptide sequences since uptake and subcellular localization may be strongly influenced by the fluorophore.⁴ In the same way, some structural modifications of cyanine-based dyes have been reported to alter the mechanism of mAb when conjugated together, and nonspecific hydrophobic interactions between the epidermal growth factor (EGF) receptor and the dye moiety in BODIPY-peptide conjugates were found to reduce peptide-receptor binding specificity.⁵ Hence, the choice of the fluorophore cannot be underestimated since it constitutes a critical parameter in ligand-targeted imaging applications.

Received: October 10, 2018

Published: January 10, 2019

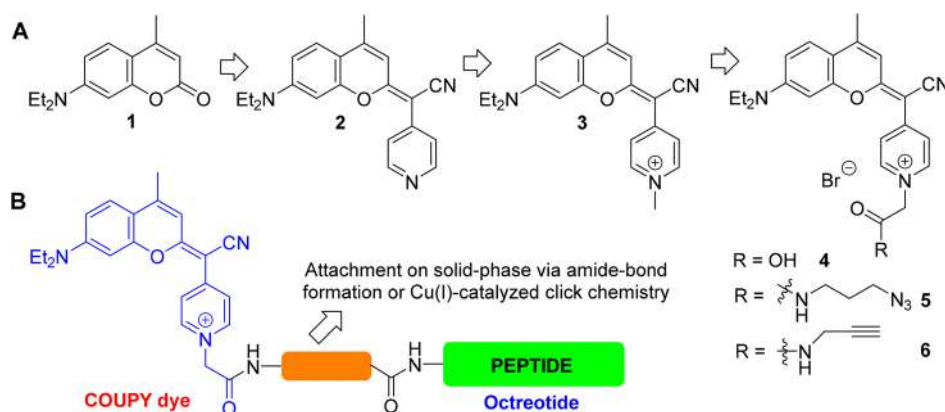
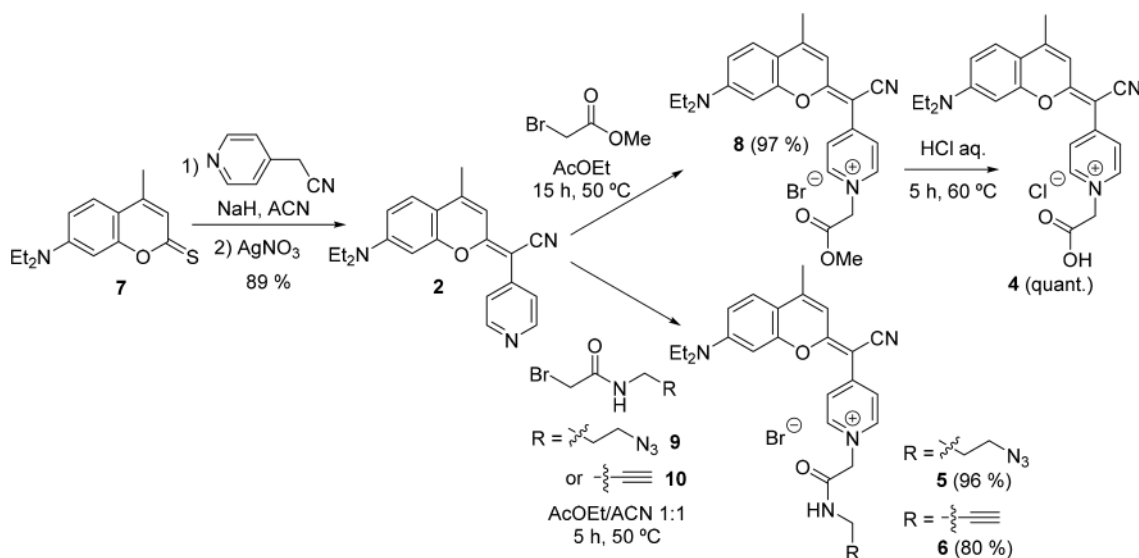


Figure 1. Rational design of conjugatable versions of COUPY dyes (A) and schematic representation of COUPY-octreotide conjugates (B).

Scheme 1. Synthesis of Conjugatable COUPY Dyes 4–6



Recently, we have developed a novel family of coumarin-based fluorophores, nicknamed COUPYs, with promising photophysical properties and great potential for imaging applications.⁶ As shown in Figure 1, replacement of the carbonyl function in coumarin 1 with the cyano(4-pyridine)-methylene moiety (e.g., compound 2) allowed us to increase the push–pull character of the conventional coumarin chromophore, which was easily transformed into pH-independent far-red/NIR-emitting fluorophores through *N*-alkylation of the pyridine heterocycle (e.g., compound 3). Although the photostability of COUPY dyes can be tuned through the incorporation of CF₃ groups at the coumarin skeleton⁶ or by replacement of *N,N*-dialkylamino groups at position 7 with the four-membered ring azetidines,^{6b} the electron-withdrawing cyano group might also have a role in their photostability as previously demonstrated in some cyanine derivatives and in other dyes.⁷ Considering the small size and the easy synthetic accessibility to COUPY dyes, these compounds are potential candidates for labeling targeting ligands, such as receptor-binding peptides. In such a context, we envisaged that conjugatable versions of COUPY dyes (e.g., compounds 4–6 in Figure 1) could be obtained from scaffold 2 through *N*-alkylation with adequate reagents, thereby providing suitable functional groups (e.g., carboxylic acid, azide or alkyne) for conjugation via amide-bond formation or

Cu(I)-catalyzed azide–alkyne cycloaddition reaction (CuAAC), respectively.⁸

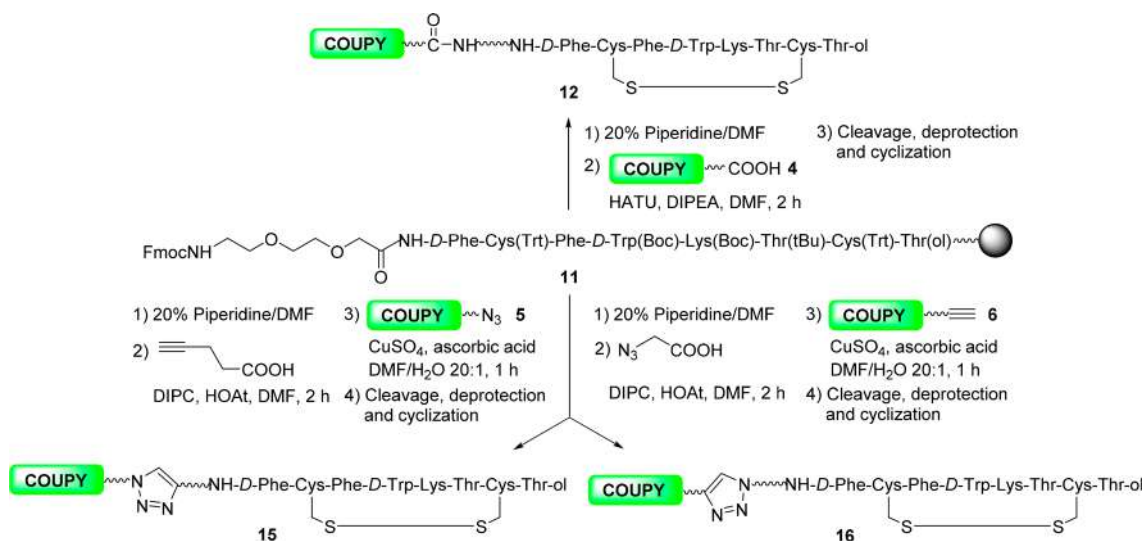
Herein, we report for the first time three straightforward solid-phase approaches for the conjugation of coumarin-based COUPY fluorophores to octreotide, an FDA-approved peptide that displays high affinity and selectivity for somatostatin receptors, mainly subtype-2 receptor (SSTR2), which is overexpressed on the membrane of various types of malignant cells.⁹ This cyclic octapeptide is a promising candidate for developing novel targeted imaging agents since some derivatives, such as [¹¹¹In-DTPA]- and [⁹⁰Y-DOTA-Tyr3]-octreotide conjugates, are routinely used in the clinics for molecular imaging and therapy of neuroendocrine tumors, respectively, and several other SSTR2-targeted radiotherapeutics are currently under clinical evaluation.^{1a} Octreotide has also been conjugated successfully to several anticancer drugs (both organic compounds and metallodrugs),¹⁰ including Ir(III) complexes useful for theranostic applications.¹¹

RESULTS AND DISCUSSION

Synthesis and Characterization of Conjugatable COUPY Dyes.

COUPY fluorophores 4–6 were easily synthesized through *N*-alkylation of 2 (Scheme 1), which was previously obtained by condensation of thiocoumarin 7^{6,12} with 4-pyridylacetonitrile. On the one hand, the reaction of 2

Scheme 2. Schematic Representation of the Three Solid-Phase Approaches Used for Labelling Octreotide with COUPY Dyes via Amide-Bond Formation (Top) or CuAAC Reaction (Bottom)



with methyl bromoacetate afforded intermediate **8** in excellent yield after silica column chromatography (97%). This compound was transformed into coumarin **4** bearing the carboxylic acid function by acidic hydrolysis (Figure S1). On the other hand, azido- (**5**) and alkylnyl- (**6**) containing fluorophores were synthesized by reaction of **2** with *N*-alkyl bromoacetamide derivatives containing the appropriate functional groups for CuAAC (compounds **9** and **10**, respectively). Compounds **5** and **6** were obtained as dark blue solids after purification (96 and 80% yields, respectively). Full characterization was carried out by HR ESI-MS and 1D (¹H and ¹³C) and 2D NMR, and the purity was assessed by reversed-phase HPLC (Figure S1). Similarly to the parent COUPY dye **3**, NOESY experiments revealed that the *E* rotamer was the major species in solution (Figures S2–S4).⁶

Synthesis and Characterization of COUPY-Octreotide Conjugates. Having at hand the conjugatable COUPY derivatives (**4–6**), we focused on labeling octreotide following a stepwise solid-phase strategy since it allows for the regioselective attachment of the fluorescent dye at the *N*-terminal end of the peptide sequence, either through amide-bond formation or by Cu(I)-catalyzed click chemistry. First, the linear octapeptide sequence incorporating a short polyethyleneglycol spacer (**11**) was assembled manually on a Rink amide resin-*p*-MBHA using standard Fmoc-*t*Bu methodology (Scheme 2). After coupling of coumarin **4** with HATU in the presence of DIPEA, side-chain deprotection and cleavage from the resin (TFA/TIS/H₂O/EDT 94:2.5:2.5:1, 2.5 h RT) and cyclization via disulfide bond formation in an aqueous buffer (pH 7–8) were carried out. Analysis by HPLC-ESI MS showed a main peak (Figure S5) that was isolated and characterized as the expected COUPY-octreotide conjugate (**12**). Finally, after purification by semipreparative HPLC and lyophilization, the formate salt of **12** (overall yield 12%) was obtained as a pink solid and fully characterized by HR ESI-MS and NMR. As shown in Figure S6, the obtained *m/z* values are consistent with the calculated values of the charged species [M]⁺, [M + H]²⁺, and [M + 2H]³⁺. In addition, the aromatic region of the ¹H NMR spectra in 8:2 H₂O/D₂O–DMSO-*d*₆ mixtures showed diagnostic peaks from the fluorophore and the peptide (amide NH protons and aromatic protons of D/L-

Phe and D-Trp residues), confirming the covalent attachment of both moieties (Figure 2). Importantly, conjugate **12** was

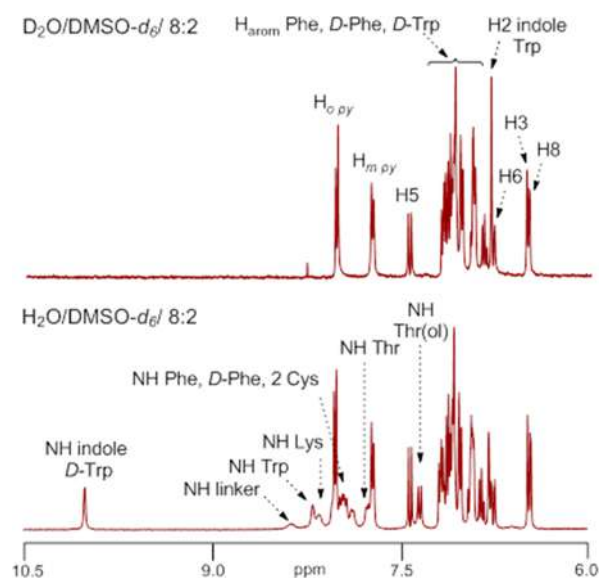


Figure 2. Aromatic region of the ¹H NMR spectra of conjugate **12** in D₂O–DMSO-*d*₆ 8:2 (top) and in H₂O–DMSO-*d*₆ 8:2 (bottom).

found stable in cell culture medium (DMEM supplemented with 10% FBS) after incubation for 24 h (Figure S7), as well as noncytotoxic in HeLa cells (Figure S8). Both prerequisites are necessary for exploring the bioimaging applications of COUPY-peptide conjugates.

Once the compatibility of COUPY dyes with solid-phase peptide synthesis (SPPS) was demonstrated, we investigated the potential applications of coumarin derivatives bearing azide (**5**) and alkylnyl (**6**) functional groups for labeling octreotide via CuAAC reaction on solid-phase, since click chemistry is routinely employed for modifying peptides, oligonucleotides, small molecules, and polymers.¹³ First, the required functional groups were incorporated at the *N*-terminal end of peptide-bound resin **11** by coupling 4-pentynoic acid or 2-azidoacetic acid, which provided alkylnyl- (**13**) and azido- (**14**) peptide-

bound resins, respectively (Figures S9–S10). Click chemistry was investigated by reacting **13** and **14** resins with **5** and **6**, respectively, in the presence of CuSO_4 (3 mol equiv) and sodium ascorbate (3 mol equiv) in DMF/ H_2O 20:1 for 18 h (Scheme 2). To our delight, after cleavage and deprotection, HPLC-MS analysis revealed the formation of the expected linear COUPY-octreotide conjugates. Since no significant side reactions derived of the presence of sodium ascorbate and Cu(I) were detected, we decided not to explore the use of Cu-stabilizing ligands. Although most click chemistry procedures reported in the literature describe the use of long reaction times (12–48 h) and even microwave irradiation for labeling peptides with organic fluorophores,^{13a} we obtained near quantitative conversions after only 1 h of reaction at RT (see Figures S11 and S14 for the HPLC-MS analyses after 1 h, 4 h and overnight reaction times), independently of the click chemistry approach used (azido-COUPY/alkynyl-peptide resin or alkynyl-COUPY/azido-peptide resin). Finally, after cyclization and purification, clicked COUPY-octreotide conjugates (**15** and **16**) were obtained as pink solids (Figures S13–S14 and S15–S16).

Photophysical Characterization of COUPY-octreotide Conjugates. The photophysical properties (absorption and emission spectra, molar absorption coefficients (ϵ), and fluorescence quantum yields (ϕ_F)) of COUPY-octreotide conjugates were studied in water and in PBS buffer, and compared with those of their respective coumarin precursors (see Table 1 and Figures 3 and S17–S20). All the compounds

Table 1. Photophysical Properties of COUPY Dyes (3, 5, 6, and 8) and COUPY-Octreotide Conjugates (12, 15–16) in PBS Buffer and in H_2O ^a

	solvent	λ_{abs} (nm)	λ_{em} (nm)	Stokes' shift (nm)	ϵ ($\text{mM}^{-1}\text{cm}^{-1}$)	ϕ_F
coumarin 3	PBS	543	603	60	34	0.14
	H_2O	543	605	62	31	0.15
coumarin 8	PBS	554	615	61	48	0.044
	H_2O	555	615	60	48	0.043
coumarin 5	PBS	554	616	62	47	0.063
	H_2O	555	615	60	50	0.066
coumarin 6	PBS	553	615	62	45	0.045
	H_2O	555	615	60	46	0.061
conjugate 12	PBS	561	620	59	24	0.14
	H_2O	561	618	57	27	0.17
conjugate 15	PBS	559	620	61	32	0.18
	H_2O	560	618	58	36	0.19
conjugate 16	PBS	559	618	59	26	0.14
	H_2O	560	618	58	30	0.19

^aThe data for coumarin derivative **3** has been included for comparison purposes.^{6a}

showed an intense absorption band in the yellow-red part of the visible spectrum, being the wavelength absorption maximum slightly red-shifted with respect to the parent dye **3** (e.g., $\lambda_{\text{abs}} = 543$ nm for **3** vs $\lambda_{\text{em}} = 555$ nm for **5–6** and **8** in H_2O) because of the additional electron-withdrawing effect of ester and amide functions. Similarly, the emission maximum was red-shifted by ca. 10 nm (e.g., $\lambda_{\text{em}} = 605$ nm for **3** vs $\lambda_{\text{em}} = 615$ nm for **5–6** and **8** in H_2O), and, consequently, the Stokes's shifts remained around 60–62 nm. An additional red-shift in absorption (ca. 4–6 nm) and emission (ca. 3–5 nm)

maxima occurred after conjugation to octreotide. As shown in Table 1, the ϕ_F of the conjugatable coumarin derivatives (**8** and **5–6**) in aqueous media was reduced when compared with **3** (e.g., $\phi_F = 0.066$ for **5** vs $\phi_F = 0.15$ for **3** in H_2O). However, a clear improvement in the fluorescent quantum yield of these fluorophores was achieved when conjugated to the peptide (e.g., $\phi_F = 0.066$ for **5** vs $\phi_F = 0.19$ for conjugate **15** in H_2O), independently of the chemical conjugation approach used.

Fluorescence Imaging of COUPY-octreotide Conjugates in Living Cells. Finally, we investigated the potential bioimaging applications of COUPY-octreotide conjugates. As a representative compound, we selected conjugate **12** and studied its cellular uptake by confocal microscopy in SSTR2-overexpressing HeLa cells after irradiation with a yellow light laser ($\lambda_{\text{ex}} = 561$ nm). Interestingly, fluorescent vesicles, mostly like endosomes, were visible in the cytoplasm of all of the examined cells after 30 min of incubation with **12**, thereby confirming the internalization and accumulation of the COUPY-octreotide conjugate in the cells (Figures 4 and S23). This pattern of staining contrasts with that of coumarin **3** (Figure S23), which accumulates preferentially in mitochondria and nucleoli,⁶ and indicates that the internalization of the COUPY-octreotide conjugate is driven exclusively by the peptide moiety and not by the coumarin tag. In order to get more insights into the cellular uptake of the conjugate, we incubated HeLa cells with **12** at 4 °C for 30 min. As shown in Figure 5, no staining was observed inside the cytoplasm, which confirms that **12** enters the cells only through an energy-dependent pathway. By contrast, the pattern of staining observed with **3** was not modified at a low temperature (Figure 5), thereby suggesting internalization through simple passive diffusion.

Next, we decided to compare the visualization ability of COUPY dyes when conjugated to octreotide with that of two common commercially available fluorophores, 5(6)-carboxy-fluorescein, which is one of the most popular fluorescent tags for labeling peptides and is typically excited at 488 nm, and Atto-Rho12, a rhodamine dye that can be excited with the same yellow light laser as our COUPY fluorophore. Atto-Rho12-octreotide (**17**) was synthesized by reaction of the corresponding succinimidyl ester derivative with octreotide, and carboxyfluorescein-octreotide (**18**) was prepared by SPPS.^{10b} As shown in Figure 4, the performance of the COUPY dye when conjugated to octreotide was comparable to that of the rhodamine dye when exciting at 561 nm under similar conditions. By contrast, COUPY fluorophore allowed a much better visualization of HeLa cells than carboxyfluorescein, even at much lower concentrations and with a more convenient excitation wavelength (561 vs 488 nm). On the other hand, it is worth noting, that conjugates involving carboxyfluorescein and Atto-Rho12 dyes (**17** and **18**) were obtained as regiomeric mixtures since both commercially available fluorophores are supplied as mixtures of isomers. However, COUPY-octreotide conjugate **12** was easily obtained as a single product, which represents a suitable alternative to many conventional fluorophores when labeled biomolecules with a well-defined structure are required for biological applications. Moreover, it is important to note, that the photostability of the COUPY-octreotide conjugate (**12**) in PBS buffer under green light irradiation (505 ± 15 nm; Figure 6) was found similar to that of the parent coumarin **3**,⁶ which indicates that peptide derivatization through the pyridine

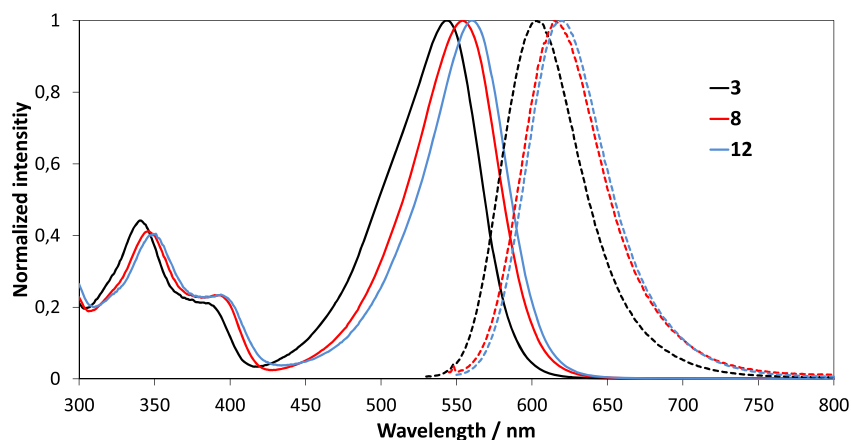


Figure 3. Comparison of the normalized absorption (solid lines) and fluorescence emission (dotted lines) spectra of coumarins 3 and 8 and of COUPY-octreotide conjugate 12.

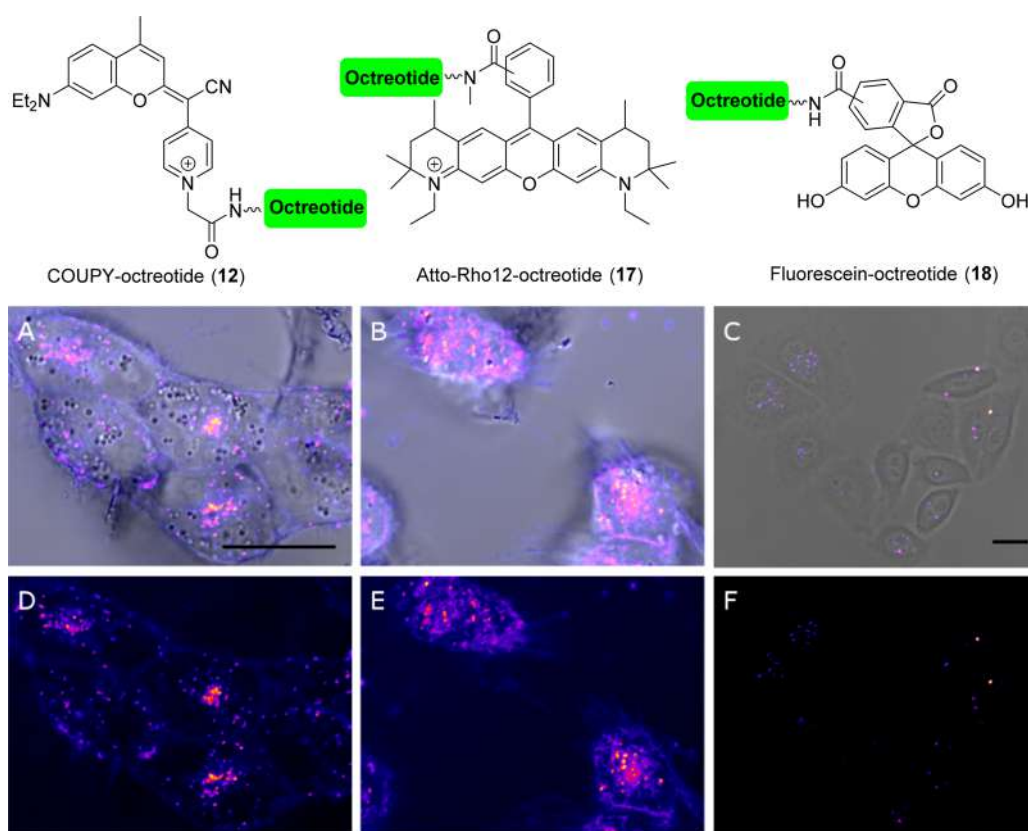


Figure 4. Comparison of the cellular uptake of COUPY- (12), Atto Rho12- (17) and fluorescein- (18) octreotide conjugates. (Top) Structures of the conjugates. (Bottom) Single confocal planes of HeLa cells incubated with 12 (A, D) and 17 (B, E) at 10 μM and 18 (C, F) at 50 μM for 30 min at 37 $^{\circ}\text{C}$. (A–C) Fluorescence images merged with bright field images. (D–F) Fluorescence images only. All fluorescence images are color coded using the Fire lookup table from Fiji. Scale bar, 20 μm . B, D, and E are the same scale as A. F is the same scale as C.

heterocycle does not significantly modify the photostability of COUPY dyes.

CONCLUSIONS

In conclusion, we have synthesized three conjugatable versions of COUPY dyes (compounds 4–6) incorporating suitable functional groups for conjugation via amide-bond formation (e.g., carboxylic acid) or a Cu(I)-catalyzed azide–alkyne cycloaddition (CuAAC) reaction (e.g., azide or alkyne). The compounds were easily obtained from a cheap, commercially available precursor, 7-*N,N*-diethylaminocoumarin, in only

three or four linear steps, with the *N*-alkylation of the pyridine ring being the key step. All the conjugatable coumarin derivatives were found fully compatible with Fmoc/*t*Bu solid-phase peptide synthesis, which allowed for the straightforward labeling of the octreotide peptide with a far-red emitting fluorophore. On the one hand, attachment of the coumarin 4 bearing a carboxylic acid function to the *N*-terminal end of the linear peptide-bound resin followed by acidic cleavage and deprotection and cyclization led to the expected COUPY-octreotide conjugate (12). This conjugate was found stable in cell culture medium as well as noncytotoxic in HeLa cells. On

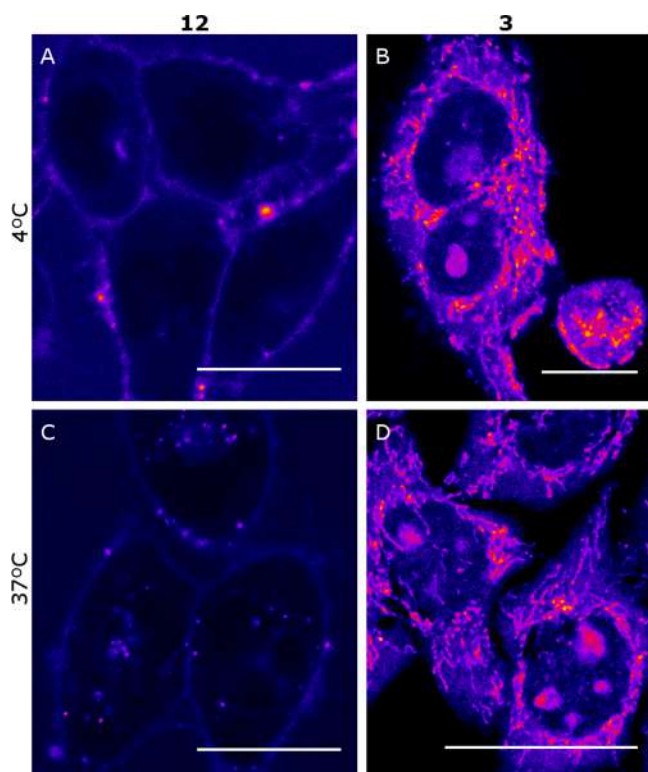


Figure 5. Comparison of the cellular uptake of COUPY-octreotide conjugate **12** and COUPY dye **3**. Single confocal planes of HeLa cells incubated with **12** (A, C) and **3** (B, D) at 10 μM or 0.5 μM , respectively, first at 4 $^{\circ}\text{C}$ for 30 min (A, B) and then incubated at 37 $^{\circ}\text{C}$ for additional 30 min (C, D). The compounds were excited at 561 nm and emission was detected from 570 to 670 nm. All images are color coded using the Fire lookup table from Fiji. Scale bar, 20 μm .

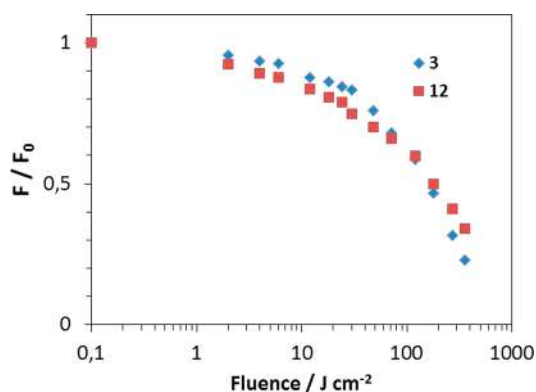


Figure 6. Fluorescence bleaching of COUPY-octreotide conjugate **12** and COUPY dye **3** in PBS buffer (5 μM) irradiated with green light (505 nm; 100 mW/cm²).

the other hand, clicked COUPY-octreotide conjugates (**15** and **16**) were efficiently obtained by CuAAC reaction on a solid-phase between azide- (**5**) and alkynyl- (**6**) containing COUPY dyes and peptide-bound resins containing the complementary functional groups.

The spectroscopic and photophysical properties of COUPY-octreotide conjugates were found similar to those of their parent coumarin dyes, being the wavelength absorption maximum located in the yellow-red part of the visible spectrum, while the emission ranged from the far red to the NIR region. Importantly, the fluorescent quantum yields of

COUPY-octreotide conjugates in water were found higher than those of their coumarin precursors. Finally, the potential bioimaging applications of COUPY-octreotide conjugates were demonstrated by confocal microscopy in SSTR2-overexpressing living HeLa cells. Both the pattern of staining and the inhibition of the cellular uptake at low temperature indicate that the internalization of the conjugates is driven by the peptide moiety and not by the coumarin tag. Moreover, the fact that the visualization ability of COUPY dyes when conjugated to octreotide was similar to that of a commercially available rhodamine fluorophore, Atto-Rho12, and much better than that of the 5(6)-carboxyfluorescein, makes them as a suitable alternative when labeled biomolecules with a well-defined structure are required for biological applications. Work is in progress in our laboratory to increase the red-shifted properties of COUPY dyes with the aim of using them in ligand-targeted imaging applications, such as fluorescence-guided surgery.

EXPERIMENTAL SECTION

Materials and Methods. Unless otherwise stated, common chemicals and solvents (HPLC grade or reagent grade quality) were purchased from commercial sources and used without further purification. Fmoc-protected amino acids, resins, and coupling reagents for solid-phase synthesis were obtained from Novabiochem, Bachem, or Iris Biotech. Fmoc-L-threoninol *p*-carboxyacetal was synthesized following previously reported procedures.¹⁴ Solid-phase peptide synthesis (SPPS) was performed manually in a polypropylene syringe fitted with a polyethylene disk. Peptides were assembled on a Rink amide resin-*p*-MBHA ($f = 0.50$ mmol/g, 100–200 mesh) using standard Fmoc/^tBu chemistry with the following side-chain protecting groups, Boc (*N*^{tert}-butoxycarbonyl, tryptophan, and *N*^{tert}-butoxycarbonyl, lysine), ^tBu (*O*-*tert*-butyl, threonine), and Trt (*S*-trityl, cysteine).

Aluminum plates coated with a 0.2 mm thick layer of silica gel 60 F₂₅₄ were used for thin-layer chromatography analyses (TLC), whereas flash column chromatography purification was carried out using silica gel 60 (230–400 mesh). Reversed-phase high-performance liquid chromatography (HPLC) analyses were carried out on a Jupiter Proteo C₁₈ column (250 mm × 4.6 mm, 90 Å 4 μm , flow rate: 1 mL/min) using linear gradients of 0.1% formic acid in H₂O (A) and 0.1% formic acid in ACN (B). NMR spectra were recorded at 25 $^{\circ}\text{C}$ in a 400 MHz spectrometer using the deuterated solvent as an internal deuterium lock. Tetramethylsilane (TMS) was used as an internal reference (0 ppm) for ¹H spectra recorded in CDCl₃ and the residual protic signal of the solvent (77.16 ppm) for ¹³C spectra. The residual protic signal of DMSO was used as a reference in ¹H and ¹³C NMR spectra recorded in DMSO-*d*₆. Chemical shifts are reported in part per million (ppm) in the δ scale, coupling constants in Hz, and multiplicity as follows, s (singlet), d (doublet), t (triplet), q (quartet), qt (quintuplet), m (multiplet), dd (doublet of doublets), dt (doublet of triplets), ddd (doublet of doublet of doublets), br (broad signal), etc. The proton signals of the *E* and *Z* rotamers were identified by simple inspection of the ¹H spectrum, and the rotamer ratio was calculated by peak integration. 2D-NOESY spectra were acquired in DMSO-*d*₆ with a mixing time of 500 ms. Electrospray ionization mass spectra (ESI-MS) were recorded on an instrument equipped with single quadrupole detector coupled to an HPLC, high-resolution (HR) ESI-MS on an LC/MS-TOF instrument.

Synthesis of Compounds 9 and 10. *N*-(3-Azidopropyl)-2-bromoacetamide (**9**). The published method with some modifications was followed to synthesize compound **9**.¹⁵ 3-Azido-1-propanamine (250 mg, 2.5 mmol) was dissolved in 10 mL of DCM, and then 10 mL of saturated aqueous NaHCO₃ was added. The mixture was vigorously stirred at -10 $^{\circ}\text{C}$ and bromoacetyl bromide (1.01 g, 5.0 mmol) was slowly added. The reaction mixture was slowly allowed to warm to room temperature. After being stirred for 3 h, the reaction mixture was partially concentrated to remove the organic solvent and

then poured into 100 mL of water. The aqueous phase was extracted with AcOEt (2 × 100 mL), and the combined organic phases were washed with saturated NaHCO₃ (100 mL), 5% aqueous HCl solution (100 mL), and saturated NaCl (100 mL). The organic phase was dried over anhydrous Na₂SO₄, filtered, and evaporated under reduced pressure. The crude product was purified by column chromatography (silica gel, 0–60% AcOEt in hexane) to give 364 mg of a pink oil (yield: 66%). TLC: *R_f* (hexane/DCM 1:1) 0.5. ¹H NMR (400 MHz, CDCl₃, δ (ppm)): 6.85 (1H, br s), 3.85 (2H, s), 3.37 (4H, m), 1.80 (2H, qt, *J* = 6.6 Hz). ¹³C{¹H} NMR (101 MHz, CDCl₃, δ (ppm)): 165.9, 49.3, 37.9, 29.1, 28.5. HRMS (ESI-TOF) (*m/z*): [M + H]⁺ Calcd for C₃H₁₀BrN₄O, 221.0033; found, 221.0027. MS (EI) (*m/z*): 220 (M⁺, s), 178 (10), 141 (25), 86 (70), 72 (100) (calcd mass for C₃H₉⁷⁹BrN₄O [M]⁺, 220; calcd mass for C₃H₉⁸¹BrN₄O [M]⁺, 222).

2-Bromo-*N*-(prop-2-yn-1-yl)acetamide (10). The published method with some modifications was followed to synthesize compound 10.¹⁶ Propargylamine (500 mg, 9.1 mmol) was dissolved in 20 mL of DCM, and then 20 mL of saturated aqueous NaHCO₃ was added. The mixture was vigorously stirred at –10 °C, and bromoacetyl bromide (3.66 g, 18.2 mmol) was slowly added. The reaction mixture was slowly allowed to warm to room temperature. After being stirred for 3 h, the reaction mixture was partially concentrated to remove the organic solvent and then poured into 100 mL of water. The aqueous phase was extracted with AcOEt (2 × 100 mL), and the combined organic phases were washed with saturated NaHCO₃ (100 mL), 5% aqueous HCl solution (100 mL), and saturated NaCl (100 mL). The organic phase was dried over anhydrous Na₂SO₄, filtered, and evaporated under reduced pressure. The crude product was purified by column chromatography (silica gel, 0–60% AcOEt in hexane) to give 0.87 g of a white solid (yield: 55%). TLC: *R_f* (hexane/DCM 1:1) 0.5. ¹H NMR (400 MHz, CDCl₃, δ (ppm)): 6.60 (1H, br s), 3.85 (2H, s), 4.09 (2H, dd, *J* = 5.6 Hz, *J* = 2.4 Hz), 3.90 (2H, s), 2.28 (1H, t, *J* = 2.4 Hz). ¹³C{¹H} NMR (101 MHz, CDCl₃, δ (ppm)): 165.2, 78.6, 72.4, 30.1, 28.8. HRMS (ESI-TOF) (*m/z*): [M + H]⁺ Calcd for C₅H₇BrNO 175.9706; found, 175.9708. MS (EI) (*m/z*): 175 (M⁺, s), 96 (100), 82 (40), 39 (35) (calcd mass for C₅H₆⁷⁹BrNO [M]⁺, 175; calcd mass for C₅H₆⁸¹BrNO [M]⁺, 177).

Synthesis of Coumarin Derivatives (4–6 and 8). **2-(Cyano(1-(2-methoxy-(2-oxoethyl))(4-pyridin-1-ium)methylene)-7-(*N,N*-diethylamino)-4-methyl-coumarin Bromide (8).** Methyl bromoacetate (140 μL, 1.51 mmol) was added to a solution of coumarin 2^{6a} (500 mg, 1.51 mmol) in AcOEt (60 mL). The mixture was stirred for 4 h at 60 °C under an Ar atmosphere and protected from light. Then, methyl bromoacetate (140 μL, 1.51 mmol) was added again, and the reaction mixture was stirred overnight at 60 °C and protected from light. The crude product was evaporated under reduced pressure and purified by column chromatography (silica gel, 0–8% MeOH in DCM) to give 713 mg of purple solid (yield, 97%). TLC: *R_f* (10% MeOH in DCM) 0.55. ¹H NMR (400 MHz, DMSO-*d*₆, δ (ppm)): 8.59 (2H, d, *J* = 7.2 Hz), 8.17 (2H, d, *J* = 7.2 Hz), 7.70 (1H, d, *J* = 9.0 Hz), 7.04 (1H, d, *J* = 2.0 Hz), 6.96 (1H, dd, *J* = 9.0 Hz, *J* = 2.8 Hz), 6.89 (1H, s), 5.51 (2H, s), 3.78 (3H, s), 3.56 (4H, q, *J* = 7.2 Hz), 2.53 (3H, s), 1.18 (6H, t, *J* = 7.2 Hz). ¹³C{¹H} NMR (101 MHz, DMSO-*d*₆, δ (ppm)): 167.6, 166.8, 154.9, 153.2, 152.1, 149.6, 144.0, 127.0, 120.1, 118.0, 112.1, 110.4, 96.5, 78.2, 58.3, 53.0, 44.2, 18.5, 12.4. HRMS (ESI-TOF) (*m/z*): [M]⁺ Calcd for C₂₄H₂₆N₃O₃, 404.1969; found, 404.1963. Analytical HPLC (30–100% B in 30 min, formic acid additive): *R_f* = 7.3 min.

2-(Cyano(1-(carboxymethyl))(4-pyridin-1-ium)methylene)-7-(*N,N*-diethylamino)-4-methyl-coumarin Chloride (4). A 1:1 (v/v) mixture of HCl (37%) and Milli-Q water (170 mL) was added to coumarin 8 (500 mg, 1.03 mmol). The reaction mixture was stirred for 5 h at 60 °C under an Ar atmosphere and protected from light. After removal of the major part of the solvent, several coevaporations from acetonitrile were carried out. The crude product was used without further purification since HPLC-MS analysis revealed that the hydrolysis reaction was quantitative. ¹H NMR (400 MHz, DMSO-*d*₆, δ (ppm)): 8.59 (2H, d, *J* = 7.4 Hz), 8.18 (2H, d, *J* = 7.4 Hz), 7.72 (1H, d, *J* = 9.2 Hz), 7.04 (1H, br s), 6.98 (1H, dd, *J* = 9.2 Hz, *J* = 2.4 Hz), 6.93 (1H, d, *J* = 2.4 Hz), 5.39 (2H, s), 3.56 (4H, q, *J* = 7.2 Hz),

2.55 (3H, s), 1.18 (6H, t, *J* = 7.2 Hz). HRMS (ESI-TOF) (*m/z*): [M]⁺ Calcd for C₂₃H₂₄N₃O₃, 390.1812; found, 390.1808. Analytical HPLC (30–100% B in 30 min, formic acid additive): *R_f* = 10.2 min).

2-(Cyano(1-(2-((3-azidopropyl)amino)-2-oxoethyl))(4-pyridin-1-ium)methylene)-7-(*N,N*-diethylamino)-4-methyl-coumarin Bromide (5). *N*-(3-Azidopropyl)-2-bromoacetamide (167 mg, 0.75 mmol) was added to a solution of coumarin 2^{6a} (250 mg, 0.75 mmol) in a 1:1 mixture of AcOEt and ACN (30 mL), which was previously heated at 50 °C. After being stirred for 2 h at 50 °C, an additional amount of compound 9 (167 mg, 0.75 mmol) was added, and the reaction mixture was stirred for 5 h at 50 °C. After evaporation under reduced pressure and purification by column chromatography (silica gel, 0–6% MeOH in DCM), 400 mg of a dark purple solid was obtained (yield: 96%). TLC: *R_f* (10% MeOH in DCM) 0.45. ¹H NMR (400 MHz, DMSO-*d*₆, δ (ppm)): 8.58 (1H, t, *J* = 5.6 Hz), 8.53 (2H, d, *J* = 7.4 Hz), 8.16 (2H, d, *J* = 7.4 Hz), 7.72 (1H, d, *J* = 9.2 Hz), 7.01 (1H, br s), 6.98 (1H, dd, *J* = 9.2 Hz, *J* = 2.4 Hz), 6.93 (1H, s), 5.24 (2H, s), 3.56 (4H, q, *J* = 7.2 Hz), 3.41 (2H, t, *J* = 6.8 Hz), 3.21 (2H, q, *J* = 6.8 Hz), 2.55 (3H, s), 1.71 (2H, qt, *J* = 6.8 Hz), 1.18 (6H, t, *J* = 7.2 Hz). ¹³C{¹H} NMR (101 MHz, DMSO-*d*₆, δ (ppm)): 166.8, 165.0, 154.9, 152.8, 152.0, 149.2, 144.2, 127.0, 120.0, 118.2, 111.9, 110.4, 96.4, 78.1, 59.5, 54.9, 48.2, 44.2, 36.3, 28.2, 18.4, 12.3. HRMS (ESI-TOF) (*m/z*): [M]⁺ Calcd for C₂₆H₃₀N₇O₂, 472.2455; found, 472.2450. Analytical HPLC (30–100% B in 30 min, formic acid additive): *R_f* = 8.0 min.

2-(Cyano(1-(2-oxo-2-(prop-2-yn-1-ylamino)ethyl))(4-pyridin-1-ium)methylene)-7-(*N,N*-diethylamino)-4-methyl-coumarin Bromide (6). 2-Bromo-*N*-(prop-2-yn-1-yl)acetamide (10) (42 mg, 0.75 mmol) was added to a solution of coumarin 2^{6a} (250 mg, 0.75 mmol) in a 1:1 mixture of AcOEt and ACN (30 mL), which was previously heated at 50 °C. After being stirred for 2 h at 50 °C, an additional amount of compound 9 (63 mg, 1.12 mmol) was added, and the reaction mixture was stirred overnight at 50 °C. After evaporation under reduced pressure and purification by column chromatography (silica gel, 0–6% MeOH in DCM), 304 mg of a dark purple solid was obtained (yield: 80%). TLC: *R_f* (10% MeOH in DCM) 0.60. ¹H NMR (400 MHz, DMSO-*d*₆, δ (ppm)): 9.01 (1H, t, *J* = 5.6 Hz), 8.53 (2H, d, *J* = 7.4 Hz), 8.16 (2H, d, *J* = 7.4 Hz), 7.72 (1H, d, *J* = 9.2 Hz), 7.01 (1H, br s), 6.98 (1H, dd, *J* = 9.2 Hz, *J* = 2.4 Hz), 6.93 (1H, s), 5.27 (2H, s), 3.98 (2H, dd, *J* = 5.6 Hz, *J* = 2.4 Hz), 3.57 (4H, q, *J* = 7.2 Hz), 3.23 (1H, t, *J* = 2.4 Hz), 2.55 (3H, s), 1.18 (6H, t, *J* = 7.2 Hz). ¹³C{¹H} NMR (101 MHz, DMSO-*d*₆, δ (ppm)): 166.8, 165.0, 154.9, 152.9, 152.0, 149.3, 144.2, 127.0, 120.0, 118.2, 111.9, 110.5, 110.4, 96.4, 80.3, 78.1, 73.8, 59.3, 44.2, 28.4, 18.4, 12.4. HRMS (ESI-TOF) (*m/z*): [M]⁺ Calcd for C₂₆H₂₇N₄O₂, 427.2129; found, 427.2127. Analytical HPLC (30–100% B in 30 min, formic acid additive): *R_f* = 7.3 min.

Synthesis and Characterization of COUPY-octreotide Conjugate 12. *Fmoc-NH-PEG-D-Phe-Cys(Trt)-Phe-D-Trp(Boc)-Lys(Boc)-Thr(tBu)-Cys(Trt)-Thr(ol)-Resin (11). Octreotide-bound resin 11 was prepared following previously reported procedures.^{9b} Briefly, the Fmoc-protected *L*-threoninol functionalized as the *p*-carboxybenzaldehyde acetal was anchored to the solid support by using DIPC (3 mol equiv) and HOBt (3 mol equiv) in anhydrous DMF for 3 h, and subsequently, the following Fmoc-protected amino acids as well as the Fmoc-protected PEG spacer, 8-(9-fluorenylmethoxycarbonyl-amino)-3,6-dioxaoctanoic acid, were incorporated using DIPC (3 mol equiv) and HOAt (3 mol equiv) in anhydrous DMF for 2 h.*

COUPY-octreotide Conjugate (12). After removal of the Fmoc protecting group from peptide-bound resin 11 with 20% piperidine in DMF (2 × 10 min), coumarin 4 (4 mol equiv) was coupled by using HATU (3.9 mol equiv) and DIPEA (2 + 2 mol equiv) in anhydrous DMF for 2 h in the dark by using the following procedure. DIPEA (2 mol equiv) was first added to a solution of coumarin 4 and HATU in anhydrous DMF, and after being stirred for 5 min at RT, the mixture was added to DMF-swollen peptide-bound resin 11. Then, DIPEA (2 mol equiv) was immediately added, and the reaction mixture was stirred for 2 h. Cleavage and deprotection of the resulting COUPY-octreotide-bound resin were simultaneously performed by treatment

with TFA/H₂O/EDT/TIS 94:2.5:2.5:1 for 2.5 h at RT and protected from light. Most of the TFA was removed by bubbling N₂ into the solution, and the resulting residue was poured onto cold diethyl ether to precipitate the target compound. The solid was isolated by centrifugation, dissolved in H₂O/ACN (9:1), and lyophilized. Cyclization was accomplished after continuously stirring an aerated solution of the crude material in a 97:3 (v/v) mixture of aqueous NH₄HCO₃ (5%) pH 7–8 and DMSO overnight at RT (1 mL solution per 1 mg of theoretical peptide). As shown in Figure S5, analytical reversed-phase HPLC-MS analysis (10–70% B in 30 min, 0.1% formic acid additive) revealed the presence of a main peak that was characterized as the expected COUPY-octreotide conjugate **12** (*R*_t = 15.6 min). The solution was lyophilized, and the conjugate was purified by semipreparative RP-HPLC (gradient from 45–100% B in 30 min; A, 0.1% TFA in H₂O; B, 0.1% TFA in ACN; flow rate, 3 mL/min; *R*_t = 6 min). Overall yield (synthesis + purification): 2.35 mg of a purple solid (from 27 mg of resin **11**), 12%. HRMS (ESI-TOF) (*m/z*): [M]⁺ Calcd for C₇₈H₉₉N₁₄O₁₅S₂, 1535.6850; found, 1535.6844; (*m/z*): [M + H]²⁺ Calcd for C₇₈H₁₀₀N₁₄O₁₅S₂, 768.3462; found, 768.3469. Analytical RP-HPLC (10–70% B in 30 min; A, 0.1% formic acid in H₂O; B, 0.1% formic acid in ACN; *R*_t = 15.6 min).

Synthesis and Characterization of COUPY-octreotide Conjugates 15 and 16. Alkynyl-PEG-*D*-Phe-Cys(*Trt*)-Phe-*D*-Trp-(*Boc*)-Lys(*Boc*)-Thr(*tBu*)-Cys(*Trt*)-Thr(*ol*)-Resin (**13**). After removal of the Fmoc protecting group from the peptide-bound resin **11** with 20% piperidine in DMF (2 × 10 min), 4-pentynoic acid (5 mol equiv) was coupled by using DIPC (5 mol equiv) and HOAt (5 mol equiv) in anhydrous DMF for 2 h. Cleavage and deprotection of an aliquot of the resulting octreotide-bound resin **13** were performed by treatment with TFA/H₂O/EDT/TIS 94:2.5:2.5:1 for 2.5 h. After evaporation of TFA by bubbling with N₂, the crude peptide was precipitated with cold diethyl ether. As shown in Figure S9, reversed-phase HPLC-MS analysis showed the presence of two peaks that were characterized as the linear alkynyl-octreotide (*R*_t = 15.2 min) and the corresponding disulfide cyclized alkynyl-octreotide (*R*_t = 14.8 min). Linear alkynyl-octreotide: LR-ESI MS, positive mode (*m/z*): 1246.54 (calcd mass for C₆₀H₈₄N₁₁O₁₄S₂ [M + H]⁺: 1246.56). Analytical HPLC (10–70% B in 30 min, 0.1% formic acid additive): *R*_t = 15.2 min. Disulfide cyclized alkynyl-octreotide: LR-ESI MS, positive mode (*m/z*): 1244.71 (calcd mass for C₆₀H₈₂N₁₁O₁₄S₂ [M + H]⁺: 1244.55). Analytical HPLC (10–70% B in 30 min, 0.1% formic acid additive): *R*_t = 14.7 min.

Azido-PEG-*D*-Phe-Cys(*Trt*)-Phe-*D*-Trp(*Boc*)-Lys(*Boc*)-Thr(*tBu*)-Cys(*Trt*)-Thr(*ol*)-Resin (**14**). After removal of the Fmoc protecting group from the peptide-bound resin **11** with 20% piperidine in DMF (2 × 10 min), 2-azidoacetic acid (5 mol equiv) was coupled by using DIPC (5 mol equiv) and HOAt (5 mol equiv) in anhydrous DMF for 2 h. Cleavage and deprotection of an aliquot of the resulting octreotide-bound resin **14** was performed by treatment with TFA/H₂O/EDT/TIS 94:2.5:2.5:1 for 2.5 h. After evaporation of TFA by bubbling with N₂, the crude peptide was precipitated with cold diethyl ether. As shown in Figure S10, reversed-phase HPLC-MS analysis showed the presence of two peaks that were characterized as the linear azido-octreotide (*R*_t = 15.2 min) and the corresponding disulfide cyclized azido-octreotide (*R*_t = 14.7 min). Linear azido-octreotide: LR-ESI MS, positive mode (*m/z*): 1249.50 (calcd mass for C₅₇H₈₁N₁₄O₄S₂ [M + H]⁺: 1249.55). Analytical HPLC (10–70% B in 30 min, 0.1% formic acid additive): *R*_t = 15.2 min. Disulfide cyclized azido-octreotide: LR-ESI MS, positive mode (*m/z*): 1247.48 (calcd mass for C₅₇H₇₉N₁₄O₄S₂ [M + H]⁺: 1247.53). Analytical HPLC (10–70% B in 30 min, 0.1% formic acid additive): *R*_t = 14.7 min.

COUPY-octreotide Conjugate (15). Five milligrams of alkynyl-peptide-bound resin **13** was transferred to a 2 mL reaction vial equipped with a magnetic stirrer. Afterward, a solution of azido-coumarin **5** (4.2 mg, 3 mol equiv), CuSO₄ (1.2 mg, 3 mol equiv), and sodium ascorbate (1.5 mg, 3 mol equiv) in 800 μL of DMF/H₂O 20:1 (v/v) was immediately added to the vial. The suspension was allowed to stir at room temperature for 1 h, 4 h, or overnight under an argon atmosphere in the dark. Then, the resin was filtered off and washed with DMF, DCM, and MeOH (5,5,5 × 4 mL). Cleavage,

deprotection, and cyclization were carried out as described above for conjugate **12**. As shown in Figure S9, analytical reversed-phase HPLC-MS analysis (10–70% B in 30 min, 0.1% formic acid additive) revealed the presence of a main peak in the three cases that were characterized as the expected COUPY-octreotide conjugate **15** (*R*_t = 15.4 min). The solution was lyophilized, and the conjugate was purified by semipreparative RP-HPLC (gradient from 45–100% B in 30 min; A, 0.1% TFA in H₂O; B, 0.1% TFA in ACN; flow rate, 3 mL/min; *R*_t = 6.5 min). Overall yield (synthesis + purification): 5.23 mg of a purple solid (from 15 mg of resin **13**), 32%. HRMS (ESI-TOF) (*m/z*): [M]⁺ Calcd for C₈₆H₁₁₁N₁₈O₁₆S₂, 1715.7861; found, 1715.7912. (*m/z*): [M + H]²⁺ Calcd for C₈₆H₁₁₂N₁₈O₁₆S₂, 858.3970; found, 858.3973. Analytical RP-HPLC (10–70% B in 30 min; A, 0.1% formic acid in H₂O; B, 0.1% formic acid in ACN): *R*_t = 15.4 min.

COUPY-octreotide Conjugate (16). Five milligrams of azido-peptide-bound resin **14** was transferred to a 2 mL reaction vial equipped with a magnetic stirrer. Afterward, a solution of alkynyl-coumarin **6** (3.8 mg, 3 mol equiv), CuSO₄ (1.2 mg, 3 mol equiv), and sodium ascorbate (1.5 mg, 3 mol equiv) in 800 μL DMF/H₂O 20:1 (v/v) was immediately added to the vial. The suspension was allowed to stir at room temperature for 1 h, 4 h, or overnight under an argon atmosphere in the dark. Then, the resin was filtered off and washed with DMF, DCM, and MeOH (5,5,5 × 4 mL). Cleavage, deprotection, and cyclization were carried out as described above for conjugate **12**. As shown in Figure S11, analytical reversed-phase HPLC-MS analysis (10–70% B in 30 min, 0.1% formic acid additive) revealed the presence of a main peak in the three cases that were characterized as the expected COUPY-octreotide conjugate **16** (*R*_t = 15.3 min). The solution was lyophilized, and the conjugate was purified by semipreparative RP-HPLC (gradient from 45–100% B in 30 min; A, 0.1% TFA in H₂O; B, 0.1% TFA in ACN; flow rate, 3 mL/min; *R*_t = 6.5 min). Overall yield (synthesis + purification): 5.23 mg of a purple solid (from 20 mg of resin **14**), 13%. HRMS (ESI-TOF) (*m/z*): [M]⁺ Calcd for C₈₃H₁₀₅N₁₈O₁₆S₂, 1673.7392; found, 1673.7388. (*m/z*): [M + H]²⁺ Calcd for C₈₃H₁₀₆N₁₈O₁₆S₂, 837.3750; found, 837.3735. Analytical RP-HPLC (10–70% B in 30 min; A, 0.1% formic acid in H₂O; B, 0.1% formic acid in ACN): *R*_t = 15.3 min.

Synthesis and Characterization of Atto-Rho12-octreotide Conjugate (17). Octreotide acetate (Bachem; 1 mg, 0.98 μmol) was allowed to react with Atto Rho12-hexanoic acid *N*-hydroxysuccinimide ester (ATTO Tech; 1 mg, 1.18 μmol) in an aqueous hydrogen carbonate buffer (100 mM, pH 7.5) for 3 h and protected from light. The solution was lyophilized, and Atto-Rho12-octreotide conjugate (**17**) was purified by analytical RP-HPLC (gradient from 30–100% in 30 min; A, 0.1% formic acid in H₂O; B, 0.1% formic acid in ACN; flow rate, 1 mL/min, *R*_t = 16.7 min). Overall yield (synthesis + purification): 0.4 mg of a pink solid, 25%. Characterization: LR ESI MS, positive mode (*m/z*): 1651.65 (calcd mass for C₉₀H₁₁₆N₁₃O₁₃S₂⁺: 1650.82).

Photophysical Characterization of the Compounds. Absorption spectra were recorded in a Varian Cary 500 UV/vis/NIR spectrophotometer at room temperature. Molar absorption coefficients (ϵ) were determined by direct application of the Beer–Lambert law, using solutions of the compounds in each solvent with concentrations ranging from 10^{−6} to 10^{−5} M. Emission spectra were registered in a Photon Technology International (PTI) fluorimeter. Fluorescence quantum yields (Φ_F) were measured by a comparative method using cresyl violet in ethanol (CV; $\Phi_{F,ref} = 0.54 \pm 0.03$) as the reference.¹⁷ Then, optically matched solutions of the compounds and CV were excited, and the fluorescence spectra were recorded. The absorbance of the sample and reference solutions was set below 0.1 at the excitation wavelength, and Φ_F were calculated using the following eq 1:

$$\Phi_{F,Sample} = \frac{Area_{Sample}}{Area_{Ref}} \left(\frac{\eta_{Sample}}{\eta_{Ref}} \right)^2 \Phi_{F,ref} \quad (1)$$

where $\text{Area}_{\text{sample}}$ and Area_{ref} are the integrated fluorescence for the sample and the reference, and η_{sample} and η_{ref} are the refractive index of sample and reference solutions, respectively. The uncertainty in the experimental value of Φ_{F} has been estimated to be approximately 10%.

Photostability studies were performed by monitoring fluorescence bleaching of a 5 μM aqueous solution (PBS buffer) of the compounds irradiated with a high power LED of 505 nm (100 mW/cm²).

Cell Culture and Treatments. HeLa Cells were maintained in DMEM (Dulbecco modified eagle medium) containing low glucose (1 g/L) and supplemented with 10% fetal calf serum (FCS), 50 U/mL of penicillin–streptomycin, and 2 mM L-glutamine. For cellular uptake experiments and posterior observation under the microscope, cells were seeded on glass bottom dishes (P35G-1.5–14-C, Mattek). Then, 24 h after cell seeding, cells were incubated for 30 min or 1 h at 37 °C with coumarin 3 (0.5 μM), COUPY-octreotide 12 (10 μM), Atto Rho12-octreotide 17 (10 μM), or fluorescein-octreotide 18 (50 μM) in supplemented DMEM. Then, cells were washed three times with DPBS (Dulbecco's phosphate-buffered saline) to remove the excess of the compounds and kept in low glucose DMEM without phenol red for fluorescence imaging.

Fluorescence Imaging. All microscopy observations were performed using a Zeiss LSM 880 confocal microscope equipped with a 405 nm laser diode, an argon-ion laser, a 561 nm laser, and a 633 nm laser. The microscope was also equipped with a full enclosure imaging chamber (XLmulti S1, Pecon) connected to a 37 °C heater and a 5% CO₂ providing system. Cells were observed using a 63× 1.2 multi immersion objective. Compounds 3, 12, and 17 were excited using the 561 nm laser and detected from 570 to 670 nm. Compound 18 was observed using the 488 nm laser line of the argon-ion laser. Image analysis was performed using Fiji.¹⁸ Unless otherwise stated, images are colorized using the Fire lookup table.

■ ASSOCIATED CONTENT

📄 Supporting Information

The Supporting Information is available free of charge on the ACS Publications website at DOI: 10.1021/acs.joc.8b02624.

Copies of HPLC traces and UV–vis absorption and fluorescence emission spectra of the compounds; additional fluorescence imaging studies; 1D NMR (¹H, ¹³C), MS, and selected 2D NMR spectra (PDF)

■ AUTHOR INFORMATION

Corresponding Author

*E-mail: vmarchan@ub.edu.

ORCID

Vicente Marchán: 0000-0002-1905-2156

Author Contributions

¹A.R. and A. Gandioso contributed equally to this work.

Notes

The authors declare no competing financial interest.

■ ACKNOWLEDGMENTS

This work was supported by funds from the Spanish Ministerio de Economía y Competitividad (grants CTQ2014-52658-R and CTQ2017-84779-R). The authors acknowledge helpful assistance of Dr. Francisco Cárdenas (NMR) and Dr. Irene Fernández and Laura Ortiz (MS) from CCIUB. A.G. was a recipient fellow of the University of Barcelona.

■ REFERENCES

(1) (a) Srinivasarao, M.; Galliford, C. V.; Low, P. S. Principles in the design of ligand-targeted cancer therapeutics and imaging agents. *Nat. Rev. Drug Discovery* **2015**, *14*, 203–219. (b) Zhang, R. R.; Schroeder, A. B.; Grudzinski, J. J.; Rosenthal, E. L.; Warram, J. M.; Pinchuk, A.

N.; Eliceiri, K. W.; Kuo, J. S.; Weichert, J. P. Beyond the margins: real-time detection of cancer using targeted fluorophores. *Nat. Rev. Clin. Oncol.* **2017**, *14*, 347–364.

(2) (a) Owens, E. A.; Henary, M.; El Fakhri, G.; Choi, H. S. Tissue-Specific Near-Infrared Fluorescence Imaging. *Acc. Chem. Res.* **2016**, *49*, 1731–1740. (b) Guo, Z.; Park, S.; Yoon, J.; Shin, I. Recent progress in the development of near-infrared fluorescent probes for bioimaging applications. *Chem. Soc. Rev.* **2014**, *43*, 16–29. (c) Haque, A.; Faizi, M. S. H.; Rather, J. A.; Khan, M. S. Next generation NIR fluorophores for tumor imaging and fluorescence-guided surgery: A review. *Bioorg. Med. Chem.* **2017**, *25*, 2017–2034.

(3) Gao, M.; Yu, F.; Lv, C.; Choo, J.; Chen, L. Fluorescent chemical probes for accurate tumor diagnosis and targeting therapy. *Chem. Soc. Rev.* **2017**, *46*, 2237–2271.

(4) (a) Birch, D.; Christensen, M. V.; Staerk, D.; Franzyk, H.; Nielsen, H. M. Fluorophore labeling of a cell-penetrating peptide induces differential effects on its cellular distribution and affects cell viability. *Biochim. Biophys. Acta, Biomembr.* **2017**, *1859*, 2483–2494. (b) Zhao, C.; Fernandez, A.; Avlonitis, N.; Vande Velde, G.; Bradley, M.; Read, N. D.; Vendrell, M. Searching for the Optimal Fluorophore to Label Antimicrobial Peptides. *ACS Comb. Sci.* **2016**, *18*, 689–696.

(5) (a) Sato, K.; Gorka, A. P.; Nagaya, T.; Michie, M. S.; Nakamura, Y.; Nani, R. R.; Coble, V. L.; Vasalatiy, O. V.; Swenson, R. E.; Choyke, P. L.; Schnermann, M. J.; Kobayashi, H. Effect of charge localization on the in vivo optical imaging properties of near-infrared cyanine dye/monoclonal antibody conjugates. *Mol. BioSyst.* **2016**, *12*, 3046–3056. (b) Zhao, N.; Williams, T. M.; Zhou, Z.; Fronczek, F. R.; Sibirian-Vazquez, M.; Jois, S. D.; Vicente, M. G. H. Synthesis of BODIPY-Peptide Conjugates for Fluorescence Labeling of EGFR Over-expressing Cells. *Bioconjugate Chem.* **2017**, *28*, 1566–1579.

(6) (a) Gandioso, A.; Bresolí-Obach, R.; Nin-Hill, A.; Bosch, M.; Palau, M.; Galindo, A.; Contreras, S.; Rovira, A.; Rovira, C.; Nonell, S.; Marchán, V. Redesigning the Coumarin Scaffold into Small Bright Fluorophores with Far-Red to Near-Infrared Emission and Large Stokes Shifts Useful for Cell Imaging. *J. Org. Chem.* **2018**, *83*, 1185–1195. (b) Gandioso, A.; Palau, M.; Bresolí-Obach, R.; Galindo, A.; Rovira, A.; Bosch, M.; Nonell, S.; Marchán, V. High Photostability in Nonconventional Coumarins with Far-Red/NIR Emission through Azetidyl Substitution. *J. Org. Chem.* **2018**, *83*, 11519–11531.

(7) (a) Shank, N. I.; Pham, H. H.; Waggoner, A. S.; Armitage, B. A. Twisted Cyanines: A Non-Planar Fluorogenic Dye with Superior Photostability and its Use in a Protein-Based Fluoromodule. *J. Am. Chem. Soc.* **2013**, *135*, 242–251. (b) Bohlaender, P. R.; Wagenknecht, H.-A. Synthesis of a Photostable Energy-Transfer Pair for "DNA Traffic Lights". *Eur. J. Org. Chem.* **2014**, *2014* (34), 7547–7551.

(8) Pickens, C. J.; Johnson, S. N.; Pressnall, M. M.; Leon, M. A.; Berkland, C. J. Practical Considerations, Challenges, and Limitations of Bioconjugation via Azide-Alkyne Cycloaddition. *Bioconjugate Chem.* **2018**, *29*, 686–701.

(9) (a) Mezo, G.; Manea, M. Receptor-mediated tumor targeting based on peptide hormones. *Expert Opin. Drug Delivery* **2010**, *7*, 79–96. (b) Janecka, A.; Zubrzycka, M.; Janecki, T. Somatostatin analogs. *J. Pept. Res.* **2001**, *58*, 91–107. (c) Reubi, J. C. Peptide receptors as molecular targets for cancer diagnosis and therapy. *Endocr. Rev.* **2003**, *24*, 389–427.

(10) (a) Sun, L.-C.; Coy, D. H. Cytotoxic conjugates of peptide hormones for cancer chemotherapy. *Drugs Future* **2008**, *33*, 217–223. (b) Barragán, F.; Carrion-Salip, D.; Gómez-Pinto, I.; González-Cantó, C.; Sadler, P. J.; de Llorens, R.; Moreno, V.; González, C.; Massaguer, A.; Marchán, V. Somatostatin Subtype-2 Receptor-Targeted Metal-Based Anticancer Complexes. *Bioconjugate Chem.* **2012**, *23*, 1838–1855. (c) Barragán, F.; Moreno, V.; Marchán, V. Solid-phase synthesis and DNA binding studies of dichloroplatinum(II) conjugates of dicarba analogues of octreotide as new anticancer drugs. *Chem. Commun.* **2009**, 4705–4707.

(11) Novohradsky, V.; Zamora, A.; Gandioso, A.; Brabec, V.; Ruiz, J.; Marchán, V. Somatostatin receptor-targeted organometallic iridium(III) complexes as novel theranostic agents. *Chem. Commun.* **2017**, *53*, 5523–5526.

(12) (a) Gandioso, A.; Palau, M.; Nin-Hill, A.; Melnyk, I.; Rovira, C.; Nonell, S.; Velasco, D.; García-Amorós, J.; Marchán, V. Sequential Uncaging with Green Light can be Achieved by Fine-Tuning the Structure of a Dicyanocoumarin Chromophore. *ChemistryOpen* **2017**, *6*, 375–384. (b) Gandioso, A.; Contreras, S.; Melnyk, I.; Oliva, J.; Nonell, S.; Velasco, D.; García-Amorós, J.; Marchán, V. Development of Green/Red-Absorbing Chromophores Based on a Coumarin Scaffold That Are Useful as Caging Groups. *J. Org. Chem.* **2017**, *82*, 5398–5408.

(13) (a) Castro, V.; Rodríguez, H.; Albericio, F. CuAAC: An Efficient Click Chemistry Reaction on Solid Phase. *ACS Comb. Sci.* **2016**, *18*, 1–14. (b) Song, X.; Wang, C.; Han, Z.; Xu, Y.; Xiao, Y. Terminal alkyne substituted O6-benzylguanine for versatile and effective syntheses of fluorescent labels to genetically encoded SNAP-tags. *RSC Adv.* **2015**, *5*, 23646–23649. (c) Yang, F.; Wang, C.; Wang, L.; Ye, Z.-W.; Song, X.-B.; Xiao, Y. Hoechst-naphthalimide dyad with dual emissions as specific and ratiometric sensor for nucleus DNA damage. *Chin. Chem. Lett.* **2017**, *28*, 2019–2022. (d) Wang, C.; Song, X.; Han, Z.; Li, X.; Xu, Y.; Xiao, Y. Monitoring Nitric Oxide in Subcellular Compartments by Hybrid Probe Based on Rhodamine Spirolactam and SNAP-tag. *ACS Chem. Biol.* **2016**, *11*, 2033–2040.

(14) Hsieh, H.-P.; Wu, Y.-T.; Chen, S.-T.; Wang, K.-T. Direct solid-phase synthesis of octreotide conjugates: precursors for use as tumor-targeted radiopharmaceuticals. *Bioorg. Med. Chem.* **1999**, *7*, 1797–1803.

(15) Sneddon, D.; Niemans, R.; Bauwens, M.; Yaromina, A.; van Kuijk, S. J. A.; Lieuwes, N. G.; Biemans, R.; Pooters, I.; Pellegrini, P. A.; Lengkeek, N. A.; Greguric, I.; Tonissen, K. F.; Supuran, C. T.; Lambin, P.; Dubois, L.; Poulsen, S.-A. Synthesis and in vivo biological evaluation of ⁶⁸Ga-labeled carbonic anhydrase IX targeting small molecules for positron emission tomography. *J. Med. Chem.* **2016**, *59*, 6431–6443.

(16) Goswami, L. N.; Cai, Q.; Ma, L.; Jalisatgi, S. S.; Hawthorne, M. F. Synthesis, relaxation properties and in vivo assessment of a carborane-GdDOTA-monoamide conjugate as an MRI blood pool contrast agent. *Org. Biomol. Chem.* **2015**, *13*, 8912–8918.

(17) Magde, D.; Brannon, J. H.; Cremers, T. L.; Olmsted, J. Absolute luminescence yield of cresyl violet. A standard for the red. *J. Phys. Chem.* **1979**, *83*, 696–699.

(18) Schindelin, J.; Arganda-Carreras, I.; Frise, E.; Kaynig, V.; Longair, M.; Pietzsch, T.; Preibisch, S.; Rueden, C.; Saalfeld, S.; Schmid, B.; Tinevez, J. Y.; White, D. J.; Hartenstein, V.; Eliceiri, K.; Tomancak, P.; Cardona, A. Fiji: an open-source platform for biological-image analysis. *Nat. Methods* **2012**, *9*, 676–682.

SUPPORTING INFORMATION

Solid-phase approaches for labelling targeting peptides with far-red emitting coumarin fluorophores

Anna Rovira,^{†,§} Albert Gandioso,^{†,§} Marina Goñalons,[†] Alex Galindo,[†] Anna Massaguer,[‡] Manel Bosch,[⊥] Vicente Marchán^{*,†}

[†]Departament de Química Inorgànica i Orgànica, Secció de Química Orgànica, IBUB, Universitat de Barcelona, Martí i Franquès 1-11, E-08028 Barcelona (Spain).

E-mail: vmarchan@ub.edu

[‡]Departament de Biologia, Universitat de Girona, E-17071 Girona (Spain).

[⊥]Unitat de Microscòpia Òptica Avançada, Centres Científics i Tecnològics, Universitat de Barcelona, E-08028 Barcelona (Spain)

[§]These authors contributed equally to this work.

Table of contents

1.- Reversed-phase HPLC analysis of coumarin derivatives 4-6 and 8	S3
2- 2D NMR characterization of coumarin derivatives	S4
3.- Synthesis and characterization of COUPY-octreotide conjugate 12	S7
4. Synthesis and characterization of COUPY-octreotide conjugates 15 and 16	
4.1. Octreotide-bound resins 13 and 14	S10
4.2. COUPY-octreotide conjugate 15	S11
4.3. COUPY-octreotide conjugate 16	S13
5.- Photophysical characterization of the compounds	S15
6.- Synthesis and characterization of Atto-Rho12-octreotide conjugate (17).	S17
7.- Fluorescence imaging.	S18
8.- ¹ H and ¹³ C NMR spectra and HR ESI-MS of the compounds	S19

1.- Reversed-phase HPLC analysis of coumarin derivatives 4-6 and 8

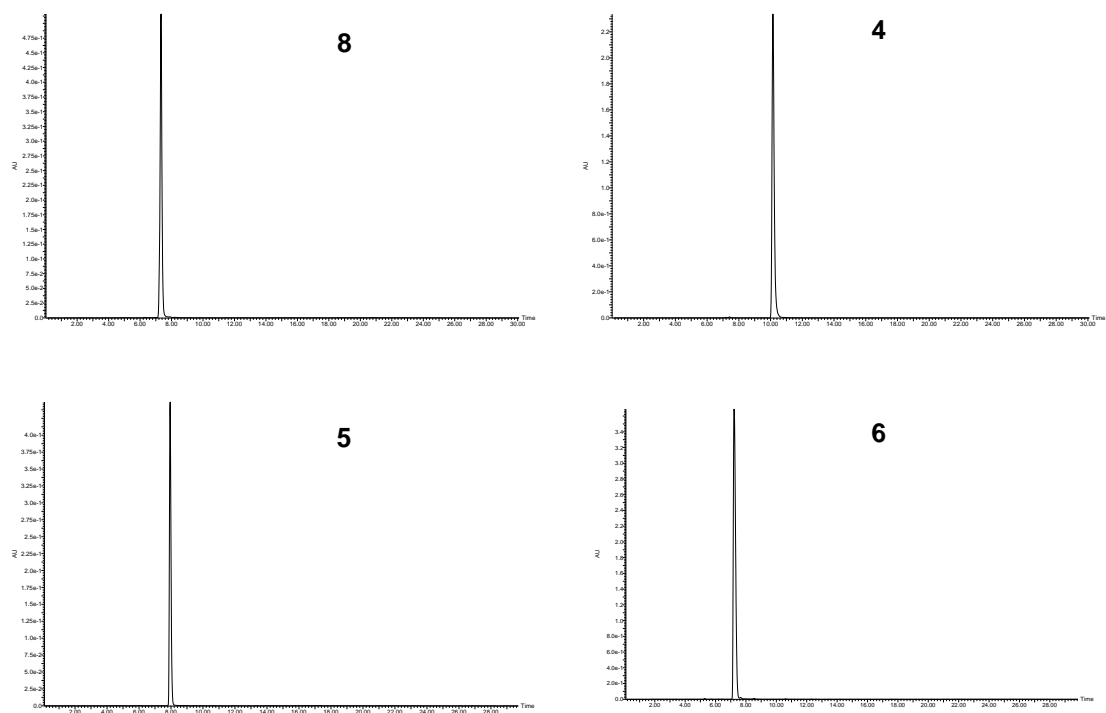


Figure S1. Reversed-phase HPLC traces of coumarins 4-6 and 8.

2.- 2D NMR characterization of coumarin derivatives

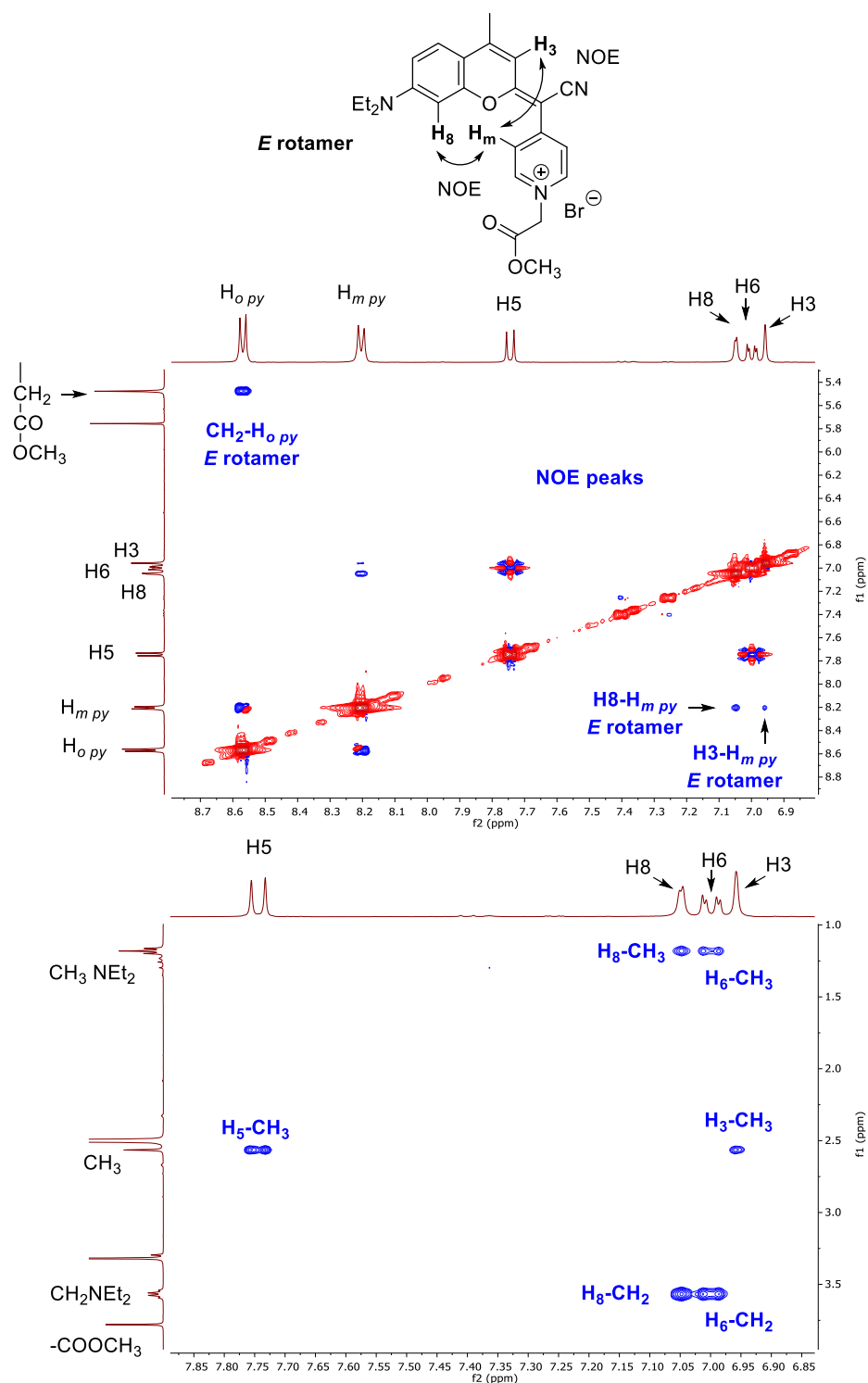


Figure S2. Structure of *E* rotamer of coumarin **8** with some diagnostic NOE cross-peaks indicated, and expansions of the NOESY spectrum ($t_m = 500$ ms) of **8** in DMSO- d_6 at 298 K.

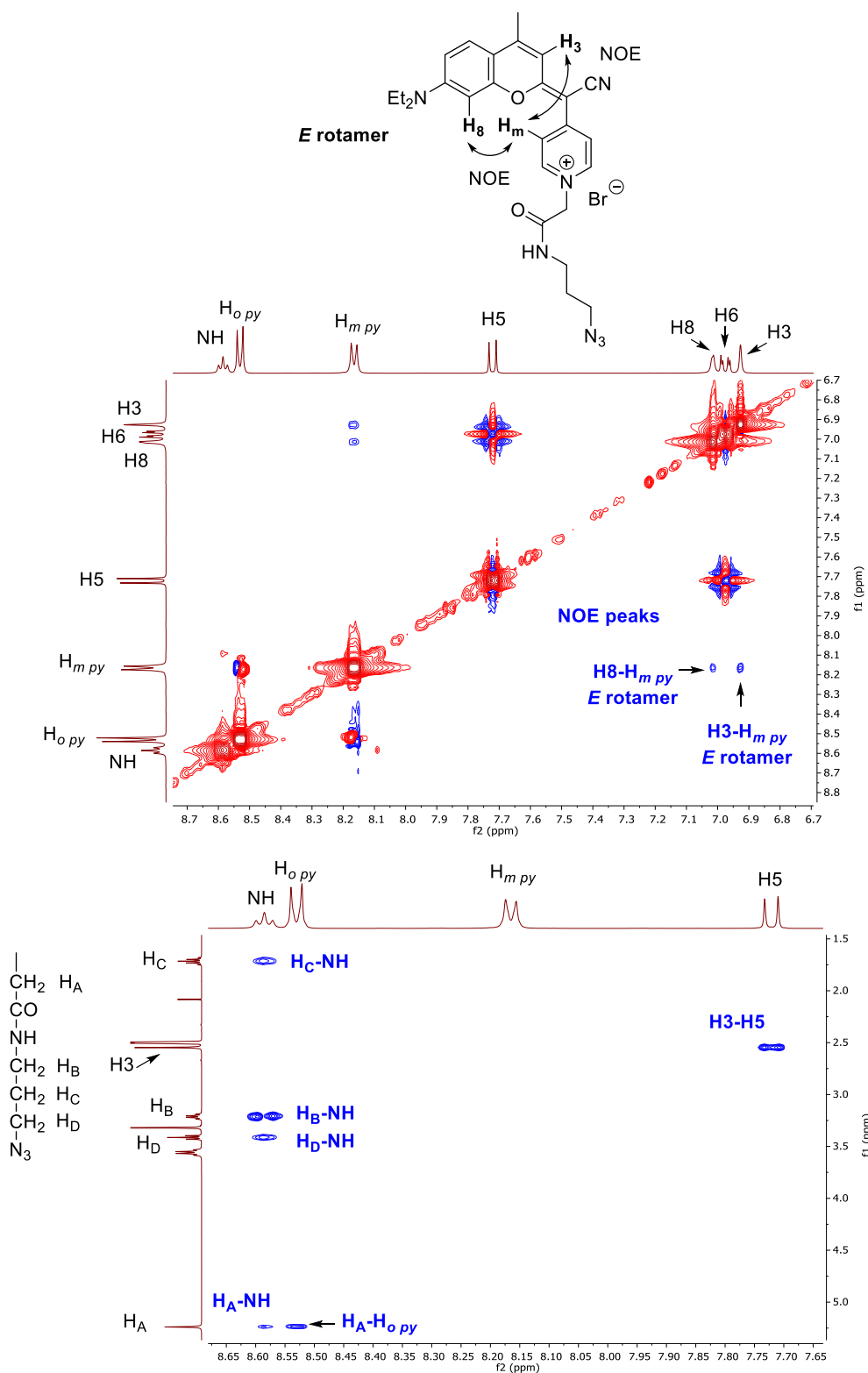


Figure S3. Structure of *E* rotamer of coumarin **5** with some diagnostic NOE cross-peaks indicated, and expansions of the NOESY spectrum ($t_m = 500$ ms) of **5** in DMSO- d_6 at 298 K.

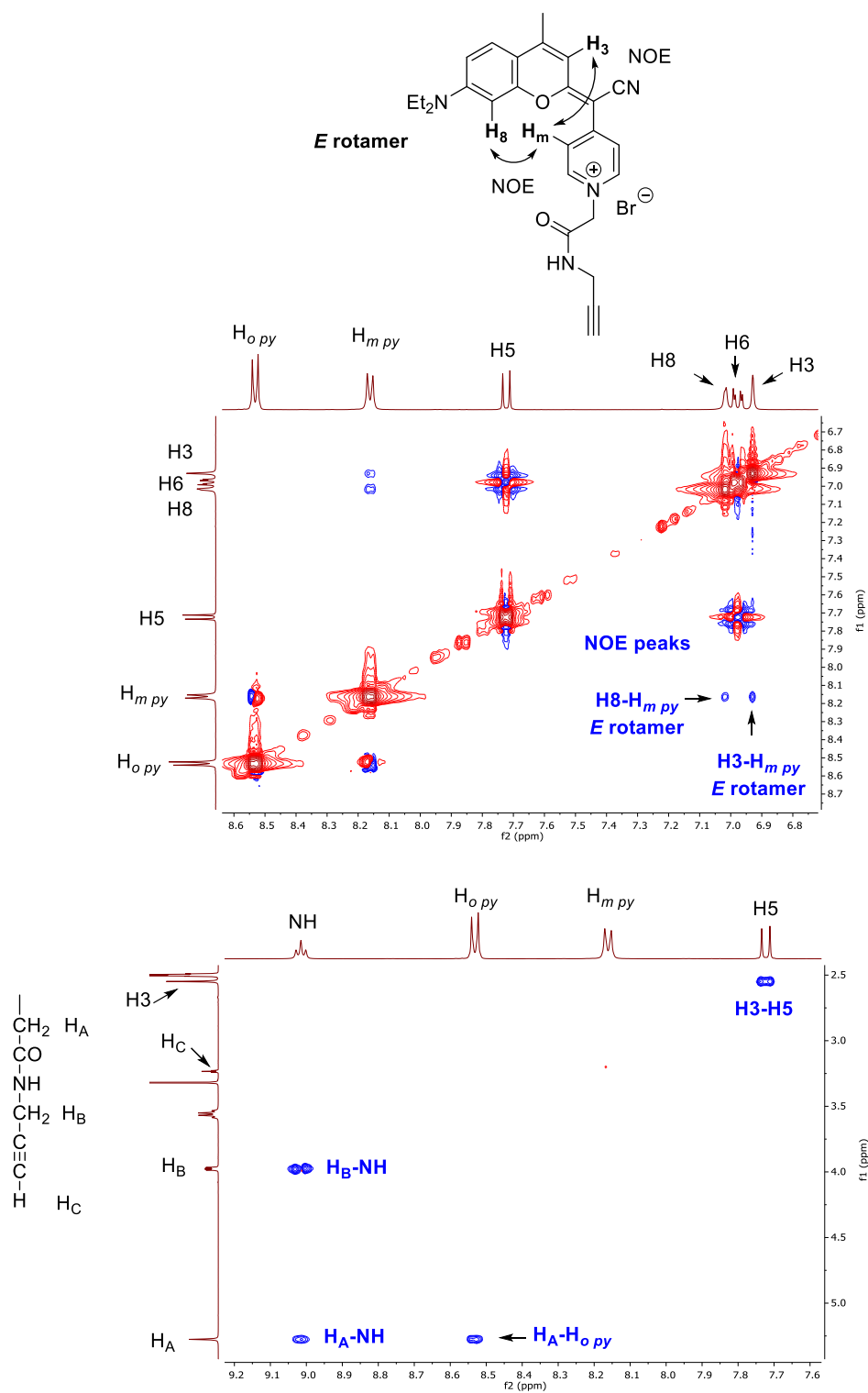


Figure S4. Structure of *E* rotamer of coumarin **6** with some diagnostic NOE cross-peaks indicated, and expansions of the NOESY spectrum ($t_m = 500$ ms) of **6** in DMSO-*d*₆ at 298 K.

3.- Synthesis and characterization of COUPY-octreotide conjugate **12**

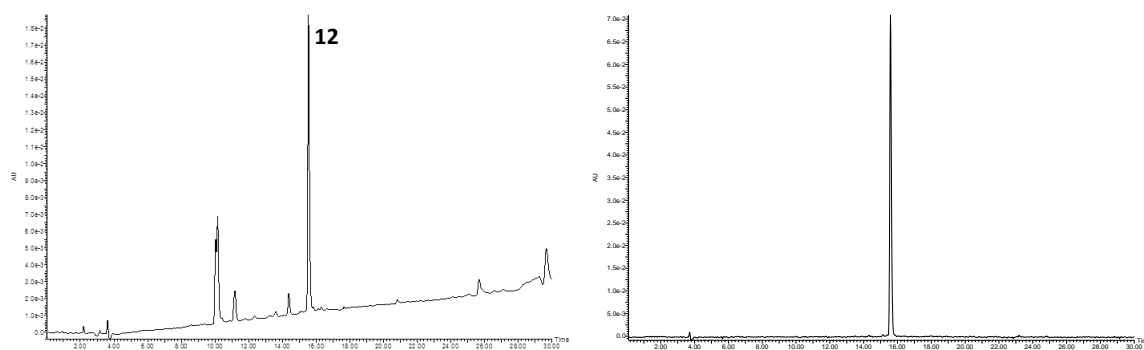
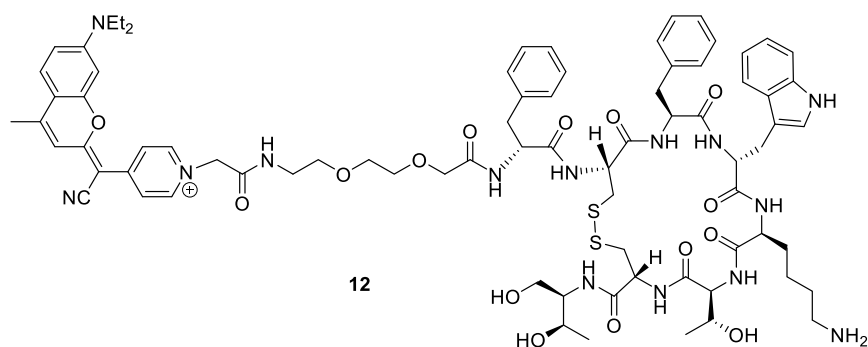


Figure S5. Reversed-phase HPLC traces for COUPY-octreotide conjugate **12**: reaction crude (left) and purified (right).

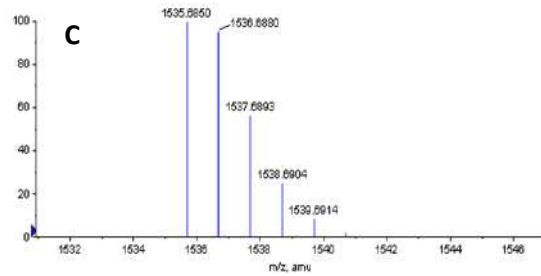
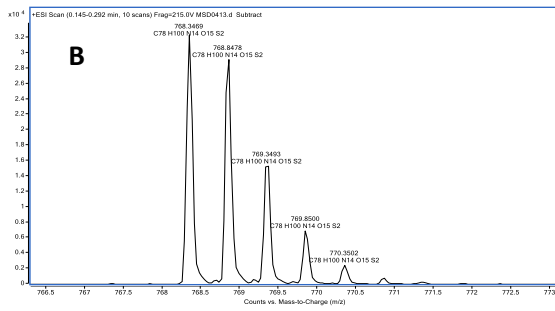
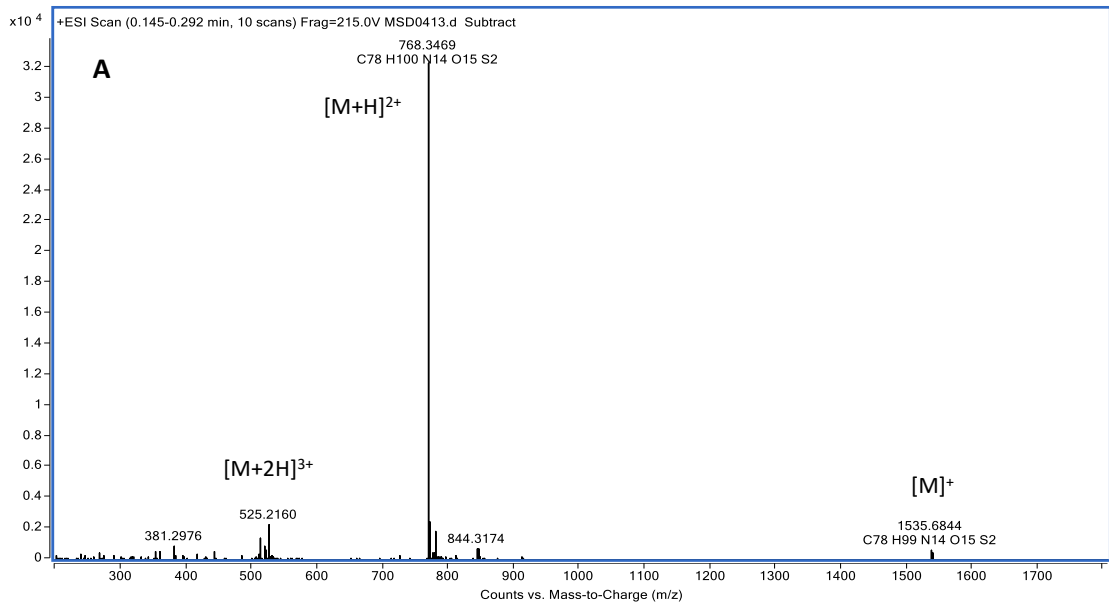


Figure S6. High resolution ESI MS of COUPY-octreotide conjugate **12**: experimental (A, B) and calculated (C).

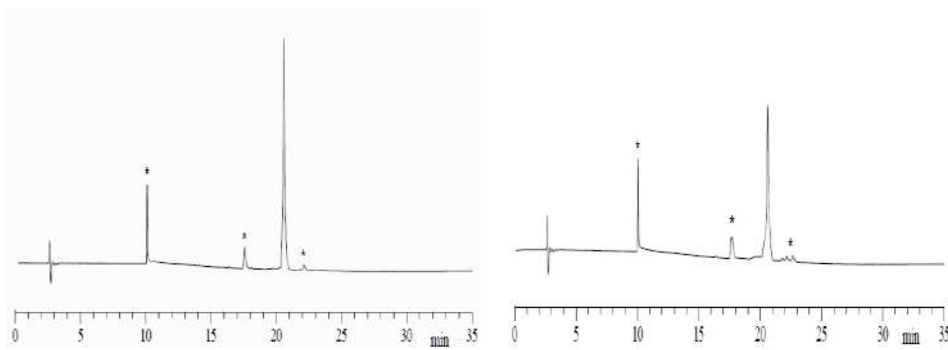


Figure S7. Reversed-phase HPLC traces for COUPY-octreotide conjugate **12** in DMEM-10% FBS at $t=0$ (left) and after incubation at 37 °C for 24 h (right). * peaks from the cell medium.

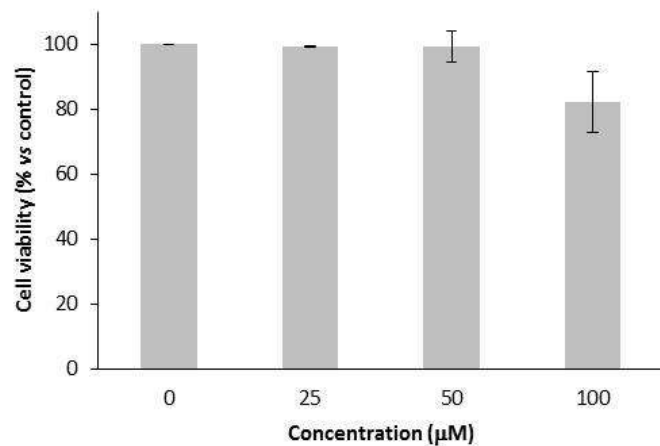


Figure S8. Effect of COUPY-octreotide conjugate **12** in the viability of HeLa cells. Cells were treated for 48 h with the indicated concentrations of the compound and the cell viability was determined by the MTT assay. Each point in the graphs represents the mean of three experiments \pm SD.

4. Synthesis and characterization of COUPY-octreotide conjugates **15** and **16**

4.1. Octreotide-bound resins **13** and **14**

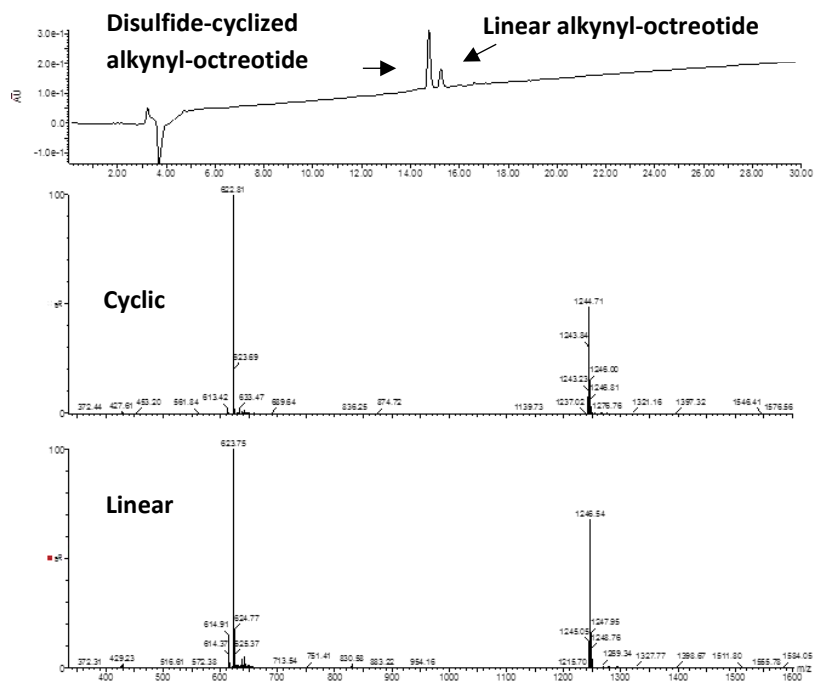


Figure S9. Reversed-phase HPLC-MS traces of the crude mixture after cleavage and deprotection of an aliquot of peptide-bound resin **13**, and ESI MS of the peaks.

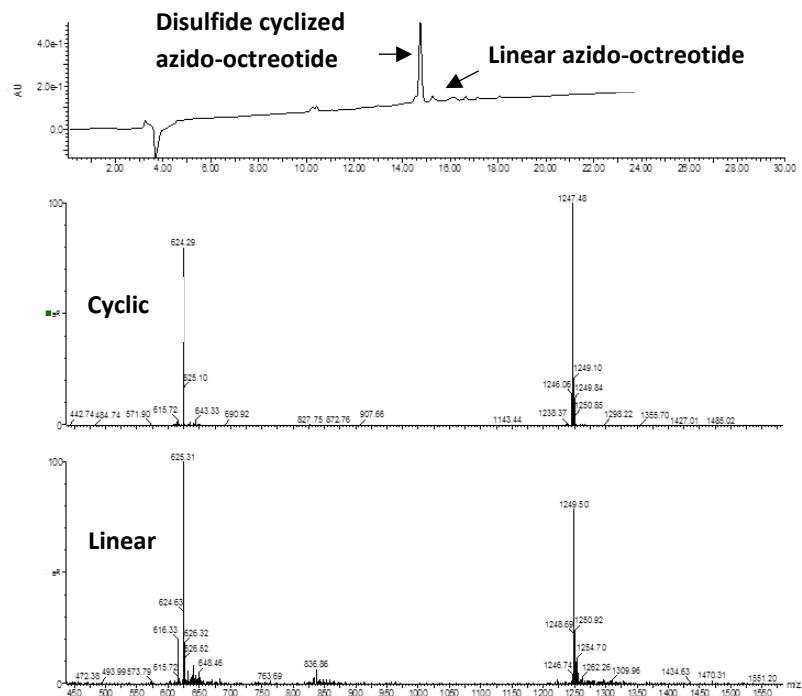


Figure S10. Reversed-phase HPLC-MS traces of the crude mixture after cleavage and deprotection of an aliquot of peptide-bound resin **14**, and ESI MS of the peaks.

4.2. COUPY-octreotide conjugate **15**

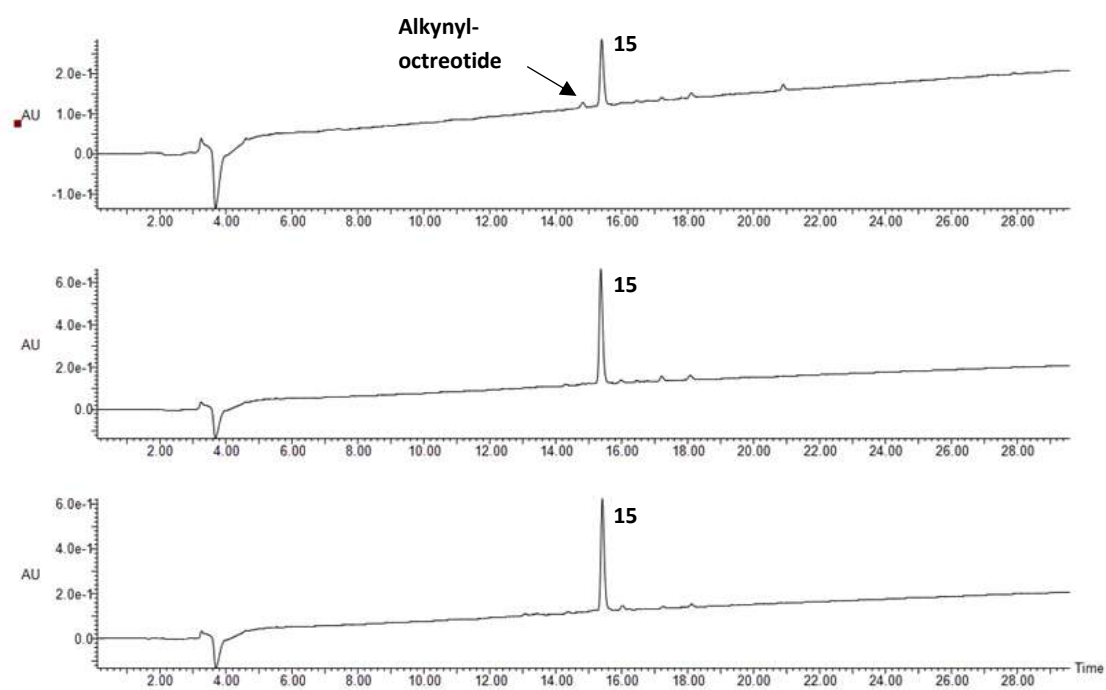
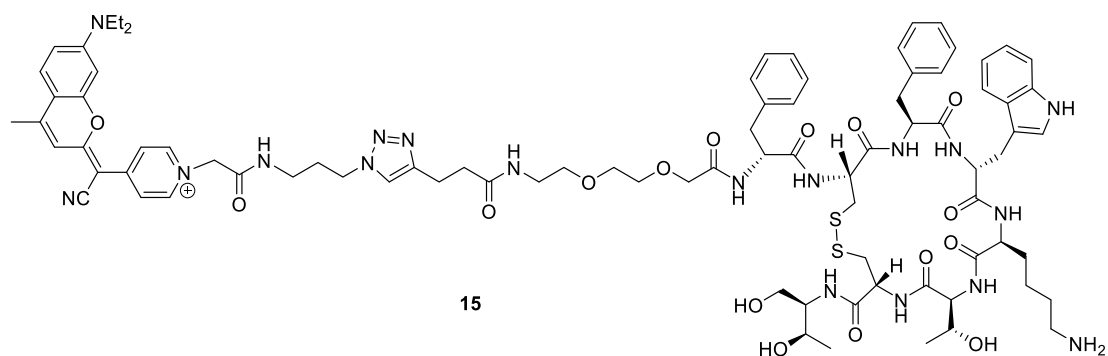


Figure S11. Reversed-phase HPLC traces for click chemistry studies between azido-coumarin **5** and alkynyl-peptide-bound resin **13**. From top to bottom: click chemistry crudes at different reaction times (1 h, 4 h or overnight) after cleavage, deprotection and cyclization.

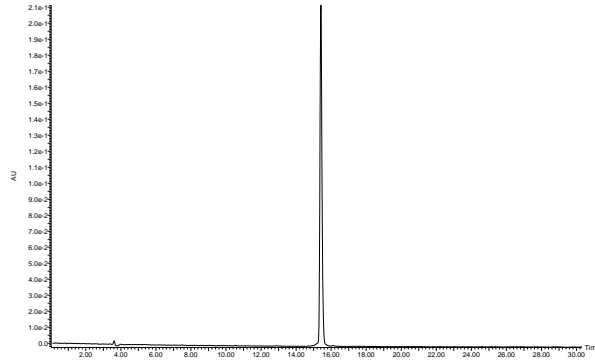


Figure S12. Reversed-phase HPLC analysis of purified COUPY-octreotide conjugate **15**.

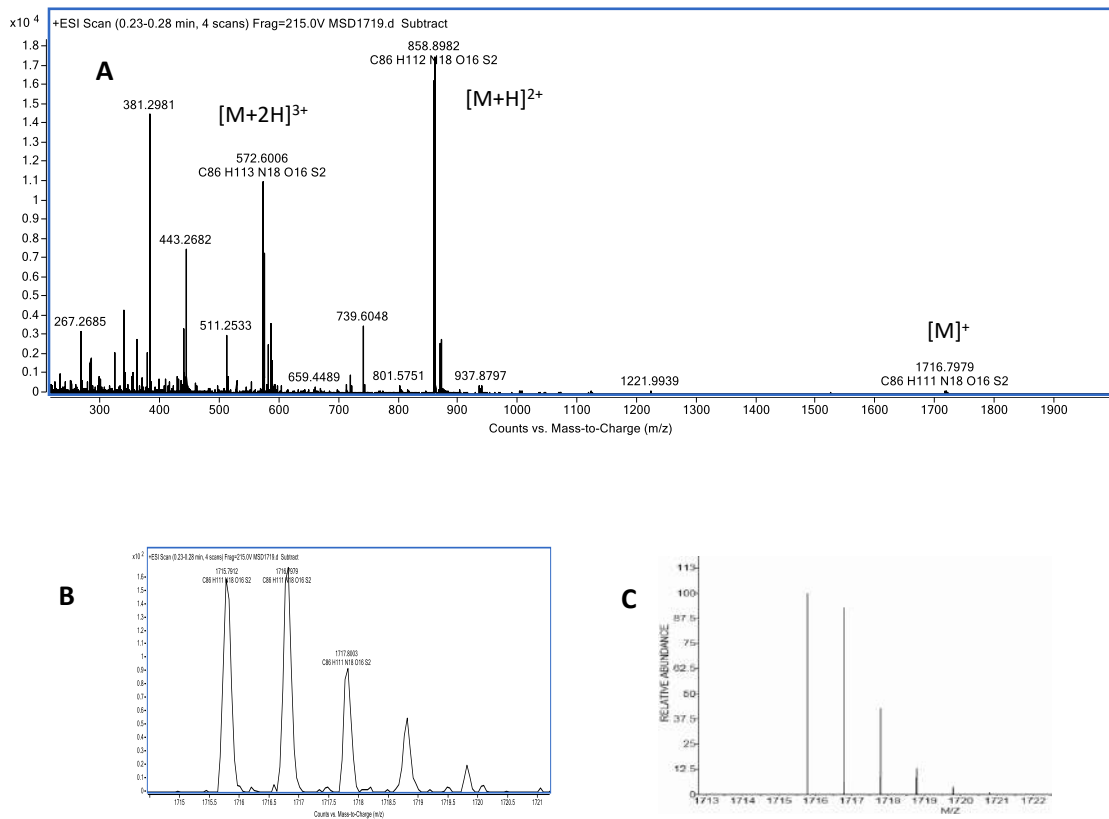


Figure S13. High resolution ESI MS of COUPY-octreotide conjugate **15**: experimental (A, B) and calculated (C).

4.3. COUPY-octreotide conjugate 16

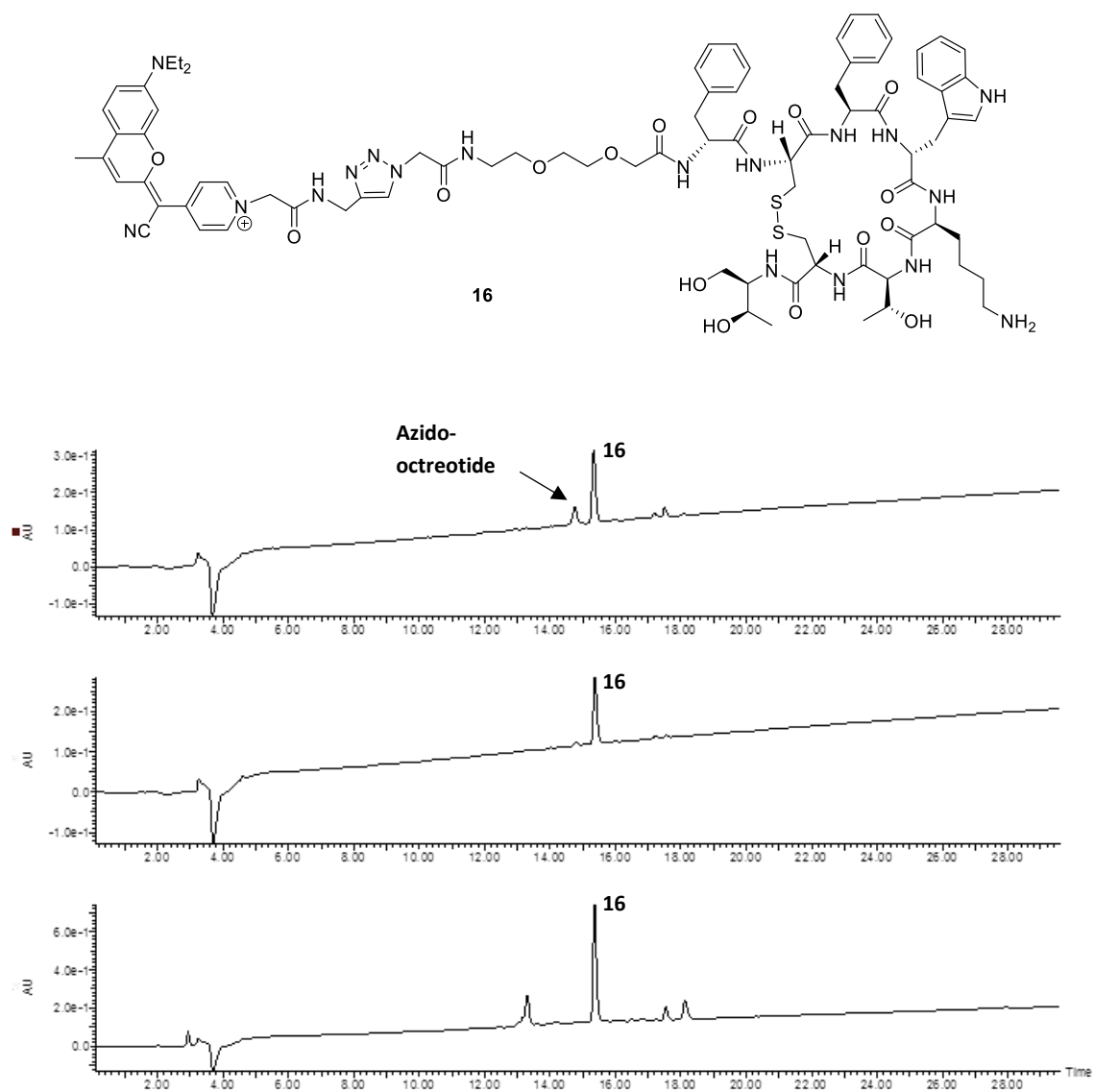


Figure S14. Reversed-phase HPLC traces for click chemistry studies between alkynyl-coumarin **6** and azide-peptide-bound resin **14**. From top to bottom: click chemistry crudes at different reaction times (1 h, 4 h or overnight) after cleavage, deprotection and cyclization.

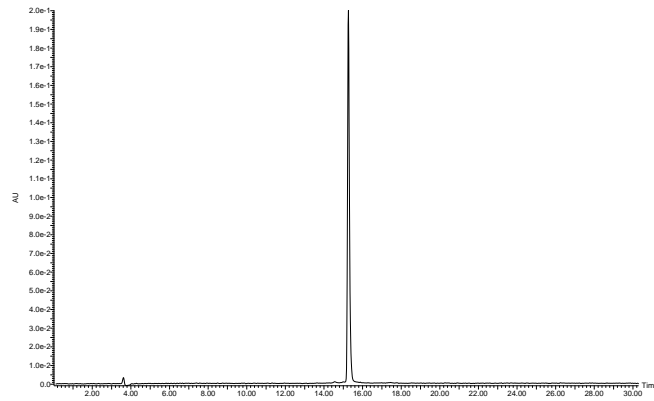


Figure S15. Reversed-phase HPLC analysis of purified COUPY-octreotide conjugate **16**.

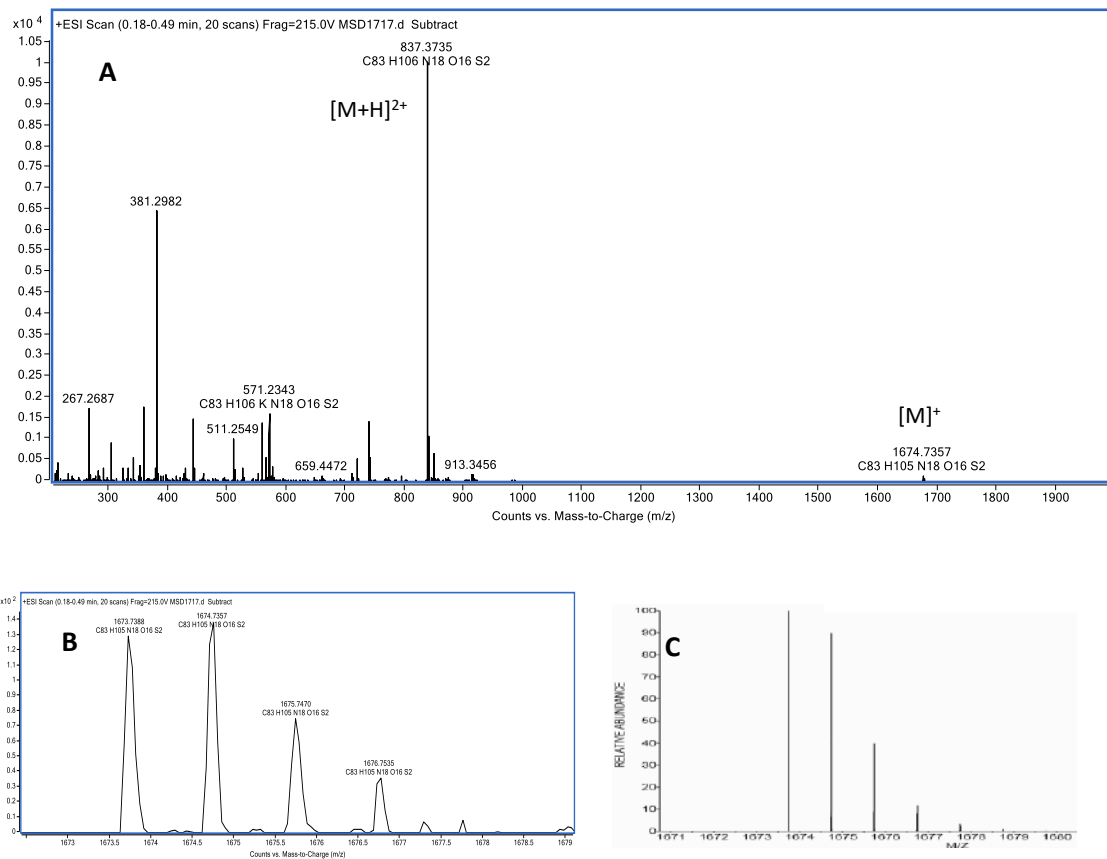


Figure S16. High resolution ESI MS of COUPY-octreotide conjugate **16**: experimental (A, B) and calculated (C).

5.- Photophysical characterization of the compounds

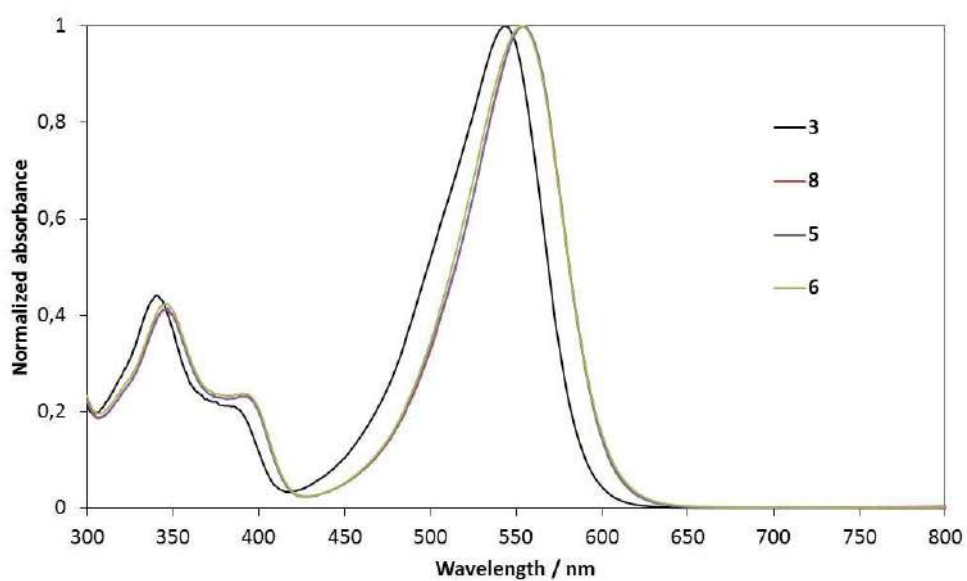


Figure S17. Normalized absorption spectra of coumarins **3**, **5-6** and **8** in PBS buffer.

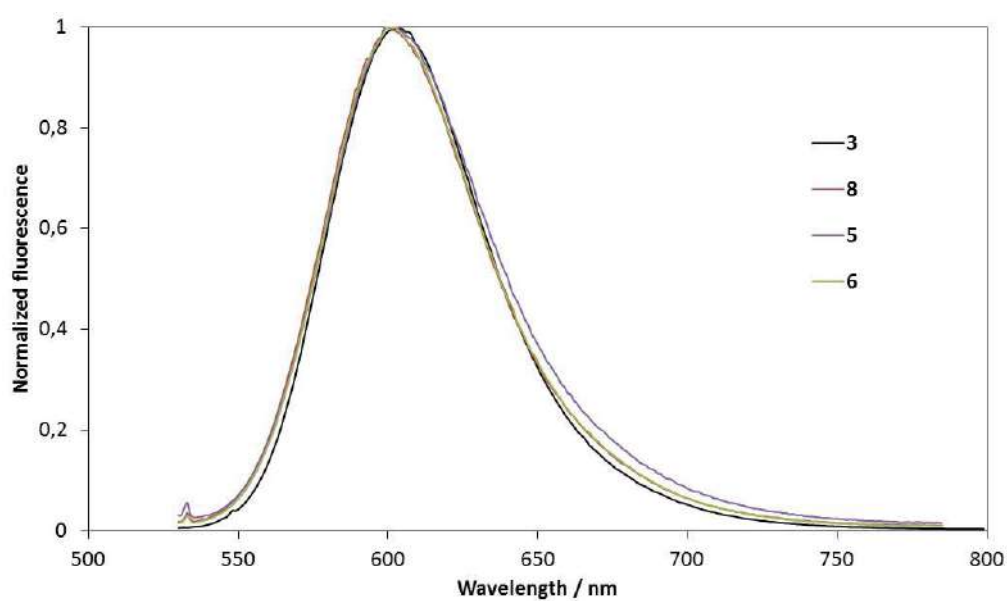


Figure S18. Normalized emission spectra of coumarins **3**, **5-6** and **8** in PBS buffer.

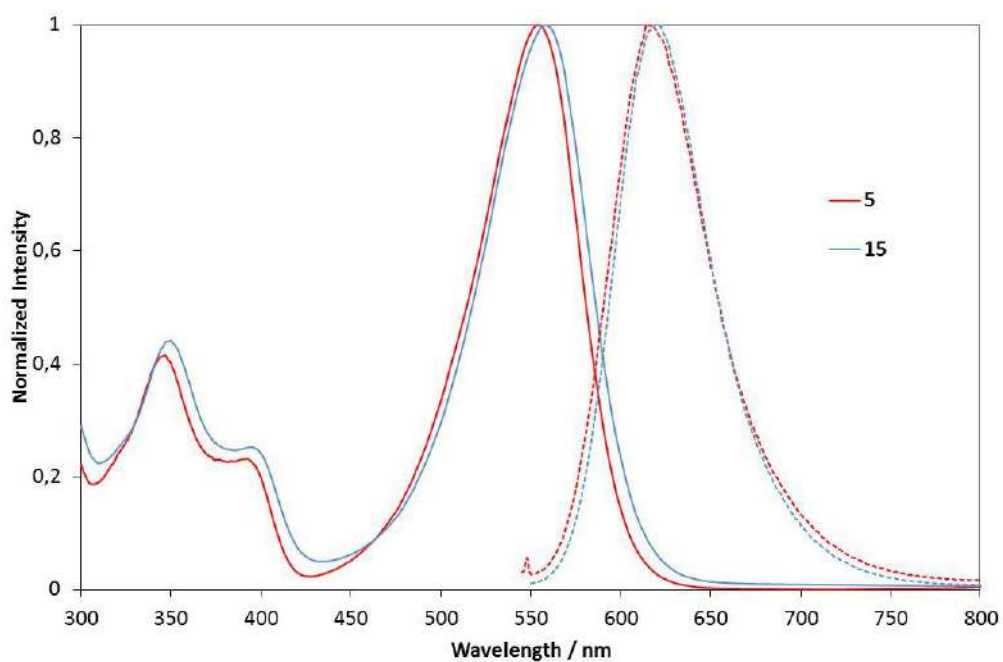


Figure S19. Comparison of the normalized absorption (solid lines) and fluorescence emission (dotted lines) spectra of coumarin **5** and conjugate **15**.

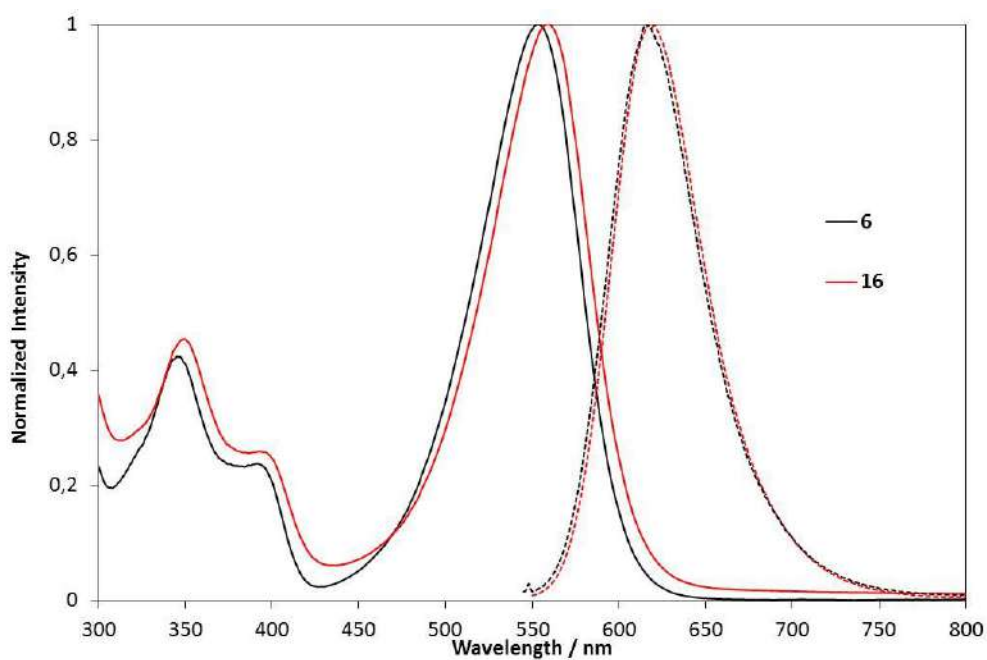


Figure S20. Comparison of the normalized absorption (solid lines) and fluorescence emission (dotted lines) spectra of coumarin **6** and conjugate **16**.

6.- Synthesis and characterization of Atto-Rho12-octreotide conjugate (17).

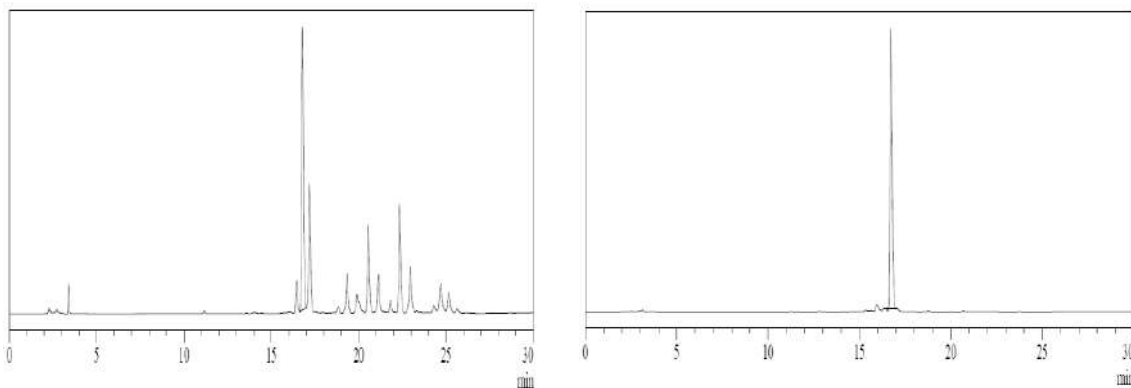


Figure S21. Reversed-phase HPLC traces for Atto Rho12-octreotide conjugate **17**: reaction crude (left) and purified (right).

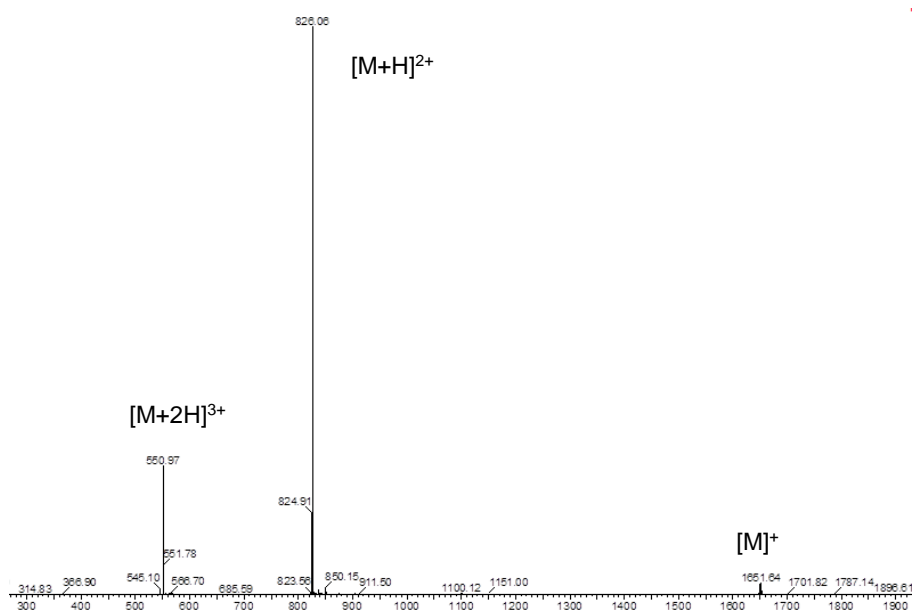


Figure S22. Low resolution ESI MS of Atto Rho12-octreotide conjugate **17**.

7.- Fluorescence imaging

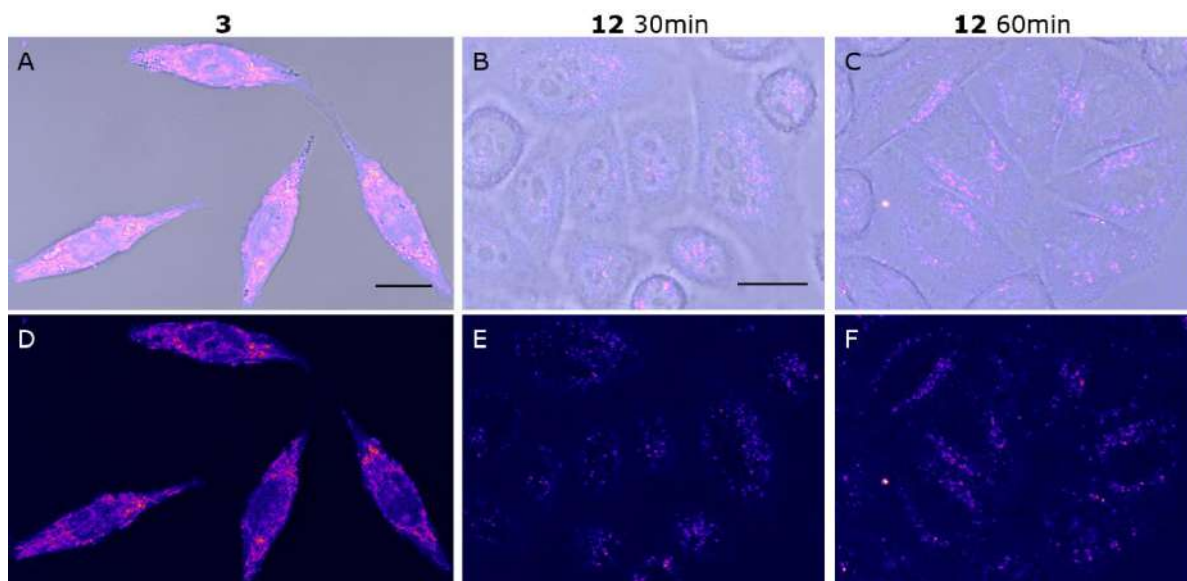


Figure S23. Comparison of the cellular uptake of coumarin **3** and COUPY-octreotide conjugate **12**. Single confocal planes of HeLa cells incubated with **3** at 1 μ M for 30 min at 37 $^{\circ}$ C (A and D) and **12** at 10 μ M for 30 min (B and E) or 60 min (C and F) at 37 $^{\circ}$ C. The compounds were excited at 561 nm and emission detected from 570 to 670 nm. (A-C) Fluorescence images merged with bright field images. (D-F) Fluorescence images only. All fluorescence images are color coded using the Fire lookup table from Fiji. Scale bar: 20 μ m. D same scale as A. C,E,F same scale as B.

8.- ^1H and ^{13}C NMR spectra and HR ESI-MS of the compounds

Coumarin 8

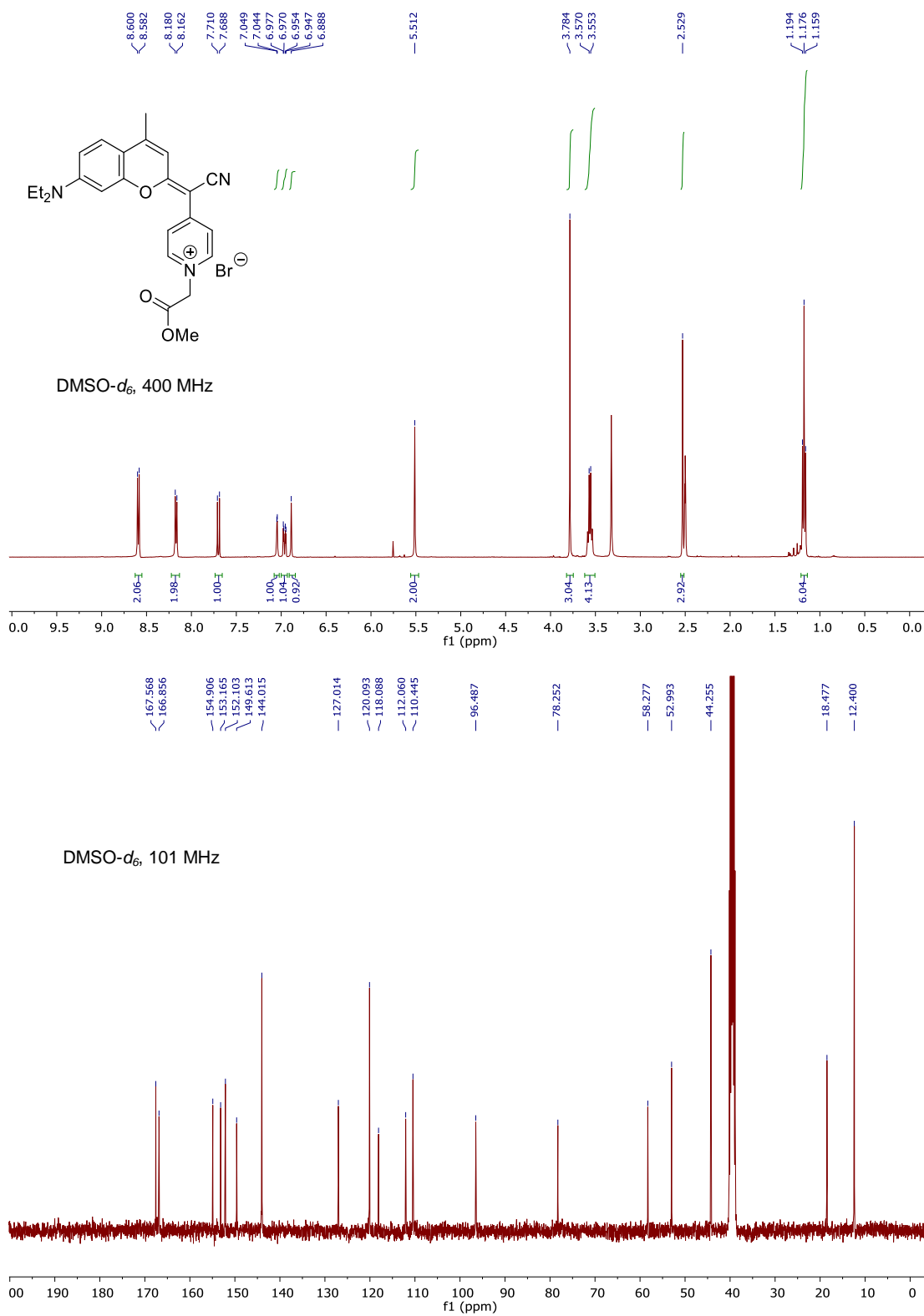


Figure S24. ^1H and ^{13}C NMR spectra of compound **8** in $\text{DMSO-}d_6$.

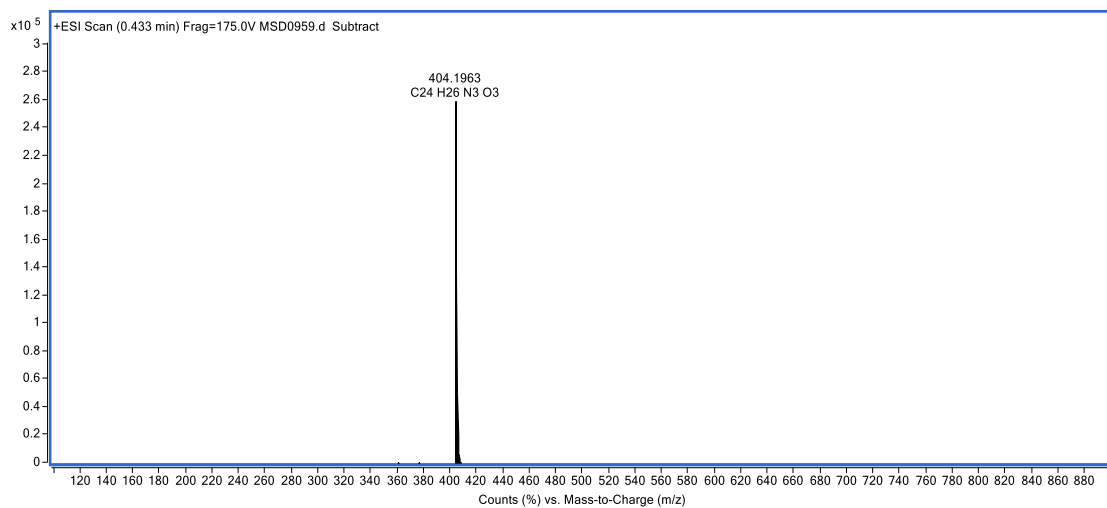


Figure S25. HR ESI-MS spectrum of compound **8**.

Coumarin 4

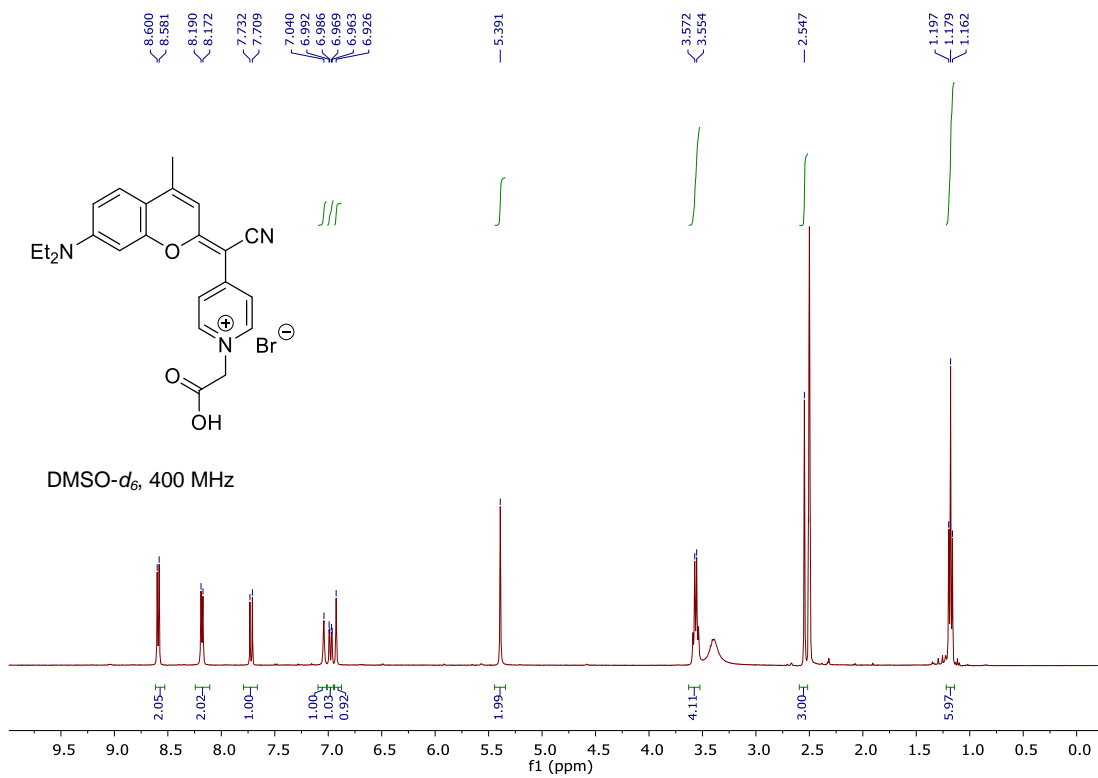


Figure S26. ¹H NMR spectra of compound 4 in DMSO-*d*₆.

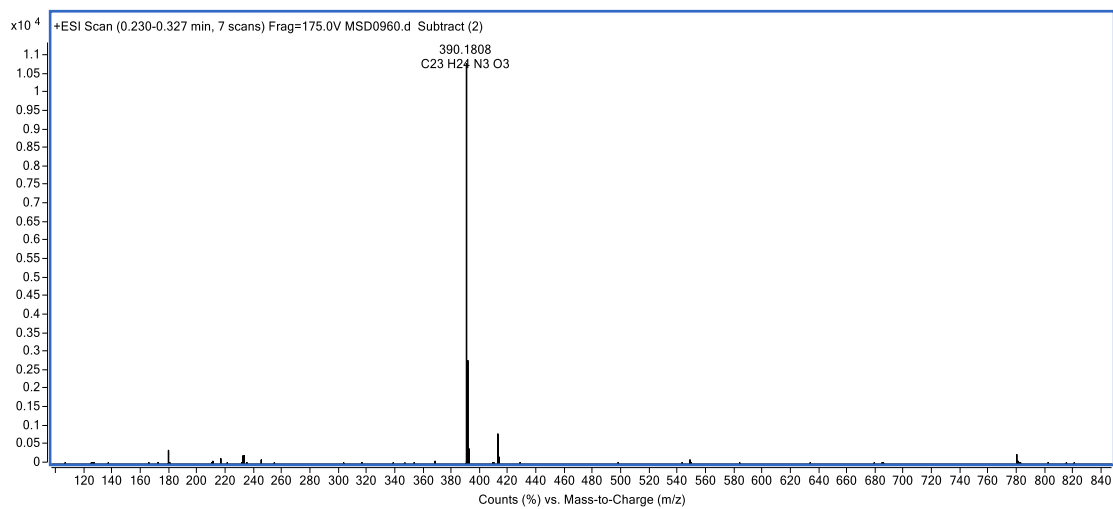


Figure S27. HR ESI-MS spectrum of compound 4.

***N*-(3-Azidopropyl)-2-bromoacetamide (9)**

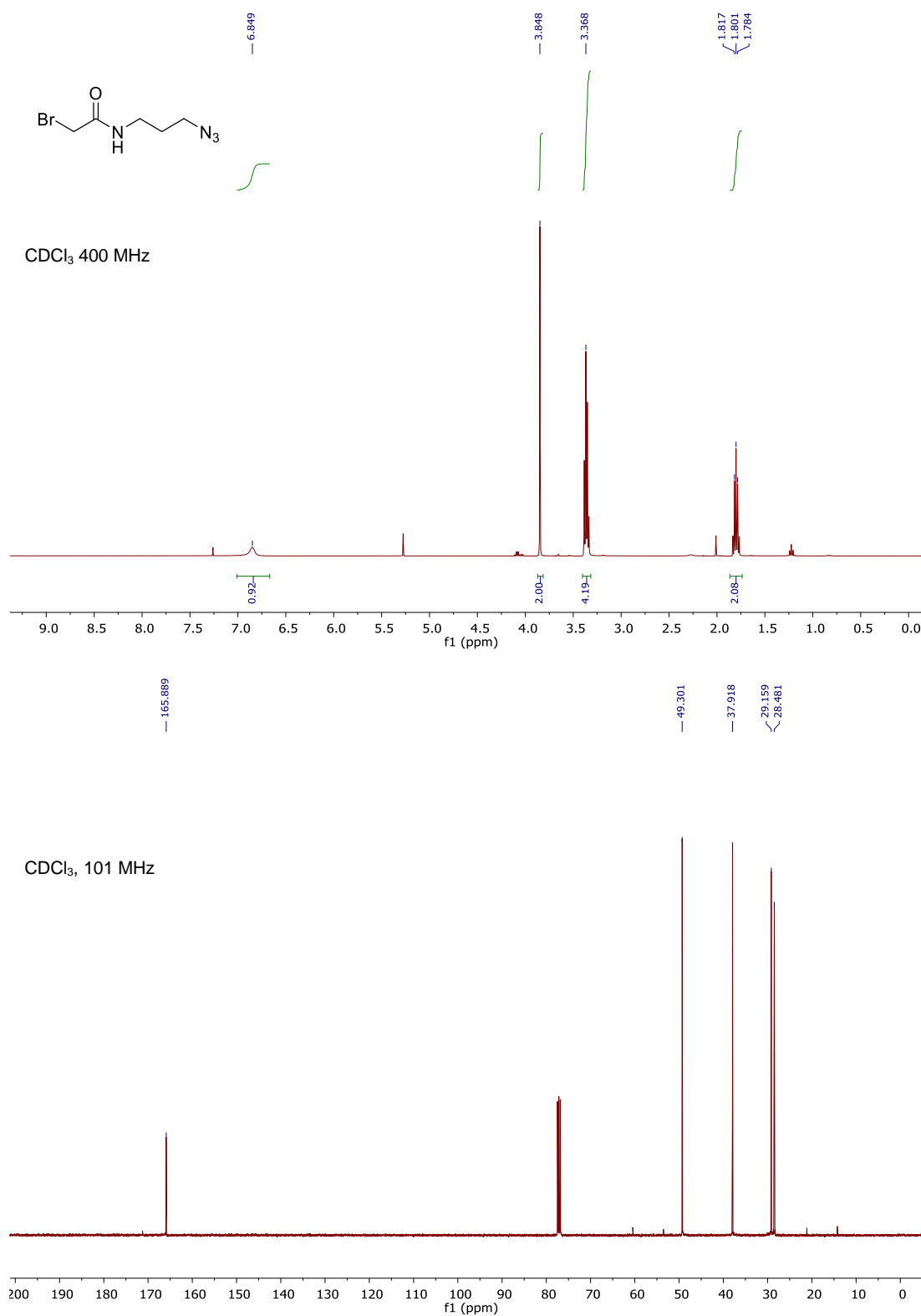


Figure S28. ¹H and ¹³C NMR spectra of compound **9** in CDCl₃.

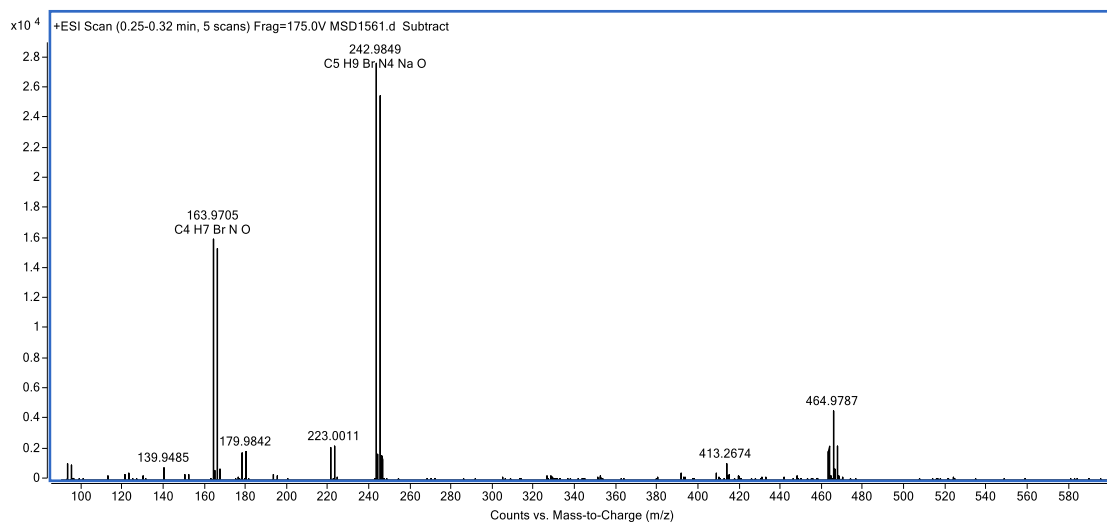


Figure S29. HR ESI-MS spectrum of compound **9**.

Coumarin 5

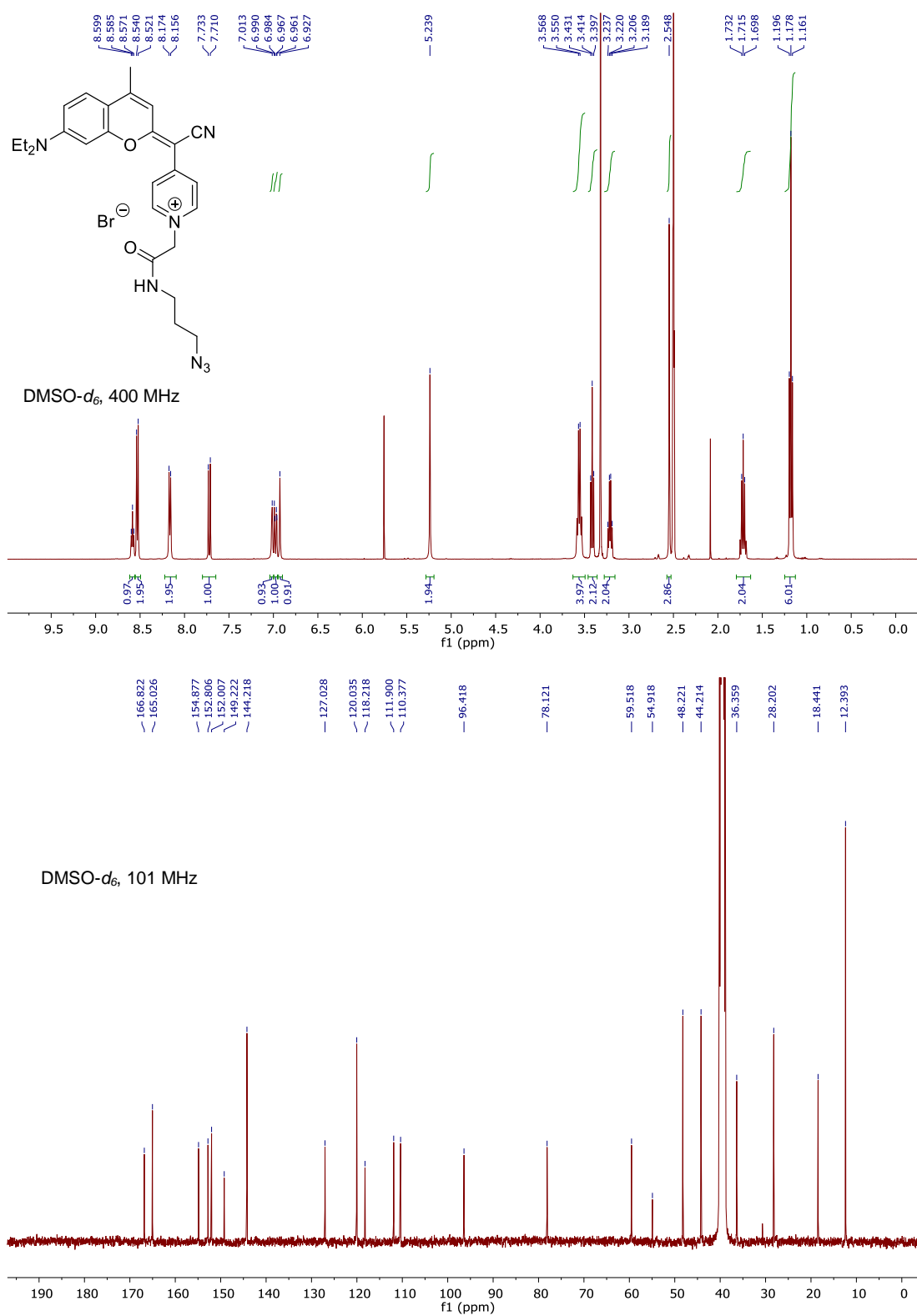


Figure S30. ¹H and ¹³C NMR spectra of compound 5 in DMSO-*d*₆.

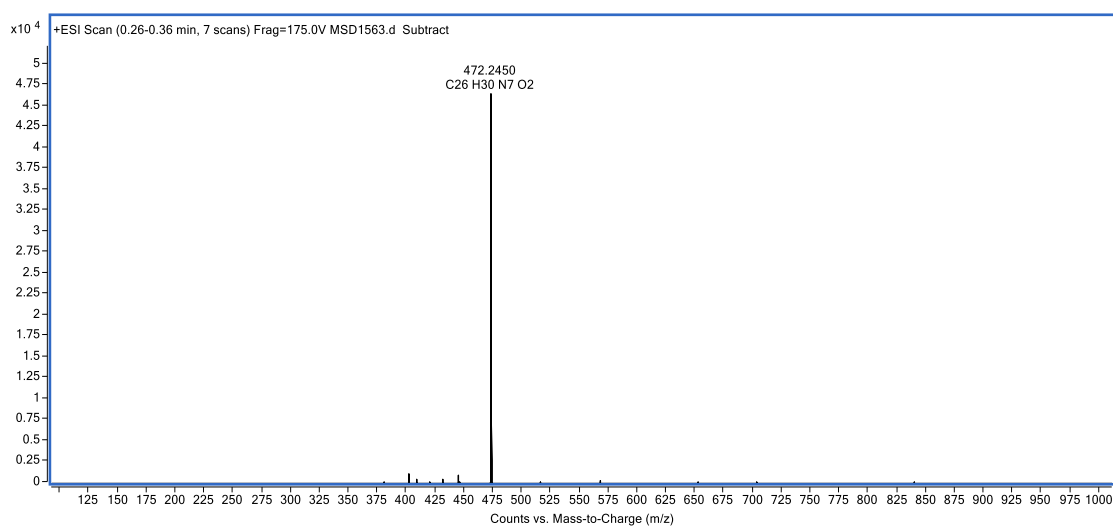


Figure S31. HR ESI-MS spectrum of compound **5**.

2-Bromo-N-(prop-2-yn-1-yl)acetamide (10)

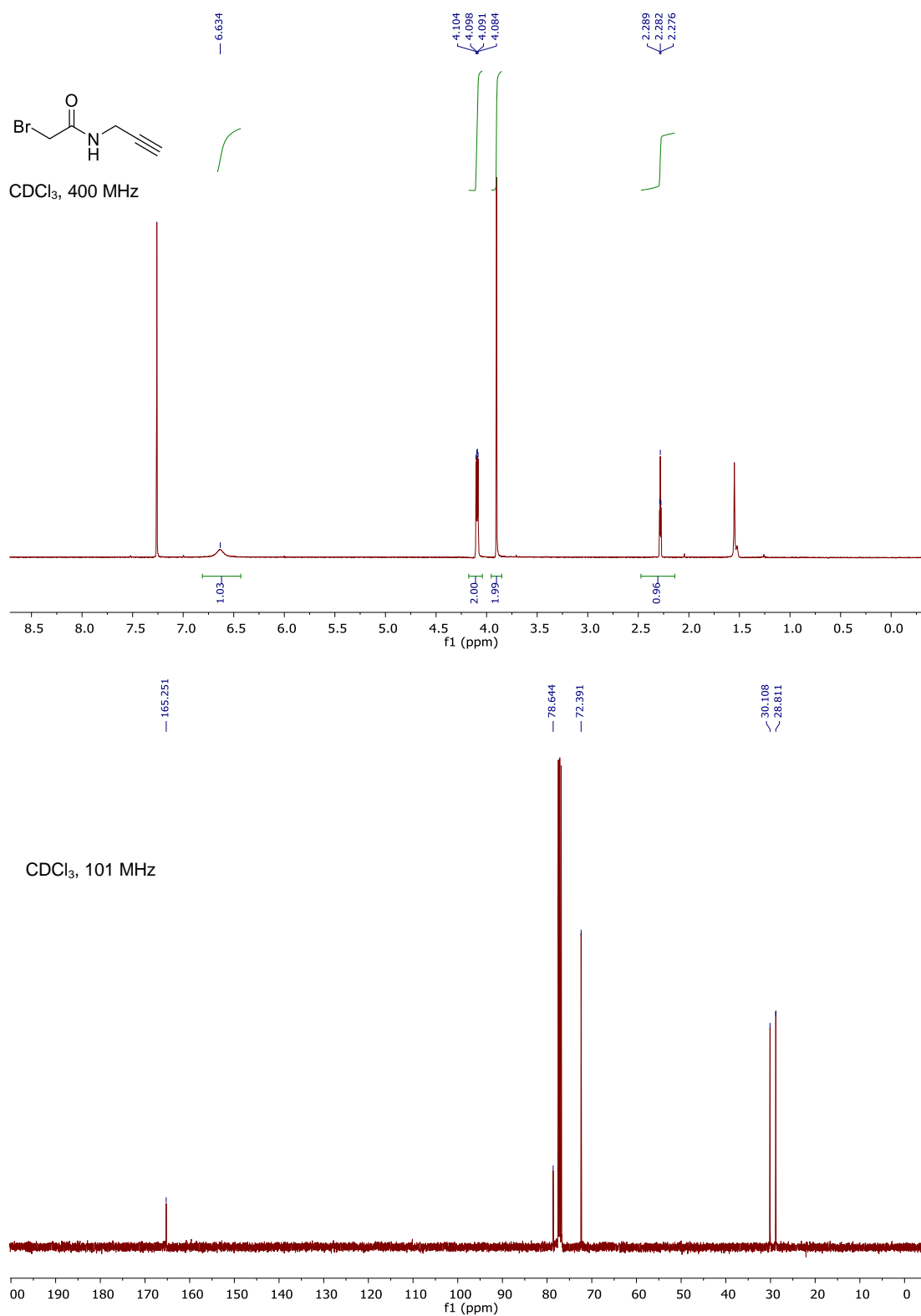


Figure S32. ^1H and ^{13}C NMR spectra of compound **10** in CDCl_3 .

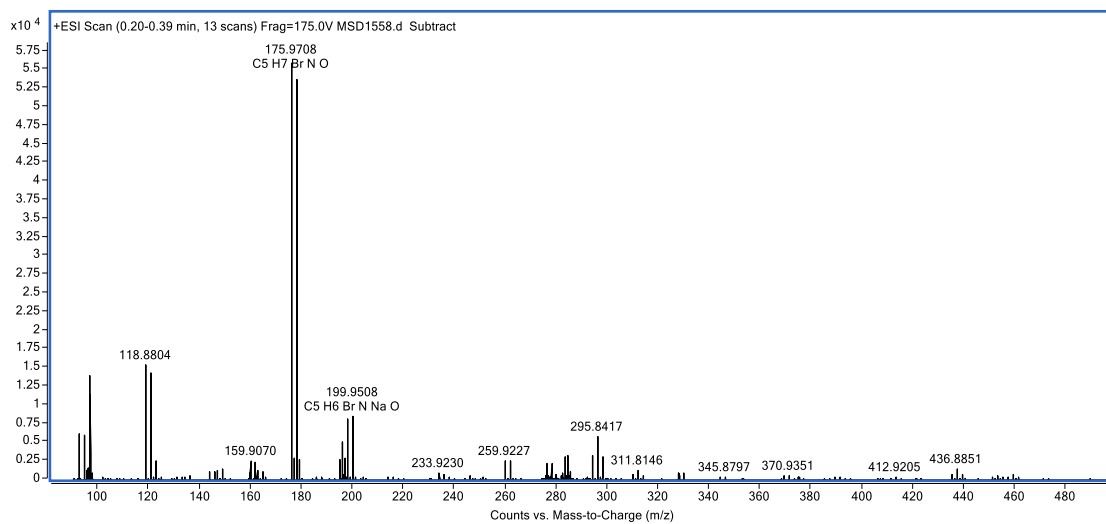


Figure S33. HR ESI-MS spectrum of compound **10**.

Coumarin 6

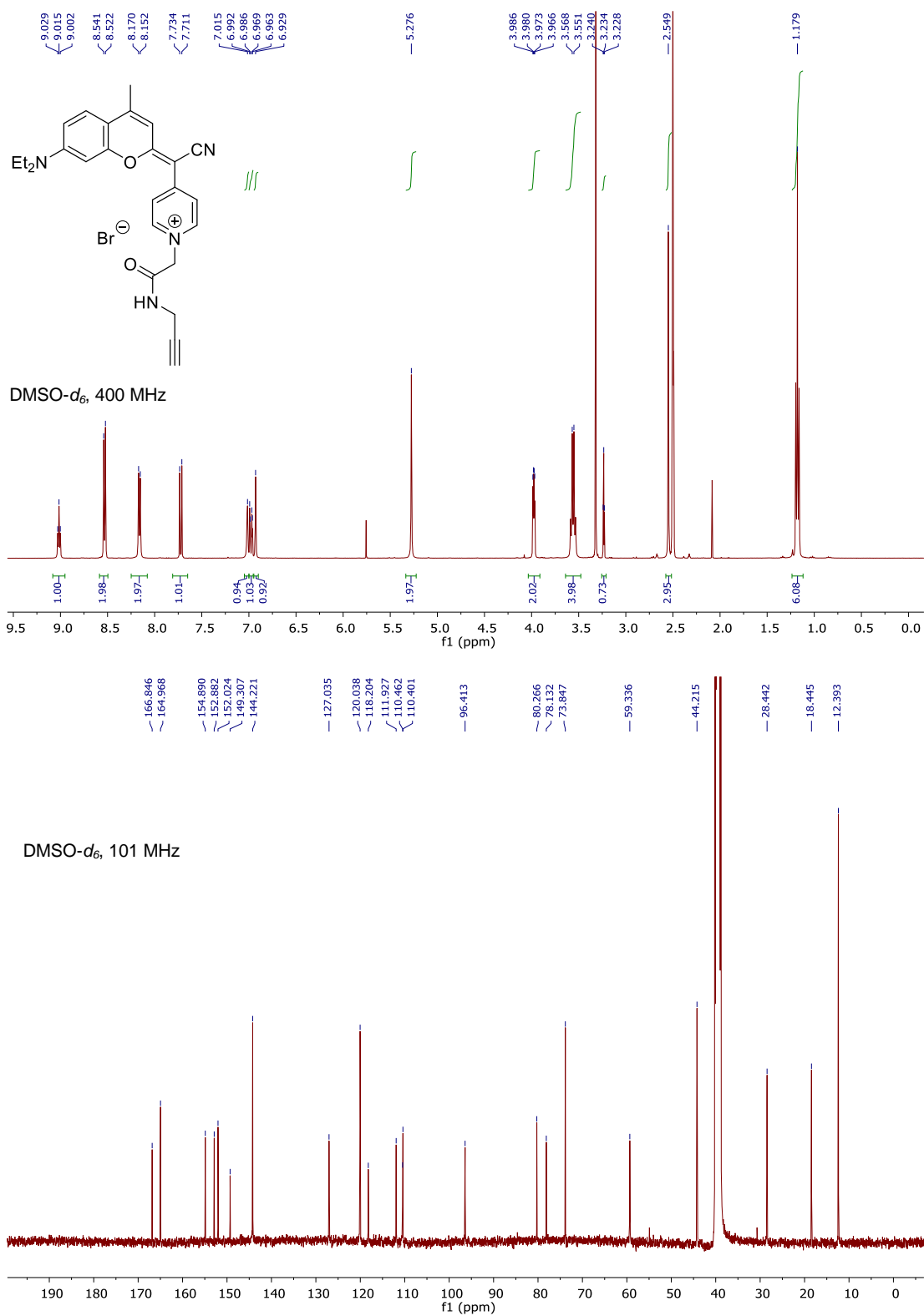


Figure S34. ¹H and ¹³C NMR spectra of compound 6 in DMSO-*d*₆.

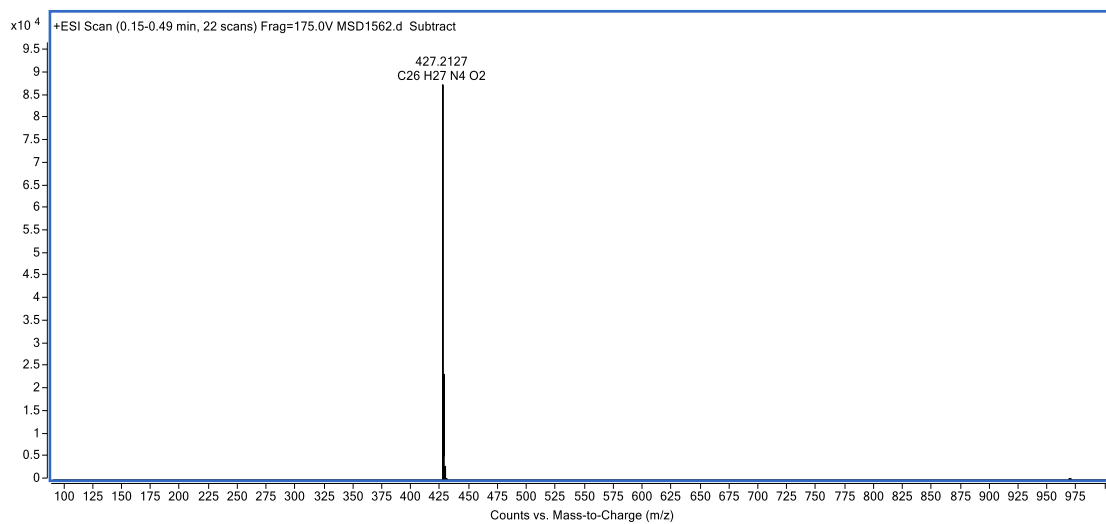


Figure S35. HR ESI-MS spectrum of compound **6**.

Chapter II

Conjugation of COUPY fluorophores to Ir(III) and
Ru(II) complexes for anticancer photodynamic
therapy

8. Chapter IIa. Publication C

Towards novel photodynamic anticancer agents generating superoxide anion radicals: a cyclometalated Ir^{III} complex conjugated to a far-red emitting coumarin.

(V. Novohradsky *et al.* *Angew. Chem. Int. Ed.* **2019**, *58*, 6311–6315)

Towards Novel Photodynamic Anticancer Agents Generating Superoxide Anion Radicals: A Cyclometalated Ir^{III} Complex Conjugated to a Far-Red Emitting Coumarin

Vojtech Novohradsky, Anna Rovira, Cormac Hally, Alex Galindo, Gloria Viguera, Albert Gandioso, Marie Svitelova, Roger Bresolí-Obach, Hana Kostrhunova, Lenka Markova, Jana Kasparkova, Santi Nonell, José Ruiz,* Viktor Brabec,* and Vicente Marchán*

Abstract: Although cyclometalated Ir^{III} complexes have emerged as promising photosensitizers for photodynamic therapy, some key drawbacks still hamper clinical translation, such as operability in the phototherapeutic window and reactive oxygen species (ROS) production efficiency and selectivity. In this work, a cyclometalated Ir^{III} complex conjugated to a far-red-emitting coumarin, Ir^{III}-COUPY, is reported with highly favourable properties for cancer phototherapy. Ir^{III}-COUPY was efficiently taken up by HeLa cells and showed no dark cytotoxicity and impressive photocytotoxicity indexes after irradiation with green and blue light, even under hypoxia. Importantly, a clear correlation between cell death and intracellular generation of superoxide anion radicals after visible light irradiation was demonstrated. This strategy opens the door to novel fluorescent photodynamic therapy agents with promising applications in theragnosis.

Cyclometalated iridium(III) complexes^[1] have gained attention as promising photosensitizers (PSs) in photodynamic therapy (PDT)^[2] since they can generate cytotoxic reactive oxygen species (ROS) under light irradiation. While direct energy transfer from the PS to the ground state of molecular oxygen in type II PDT yields singlet oxygen (¹O₂), the photochemical pathway of type I PDT more complex and involves the production of several types of ROS.^[1c] To date,

very few Ir^{III}-based PSs operate in the phototherapeutic window, which represents a serious drawback for clinical translation owing to the poor tissue penetration and toxicity of high energetic wavelengths, which inevitably cause off-target toxicity. However, the choice of the optimal wavelength range will depend on the tumor invasion depth since unnecessary deeper tissue penetration could also impair PDT potency and damage underlying healthy tissues.^[2e] Ideally, metal-based PSs should also operate under hypoxia^[3] and exhibit strong photocytotoxicity (i.e., high photocytotoxicity indexes). This might be a problematic issue in the case of cyclometalated Ir^{III} complexes due to their inherent high dark cytotoxicity and strong dependence on photocytotoxicity with ¹O₂ production.^[1,4] To address these problems, research efforts have been dedicated over the last few years to the development of novel PDT agents by combining organic fluorophores and metal complexes, either by integrating the chromophore within the metal coordination sphere via π -conjugated linkers or by simply attaching them together through a non- π -conjugated linker. This strategy takes advantage of the rich photophysical properties of organic fluorophores and of the well-established anticancer activities of metal complexes.^[1] Examples of this approach include boron-dipyrromethene (BODIPY) fluorophores^[5] and their conjugation to cyclometalated iridium(III) complexes.^[6] Conventional coumarins have also been conjugated to Ir^{III} complexes, either to increase singlet oxygen quantum yield^[7] or to target mitochondria.^[8]

Fluorophores based on small organic molecules have become essential daily tools in bioimaging applications, both in basic research and in diagnoses and therapy.^[9] Recently, we have described a novel class of far-red/NIR-emitting fluorophores, nicknamed COUPYs, in which the carbonyl group of conventional coumarin **1** (Scheme 1) was replaced with N-alkylated cyano(4-pyridine)methylene moieties (for example, compound **2**) to increase the push-pull character of the aromatic system.^[10] Besides operating within the optical window of biological tissues, COUPY dyes exhibit several appealing features, such as brightness, high photostability, and large Stokes' shifts.^[10]

Based on these antecedents, we envisaged COUPY fluorophores as promising candidates for developing novel fluorescent PDT agents in combination with highly potent cyclometalated Ir^{III} anticancer complexes, which contain a 2-quinolinylbenzimidazole N[^]N ligand (for example, complex **3**).^[11] Herein, we report for the first time the synthesis

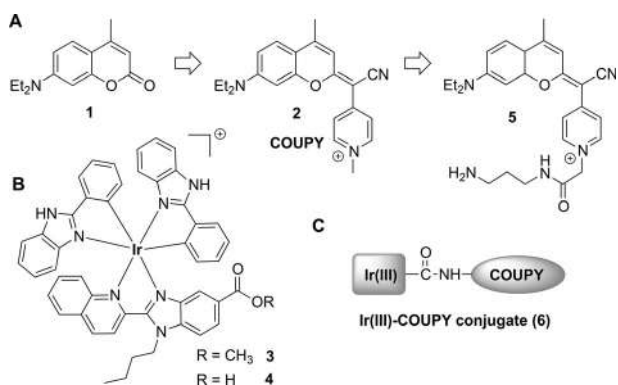
[*] Dr. V. Novohradsky, M. Svitelova, Dr. H. Kostrhunova, Dr. L. Markova, Dr. J. Kasparkova, Prof. V. Brabec
Institute of Biophysics of the Czech Academy of Sciences,
Kralovopolska 135, CZ-61265 Brno (Czech Republic)
E-mail: brabec@ibp.cz

A. Rovira, A. Galindo, Dr. A. Gandioso, Dr. V. Marchán
Departament de Química Inorgànica i Orgànica,
Secció de Química Orgànica, IBUB, Universitat de Barcelona
Martí i Franquès 1–11, E-08028 Barcelona (Spain)
E-mail: vmarchan@ub.edu

C. Hally, Dr. R. Bresolí-Obach, Prof. S. Nonell
Institut Químic de Sarrià, Universitat Ramon Llull
Via Augusta 390, E-08017 Barcelona (Spain)

G. Viguera, Prof. J. Ruiz
Departamento de Química Inorgànica, Universidad de Murcia and
Institute for Bio-Health Research of Murcia (IMIB-Arrixaca)
Campus de Espinardo, E-30071 Murcia (Spain)
E-mail: jruiz@um.es

Supporting information and the ORCID identification number(s) for the author(s) of this article can be found under:
<https://doi.org/10.1002/anie.201901268>.



Scheme 1. A) Rational design of COUPY fluorophores. B) Structure of cyclometalated iridium(III) complexes. C) Schematic representation of the Ir^{III}-COUPY conjugate described in this work.

and biological evaluation of a potential PS agent that combines a cyclometalated Ir^{III} complex with a representative COUPY dye (Scheme 1), and demonstrate a good correlation between cell death and the production of superoxide anion radicals, which were selectively generated after visible-light irradiation.

The attachment of the Ir^{III} complex to the fluorophore was carried out through the formation of an amide bond between the carboxylic acid functional group of **4** and the free amino group of coumarin **5** (see Scheme 1 and the Supporting Information for further details). The expected Ir^{III}-COUPY conjugate (**6**) was obtained as a dark purple solid after purification by silica column chromatography, and fully characterized by HR ESI-MS and ¹H and ¹³C NMR spectroscopy. Conjugate **6** was found to be completely soluble in water, which is an important improvement with respect to the metal complex, and is stable in cell culture medium (DMEM supplemented with 10% FBS) (Supporting Information, Figure S2).

The photophysical properties of conjugate **6** were studied in four solvents of different polarity and compared with those of coumarin **2** and Ir^{III} complex **3** (Figure 1 and Supporting Information, Table S1 and Figures S3–S9). The most relevant findings are that the Ir^{III} complex showed strong red phosphorescence (660 nm),^[12] whose intensity decreased in the conjugate in a solvent-dependent manner, indicating that competitive excited-state processes take place. Regarding the coumarin, it showed strong fluorescence (599–609 nm), whose intensity and lifetime decreased strongly in the conjugate,

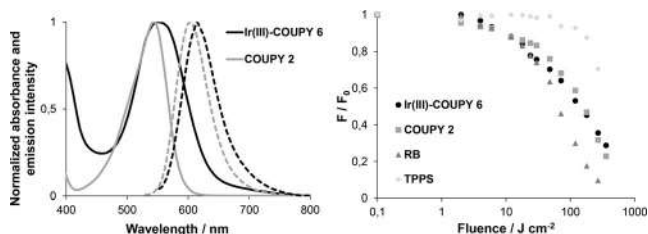


Figure 1. Left: Comparison of the normalized absorption (solid lines) and fluorescence emission (dotted lines) spectra of the compounds in PBS buffer. Right: Fluorescence bleaching of the compounds irradiated with green light.

again indicating the existence of competitive excited-state processes. Fluorescence of the coumarin could also be observed when the Ir^{III} complex was selectively photoexcited in the conjugate, indicating fast energy transfer from the Ir^{III} complex to the coumarin moiety. In the presence of oxygen, the Ir^{III} complex produced ¹O₂ in all organic solvents but not in phosphate-buffered saline (PBS). The coumarin was a much worse PS in all solvents; however, its ¹O₂ quantum yield increased by one order of magnitude in the conjugate, indicating an enhanced intersystem crossing induced by the heavy Ir^{III} ion, which is consistent with the shortening of its fluorescence lifetime. Nevertheless, no generation could be detected in PBS. Very similar quantum yields were observed when either the Ir^{III} complex or the coumarin moiety were selectively photoexcited in organic solvents in conjugate **6**, indicating almost 100% efficient singlet–singlet energy transfer from the Ir^{III} complex to the coumarin. In PBS, no ¹O₂ was detected at either excitation wavelength for any of the compounds.

Besides operability in the phototherapeutic window, good photostability is desirable in a PS to allow visualization of the tumor for a sufficiently long period. The photostability of **6** was evaluated under green light irradiation and compared with that of three control compounds, the parent COUPY **2**, Rose Bengal (RB), and *meso*-tetra(4-sulfonatophenyl)porphyrin (TPPS). As shown in Figure 1, conjugate **6** was slightly more resistant to photobleaching than RB, which is a commonly used PS for studies in biological systems. As expected, TPPS was the most photostable compound. Nevertheless, it is worth noting that conjugate **6** was found to be photostable up to light fluences larger than those typically used for cell imaging purposes.^[10a]

The cellular uptake of conjugate **6** was studied in living HeLa cells by confocal microscopy by irradiation with a yellow light laser ($\lambda_{\text{ex}} = 561 \text{ nm}$). As shown in Figure 2, **6** was efficiently taken up by the cells since fluorescent vesicles were clearly observed in the cytoplasm of all the examined cells. In contrast, COUPY **2** accumulated preferentially in mitochondria and nucleoli.^[10a] To further investigate the cellular uptake of the conjugate, Ir accumulation was quantitatively determined by inductively coupled plasma mass spectrometry (ICP-MS) after incubation of HeLa cells with Ir compounds. As shown in Table 1, the accumulation of **6** at 37 °C was slightly higher (about 1.6-fold) than that of the parent complex (**3**), which indicates that conjugation to the coumarin has a positive effect both on internalization and

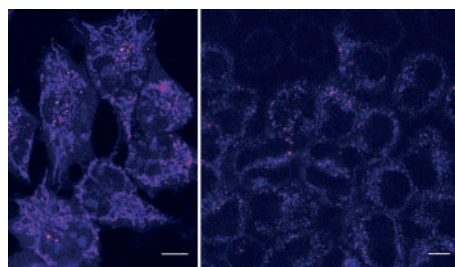


Figure 2. Comparison of the cellular uptake of Ir^{III}-COUPY conjugate **6** and COUPY **2**. Single confocal planes of HeLa cells incubated with **2** (left) and **6** (right) for 30 min at 37 °C. Scale bar: 10 µm.

Table 1: Cellular Ir accumulation determined by ICP-MS in HeLa cells at 4 °C and 37 °C.^[a]

	ng Ir/10 ⁶ cells		pmol Ir/10 ⁶ cells	
	4 °C	37 °C	4 °C	37 °C
Ir ^{III} complex 3	1.3 ± 0.2	7.6 ± 0.4	6.5 ± 1.0	39.4 ± 2.2
Ir ^{III} -COUPY 6	11.6 ± 1.0	12.1 ± 0.7	60.4 ± 5.2	62.8 ± 3.4

[a] HeLa cells were incubated for 2 h with 5 μM of Ir compounds at 4 °C or 37 °C. Results are the mean ± SDs from three independent experiments.

accumulation. Very interestingly, the accumulation of conjugate **6** was not modified when incubation was carried out at 4 °C. In contrast, the amount of cellular Ir accumulation was considerably reduced after incubation with **3** at low temperature, which points to an energy-dependent uptake pathway. The overall cellular uptake experiments indicate that the internalization pathway of the Ir^{III}-COUPY conjugate differs from that of the two separated moieties, since it does not accumulate in specific organelles, such as mitochondria or nucleoli but in the cytoplasm, and enters the cells through an energy-independent uptake mechanism.

The *in vitro* antitumor activity of **6** was tested in HeLa cells first in normoxic conditions (21 % O₂). Photocytotoxicity was also assessed via irradiation with visible light, either with a dose of 28 J cm⁻² of blue light or with 21 J cm⁻² of green light. Such doses of blue and green light are typically used in photocytotoxicity studies with metallodrugs.^[13] The parent compounds (COUPY **2** and complex **3**) were also tested to investigate the effect of conjugation. In both cases, the MTT assay was performed after 72 h of incubation. As shown in Table 2, conjugation between the Ir^{III} complex and the fluorophore resulted in a decrease in cytotoxicity. This result is particularly surprising considering the higher accumulation of the conjugate compared with the parent complex (Table 1). To our delight, visible-light irradiation clearly improved the antitumor activity of the conjugate, leading to IC₅₀ values of 2.51 and 1.32 μM upon irradiation with green and blue light, respectively. Furthermore, the low dark cytotoxicity of conjugate **6** led to excellent photocytotoxicity indexes (PIs) of 85 and 161 after irradiation with green and blue light, respectively. The PI of **6** after irradiation with biologically compatible green light is particularly impressive when compared with that of complex **3** (85 vs. 2.9, respec-

Table 2: Cytotoxicity of the compounds towards HeLa cells.^[a]

		Dark		PI ^[b]	Blue	
		IC ₅₀ [μM]	IC ₅₀ [μM]		IC ₅₀ [μM]	PI ^[b]
COUPY 2	Normoxia	38.7 ± 4.1	0.34 ± 0.11	114	0.37 ± 0.09	105
	Hypoxia	46.3 ± 3.1	0.46 ± 0.08	101	0.44 ± 0.13	105
Ir ^{III} comp. 3	Normoxia	95.2 ± 6.4	32.7 ± 4.9	2.9	2.02 ± 0.24	47
	Hypoxia	101 ± 10	31.5 ± 3.3	3.2	2.52 ± 0.19	40
Ir ^{III} -COUPY 6	Normoxia	213 ± 14	2.51 ± 0.32	85	1.32 ± 0.09	161
	Hypoxia	219 ± 6	2.77 ± 0.20	79	1.43 ± 0.11	153

[a] Cells were treated for 2 h (1 h of incubation, 1 h of irradiation at doses of 28 J cm⁻² of blue or 21 J cm⁻² of green light) followed by 70 h of incubation in drug-free medium. Control cells were left in the dark. Cells were cultured under normoxia (21 % O₂) and hypoxia (2 % O₂). Results are the means ± SDs from three independent experiments. [b] PI (Phototoxicity index) was calculated using the following formula: PI (Blue, Green) = IC₅₀ (dark-non-irradiated cells)/IC₅₀ (irradiated cells; blue, green).

tively). Although not investigated in this work, yellow and even red light could be used to activate conjugate **6** by taking advantage of the absorption spectrum of the coumarin moiety. The high photocytotoxicity of COUPY **2** suggests a disruption of the mitochondrial function, given its preferred accumulation in this organelle.^[10a]

Having confirmed a close relationship between visible-light irradiation and cytotoxicity, we investigated ROS generation inside the cells, either in the dark or after irradiation. Although the three compounds generated a basal level of intracellular ROS in the dark (Figure 3 and Supporting Information, Figure S6), a remarkable increase in ROS

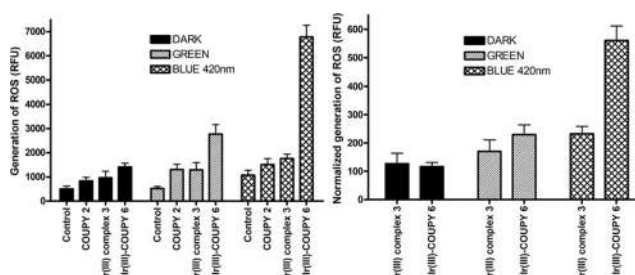


Figure 3. Left: Quantification of ROS determined by flow cytometry in HeLa cells. Cells were treated with 10 μM of the compounds for 1 h in the dark followed by 1 h of irradiation with green (21 J cm⁻²) or blue light (28 J cm⁻²). Right: Quantification of ROS normalized to the level of cellular uptake (ng Ir/10⁶ cells) of Ir compounds determined at 37 °C. Bars represent the mean relative fluorescence intensities coming from CellRox[®] reagent. Error bars were calculated from three independent experiments.

production occurred in the case of conjugate **6** after visible-light irradiation when compared with parent compounds **2** and **3**, especially with blue light, which cannot be exclusively attributed to a higher accumulation (see ROS quantification of **3** and **6** normalized to the level of cellular Ir accumulation in Figure 3). Overall, these results show a clear correlation between the photocytotoxicity of the Ir^{III}-COUPY conjugate and intracellular ROS generation, which confirms its potential applications as a PS since the production of ROS is the main mechanism for PDT-initiated cell death. To gain more insights into the photocytotoxicity of the conjugate, the antiproliferative activity of all the compounds was tested under low-oxygen conditions (2 % O₂). Interestingly, the cytotoxicity of the compounds was similar in both normoxic and hypoxic conditions (Table 2), which makes Ir^{III}-COUPY conjugates ideal candidates for the treatment of hypoxic tumors.

We then focused on identifying the specific cytotoxic ROS involved in cell death. Although cyclometalated Ir^{III} complexes typically produce ¹O₂,^[1] many other cytotoxic ROS can also be generated through type I photochemical

processes, such as hydrogen peroxide (H_2O_2), hydroxyl radicals ($\cdot\text{OH}$), superoxide anion radicals ($\cdot\text{O}_2^-$), and peroxynitrite anion (ONOO^-).^[14] To determine the specific ROS generated after treatment with Ir^{III} -COUPY conjugate **6**, HeLa cells were previously treated with several selective ROS scavengers, including sodium pyruvate (H_2O_2), D-mannitol ($\cdot\text{OH}$), tiron ($\cdot\text{O}_2^-$), sodium azide ($^1\text{O}_2$), and ebselen (ONOO^-). As shown in Figure 4 and Figure S11 in the Supporting Information, only the use of tiron was able to prevent the intracellular production of ROS, which suggests the generation of superoxide anion radicals in the cells after irradiation with visible (blue or green) light in the presence of Ir^{III} -COUPY conjugate **6**. Interestingly, scavenging studies ruled out the production of other types of ROS from conjugate **6**, including that of $^1\text{O}_2$, which agrees with the photophysical studies in PBS. In contrast, neither of the two components separately, COUPY **2** and Ir^{III} complex **3**, led to a significant production of ROS in HeLa cells, including $\cdot\text{O}_2^-$ (Supporting Information, Figures S12–S15).

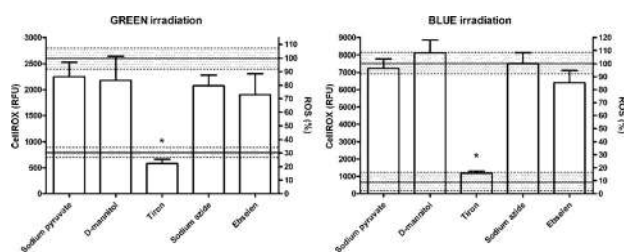


Figure 4. Data analysis for determination of ROS in HeLa cells by flow cytometry after irradiation with green (left) or blue light (right). Cells were pre-incubated with specific ROS scavengers and then treated with **6** (1 h in the dark followed by 1 h under irradiation).

Further confirmation of the generation of superoxide anion radicals from conjugate **6** was obtained by using a cell-based assay for the measurement of $\cdot\text{O}_2^-$ status in whole cells.^[15] As shown in Figure S16 in the Supporting Information, a significant increase in the luminescence signal with irradiation time of HeLa cells pre-treated with **6** was observed, indicating oxidation of luminol substrate. The oxidation of luminol was likely due to the generation of superoxide anion radicals, suggesting the reduction of the signal in the presence of superoxide dismutase (SOD), an enzyme that catalyzes $\cdot\text{O}_2^-$ disproportionation reactions to form H_2O_2 and O_2 .^[16] Furthermore, the use of dihydrorhodamine 123 (DHR123), a non-fluorescent probe that emits green fluorescence after reaction with $\cdot\text{O}_2^-$, allowed the confirmation of the generation of superoxide anion radicals in cell-free media.^[16] As shown in Figure S17 in the Supporting Information, conjugate **6** increased fluorescence intensity of DHR123 markedly more than the Ir^{III} complex **3** and COUPY **2**. Moreover, that increase was significantly suppressed in the presence of SOD and ascorbate (Supporting Information, Figure S18), thereby confirming the involvement of $\cdot\text{O}_2^-$ in oxidation processes leading to the fluorescence signal. Interestingly, SOD did not show any effect in the case of COUPY **2**, in contrast to the nonspecific reductant sodium ascorbate, which suggests that processes other than

$\cdot\text{O}_2^-$ production might be responsible for the photo effects of **2**. Furthermore, laser flash photolysis experiments revealed the production of different transient species (Supporting Information, Figure S9). Thus, at 570 nm the decay was dominated by the lifetime of the coumarin triplet state (3.8 and 0.6 μs in the absence and presence of oxygen, respectively). At 630 nm a longer-lived transient was observed, whose lifetime decreased strongly in the presence of oxygen. We interpret this as a reduced form of the Ir^{III} complex that is scavenged by oxygen to produce $\cdot\text{O}_2^-$. Finally, a third species was observed at 490 nm, whose lifetime increased in the presence of oxygen. This is interpreted as the cation radical of the coumarin moiety^[17] since reoxidation of the reduced form of the Ir^{III} complex by oxygen prevents intramolecular charge recombination. Nevertheless, a complete unravelling of the photochemical behaviour of Ir^{III} -COUPY conjugates requires further experiments. To our knowledge, this is the first example of selective production of superoxide anion radicals from a compound based on a cyclometalated Ir^{III} complex after visible-light irradiation in cells.^[18] Hence, the covalent attachment of the coumarin-based COUPY fluorophore to the metal complex not only improves cellular uptake and photocytotoxicity under visible-light irradiation but also triggers the production of highly cytotoxic $\cdot\text{O}_2^-$.

Finally, to investigate the involvement of superoxide anion radicals in cell death, we determined the viability of HeLa cells after treatment with conjugate **6** under the irradiating conditions, both in the absence and in the presence of tiron. As shown in Figure S19 in the Supporting Information, the photocytotoxicity of **6** was completely abolished in the cells pre-treated with the ROS scavenger, which confirms the active role of $\cdot\text{O}_2^-$ in cell death. Excessive $\cdot\text{O}_2^-$, which is one of the most toxic ROS, is known to irreversibly damage cellular components by reacting with proteins, DNA, and lipids.^[19] Moreover, disproportionation reactions involving $\cdot\text{O}_2^-$ might trigger the formation of other highly toxic ROS.

In summary, we have reported the first example of a novel PS agent based on the conjugation of a cyclometalated Ir^{III} complex to a coumarin-based COUPY fluorophore. The Ir^{III} -COUPY conjugate (**6**) exhibits several interesting features for cancer phototherapy, such as aqueous solubility, excellent cellular uptake, and high photocytotoxicity under visible-light irradiation, both in normoxia and hypoxia, with the PI values after blue and green light irradiation being particularly appealing, owing to the low dark cytotoxicity compared with the parent compounds, especially in the case of coumarin. Importantly, treatment with **6** generates a specific type I ROS in living cells upon visible-light irradiation, superoxide anion radicals ($\cdot\text{O}_2^-$), whose production has been further confirmed through spectroscopic methods and correlated with cell death, according to cellular viability experiments with tiron scavenger. Moreover, HeLa cells could be visualized by confocal microscopy by using a yellow light laser owing to the spectroscopic properties of the organic fluorophore in the Ir^{III} -COUPY conjugate. Overall, these properties indicate that conjugation between far-red/NIR-emitting COUPY coumarins and highly potent cyclometalated Ir^{III} complexes can be exploited to overcome some of the drawbacks of traditional PSs, such as poor tissue penetration

and O₂-tension dependency,^[16,20] leading to fluorescent PDT agents with promising applications in diagnosis and PDT against hypoxic tumors. Work is in progress in our laboratory to develop novel Ir^{III}-fluorophore conjugates operating in the phototherapeutic window, especially in the far-red and NIR region, with the aim of using them in targeted PDT.

Acknowledgements

This work was supported by funds from the Spanish Ministerio de Economía y Competitividad and FEDER funds (grants CTQ2014-52658-R, CTQ2015-64319-R, CTQ2016-78454-C2-1-R and CTQ2017-84779-R) and the Generalitat de Catalunya (2017 DI 072). The authors acknowledge helpful assistance of Dr. Francisco Cárdenas (NMR), Dr. Manel Bosch (Confocal Microscopy), and Dr. Irene Fernández and Laura Ortiz (MS) from CCiTUB. A.G. was a recipient fellow of the University of Barcelona. G.V. thanks the University of Murcia for a grant (R-1034/2016). C.H. thanks the European Social Funds and the SUR of DEC of the Generalitat de Catalunya for his predoctoral fellowships (Grants No. 2017 FI_B 00617, 2018 FI_B1 00174 and 2019 FI_B2 00167). V.N., M.S., H.K., L.M., J.K., and V.B. acknowledge the support from the Czech Science Foundation, Grant No. 18-09502S.

Conflict of interest

The authors declare no conflict of interest.

Keywords: conjugation · coumarin · cyclometalated iridium(III) complexes · photodynamic therapy · photosensitizer

How to cite: *Angew. Chem. Int. Ed.* **2019**, *58*, 6311–6315
Angew. Chem. **2019**, *131*, 6377–6381

- [1] a) Z. Liu, P. J. Sadler, *Acc. Chem. Res.* **2014**, *47*, 1174–1185; b) C. C. Konkankit, S. C. Marker, K. M. Knopf, J. J. Wilson, *Dalton Trans.* **2018**, *47*, 9934–9974; c) A. Zamora, G. Viguera, V. Rodríguez, M. D. Santana, J. Ruiz, *Coord. Chem. Rev.* **2018**, *360*, 34–76.
- [2] a) D. E. Dolmans, D. Fukumura, R. K. Jain, *Nat. Rev. Cancer* **2003**, *3*, 380–387; b) F. Heinemann, J. Karges, G. Gasser, *Acc. Chem. Res.* **2017**, *50*, 2727–2736; c) X. Li, S. Lee, J. Yoon, *Chem. Soc. Rev.* **2018**, *47*, 1174–1188; d) B. M. Luby, C. D. Walsh, G. Zheng, *Angew. Chem. Int. Ed.* **2018**, *57*, 2558–2569; *Angew. Chem.* **2018**, *130*, 2580–2591; e) S. Monro, K. L. Colón, H. Yin, J. Roque, P. Konda, S. Gujar, R. P. Thummel, L. Lilge, C. G. Cameron, S. A. McFarland, *Chem. Rev.* **2019**, *119*, 797–828.
- [3] X. Li, N. Kwon, T. Guo, Z. Liu, J. Yoon, *Angew. Chem. Int. Ed.* **2018**, *57*, 11522–11531; *Angew. Chem.* **2018**, *130*, 11694–11704.
- [4] a) K. V. Sudheesh, P. S. Jayaram, A. Samanta, K. S. Bejoymohandas, R. S. Jayasree, A. Ajayaghosh, *Chem. Eur. J.* **2018**, *24*, 10999–11007; b) P. Zhang, H. Huang, S. Banerjee, G. J. Clarkson, C. Ge, C. Imberti, P. J. Sadler, *Angew. Chem. Int. Ed.* **2019**, *58*, 2350–2354; *Angew. Chem.* **2019**, *131*, 2372–2376.
- [5] B. Bertrand, K. Passador, C. Goze, F. Denat, E. Bodio, M. Salmain, *Coord. Chem. Rev.* **2018**, *358*, 108–124.
- [6] a) E. Palao, R. Sola-Llano, A. Tabero, H. Manzano, A. R. Agarrabeitia, A. Villanueva, I. López-Arbeloa, V. Martínez-Martínez, M. J. Ortiz, *Chem. Eur. J.* **2017**, *23*, 10139–10147; b) L. Tabrizi, H. Chiniforoshan, *RSC Adv.* **2017**, *7*, 34160–34169; c) P. Majumdar, X. Yuan, S. Li, B. L. Guenic, J. Ma, C. Zhang, D. Jacquemin, J. Zhao, *J. Mater. Chem. B* **2014**, *2*, 2838–2854.
- [7] Y. Lu, R. Conway-Kenny, J. Wang, X. Cui, J. Zhao, S. M. Draper, *Dalton Trans.* **2018**, *47*, 8585–8589.
- [8] R.-R. Ye, C.-P. Tan, L.-N. Ji, Z.-W. Mao, *Dalton Trans.* **2016**, *45*, 13042–13051.
- [9] a) M. Srinivasarao, C. V. Galliford, P. S. Low, *Nat. Rev. Drug Discovery* **2015**, *14*, 203–219; b) R. R. Zhang, A. B. Schroeder, J. J. Grudzinski, E. L. Rosenthal, J. M. Warram, A. N. Pinchuk, K. W. Eliceiri, J. S. Kuo, J. P. Weichert, *Nat. Rev. Clin. Oncol.* **2017**, *14*, 347–364; c) M. Gao, F. Yu, C. Lv, J. Choo, L. Chen, *Chem. Soc. Rev.* **2017**, *46*, 2237–2271.
- [10] a) A. Gandioso, R. Bresolí-Obach, A. Nin-Hill, M. Bosch, M. Palau, A. Galindo, S. Contreras, A. Rovira, C. Rovira, S. Nonell, V. Marchán, *J. Org. Chem.* **2018**, *83*, 1185–1195; b) A. Gandioso, M. Palau, R. Bresolí-Obach, A. Galindo, A. Rovira, M. Bosch, S. Nonell, V. Marchán, *J. Org. Chem.* **2018**, *83*, 11519–11531; c) A. Rovira, A. Gandioso, M. Goñalons, A. Galindo, A. Massagué, M. Bosch, V. Marchán, *J. Org. Chem.* **2019**, *84*, 1808–1817.
- [11] a) J. Yellol, S. A. Pérez, G. Yellol, J. Zajac, A. Donaire, G. Viguera, V. Novohradsky, C. Janiak, V. Brabec, J. Ruiz, *Chem. Commun.* **2016**, *52*, 14165–14168; b) V. Novohradsky, A. Zamora, A. Gandioso, V. Brabec, J. Ruiz, V. Marchán, *Chem. Commun.* **2017**, *53*, 5523–5526.
- [12] a) T. Huang, Q. Yu, S. Liu, K. Yin Zhang, W. Huang, Q. Zhao, *ChemBioChem* **2019**, *20*, 576–586; b) J. Pracharova, G. Viguera, V. Novohradsky, N. Cutillas, C. Janiak, H. Kostrhunova, J. Kasparkova, J. Ruiz, V. Brabec, *Chem. Eur. J.* **2018**, *24*, 4607–4619.
- [13] a) S. L. Hopkins, B. Siewert, S. H. C. Askes, P. Veldhuizen, R. Zwier, M. Heger, S. Bonnet, *Photochem. Photobiol. Sci.* **2016**, *15*, 644–653; b) V. H. S. van Rixel, B. Siewert, S. L. Hopkins, S. H. C. Askes, A. Busemann, M. A. Siegler, S. Bonnet, *Chem. Sci.* **2016**, *7*, 4922–4929.
- [14] T. P. Devasagayam, J. C. Tilak, K. K. Boloor, K. S. Sane, S. S. Ghaskadbi, R. D. Lele, *J. Assoc. Physicians India* **2004**, *52*, 794–804.
- [15] D. Mihov, J. Vogel, M. Gassmann, A. Bogdanova, *Am. J. Physiol. Cell Physiol.* **2009**, *297*, C378–C388.
- [16] M. Li, J. Xia, R. Tian, J. Wang, J. Fan, J. Du, S. Long, X. Song, J. W. Foley, X. J. Peng, *J. Am. Chem. Soc.* **2018**, *140*, 14851–14859.
- [17] A. Aspée, E. Alarcon, E. Pino, S. I. Gorelsky, J. C. Scaiano, *J. Phys. Chem. A* **2012**, *116*, 199–206.
- [18] a) L. He, K.-N. Wang, Y. Zheng, J.-J. Cao, M.-F. Zhang, C.-P. Tan, L.-N. Ji, Z.-W. Mao, *Dalton Trans.* **2018**, *47*, 6942–6953; b) J.-S. Nam, M.-G. Kang, J. Kang, S.-Y. Park, S. J. C. Lee, H.-T. Kim, J. K. Seo, O.-H. Kwon, M. H. Lim, H.-W. Rhee, T.-H. Kwon, *J. Am. Chem. Soc.* **2016**, *138*, 10968–10977.
- [19] G.-Y. Liou, P. Storz, *Free Radical Res.* **2010**, *44*, 479–496.
- [20] H. Abrahamse, M. R. Hamblin, *Biochem. J.* **2016**, *473*, 347–364.

Manuscript received: January 29, 2019

Revised manuscript received: March 18, 2019

Accepted manuscript online: March 19, 2019

Version of record online: April 4, 2019

Supporting Information

Towards Novel Photodynamic Anticancer Agents Generating Superoxide Anion Radicals: A Cyclometalated Ir^{III} Complex Conjugated to a Far-Red Emitting Coumarin

Vojtech Novohradsky, Anna Rovira, Cormac Hally, Alex Galindo, Gloria Viguera, Albert Gandioso, Marie Svitelova, Roger Bresolí-Obach, Hana Kostrhunova, Lenka Markova, Jana Kasparkova, Santi Nonell, José Ruiz, Viktor Brabec,* and Vicente Marchán**

anie_201901268_sm_miscellaneous_information.pdf

Author Contributions

V.N. Data curation: Lead; Investigation: Lead; Methodology: Lead; Supervision: Lead; Writing—Review & Editing: Lead

A.R. Data curation: Lead; Investigation: Lead; Methodology: Lead

C.H. Data curation: Lead; Investigation: Lead; Methodology: Lead

A.G. Investigation: Lead; Methodology: Lead

G.V. Investigation: Lead; Methodology: Lead

A.G. Investigation: Supporting; Methodology: Supporting

M.S. Data curation: Equal; Investigation: Equal; Methodology: Equal

R.B. Data curation: Lead; Methodology: Lead

H.K. Investigation: Supporting; Methodology: Supporting

L.M. Investigation: Supporting; Methodology: Supporting

J.K. Funding acquisition: Equal; Project administration: Equal; Supervision: Equal

S.N. Funding acquisition: Lead; Project administration: Lead; Supervision: Lead; Writing—Review & Editing: Lead

J.R. Funding acquisition: Lead; Project administration: Lead; Supervision: Lead; Writing—Review & Editing: Lead

V.B. Funding acquisition: Lead; Project administration: Lead; Supervision: Lead; Writing—Review & Editing: Lead

V.M. Conceptualization: Lead; Data curation: Lead; Formal analysis: Lead; Funding acquisition: Lead; Project administration: Lead; Supervision: Lead; Validation: Lead; Writing—Original Draft: Lead; Writing—Review & Editing: Lead.

Table of contents

1. Synthesis and characterization of Ir(III)-COUPY conjugate 6	
1.1. Materials and Methods	S3
1.2. Synthesis of cyclometalated Ir(III) complexes 3 and 4	S4
1.3. Synthesis of coumarin derivative 5	S7
1.4. Synthesis of Ir(III)-COUPY conjugate 6	S9
2.- Photophysical characterization of the compounds	S11
3.- Fluorescence imaging.	S18
4.- Biological studies	S19
4.1. Cytotoxicity	
4.2. Cellular accumulation	
4.3. Determination of ROS induced after the treatment with the compounds in HeLa cells	
4.4. Selective scavenging of ROS in HeLa cells after the treatment with COUPY 2 , Ir(III) complex 3 and Ir(III)-COUPY conjugate 6	
4.5. Superoxide anion radical production by HeLa cells after treatment with Ir(III)-COUPY conjugate 6 .	
4.6. Superoxide anion radical production and characterization using DHR123 as fluorescence probe.	
4.7. Impact of selective superoxide anion scavenger tiron on the viability of HeLa cells	
5.- ^1H and ^{13}C NMR spectra and HR ESI-MS of the compounds	S31
6.- References	S37

1.- Synthesis and characterization of Ir(III)-COUPY conjugate 6

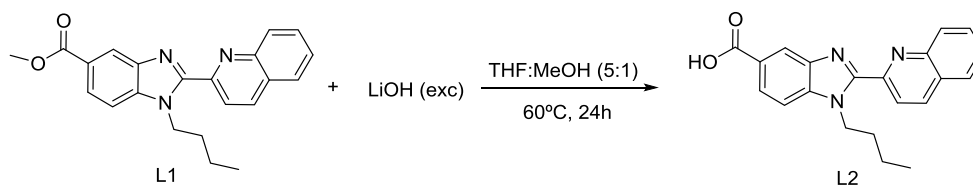
1.1.- Materials and Methods

Unless otherwise stated, common chemicals and solvents (HPLC grade or reagent grade quality) were purchased from commercial sources and used without further purification. Aluminium plates coated with a 0.2 mm thick layer of silica gel 60 F₂₅₄ were used for thin-layer chromatography analyses (TLC), whereas flash column chromatography purification was carried out using silica gel 60 (230-400 mesh). Reversed-phase high-performance liquid chromatography (HPLC) analyses were carried out on a Jupiter Proteo C₁₈ column (250x4.6 mm, 90 Å 4 µm, flow rate: 1 mL/min) using linear gradients of 0.1% formic acid in H₂O (A) and 0.1% formic acid in ACN (B). NMR spectra were recorded at 25 °C in a 400 MHz spectrometer using the deuterated solvent as an internal deuterium lock. Tetramethylsilane (TMS) was used as an internal reference (0 ppm) for ¹H spectra recorded in CDCl₃ and the residual protic signal of the solvent (77.16 ppm) for ¹³C spectra. The residual protic signal of DMSO was used as a reference in ¹H and ¹³C NMR spectra recorded in DMSO-*d*₆. Chemical shifts are reported in part per million (ppm) in the δ scale, coupling constants in Hz and multiplicity as follows: s (singlet), d (doublet), t (triplet), q (quartet), qt (quintuplet), m (multiplet), dd (doublet of doublets), dt (doublet of triplets), td (triplet of doublets), ddd (doublet of doublet of doublets), br (broad signal), etc. Electrospray ionization mass spectra (ESI-MS) were recorded on an instrument equipped with single quadrupole detector coupled to an HPLC, high-resolution (HR) ESI-MS on an LC/MS-TOF instrument.

1.2.- Synthesis of cyclometalated Ir(III) complexes **3** and **4**.

-Preparation of N^N ligands **L1** and **L2**.

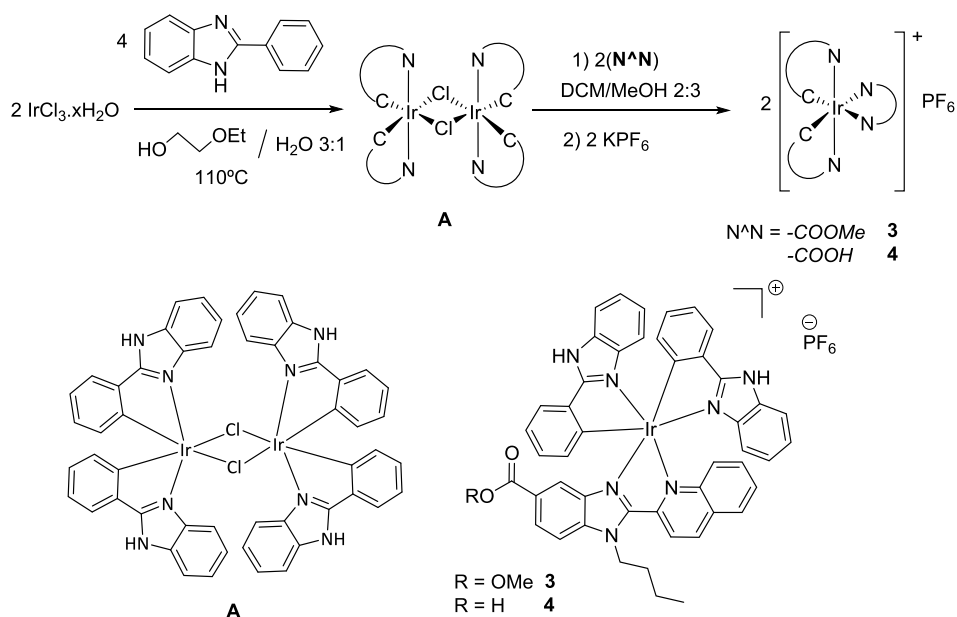
Methyl 1-butyl-2-(quinolin-2-yl)-1H-benzo[d]imidazole-5-carboxylate, **L1**, was synthesized as previously reported.¹



Scheme S1. Synthesis of N^N ligand **L2**.

1-Butyl-2-(quinolin-2-yl)-1H-benzo[d]imidazole-5-carboxylic acid, **L2**, was synthesized by hydrolysis of **L1**. **L1** (0.446 mmol) was dissolved in 10 mL of THF/MeOH (5:1). A saturated solution of LiOH was added slowly with constant stirring until pH = 8-9. The reaction mixture was stirred at 60 °C for 24 h, and the progress of the reaction was monitored by TLC. After completion of the reaction, the solvent was removed under reduced pressure and the resulting residue was suspended in a mixture of water and diethyl ether. The aqueous layer was separated and concentrated using a rotary evaporator to remove any traces of diethyl ether. Next, HCl 10% was carefully added dropwise until pH = 5-6. The precipitated solid was filtered and washed with water. White solid (75%); ¹H NMR (400 MHz, CDCl₃) δ (ppm): 8.80 (2H, br), 8.41 (1H, d, *J* = 9.2 Hz), 8.22 (1H, d, *J* = 8.5 Hz), 8.15 (1H, d, *J* = 8.5 Hz), 7.94 (1H, d, *J* = 8.2 Hz), 7.82 (1H, m), 7.67 (1H, m), 7.61 (1H, d, *J* = 8.2 Hz), 5.10 (2H, t, *J* = 7.1 Hz), 2.06 (2H, m), 1.53 (2H, m), 1.03 (3H, t, *J* = 7.2 Hz). HRMS (ESI-TOF) *m/z*: [M+H]⁺ Calcd for C₂₁H₂₀N₃O₂ 346.1556; Found 346.1546. Elemental analysis calcd for C₂₁H₁₉N₃O₂: C 73.0, H 5.5, N 12.2; found: C 73.1, H 5.5, N 12.3 (%).

-Preparation of dimer A



Scheme S2. Synthesis of dimer **A** and cyclometalated complexes **3** and **4**.

The cyclometalating pro-ligand 2-phenyl-1H-benzo[d]imidazole is commercial.

Dimer **A** was synthesized with a slight modification of the standard literature procedures for other bridged-chloride dimers.² $\text{IrCl}_3 \cdot \text{H}_2\text{O}$ (1 mmol) and the cyclometalating pro-ligand 2-phenyl-1H-benzo[d]imidazole (2.2 mmol) were dissolved in 2-ethoxyethanol/deionized H_2O (3:1). The mixture was stirred at 110 °C for 24 h under nitrogen atmosphere. Then, the reaction mixture was cooled down to room temperature and the resultant solid was collected by filtration. The solid was washed with water and ethanol and used in subsequent reaction without further purification.

-Preparation of cyclometalated Ir(III) complexes **3** and **4**

The cyclometalated iridium(III) chloro-bridged dimer **A** (1.0 mmol) and the corresponding $\text{N}^{\wedge}\text{N}$ ligand (2.1 mmol) were dissolved in DCM/MeOH (2:3, v/v). The reaction mixture was stirred at 58 °C for 24 h under nitrogen atmosphere. After cooling down the solution to room temperature, an excess of KPF_6 (2.5 mmol) was added and stirred for 30 min. The solvent was concentrated under reduced pressure, and the product was washed with water and recrystallized using dichloromethane and diethyl ether.

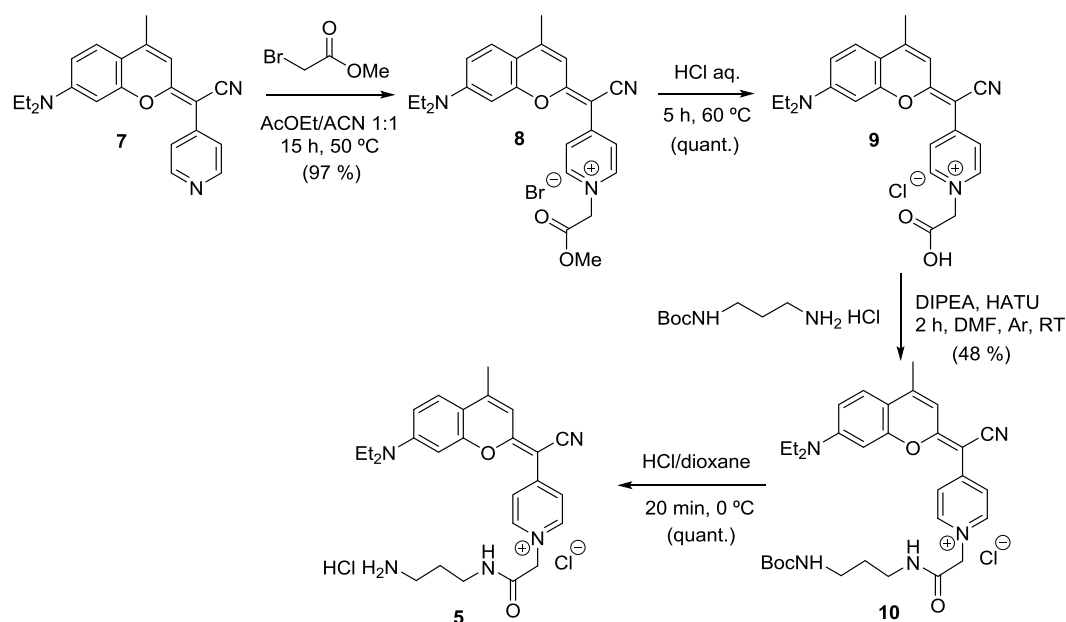
Complex 3. Orangish red solid. Reported in reference 1.

Complex 4. Dark red solid. Isolated yield: 62%. $^1\text{H-NMR}$ (400 MHz, $\text{DMSO-}d_6$) δ (ppm): 13.92 (1H, s), 13.78 (1H, s), 12.70 (1H, br s), 8.88 (1H, d, $J = 8.7$ Hz), 8.68 (1H, d, $J = 8.8$ Hz), 8.27 (1H, d, $J = 9.2$ Hz), 8.14 (1H, d, $J = 8.2$ Hz), 8.08 (1H, d, $J = 8.8$ Hz), 7.95 (1H, dd, J

= 8.8, 1.5 Hz), 7.87 (1H, d, $J = 7.7$ Hz), 7.8 (1H, d, $J = 7.6$ Hz), 7.64 (1H, t, $J = 7.8$ Hz), 7.53 (1H, d, $J = 8.1$ Hz), 7.47 (1H, d, $J = 8.0$ Hz), 7.15 (3H, m), 7.02 (2H, m), 6.95 (1H, d, $J = 1.1$ Hz), 6.89 (1H, td, $J = 7.5, 1.3$ Hz), 6.81 (1H, td, $J = 7.6, 1.2$ Hz), 6.76 (2H, m), 6.33 (1H, d, $J = 7.4$ Hz), 6.14 (1H, d, $J = 7.6$ Hz), 5.95 (1H, d, $J = 8.2$ Hz), 5.72 (1H, d, $J = 8.2$ Hz), 5.07 (2H, m), 1.72 (2H, m), 0.99 (2H, m), 0.66 (3H, t, $J = 7.2$ Hz). ^{13}C - NMR (150 MHz, DMSO- d_6) δ (ppm): 166.49, 164.44, 163.83, 156.00, 152.27, 149.73, 148.47, 142.95, 141.32, 139.47, 139.18, 138.96, 134.04, 132.09, 131.27, 130.36, 129.42, 128.95, 128.79, 127.88, 126.42, 124.46, 124.14, 123.23, 123.06, 122.61, 121.66, 120.60, 120.32, 118.08, 113.41, 113.02, 112.88, 46.00, 31.84, 19.04, 13.44. HRMS (ESI-TOF) m/z : $[\text{M-PF}_6]^+$ Calcd for $\text{C}_{47}\text{H}_{37}\text{IrN}_7\text{O}_2$ 924.2638; Found 924.2648. Elemental analysis calcd. for $\text{C}_{47}\text{H}_{37}\text{F}_6\text{IrN}_7\text{O}_2\text{P}$: C, 52.81; H, 3.49; N, 9.17; found: C, 52.80, H, 3.50; N, 9.16 (%).

1.3.- Synthesis of coumarin derivative 5.

As shown in Scheme S2, coumarin derivative **9** was synthesized from COUPY scaffold **7** in two linear steps following previously reported procedures.³ Reaction of **9** with *N*-Boc-1,3-propanediamine hydrochloride by using HATU as a coupling reagent in the presence of DIPEA afforded coumarin **10**. Finally, removal of the Boc protecting group afforded coumarin derivative **5**.



Scheme S3. Synthesis of coumarin derivative **5**.

Coumarin derivative 10.

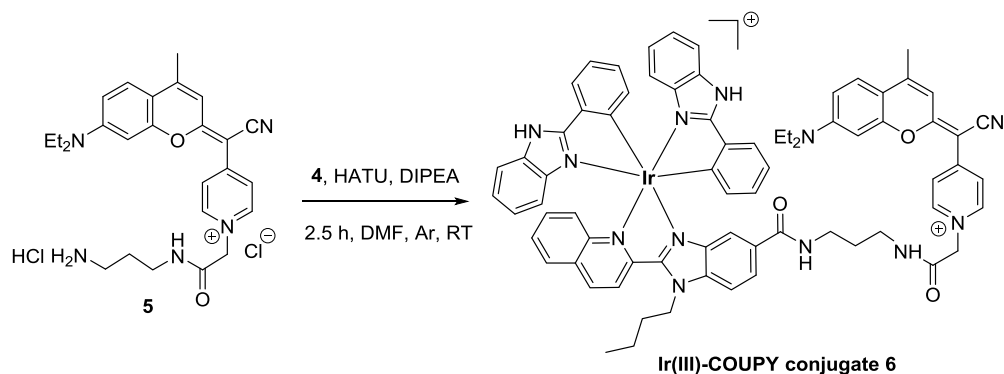
Coumarin **9** (317 mg, 0.74 mmol) and HATU (300 mg, 0.74 mmol) were dissolved in anhydrous DMF (15 mL) under an Ar atmosphere. After addition of DIPEA (131 μ L, 0.74 mmol), the reaction mixture was stirred for 5 min under Ar at room temperature and protected from light. On the other hand, DIPEA (131 μ L, 0.74 mmol) was added to a solution of *N*-Boc-1,3-propanediamine hydrochloride (157 mg, 0.74 mmol) in anhydrous DMF (15 mL), and the resulting mixture was combined with the coumarin solution. After addition of DIPEA (131 μ L, 0.74 mmol), the reaction mixture was stirred for 2 h at room temperature under Ar and protected from light. The crude product was evaporated under reduced pressure and purified by column chromatography (silica gel, 0-9.0% MeOH in DCM) to give 206 mg of purple solid (yield: 48 %). TLC: R_f (10% MeOH in DCM) 0.30. ¹H NMR (400 MHz, DMSO-*d*₆) δ (ppm): 8.59 (1H, t, J = 5.6 Hz), 8.53 (2H, d, J = 7.2 Hz), 8.16 (2H, d, J = 7.2 Hz), 7.72 (1H, d, J = 9.2 Hz), 7.02 (1H, br s), 6.97 (1H, dd, J = 9.2 Hz, J = 2.8 Hz), 6.93 (1H, s), 6.82 (1H, t, J = 5.6 Hz), 5.24 (2H, s), 3.56 (4H, q, J = 7.2 Hz), 3.13 (2H, q, J = 6 Hz), 2.96 (2H, q, J = 6

Hz), 2.55 (3H, s), 1.57 (2H, qt, $J = 6.8$ Hz), 1.37 (9H, s), 1.18 (6H, t, $J = 7.2$ Hz). $^{13}\text{C}\{^1\text{H}\}$ NMR (101 MHz, DMSO- d_6) δ (ppm): 166.82, 164.84, 155.60, 154.88, 152.79, 152.01, 149.20, 144.19, 127.03, 120.05, 118.22, 111.89, 110.37, 96.43, 78.12, 77.53, 59.56, 53.37, 44.21, 37.54, 36.82, 29.33, 28.25, 18.44, 12.39. HRMS (ESI-TOF) m/z : $[\text{M}]^+$ Calcd for $\text{C}_{31}\text{H}_{40}\text{N}_5\text{O}_4$ 546.3075; Found 546.3073. Analytical HPLC (30 to 100% B in 30 min, formic acid additive): $R_t = 8.8$ min

Coumarin derivative 5.

A cooled down solution of hydrochloric acid in dioxane (4 M, 43 mL) was added to coumarin **10** (172 mg, 0.30 mmol). The reaction mixture was stirred for 20 min in an ice bath under an Ar atmosphere and protected from light. After removal of the solvent, several co-evaporations from acetonitrile were carried out. The crude product was used without further purification since HPLC-MS analysis revealed that the removal of the Boc group was quantitative. LRMS (ESI-TOF) m/z : $[\text{M}]^+$ Calcd for $\text{C}_{26}\text{H}_{32}\text{N}_5\text{O}_2$ 446.26; Found 446.18. Analytical HPLC (0 to 50% B in 30 min, formic acid additive): $R_t = 18.2$ min.

1.4.- Synthesis of Ir(III)-COUPY conjugate **6**.



Scheme S4. Synthesis of Ir(III)-COUPY conjugate **6**.

To a solution of complex **4** (7.25 mg, 6.78 μmol) and HATU (2.6 mg, 6.78 μmol) in anhydrous DMF (1.5 mL) under an Ar atmosphere, DIPEA (2 μL , 11.5 μmol) was added and the mixture stirred for 10 min under Ar at room temperature and protected from light. After addition of a solution of coumarin **5** (11 mg, 21.4 μmol) and DIPEA (10 μL , 57.5 μmol) in anhydrous DMF (2 mL), the reaction mixture was stirred for 2.5 h at room temperature under Ar and protected from light. After evaporation under reduced pressure, the crude was purified by column chromatography (silica gel, 0-9.5% MeOH in DCM) to give 3 mg of purple solid (yield: 30 %). TLC: R_f (10% MeOH in DCM) 0.28. ^1H NMR (400 MHz, $\text{DMSO-}d_6$) δ (ppm): 8.85 (1H, d, $J = 8.8$ Hz), 8.67 (1H, d, $J = 8.8$ Hz), 8.59 (1H, t, $J = 5.6$ Hz), 8.53 (2H, d, $J = 7.6$ Hz), 8.38 (1H, d, $J = 9.2$ Hz), 8.30 (1H, s), 8.16 (2H, d, $J = 7.2$ Hz), 8.13 (1H, d, $J = 8.2$ Hz), 8.05 (1H, d, $J = 8.8$ Hz), 7.81 (2H, m), 7.72 (2H, m), 7.62 (1H, t, $J = 7.6$ Hz), 7.42 (2H, m), 7.16 (1H, m), 6.97 (6H, m), 6.80 (1H, t, $J = 7.2$ Hz), 6.74 (1H, t, $J = 7.6$ Hz), 6.67 (1H, d, $J = 1.2$ Hz), 6.59 (2H, m), 6.25 (1H, d, $J = 7.6$ Hz), 6.16 (1H, d, $J = 7.6$ Hz), 5.82 (1H, m), 5.63 (1H, m), 5.26 (2H, s), 5.08 (2H, m), 3.53 (4H, q, $J = 7.2$ Hz), 3.20 (4H, m), 2.55 (3H, s), 1.73 (4H, m), 1.15 (6H, t, $J = 7.2$ Hz), 1.01 (2H, m), 0.67 (3H, t, $J = 7.2$ Hz). $^{13}\text{C}\{^1\text{H}\}$ NMR (101 MHz, $\text{DMSO-}d_6$) δ (ppm): 166.86, 165.72, 164.91, 164.40, 155.61, 154.89, 154.72, 152.87, 152.79, 152.00, 149.77, 149.41, 149.22, 148.71, 148.63, 144.22, 140.95, 139.69, 137.91, 132.51, 132.46, 132.15, 131.75, 131.71, 131.00, 129.48, 129.41, 129.26, 128.78, 128.56, 127.03, 124.65, 124.03, 121.96, 121.27, 120.39, 118.24, 117.73, 114.01, 112.77, 112.55, 112.49, 111.89, 110.38, 96.44, 55.59, 45.86, 44.20, 37.03, 31.94, 29.02, 28.91, 19.05, 18.43, 13.47, 12.38. HRMS (ESI-TOF) m/z : $[\text{M}]^{2+}$ Calcd for $\text{C}_{73}\text{H}_{67}\text{IrN}_{12}\text{O}_3$ 676.2541; Found 676.2537. Analytical HPLC (30 to 100% B in 30 min, formic acid additive): $R_t = 8.9$ min

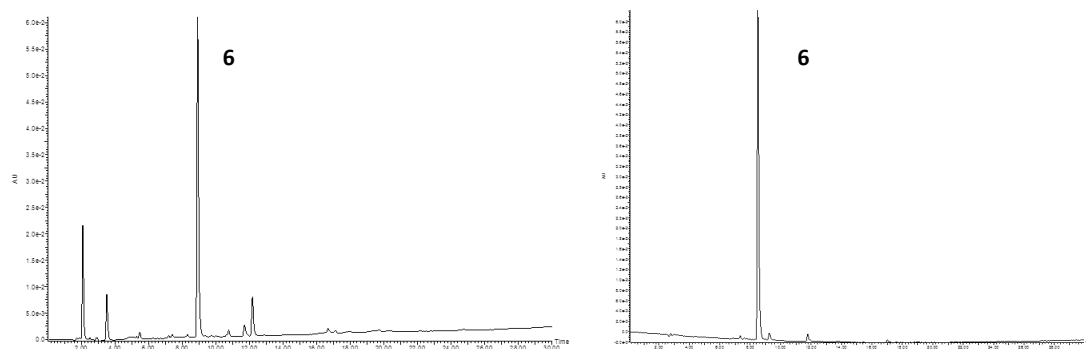


Figure S1. Reversed-phase HPLC traces for Ir(III)-COUPY conjugate (**6**): reaction crude (left) and purified (right).

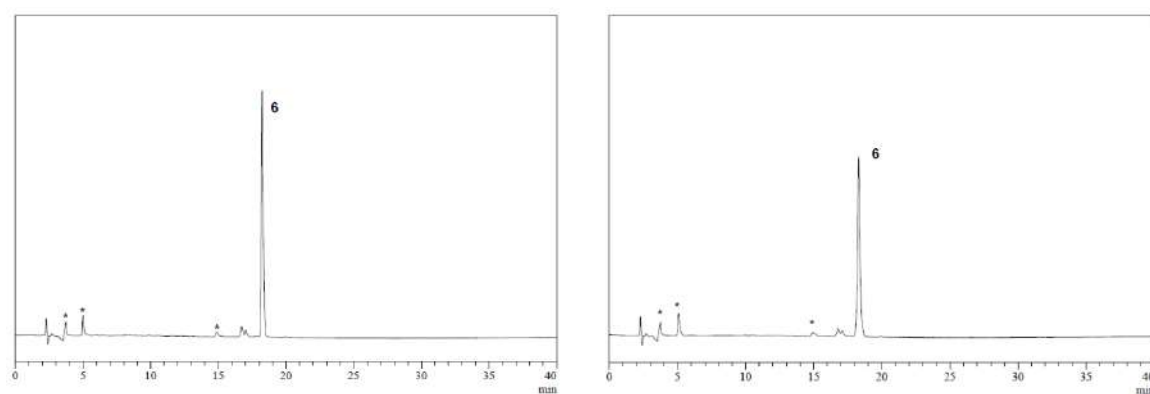


Figure S2. Reversed-phase HPLC traces for Ir(III)-COUPY conjugate (**6**) in DMEM-10% FBS at $t=0$ (left) and after incubation at 37 °C for 24 h (right). * peaks from the cell medium.

2.- Photophysical characterization of the compounds.

For photophysical measurements, all solvents used were spectroscopic grade. Absorption spectra were recorded in a Varian Cary 500 UV/Vis/NIR or Varian Cary 6000i spectrophotometer at room temperature. Molar absorption coefficients (ϵ) were determined by direct application of the Beer-Lambert law, using solutions of the compounds in each solvent with concentrations ranging from 10^{-6} to 10^{-5} M. Emission spectra were registered in a Photon Technology International (PTI) fluorimeter or in a Spex Fluoromax-4 spectrofluorometer. Fluorescence quantum yields (Φ_F) were measured by comparative method using cresyl violet in ethanol (CV; $\Phi_{F;Ref} = 0.54 \pm 0.03$) as reference.⁴ Then, optically-matched solutions of the compounds and CV were excited and the fluorescence spectra was recorded. The absorbance of sample and reference solutions was set below 0.1 at the excitation wavelength and Φ_F were calculated using the following equation (1):

$$\Phi_{F;Sample} = \frac{Area_{Sample}}{Area_{Ref}} \times \left(\frac{\eta_{Sample}}{\eta_{Ref}} \right)^2 \times \Phi_{F;ref} \quad (1)$$

where $Area_{Sample}$ and $Area_{Ref}$ are the integrated fluorescence for the sample and the reference and η_{Sample} and η_{Ref} are the refractive index of sample and reference solutions respectively. The uncertainty in the experimental value of Φ_F has been estimated to be approximately 10%. Phosphorescence quantum yields (Φ_P) of the iridium complex were determined analogously to Φ_F , using argon-saturated meso-tetra-5,10,15,20-phenylporphine as reference ($\Phi_F = 0.11$ in toluene).⁵

Time-resolved fluorescence decays were registered with a time-correlated single photon counting system (Fluotime 200, PicoQuant GmbH, Berlin, Germany). The samples were excited at 375 or 504 nm by means of a picosecond laser diode or a pulsed LED, respectively, working at 10 MHz repetition rate. Fluorescence decays were acquired at the emission maxima using a red-sensitive Hamamatsu H5783 photosensor module was used for detection, and they were analyzed using the PicoQuant FluoFit 4.6.6 data analysis software. The counting frequency was always kept below 1%.

Singlet oxygen generation was studied by time-resolved near-infrared phosphorescence by means of a customised setup. Briefly, a pulsed Nd:YAG laser (FTSS355-Q, Crystal Laser, Berlin, Germany) working at 1 or 10 kHz repetition rate at 355 nm (0.5 μ J per pulse) or 523 nm (1.2 μ J per pulse) was used to excite the sample. A 1064-nm rugate notch filter (Edmund Optics) and an uncoated SKG-5 filter (CVI Laser Corporation) were placed in the laser path

to remove any NIR emission. The light emitted by the sample was filtered with a 1000-nm long-pass filter (Edmund Optics) and later by a narrow bandpass filter at 1275 nm (BK-1270-70-B, bk Interferenzoptik). A thermoelectric-cooled NIR-sensitive photomultiplier tube assembly (H9170-45, Hamamatsu Photonics, Hamamatsu, Japan) was used as detector. Photon counting was achieved with a multichannel scaler (NanoHarp 250, PicoQuant). The time dependence of the $^1\text{O}_2$ phosphorescence with the signal intensity $S(t)$ is described by Equation 2, in which τ_T and τ_Δ are the lifetimes of the photosensitizer triplet state and of $^1\text{O}_2$ respectively, and S_0 a preexponential parameter proportional to Φ_Δ .

$$S_{1275}(t) = S_{1275}(0) \times \frac{\tau_\Delta}{\tau_\Delta - \tau_T} \times \left(e^{-t/\tau_\Delta} - e^{-t/\tau_T} \right) \quad (2)$$

The Φ_Δ values of the different samples were obtained by comparing S_0 values of optically matched samples and using an appropriate reference, by means of equation 3.

$$\Phi_{\Delta, \text{sample}} = \Phi_{\Delta, \text{ref}} \times \frac{S_{0, \text{sample}}}{S_{0, \text{Ref}}} \quad (3)$$

The same setup was used to monitor the phosphorescence of the complex and the conjugate, except that the red-sensitive Hamamatsu H5783 photosensor module was used for detection. Transient absorption spectra (Figure S3) were monitored by nanosecond laser flash photolysis using a Q-switched Nd:YAG Laser (Surelite I-10, Continuum) with right-angle geometry and an analysing beam produced by a Xe lamp (PTI, 75 W) in combination with a dual-grating monochromator (mod. 101, PTI) coupled to a UV-Vis radiation detector (PTI 710). The signal was fed to a Lecroy WaveSurfer 454 oscilloscope for digitizing and averaging (typically 10 shots) and finally transferred to a PC for data storage and analysis.

Photostability studies were performed by monitoring fluorescence bleaching of a 5 μM PBS solution of the compounds at 37 $^\circ\text{C}$ irradiated with a high power 505 nm LED (100 mW/cm^2). Fluorescence intensity values were recorded at $t = 0$ (F_0) and after different irradiation times (F)

Table S1. Photophysical properties of the compounds in different solvents at room temperature.

Compound	Solvent	λ_{abs} [nm]	ϵ [mM ⁻¹ cm ⁻¹]	λ_{em} [nm]	Stokes' Shift [cm ⁻¹]	$\phi_{\text{F}}/\phi_{\text{P}}$	τ_{F} [ns]	τ_{P} [ns]	Φ_{Δ} at 355 nm at 532 nm
COUPY 2	PBS	545	34	604	1792	0.14	0.9	-	<0.01
	ACN	548	75	609	1828	0.18	1.4	-	<0.01 <0.01
	DCM	569	67	607	1100	0.70	5.4	-	<0.01 0.03
	benzene	566	63	599	973	0,90	4.2	-	0.02 0.02
Ir(III) complex 3	PBS	305	40	656	17543	>0,01	-	55 (93%) 281 (7%)	<0.01 N/A
	ACN	302	41	660	17961	0,03	-	187	0.42 N/A
	DCM	303	42	665	17966	0,07	-	315	0.23 N/A
	benzene	304	45	678	18145	0,09	-	162	0.30 N/A
Ir(III)- COUPY 6	PBS	550	17	615	1921	0.004	0.37 (73%) 3.3 (27%)	-	<0.01 <0.01
	ACN	555	22	615	1758	0.08	0.51	45 (86%) 269 (14%)	0.23 0.24
	DCM	566	44	602	1056	0.07	0.25	121 (70%) 392 (30)	0.37 0.34
	benzene	565	43	601	1060	0,07	0.24	96 (70%) 234 (30%)	0.19 0.21

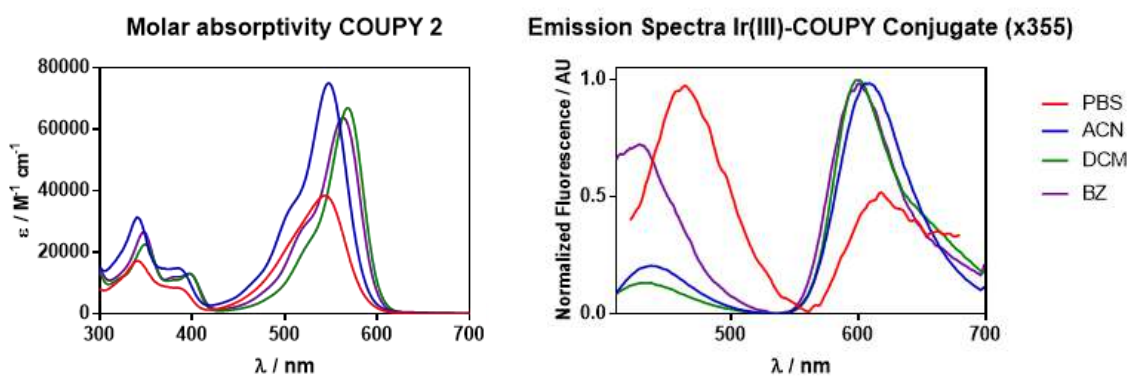


Figure S3. Comparison of the absorption (left) and emission spectra (right) of COUPY **2** in different solvents (PBS buffer, ACN, DCM and benzene).

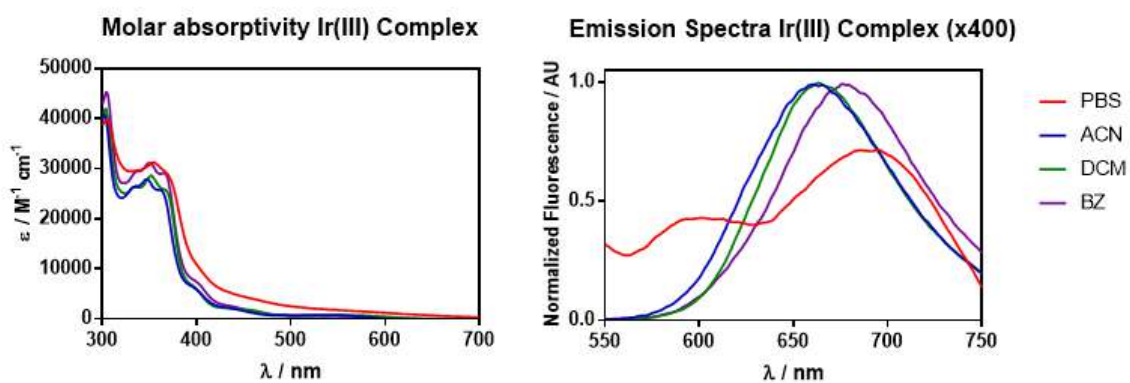


Figure S4. Comparison of the absorption (left) and emission spectra (right) of Ir(III) complex **3** in different solvents (PBS buffer, ACN, DCM and benzene).

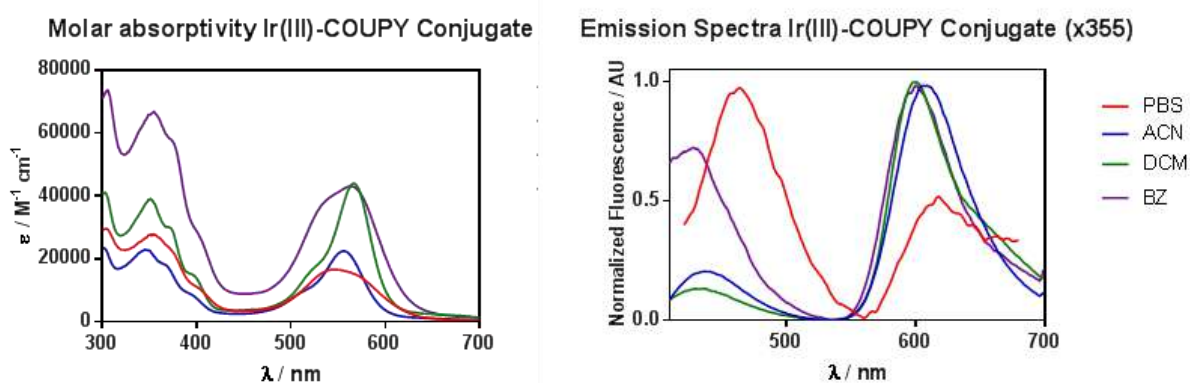


Figure S5. Comparison of the absorption (left) and emission spectra (right) of Ir(III)-COUPY conjugate **6** in different solvents (PBS buffer, ACN, DCM and benzene).

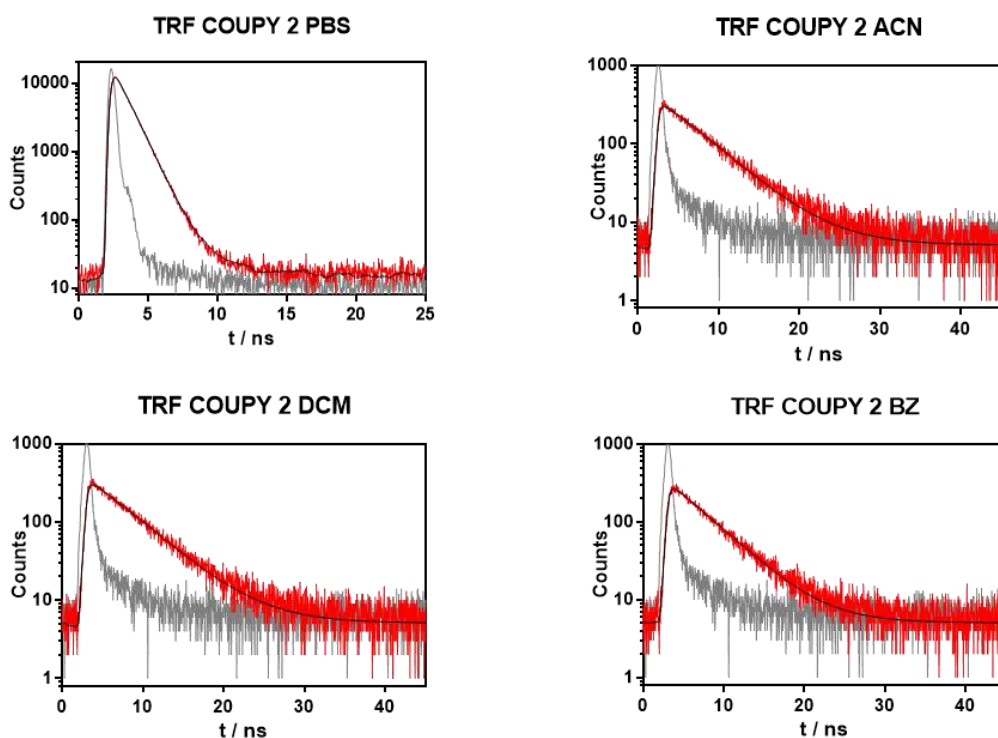


Figure S6. Fluorescence emission decay kinetics of COUPY **2** in PBS, ACN, DCM and benzene, exciting at 375 nm and observing at 600 nm.

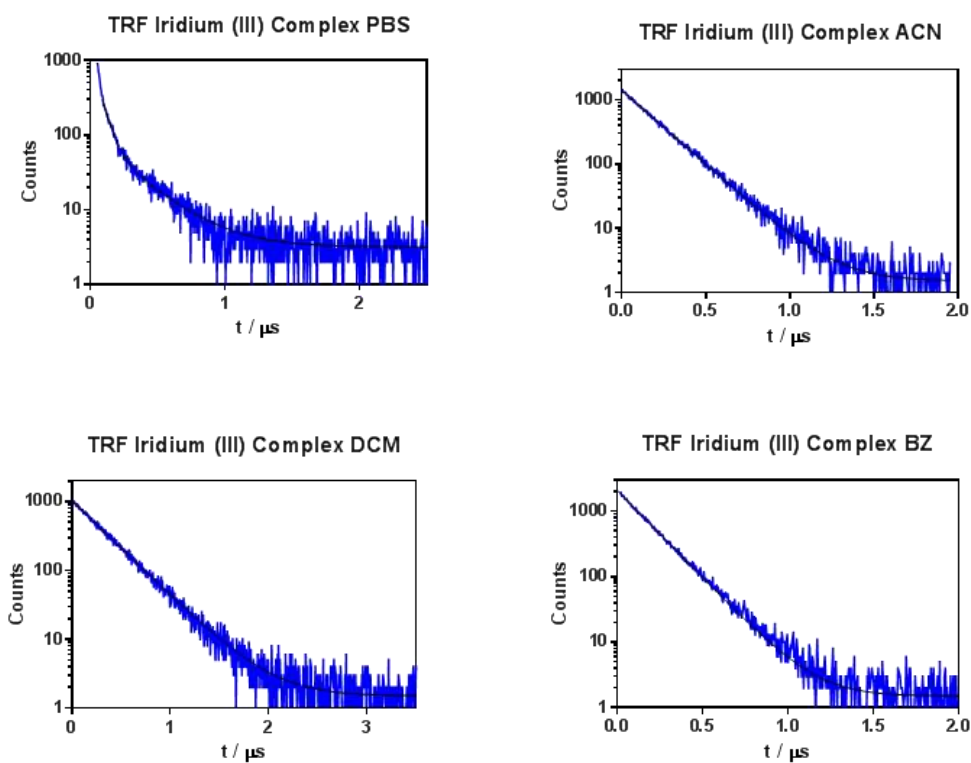


Figure S7. Fluorescence emission decay kinetics of Ir(III) complex **3** in PBS, ACN, DCM and benzene, exciting at 375 nm and observing at 660 nm.

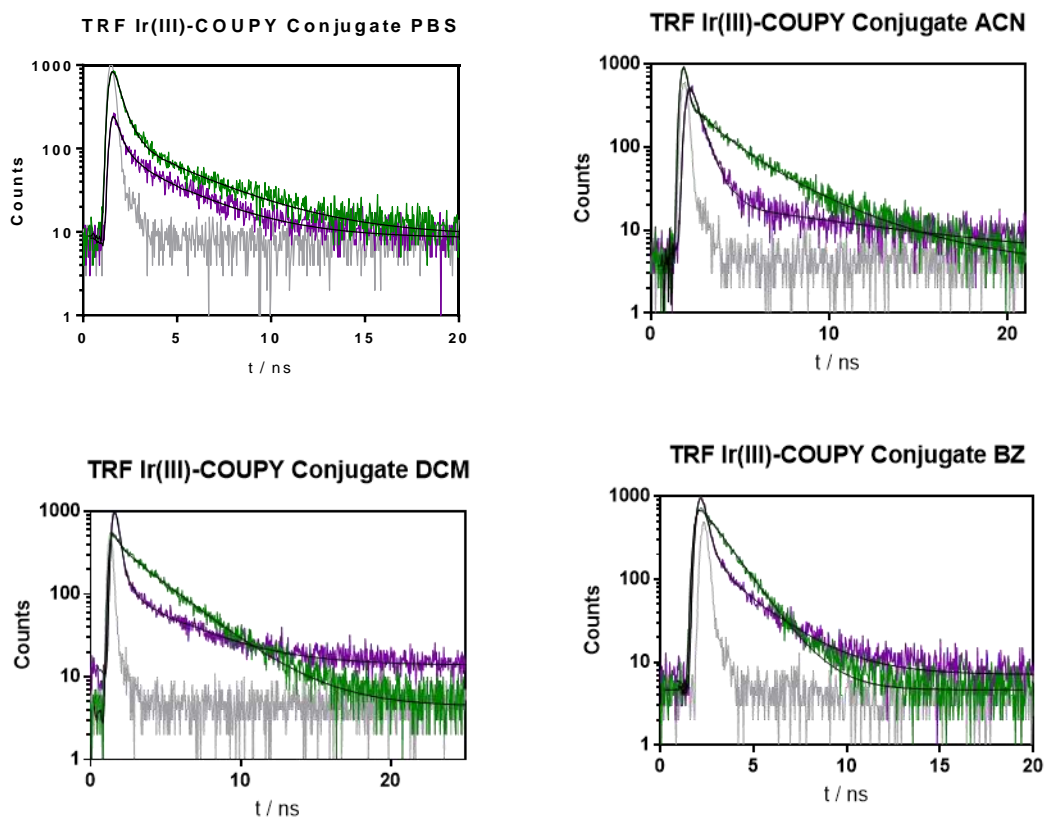


Figure S8. Fluorescence emission decay kinetics of Ir(III)-COUPY conjugate **6** in PBS, ACN, DCM and benzene, excited at 375 nm and observed at 430 nm (green) and 600 nm (purple).

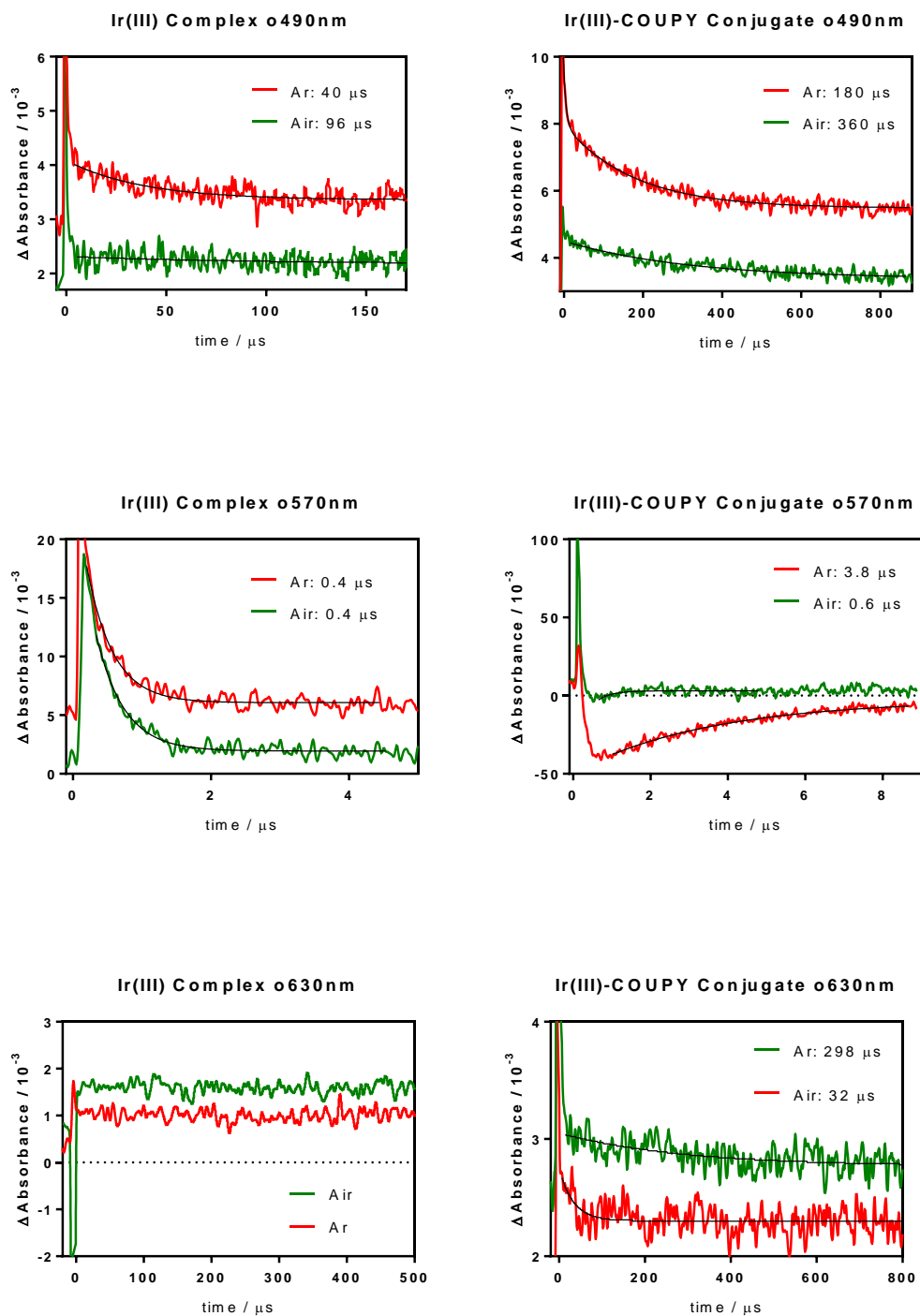


Figure S9. Comparative transient absorption decays of the Ir(III) complex **3** and its coumarin conjugate **6** in argon- or air-saturated dichloromethane solutions upon 355 nm laser flash photolysis. Top: Transient absorption at 490 nm. Lifetime increases in the presence of oxygen. Middle: Transient absorption at 570 nm. Lifetime decreases in the presence of oxygen. Bottom: Transient absorption at 630 nm. A new very long-lived species is formed in the case of the complex, while a decrease in the lifetime is observed for the conjugate.

3.- Fluorescence imaging

HeLa Cells were maintained in DMEM (Dulbecco Modified Eagle Medium) containing low glucose (1 g/L) and supplemented with 10% foetal calf serum (FCS), 50U/mL penicillin-streptomycin and 2 mM *L*-glutamine. For cellular uptake experiments and posterior observation under the microscope, cells were seeded on glass bottom dishes (P35G-1.5-14-C, Mattek). 24 h after cell seeding, cells were incubated at 37 °C for 30 min with coumarin **2** (0.5 μM) or Ir(III)-COUPY conjugate **6** (5 μM) in supplemented DMEM. Then, cells were washed three times with DPBS (Dulbecco's Phosphate-Buffered Saline) to remove the excess of the compounds and kept in low glucose DMEM without phenol red for fluorescence imaging.

All microscopy observations were performed using a Zeiss LSM 880 confocal microscope equipped with a 561 nm laser. The microscope was also equipped with a full enclosure imaging chamber (XLmulti S1, Pecon) connected to a 37 °C heater and a 5% CO₂ providing system. Cells were observed using a 63X 1.2 multi immersion objective. The compounds were excited using the 561 nm laser and emission detected from 570 to 670 nm. Image analysis was performed using Fiji.⁶ All images are colorized using the Fire lookup table from Fiji.

4.- Biological studies

4.1.- Cytotoxicity

HeLa cells were used to determine photo-activation properties of the investigated compounds. Cells were seeded on the 96-well plates at the density of 5000 cells/well and incubated overnight. Subsequently, the medium was removed, cells were washed with HBSS and treated with increasing concentrations of the tested compounds diluted in HBSS (without antibiotics). Hypoxic conditions were induced by nitrogen atmosphere in CO₂/O₂ controlled humidified incubator. Hypoxic samples were kept in the oxygen-starved atmosphere during the whole experiment. The treatment schedule was as follows: 1 h of incubation in the dark, followed by 1 h incubation under irradiation conditions (irradiated) [using Photoreactor LZC-ICH2 from Luzchem (Canada) fitted with Vis lamps (cool white fluorescent tubes, 400–700 nm, with mounted green filter ($\lambda_{\text{max}} = 550 \text{ nm}$, the final light intensity applied to the samples was 58 W m^{-2} , 21 J cm^{-2}). Samples were also irradiated with lamps centered at 420 nm (blue light) with the final intensity of 77 W m^{-2} (28 J cm^{-2}). The temperature in the light chamber during irradiation was $37 \text{ }^{\circ}\text{C}$. Control samples were stored in the dark (non-irradiated) and then incubated again for 1 h in the humidified CO₂ incubator. After that the cells were washed again with HBSS and the wells were loaded with 200 μL of culture medium. The MTT assay was performed after 70 h of recovery time since the end of the incubation with the investigated compounds. 10 μL of a freshly diluted MTT solution (2.5 mg mL^{-1}) was added to each well and the plate was incubated at $37 \text{ }^{\circ}\text{C}$ in a humidified 5% CO₂ atmosphere for 4 h. At the end of the incubation period the medium was removed and the formazan product was dissolved in 100 μL of DMSO. The cell viability was evaluated by measurement of the absorbance of 570 nm, using an Absorbance Reader SUNRISE TECAN SCHOELLER. IC₅₀ values were calculated from curves constructed by plotting cell survival (%) *versus* drug concentration (μM). All experiments were made in triplicate. The reading values were converted to the percentage of control (% cell survival). Cytotoxic effects were expressed as IC₅₀.

4.2.- Cellular accumulation

Cellular accumulation of iridium from iridium compounds was measured in HeLa cells. The cells were seeded in 100 mm petri dishes at a density of $1 \cdot 10^6$ cells/dish. For determination of energy-dependent uptake mechanisms of Ir compounds the cells were treated with 5 μM of the investigated compounds and incubated for 2 h at 4 °C (energy-dependent mechanisms inhibition) or at 37 °C (physiological conditions). The cells were subsequently washed with PBS, harvested, counted and pelleted by centrifugation at 300 g, 3 min, 4 °C. Cell pellets were digested by a high-pressure microwave digestion system (MARS5, CEM) with HCl (11 M) to give a fully homogenized solution, and the final iridium content was determined by ICP-MS (Agilent Technologies, CA, USA).

4.3.- Determination of ROS induced after the treatment with the compounds in HeLa cells

Reactive oxygen species were determined by using CellRox[®] Oxidative stress Deep red reagent (Life Technologies[™], USA). HeLa cells were seeded on the 6-well plate at the density of 1.5×10^5 cells/well and incubated overnight in the humidified CO₂ incubator. The cells were subsequently washed with PBS and treated with 10 μM of the investigated compounds for 1 h in HBSS followed by the irradiation schedule described in the section “Cytotoxicity” (4.1). After 1 h of irradiation (or incubation in the dark), the samples were treated with the CellRox[®] deep red reagent at the final concentration 2.5 μM and incubated for 30 min at 37°C. The cells were finally harvested and analyzed on the flow cytometer (BD FACSVerser). Single cells (3×10^4) were analyzed and plotted to the histogram with bi-exponential scale on the x-axis.

Supplementary legend to Figure 4. Data analysis for determination of ROS in HeLa cells by the flow cytometry after the irradiation with green (left) of blue light (right). Cells were pre-incubated with specific ROS scavengers and then treated with 6 (1 h in the dark followed by 1 h under the irradiation with green (21 J cm^{-2}) or blue light (28 J cm^{-2})). Scavengers remained throughout the experiment. Positive control (irradiated cells treated with 6 without scavengers), negative controls (untreated, irradiated cells) are indicated as the horizontal lines with SDs (dashed lines). Data are the mean of three independent experiments. Star at the top of the bar indicate a significant difference from positive control with $p \leq 0.01$ calculated by using analysis of variance (ANOVA) and non-parametric student's t-test. Error bars are the SDs.

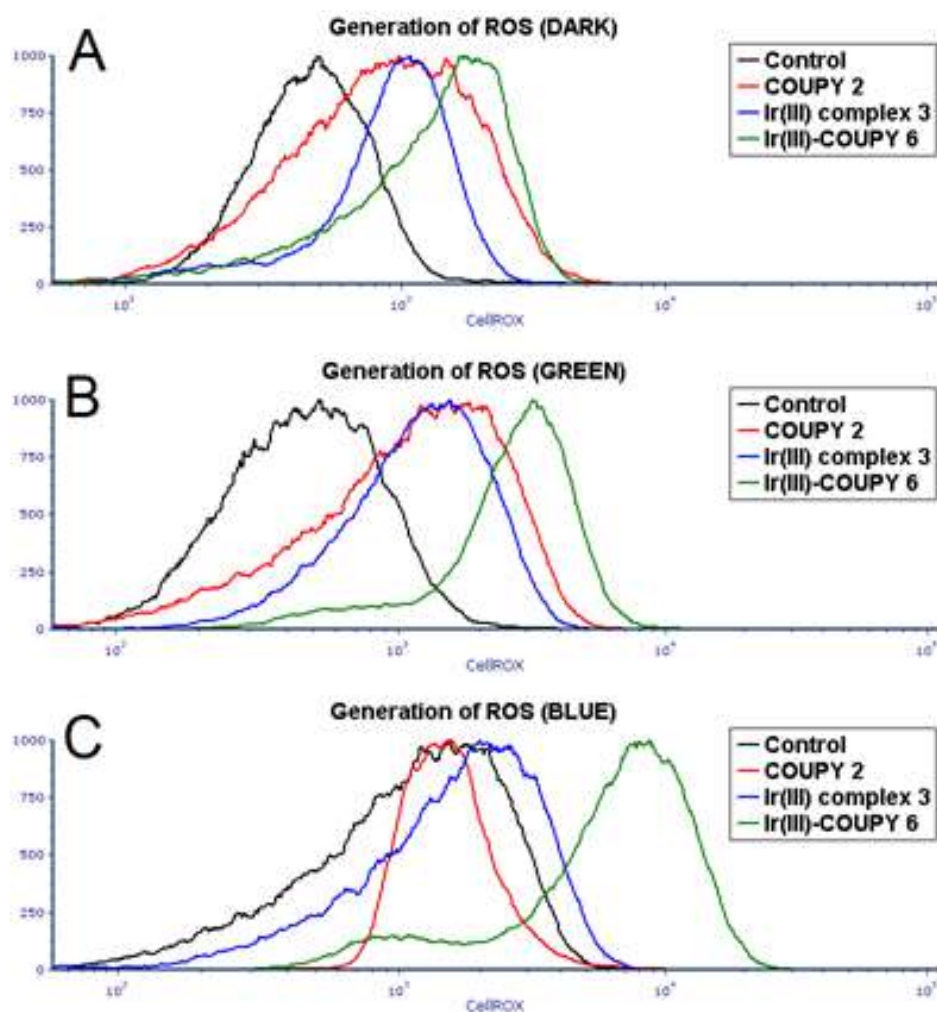


Figure S10. Original FC histograms for determination of ROS in HeLa cells. A) Control, non-irradiated cells, B) cells irradiated with blue light (28 J cm^{-2}) and C) cells irradiated with green light (21 J cm^{-2}). Cells were treated with $10 \text{ }\mu\text{M}$ of tested compounds. Control histograms black line, coumarin 2 red line, Ir(III) complex 3 blue line and Ir(III)-COUPY conjugate 6 green line. $3 \cdot 10^4$ cells were analyzed, and the representative histograms from three independent experiments were expressed on the bi-exponential scale.

4.4.- Selective scavenging of ROS in HeLa cells after the treatment with COUPY 2, Ir(III) complex 3 and Ir(III)-COUPY conjugate 6

Chemicals

Sodium pyruvate, D-mannitol, sodium azide, tiron (4,5-Dihydroxy-1,3-benzenedisulfonic acid disodium salt monohydrate) and ebselen (2-Phenyl-1,2-benzisoselenazol-3(2H)-one) were from Sigma Aldrich, Darmstadt, Germany.

Selective scavenging of ROS in HeLa cells

HeLa cells were seeded at the density of 15000 cells/cm² on the 6-well plates and incubated overnight. For determination of specific ROS generated in HeLa cells, the cells were pre-treated with selective ROS scavengers, incubated for 1 h at 37 °C and subsequently treated with COUPY 2, Ir(III) complex 3 or Ir(III)-COUPY conjugate 6 (10 μM). Formation of hydrogen peroxide (H₂O₂) was prevented by the use of sodium pyruvate at the final concentration of 10 mM,⁷ hydroxyl radicals ([•]OH⁻) were scavenged by D-mannitol applied at the concentration of 50 mM,^{8,9} generation of superoxide anions ([•]O₂⁻) was silenced by the treatment with 5 mM of tiron (4,5-Dihydroxy-1,3-benzenedisulfonic acid disodium salt monohydrate),^{10,11} singlet oxygen (¹O₂) was eliminated with sodium azide at the concentration of 5 mM,⁷ Generation of peroxynitrite anion species was prevented by the pre-treatment with 50 μM of ebselen (2-Phenyl-1,2-benzisoselenazol-3(2H)-one).^{11,12,13,14} The antioxidants remained throughout the experiment. After the pre-treatment with selective ROS scavengers, the cells were treated for 2 h with 10 μM of conjugate 6 (1 h of incubation in the dark followed by 1 h of irradiation with green light 550 nm; 58.2 W m⁻² (21 J cm⁻²) or blue light 420 nm; 76.8 ± 2.9 W m⁻²; 28 J cm⁻²). After the irradiation, the cells were collected, stained by using CellRox[®] Oxidative stress Deep red reagent (Life Technologies[™], USA) and analyzed on the flow cytometer (BD FACSVerser). Data were analyzed by using FCS Express 6 (DeNovo software; Glendale, CA).

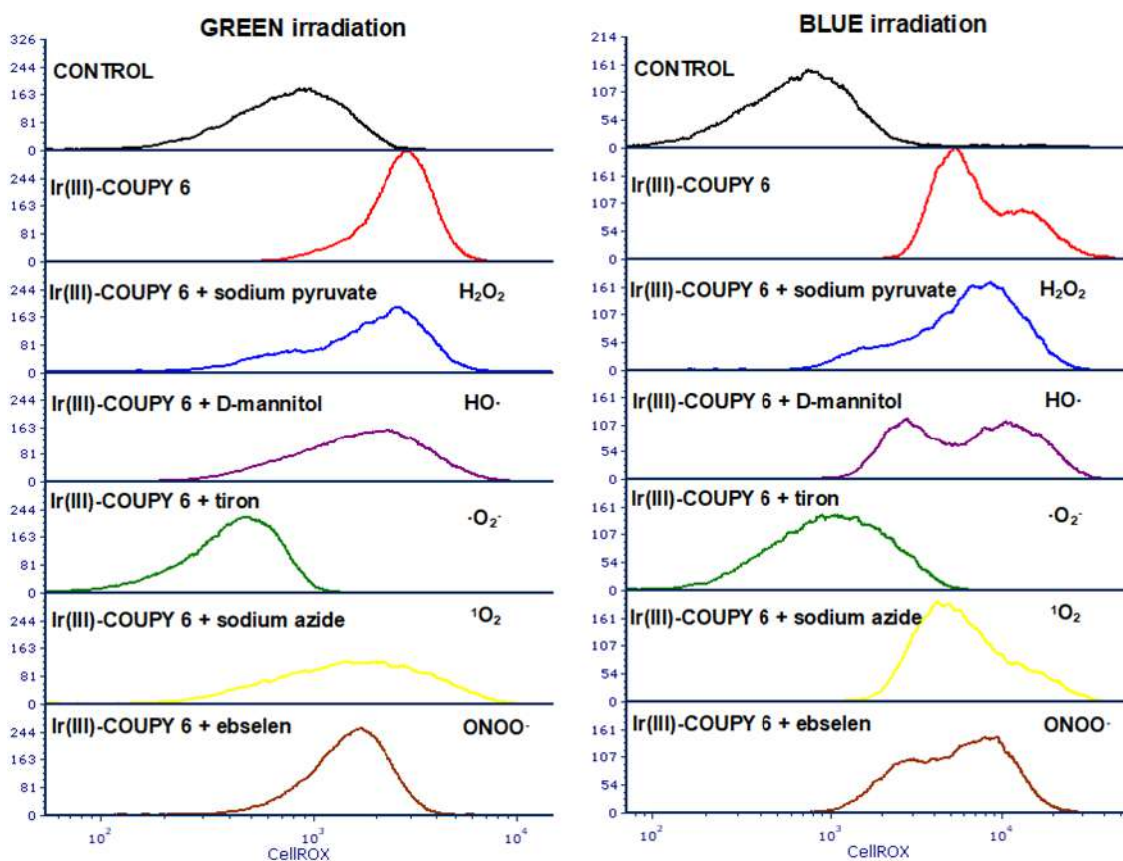


Figure S11. Original histograms for determination of ROS in HeLa cells by the flow cytometry after the irradiation with green (left) of blue light (right panel). Cells were pre-incubated for 1 h with specific ROS scavengers: sodium pyruvate (10 mM), D-mannitol (50 mM), tiron (5 mM), sodium azide (5 mM) and ebselen (50 μ M). Cells were treated with 10 μ M of Ir(III)-COUPY conjugate **6**, incubated for 1 h in the dark followed by 1 h under the irradiation with green (21 J cm^{-2}) or blue light (28 J cm^{-2}). Controls were treated with an appropriate amount of DMSO. Scavengers remained throughout the experiment. Data are the representatives of three independent experiments expressed on the histograms with bi-exponential scale.

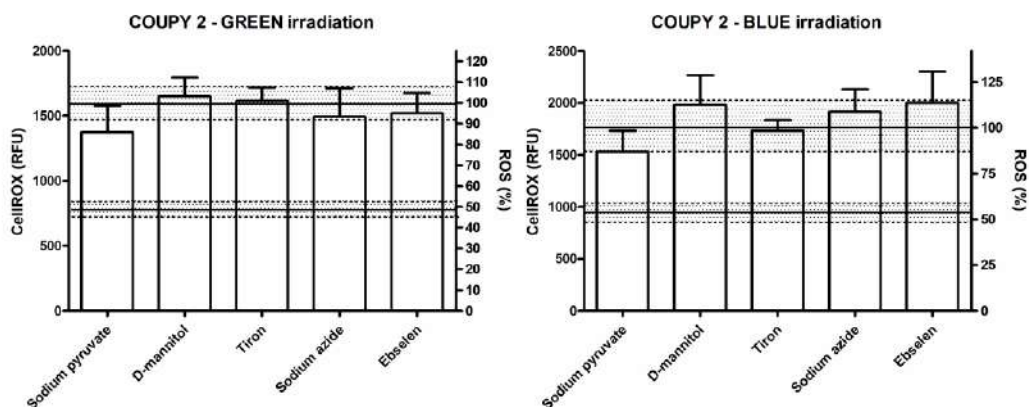


Figure S12. Data analysis for the determination of ROS in HeLa cells by flow cytometry after the irradiation with green (left) or blue light (right). Cells were pre-incubated with specific ROS scavengers and then treated with COUPY **2** (1 h in the dark followed by 1 h under the irradiation with green (21 J cm^{-2}) or blue light (28 J cm^{-2})). Scavengers remained throughout the experiment. Positive control (irradiated cells treated with COUPY **2** without scavengers), negative controls (untreated, irradiated cells) are indicated as the horizontal lines with SDs (dashed lines). Data are the mean of three independent experiments. Error bars are the SDs.

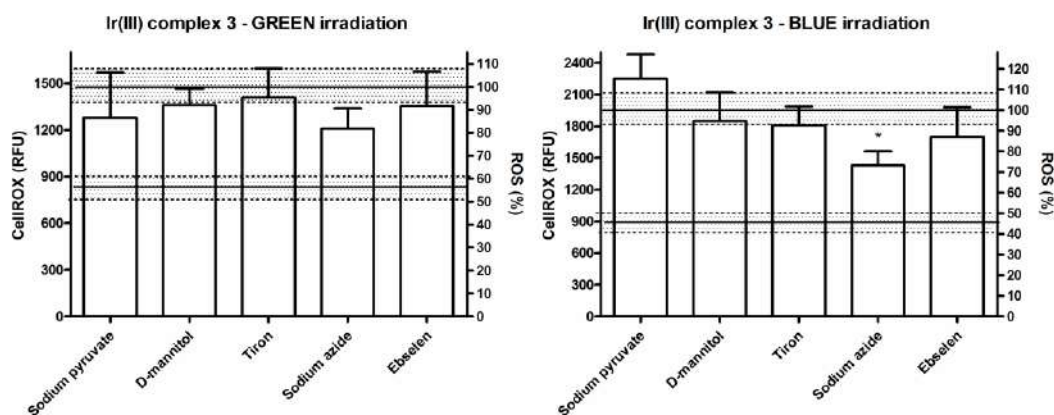


Figure S13. Data analysis for the determination of ROS in HeLa cells by flow cytometry after the irradiation with green (21 J cm^{-2}) (left) or blue light (28 J cm^{-2}) (right). Cells were pre-incubated with specific ROS scavengers and then treated with Ir(III) complex **3** (1 h in the dark followed by 1 h under the irradiation). Scavengers remained throughout the experiment. Positive control (irradiated cells treated with **3** without scavengers), negative controls (untreated, irradiated cells) are indicated as the horizontal lines with SDs (dashed lines). Data are the mean of three independent experiments. Star at the top of the bar indicates a significant difference from positive control with $p \leq 0.01$ calculated by using analysis of variance (ANOVA) and non-parametric student's t-test. Error bars are the SDs.

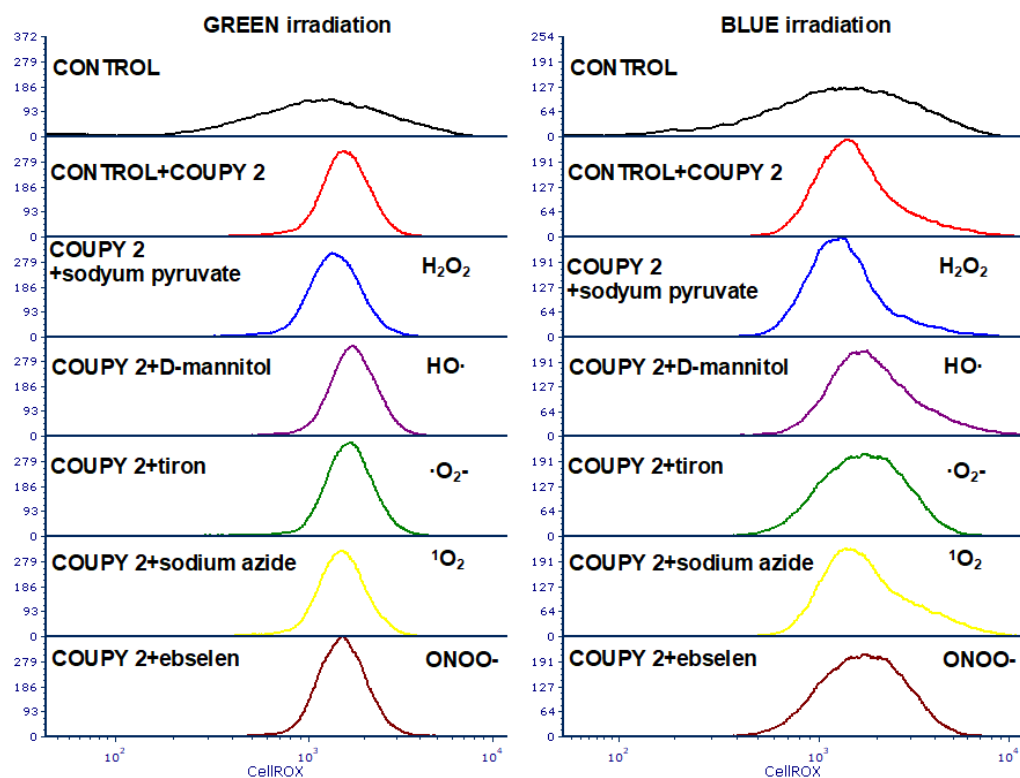


Figure S14. Original histograms for the determination of ROS in HeLa cells by flow cytometry after the irradiation with green (21 J cm^{-2}) (left) or blue light (28 J cm^{-2}) (right panel). Cells were pre-incubated for 1 h with specific ROS scavengers: sodium pyruvate (10 mM), D-mannitol (50 mM), tiron (5 mM), sodium azide (5 mM) and ebselen ($50 \mu\text{M}$). Cells were subsequently treated with $10 \mu\text{M}$ of COUPY 2, incubated for 1 h in the dark followed by 1 h under the irradiation. Controls were treated with an appropriate amount of DMSO. Scavengers remained throughout the experiment. Data are the representatives of three independent experiments expressed on the histograms with bi-exponential scale.

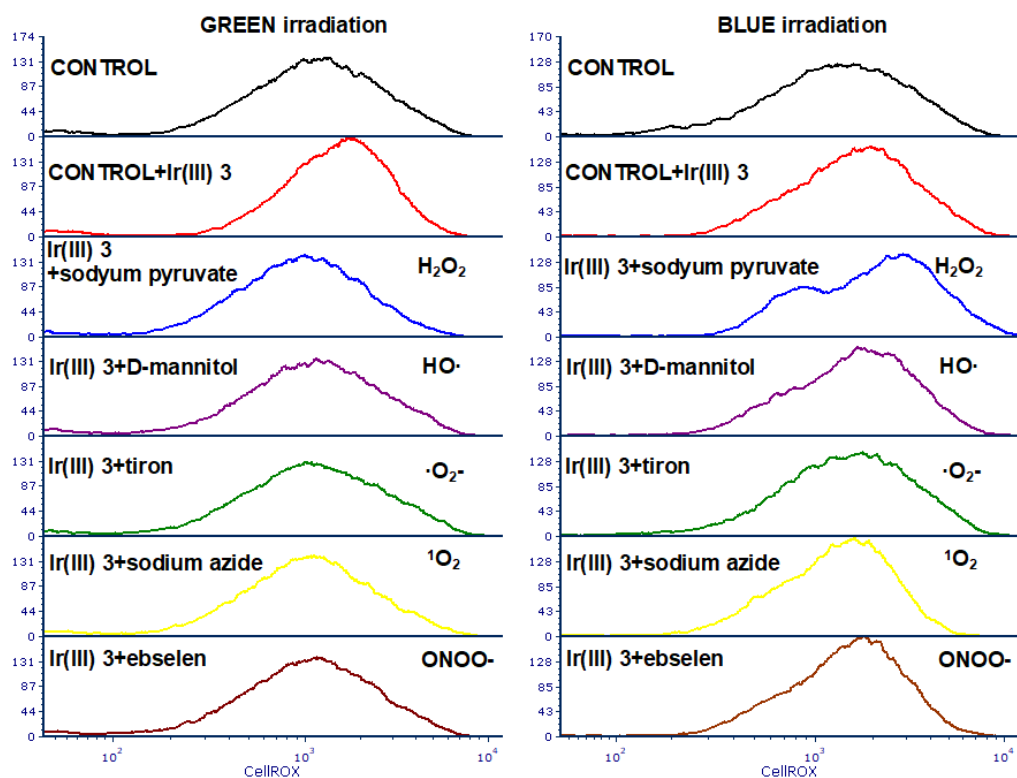


Figure S15. Original histograms for the determination of ROS in HeLa cells by flow cytometry after the irradiation with green (21 J cm^{-2}) (left) or blue light (28 J cm^{-2}) (right panel). Cells were pre-incubated for 1 h with specific ROS scavengers: sodium pyruvate (10 mM), D-mannitol (50 mM), tiron (5 mM), sodium azide (5 mM) and ebselen (50 μM). Cells were subsequently treated with 10 μM of Ir(III) complex **3**, incubated for 1 h in the dark followed by 1 h under the irradiation. Controls were treated with an appropriate amount of DMSO. Scavengers remained throughout the experiment. Data are the representatives of three independent experiments expressed on the histograms with the bi-exponential scale.

4.5.- Superoxide anion radical production by HeLa cells after treatment with Ir(III)-COUPY 6.

For detection of superoxide anion radicals in HeLa cells, a commercial superoxide anion radical assay kit from Sigma was used.¹⁵ Cells were seeded at the density of 7.5×10^5 per well on 96w-plate, treated with $10 \mu\text{M}$ of Ir(III) COUPY 6 for 1 h in the dark, followed by 1 h under the irradiation with blue light (420 nm , 28 J cm^{-2}). To test the effect of superoxide dismutase (SOD), samples were incubated with 10 units of SOD included in the assay kit. The assay is based on the oxidation of luminol by superoxide anion radicals. The oxidation of luminol produces chemiluminescence light, which was detected after the incubation with the enhancer solution on Infinite M200 chemiluminescence reader.

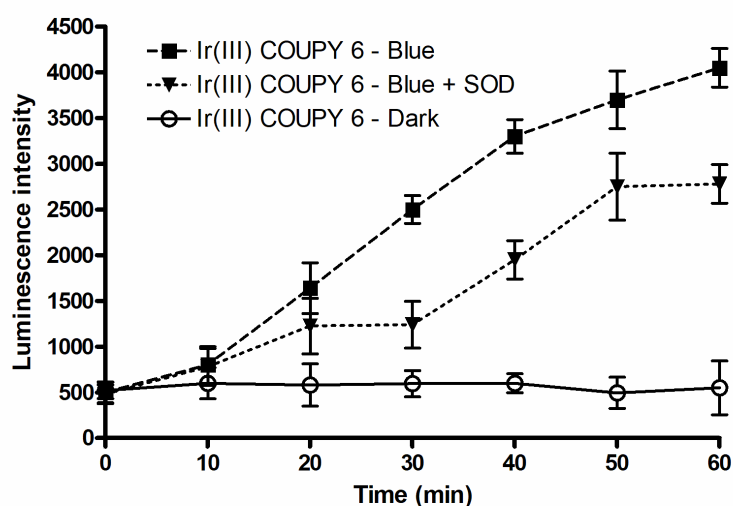


Figure S16. Superoxide anion production by HeLa cells after the treatment with $10 \mu\text{M}$ Ir(III)-COUPY 6. Cells were incubated for 1 h in the dark, followed by 1 h incubation under the irradiation with blue light (28 J cm^{-2}) (420 nm) or in the dark and in the presence or absence of superoxide dismutase (SOD). Luminescence intensity was monitored for 1 h.

4.6.- Superoxide anion radical production and characterization using DHR123 as fluorescence probe.

Dihydrorhodamine 123 was used as the superoxide anion radical indicator.¹⁶ It can be oxidized by $\cdot\text{O}_2^-$, to the fluorescent rhodamine 123. All compounds (10 μM) were prepared in PBS (0.2 % DMSO). To this solution, DHR123 was added so that its final concentration was 10 μM . Then the samples were irradiated in 0.5 x 0.5 cm cuvette by blue light (455 nm centered LED) for indicated time intervals. Immediately, the fluorescence spectra were collected by using Varian Cary Eclipse spectrofluorophotometer. The excitation wavelength was set to 500 nm, the excitation and emission slit widths were 5 nm, and the integration time was set to 5 s.

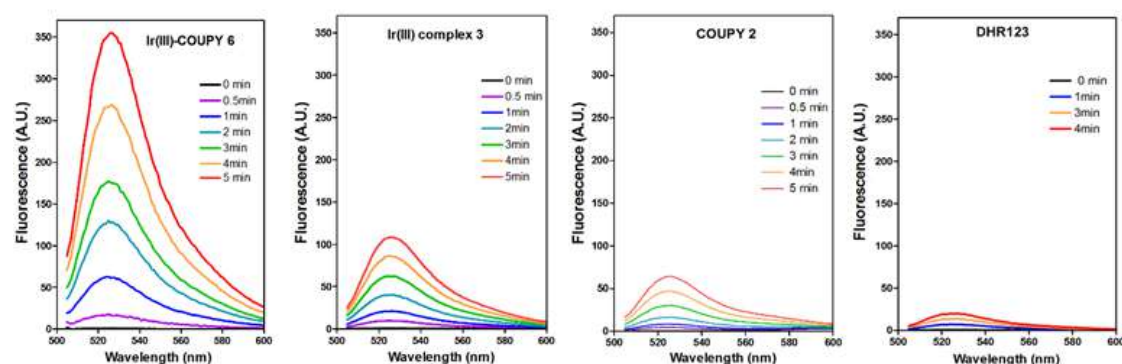


Figure S17. Fluorescence spectra of DHR123 induced by irradiation with blue light (455 nm) in the presence of Ir(III)-COUPY **6** (first panel), Ir(III) complex **3** (second panel), COUPY **2** (third panel) or without any compound (DHR 123 alone, forth panel).

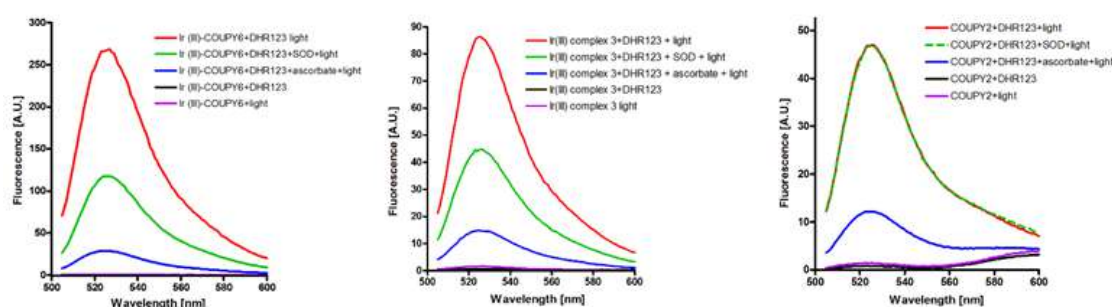


Figure S18. The effect of SOD (100 U mL^{-1}) and sodium ascorbate (100 μM) on DHR123 fluorescence induced by irradiation in the presence of Ir(III)-COUPY **6** (left panel), Ir(III) complex **3** (central panel) and COUPY **2** (right panel). The samples were irradiated by blue light (455nm) for 4 min.

4.7.- Impact of selective superoxide anion scavenger tiron on the viability of HeLa cells

HeLa cells were seeded on the 96-well plates at the density of 5000 cells/well and incubated overnight. Then the medium was removed, cells were washed with HBSS and pre-treated with 5 mM of tiron. After 1 h of incubation, the cells were treated with increasing concentration of Ir(III)-COUPY conjugate **6** diluted in HBSS (without antibiotics; tiron remained). Treatment schedule was as following: 1 h of incubation in the dark, followed by 1 h incubation under irradiation conditions (irradiated) [using Photoreactor LZC-ICH2 from Luzchem (Canada) fitted with Vis lamps (cool white fluorescent tubes, 400–700 nm, with mounted green filter; the final light intensity applied to the samples was 58.2 W m^{-2} (21 J cm^{-2}); the temperature in the light chamber during irradiation was $37 \text{ }^\circ\text{C}$), samples irradiated with blue lamps (420 nm) were irradiated with the final intensity of 76.8 W m^{-2} (28 J cm^{-2}). After that, the cells were washed again with HBSS, and the wells were loaded with 200 μL of culture medium. The MTT assay was performed after 70 h of recovery time since the end of the incubation with the compounds. 10 μL of a freshly diluted MTT solution (2.5 mg mL^{-1}) was added to each well, and the plate was incubated at $37 \text{ }^\circ\text{C}$ in a humidified 5% CO_2 atmosphere for 4 h. At the end of the incubation period, the medium was removed, and the formazan product was dissolved in 100 μL of DMSO. The cell viability was evaluated by measurement of the absorbance of 570 nm, using an Absorbance Reader SUNRISE TECAN SCHOELLER. IC_{50} values were calculated from curves constructed by plotting cell survival (%) versus drug concentration (μM). All experiments were made in triplicate. The reading values were converted to the percentage of control (% cell survival).

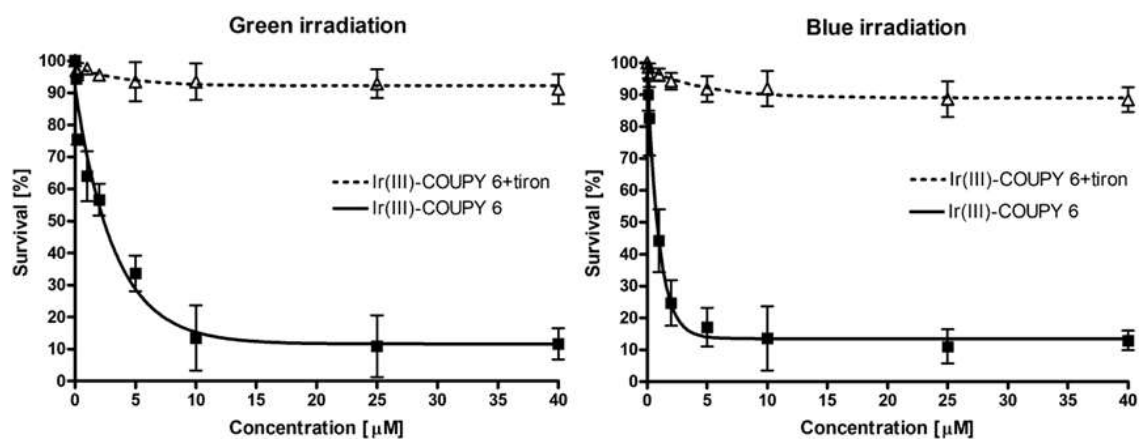
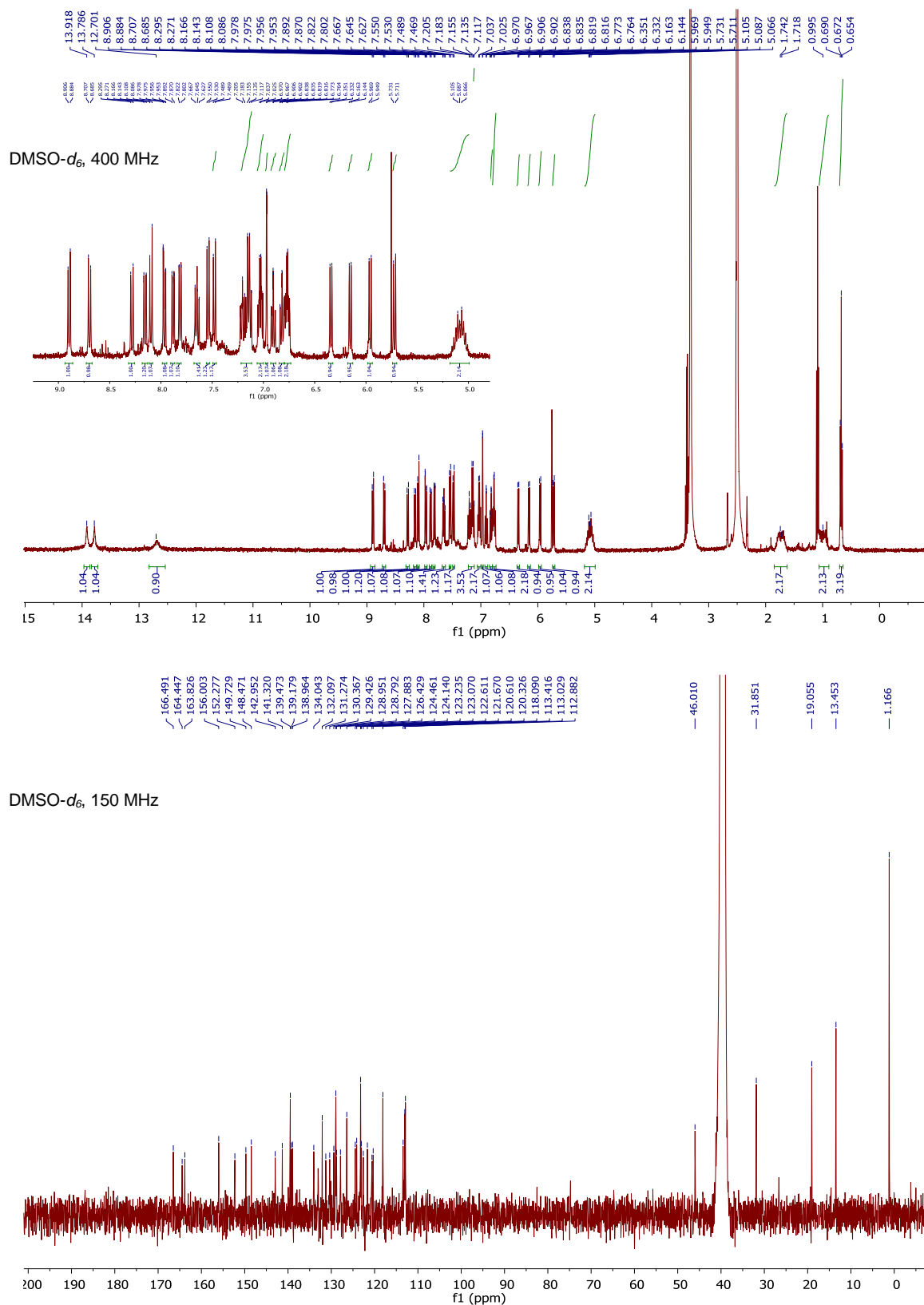


Figure S19. Impact of selective superoxide anion radical scavenger tiron on the viability of HeLa cells under the irradiating conditions. Cells were pretreated for 1 h with 5 mM of tiron before the test of cellular viability determined for **6**. Tiron remained throughout the treatment with **6** [1 h of incubation followed by 1 h of irradiation with green (21 J cm^{-2}) or blue light (28 J cm^{-2}) (green-left panel; blue-right panel)] but not during the 70 h of the recovery time. Error bars are the SDs calculated from three independent experiments.

5. ^1H and ^{13}C NMR spectra and HR ESI-MS of the compounds

Complex 4



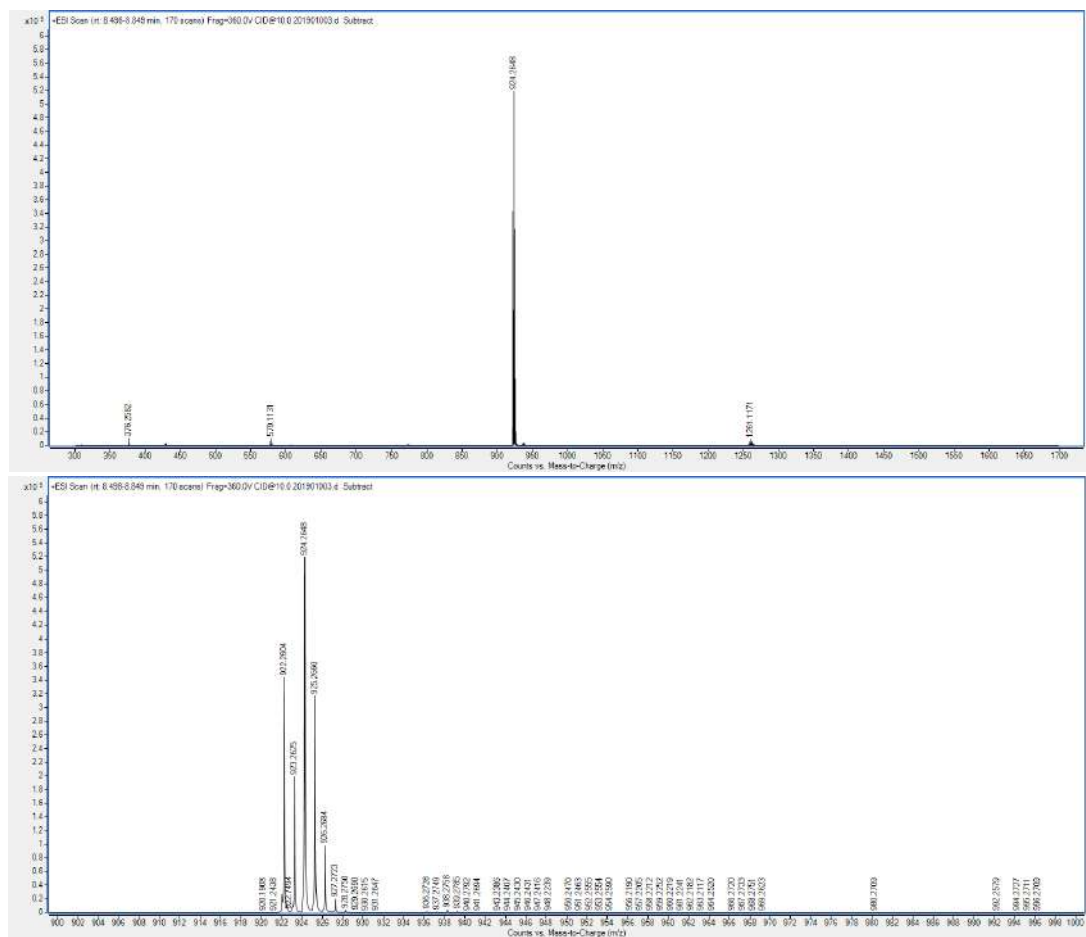


Figure S21. HR ESI-MS spectrum of complex 4.

Coumarin 10

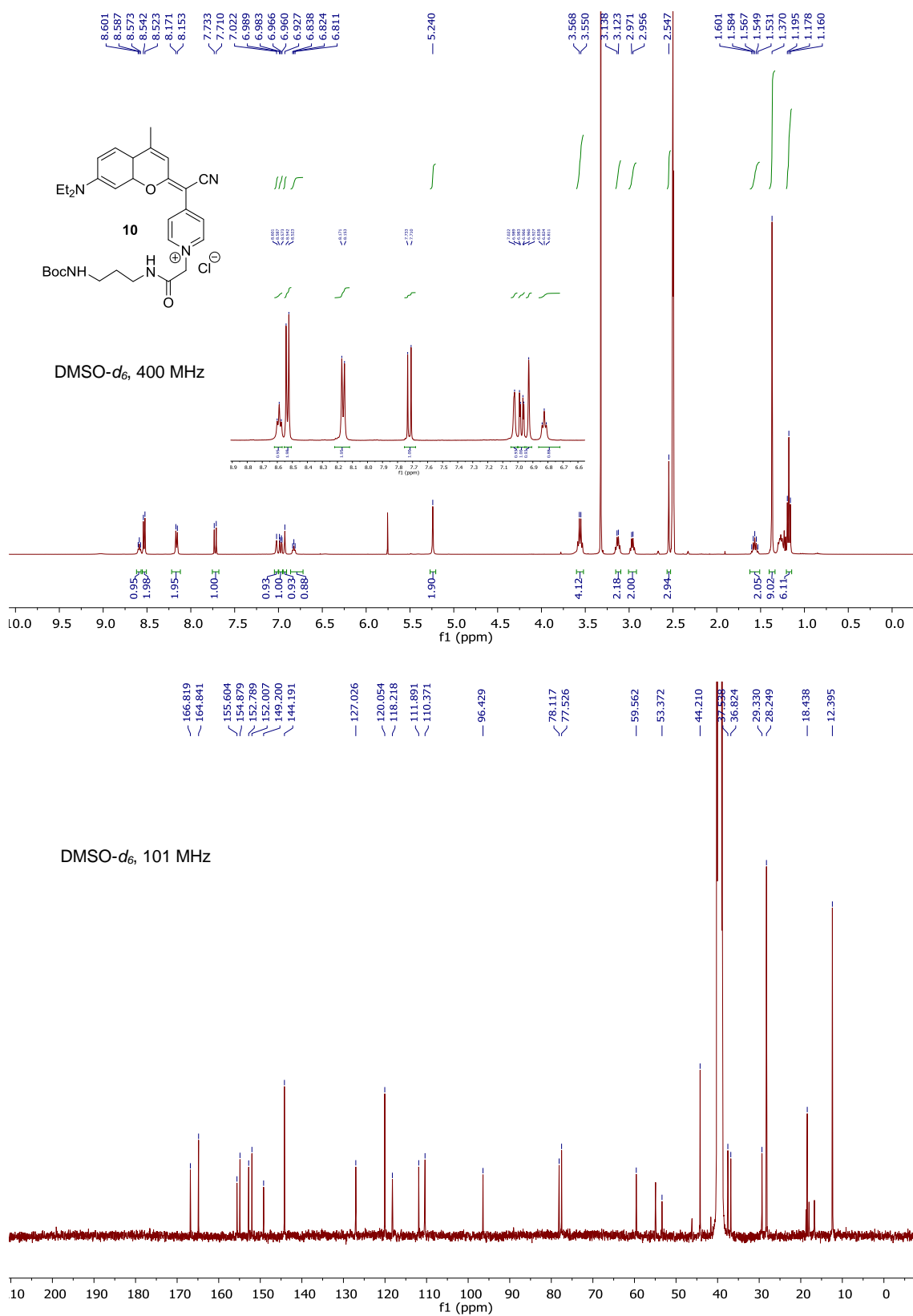


Figure S22. ¹H and ¹³C NMR spectra of coumarin 10 in DMSO-*d*₆.

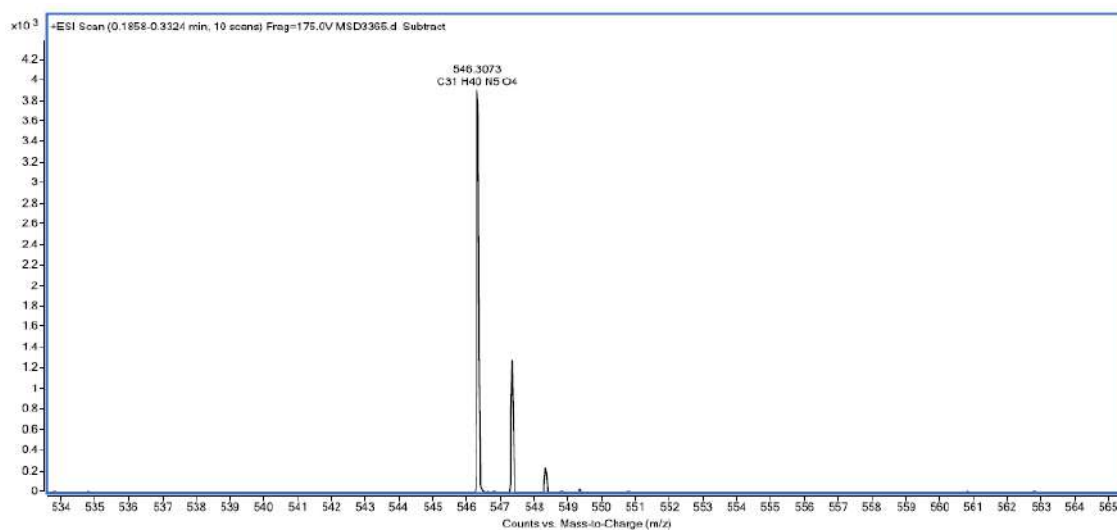
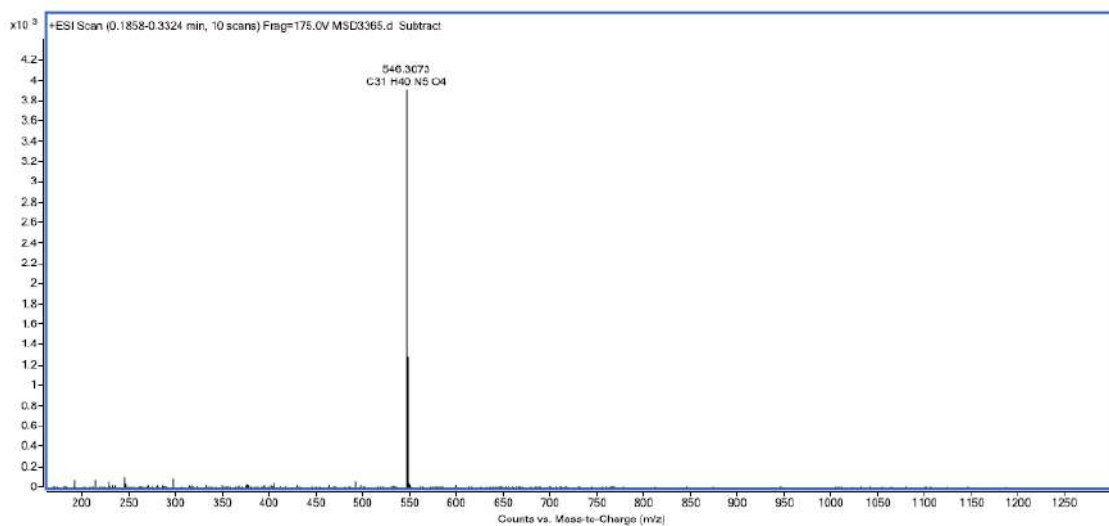


Figure S23. HR ESI-MS spectrum of coumarin 10.

Ir(III)-COUPY conjugate 6

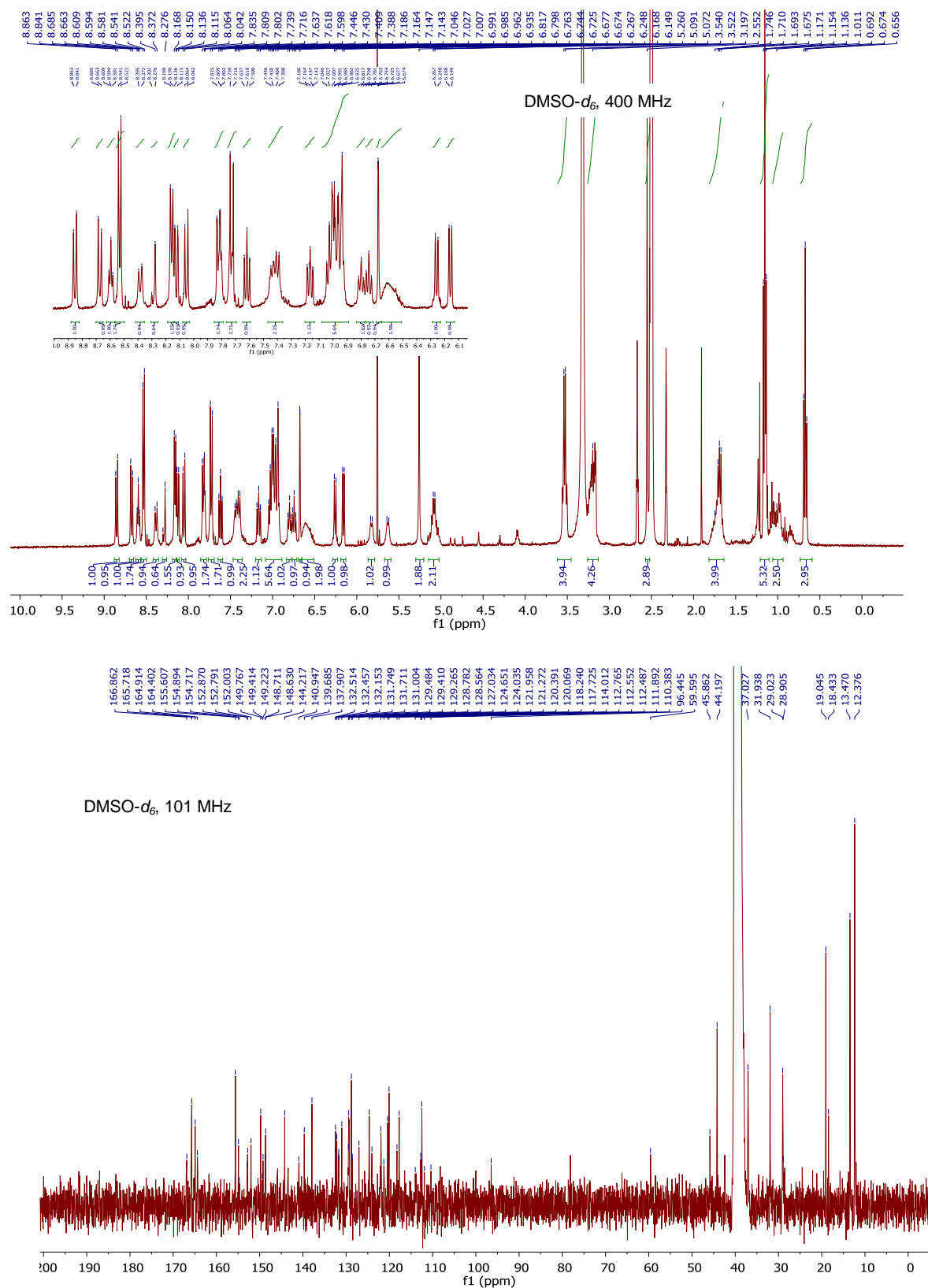


Figure S24. ^1H and ^{13}C NMR spectra of Ir(III)-COUPY conjugate 6 in $\text{DMSO-}d_6$.

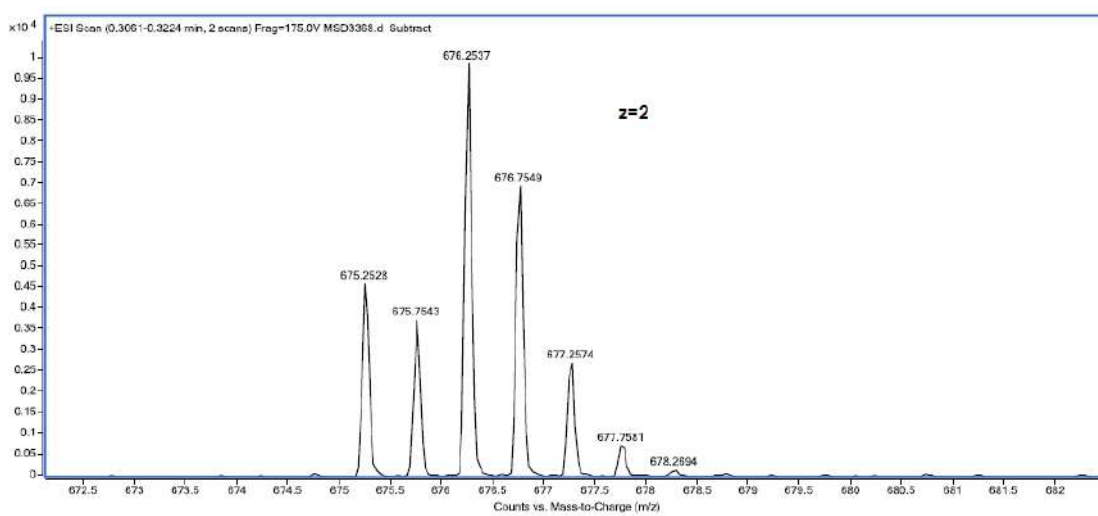
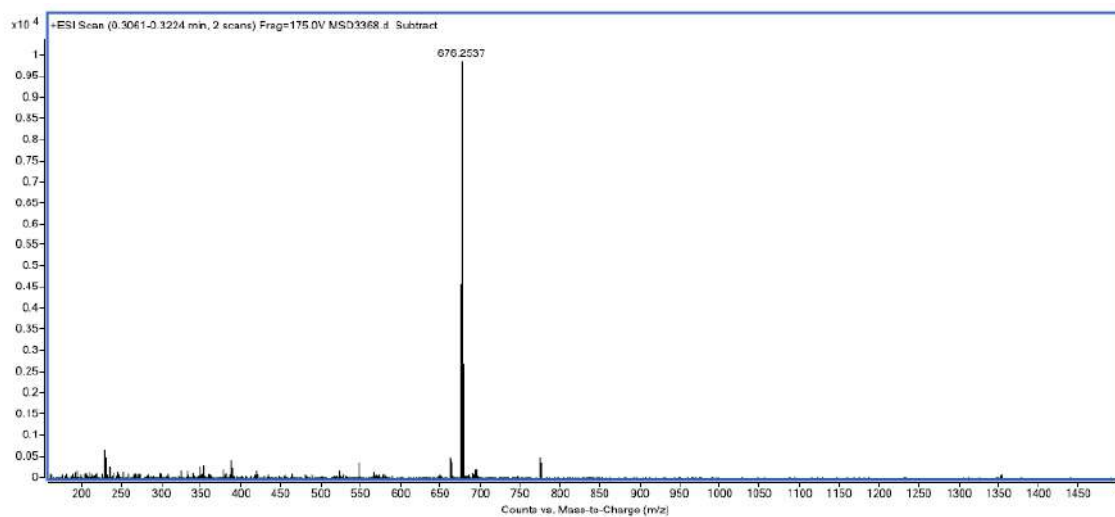


Figure S25. HR ESI-MS spectrum of Ir(III)-COUPY conjugate **6**.

6.- References

- (1) Yellol, J.; Perez, S. A.; Yellol, G.; Zajac, J.; Donaire, A.; Viguera, G.; Novohradsky, V.; Janiak, C.; Brabec, V.; Ruiz, J. *Chem. Commun.* **2016**, *52*, 14165–14168.
- (2) a) Ma, D.-L.; Lin, S.; Lu, L.; Wang, M.; Hu, C.; Liu, L.-J.; Ren, K.; Leung, C.-H. *J. Mater. Chem. B* **2015**, *3*, 4780-4785; b) Jones, J. E.; Jenkins, R. L.; Hicks, R. S.; Hallett, A. J.; Pope, S. J. A. *Dalton Trans.* **2012**, *41*, 10372-10381.
- (3) a) Gandioso, A.; Bresolí-Obach, R.; Nin-Hill, A.; Bosch, M.; Palau, M.; Galindo, A.; Contreras, S.; Rovira, A.; Rovira, C.; Nonell, S.; Marchán, V. Redesigning the Coumarin Scaffold into Small Bright Fluorophores with Far-Red to Near-Infrared Emission and Large Stokes Shifts Useful for Cell Imaging. *J. Org. Chem.* **2018**, *83*, 1185–1195; b) Rovira, A.; Gandioso, A.; Goñalons, M.; Galindo, A.; Massaguer, A.; Bosch, M.; Marchán, V. Solid-phase approaches for labelling targeting peptides with far-red emitting coumarin fluorophores. *J. Org. Chem.* **2019**, dx.doi.org/10.1021/acs.joc.8b02624.
- (4) Magde, D.; Brannon, J. H.; Cremers, T. L.; Olmsted, J. Absolute luminescence yield of cresyl violet. A standard for the red. *J. Phys. Chem.* **1979**, *83*, 696–699.
- (5) Seybold, P. G.; Gouterman, M. Porphyrins XIII: Fluorescence Spectra and Quantum Yields. *J. Mol. Spectrosc.* **1969**, *31*, 1–13.
- (6) Schindelin, J.; Arganda-Carreras, I.; Frise, E.; Kaynig, V.; Longair, M.; Pietzsch, T.; Preibisch, S.; Rueden, C.; Saalfeld, S.; Schmid, B.; Tinevez, J. Y.; White, D. J.; Hartenstein, V.; Eliceiri, K.; Tomancak, P.; Cardona, A. Fiji: an open-source platform for biological-image analysis. *Nat. Methods* **2012**, *9*, 676–682.
- (7) Bello, R. I.; Gómez-Díaz, C.; Navarro, F.; Alcaín, F. J.; Villalba, J. M. Expression of NAD(P)H:Quinone Oxidoreductase 1 in HeLa Cells. *J. Biol. Chem.* **2001**, *276*, 44379–44384.
- (8) Ding, X.; Xu, Q.; Liu, F.; Zhou, P.; Gu, Y.; Zeng, J.; An, J.; Dai, W.; Li, X. Hematoporphyrin monomethyl ether photodynamic damage on HeLa cells by means of reactive oxygen species production and cytosolic free calcium concentration elevation. *Cancer Lett.* **2004**, *216*, 43–54.
- (9) Zhang, X.; Rosenstein, B. S.; Wang, Y.; Lebwohl, M.; Wei, H. Identification of possible reactive oxygen species involved in ultraviolet radiation-induced oxidative DNA damage. *Free Radic. Biol. Med.* **1997**, *23*, 980–985.

- (10) Krishna, C. M.; Liebmann, J. E.; Kaufman, D.; DeGraff, W.; Hahn, S. M.; McMurry, T.; Mitchell, J. B.; Russo, A. The catecholic metal sequestering agent 1,2-dihydroxybenzene-3,5-disulfonate confers protection against oxidative cell damage . *Arch.Biochem.Biophys.* **1992**, *294*, 98–106.
- (11) Yamada, J.; Yoshimura, S.; Yamakawa, H.; Sawada, M.; Nakagawa, M.; Hara, S.; Kaku, Y.; Iwama, T.; Naganawa, T.; Banno, Y.; Nakashima, S.; Sakai, N. Cell permeable ROS scavengers, Tiron and Tempol, rescue PC12 cell death caused by pyrogallol or hypoxia/reoxygenation. *Neurosci. Res.* **2003**, *45*, 1–8.
- (12) Antony, S.; Bayse, C. A. Modeling the mechanism of the glutathione peroxidase mimic ebselen. *Inorg. Chem.* **2011**, *50*, 12075–12084.
- (13) Bhowmick, D.; Srivastava, S.; D’Silva, P.; Mugesh, G. Highly Efficient Glutathione Peroxidase and Peroxiredoxin Mimetics Protect Mammalian Cells against Oxidative Damage. *Angew. Chem. Int. Ed.* **2015**, *54*, 8449–8453.
- (14) Ishikawa, K.; Takenaga, K.; Akimoto, M.; Koshikawa, N.; Yamaguchi, A.; Imanishi, H.; Nakada, K.; Honma, Y.; Hayashi, J. ROS-Generating Mitochondrial DNA Mutations Can Regulate Tumor Cell Metastasis. *Science* **2008**, *320*, 661–664.
- (15) D. Mihov, J. Vogel, M. Gassmann, A. Bogdanova. Erythropoietin activates nitric oxide synthase in murine erythrocytes. *Am. J. Physiol. Cell Physiol.* **2009**, *297*: C378–C388.
- (16) M. Li, J. Xia, R. Tian, J. Wang, J. Fan, J. Du, S. Long, X. Song, J. W. Foley, X. J. Peng. Near-Infrared Light-Initiated Molecular Superoxide Radical Generator: Rejuvenating Photodynamic Therapy against Hypoxic Tumors *J. Am. Chem. Soc.* **2018**, *140*, 14851-14859.

9. Chapter IIb. Publication D

Exploring structure–activity relationships in photodynamic therapy anticancer agents based on Ir(III)-COUPY conjugates.

(A. Rovira *et al.* *Manuscript under preparation*)

Exploring structure–activity relationships in photodynamic therapy anticancer agents based on Ir(III)-COUPY conjugates

Anna Rovira,^{1,#} Enrique Ortega-Forte,^{2,#} Cormac Hally,³ Mireia Jordà,³ Gloria Viguera,² Manel Bosch,⁴ Santi Nonell,³ José Ruiz,^{2,*} Vicente Marchán^{1,*}

¹ Departament de Química Inorgànica i Orgànica, Secció de Química Orgànica, Universitat de Barcelona (UB), and Institut de Biomedicina de la Universitat de Barcelona (IBUB), Martí i Franquès 1-11, E-08028 Barcelona, Spain. Email: vmarchan@ub.edu

² Departamento de Química Inorgànica, Universidad de Murcia, and Institute for Bio-Health Research of Murcia (IMIB-Arrixaca), E-30071 Murcia, Spain. Email: jruiz@um.es

³ Institut Químic de Sarrià, Universitat Ramon Llull, Vía Augusta 390, E-08017 Barcelona (Spain)

⁴ Unitat de Microscòpia Òptica Avançada, Centres Científics i Tecnològics, Universitat de Barcelona, Av. Diagonal 643, E- 08028 Barcelona (Spain)

These authors contributed equally

KEYWORDS: coumarin – cyclometalated iridium(III) complexes – photodynamic therapy – anticancer agents – drug design – photosensitizer

ABSTRACT

Photodynamic therapy holds great promise as a non-invasive anticancer tool against drug-resistant cancers. However, highly effective, non-toxic and reliable photosensitizers with operability under hypoxic conditions remain to be developed. Herein, we took the advantageous properties of both COUPY fluorophores and cyclometalated Ir(III) complexes to develop a novel family of PDT agents based on Ir(III)-COUPY conjugates with the aim of establishing structure–activity relationships. The structural modifications carried out within the coumarin scaffold had a strong impact on the photophysical properties and cellular uptake of the Ir(III)-COUPY conjugates. In addition, all conjugates exhibited high phototoxicity under green light irradiation, which was attributed to the photogeneration of ROS, while remaining non-toxic in the dark regardless of the cancer cell lines studied. Among them, two hit conjugates showed excellent phototherapeutic indexes in cisplatin-resistant A2780cis cancer cells, both in normoxia (≥ 269) and in hypoxia (≥ 147), suggesting that photoactive therapy approaches based on the conjugation of far-red/NIR-emitting COUPY dyes and transition metal complexes could effectively tackle *in vitro* acquired-resistance to cisplatin.

INTRODUCTION

Photodynamic therapy (PDT) has gained great attention in recent years as a promising cancer treatment modality.^{1,2} Unlike conventional approaches based on surgery or chemotherapy, PDT offers several advantages including low invasiveness, high selectivity and efficiency, and reduced toxic side effects that usually compromise patient's health. Upon light irradiation, the interaction of a non-toxic photosensitizer (PS) and oxygen triggers local cytotoxicity through the generation of reactive oxygen species (ROS), that oxidize biomolecules in cells and lead to irreversible damage on tumor cell structures (e.g., membranes and organelles), as well as on the vasculature that deprive the tumor of oxygen and nutrients.³ In addition, increasing evidences show that PDT can trigger the activation of the anticancer immune system throughout the body by immunogenic cell death (ICD).⁴ Depending on the reaction mechanism, PDT can be classified into two main types (I and II).⁵ While type II pathway involves the transformation of molecular oxygen ($^3\text{O}_2$) into singlet oxygen ($^1\text{O}_2$) via an energy transfer process, several other cytotoxic reactive species, mainly superoxide radicals ($\text{O}_2^{\cdot-}$), hydroxyl radicals ($\cdot\text{OH}$) and hydrogen peroxide, are generated in type I photochemical pathways via an electron transfer mechanism.⁶ Although type II photochemical processes are generally considered as the main photosensitization mechanism of most of the conventional PSs, the availability of PDT agents operating at low-oxygen concentrations in the phototherapeutic window (e.g., 650-800 nm) is highly desirable to combat deep-seated hypoxic tumors and to avoid toxicity associated to short wavelengths of light.^{7,8,9}

Transition metal complexes have emerged as promising therapeutic tools in photopharmacology due to several unique properties, including a wide range of coordination numbers, oxidation states and geometries.^{10,11} Among transition metals, Pt(IV), Ru(II), Rh(III), Ir(III) and Os(II) are very attractive candidates for PDT applications since they tend to absorb in the visible region of the electromagnetic spectrum and exhibit relatively high photostability, and long luminescence lifetimes (>100 ns), being an interesting alternative to PSs based on organic fluorophores on clinical use such as porphyrins or chlorins.^{12,13,14,15,16,17} In this context, cyclometalated iridium(III) complexes show excellent anticancer activities and a great potential to overcome some of the main drawbacks of conventional platinum-based chemotherapy (i.e. resistance and toxic side effects).^{18,19} Such metal complexes are likely good candidates for PDT applications as they combine appealing photophysical and photochemical properties within a single compound, including large Stokes' shifts, high luminescent quantum yield, and high efficient singlet oxygen production upon light irradiation. However, most reported

cyclometalated iridium(III) complexes are quite cytotoxic in the dark and only activatable with short wavelengths of light, which compromises further development as efficient PDT agents.

By taking advantage of the well-established anticancer properties of transition metal complexes and of the rich and tunable photophysical and physicochemical properties of small organic chromophores, their conjugation can be exploited for developing theranostic agents for imaging-guided PDT. Examples of this strategy include the conjugation and/or integration of cyclometalated Ir(III) complexes with organic fluorophores such as boron-dipyrromethene (BODIPY)^{20, 21, 22, 23} porphyrin,²⁴ xanthene,²⁵ and rhodamine derivatives.²⁶ Coumarins, which are well-known anticancer scaffolds^{27, 28, 29} and the basis for the development of novel organic fluorophores,³⁰ have also been covalently attached to Ir(III) complexes and used as cyclometalating ligands.^{31, 32, 33, 34} In this context, we have been pioneers in describing a novel class of PDT agents based on the conjugation of a far red to NIR emitting COUPY coumarin to a cyclometalated Ir(III) complex (compounds **1a** and **2a**, respectively, in Figure 1).^{35, 36} The resulting Ir(III)-COUPY conjugate (compound **3a**) was found non-cytotoxic in the dark but highly photocytotoxic after irradiation with visible light, even under hypoxia, the latter being attributable to the selective generation of type I superoxide anion radicals.³⁵ Owing to a strong push-pull character due to the replacement of the carbonyl group of the lactone in the conventional coumarin scaffold by *N*-alkylated cyano(4-pyridine)methylene moieties, COUPY dyes possess several attractive features for bioimaging applications such as absorption and emission within the phototherapeutic window, brightness, high photostability, and large Stokes' shifts.^{37, 38, 39, 40} In addition, we have recently demonstrated that some COUPY dyes exhibit effective in vitro anticancer activities upon visible-light irradiation both under normoxia and hypoxia conditions while exhibiting minimal toxicity towards normal cells, which position them as promising PS candidates for anticancer PDT.⁴¹

Herein, we have synthesized a family of new Ir(III)-COUPY conjugates (compounds **3b-3e**) with the aim of establishing structure–activity relationships (SARs), specially to investigate how the structural modifications within the COUPY scaffold influence the photophysical, photochemical and biological properties of the resulting PSs. As shown in Figure 1, the newly synthesized Ir(III)-COUPY conjugates combine the highly potent cyclometalated Ir(III) complex **2a** and three COUPY derivatives (**1a-1c**) which were connected through flexible or rigid linkers. The absence of the *N,N*-diethylamino electron-donating group (EDG) at the 7-position of the coumarin moiety (**1b**) could provide insights on the involvement of this group on the generation of ROS in the resulting Ir(III)-COUPY conjugate **3b**. Moreover, the

incorporation of a julolidine-fused analogue (**1c**) in Ir(III)-COUPY conjugate **3c** was expected to prevent the twisted intramolecular charge transfer (TICT) state by incorporating the nitrogen atom into a system of fused rings,⁴² which would also influence electron charge transfer between the metal center and the coumarin moiety. Besides investigating the photophysical and photochemical properties of all of the compounds, the results from cellular uptake and cyto- and phototoxicity studies in several cancer cells allowed us to select two Ir(III)-COUPY conjugates (**3d** and **3e**) as promising PSs owing to their excellent phototoxicities in both normoxic and hypoxic conditions upon green light irradiation and reduced *in vitro* dark toxicity.

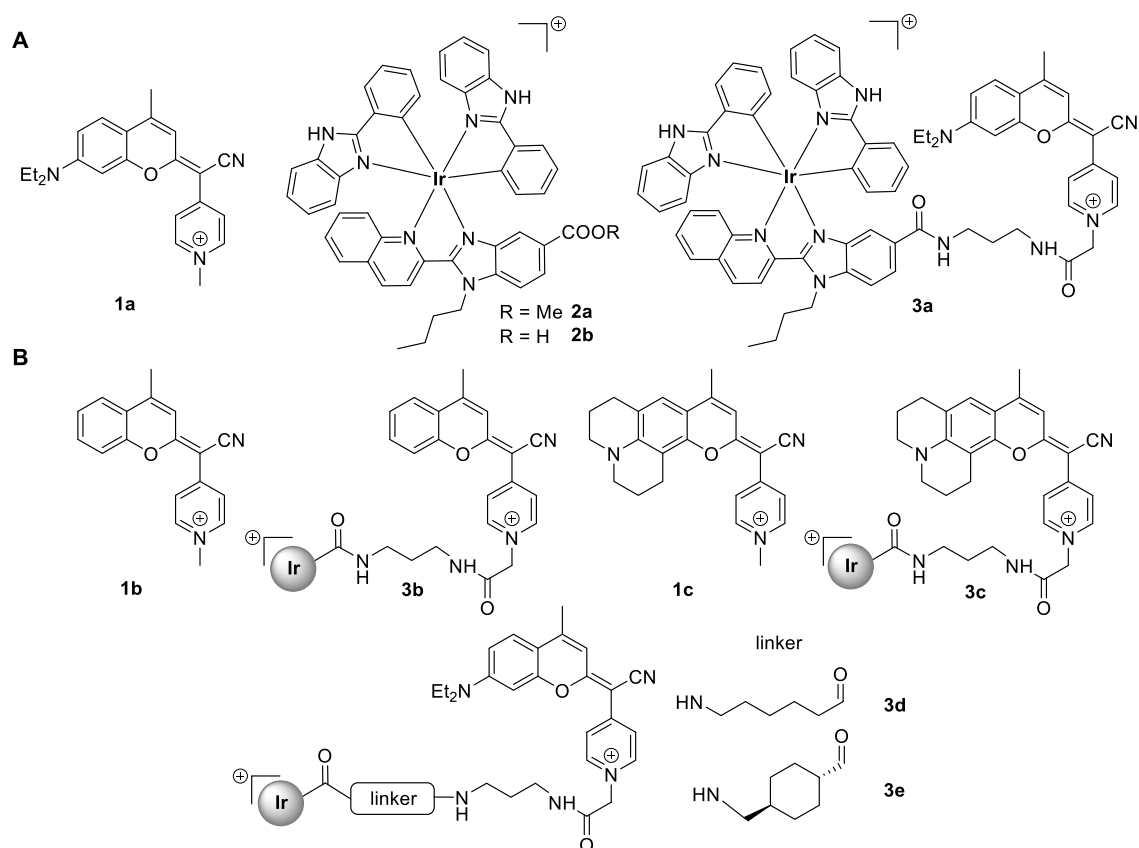
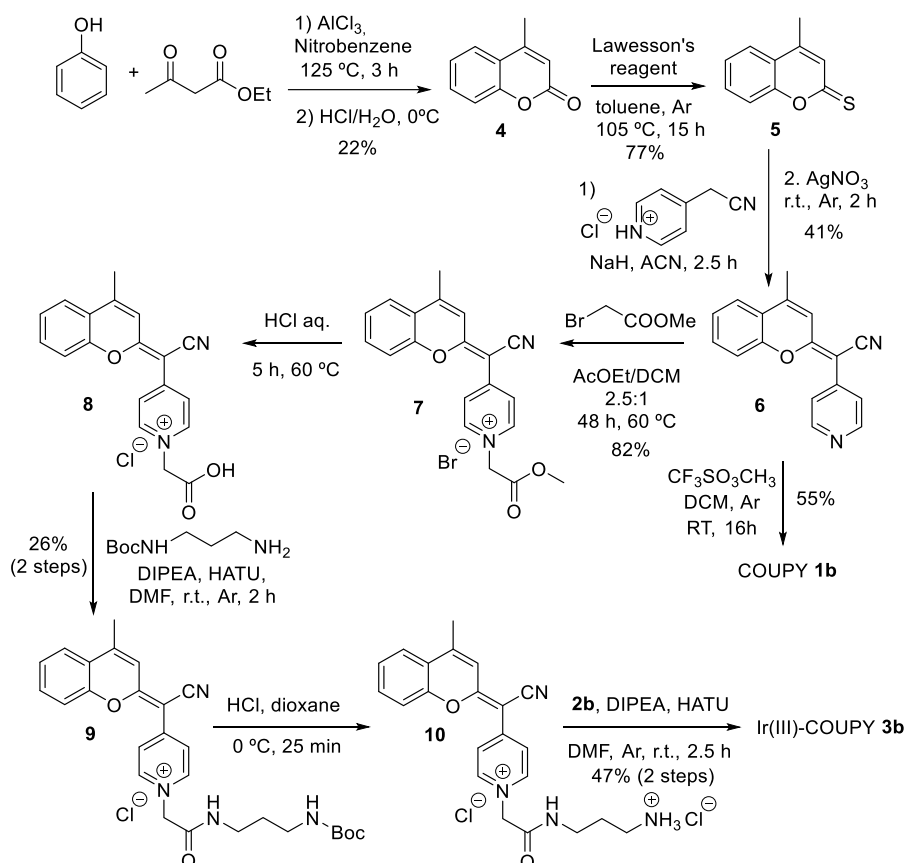


Figure 1. A) Structure of previously evaluated compounds: COUPY coumarin **1a**, cyclometalated Ir(III) complex **2a** and the corresponding Ir(III)-COUPY conjugate **3a**. B) Structure of the new COUPY coumarins (**1b-1c**) and Ir(III)-COUPY conjugates (**3b-3e**) investigated in this work.

RESULTS

Synthesis and characterization of Ir(III)-COUPY conjugates

Synthesis of Ir(III)-COUPY conjugate 3b. As shown in Scheme 1, a convergent approach was used for the synthesis of Ir(III)-COUPY conjugate **3b** in which the carboxylic group of the Ir(III) complex **2b** (Figure 1) was linked to the amino group of coumarin **10** through the formation of an amide bond. As previously indicated, the synthesis of a COUPY derivative lacking the dialkylamino group at the 7-position of the coumarin skeleton was proposed to explore the contribution of this EDG to ROS generation when conjugated to the metal complex.

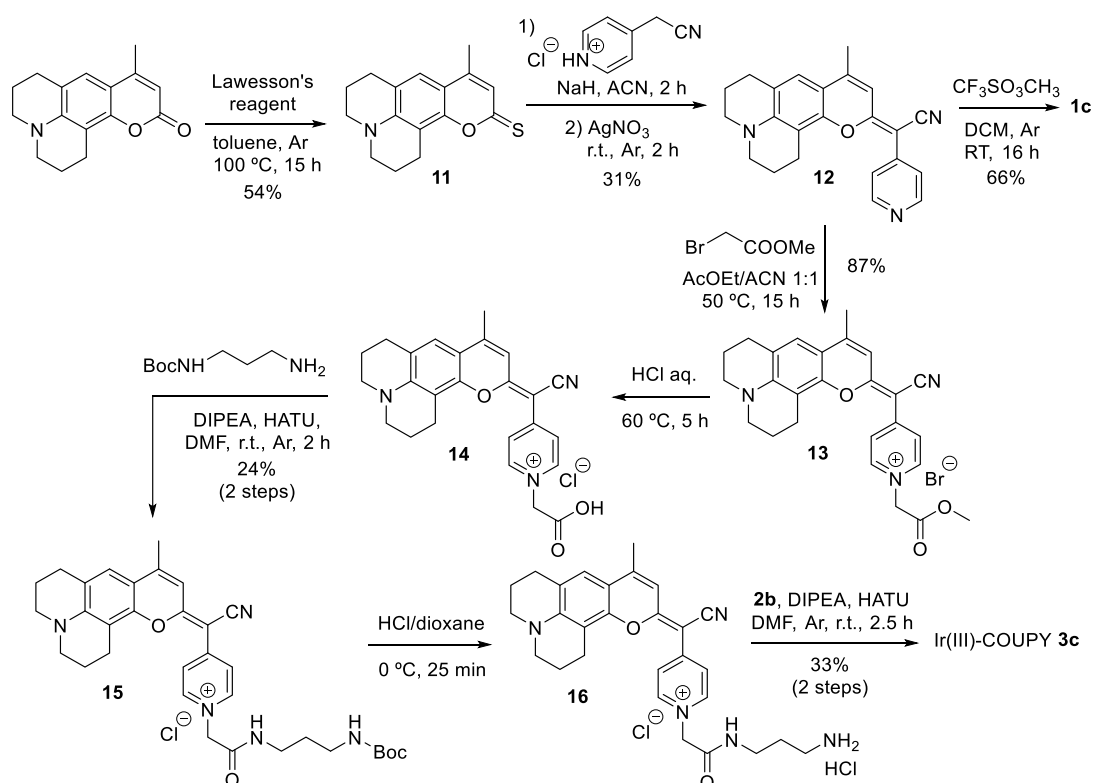


Scheme 1. Synthesis of Ir(III)-COUPY conjugate **3b** and of control COUPY coumarin **1b**.

The synthesis route for COUPY derivative **10** (Scheme 1) involved seven steps starting with a Pechmann condensation between phenol and ethyl acetoacetate that afforded the desired coumarin skeleton (**4**).⁴³ Next, coumarin **4** was reacted with Lawesson's reagent (LW) to provide thiocoumarin **5**, which was condensed with 4-pyridylacetonitrile to give compound **6**. Coumarin ester **7** was obtained with good yield by alkylation of **6** with methyl bromoacetate. After acid hydrolysis, the carboxyl group of coumarin **8** was reacted with *N*-Boc-1,3-propanediamine hydrochloride with the assistance of HATU coupling reagent and DIPEA to yield coumarin **9**, whose Boc protecting group was removed under acidic conditions to give

coumarin derivative **10**. Finally, Ir(III)-COUPY conjugate **3b** was obtained as a dark yellow solid after attachment of the Ir(III) complex to the fluorophore via the formation of an amide bond. All of the compounds depicted in Scheme 1 were purified by silica column chromatography and fully characterized by high-resolution mass spectrometry (HRMS) and ^1H and ^{13}C NMR spectroscopy.

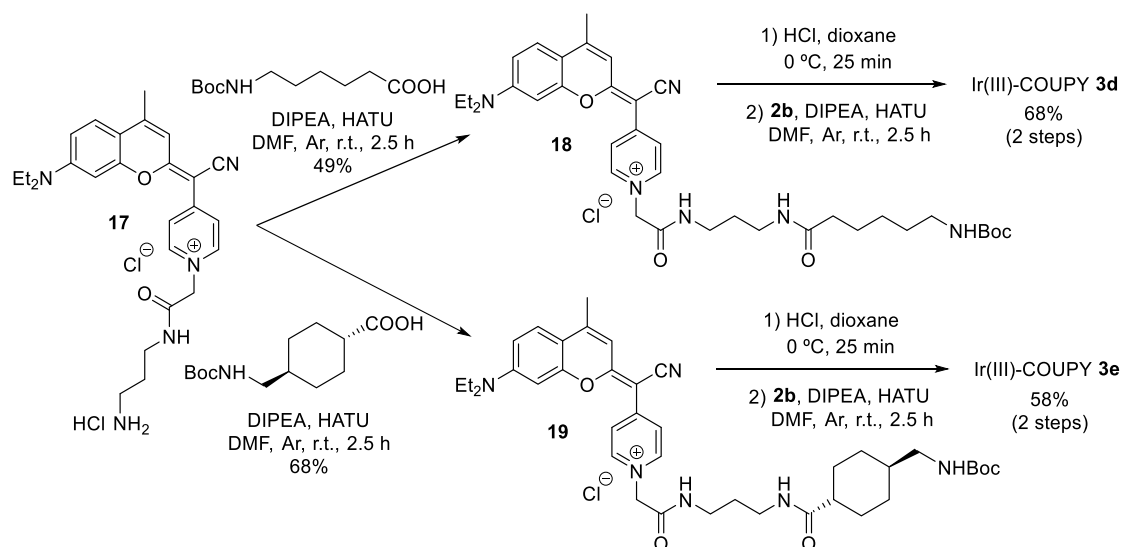
Synthesis of Ir(III)-COUPY conjugate 3c. For the synthesis of Ir(III)-COUPY conjugate **3c** (Scheme 2), we selected a julolidine-fused coumarin analogue to red-shift the absorption maximum with respect to the parent 7-dialkylaminocoumarin. Moreover, as previously stated, rigidification of the amino group was anticipated to have an impact on the photophysical and photochemical properties of the compounds since rotation around the N-C bond is not possible because of the fusion of the six-membered alkyl rings to the aromatic ring. The required amino-containing COUPY derivative **16** was synthesized from a commercially available coumarin precursor following the same procedure as for COUPY **10**. The conjugation between **16** and the Ir(III) complex **2b** afforded Ir(III)-COUPY conjugate **3c** as a dark blue solid after silica column purification. All the compounds were characterized by ^1H and ^{13}C NMR spectroscopy and high-resolution mass spectrometry (HRMS).



Scheme 2. Synthesis of Ir(III)-COUPY conjugate **3c** and control COUPY coumarin **1c**.

Synthesis of Ir(III)-COUPY conjugates 3d and 3e. With the aim of investigating the effect of the distance between the COUPY fluorophore and the Ir(III) complex in the parent Ir(III)-COUPY conjugate **3a** on the photophysical and photochemical properties of the compounds, we designed two analogues incorporating a longer spacer between both moieties. As shown in Scheme 3, we selected flexible (**3d**) and rigid (**3e**) spacers with the same number of atoms separating the two moieties. The incorporation of both linkers was carried out through the formation of an amide bond between the carboxylic group of each Boc-protected precursor and the free amino group of coumarin **17**,³⁵ which afforded COUPY derivatives **18** and **19** containing the flexible and rigid spacers, respectively. Finally, after acidic Boc removal, the conjugation of coumarins **20** and **21** to the Ir(III) complex **2b** provided Ir(III)-COUPY conjugates **3d** and **3e**, respectively, as dark blue solids after silica column purification, which were characterized by ¹H and ¹³C NMR spectroscopy and high-resolution mass spectrometry (HRMS).

Synthesis of control COUPY coumarin 1b and 1c. For the synthesis of the corresponding *N*-methylated COUPY dyes **1b** and **1c** to be used as control compounds, coumarin **6** (Scheme 1) or coumarin **12** (Scheme 2) were reacted with methyl trifluoromethanesulfonate in DCM at room temperature yielding the expected compounds as yellow and dark blue solids, respectively.



Scheme 3. Synthesis of Ir(III)-COUPY conjugates **3d** and **3e**.

Photophysical and photochemical characterization of the compounds

The photophysical and photochemical properties (absorption and emission spectra, molar absorption coefficients (ϵ), fluorescence (Φ_F) or phosphorescence (Φ_P) quantum yields, fluorescence (τ_F) or phosphorescent (τ_P) lifetimes, and singlet oxygen quantum yield (Φ_{Δ}) of the four new Ir(III)-COUPY conjugates (**3b-3e**) along with the two new coumarins (**1b-1c**) were studied in three solvents of different polarity (phosphate-buffered saline PBS, CH₃CN and CH₂Cl₂), and compared with those of the previously reported parent compounds (COUPY dye **1a** and Ir(III)-COUPY conjugate **3a**).³⁵ The UV-vis absorption and emission spectra are shown in Figure 2 and Figures S1-S2, and their photophysical properties are summarized in Tables S1 and S2.

As shown in Table S1, the structural modifications carried out within the coumarin scaffold have a strong impact on the photophysical properties of the compounds. Indeed, the newly synthesized COUPY dyes showed either a bathochromic shift (about 20-30 nm for coumarin **1c**) or a hypsochromic shift (about 100-120 nm for coumarin **1b**) in their absorption and emission maxima compared with those of the parent coumarin **1a** (e.g. in ACN, $\lambda_{\text{abs}} = 548$ nm and $\lambda_{\text{em}} = 609$ nm for **1a** vs $\lambda_{\text{abs}} = 446$ nm and $\lambda_{\text{em}} = 492$ nm for **1b**, and $\lambda_{\text{abs}} = 572$ nm and $\lambda_{\text{em}} = 635$ nm for **1c**). The replacement of the *N,N*-dialkylamino group at position 7 of the coumarin skeleton by the strong electron-donating julolidine-fused analogue in coumarin **1c** caused the observed red-shifting in the wavelength at the absorption and emission maximum. On the contrary the absence of an EDG in coumarin **1b** had a negative effect on the spectroscopic properties of the fluorophore since both absorption and emission maxima were strongly blue-shifted due to the decreased push-pull character of the chromophore. On the other hand, the fluorescent quantum yields were slightly lower for coumarin **1c** in DCM and PBS, compared with the original COUPY **1a**, whereas coumarin **1b** was found to be very weakly fluorescent.

As we had already reported,³⁵ the Ir(III) complex **2a** showed a strong phosphorescence band around 660 nm, whose intensity decreased in the Ir(III)-COUPY conjugate **3a**, suggesting the existence of competitive excited-state processes. As shown in Table S2, a similar behaviour was observed in the three new conjugates incorporating a far-red emitting coumarin (**3c-3e**). Among them, conjugate **3c** containing the julolidine-fused coumarin showed the higher red-shifted absorption and emission maxima (*ca* 25-30 nm depending on the solvent), which parallels the spectroscopic properties of COUPY **1c** (**3c**, $\lambda_{\text{abs}} = 580$ nm and $\lambda_{\text{em}} = 647$ nm in ACN). Interestingly, the fluorescent quantum yield of **3c** was higher than that of the parent conjugate **3a** in DCM, but similar values were obtained in ACN and PBS. As expected,

conjugates **3d** and **3e** containing the flexible and the rigid spacer, respectively, showed similar absorption and emission maxima in all investigated solvents compared to the original conjugate **3a** since they contain the same coumarin (about $\lambda_{\text{abs}} = 555$ nm and $\lambda_{\text{em}} = 610$ nm in ACN). The fluorescent quantum yield values were also similar for the three conjugates, about 0.1 in DCM and ACN, and values below 0.02 in PBS. In good agreement with the behavior of COUPY dye **1b**, the Ir(III)-COUPY conjugate **3b** practically did not show any fluorescence in all of the solvents investigated and, as shown in Table S2, only phosphorescence lifetime values associated to the Ir(III) complex could be determined. Finally, it is worth noting that the maximum absorption wavelengths of all of the compounds (COUPY dyes and Ir(III)-COUPY conjugates) gradually decrease according to the following order $\text{CH}_2\text{Cl}_2 < \text{CH}_3\text{CN} < \text{PBS}$, which agrees with a negative solvatochromism phenomenon (Figure 2).

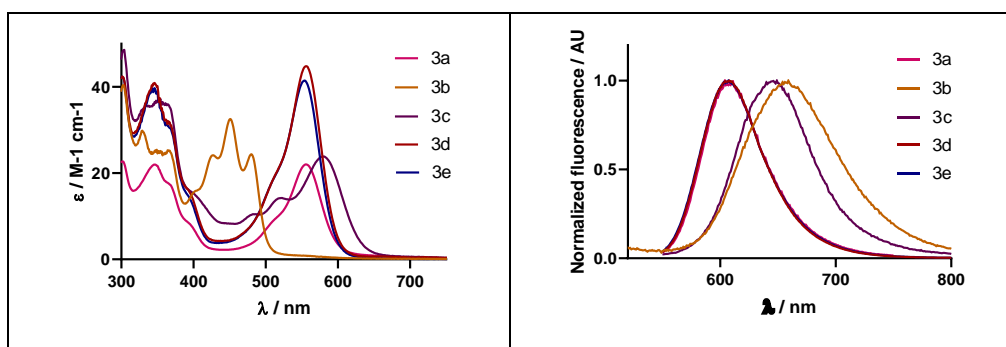


Figure 2. Comparison of the molar absorptivity (left) and emission spectra (right) of Ir(III)-COUPY conjugates **3a-3d** in ACN.

Next, we focused on investigating the impact of the structural modifications on the generation of ROS by Ir(III)-COUPY conjugates. As we previously reported,³⁵ the Ir(III) complex **2a** produced singlet oxygen in all of the organic solvents evaluated but not in PBS, while COUPY **1a** did not showed significant $^1\text{O}_2$ quantum yields in any solvent (Table S1). However, the conjugation of Ir(III) complex **2a** to the COUPY fluorophore **1a** led to an increase of $^1\text{O}_2$ quantum yield by one order of magnitude, suggesting the promotion of the intersystem crossing (ISC) process in conjugate **3a**, which provides more time for the triplet excited state (T_1) to interact with $^3\text{O}_2$ (Table S2). Based on these antecedents, the ability of all newly synthesized Ir(III)-COUPY conjugates (**3b-3e**) and control COUPY fluorophores (**1b-1c**) to produce $^1\text{O}_2$ was evaluated spectroscopically by the observation of $^1\text{O}_2$ emission at 1275 nm upon excitation at two wavelengths (355 and 532 nm). In the same way as for the original COUPY derivative **1a**, neither **1b** nor **1c** generated significant $^1\text{O}_2$. Interestingly, $^1\text{O}_2$ emission was observed in all

new Ir(III)-COUPY conjugates in DCM and ACN, but not in PBS. Conjugates **3d** and **3e** containing the same coumarin derivative as the parent compound (**3a**) showed similar oxygen singlet quantum yields (*ca* 0.30-0.40 in DCM upon excitation at both wavelengths) regardless of the spacer linking both moieties, while the conjugates with new coumarin derivatives, **3b** and **3c**, exhibited lower values (*ca* 0.20 in DCM).

Considering that one of the main features of the parent Ir(III)-COUPY conjugate **3a** is the generation of superoxide anion radical ($\text{O}_2^{\bullet-}$) in living cells upon visible light,³⁵ we next investigated the ability of the new conjugates to produce this specific type I ROS by using a spectroscopic method which is based on the oxidation of the non-fluorescent dihydrorhodamine 123 (DHR123) probe by $\text{O}_2^{\bullet-}$ to the correspondent fluorescent rhodamine 123 derivative. As shown in Figure 3 and Figure S3, Ir(III)-COUPY conjugates did not produce any measurable quantity of superoxide anion radical before irradiation, being this result comparable to that obtained with DHR123 alone after irradiation, which was used as a negative control. Surprisingly, under green light irradiation, all of the new conjugates, including the one containing the coumarin fluorophore lacking the amino group at the 7-position, clearly increased the fluorescence intensity of DHR123 to a greater extent than the Ir(III) complex **2a** and COUPY derivatives **1a-1c**, indicating the generation of superoxide anion radical. Remarkably, all the new conjugates led to a faster $\text{O}_2^{\bullet-}$ generation rate in comparison to the parent compound **3a**. It is worth noting that the Ir(III)-COUPY conjugate containing the julolidine-fused system (**3c**) showed the fastest rates in superoxide generation, thereby demonstrating the importance of incorporating a strong EDG in the coumarin scaffold, which not only red-shifts absorption and emission maxima but also triggers the production of more $\text{O}_2^{\bullet-}$. On the other hand, to our surprise, the Ir(III)-COUPY conjugate **3b** reached the highest maximum emission intensity of superoxide generation after 3 min of irradiation, indicating that the amino group at the 7-position of the coumarin moiety is not strictly necessary to trigger the generation of $\text{O}_2^{\bullet-}$.

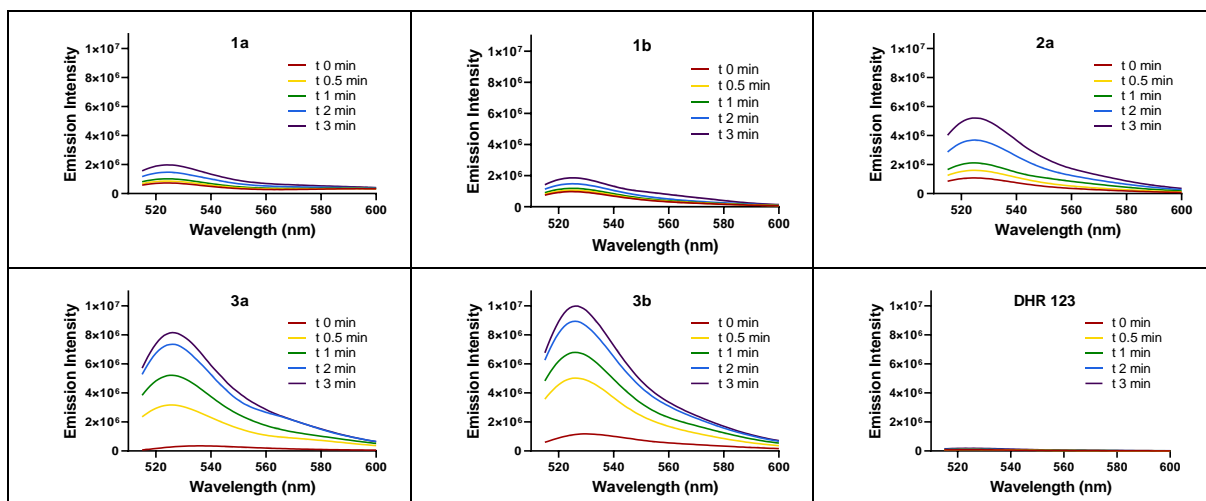


Figure 3. Fluorescence spectra of DHR123 induced by irradiation with visible light (505 nm) in the presence of COUPY coumarins **1a** and **1b**, Ir(III) complex **2a**, Ir(III)-COUPY conjugates **3a** and **3b** or without any compound (DHR 123 alone).

Cellular uptake and localization of Ir(III)-COUPY fluorophores

The cellular uptake of the conjugates was first investigated using Inductively Coupled-Plasma Mass Spectrometry (ICP-MS). After 2 h incubation, the iridium content inside cancer cells treated with Ir(III)-COUPY conjugates at 10 μM yielded similar results, with metal accumulations 4- to 9-fold higher than that of those found in cisplatin-treated cells (Figure 4a). Intracellular Ir levels varied from 185 ± 40 to 261 ± 25 ng/ 10^6 cells for Ir(III)-COUPY-treated cells and were comparable to those incubated with Ir(III) complex **2a** (276 ± 12). Strikingly, the amount of metal in cells treated with conjugate **3c** doubled that accumulation (461 ± 74 ng Ir per million cells), indicating that the julolidine-fused system of **3c** greatly improved cellular internalization.

To gain more insights on cellular uptake, the compounds were incubated with living cancer cells and examined under a confocal microscopy using yellow light laser ($\lambda_{\text{ex}}=561$ nm) excitation. As shown in Figure 4b, fluorescence signals from all of the new conjugates containing a far-red emitting coumarin, compounds **3c-3e**, were appreciated inside cells, thereby confirming an excellent cellular uptake. In agreement with ICP-MS results, intracellular fluorescence was slightly higher in **3c**-stained cells than with other conjugates (Figure 4a). Overall, the Ir(III)-COUPY conjugates **3c-3e** showed the same internalization pattern than the parent conjugate **3a**,³⁵ characterized by fluorescent vesicles in the cytoplasm.

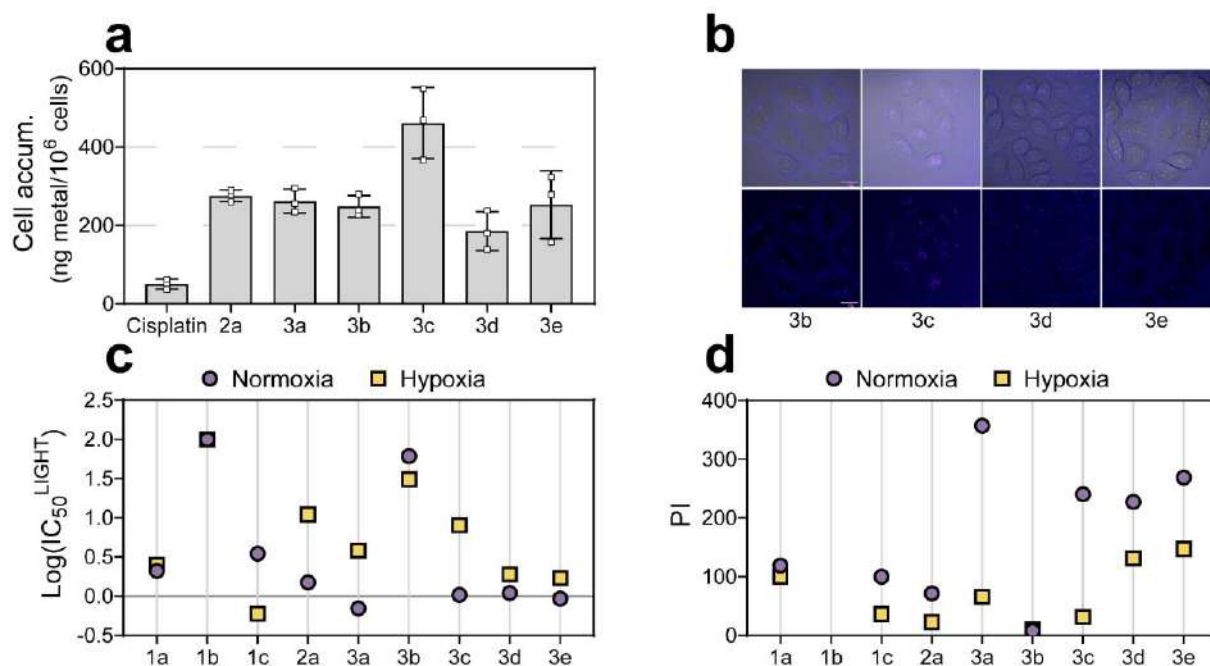


Figure 4. |Cellular uptake and photocytotoxicity of Ir-COUPY conjugates in cancer cells. **a)** Intracellular accumulation of Ir(III) compounds and cisplatin in A2780cis cells after 2 h treatment at 10 μM . Data expressed as mean \pm SD from three independent measurements. **b)** Single confocal planes of HeLa cells incubated with the compounds for 30 min at 37°C. Upper row: merge of bright field and fluorescence images. Lower row: fluorescence images of the compounds. Scale bar: 20 μm . **c – d)**, summary of *in vitro* photocytotoxicity for compounds **1a-1c**, **2a** and **3a-3e** in A2780cis cells after light irradiation (520 nm, 1.5 mW cm^{-2} , 1 h) under normoxia (21% O_2) or hypoxia (2% O_2) represented as $\text{Log}(\text{IC}_{50}^{\text{LIGHT}})$ and phototherapeutic indexes (PI), defined as the ratio of dark to light IC_{50} values. IC_{50} , PI values and their corresponding SD errors are listed in the Supplementary Information (Table S3).

Photobiological studies.

Having shown that the Ir(III)-COUPY conjugates can sensitize both type I and II ROS through spectroscopic techniques and readily internalize into living cells, their photocytotoxicity was screened in various cancer cell lines. This screening included two representative melanoma cell lines (female human A375 and male human SK-MEL-28) and cancer cells with resistance to the clinical drug cisplatin. For the latter, both sensitive and cisplatin-resistant ovarian cancer cells (A2780 and A2780cis) as well as HeLa cells, which also shows a degree of chemoresistance to the platinum anticancer drug *in vitro*,⁴⁴ were used. For the determination of dark and light cytotoxicity, dose-response curves were assayed from both conditions to provide the correspondent IC_{50} values, which correspond to the concentration needed for inhibition of cell growth by 50%. Phototherapeutic index (PI) was calculated as the ratio of dark to light IC_{50} value for each compound.

Dark cytotoxicity. Except for compound **1c**, all the compounds were found non-toxic in the absence of the light trigger ($IC_{50} > 100 \mu M$) regardless of the cell line (Table 1 and Tables S3-S4). From this, it was clear that the julolidine-fused system of **1c** impacted on dark cytotoxicity, rendering dark IC_{50} values that oscillated between 5 and 26 μM in the studied cancer cell lines. Noteworthy, conjugate **3c**, which also contains **1c** as a coumarin moiety showed no dark cytotoxicity up to 100 μM .

Photocytotoxicity in normoxia. First, photoactivation of **3a**, **3b** and **3c** was evaluated in cancer cells, along with their coumarin precursors **1a-1c** and the parent Ir(III) complex **2a**. Light treatments were applied at doses of 1.5 mW cm^{-2} using single green wavelength (520 nm) LED irradiation. Overall, the compounds triggered cell death upon light exposure at 520 nm in all cancer cell lines studied, with IC_{50} values in the low micromolar range (Table 1). COUPY **1b**, which lacks the *N,N*-dialkylamino group at position 7, did not display antiproliferative activity after light irradiation towards the investigated cancer cells, probably due to its blue-shifted absorption (Figure S2). In contrast, the original COUPY derivative **1a** exerted higher phototoxic action, particularly against melanoma cells, resulting in more than 86-fold differences in bioactivity upon irradiation (Table 1). The correspondent conjugate (**3b**) showed a slight increase in phototoxic activity compared to **1b**. This might be ascribable to the Ir(III) core of the PS because the Ir(III) complex **2a** also presented reasonable inhibitory activity after irradiation. Nonetheless, the green-light photocytotoxicity of **3b** was lower than that of **3a** in all cancer cell lines (light IC_{50} values between 3 – 78 μM compared to 0.7 – 18 μM). To test whether the poor phototoxicity of **3b** was due to a blue-shifted absorption, photoactivation upon blue light (465 nm) was also assayed. As shown in Table S4, A2780cis cells dosed with **3b** rendered light IC_{50} values that were very similar to those obtained for **3a** after blue light irradiation (2.4 and 1.9 μM , respectively). On the other hand, replacement of *N,N*-dialkylamino group of the coumarin by a julolidine-fused system decreased the phototoxicity of conjugate **3c** in A375, SK-MEL-28 and HeLa cells compared to **3a**. Nevertheless, the behavior of **3c** after green light irradiation was similar to that of **3a** in A2780 and A2780cis cancer cells, with light IC_{50} values between 0.7 and 2.1 μM .

Table 1. Photocytotoxicity of the compounds towards cancer cells.^a

	A375		SK-MEL-28		HeLa		A2780		A2780cis	
	Dark	Light	Dark	Light	Dark	Light	Dark	Light	Dark	Light
1a	>100	1.1 ± 0.1 [>89]	>100	1.2 ± 0.1 [>86]	>100	5.8 ± 0.4 [>17]	>100	5.2 ± 0.5 [>19]	>100	2.1 ± 0.2 [>48]
1b	>100	10 ± 2 [>10]	>100	>100 [n.d.]	>100	>100 [n.d.]	>100	>100 [n.d.]	>100	>100 [n.d.]
1c	9.9 ± 0.5	0.31 ± 0.02 [32]	12 ± 1	0.2 ± 0.01 [60]	26 ± 4	1.1 ± 0.8 [24]	5.1 ± 0.9	0.09 ± 0.01 [57]	15 ± 2	0.15 ± 0.04 [100]
2a	>100	2.1 ± 0.3 [>48]	>100	2.8 ± 0.3 [>36]	>100	75 ± 6 [>1.3]	>100	4 ± 1 [>25]	>100	3.5 ± 0.4 [>29]
3a	>100	18 ± 3 [>6]	>100	1.5 ± 0.1 [>67]	>100	8.6 ± 0.7 [>12]	>100	1.07 ± 0.07 [>94]	>100	0.70 ± 0.06 [>143]
3b	>100	78 ± 6 [>1.3]	>100	2.1 ± 0.2 [>48]	>100	18 ± 2 [>6]	>100	7.1 ± 0.1 [>14]	>100	61 ± 8 [>1.6]
3c	>100	38 ± 5 [>3]	>100	>100 [n.d.]	>100	45 ± 4 [>2.2]	>100	2.1 ± 0.2 [>48]	>100	1.04 ± 0.02 [>96]
3d	>100	46 ± 4 [>2.2]	>100	2.5 ± 0.2 [>40]	>100	2.0 ± 0.4 [>50]	>100	1.78 ± 0.07 [>56]	>100	1.1 ± 0.2 [>91]
3e	>100	19 ± 3 [>5]	>100	7.6 ± 0.9 [>13]	>100	9.3 ± 0.8 [>11]	>100	1.9 ± 0.2 [>53]	>100	0.93 ± 0.04 [>108]

^aCells were treated for 2 h (1 h of incubation, 1 h of irradiation with green light at 520 nm, 1.5 mW cm⁻²) followed by 48 h incubation in drug-free medium. Dark analogues were kept in the dark. Data expressed as mean ± SD from three independent experiments.

*n.d. = not determined. PI (phototherapeutic index) is given in brackets; PI defined as IC₅₀ (dark-non-irradiated cells)/IC₅₀ (irradiated cells).

Phototherapeutic index (PI). To explore the phototherapeutic potential of the Ir(III)-COUPY conjugates, we performed a SAR analysis derived from their phototoxic activity in cancer cells. For the identification of the best performing anticancer PDT agents, PI determination was used. Noticeably, PIs differed from one cancer cell line to another. For instance, A375 melanoma cells, which exhibit the most aggressive melanoma phenotype,⁴⁵ were less sensitive to Ir(III)-COUPY phototoxicities (PI values not exceeding >6) than SK-MEL-28 melanoma cells, where PIs reached up to >67 (Table 1). The conjugates also exerted mild phototoxic activity in HeLa cancer cells (PIs ranging from 2.2 to >50). The order of potency toward cancer cells generally was **3a** > **3c** ≈ **3d** ≈ **3e** > **3b**, with small discrepancies in this trend depending on cell line. Nevertheless, the most potent green-light photoactivation was found in ovarian cancer cells, particularly in resistant A2780cis cells, where PI values were markedly higher both for the conjugates containing the parent COUPY dye **1a** regardless of the type and length of the spacer, and the one incorporating the julolidine-fused system (>143 for **3a**, >96 for **3c**, >91 for **3d** and >108 for **3e**). Overall, these results led us to initially select **3a** and **3c-3e** due to their good photocytotoxic profiles, especially in A2780cis cancer cells. However, since **3c** accumulated in cancer cells to a greater extent than **3a** or **3d-3e** (Figure 4a), we hypothesized that **3c** was less efficient as PS as it would require more intracellular amount of compound to induce similar phototoxic outcomes. Therefore, **3a** was considered as the best hit Ir(III)-COUPY candidate for

green-light PDT *in vitro*, followed by **3d** and **3e**, which contain the same coumarin and Ir(III) complex moieties.

Photocytotoxicity in hypoxia. Since A2780cis cells were strongly inhibited by Ir(III)-COUPY photosensitizers upon green light irradiation, this cell line was used for further SARS evaluation. The phototoxic action of the compounds was assessed toward A2780cis cells under hypoxic conditions (2% O₂) and compared to the clinically-approved PS 5-aminolevulinic acid (5-ALA). In this second photocytotoxicity testing, dark cytotoxicity was recalculated using higher concentrations given that the compounds were deemed as inactive at 100 μM. Except for **1c**, no dark IC₅₀ values could be determined either in normoxia or hypoxia up to 250 μM (Table S3), which is highly desirable for PDT agents. As shown in Table S5, although none of them inhibited cell growth completely at 250 μM, some conjugates were relatively toxic at this dose. For instance, conjugates **3a**, **3b** and **3c** provided 45 – 76% of cell killing, while linker-containing conjugates **3d** and **3e** barely exhibited dark cytotoxicity at 250 μM (cell growth inhibition between 12 and 27%).

Under hypoxia, poorer PI values were found compared to those under normoxia, which can be explained in terms of photodynamic effect restriction by the lack of oxygen (Figure 4d and Table S3). All the compounds exhibited higher phototherapeutic effects against A2780cis cells than the protoporphyrin IX (PpIX) precursor 5-ALA (Table S3). The highest PI values in normoxia were achieved by **3a** (>357) followed by the conjugates containing the longer linkers **3d** and **3e** (>227 and >269, respectively). However, under hypoxia the photodynamic effect of **3a** significantly decreased (PI >66), whereas **3d** and **3e** yielded comparably higher photocytotoxicity, with PI values of >131 and >147, respectively. As depicted in Figure 4d, julolidine-containing conjugate **3c** displayed a similar PI value under normoxia (>240), but was much less photoactive under hypoxia (PI >31). On the other hand, no obvious photocytotoxicity was observed for **3b** upon green light irradiation neither in normoxia nor in hypoxia (light IC₅₀ values of 61 and 31 μM, respectively).

Photogeneration of ROS. Once demonstrated the photocytotoxicity of the compounds against cancer cells, the induction of cellular oxidative stress after irradiation was explored under both normoxia and hypoxia using the ROS probe 2,7-dichlorodihydrofluorescein diacetate (DCFH-DA) (Figure 5). In dark conditions, ROS levels from untreated, control cells remained similar to those treated with COUPY compounds **1a-1c** or with iridium(III) complex **2a** regardless the oxygen tension. Noticeably, conjugates **3a** and its linker-containing derivatives **3d** and **3e** slightly increased ROS levels under normoxia in the absence of light (Figure 5a).

Upon 520 nm light application, a strong fluorescence signal from DCFH-DA probe was observed in normoxic cells treated with **3a**, **3c**, **3d** and **3e**, indicating efficient photogeneration of ROS. Although this photogeneration was comparably lower under hypoxia, differences between dark and light conditions were still markedly significant under low oxygen environment. Strikingly, despite poor phototoxicity was achieved for **3b** in cellular assays under hypoxia (Figure 4d), a slight increase in ROS levels was found after green-light irradiation in A2780cis cells; these differences being significantly much larger for the other conjugates (Figure 5b).

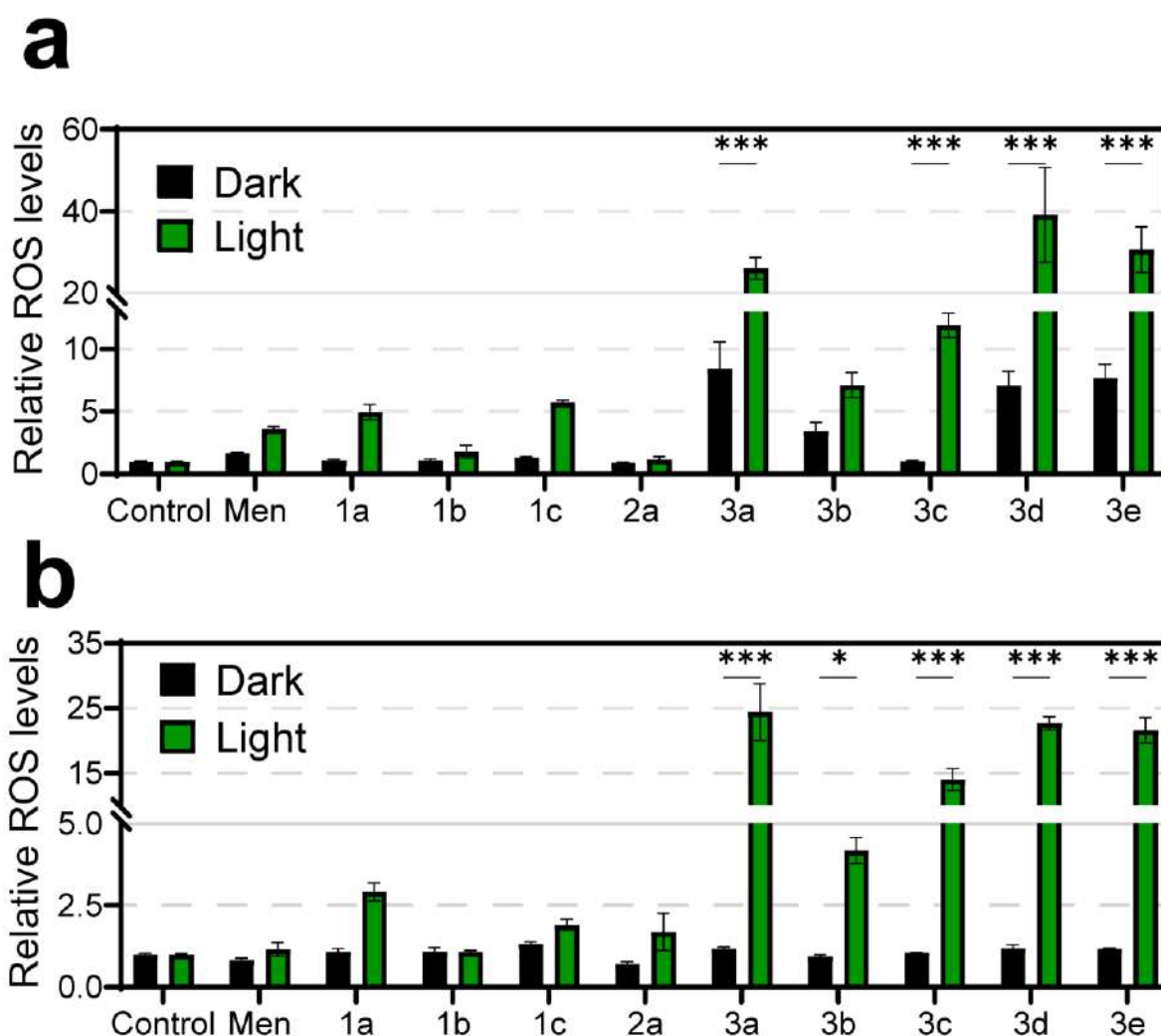


Figure 5. Photogeneration of ROS in cancer cells. **a)** Relative ROS levels in A2780cis cells under normoxia (21% O₂) and **b)** under hypoxia (2% O₂) after treatment with the compounds at 10 μ M in dark or upon light irradiation (520 nm, 1.5 mW cm⁻², 1 h) as measured with the DCFH-DA probe. Data expressed as mean \pm SD from three independent measurements. Statistical significance * p <0.05, ** p <0.01, *** p <0.001 from two-way ANOVA test.

DISCUSSION AND CONCLUSIONS

PDT holds great promise as a non-invasive anticancer tool against drug-resistant cancers.⁴⁶ However, highly effective, non-toxic and reliable PSs remain to be developed. Herein, we took the advantageous properties of both organic fluorophores and transition metal-based complexes to develop a novel family of PDT agents. Inspired by our previous encouraging results with this type of compounds,³⁵ we synthesized four new PSs based on the conjugation of COUPY coumarins with far-red/NIR emission to a cyclometalated Ir(III) complex.

The photophysical properties of the COUPY fluorophores were highly influenced by the structural modifications carried out within the coumarin scaffold. In particular, the incorporation of a strong EDG at position 7 of the coumarin skeleton in the newly synthesized COUPY dye **1c** through fusion of the julolidine system was found to induce a bathochromic shift in the absorption and emission maxima compared to the 7-*N,N*-dialkylamino-containing parent coumarin **1a**. On the other hand, the decreased push-pull character of the π -delocalized system in COUPY **1b** as a consequence of removing the EDG at the 7-position led to a clear blue-shift in the absorption and emission maxima and reduced significantly its fluorescence emission. In parallel, the spectroscopic properties of the conjugates could be also tuned depending on the COUPY fluorophore attached to the Ir(III) core. For instance, attachment of julolidine-fused COUPY coumarin **1c** to the Ir(III) complex red-shifted the absorption maximum of the resultant conjugate **3c** compared to **3a**, which contain the parent COUPY dye **1a**. In contrast, **3b** lost its fluorescence due to the absence of EDG in the coumarin moiety **1b**. This reveals the feasibility of these molecules as theragnostic agents, which can be tuned to act in different regions of the visible spectra depending on minimal structural modifications that do not considerably alter the overall molecular size. In fact, owing to a strong luminescence, Ir(III)-COUPY conjugates could be easily tracked inside cancer cells by confocal microscopy. These experiments revealed that the compounds are highly biocompatible, showing excellent cellular uptake and forming fluorescent vesicles in the cytosol (Figure 4b). Noteworthy, the julolidine-fused system also increased cell accumulation of the resulting conjugate **3c** (Figure 4a), which add emphasis on how the COUPY scaffold can act as a handle to modulate not only key photophysical properties (e.g., absorption and emission within the phototherapeutic window) but also key biological parameters such as cell entry and accumulation. Another relevant aspect was that COUPY fluorophores and their Ir(III) conjugates meet an important requirement for being considered as promising PDT agents: their minimal toxicity in the dark (Table S3 and Table S5). Only coumarin **1c** exhibited dark cytotoxicity in cancer cells, but its

correspondent conjugate (**3c**) was found inactive, thus revealing that conjugation can be used to diminish undesired dark toxicity of PSs based on cyclometalated Ir(III) complexes or their derivatives (Table 1 and Table S3).

The prospect of using Ir(III)-COUPY photosensitizers was very attractive since conjugation of COUPY fluorophore to the metal complex increased by a factor of ten the $^1\text{O}_2$ quantum yield of all the resulting conjugates compared with the corresponding free coumarins upon excitation at 532 nm (Tables S1 and S2). Compared to the rest of conjugates, **3a** and its spacer-containing derivatives **3d** and **3e** had the largest $^1\text{O}_2$ quantum yields, thereby confirming their capacity to sensitize highly toxic singlet oxygen after visible light irradiation independently of the length and rigidity of the spacer linking both moieties. In addition, all Ir(III)-COUPY conjugates were able to promote superoxide ($\text{O}_2^{\cdot-}$) generation through type I PDT reactions (Figure 3 and Figure S3). Particularly, the julolidine-fused system-containing conjugate (**3c**) photogenerated $\text{O}_2^{\cdot-}$ with the fastest rates, thereby demonstrating the importance of incorporating a strong EDG in the coumarin scaffold, which not only red-shifts absorption and emission maxima but also triggers the production of more superoxide anion radical. Surprisingly, we also observed that **3b** rapidly generated $\text{O}_2^{\cdot-}$ after visible light irradiation, indicating that the amino group at the 7-position of the coumarin moiety is not strictly necessary to trigger superoxide generation.

As anticipated, Ir(III)-COUPY conjugates with higher quantum yields for $^1\text{O}_2$ sensitization gave the largest PI values in the cancer cell lines studied herein. This preliminary SARS rationale enabled us to identify of **3a**, **3d** and **3e** as best hit candidates for green light-mediated anticancer therapy. Interestingly, we detected that A2780cis cells were strongly inhibited by light-driven treatments, suggesting that *in vitro* acquired-resistance mechanisms to cisplatin could be tackled by Ir(III)-COUPY-based photoactive therapy.

Local hypoxia within deep-seated tumors is a serious impediment for anticancer PDT.⁴⁷ Given that Ir(III)-COUPY PSs possess the ability to generate $\text{O}_2^{\cdot-}$ and $^1\text{O}_2$ at the same time, which would overcome the limitation of traditional Type II PDT agents under low oxygen environments, we tested their photoactivity under hypoxic conditions. In general, hypoxia decreased the anticancer activity of the conjugates, which confirmed ROS-generating PDT reactions as source of photocytotoxicity (Figure 4d). In particular, **3a** photocytotoxicity was greatly reduced under low oxygen environment. However, the incorporation of a spacer between the coumarin moiety and the Ir(III) complex enhanced the phototoxic activity under hypoxia, rendering higher PI values for **3d** and **3e** compared to the parent Ir(III)-COUPY conjugate **3a**. These findings suggested that the addition of rigid or flexible linkers between the

metal- and the organic-based scaffold can be used to improve the phototherapeutic profile of these PSs not only increasing the PI under challenging hypoxia condition but also reducing undesired *in vitro* dark toxicity (Figure 4d and Table S5).

Besides, we further verified the potential of these PSs by measuring intracellular ROS levels in A2780cis cells. In agreement with $^1\text{O}_2$ and PI values, conjugate **3a** along with **3d** and **3e** produced higher ROS photogeneration than other compounds even under low oxygen conditions (Figure 5). Worthy of note, **3c** also raised ROS levels that were comparable to those produced by **3a**, **3d** and **3e**. However, given that the intracellular amount of **3c** was considerably higher than that found for the other conjugates, it could be reasoned that **3c** is less efficient as PS because a higher amount of compound is required to catalytically photogenerate similar levels of ROS within cancer cells.

In conclusion, we have synthesized four new PDT agents based on the conjugation between far-red/NIR emitting COUPY fluorophores and a highly potent cyclometalated Ir(III) complex, with the aim of finding rational relationships between chemical structure and biological activity. The structural modifications introduced within the coumarin skeleton clearly influenced the photophysical and biological properties of the resulting Ir(III)-COUPY PSs. On the one hand, the conjugates exhibited appealing features for PDT therapy, including emission in the phototherapeutic window, excellent cellular uptake, no dark cytotoxicity and high photoinduced toxicity under green-light irradiation, which lead to excellent PI values in several cancer cell lines. On the other hand, the photoinduced generation of different types of ROS (Type II $^1\text{O}_2$ and Type I $\text{O}_2^{\bullet-}$) for all of the conjugates was demonstrated through spectroscopic methods, which would facilitate overcoming the limitations of conventional PSs under low oxygen environments. Remarkably, ROS generation was also confirmed in cisplatin-resistant A2780cis cancer cells for all the Ir(III)-COUPY conjugates, in both normoxia and hypoxia. Overall, three hit conjugates (**3a**, **3d** and **3e**) containing the same COUPY fluorophore were identified in this SAR study as promising PSs owing to their excellent phototoxicity in A2780cis cells in normoxia upon green light irradiation (PI = 357.1 for **3a**, 227.3 for **3d**, and 268.8 for **3e**). Among them, the linker-containing derivatives **3d** and **3e** are particularly interesting since they exhibited an enhanced phototoxic activity under hypoxic conditions compared with the parent Ir(III)-COUPY conjugate **3a** (PI = 65.8 for **3a**, 131.6 for **3d**, and 147.1 for **3e**), as well as reduced undesired *in vitro* dark toxicity. The high anticancer activity under normoxia and hypoxia conditions and the non-cytotoxicity in the dark, together with the excellent and tunable photophysical and photochemical properties of the Ir(III)-COUPY

conjugates make them useful tools in PDT to deliver efficient ROS-mediated anticancer activity toward chemo-resistant cancer cells using low doses of clinically-relevant green light activation.

EXPERIMENTAL SECTION

Materials and Methods

Unless otherwise stated, common chemicals and solvents (HPLC grade or reagent grade quality) were purchased from commercial sources and used without further purification. Aluminium plates coated with a 0.2 mm thick layer of silica gel 60 F₂₅₄ were used for thin-layer chromatography analyses (TLC), whereas flash column chromatography purification was carried out using silica gel 60 (230-400 mesh). NMR spectra were recorded at 25 °C in a 400 MHz spectrometer using the deuterated solvent as an internal deuterium lock. The residual protic signal of CHCl₃ and DMSO was used as a reference in ¹H and ¹³C NMR spectra recorded in CDCl₃ and DMSO-*d*₆, respectively. Chemical shifts are reported in part per million (ppm) in the δ scale, coupling constants in Hz and multiplicity as follows: s (singlet), d (doublet), t (triplet), q (quartet), qt (quintuplet), m (multiplet), dd (doublet of doublets), dt (doublet of triplets), td (triplet of doublets), br (broad signal), etc. Electrospray ionization mass spectra (ESI-MS) were recorded on an instrument equipped with single quadrupole detector coupled to an HPLC and high-resolution (HR) ESI-MS on an LC/MS-TOF instrument. The purity of final compounds was determined by reversed-phase high performance liquid chromatography (HPLC) analyses on a Jupiter Proteo C12 column (250 × 4.6 mm, 90 Å, 4 μm, flow rate: 1 mL/min) using linear gradients of 0.1% formic acid in Milli-Q H₂O (A) and 0.1% formic acid in ACN (B). The HPLC column was maintained at 25 °C. All final compounds were >95% pure by this method.

Synthesis of COUPY 1b

Synthesis of compound 4

Phenol (10 g, 106 mmol) and ethyl acetoacetate (13.6 mL, 106 mmol) were mixed and heated to 100 °C in nitrobenzene (10 mL). In a separate flask, AlCl₃ (28.1 g, 213 mmol) was dissolved in nitrobenzene (100 mL) at 0 °C – the AlCl₃ was added in six portions and left to stir at room temperature for 15-30 min. Then, the AlCl₃ solution was decanted from excess and added dropwise to the phenol and ethyl acetoacetate solution over 45 min. Once the addition was completed, the temperature was increased to 125 °C and the reaction mixture was stirred under reflux for 3 h. The reaction was then cooled to 0 °C and a 1:1 (v/v) mixture of HCl/H₂O (100 mL) was added. The mixture was then filtrated and the solid washed with ethyl acetate. The

filtrate was transferred to a separating flask where the aqueous and organic layers were separated: The organic layer was dried over anhydrous Na₂SO₄ and filtered. The ethyl acetate was removed by evaporation under reduced pressure and nitrobenzene by distillation *in vacuo*. The crude product was then purified by column chromatography (silica gel, 0-100% DCM in hexanes) to give 3.79 g (22%) of a brown solid. TLC: R_f (DCM) 0.34. ¹H NMR (400 MHz, CDCl₃) δ(ppm) 7.61 (1H, dd, *J* = 8.0, 1.6 Hz), 7.54 (1H, m), 7.32 (2H, m), 6.30 (1H, s), 2.45 (3H, s). ¹³C{¹H} NMR (101 Hz, CDCl₃) δ(ppm) 160.9, 153.6, 152.5, 131.9, 124.7, 124.3, 120.1, 117.2, 115.2, 18.8. LRMS (ESI-TOF) *m/z*: [M + H]⁺ Calcd for C₁₀H₉O₂ 161.06; Found 160.83.

Synthesis of compound 5

Coumarin **4** (4.48 g, 28.0 mmol) was mixed with Lawesson's Reagent (5.66 g, 14.0 mmol) in toluene (150 mL) and refluxed for 19 h at 105 °C. The crude was then evaporated under reduced pressure and purified by column chromatography (silica gel, 0-50% DCM in hexanes) to obtain 3.80 g of a yellow solid (77% yield). TLC: R_f (75:25, DCM:hexanes) 0.88. ¹H NMR (400 MHz, CDCl₃) δ(ppm) 7.65 (1H, dd, *J* = 8.0, 1.6 Hz), 7.59 (1H, m), 7.49 (1H, m), 7.36 (1H, m), 7.18 (1H, m), 2.38 (3H, s). ¹³C{¹H} NMR (101 Hz, CDCl₃) δ(ppm) 197.6, 156.2, 144.3, 132.2, 129.1, 125.5, 124.6, 121.6, 117.1, 18.1. HRMS (ESI-TOF) *m/z* [M + H]⁺ calcd for C₁₀H₉OS 177.0369, found 177.0369.

Synthesis of compound 6

4-Pyridylacetonitrile hydrochloride (1.71 g, 11.08 mmol) and NaH (3.41 g of a 60 % dispersion in mineral oil, 85.2 mmol) were dried together in a desiccator alongside compound **5** (1.50 g, 8.52 mmol) in a separate flask. Both were then dissolved in anhydrous ACN (90 mL and 30 mL, respectively) and the first solution passed to the second and the resulting mixture stirred for 2.5 h at room temperature and under an argon atmosphere. Afterwards, AgNO₃ (3.18 g, 18.74 mmol) was added and the mixture stirred for 2 h under Ar atmosphere and protected from light. The crude product was then evaporated under reduced pressure and purified by column chromatography (silica gel, 50-100% DCM in hexanes first, then 0-0.65% MeOH in DCM) to give 913 mg (41% yield) of brown solid. TLC: R_f (DCM/AcOEt 1:1) 0.48. ¹H NMR (400 MHz, CDCl₃) δ(ppm) 8.61 (2H, d, *J* = 5.8 Hz), 7.75 (2H, d, *J* = 5.8 Hz), 7.51 (2H, m), 7.32 (2H, m), 7.04 (1H, s), 2.42 (3H, s). ¹³C{¹H} NMR (101 Hz, CDCl₃) δ(ppm) 161.9, 152.1, 150.1, 142.8, 140.1, 131.9, 125.3, 124.6, 121.3, 121.2, 118.9, 118.0, 116.4, 84.8, 18.7. HRMS (ESI-TOF) *m/z* [M + H]⁺ calcd for C₁₇H₁₃N₂O 261.1022, found 261.1026.

Synthesis of compound 1b

Methyl trifluoromethanesulfonate (16 μ L, 0.14 mmol) was added to a solution of coumarin **6** (18.1 mg, 0.070 mmol) in DCM (10 mL) under an argon atmosphere. The mixture was stirred overnight at room temperature and protected from light. The reaction mixture was evaporated under reduced pressure and purified by column chromatography (silica gel, 0–10% MeOH in DCM) to give 16.1 mg of a yellow solid (yield 55%). TLC: R_f (10% MeOH in DCM) 0.34. ¹H NMR (400 MHz, DMSO-*d*₆) δ (ppm) 8.73 (2H, d, *J* = 8.0 Hz), 8.32 (2H, d, *J* = 7.6 Hz), 7.92 (2H, m), 7.81 (1H, m), 7.56 (1H, m), 7.30 (1H, d, *J* = 1.6 Hz), 4.27 (3H, s), 2.62 (3H, d, *J* = 1.2 Hz). ¹³C{¹H} NMR (101 Hz, DMSO-*d*₆) δ (ppm) 165.9, 151.6, 150.3, 147.9, 144.5, 133.3, 126.5, 125.6, 122.3, 120.8, 117.4, 117.1, 116.8, 81.3, 46.6, 18.5. HRMS (ESI-TOF) *m/z* [M]⁺ calcd for C₁₈H₁₅N₂O 275.1179, found 275.1179.

Synthesis of Ir(III)-COUPY conjugate 3b

Synthesis of compound 7

A solution of methyl bromoacetate (0.9 mL, 9.25 mmol) and coumarin **6** (481 mg, 1.85 mmol) in a 2.5:1 (v/v) mixture of AcOEt and DCM (35 mL) was stirred under reflux at 60 °C for 48 h. The reaction mixture was then evaporated under reduced pressure and purified by column chromatography (silica gel, 0–6.5% MeOH in DCM) to give 623 mg (81% yield) of an orange solid. TLC: R_f (10% MeOH in DCM) 0.37. ¹H NMR (400 MHz, DMSO-*d*₆) δ (ppm) 8.76 (2H, d, *J* = 7.4 Hz), 8.41 (2H, d, *J* = 7.4 Hz), 8.04 (1H, d, *J* = 7.6 Hz), 7.95 (1H, dd, *J* = 8.0, 1.6 Hz), 7.83 (1H, td, *J* = 8.0, 1.6 Hz), 7.58 (1H, m), 7.35 (1H, s), 5.60 (2H, s), 3.79 (3H, s), 2.65 (3H, s). ¹³C{¹H} NMR (101 Hz, DMSO-*d*₆) δ (ppm) 167.3, 166.5, 151.7, 151.3, 149.3, 144.9, 133.5, 126.6, 125.6, 122.0, 120.8, 117.4, 117.3, 116.9, 81.6, 58.9, 53.0, 18.6. HRMS (ESI-TOF) *m/z* [M]⁺ calcd for C₂₀H₁₇N₂O₃ 333.1234, found 333.1243.

Synthesis of compound 8

Compound **7** (214 mg, 0.52 mmol) was refluxed in a solution containing concentrated HCl (43 mL, 520 mmol) and H₂O (86 mL, Milli-Q quality) at 60 °C for 5.5 h. The crude mixture was then evaporated under reduced pressure to give a red solid, which was used without further purification in the next step. Analytical HPLC (10 to 100% B in 30 min, formic acid additive): R_t = 12.5 min. LRMS (ESI-TOF) *m/z*: [M]⁺ Calcd for C₁₉H₁₅N₂O₃ 319.11; Found 319.53.

Synthesis of compound 9

Coumarin **8** (80.4 mg, 0.23 mmol) and HATU (88.8 mg, 0.23 mmol) were dissolved in anhydrous DMF (8 mL) under an Ar atmosphere. After addition of DIPEA (40 μ L, 0.23 mmol), the reaction mixture was stirred for 5 min under Ar at room temperature and protected from

light. On the other hand, DIPEA (40 μ L, 0.23 mmol) was added to a solution of *N*-Boc-1,3-propanediamine hydrochloride (57.3 mg, 0.27 mmol) in anhydrous DMF (5 mL), and the resulting mixture was combined with the coumarin solution. After addition of DIPEA (40 μ L, 0.23 mmol), the reaction mixture was stirred for 2 h at room temperature under Ar and protected from light. The crude product was evaporated under reduced pressure and purified by column chromatography (silica gel, 0-12% MeOH in DCM) to give 30.5 mg of purple solid (yield: 26%). TLC: R_f (10% MeOH in DCM) 0.26. ¹H NMR (400 MHz, DMSO-*d*₆) δ (ppm) 8.69 (2H, d, *J* = 7.4 Hz), 8.52 (1H, t, *J* = 5.6 Hz), 8.36 (2H, d, *J* = 7.4 Hz), 7.98 (1H, dd, *J* = 8.4, 1.2 Hz), 7.94 (1H, dd, *J* = 8.0, 1.2 Hz), 7.82 (1H, td, *J* = 7.2 Hz, *J* = 1.6 Hz), 7.57 (1H, td, *J* = 8.3, 0.8 Hz), 7.33 (1H, d, *J* = 1.2 Hz), 6.82 (1H, t, *J* = 5.6 Hz), 5.33 (2H, s), 3.15 (2H, q, *J* = 6.4 Hz), 2.97 (2H, q, *J* = 6.4 Hz), 2.64 (3H, d, *J* = 1.2 Hz), 1.58 (2H, qt, *J* = 7.0 Hz), 1.37 (9H, s). ¹³C{¹H} NMR (101 Hz, DMSO-*d*₆) δ (ppm) 166.3, 164.6, 155.6, 151.7, 150.8, 148.7, 145.0, 133.4, 126.6, 125.7, 121.8, 120.8, 117.4, 116.9, 81.5, 77.5, 60.1, 37.5, 36.9, 29.3, 28.2, 18.6. HRMS (ESI-TOF) *m/z* [M]⁺ calcd for C₂₇H₃₁N₄O₄ 475.2340, found 475.2336.

Synthesis of compound 10

A cooled down solution of hydrochloric acid in dioxane (4 M, 3 mL) was added to coumarin **9** (10 mg, 0.021 mmol). The reaction mixture was stirred for 25 min in an ice bath under an Ar atmosphere and protected from light. After removal of the solvent under reduced pressure, several co-evaporations from acetonitrile were carried out. The crude product was used without further purification in the next step since HPLC-MS analysis revealed that the removal of the Boc group was quantitative. Analytical HPLC (10 to 100% B in 30 min, formic acid additive): R_t = 5.5 min. LRMS (ESI-TOF) *m/z* [M]⁺ Calcd for C₂₂H₂₃N₄O₂ 375.18; Found 375.19.

Synthesis of Ir(III)-COUPY conjugate 3b

To a solution of Ir complex **2b** (15.6 mg, 14.6 μ mol) and HATU (5.7 mg, 14.6 μ mol) in anhydrous DMF (2.5 mL) under an Ar atmosphere, DIPEA (3 μ L, 14.6 μ mol) was added and the mixture stirred for 10 min under Ar at room temperature and protected from light. After addition of a solution of coumarin **10** (9.8 mg, 21.9 μ mol) and DIPEA (15 μ L, 73 μ mol) in anhydrous DMF (3 mL), the reaction mixture was stirred for 2.5 h at room temperature under Ar and protected from light. After evaporation under reduced pressure, the crude was purified by column chromatography (silica gel, 0-12.5% MeOH in DCM) to give 10.1 mg of yellow solid (yield: 47%). Analytical HPLC (10 to 100% B in 30 min, formic acid additive): R_t = 12.6 min. HRMS (ESI-TOF) *m/z*: [M]²⁺ Calcd for C₆₉H₅₈IrN₁₁O₃ 640.7171; Found 640.7169.

Synthesis of COUPY 1c

Synthesis of compound 11

Coumarin 102 (1.17 g, 4.58 mmol) and Lawesson's reagent (1.11 g, 2.75 mmol) were dissolved in toluene (30 mL) and heated at 100 °C for 15 h. After evaporation under reduced pressure, the residue was purified by column chromatography (silica gel, 50-70% DCM in hexanes) to give an orange solid (666 mg, 54%): TLC R_f (DCM) 0.53. ¹H NMR (400 MHz, CDCl₃) δ(ppm) 7.03 (1H, s), 6.91 (1H, br q, *J* = 0.8 Hz), 3.29 (4H, q, *J* = 6.8 Hz), 3.00 (2H, t, *J* = 6.4 Hz), 2.79 (2H, t, *J* = 6.4 Hz), 2.27 (3H, d, *J* = 0.8 Hz), 1.98 (4H, m). ¹³C{¹H} NMR (101 Hz, CDCl₃) δ(ppm) 196.4, 154.5, 146.5, 146.4, 123.4, 121.8, 120.2, 111.2, 106.1, 50.1, 49.8, 28.0, 21.5, 20.7, 20.5, 18.1; HRMS (ESI-TOF) *m/z* [M + H]⁺ calcd for C₁₆H₁₈NOS 272.1104, found 272.1108.

Synthesis of compound 12

To a solution of 4-pyridylacetonitrile hydrochloride (256.4 mg, 1.66 mmol) and NaH (60% dispersion in mineral oil, 442.2 mg, 11.06 mmol) in dry ACN (50 mL) under an Ar atmosphere and protected from light, a solution of coumarin **11** (300 mg, 1.11 mmol) in dry ACN (10 mL) was added. After the mixture was stirred for 2 h at room temperature, silver nitrate (413.2 mg, 2.43 mmol) was added, and the reaction mixture was stirred at room temperature for 2 h under an Ar atmosphere and protected from light. The crude product was evaporated under reduced pressure and purified by column chromatography (silica gel, 0–3.5% MeOH in DCM) to give 120.6 mg of an orange solid (yield 31%). TLC: R_f (10% MeOH in DCM) 0.67. ¹H NMR (400 MHz, CDCl₃) δ(ppm) 8.54 (2H, m), 7.69 (2H, m), 6.94 (1H, s), 6.72 (1H, br q, *J* = 0.8 Hz), 3.27 (4H, m), 2.90 (2H, t, *J* = 6.5 Hz), 2.78 (2H, t, *J* = 6.3 Hz), 2.31 (3H, d, *J* = 0.8 Hz), 2.00 (4H, m). ¹³C{¹H} NMR (101 Hz, CDCl₃) δ(ppm) 163.2, 149.2, 145.4, 144.0, 140.9, 121.4, 120.5, 119.9, 118.4, 111.5, 109.5, 106.0, 80.3, 49.6, 48.9, 27.3, 21.1, 21.0, 20.5, 18.1. HRMS (ESI-TOF) *m/z* [M + H]⁺ calcd for C₂₃H₂₂N₃O 356.1757, found 356.1761.

Synthesis of compound 1c

Methyl trifluoromethanesulfonate (32 μL, 0.28 mmol) was added to a solution of coumarin **12** (49 mg, 0.14 mmol) in DCM (25 mL) under an argon atmosphere. The mixture was stirred overnight at room temperature and protected from light. The reaction mixture was evaporated under reduced pressure and purified by column chromatography (silica gel, 0–6% MeOH in DCM) to give 47 mg of a red solid (yield 66%). TLC: R_f (10% MeOH in DCM) 0.33. ¹H NMR (400 MHz, DMSO-*d*₆) δ(ppm) 8.60 (2H, d, *J* = 7.2 Hz), 7.99 (2H, d, *J* = 7.2 Hz), 7.37 (1H, s), 6.87 (1H, s), 4.13 (3H, s), 3.37 (4H, m), 2.93 (2H, t, *J* = 6.4 Hz), 2.81 (2H, t, *J* = 6.2 Hz), 2.50

(3H, s), 1.96 (2H, m), 1.90 (2H, m). $^{13}\text{C}\{^1\text{H}\}$ NMR (101 Hz, DMSO- d_6) δ (ppm) 166.2, 152.4, 150.4, 148.8, 147.4, 143.5, 122.7, 121.4, 120.1, 118.6, 110.3, 105.0, 77.1, 49.5, 48.7, 45.9, 27.1, 20.8, 20.4, 19.8, 18.5. HRMS (ESI-TOF) m/z $[\text{M}]^+$ calcd for $\text{C}_{24}\text{H}_{24}\text{N}_3\text{O}$ 370.1912, found 370.1914.

Synthesis of Ir(III)-COUPY conjugate 3c

Synthesis of compound 13

Methyl bromoacetate (52 μL , 0.56 mmol) was added to a solution of coumarin **12** (100 mg, 0.28 mmol) in AcOEt/ACN 1:1 (20 mL). The mixture was stirred overnight at 50 $^\circ\text{C}$ under an Ar atmosphere and protected from light. The crude product was evaporated under reduced pressure and purified by column chromatography (silica gel, 0–8% MeOH in DCM) to give 124 mg of blue solid (yield, 87%). TLC: R_f (10% MeOH in DCM) 0.40. ^1H NMR (400 MHz, CDCl_3) δ (ppm) 8.81 (2H, d, $J = 6.8$ Hz), 8.01 (2H, d, $J = 6.8$ Hz), 7.15 (1H, s), 6.90 (1H, s), 5.80 (2H, s), 3.85 (3H, s), 3.39 (4H, m), 3.05 (2H, t, $J = 6.4$ Hz), 2.84 (2H, t, $J = 6.4$ Hz), 2.49 (3H, s), 2.16 (2H, m), 2.01 (2H, m). $^{13}\text{C}\{^1\text{H}\}$ NMR (101 Hz, CDCl_3) δ (ppm) 167.3, 167.2, 152.7, 151.5, 150.8, 148.4, 143.5, 122.5, 122.4, 119.8, 118.5, 111.4, 111.0, 106.0, 79.2, 58.7, 53.6, 50.4, 49.8, 28.1, 21.9, 21.0, 20.3, 19.2. HRMS (ESI-TOF) m/z $[\text{M}]^+$ calcd for $\text{C}_{26}\text{H}_{26}\text{N}_3\text{O}_3$ 428.1969, found 428.1974.

Synthesis of compound 14

A 1:2 (v/v) mixture of HCl (37%) and Milli-Q water (51 mL) was added to coumarin **13** (98.9 mg, 0.19 mmol). The reaction mixture was stirred for 5 h at 60 $^\circ\text{C}$ under an Ar atmosphere and protected from light. After removal of the major part of the solvent, several coevaporations from acetonitrile were carried out. The crude product was used without further purification in the next step. Analytical HPLC (10 to 100% B in 30 min, formic acid additive): $R_t = 16.6$ min. LRMS (ESI-TOF) m/z $[\text{M}]^+$ calcd for $\text{C}_{25}\text{H}_{24}\text{N}_3\text{O}_3$ 414.18, found 413.81

Synthesis of compound 15

Coumarin **14** (87.5 mg, 0.19 mmol) and HATU (76 mg, 0.19 mmol) were dissolved in anhydrous DMF (8 mL) under an Ar atmosphere. After addition of DIPEA (70 μL , 0.39 mmol), the reaction mixture was stirred for 5 min under Ar at room temperature and protected from light. On the other hand, DIPEA (35 μL , 0.19 mmol) was added to a solution of *N*-Boc-1,3-propanediamine hydrochloride (62 mg, 0.29 mmol) in anhydrous DMF (5 mL), and the resulting mixture was combined with the coumarin solution. After addition of DIPEA (70 μL , 0.39 mmol), the reaction mixture was stirred for 2 h at room temperature under Ar and protected from light. The crude product was evaporated under reduced pressure and purified by column

chromatography (silica gel, 0-12.0% MeOH in DCM) to give 29 mg of purple solid (yield: 24%). TLC: Rf (10% MeOH in DCM) 0.59. ¹H NMR (400 MHz, DMSO-*d*₆) δ(ppm) 8.69 (1H, br s), 8.55 (2H, d, *J* = 6.8 Hz), 7.96 (2H, d, *J* = 6.6 Hz), 7.35 (1H, s), 6.84 (2H, m), 5.19 (2H, s), 3.37 (4H, m), 3.13 (2H, q, *J* = 6.6 Hz), 2.95 (4H, m), 2.80 (2H, m), 2.49 (3H, s), 1.92 (4H, m), 1.57 (2H, quint, *J* = 6.9 Hz), 1.37 (9H, s). ¹³C NMR (101 MHz, DMSO-*d*₆) δ(ppm) 166.2, 164.8, 155.6, 152.8, 150.5, 149.3, 147.6, 143.9, 122.7, 121.7, 119.3, 118.5, 110.5, 109.8, 104.9, 77.5, 77.5, 59.5, 49.6, 48.7, 40.2, 37.5, 36.8, 31.3, 29.3, 29.0, 28.2, 27.1, 22.1, 20.8, 20.4, 19.8, 18.5, 14.0. HRMS (ESI-TOF) *m/z* [M]⁺ calcd for C₃₃H₄₀N₅O₄ 570.3075, found 570.3079.

Synthesis of compound 16

A cooled down solution of hydrochloric acid in dioxane (4 M, 8 mL) was added to coumarin **15** (19 mg, 0.031 mmol). The reaction mixture was stirred for 25 min in an ice bath under an Ar atmosphere and protected from light. After removal of the solvent, several co-evaporations from acetonitrile were carried out. The crude product was used without further purification since HPLC-MS analysis revealed that the removal of the Boc group was quantitative. Analytical HPLC (10 to 100% B in 30 min, formic acid additive): Rt = 10.6 min. LRMS (ESI-TOF) *m/z*: [M]⁺ Calcd for C₂₈H₃₂N₅O₂ 470.26; Found 470.11.

Synthesis of Ir(III)-COUPY conjugate 3c

To a solution of Ir complex **2b** (30 mg, 28.1 μmol) and HATU (11.0 mg, 28.1 μmol) in anhydrous DMF (5 mL) under an Ar atmosphere, DIPEA (10 μL, 56.1 μmol) was added and the mixture stirred for 10 min under Ar at room temperature and protected from light. After addition of a solution of coumarin **16** (16.9 mg, 31.2 μmol) and DIPEA (25 μL, 140.3 μmol) in anhydrous DMF (6 mL), the reaction mixture was stirred for 2.5 h at room temperature under Ar and protected from light. After evaporation under reduced pressure, the crude was purified by column chromatography (silica gel, 0-12% MeOH in DCM) to give 14.5 mg of dark blue solid (yield: 33%). TLC: Rf (10% MeOH in DCM) 0.47. ¹H NMR (400 MHz, DMSO-*d*₆) δ(ppm) 8.88 (1H, d, *J* = 8.8 Hz), 8.69 (1H, d, *J* = 9.0 Hz), 8.66 (1H, m), 8.55 (2H, d, *J* = 7.0 Hz), 8.30 (1H, d, *J* = 9.0 Hz), 8.15 (1H, d, *J* = 8.3 Hz), 8.08 (1H, d, *J* = 8.9 Hz), 7.99 (2H, d, *J* = 7.2 Hz), 7.93 (1H, d, *J* = 7.7 Hz), 7.83 (2H, m), 7.72 (1H, m), 7.63 (1H, t, *J* = 7.8 Hz), 7.51 (1H, d, *J* = 8.1 Hz), 7.45 (1H, d, *J* = 8.1 Hz), 7.40 (1H, s), 7.19 (1H, t, *J* = 8.7 Hz), 7.09 (3H, m), 7.00 (1H, t, *J* = 7.4 Hz), 6.90 (2H, m), 6.81 (1H, t, *J* = 7.5 Hz), 6.73 (2H, m), 6.68 (1H, s), 6.30 (1H, d, *J* = 7.6 Hz), 6.19 (1H, d, *J* = 7.6 Hz), 5.95 (1H, d, *J* = 8.2 Hz), 5.70 (1H, d, *J* = 8.2 Hz), 5.21 (2H, s), 5.10 (2H, m), 3.19 (4H, sext, *J* = 7.2 Hz), 2.92 (2H, t, *J* = 6.1 Hz), 2.81 (2H, t, *J* = 6.0 Hz), 1.91 (4H, m), 1.68 (5H, m), 1.23 (4H, m), 0.94 (4H, m), 0.66 (3H, t, *J* = 7.2 Hz).

^{13}C NMR (101 MHz, DMSO-*d*₆) δ (ppm) 165.8, 164.9, 164.0, 155.6, 152.9, 152.4, 150.6, 149.8, 149.4, 148.5, 147.6, 143.9, 141.2, 139.5, 137.9, 132.4, 132.1, 132.0, 131.2, 130.2, 129.9, 129.3, 129.0, 128.9, 128.7, 124.7, 124.5, 124.2, 124.2, 123.0, 122.9, 122.8, 122.7, 122.3, 121.7, 121.6, 120.5, 119.4, 118.5, 117.7, 113.4, 113.3, 113.1, 113.0, 112.8, 112.6, 110.6, 105.0, 77.4, 67.5, 59.5, 49.6, 48.7, 45.9, 37.0, 31.9, 29.0, 27.1, 20.8, 20.4, 19.8, 19.0, 18.8, 18.5, 13.4. HRMS (ESI-TOF) m/z : $[\text{M}]^{2+}$ Calcd for $\text{C}_{75}\text{H}_{67}\text{IrN}_{12}\text{O}_3$ 688.2539; Found 688.2545. Analytical HPLC (10 to 100% B in 30 min, formic acid additive): R_t = 15.5 min

Synthesis of Ir(III)-COUPY conjugate **3d**

Synthesis of compound 18

To a solution of Boc-6-aminohexanoic acid (42.8 mg, 0.19 mmol) and HATU (72.5 mg, 0.19 mmol) in anhydrous DMF (6 mL) under an Ar atmosphere, DIPEA (65 μL , 0.37 mmol) was added and the mixture stirred for 10 min under Ar at room temperature and protected from light. After addition of a solution of coumarin **17** (32 mg, 0.062 mmol) and DIPEA (54 μL , 0.31 mmol) in anhydrous DMF (6 mL), the reaction mixture was stirred for 2.5 h at room temperature under Ar and protected from light. After evaporation under reduced pressure, the crude was purified by column chromatography (silica gel, 0-12% MeOH in DCM) to give 19.7 mg of pink solid (yield: 49 %). TLC: R_f (10% MeOH in DCM) 0.43. ^1H NMR (400 MHz, DMSO-*d*₆) δ (ppm) 8.59 (1H, br s), 8.53 (2H, d, J = 6.2 Hz), 8.16 (2H, d, J = 6.4 Hz), 7.81 (1H, br s), 7.72 (1H, d, J = 9.0 Hz), 6.99 (3H, m), 6.74 (1H, br s), 5.24 (2H, s), 3.55 (4H, m), 3.10 (4H, m), 2.86 (2H, m), 2.55 (3H, s), 2.03 (2H, m), 1.58 (2H, m), 1.46 (2H, m), 1.36 (11H, m), 1.18 (8H, m). ^{13}C NMR (101 MHz, DMSO-*d*₆) δ (ppm) 172.1, 166.8, 164.8, 155.6, 154.9, 152.8, 152.0, 149.2, 144.2, 127.0, 120.1, 118.2, 111.9, 110.5, 110.4, 96.4, 78.1, 77.3, 59.6, 44.2, 36.9, 36.1, 35.4, 29.3, 29.0, 28.3, 26.0, 25.1, 18.4, 12.4. HRMS (ESI-TOF) m/z $[\text{M}]^+$ calcd for $\text{C}_{37}\text{H}_{51}\text{N}_6\text{O}_5$ 659.3915, found 659.3928.

Synthesis of compound 20

A cooled down solution of hydrochloric acid in dioxane (4 M, 6 mL) was added to coumarin **18** (16.1 mg, 0.023 mmol). The reaction mixture was stirred for 20 min in an ice bath under an Ar atmosphere and protected from light. After removal of the solvent, several co-evaporations from acetonitrile were carried out. The crude product was used without further purification since HPLC-MS analysis revealed that the removal of the Boc group was quantitative. Analytical HPLC (10 to 100% B in 30 min, formic acid additive): R_t = 8.5 min. LRMS (ESI-TOF) m/z : $[\text{M}]^+$ Calcd for $\text{C}_{32}\text{H}_{43}\text{N}_6\text{O}_3$ 559.34; Found 559.49.

Synthesis of Ir(III)-COUPY conjugate 3d

To a solution of Ir complex **2b** (20.6 mg, 19.3 μmol) and HATU (7.4 mg, 19.3 μmol) in anhydrous DMF (4 mL) under an Ar atmosphere, DIPEA (7 μL , 38.6 μmol) was added and the mixture stirred for 10 min under Ar at room temperature and protected from light. After addition of a solution of coumarin **20** (14.6 mg, 23.2 μmol) and DIPEA (17 μL , 96.4 μmol) in anhydrous DMF (5 mL), the reaction mixture was stirred for 2.5 h at room temperature under Ar and protected from light. After evaporation under reduced pressure, the crude was purified by column chromatography (silica gel, 0-12% MeOH in DCM) to give 27.9 mg of purple solid (yield: 68%). ^1H NMR (400 MHz, DMSO- d_6) δ (ppm) 14.16 (2H, br s), 8.88 (1H, d, $J = 8.7$ Hz), 8.69 (1H, d, $J = 8.9$ Hz), 8.65 (1H, t, $J = 5.5$ Hz), 8.53 (2H, d, $J = 7.5$ Hz), 8.29 (1H, d, $J = 9.0$ Hz), 8.15 (3H, m), 8.07 (1H, d, $J = 8.9$ Hz), 7.96 (1H, d, $J = 7.5$ Hz), 7.92 (1H, t, $J = 5.6$ Hz), 7.87 (1H, d, $J = 7.6$ Hz), 7.83 (1H, dd, $J = 8.8$ Hz, $J = 1.5$ Hz), 7.70 (1H, d, $J = 9.2$ Hz), 7.63 (1H, t, $J = 8.0$ Hz), 7.53 (2H, m), 7.46 (1H, d, $J = 8.1$ Hz), 7.19 (1H, t, $J = 8.8$ Hz), 7.00 (8H, m), 6.81 (1H, td, $J = 7.6$ Hz, $J = 1.3$ Hz), 6.74 (2H, m), 6.64 (1H, d, $J = 1.1$ Hz), 6.30 (1H, d, $J = 7.3$ Hz), 6.19 (1H, d, $J = 7.4$ Hz), 5.95 (1H, d, $J = 8.3$ Hz), 5.70 (1H, d, $J = 8.2$ Hz), 5.25 (2H, m), 5.09 (2H, m), 3.53 (4H, q, $J = 6.9$ Hz), 3.11 (6H, m), 2.53 (2H, d, $J = 0.8$ Hz), 2.09 (2H, t, $J = 7.4$ Hz), 1.71 (2H, m), 1.51 (6H, m), 1.25 (3H, m), 1.15 (6H, t, $J = 7.0$ Hz), 0.99 (2H, m), 0.65 (3H, t, $J = 7.2$ Hz). ^{13}C NMR (101 MHz, DMSO- d_6) δ (ppm) 172.1, 166.8, 165.5, 164.8, 164.6, 164.0, 155.6, 154.9, 152.8, 152.4, 152.0, 149.8, 149.2, 148.5, 144.2, 143.4, 141.2, 139.6, 139.5, 139.3, 137.8, 134.5, 134.3, 132.4, 132.1, 132.0, 131.2, 130.2, 129.8, 129.0, 128.8, 128.8, 127.0, 124.8, 124.5, 124.3, 123.0, 123.0, 122.2, 121.6, 120.5, 120.1, 118.2, 117.5, 113.3, 113.1, 112.8, 112.6, 111.9, 110.5, 110.4, 96.4, 78.1, 59.6, 45.9, 44.2, 36.9, 36.2, 35.4, 31.9, 29.0, 26.2, 25.1, 19.0, 18.4, 13.4, 12.4. HRMS (ESI-TOF) m/z : $[\text{M}]^{2+}$ Calcd for $\text{C}_{79}\text{H}_{78}\text{IrN}_{13}\text{O}_4$ 732.7959; Found 732.7973. Analytical HPLC (10 to 100% B in 30 min, formic acid additive): $R_t = 13.7$ min

Synthesis of Ir(III)-COUPY conjugate 3e

Synthesis of compound 19

To a solution of *trans*-4-N-Boc-aminomethyl-cyclohexanecarboxylic acid (56 mg, 0.22 mmol) and HATU (85.3 mg, 0.22 mmol) in anhydrous DMF (6 mL) under an Ar atmosphere, DIPEA (77 μL , 0.44 mmol) was added and the mixture stirred for 10 min under Ar at room temperature and protected from light. After addition of a solution of coumarin **17** (37.6 mg, 0.073 mmol) and DIPEA (64 μL , 0.36 mmol) in anhydrous DMF (6 mL), the reaction mixture was stirred for 2.5 h at room temperature under Ar and protected from light. After evaporation

under reduced pressure, the crude was purified by column chromatography (silica gel, 0-11% MeOH in DCM) to give 35.4 mg of pink solid (yield: 68 %). TLC: R_f (10% MeOH in DCM) 0.38. ¹H NMR (400 MHz, DMSO-*d*₆) δ(ppm) 8.60 (1H, m), 8.53 (2H, d, *J* = 7.2 Hz), 8.16 (2H, d, *J* = 7.2 Hz), 7.73 (1H, m), 7.72 (1H, d, *J* = 9.2 Hz), 7.02 (1H, m), 6.98 (1H, dd, *J* = 9.2, 2.4 Hz), 6.93 (1H, s), 6.78 (1H, t, *J* = 6.0 Hz), 5.24 (2H, s), 3.56 (4H, q, *J* = 7.2 Hz), 3.13 (2H, q, *J* = 6.4 Hz), 3.07 (2H, q, *J* = 6.0 Hz), 2.75 (2H, t, *J* = 6.4 Hz), 2.55 (3H, s), 2.00 (1H, m), 1.68 (4H, m), 1.57 (2H, qt, *J* = 6.8 Hz), 1.36 (9H, s), 1.26 (4H, m), 1.18 (6H, t, *J* = 7.2 Hz), 0.84 (2H, m). ¹³C {¹H} NMR (101 Hz, DMSO-*d*₆) δ(ppm) 175.2, 166.8, 164.8, 155.7, 154.9, 152.8, 152.0, 149.2, 144.2, 127.0, 120.1, 118.2, 111.9, 110.5, 110.4, 96.4, 78.1, 77.3, 59.6, 46.1, 44.2, 44.1, 37.4, 36.8, 36.0, 29.5, 29.0, 28.8, 28.3, 18.4, 12.4. HRMS (ESI-TOF) *m/z* [M]⁺ calcd for C₃₉H₅₃N₆O₅ 685.4072, found 685.4072.

Synthesis of compound 21

A cooled down solution of hydrochloric acid in dioxane (4 M, 11 mL) was added to coumarin **19** (28 mg, 0.039 mmol). The reaction mixture was stirred for 20 min in an ice bath under an Ar atmosphere and protected from light. After removal of the solvent, several co-evaporations from acetonitrile were carried out. The crude product was used without further purification since HPLC-MS analysis revealed that the removal of the Boc group was quantitative. Analytical HPLC (10 to 100% B in 30 min, formic acid additive): R_t = 8.6 min. LRMS (ESI-TOF) *m/z*: [M]⁺ Calcd for C₃₄H₄₅N₆O₃ 585.35; Found 585.31.

Synthesis of Ir(III)-COUPY conjugate 3e

To a solution of Ir complex **2b** (34.6 mg, 32.3 μmol) and HATU (12.7 mg, 32.3 μmol) in anhydrous DMF (5 mL) under an Ar atmosphere, DIPEA (12 μL, 64.7 μmol) was added and the mixture stirred for 10 min under Ar at room temperature and protected from light. After addition of a solution of coumarin **21** (25.5 mg, 38.8 μmol) and DIPEA (29 μL, 161.7 μmol) in anhydrous DMF (6 mL), the reaction mixture was stirred for 2.5 h at room temperature under Ar and protected from light. After evaporation under reduced pressure, the crude was purified by column chromatography (silica gel, 0-12% MeOH in DCM) to give 34.7 mg of purple solid (yield: 58%). ¹H NMR (400 MHz, DMSO-*d*₆) δ(ppm) 14.40 (2H, br s), 8.89 (1H, d, *J* = 8.8 Hz), 8.70 (2H, m), 8.54 (2H, d, *J* = 7.5 Hz), 8.28 (1H, d, *J* = 9.0 Hz), 8.15 (3H, m), 8.07 (1H, d, *J* = 8.9 Hz), 7.97 (1H, d, *J* = 6.9 Hz), 7.91 (1H, d, *J* = 7.6 Hz), 7.82 (2H, m), 7.70 (1H, d, *J* = 9.2 Hz), 7.62 (2H, m), 7.52 (1H, d, *J* = 8.1 Hz), 7.46 (1H, d, *J* = 8.1 Hz), 7.19 (1H, t, *J* = 8.8 Hz), 7.12 (2H, q, *J* = 7.9 Hz), 6.95 (6H, m), 6.80 (1H, t, *J* = 7.6 Hz), 6.75 (2H, t, *J* = 7.4 Hz), 6.63 (1H, s), 6.30 (1H, d, *J* = 7.2 Hz), 6.19 (1H, d, *J* = 7.4 Hz), 5.96 (1H, d, *J* = 8.3 Hz), 5.73 (1H,

d, $J = 8.2$ Hz), 5.26 (2H, s), 5.10 (2H, m), 3.54 (4H, q, $J = 6.9$ Hz), 3.07 (7H, m), 2.53 (2H, s), 2.07 (1H, m), 1.73 (6H, m), 1.58 (2H, qt, $J = 6.9$ Hz), 1.35 (3H, m), 1.16 (6H, t, $J = 7.0$ Hz), 0.92 (4H, m), 0.63 (3H, t, $J = 7.2$ Hz). ^{13}C NMR (101 MHz, DMSO- d_6) δ (ppm) 175.2, 166.8, 165.8, 164.8, 164.5, 163.8, 155.6, 154.9, 152.8, 152.3, 152.0, 149.8, 149.2, 148.5, 144.2, 143.4, 141.3, 139.5, 139.2, 137.8, 134.5, 134.3, 134.2, 133.2, 133.1, 132.3, 132.3, 132.0, 131.2, 130.3, 129.9, 129.4, 128.9, 128.9, 128.8, 127.6, 127.0, 124.8, 124.6, 124.3, 123.1, 123.0, 122.9, 122.2, 121.6, 120.6, 120.1, 119.3, 118.2, 117.5, 113.3, 113.0, 112.9, 112.5, 111.9, 110.5, 110.4, 96.5, 78.1, 59.6, 45.9, 45.3, 44.2, 44.1, 37.1, 36.9, 36.0, 31.9, 29.7, 29.0, 28.9, 19.0, 18.4, 13.4, 12.4. HRMS (ESI-TOF) m/z : $[\text{M}]^{2+}$ Calcd for $\text{C}_{81}\text{H}_{80}\text{IrN}_{13}\text{O}_4$ 745.8037; Found 745.8047. Analytical HPLC (10 to 100% B in 30 min, formic acid additive): $R_t = 15.8$ min

Photophysical and photochemical characterization

For photophysical measurements, all solvents used were spectroscopic grade. Absorption spectra were recorded in a Varian Cary 500 UV/Vis/NIR or Varian Cary 6000i spectrophotometer at room temperature. Molar absorption coefficients (ϵ) were determined by direct application of the Beer-Lambert law, using solutions of the compounds in each solvent with concentrations ranging from 10^{-6} to 10^{-5} M. Emission spectra were registered in a Photon Technology International (PTI) fluorimeter or in a Spex Fluoromax-4 spectrofluorometer. Fluorescence quantum yields (Φ_F) were measured by comparative method using cresyl violet in ethanol (CV; $\Phi_{F;\text{Ref}} = 0.54 \pm 0.03$) as reference.⁴⁸ Then, optically-matched solutions of the compounds and CV were excited and the fluorescence spectra was recorded. The absorbance of sample and reference solutions was set below 0.1 at the excitation wavelength and Φ_F were calculated using the following equation (1):

$$\Phi_{F;\text{Sample}} = \frac{\text{Area}_{\text{Sample}}}{\text{Area}_{\text{Ref}}} \times \left(\frac{\eta_{\text{Sample}}}{\eta_{\text{Ref}}} \right)^2 \times \Phi_{F;\text{ref}} \quad (1)$$

where $\text{Area}_{\text{Sample}}$ and Area_{Ref} are the integrated fluorescence for the sample and the reference and η_{Sample} and η_{Ref} are the refractive index of sample and reference solutions respectively. The uncertainty in the experimental value of Φ_F has been estimated to be approximately 10%.

Phosphorescence quantum yields (Φ_P) of the iridium complex were determined analogously to Φ_F , using argon-saturated meso-tetra-5,10,15,20-phenylporphine as reference ($\Phi_F = 0.11$ in toluene).⁴⁹

Singlet oxygen generation was studied by time-resolved near-infrared phosphorescence by means of a customised setup. Briefly, a pulsed Nd:YAG laser (FTSS355-Q, Crystal Laser,

Berlin, Germany) working at 1 or 10 kHz repetition rate at 355 nm (0.5 μJ per pulse) or 532 nm (1.2 μJ per pulse) was used to excite the sample. A 1064-nm rugate notch filter (Edmund Optics) and an uncoated SKG-5 filter (CVI Laser Corporation) were placed in the laser path to remove any NIR emission. The light emitted by the sample was filtered with a 1000-nm long-pass filter (Edmund Optics) and later by a narrow bandpass filter at 1275 nm (BK-1270-70-B, bk Interferenzoptik). A thermoelectric-cooled NIR-sensitive photomultiplier tube assembly (H9170-45, Hamamatsu Photonics, Hamamatsu, Japan) was used as detector. Photon counting was achieved with a multichannel scaler (NanoHarp 250, PicoQuant). The time dependence of the $^1\text{O}_2$ phosphorescence with the signal intensity $S(t)$ is described by Equation 2, in which τ_T and τ_Δ are the lifetimes of the photosensitizer triplet state and of $^1\text{O}_2$ respectively, and S_0 a preexponential parameter proportional to Φ_Δ .

$$S_{1275}(t) = S_{1275}(0) \times \frac{\tau_\Delta}{\tau_\Delta - \tau_T} \times \left(e^{-t/\tau_\Delta} - e^{-t/\tau_T} \right) \quad (2)$$

The Φ_Δ values of the different samples were obtained by comparing S_0 values of optically matched samples and using an appropriate reference, by means of equation 3.

$$\Phi_{\Delta, \text{sample}} = \Phi_{\Delta, \text{ref}} \times \frac{S_{0, \text{sample}}}{S_{0, \text{ref}}} \quad (3)$$

The same setup was used to monitor the phosphorescence of the complex and the conjugate, except that the red-sensitive Hamamatsu H5783 photosensor module was used for detection.

Superoxide anion radical generation and characterization using DHR123

All compounds (10 μM) were prepared in PBS (0.2 % DMSO). To this solution, DHR123 was added so that its final concentration was 10 μM . Then the samples were irradiated in 1.0 x 0.5 cm cuvette by green light (505 nm centered LED) for indicated time intervals. Immediately, the fluorescence spectra were collected by using a Photon Technology International (PTI) fluorimeter. The excitation wavelength was set to 500 nm, the excitation and emission slit widths were 2 nm, and the integration time was set to 1 s.

Cell Culture and Cell Lines

A375, HeLa and SK-MEL-28 cells were cultured in Dulbecco's modified Eagle medium (DMEM) supplemented with 10% FBS, l-glutamine, 1% penicillin–streptomycin. A2780 and A2780cis cells were grown in RPMI-1640 cell medium supplemented with 10% fetal bovine serum (FBS) and 2 mM l-glutamine. Acquired resistance to cisplatin in A2780cis cell line was maintained by adding cisplatin 1 μM to culture medium every second passage. Cells were cultured in a humidified incubator at 310 K with 5% CO_2 atmosphere and subcultured two or

three times a week with appropriate densities and were confirmed to be mycoplasma-free using a standard Hoechst DNA staining method.

Fluorescence imaging

HeLa Cells were maintained in DMEM (Dulbecco Modified Eagle Medium) containing low glucose (1 g/L) and supplemented with 10% fetal bovine serum (FBS), 50U/mL penicillin-streptomycin and 2 mM *L*-glutamine. For cellular uptake experiments and posterior observation under the microscope, cells were seeded on glass bottom dishes (P35G-1.5-14-C, Mattek). 24 h after cell seeding, cells were incubated at 37 °C for 30 min with Ir(III)-COUPY conjugates **3a-3e** (5 μM) in supplemented DMEM. Then, cells were washed three times with DPBS (Dulbecco's Phosphate-Buffered Saline) to remove the excess of the compounds and kept in low glucose DMEM without phenol red supplemented with 10 mM Hepes for fluorescence imaging.

All microscopy observations were performed using a Zeiss LSM 880 confocal microscope equipped with a 561 nm laser. The microscope was also equipped with a heating insert (P Lab-Tek S, Pecon) to keep cells at 37 °C. Cells were observed using a 63X 1.4 oil immersion objective. The compounds were excited using the 561 nm laser and emission detected from 570 to 670 nm. Image analysis was performed using Fiji.⁵⁰ All images are colorized using the Fire lookup table from Fiji.

Cellular accumulation by ICP-MS

Briefly, A2780cis cells were seeded onto 12-well plate (3×10^5 cells/well). Treatments with tested agents for 2 h were applied at 10 μM. Cisplatin was included for comparative purposes. Cells were then trypsinized, and pellets were counted. Samples were then digested with 30% HNO₃ suprapur acid (Sigma Aldrich) and subjected to Inductively Coupled Plasma Mass Spectrometry analysis in Agilent 7900 ICP-MS. ⁹⁹Ru, ¹⁰¹Ru, ¹⁹⁴Pt and ¹⁹⁵Pt isotopes were measured. Three independent experiments were performed ($n = 2$ replicates).

Photo- and cytotoxic activity determination

A2780, A2780cis, HeLa, A375 and SK-MEL-28 cells were maintained at logarithmic growth-phase and cultured in 96-well plates at a density of 5000 cells/well in complete medium for 24 h at 310 K, 5% CO₂ in a humidified incubator. For hypoxia experiments, a Hypoxia condition was set up by Tissue Culture Service at University of Murcia using nitrogen (N₂) to displace O₂ down to a minimum of 2% in a Forma™ Steri-Cycle™ i160 incubator (ThermoFisher Scientific). Serial dilutions of the compounds were added at the final

concentrations in the range of 0 to 100 μM in a final volume of 100 μL per well. Light-based treatment schedule was performed as follows: 1 h incubation with the compounds in the dark followed by 1 h incubation under irradiation conditions by placing the Photoreactor EXPO-LED from Luzchem (Canada) fitted with green lamps (final light intensity applied of 1.5 mW/cm^2 at $\lambda_{\text{max}}=520$ nm) inside the CO_2 incubator. All the cell culture plates subjected to light irradiation included untreated controls to verify that cell viability was not affected by light. Then, treatment-containing media was removed, and fresh media added for a 48 h cell recovery period; the temperature throughout the experiment remaining at 310 K. Dark control samples were placed in the same dark conditions and then kept incubated for 1 h in the dark in the humidified CO_2 incubator. Medium was then aspirated by suction, cells were loaded with 50 μL of MTT solution (1 mg/mL) for additional 4 h, then removed and 50 μL DMSO was added to solubilize the purple formazan crystals formed in active cells. The absorbance was measured at 570 nm using a microplate reader (FLUOstar Omega) and the IC_{50} values were calculated based on the inhibitory rate curves using the following equation:

$$I = \frac{I_{\text{max}}}{1 + \left(\frac{\text{IC}_{50}}{C}\right)^n} \quad (4)$$

Where I represent the percentage inhibition of viability observed, I_{max} is the maximal inhibitory effect, IC_{50} is the concentration that inhibits 50% of maximal growth, C is the concentration of the treatment and n is the slope of the semi-logarithmic dose-response sigmoidal curves. The non-linear fitting was performed using SigmaPlot 14.0 software. All experiments were performed in three independent studies with $n=3$ replicates per concentration level. For a detailed phototoxicity procedure, reference 41 includes technical explanations.

ROS photogeneration in A2780cis cells

ROS levels were determined using the 2'-7'-dichlorofluorescein diacetate (DCFH-DA) probe. A2780cis cells were seeded onto 96-well black plates at 2×10^4 cells/well for 24 h in a humidified CO_2 incubator either in normoxia (21% O_2) or hypoxia (2% O_2). Tested compounds were then administered in cell media for the allowed time. Treatments were then removed, and cells were stained with 10 μM of DCFH-DA for 0.5 h. After staining, cells were washed with PBS twice and irradiated for 1 h with LED source light from Luzchem photoreactor (Canada) fitted with green lamps (final light intensity applied of 1.5 mW/cm^2 at $\lambda_{\text{max}} = 520$ nm). Fluorescence readings were performed in FLUOstar Omega ($\lambda_{\text{exc}} = 488$ nm and $\lambda_{\text{em}} = 530 \pm 30$ nm). Non-irradiated plates were used for dark conditions whereas treated, unstained cells were used

to subtract basal fluorescence of compounds and correct fluorescence readings. Unstained cells served as blank. Three independent experiments were performed with n=3 replicates.

ASSOCIATED CONTENT

Supporting Information. The Supporting Information is available free of charge at <https://pubs.acs.org/doi/XXX>

Additional tables and figures for photophysical and photochemical characterization of the compounds and copies of NMR and MS spectra. This material is available free of charge via the Internet at <http://pubs.acs.org>.

AUTHOR INFORMATION

Corresponding Authors

Vicente Marchán - Departament de Química Inorgànica i Orgànica, Secció de Química Orgànica, IBUB, Universitat de Barcelona, E-08028 Barcelona, Spain; orcid.org/0000-0002-1905-2156; E-mail: vmarchan@ub.edu

José Ruiz - Departamento de Química Inorgánica, Universidad de Murcia and Institute for Bio-Health Research of Murcia (IMIB-Arrixaca), E-30071 Murcia, Spain; orcid.org/0000-0002-0834-337X; E-mail: jruiz@um.es

Author Contributions

V.M. designed the research. A.R. synthesized and characterized all coumarin derivatives and Ir(III)-COUPY conjugates. G.V. synthesized and characterized the Ir(III) complexes. A.R., C.H. and M.J. investigated the photophysical and photochemical properties of all of the compounds. A.R. and M.B. performed confocal microscopy studies. E.O.-F. performed all biological experiments (cyto- and phototoxicity, ROS determination and cellular accumulation by ICP-MS). A.R., E.O.-F. and V.M. wrote the manuscript, which was contributed by all authors. All authors have approved the final version of the manuscript.

Funding Sources

This work was supported by funds from the Spanish Ministerio de Ciencia e Innovación-Agencia Estatal de Investigación (MCI/AEI/10.13039/501100011033) and FEDER funds (Projects CTQ2017-84779-R, RTI2018-096891-B-I00 and PID2020-117508RB-I00).

ACKNOWLEDGMENTS

The authors wish to thank Nicole Miller for synthesizing some coumarin precursors. A.R. and M.L.-C. were recipient fellows of the University of Barcelona (APIF) and of the Generalitat de Catalunya (FI-SDUR), respectively. E. O.-F thanks AECC (Project PRDMU19003ORTE).

ABBREVIATIONS

ACN, acetonitrile; A2780, cisplatin-sensitive ovarian carcinoma; A2780cis, cisplatin-resistant ovarian carcinoma; A-375, female human malignant melanoma cell line; DCM, dichloromethane; DCFH-DA, 2'-7'-dichlorofluorescein diacetate; DHE, dihydroethidium; DHR123, dihydrorhodamine 123; DIPEA, *N,N*-diisopropylethylamine; DMEM, Dullbecco Modified Eagle Medium; DMSO, dimethylsulfoxide; EDG, electron-donating group; ESI, electrospray ionization; FBS, fetal bovine serum; HATU, 1-[bis(dimethylamino)methylene]-1H-1,2,3-triazolo[4,5-b]pyridinium 3-oxid hexafluorophosphate; HeLa, cervical carcinoma cell line; HRMS, high-resolution mass spectrometry; ICD, immunogenic cell death; ICP-MS, Inductively Coupled-Plasma Mass Spectrometry; ISC, intersystem crossing; LW, Lawesson's reagent; NIR, near-infrared; NMR, nuclear magnetic resonance; PBS, phosphate-buffered saline; PDT, photodynamic therapy; PI, phototherapeutic index; PpIX, protoporphyrin IX; PS, photosensitizer; ROS, reactive oxygen species; SK-MEL-28, male human malignant melanoma cell line; TLC, thin layer chromatography.

REFERENCES

-
- ¹ van Straten, D.; Mashayekhi, V.; de Bruijn, H. S.; Oliveira, S.; Robinson, D. J. Oncologic Photodynamic Therapy: Basic Principles, Current Clinical Status and Future Directions. *Cancers* **2017**, *9*, 19.
- ² Dos Santos, A. F.; De Almeida, D. R. Q.; Terra, L. F.; Baptista, M. S.; Labriola, L. Photodynamic Therapy in Cancer Treatment – An Update Review. *J. Cancer Metastasis Treat.* **2019**, *5*, 25.
- ³ Pham, T. S.; Nguyen, V.-N.; Choi, Y.; Lee, S.; Yoon, J. Recent Strategies to Develop Innovative Photosensitizers for Enhanced Photodynamic Therapy. *Chem. Rev.* **2021**, *121*, 13454–13619.
- ⁴ Alzeibak, R.; Mishchenko, T. A.; Shilyagina, N. Y.; Balalaeva, I. V.; Vedunova, M. V.; Krysko, D. V. Targeting immunogenic cancer cell death by photodynamic therapy: past, present and future. *J. Immunother. Cancer* **2021**, *9*, e001926.
- ⁵ Dąbrowski, J. M. Reactive Oxygen Species in Photodynamic Therapy: Mechanisms of Their Generation and Potentiation. *Adv. Inorg. Chem.* **2017**, *70*, 343–394.
- ⁶ Chen, D.; Xu, Q.; Wang, W.; Shao, J.; Huang, W.; Dong, X. Type I Photosensitizers Revitalizing Photodynamic Oncotherapy. *Small* **2021**, *17*, 1–21.
- ⁷ Zhao, X.; Liu, J.; Fan, J.; Chao, H.; Peng, X. Recent progress in photosensitizers for overcoming the challenges of photodynamic therapy: from molecular design to application. *Chem. Soc. Rev.* **2021**, *50*, 4185–4219.
- ⁸ Wenpei, F.; Peng, H.; Chen, X. Overcoming the Achilles' heel of photodynamic therapy. *Chem. Soc. Rev.* **2016**, *45*, 6488–6519.
- ⁹ Li, X.; Kwon, N.; Guo, T.; Liu, Z.; Yoon, J. Innovative Strategies for Hypoxic-Tumor Photodynamic Therapy. *Angew. Chem. Int. Ed.* **2018**, *57*, 11522–11531.
- ¹⁰ Li, J.; Chen, T. Transition metal complexes as photosensitizers for integrated cancer theranostic applications. *Coord. Chem. Rev.* **2020**, *418*, 213355.
- ¹¹ Stacey, O. J.; Pope, S. J. A. New avenues in the design and potential application of metal complexes for photodynamic therapy. *RSC Adv.* **2013**, *3*, 25550–25564.
- ¹² Monroe, S.; Colon, K. L.; Yin, H. M.; Roque, J.; Konda, P.; Gujar, S.; Thummel, R. P.; Lilge, L.; Cameron, C. G.; McFarland, S. A. Transition Metal Complexes and Photodynamic Therapy from a Tumor-Centered Approach: Challenges, Opportunities, and Highlights from the Development of TLD1433. *Chem. Rev.* **2019**, *119*, 797–828.
- ¹³ McFarland, S. A.; Mandel, A.; Dumoulin-White, R.; Gasser, G. Metal-based photosensitizers for photodynamic therapy: the future of multimodal oncology? *Curr. Opin. Chem. Biol.* **2020**, *56*, 23–27.
- ¹⁴ Lisa, G.; Carioua, K.; Gasser, G. Phototherapeutic Anticancer Strategies with First-Row Transition Metal Complexes: a Critical Review. *Chem. Soc. Rev.* **2022**, *51*, 1167–1195.

-
- ¹⁵ Karges, J. Clinical Development of Metal Complexes as Photosensitizers for Photodynamic Therapy of Cancer. *Angew. Chem. Int. Ed.* **2022**, *61*, e202112236.
- ¹⁶ Wu, Y.; Li, S.; Chen, Y.; He, W.; Guo, Z. Recent advances in noble metal complex based photodynamic therapy. *Chem. Sci.* **2022**, *13*, 5085–5106.
- ¹⁷ Lee, L. C.-C.; Lo, K. K.-W. Luminescent and Photofunctional Transition Metal Complexes: From Molecular Design to Diagnostic and Therapeutic Applications. *J. Am. Chem. Soc.* **2022**, *144*, 14420-14440.
- ¹⁸ Sharma S, A., P, S.; Roy, N.; Paira, P. Advances in novel iridium (III) based complexes for anticancer applications: A review. *Inorg. Chim. Acta* **2020**, *513*, 119925.
- ¹⁹ Zamora, A.; Vigueras, G.; Rodríguez, V.; Santana, M. D.; Ruiz, J. Cyclometalated iridium(III) luminescent complexes in therapy and phototherapy. *Coord. Chem. Rev.* **2018**, *360*, 34-76.
- ²⁰ Majumdar, P.; Yuan, X.; Li, S.; Guennic, B. L.; Ma, J.; Zhang, C.; Jacquemin, D.; Zhao, J. *J. Mater. Chem. B* **2014**, *2*, 2838–2854.
- ²¹ Palao, E.; Sola-Llano, R.; Tabero, A.; Manzano, H.; Agarrabeitia, A. R.; Villanueva, A.; López-Arbeloa, I.; Martínez-Martínez, V.; Ortiz, M. J. AcetylacetonateBODIPY-Biscyclometalated Iridium(III) Complexes: Effective Strategy towards Smarter Fluorescent Photosensitizer Agents. *Chem. Eur. J.* **2017**, *23*, 10139–10147.
- ²² Tabrizi, L.; Chiniforoshan, H. New cyclometalated Ir(III) complexes with NCN pincer and meso-phenylcyanamide BODIPY ligands as efficient photodynamic therapy agents. *RSC Adv.* **2017**, *7*, 34160–34169.
- ²³ Qiao, L.; Liu, J.; Kuang, S.; Liao, X.; Kou, J.; Ji, L.; Chao, H. A mitochondrion-targeted BODIPY-Ir(III) conjugate as a photoinduced ROS generator for the oxidative destruction of triple-negative breast cancer cells. *Dalton Trans.* **2021**, *50*, 14332-14341.
- ²⁴ Zhang, L.; Geng, Y.; Li, L.; Tong, X.; Liu, S.; Liu, X.; Su, Z.; Xie, Z.; Zhu, D.; Bryce, M. R. Rational design of iridium-porphyrin conjugates for novel synergistic photodynamic and photothermal therapy anticancer agents. *Chem. Sci.* **2021**, *12*, 5918-5925.
- ²⁵ Wu, Y.; Wu, J.; Wong, W.-Y. A new near-infrared phosphorescent iridium(III) complex conjugated to a xanthene dye for mitochondria-targeted photodynamic therapy. *Biomater. Sci.* **2021**, *9*, 4843-4853
- ²⁶ Liu, C.; Zhou, L.; Wei, F.; Li, L.; Zhao, S.; Gong, P.; Cai, L.; Wong, K. M.-C. Versatile Strategy To Generate a Rhodamine Triplet State as Mitochondria-Targeting Visible-Light Photosensitizers for Efficient Photodynamic Therapy. *ACS Appl. Mater. Interfaces* **2019**, *11*, 8797-8806
- ²⁷ Medina, F. G.; Marrero, J. G.; Macías-Alonso, M.; González, M. C.; Córdova-Guerrero, I.; Teissier García, A. G.; Osegueda-Robles, S. Coumarin Heterocyclic Derivatives: Chemical Synthesis and Biological Activity. *Nat. Prod. Rep.* **2015**, *32*, 1472–1507.
- ²⁸ Al-Warhi, T.; Sabt, A.; Elkaeed, E. B.; Eldehna, W. M. Recent Advancements of Coumarin-Based Anticancer Agents: An up-to-Date Review. *Bioorg. Chem.* **2020**, *103*, No. 104163.
- ²⁹ Emami, S.; Dadashpour, S. Current Developments of Coumarin-Based Anti-Cancer Agents in Medicinal Chemistry. *Eur. J. Med. Chem.* **2015**, *102*, 611–630.

-
- ³⁰ Sharma, S. J.; Sekar, N. Deep-red/NIR emitting coumarin derivatives - Synthesis, photophysical properties, and biological applications. *Dyes Pigm.* **2022**, *202*, 110306.
- ³¹ Ye, R.-R.; Tan, C.-P.; Ji, L.-N.; Mao, Z.-W.. Coumarin-appended phosphorescent cyclometalated iridium(III) complexes as mitochondria-targeted theranostic anticancer agents. *Dalton Trans.* **2016**, *45*, 13042-13051.
- ³² Ye, R.-R.; Tan, C.-P.; He, L.; Chen, M.-H.; Ji, L.-N.; Mao, Z.-W.. Cyclometalated Ir(III) complexes as targeted theranostic anticancer therapeutics: combining HDAC inhibition with photodynamic therapy. *Chem. Commun.* **2014**, *50*, 10945-10948.
- ³³ Yu, T.; Xu, Z.; Su, W.; Zhao, Y.; Zhang, H.; Bao, Y. Highly efficient phosphorescent materials based on Ir(III) complexes-grafted on a polyhedral oligomeric silsesquioxane core. *Dalton Trans.* **2016**, *45*, 13491-13502.
- ³⁴ Fan, Z.; Xie, J.; Sadhukhan, T.; Liang, C.; Huang, C.; Li, W.; Li, T.; Zhang, P.; Banerjee, S.; Raghavachari, K.; Huang, H. Highly Efficient Ir(III)-Coumarin Photo-Redox Catalyst for Synergetic Multi-Mode Cancer Photo-Therapy. *Chem. Eur. J.* **2022**, *28*, e202103346.
- ³⁵ Novohradsky, V.; Rovira, A.; Hally, C.; Galindo, A.; Viguera, G.; Gandioso, A.; Svitelova, M.; Bresolí-Obach, R.; Kosthunova, H.; Markova, L.; Kasparkova, J.; Nonell, S.; Ruiz, J.; Brabec, V.; Marchán, V. Towards Novel Photodynamic Anticancer Agents Generating Superoxide Anion Radicals: A Cyclometalated Ir(III) Complex Conjugated to a Far-Red Emitting Coumarin. *Angew. Chem. Int. Ed.* **2019**, *58*, 6311-6315.
- ³⁶ Novohradsky, V.; Markova, L.; Kosthunova, H.; Kasparkova, J.; Ruiz, J.; Marchán, V.; Brabec, V. A Cyclometalated Ir(III) Complex Conjugated to a Coumarin Derivative Is a Potent Photodynamic Agent against Prostate Differentiated and Tumorigenic Cancer Stem Cells. *Chem. Eur. J.* **2021**, *27*, 8547-8556.
- ³⁷ Gandioso, A.; Bresolí-Obach, R.; Nin-Hill, A.; Bosch, M.; Palau, M.; Galindo, A.; Contreras, S.; Rovira, A.; Rovira, C.; Nonell, S.; Marchán, V. Redesigning the Coumarin Scaffold into Small Bright Fluorophores with Far-Red to Near-Infrared Emission and Large Stokes Shifts Useful for Cell Imaging. *J. Org. Chem.* **2018**, *83*, 1185-1195.
- ³⁸ Gandioso, A.; Palau, M.; Bresolí-Obach, R.; Galindo, A.; Rovira, A.; Bosch, M.; Nonell, S.; Marchán, V. High Photostability in Nonconventional Coumarins with Far-Red/NIR Emission through Azetidinylation. *J. Org. Chem.* **2018**, *83*, 11519-11531.
- ³⁹ Rovira, A.; Pujals, M.; Gandioso, A.; López-Corrales, M.; Bosch, M.; Marchán, V. Modulating Photostability and Mitochondria Selectivity in Far-Red/NIR Emitting Coumarin Fluorophores through Replacement of Pyridinium by Pyrimidinium. *J. Org. Chem.* **2020**, *85*, 6086-6097.
- ⁴⁰ Rovira, A.; Gandioso, A.; Goñalons, M.; Galindo, A.; Massaguer, A.; Bosch, M.; Marchán, V. Solid-Phase Approaches for Labeling Targeting Peptides with Far-Red Emitting Coumarin Fluorophores. *J. Org. Chem.* **2019**, *84*, 1808-1817.
- ⁴¹ Ortega-Forte, E.; Rovira, A.; Gandioso, A.; Bonelli, J.; Bosch, M.; Ruiz, J.; Marchán, V. COUPY Coumarins as Novel Mitochondria-Targeted Photodynamic Therapy Anticancer Agents. *J. Med. Chem.* **2021**, *64*, 17209-17220.

-
- ⁴² Bassolino, G.; Nançoz, C.; Thiel, Z.; Bois, E.; Vauthey, E.; Rivera-Fuentes, P. Photolabile coumarins with improved efficiency through azetidiny substitution. *Chem. Sci.* **2018**, *9*, 387–391.
- ⁴³ Brimiouille, R.; Guo, H.; Bach, T. Enantioselective intramolecular [2+2] photocycloaddition reactions of 4-substituted coumarins catalyzed by a chiral Lewis acid. *Chem. Eur. J.* **2012**, *18*, 7552–7560.
- ⁴⁴ Ortega-Forte, E.; Hernández-García, S.; Viguera, G.; Henarejos-Escudero, P.; Cutillas, N.; Ruiz, J.; Gandía-Herrero, F. Potent anticancer activity of a novel iridium metallodrug via oncosis. *Cell. Mol. Life Sci.* **2022**, *79*, 510.
- ⁴⁵ Rossi, S.; Cordella, M.; Tabolacci, C.; Nassa, G.; D’Arcangelo, D.; Senatore, C.; Pagnotto, P.; Magliozzi, R.; Salvati, A.; Weisz, A.; Facchiano, A.; Facchiano, F. TNF-alpha and metalloproteases as key players in melanoma cells aggressiveness. *J. Exp. Clin. Cancer Res.* **2018**, *37*, 326.
- ⁴⁶ Karges, J.; Yempala, T.; Tharaud, M.; Gibson, D.; Gasser, G. A Multi-action and Multitarget Ru(II)-Pt(IV) Conjugate Combining Cancer Activated Chemotherapy and Photodynamic Therapy to Overcome Drug Resistant. *Cancers. Angew. Chem. Int. Ed.* **2020**, *59*, 7069-7075.
- ⁴⁷ Casas, A.; Di Venosa, G.; Hasan, T.; Batlle, A. Mechanisms of Resistance to Photodynamic Therapy. *Curr. Med. Chem.* **2011**, *18*, 2486–2515.
- ⁴⁸ Magde, D.; Brannon, J. H.; Cremers, T. L.; Olmsted, J. Absolute luminescence yield of cresyl violet. A standard for the red. *J. Phys. Chem.* **1979**, *83*, 696-699
- ⁴⁹ Seybold, P. G.; Gouterman, M. Porphyrins XIII: Fluorescence Spectra and Quantum Yields. *J. Mol. Spectrosc.* **1969**, *31*, 1–13.
- ⁵⁰ Schindelin, J.; Arganda-Carreras, I.; Frise, E.; Kaynig, V.; Longair, M.; Pietzsch, T.; Preibisch, S.; Rueden, C.; Saalfeld, S.; Schmid, B.; Tinevez, J. Y.; White, D. J.; Hartenstein, V.; Eliceiri, K.; Tomancak, P.; Cardona, A. Fiji: an open-source platform for biological-image analysis. *Nat. Methods* **2012**, *9*, 676-682.

SUPPORTING INFORMATION

Exploring structure–activity relationships in photodynamic therapy anticancer agents based on Ir(III)-COUPY conjugates

Anna Rovira,^{1,#} Enrique Ortega-Forte,^{2,#} Cormac Hally,³ Mireia Jordà,³ Gloria Viguera,² Manel Bosch,⁴ Santi Nonell,³ José Ruiz,^{2,*} Vicente Marchán^{1,*}

¹ Departament de Química Inorgànica i Orgànica, Secció de Química Orgànica, Universitat de Barcelona (UB), and Institut de Biomedicina de la Universitat de Barcelona (IBUB), Martí i Franquès 1-11, E-08028 Barcelona, Spain. Email: vmarchan@ub.edu

² Departamento de Química Inorgànica, Universidad de Murcia, and Institute for Bio-Health Research of Murcia (IMIB-Arrixaca), E-30071 Murcia, Spain. Email: jruiz@um.es

³ Institut Químic de Sarrià, Universitat Ramon Llull, Vía Augusta 390, E-08017 Barcelona (Spain)

⁴ Unitat de Microscòpia Òptica Avançada, Centres Científics i Tecnològics, Universitat de Barcelona, Av. Diagonal 643, E- 08028 Barcelona (Spain)

These authors contributed equally

Table of contents

1.- Photophysical and photochemical characterization of the compounds	S3
2.- <i>In vitro</i> photobiological studies	S8
3.- ^1H and ^{13}C NMR spectra and HR ESI-MS of the compounds	S10

1. Photophysical and photochemical characterization of the compounds

Table S1. Photophysical and photochemical properties of the control compounds (coumarins **1a-1c** and complex **2a**) in different solvents at room temperature.

Comp.	Solvent	λ_{abs} [nm]	ϵ [mM·cm ⁻¹]	λ_{em} [nm]	Stokes' shift [nm]	ϕ_F/ϕ_P	τ_F [ns]	τ_P [ns]	Φ_{Δ} at 355 nm	Φ_{Δ} at 532 nm
1a	DCM	569	67	607	38	0.70	5.4	-	<0.01	0.03
	ACN	548	75	609	61	0.18	1.4	-	<0.01	<0.01
	PBS	545	34	604	59	0.14	0.9	-	≈ 0	<0.01
1b	DCM	456	23	506	50	0.007	3.52	-	0.01	-
	ACN	446	24	492	46	0.002	4	-	0.01	<0.01
	PBS	443	23	486	43	0.002	3.37	-	≈ 0	<0.01
1c	DCM	597	61	631	34	0.53	5.46	-	0.03	0.03
	ACN	572	60	635	63	0.22	2.03	-	≈ 0	0.01
	PBS	557	38	629	72	0.031	0.031	-	≈ 0	<0.01
2a	DCM	303	42	665	362	0.07	-	315	0.23	-
	ACN	302	41	660	358	0.03	-	187	0.42	-
	PBS	305	40	656	351	>0.01	-	55 (93%) 281 (7%)	<0.01	-

Table S2. Photophysical and photochemical properties of the Ir(III)-COUPY conjugates **3a-3e** in different solvents at room temperature.

Comp.	Solvent	λ_{abs} [nm]	ϵ [mM·cm ⁻¹]	λ_{em} [nm]	Stokes' shift [nm]	ϕ_f/ϕ_p	τ_F [ns]	τ_P [ns]	Φ_{Δ} at 355 nm	Φ_{Δ} at 532 nm
3a	DCM	566	44	602	36	0.07	0.25	121 (70%) 392 (30)	0.37	0.34
	ACN	555	22	615	60	0.08	0.51	45 (86%) 269 (14%)	0.23	0.24
	PBS	550	17	615	65	0.004	0.37 (73%) 3.3 (27%)	-	<0.01	<0.01
3b	DCM	457	26	664	-	0.01	-	329	0.21	-
	ACN	451	33	650 (480)	-	0.002	-	173	0.30	0.32
	PBS	436	17	-	-	0.00049	-	39 (52%) 211 (48%)	<0.01	<0.01
3c	DCM	592	26	629	37	0.17	2.66	69 (80%) 298 (20%)	0.20	0.16
	ACN	580	24	647	67	0.08	0.9 (74%) 3.534 (26%)	264	0.14	0.12
	PBS	575	13	610	35	0.003	1.4	317 (78%) 43 (22%)	<0.01	<0.01
3d	DCM	567	45	599	32	0.09	2.94	333 (89%) 59 (11%)	0.39	0.35
	ACN	556	45	608	52	0.07	2.94 (70%) 0.79 (30%)	263	0.32	0.30
	PBS	550	21	612	62	0.017	1.11	307 (72%) 1900 (28%)	<0.01	<0.01
3e	DCM	566	40	600	34	0.08	0.55 (62%) 3.34 (38%)	377 (64%) 109 (36%)	0.34	0.28
	ACN	554	41	607	53	0.16	1	159 (56%) 40 (44%)	0.31	0.22
	PBS	541	20	618	77	0.006	1.03	315 (68%) 1913 (32%)	<0.01	<0.01

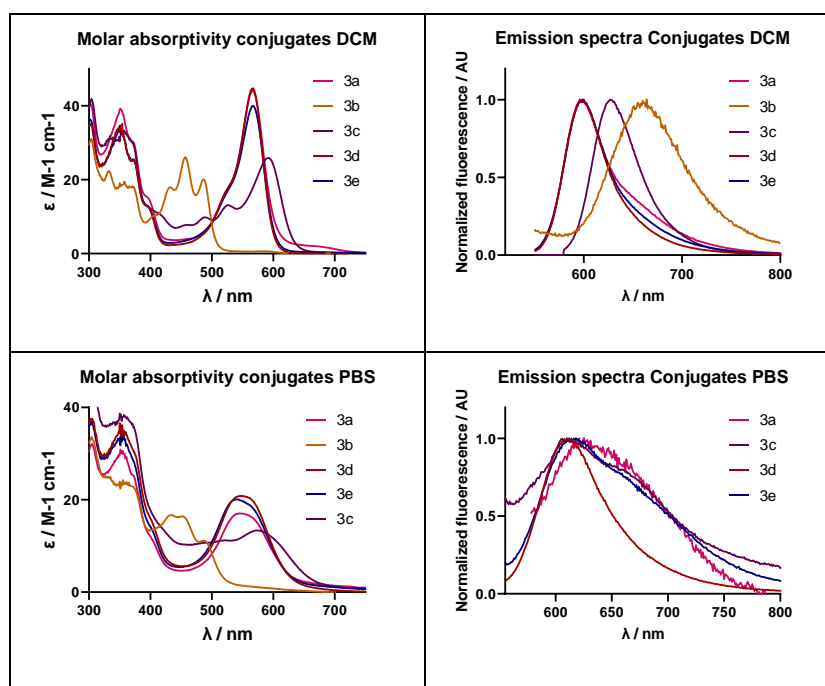


Figure S1. Comparison of the absorption (left) and emission spectra (right) of Ir(III)-COUPY conjugates **3a-3e** in DCM and PBS.

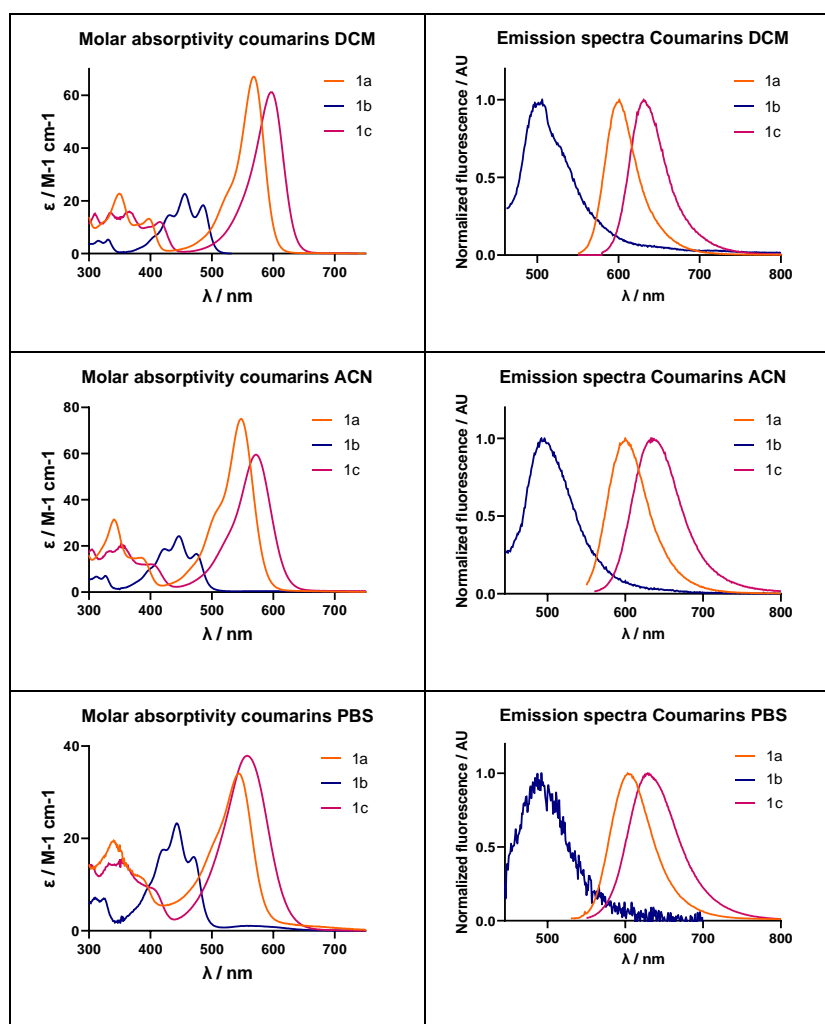


Figure S2. Comparison of the absorption (left) and emission spectra (right) of COUPY dyes **1a-1c** in DCM, ACN and PBS.

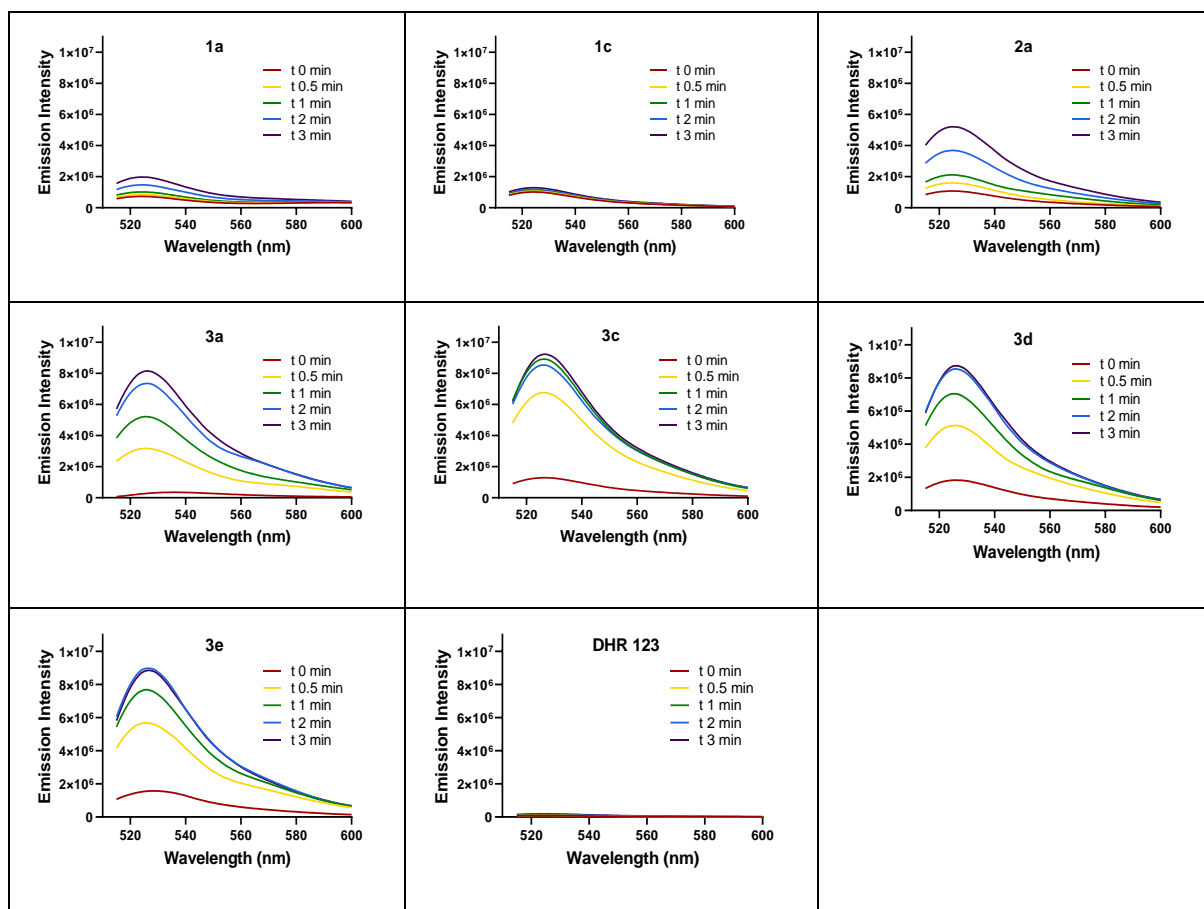


Figure S3. Fluorescence spectra of DHR123 induced by irradiation with visible light (505 nm) in the presence of COUPY coumarins **1a** and **1c**, Ir(III) complex **2a**, Ir(III)-COUPY conjugates **3a**, **3c**, **3d** and **3e**, or without any compound (DHR 123 alone).

2. *In vitro* photobiological studies

Table S3. Phototoxicity of the compounds towards A2780cis cells under normoxia and hypoxia.^a

	Normoxia			Hypoxia		
	Dark	520 nm	PI ^b	Dark	520 nm	PI ^b
1a	>250	2.1 ± 0.2	>119.1	>250	2.5 ± 0.2	>100.0
1b	>250	>250	n.d.	>250	>250	n.d.
1c	15 ± 2	0.15 ± 0.04	100.0	20 ± 2	0.6 ± 0.1	36.4
2a	>250	3.5 ± 0.4	>71.4	>250	11 ± 2	>22.7
3a	>250	0.70 ± 0.06	>357.1	>250	3.8 ± 0.3	>65.8
3b	>250	61 ± 8	>4.1	>250	31 ± 7	>8.1
3c	>250	1.04 ± 0.02	>240.4	>250	8 ± 1	>31.3
3d	>250	1.1 ± 0.2	>227.3	>250	1.9 ± 0.2	>131.6
3e	>250	0.93 ± 0.04	>268.8	>250	1.7 ± 0.3	>147.1
5-ALA	>250	62 ± 12	>4.0	>250	>250	n.d.

^aCells were treated for 2 h (1 h incubation and 1 h irradiation with green light) followed by 48 h of incubation in drug-free medium either under normoxic (21 % O₂) or hypoxic (2 % O₂) conditions. Dark analogues were kept in the dark. Data expressed as mean ± SD from three independent experiments.

^bPI = phototherapeutic index defined as IC₅₀ (dark-non-irradiated cells)/IC₅₀ (irradiated cells).

Table S4. Phototoxicity of the **3a** and **3b** towards A2780cis cells using blue light (465 nm).^a

	Dark	465 nm	PI ^b
3a	>100	1.9 ± 0.3	>52.6
3b	>100	2.4 ± 0.2	>41.7

^aCells were treated for 2 h (1 h incubation and 1 h irradiation with blue light, 5 mW/cm²) followed by 48 h of incubation in drug-free medium. Dark analogues were kept in the dark. Data expressed as mean ± SD from three independent experiments. ^bPI = phototherapeutic index defined as IC₅₀ (dark-non-irradiated cells)/IC₅₀ (irradiated cells).

Table S5. Partial inhibition (% of cell growth inhibition with respect to untreated controls) of compounds at 250 μ M in A2780cis after 2 h incubation in the dark followed by 48 h drug-free recovery period.

	Normoxia	Hypoxia
1a	3.5 \pm 0.9	2.1 \pm 0.4
1b	24 \pm 3	4.5 \pm 0.6
1c	100	100
2a	62 \pm 4	56 \pm 6
3a	58 \pm 7	49 \pm 4
3b	63 \pm 5	45 \pm 6
3c	74 \pm 10	61 \pm 8
3d	21 \pm 1	27 \pm 4
3e	18 \pm 1	12 \pm 3
5-ALA	3.5 \pm 0.4	1.0 \pm 0.2

3. ^1H and ^{13}C NMR spectra and HR ESI-MS of the compounds

Compound 4

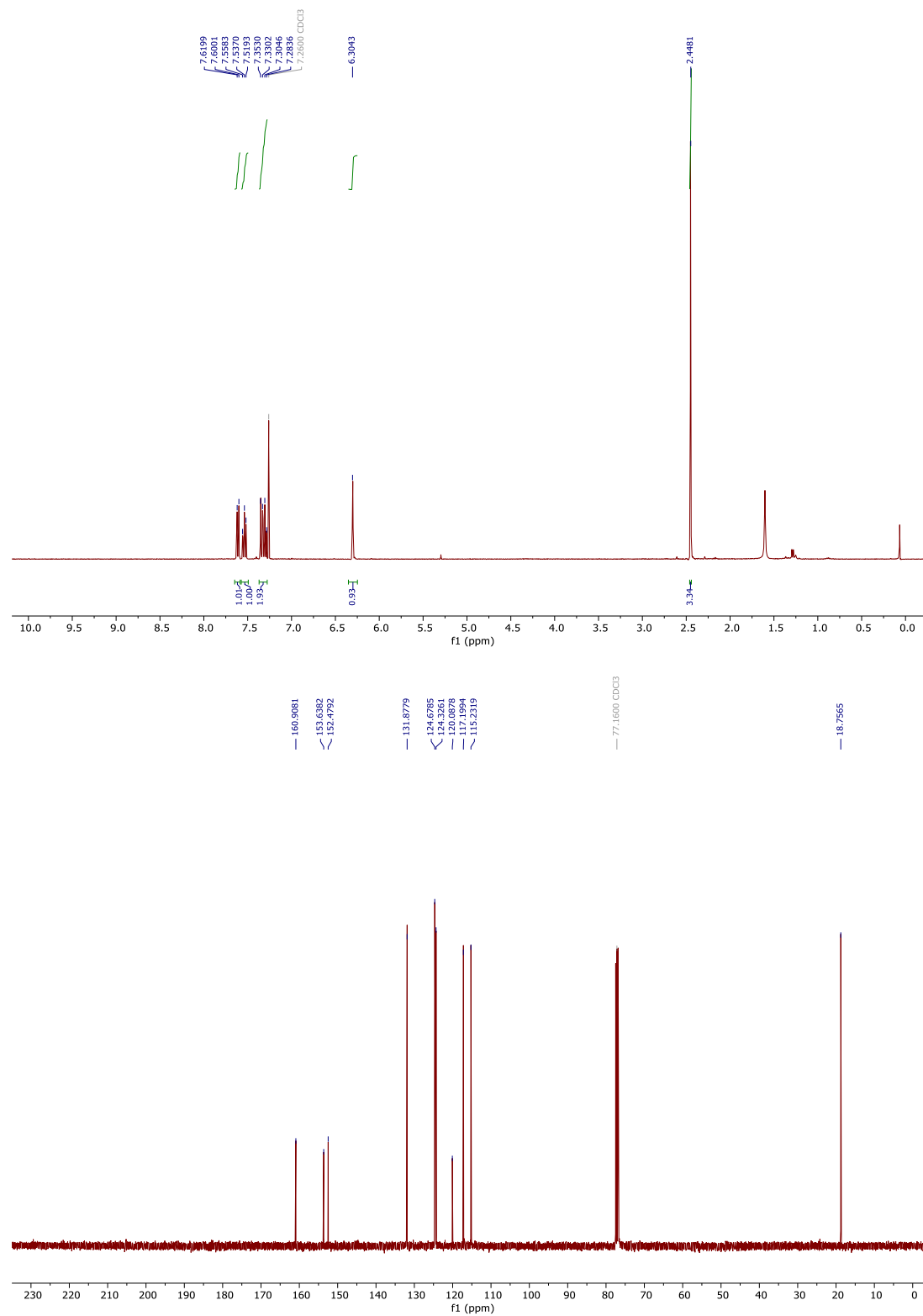


Figure S4. ^1H and ^{13}C NMR spectra of compound 4 in CDCl_3 .

Compound 5

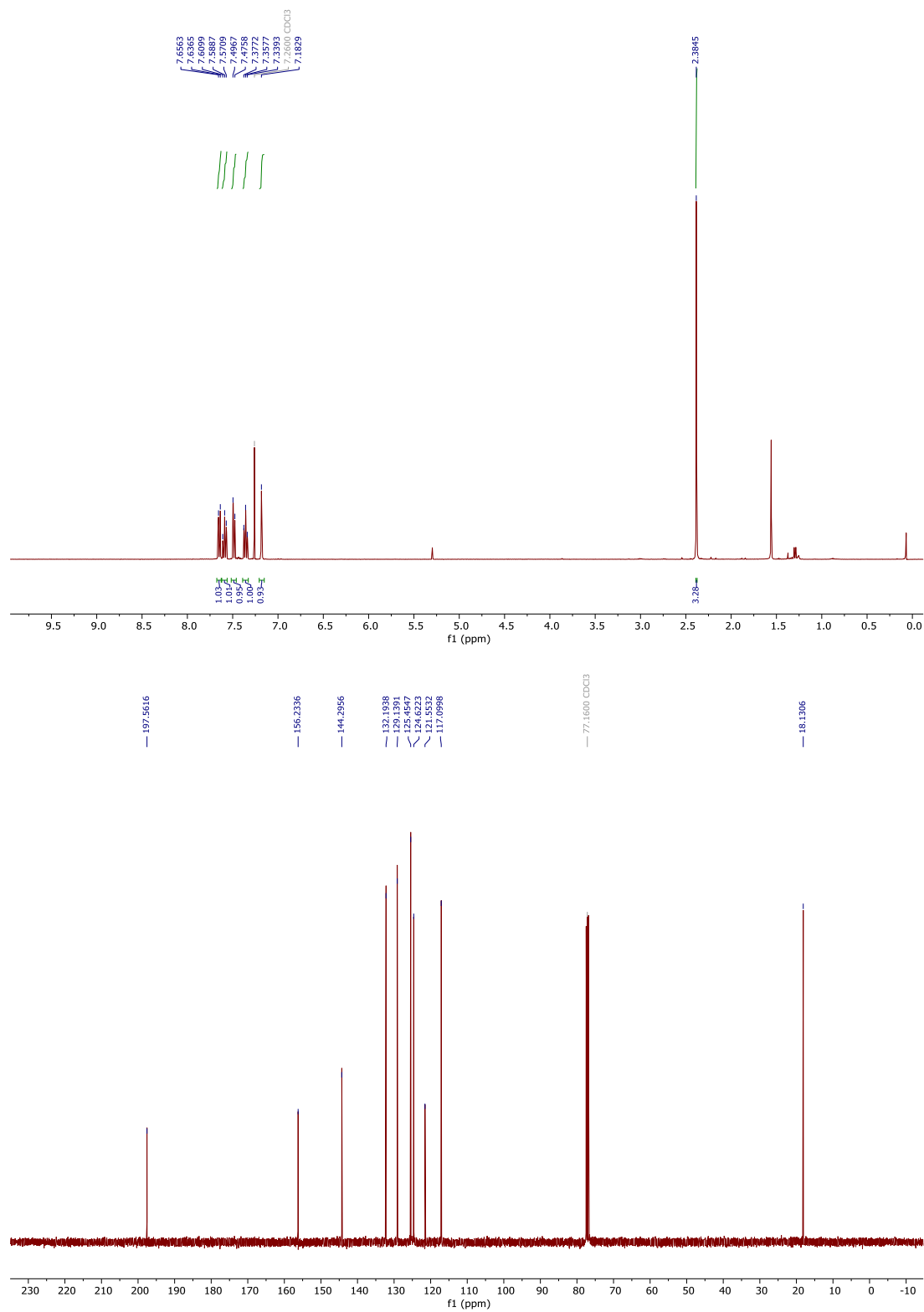


Figure S5. ¹H and ¹³C NMR spectra of compound 5 in CDCl₃.

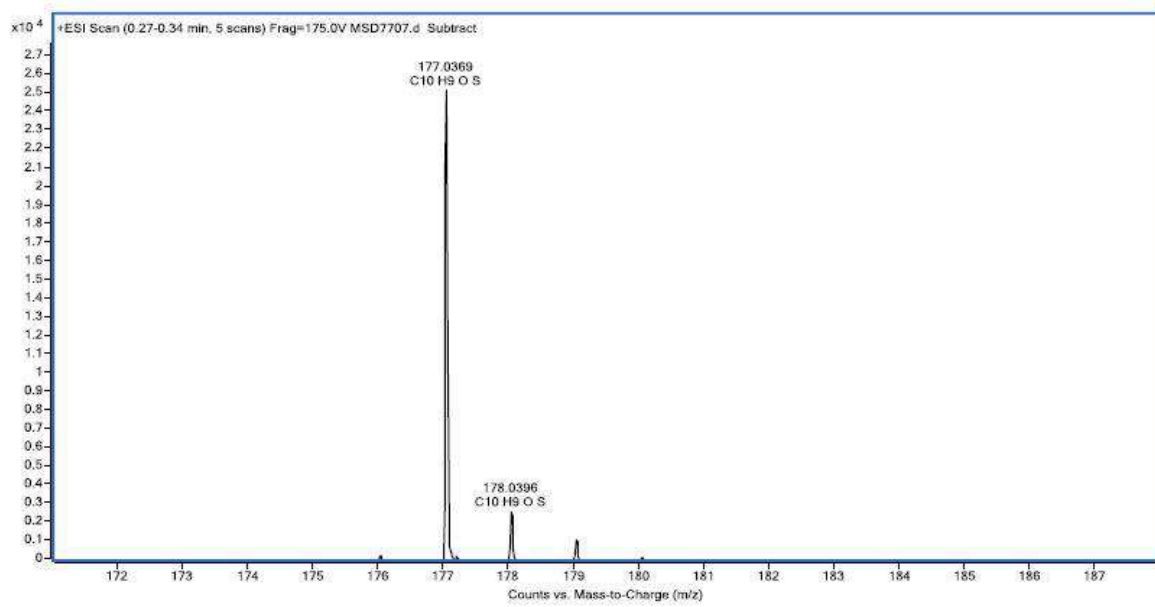
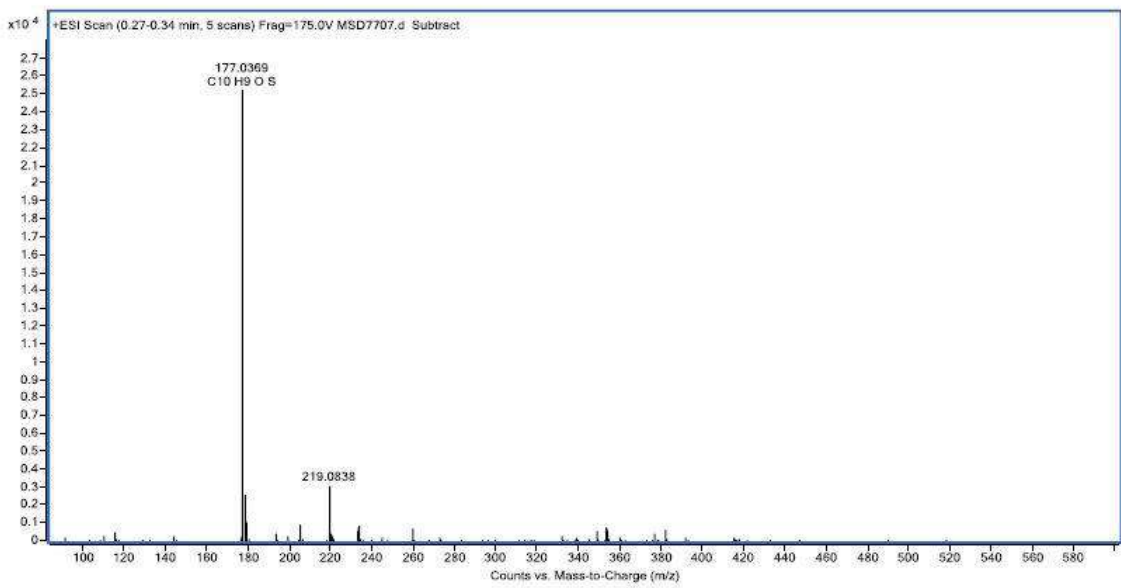


Figure S6. HR ESI-MS spectrum of compound 5.

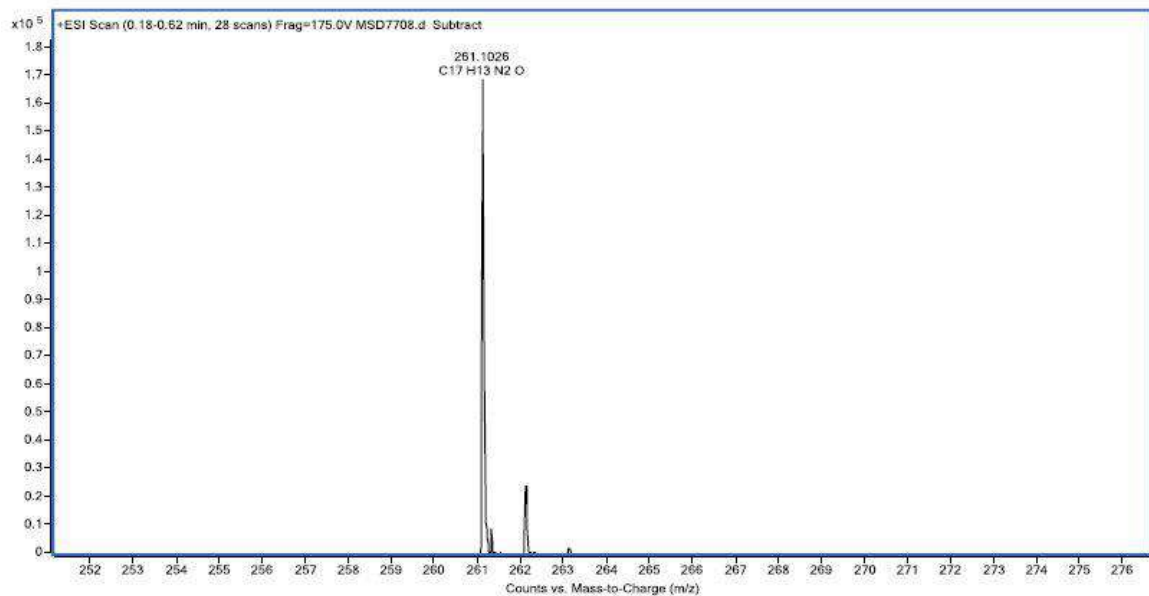
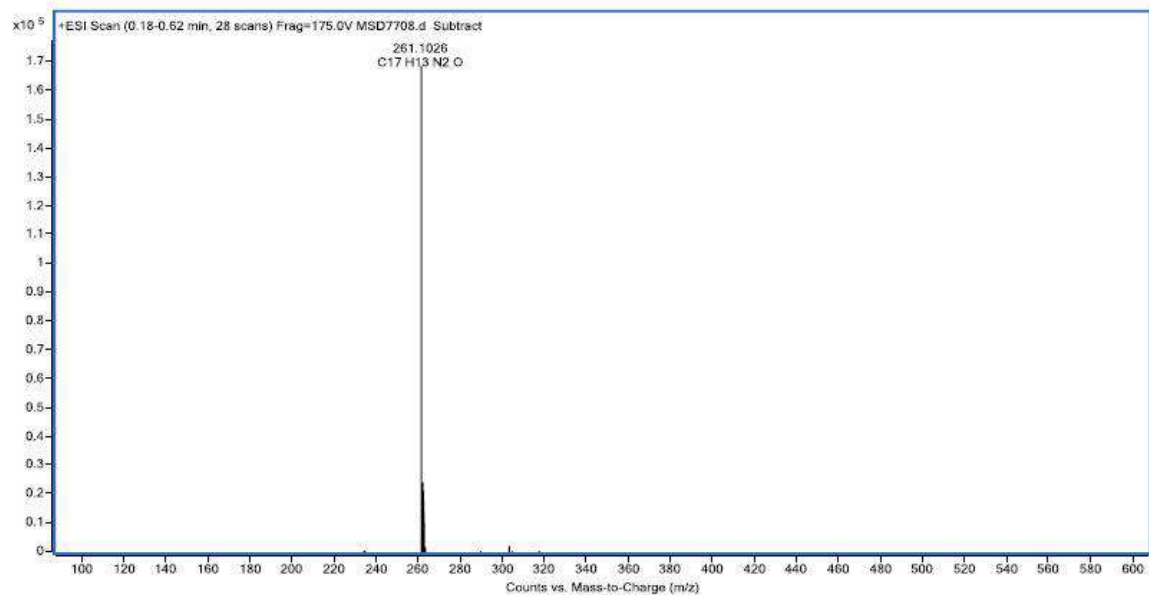


Figure S8. HR ESI-MS spectrum of compound **6**.

Compound 7

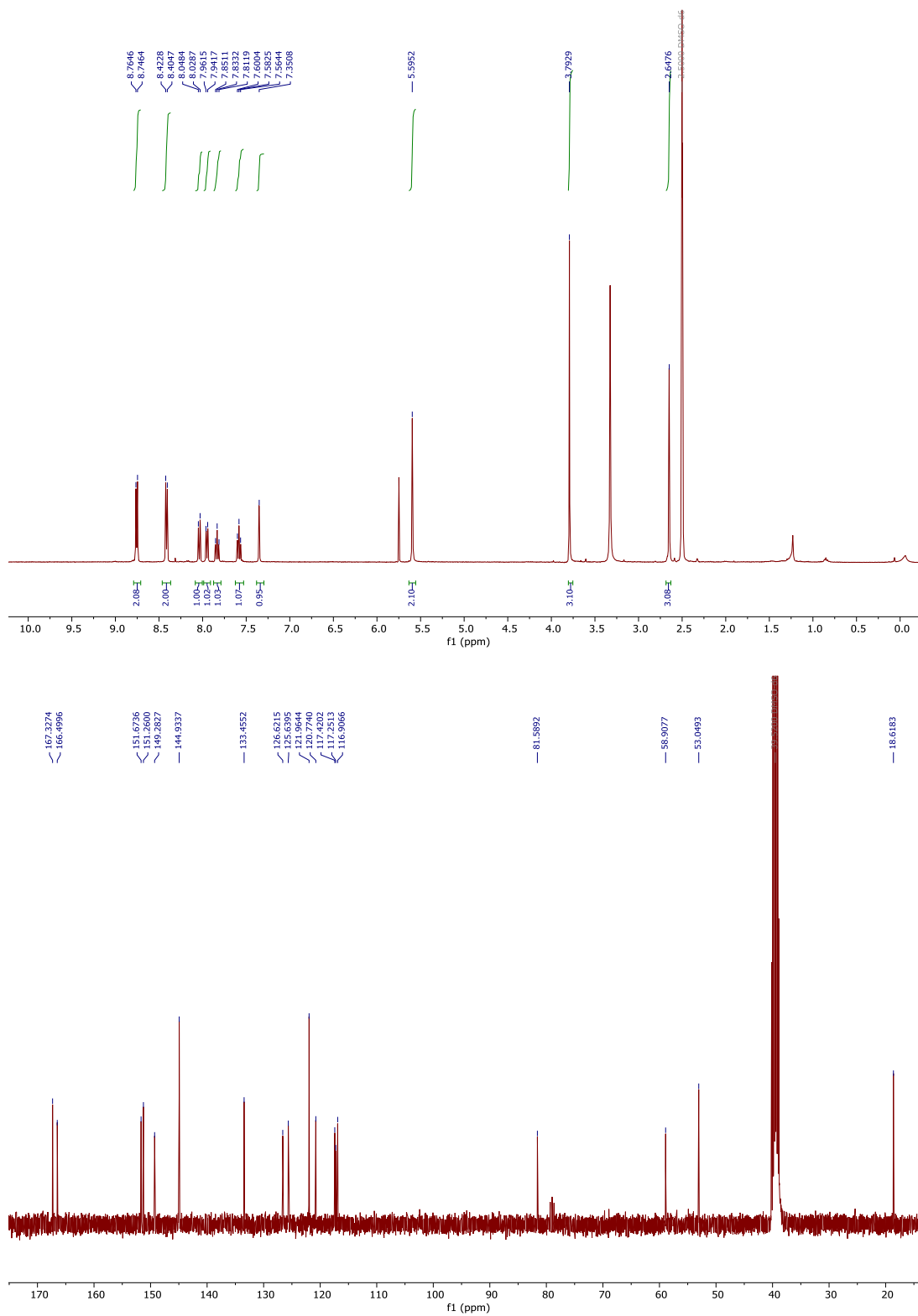


Figure S9. ¹H and ¹³C NMR spectra of compound 7 in DMSO-*d*₆.

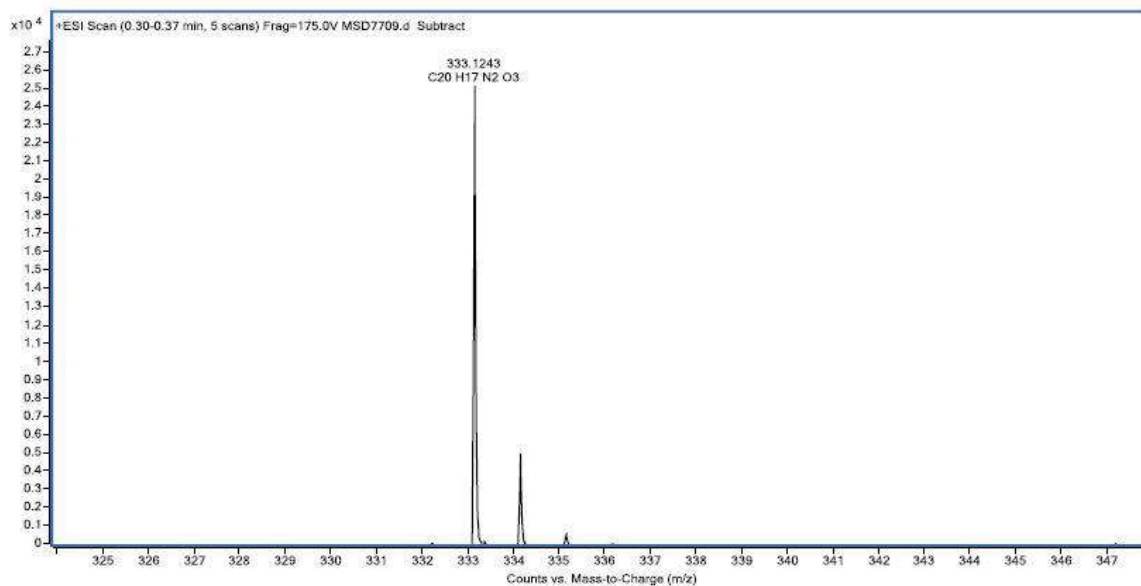
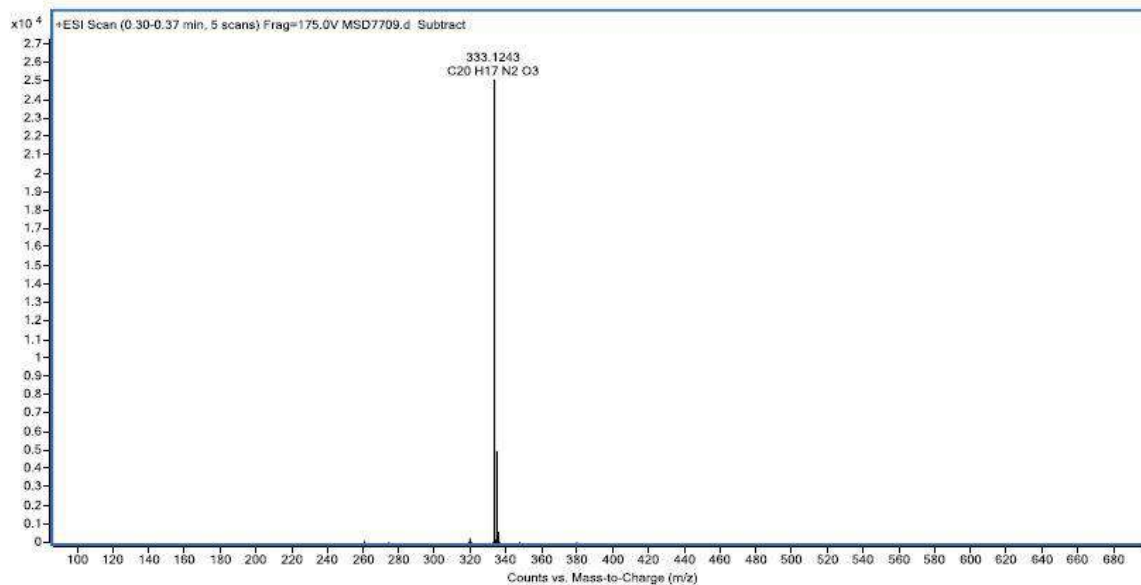


Figure S10. HR ESI-MS spectrum of compound 7.

Compound 9

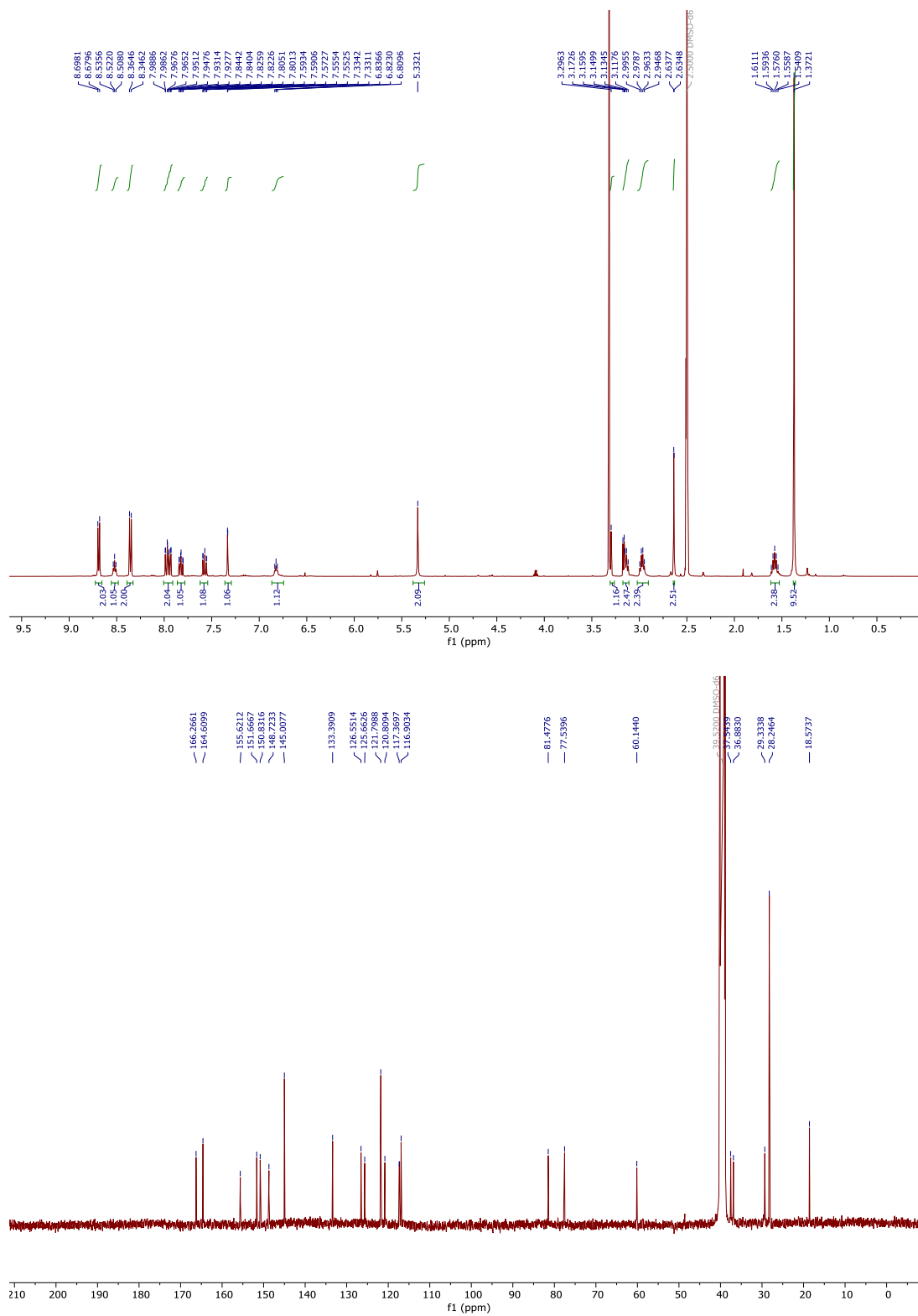


Figure S11. ¹H and ¹³C NMR spectra of compound 9 in DMSO-d₆.

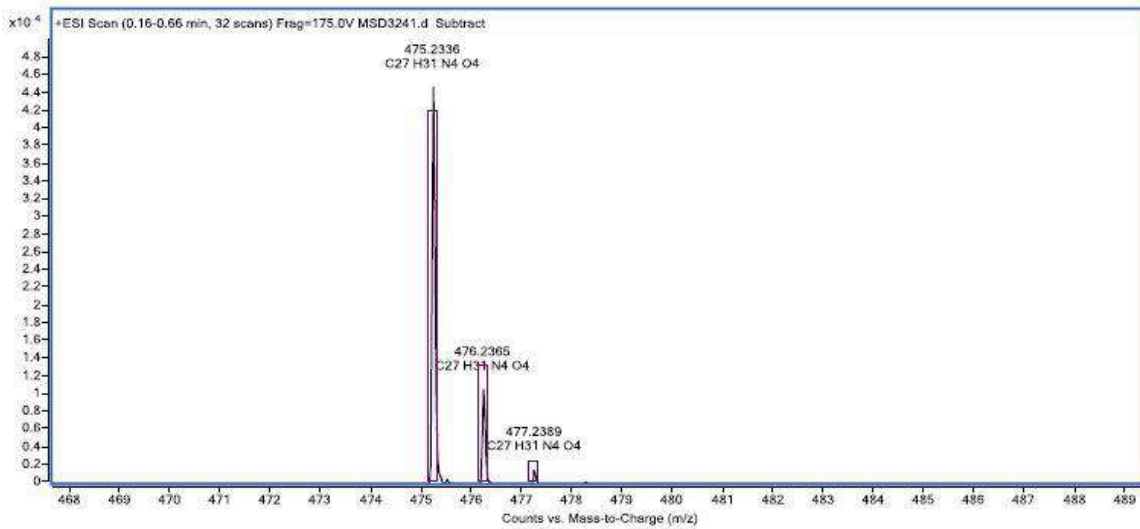
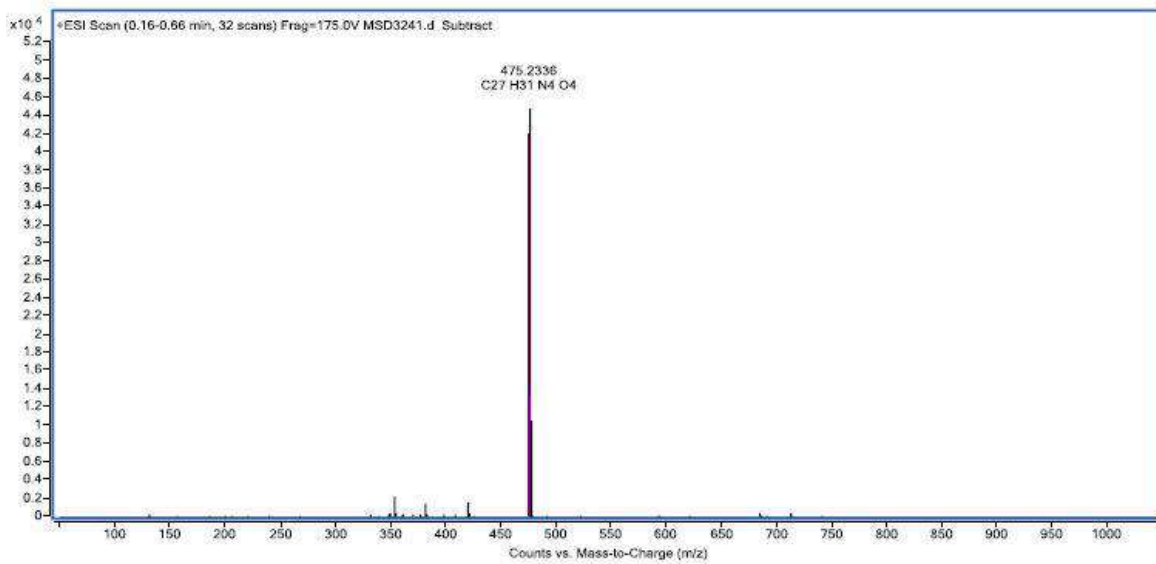


Figure S12. HR ESI-MS spectrum of compound **9**.

Compound 11

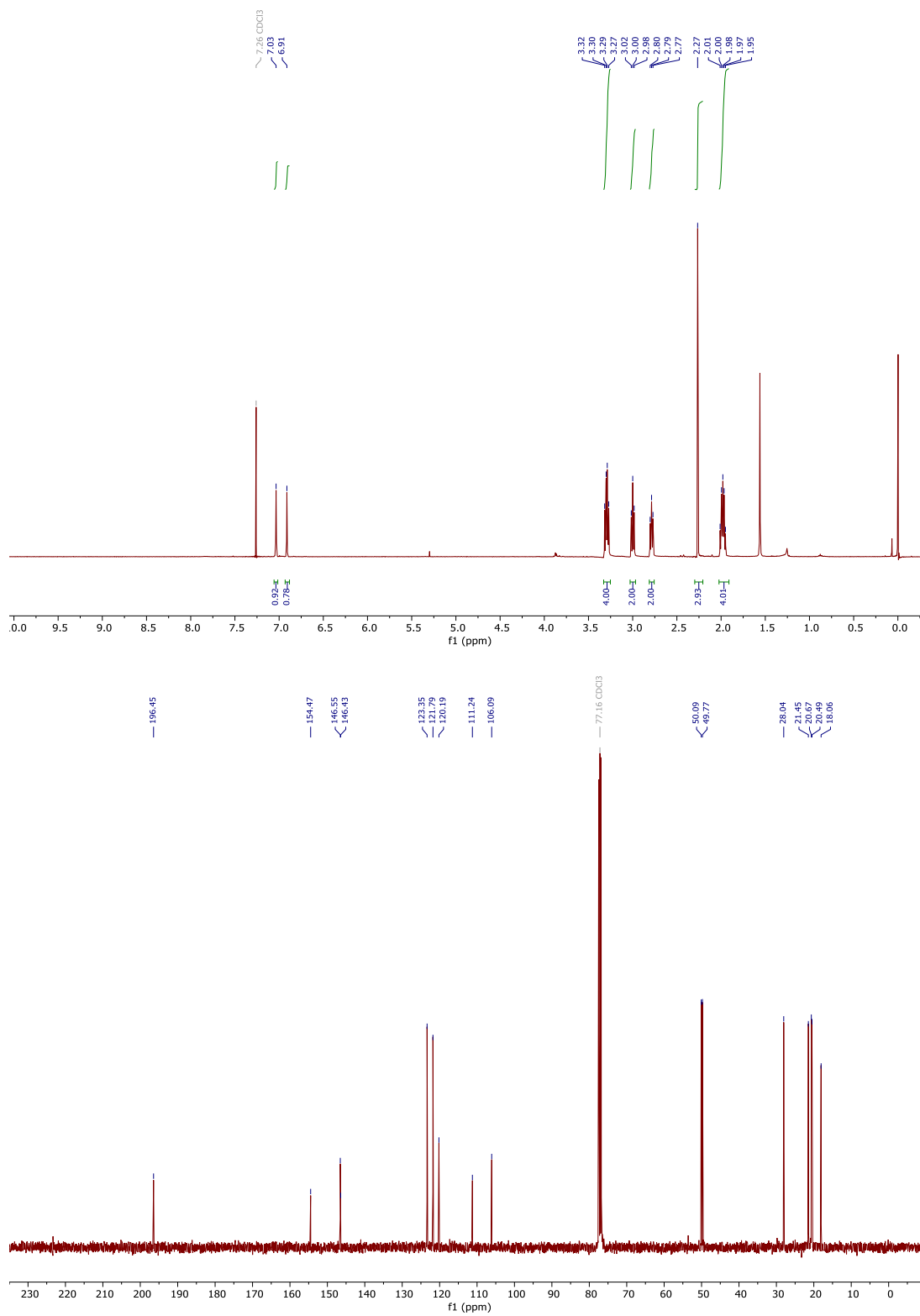


Figure S13. ¹H and ¹³C NMR spectra of compound 11 in CDCl₃.

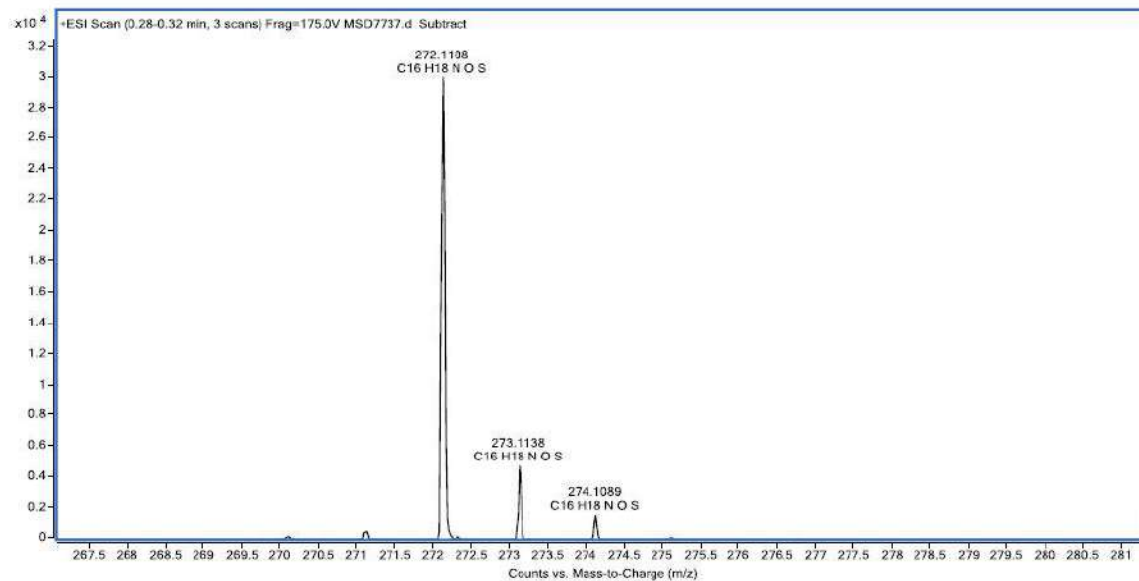
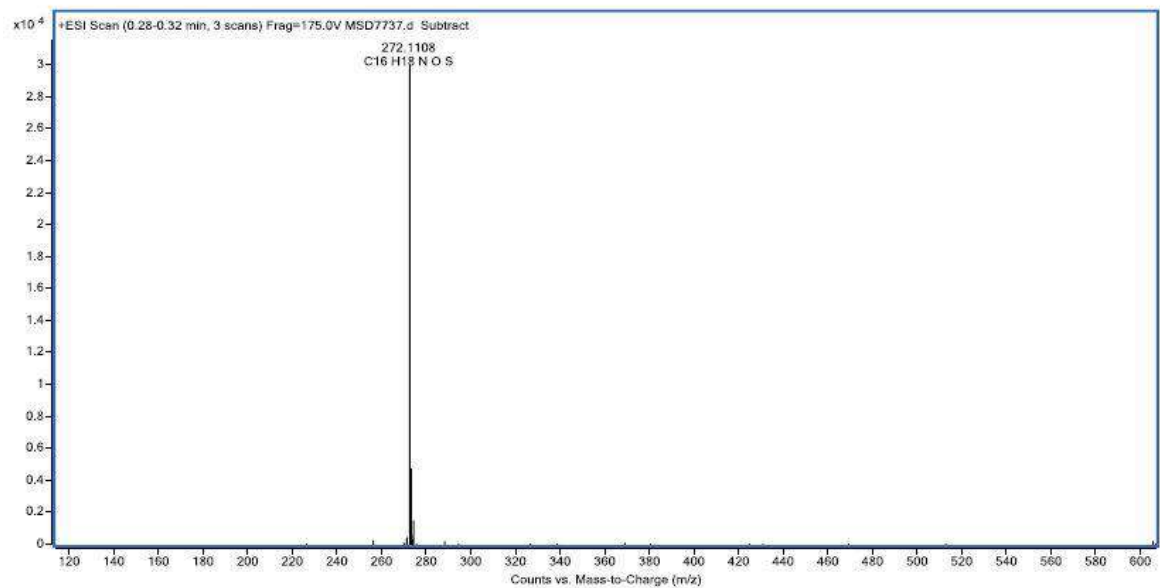


Figure S14. HR ESI-MS spectrum of compound **11**.

Compound 12

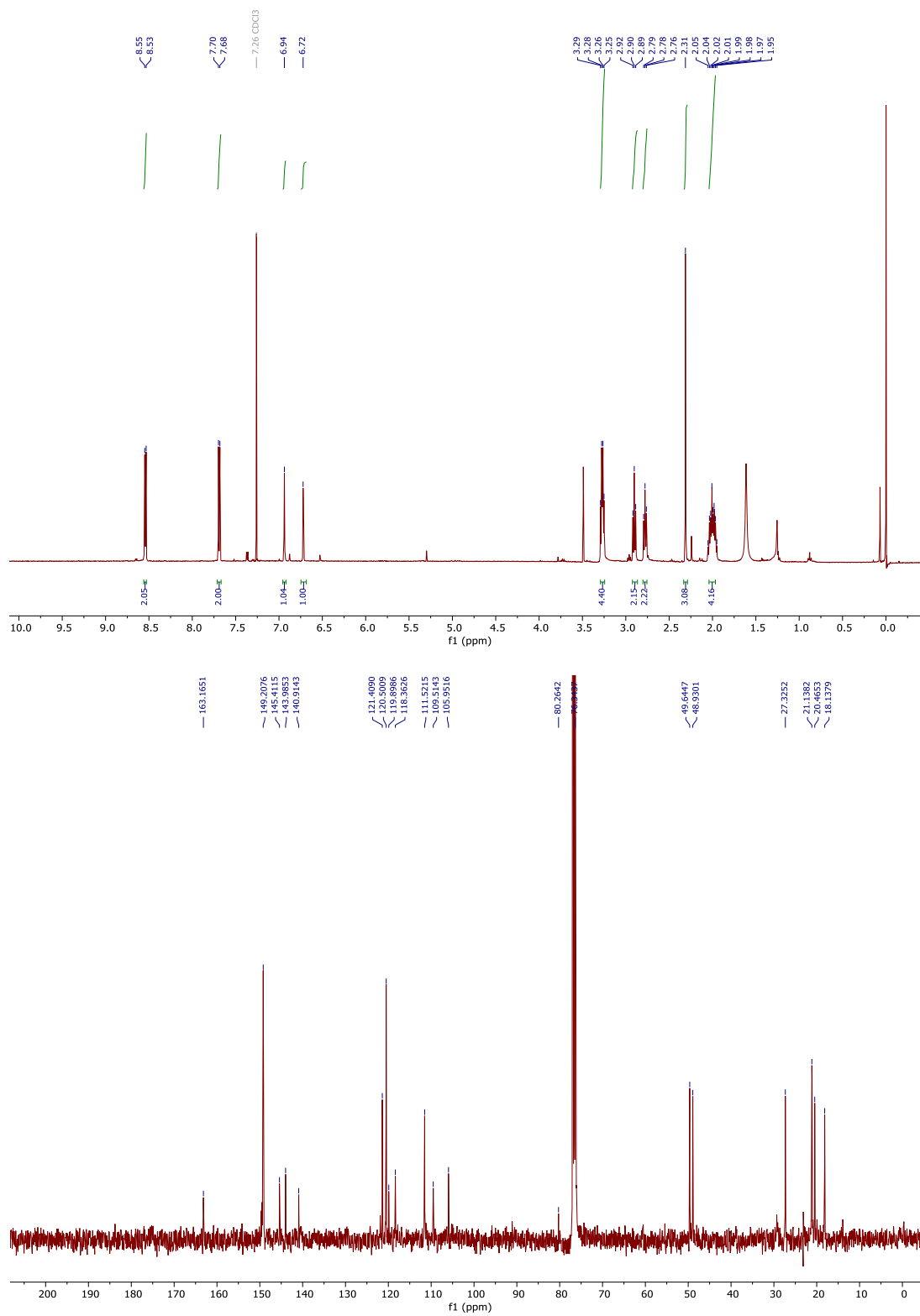


Figure S15. ¹H and ¹³C NMR spectra of compound 12 in CDCl₃.

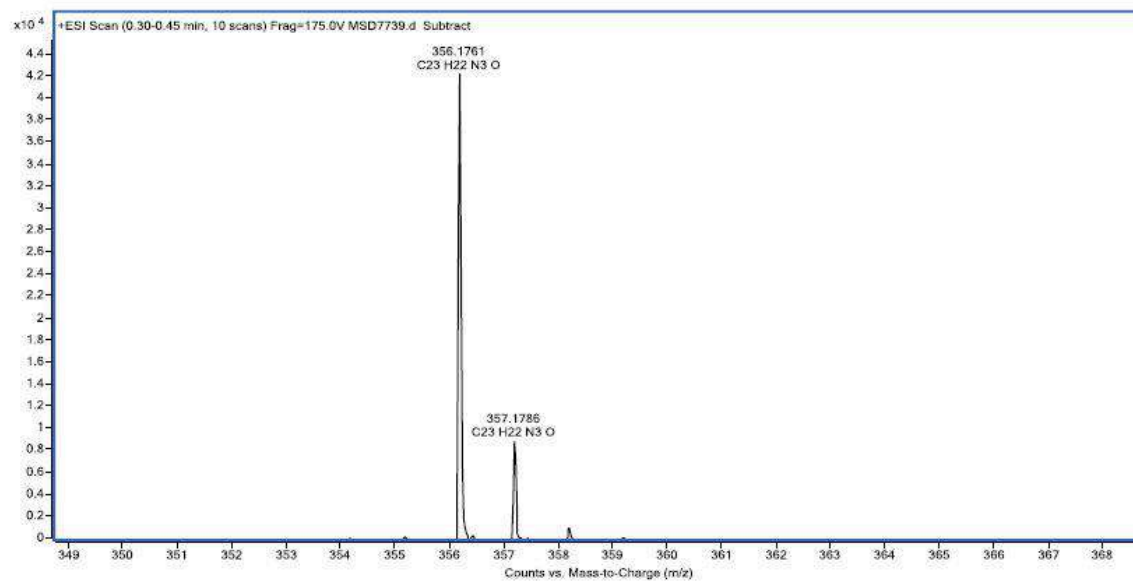
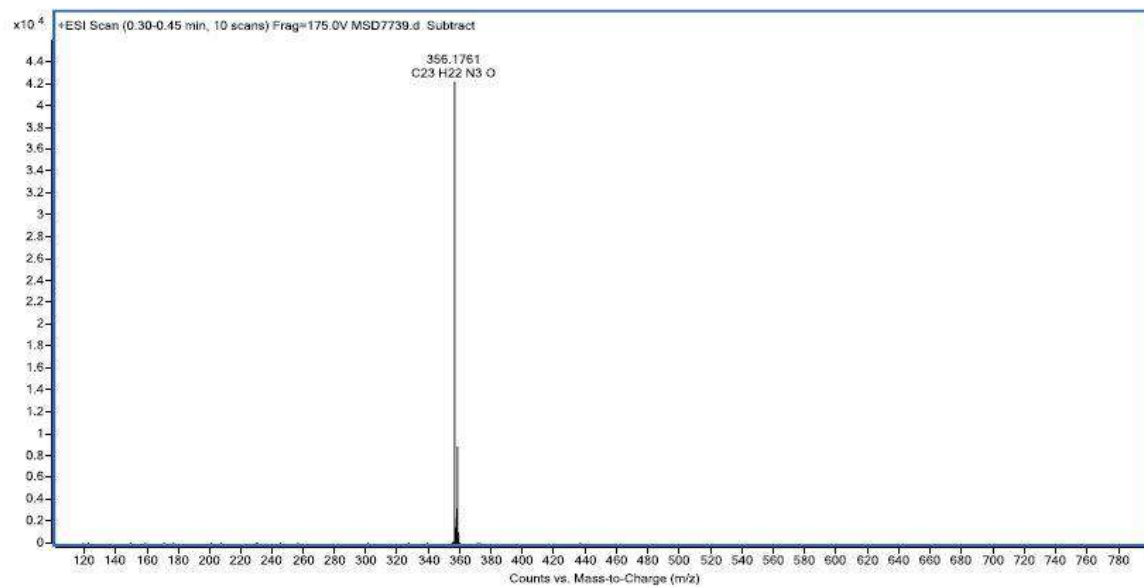


Figure S16. HR ESI-MS spectrum of compound 12.

Compound 13

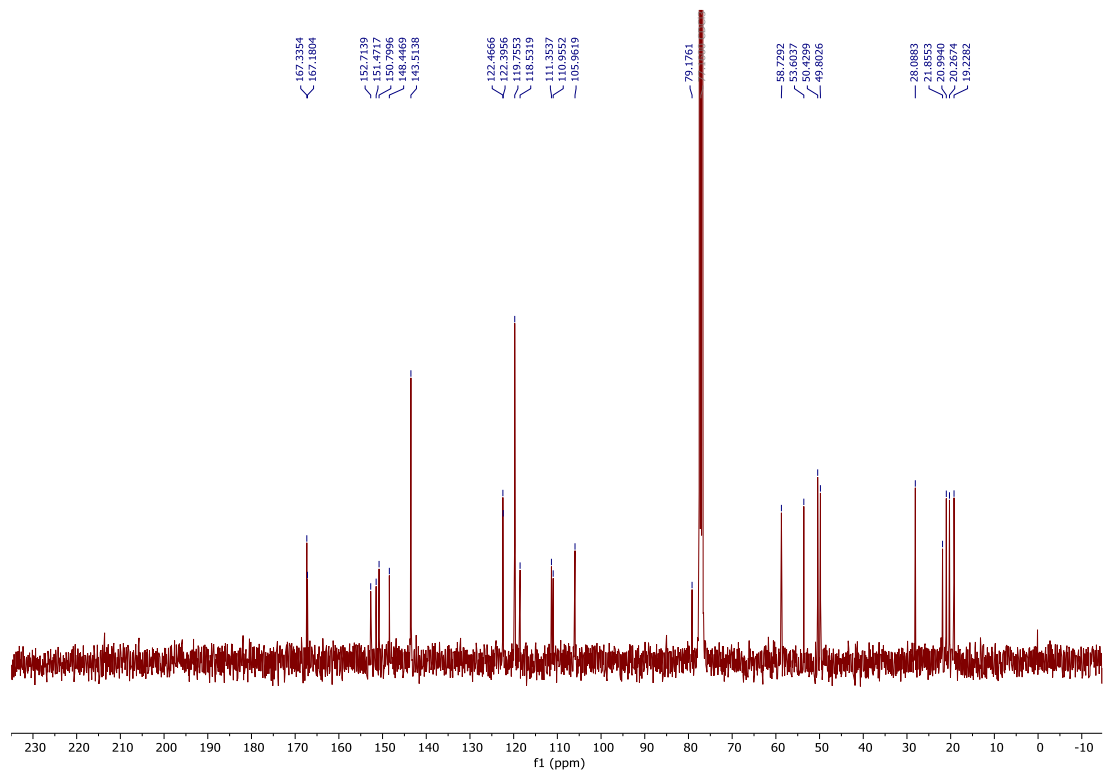
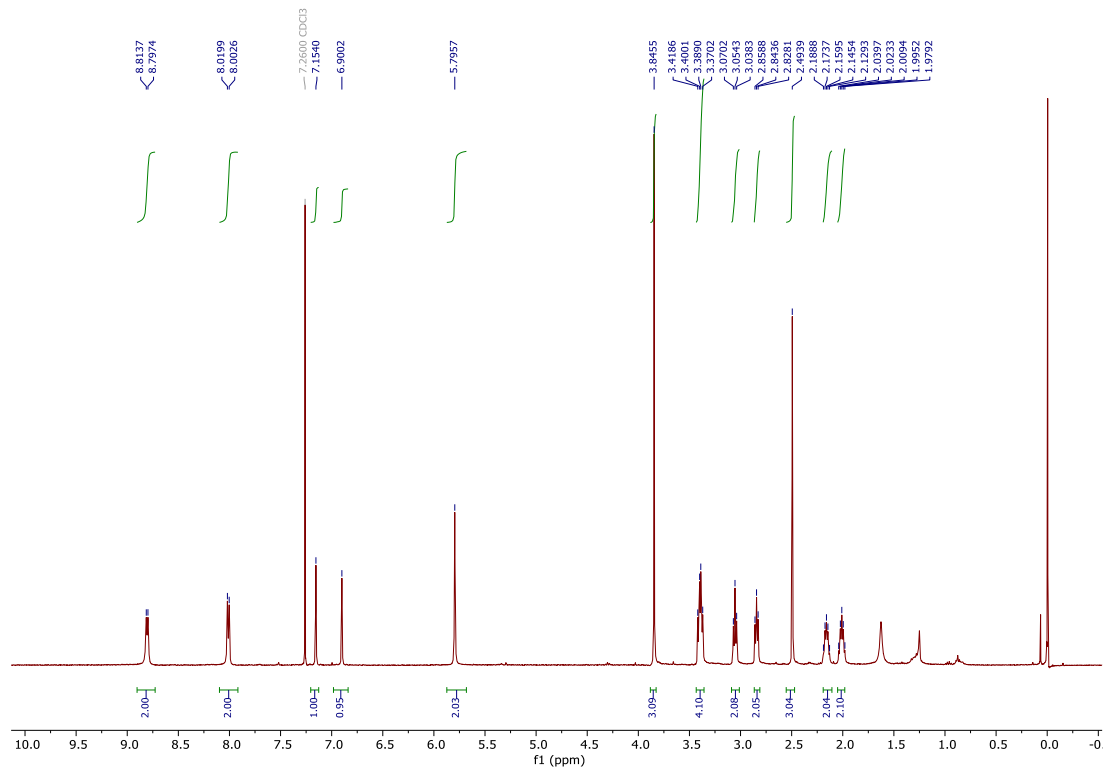


Figure S17. ¹H and ¹³C NMR spectra of compound 13 in CDCl₃.

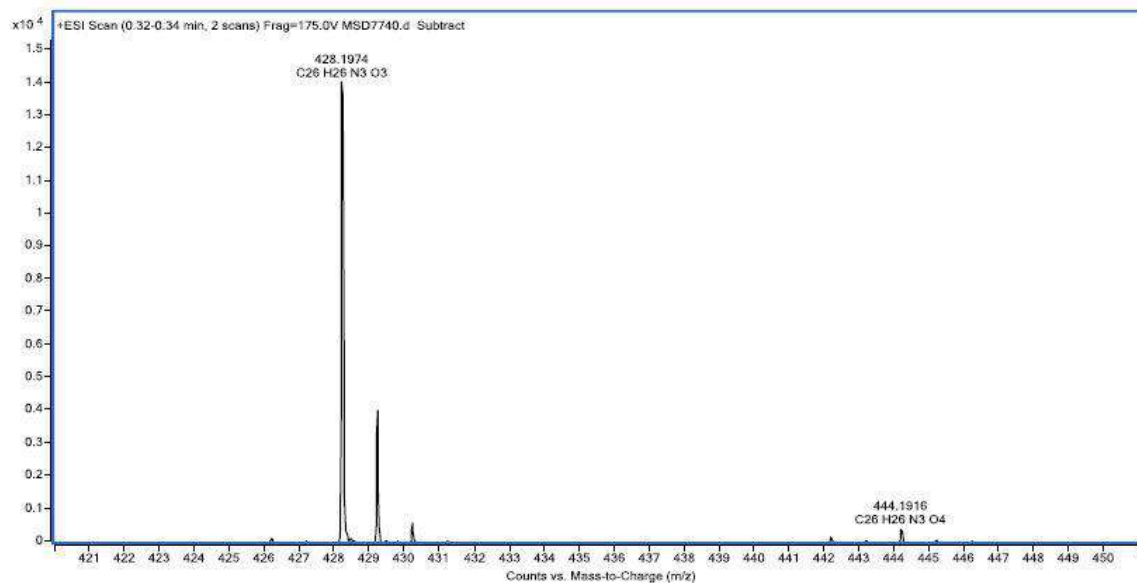
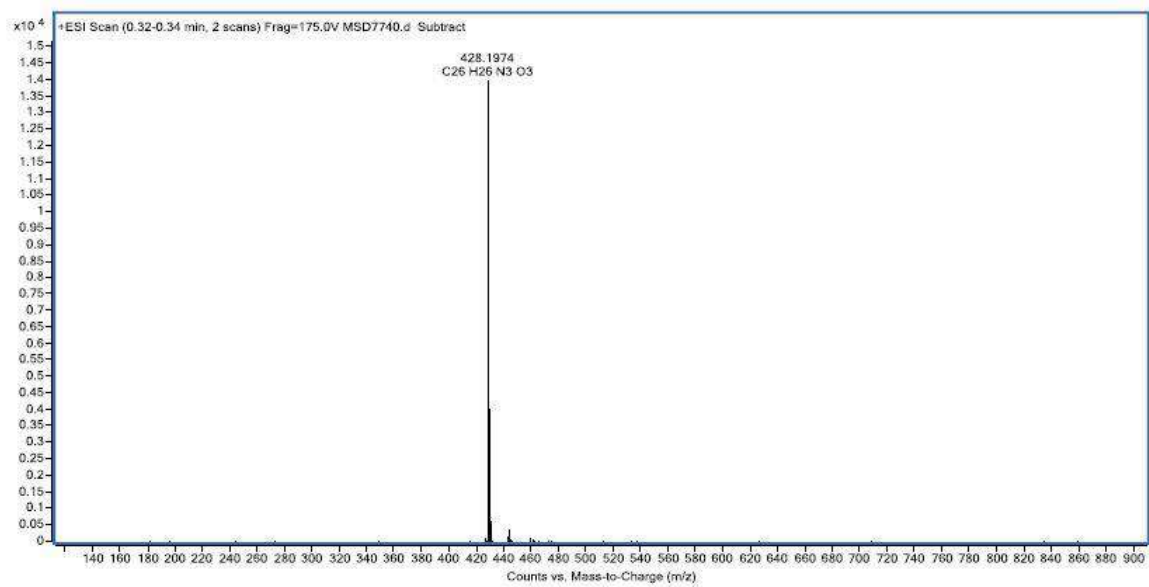


Figure S18. HR ESI-MS spectrum of compound 13.

Compound 15

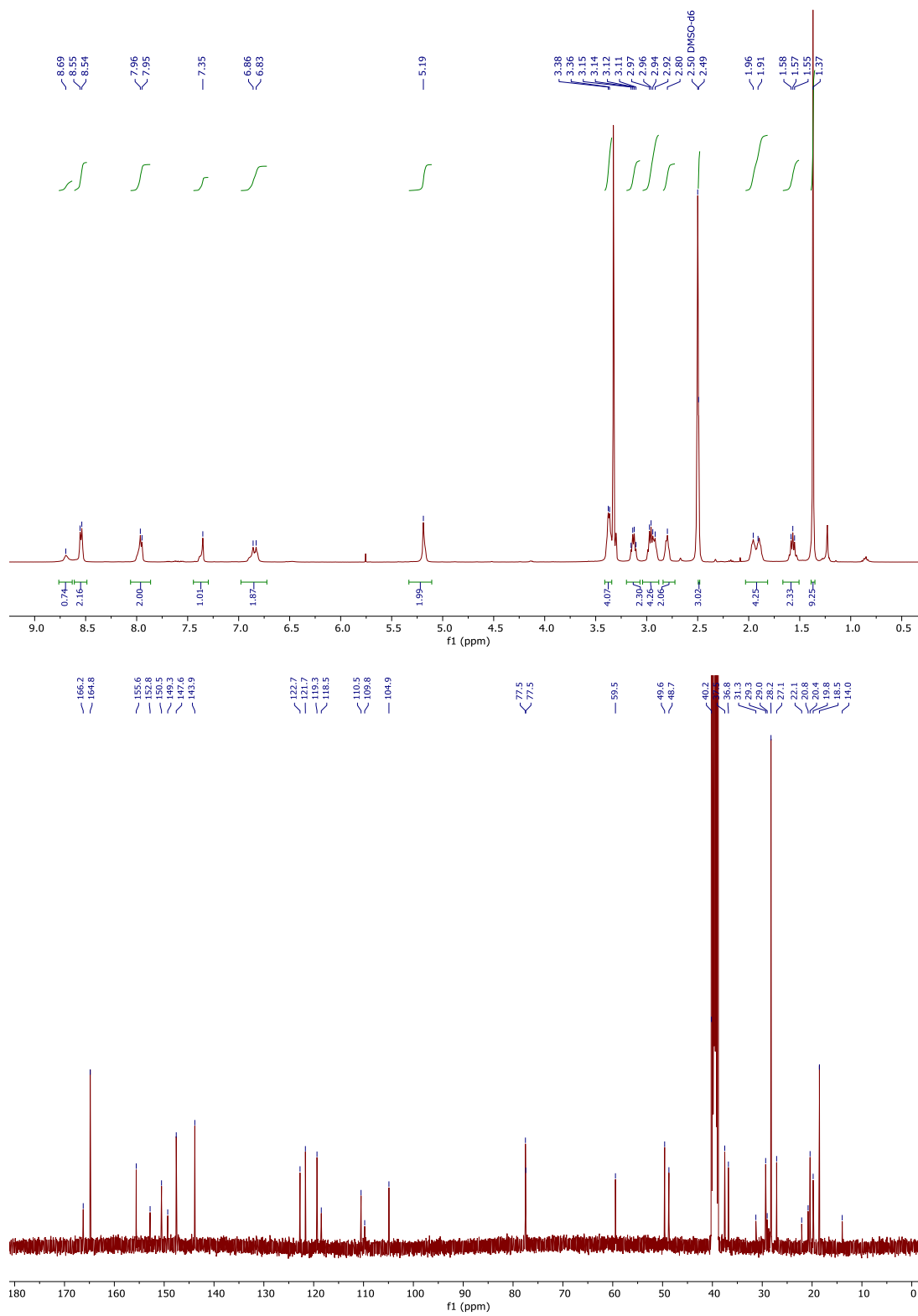


Figure S19. ¹H and ¹³C NMR spectra of compound **15** in CDCl₃.

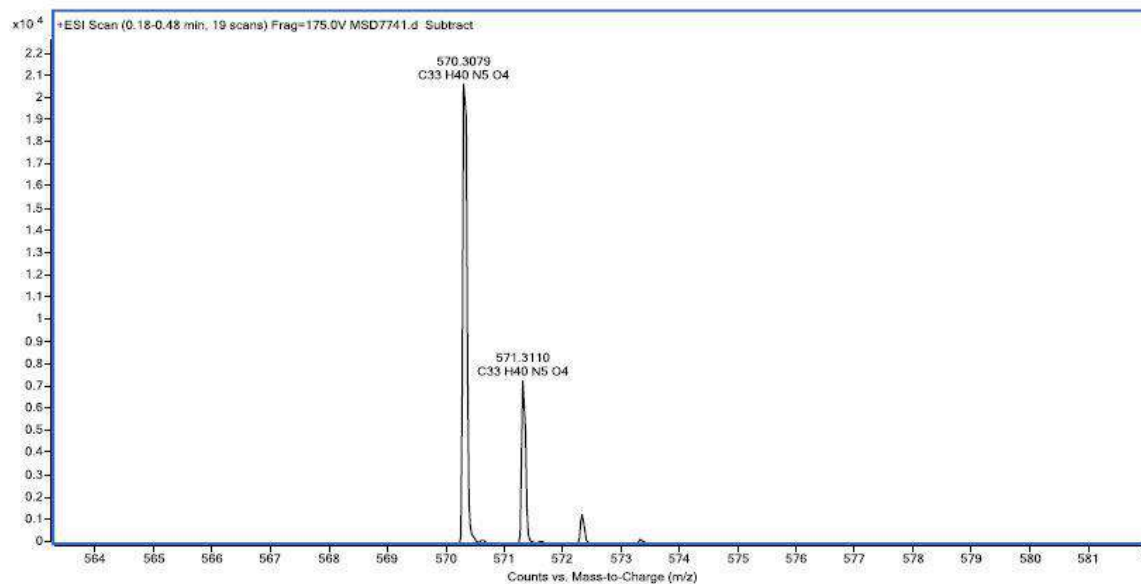
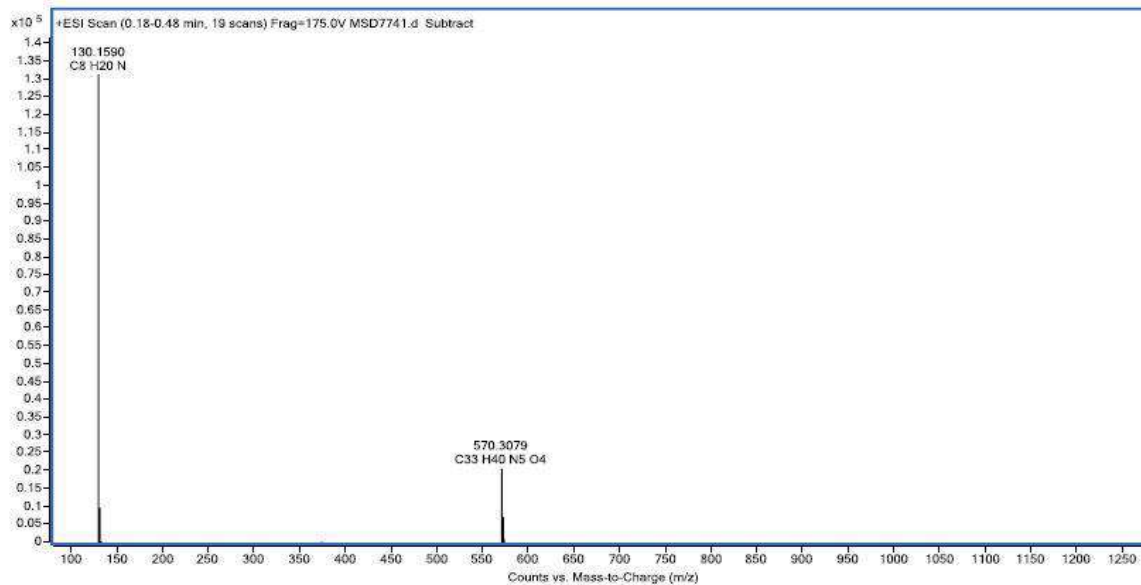


Figure S20. HR ESI-MS spectrum of compound 15.

Compound 18

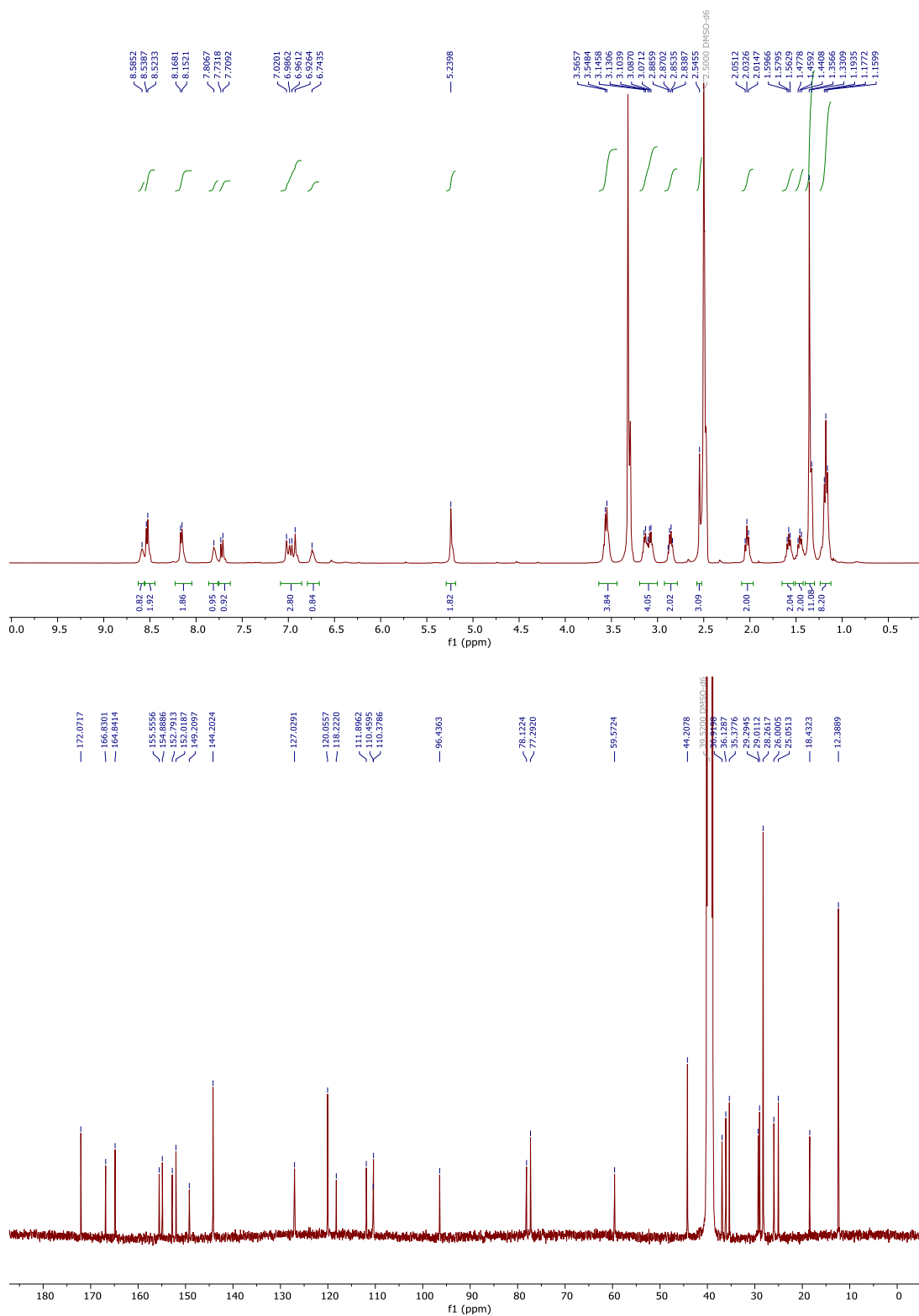


Figure S21. ¹H and ¹³C NMR spectra of compound 18 in DMSO-d₆.

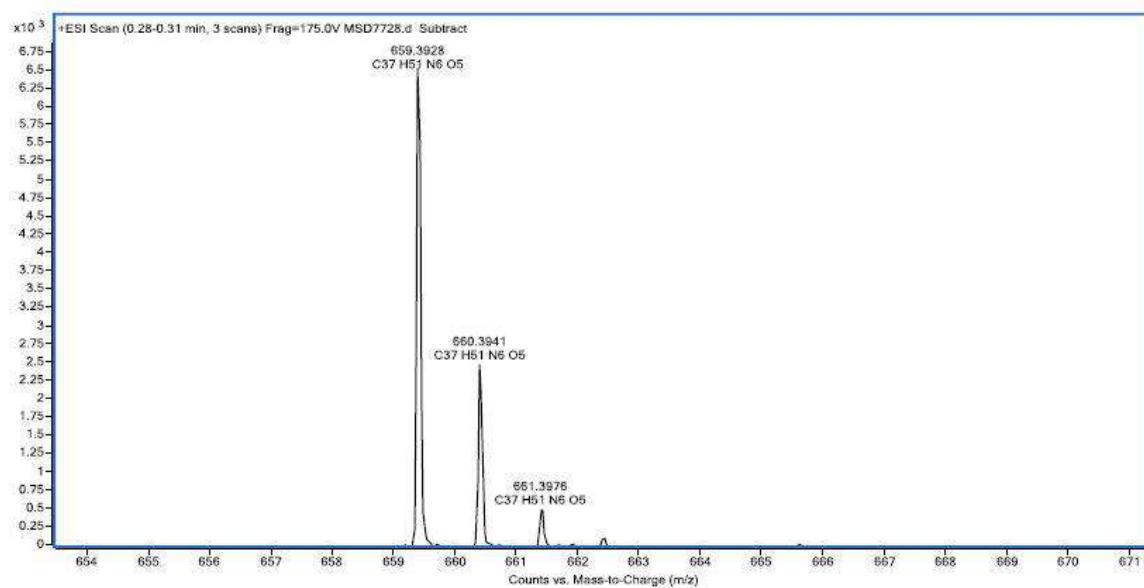
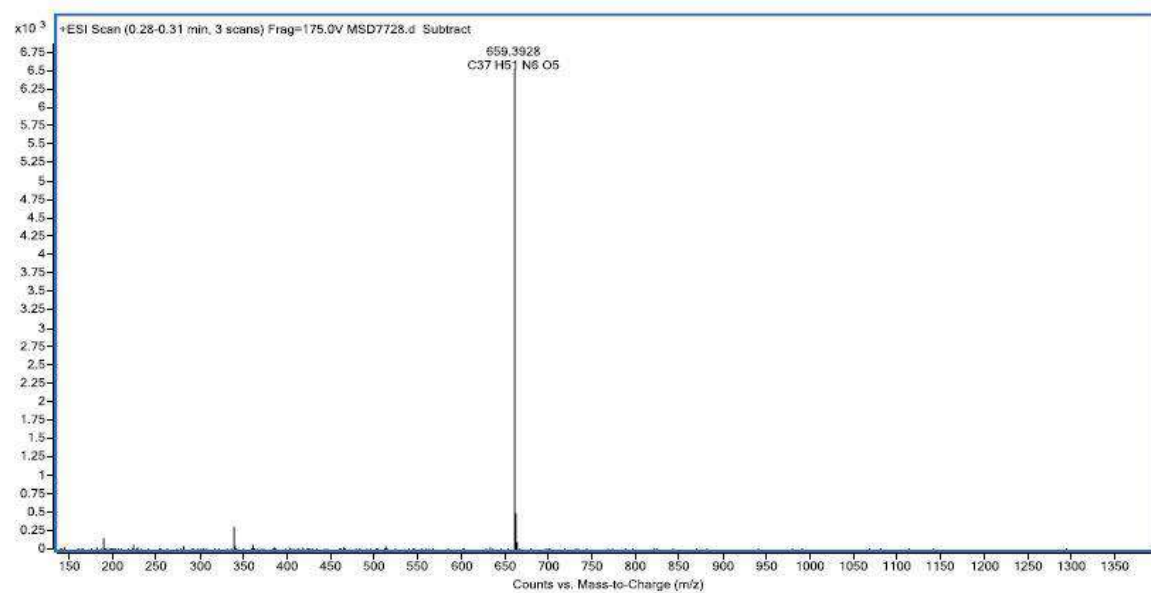


Figure S22. HR ESI-MS spectrum of compound **18**

Compound 19

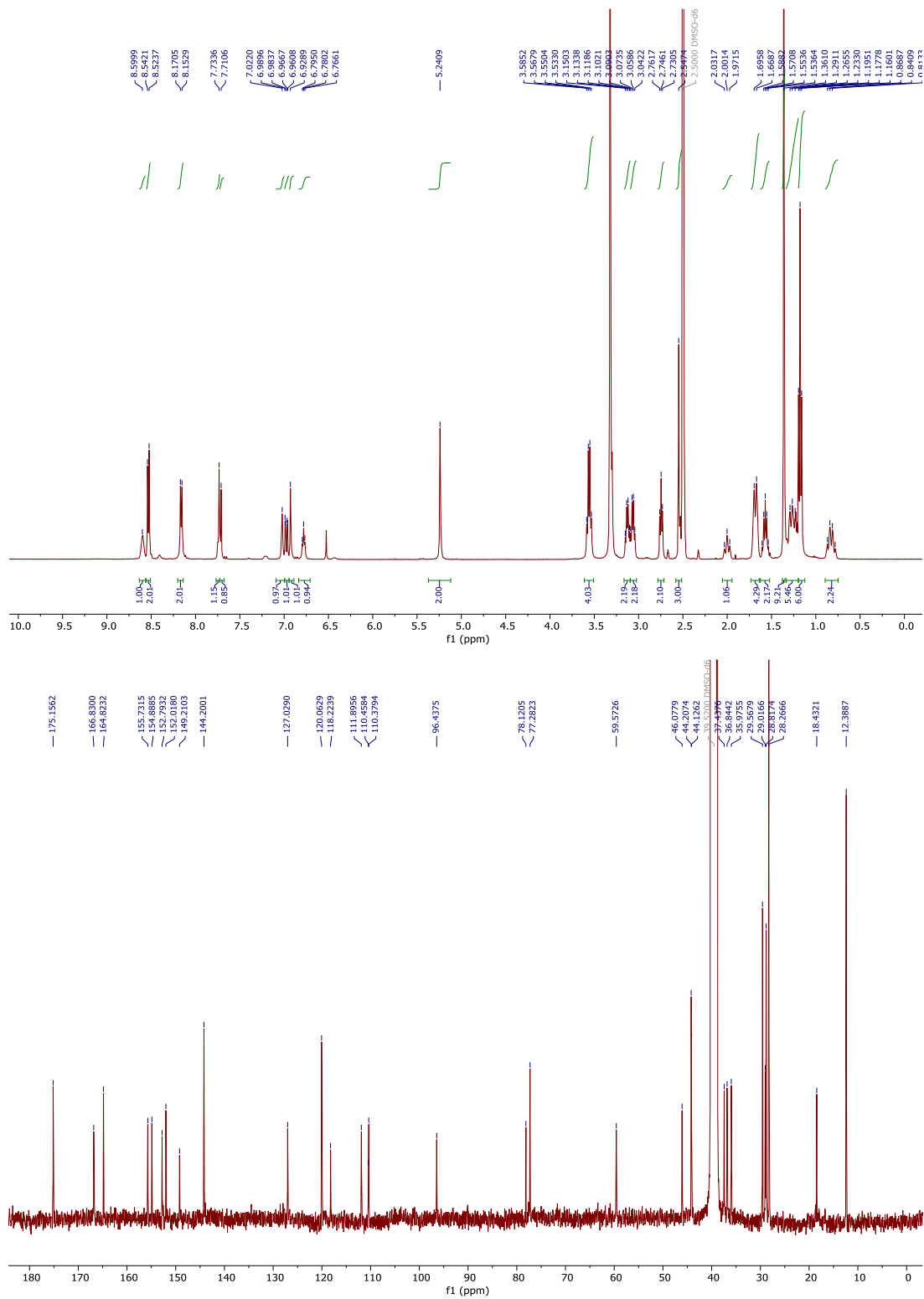


Figure S23. ¹H and ¹³C NMR spectra of compound 19 in DMSO-d₆.

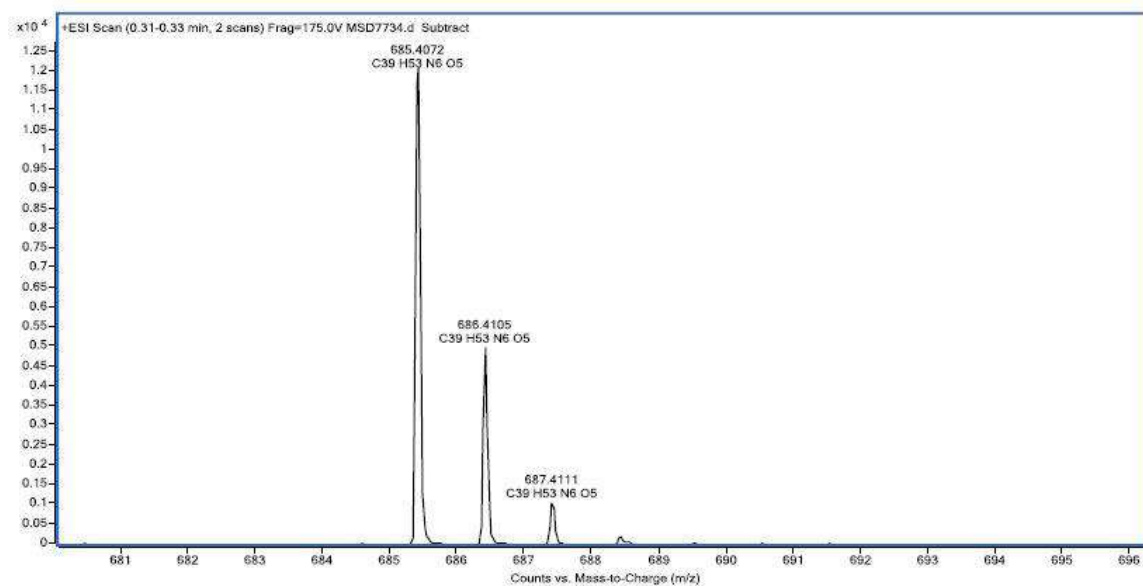
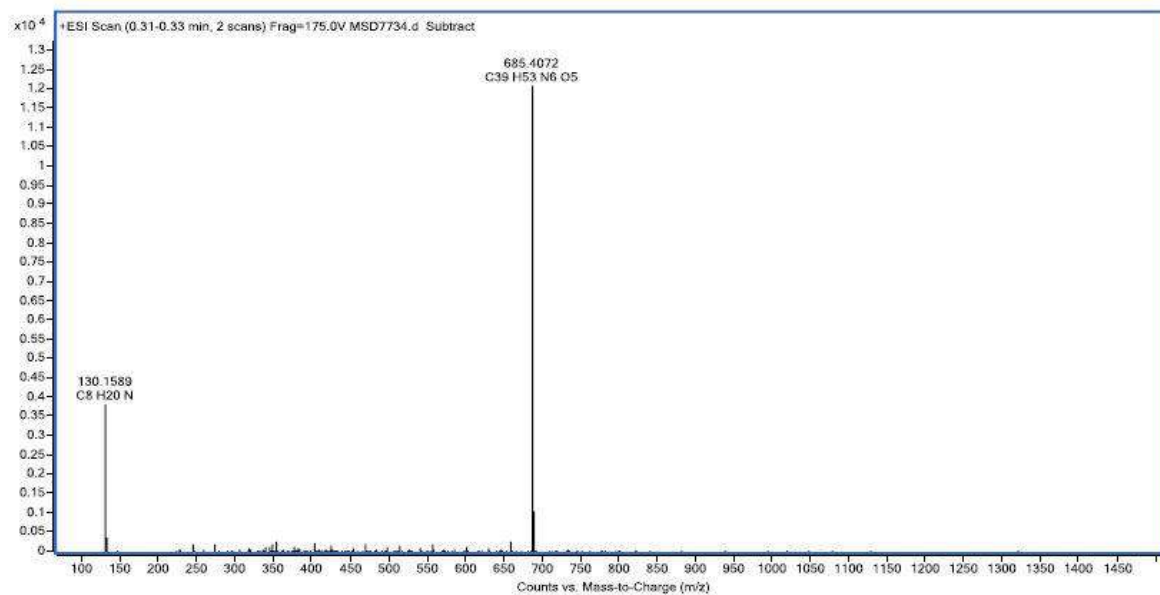


Figure S24. HR ESI-MS spectrum of compound 19

COUPY 1b

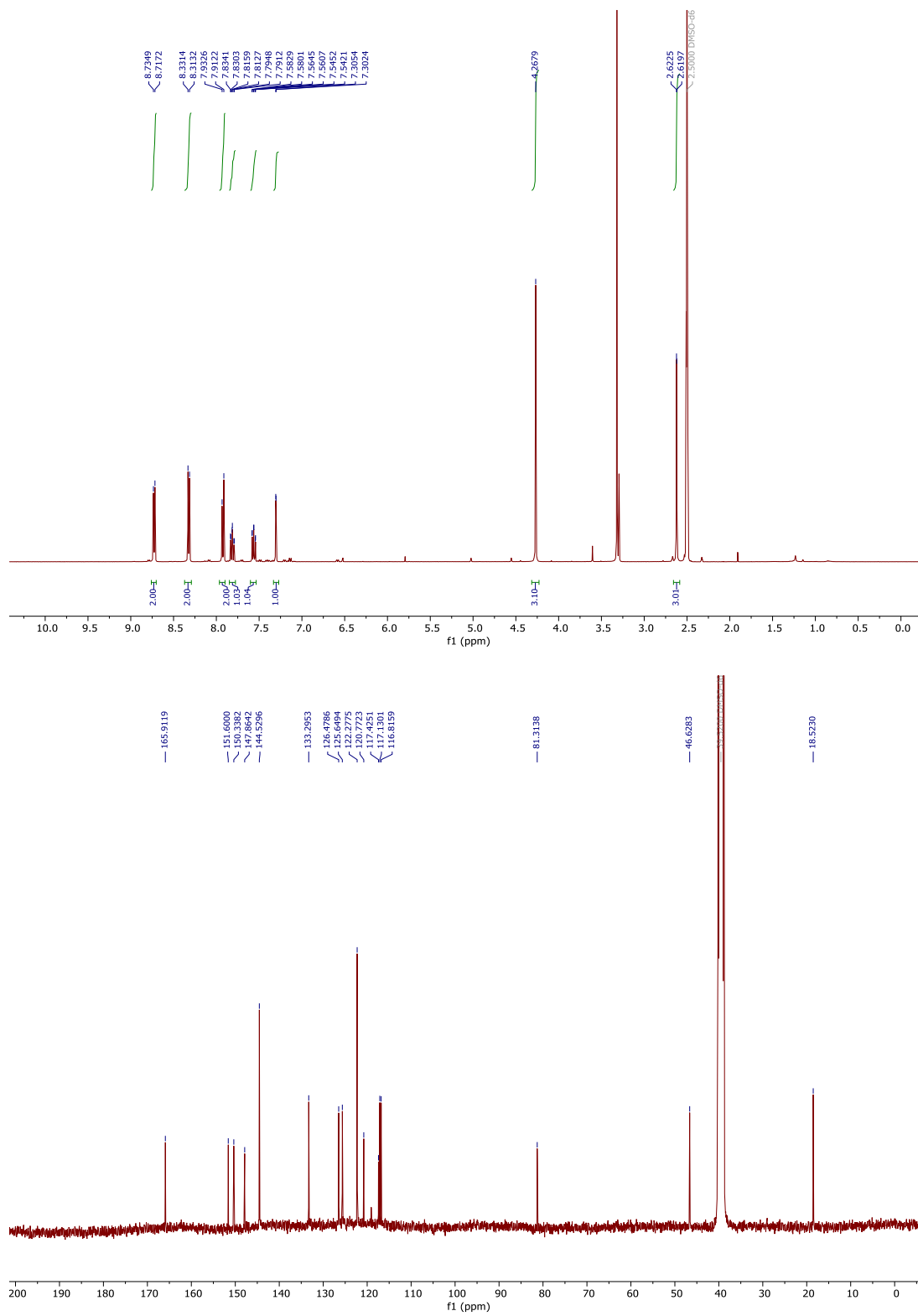


Figure S25. ¹H and ¹³C NMR spectra of compound 1b in DMSO-d₆.

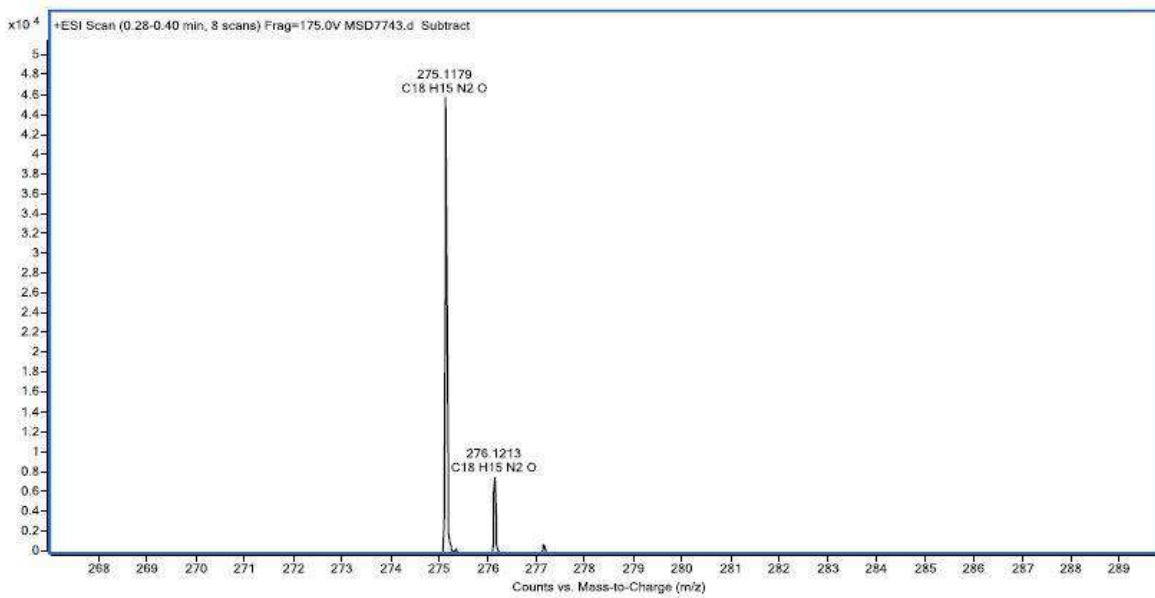
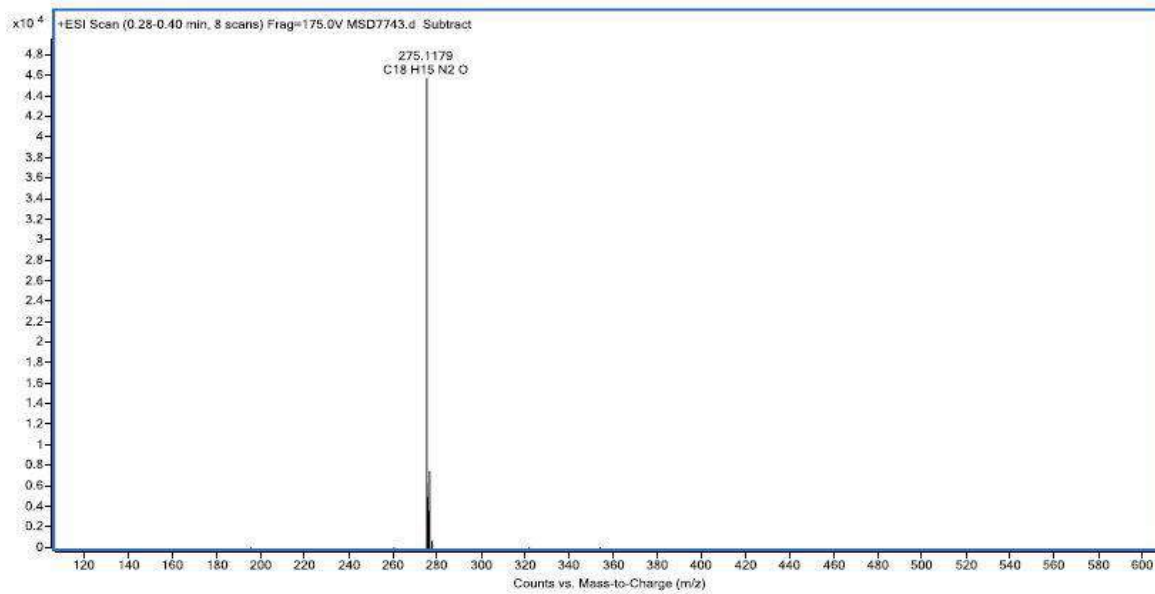


Figure S26. HR ESI-MS spectrum of compound **1b**.

COUPY 1c

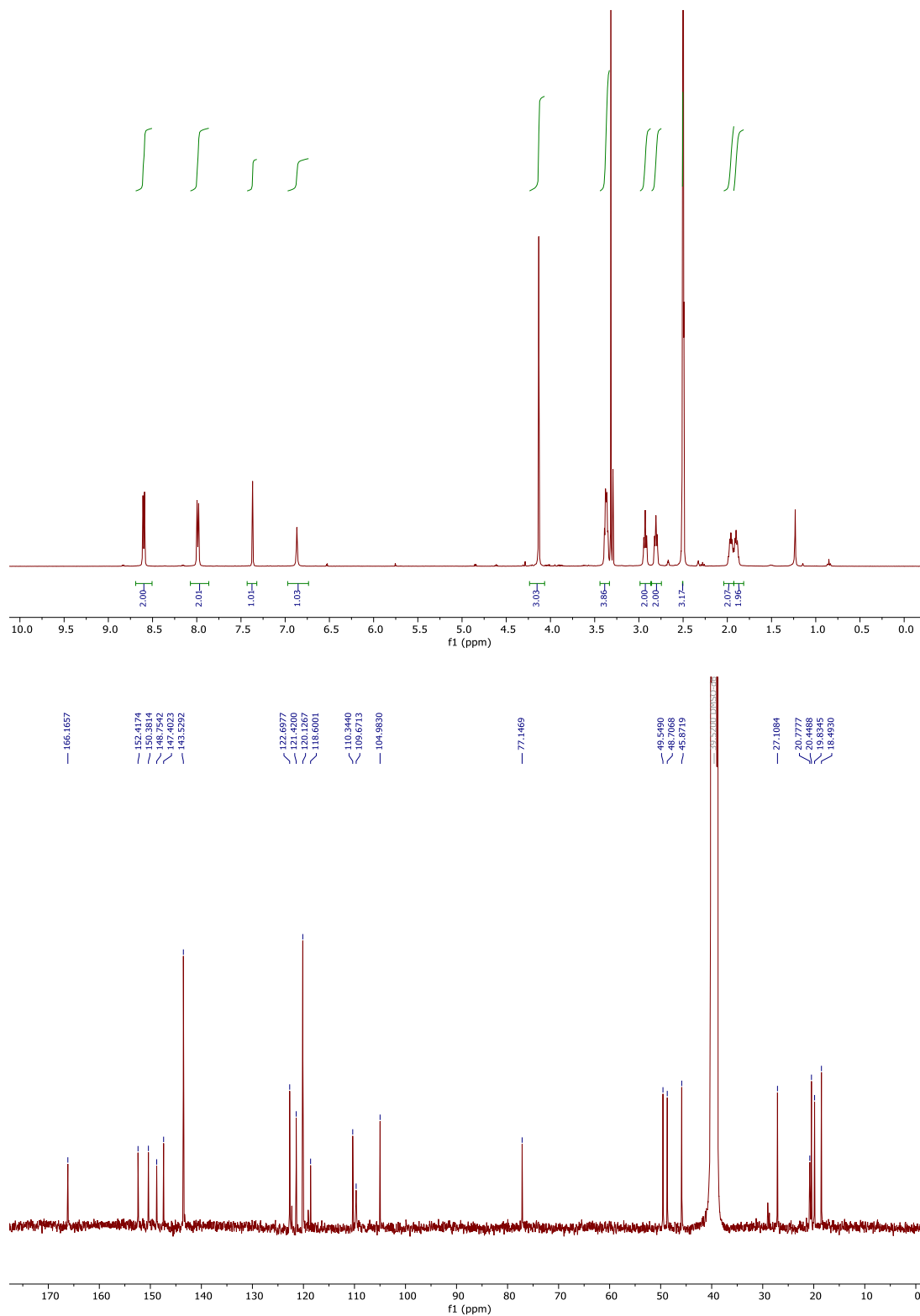


Figure S27. ¹H and ¹³C NMR spectra of compound 1c in DMSO-d₆.

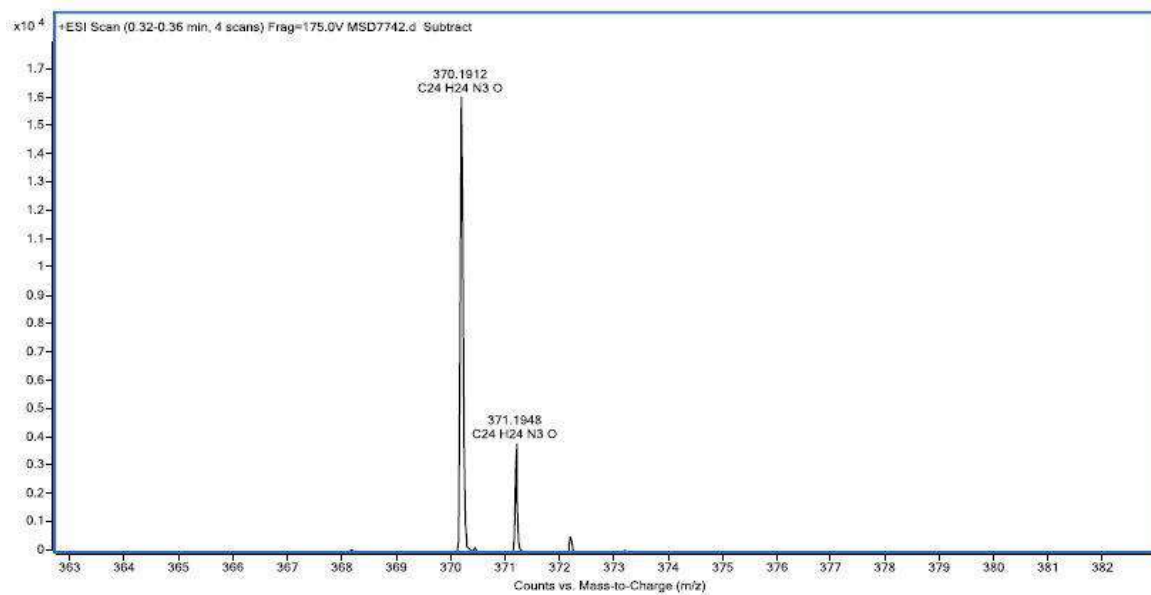
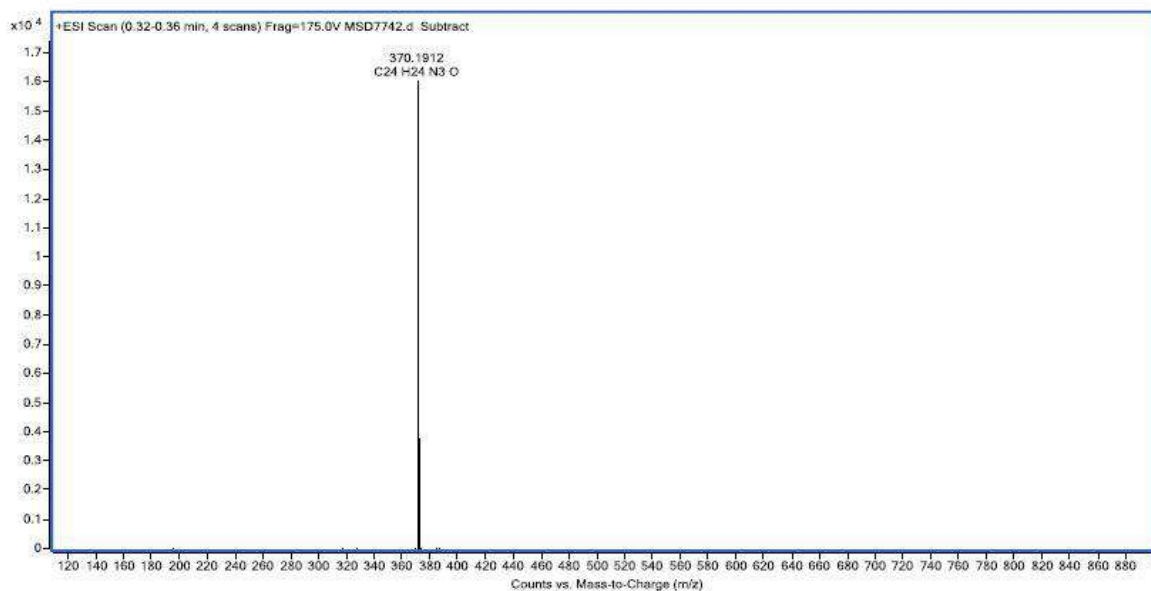


Figure S28. HR ESI-MS spectrum of compound **1c**.

Ir(III)-COUPY conjugate 3b

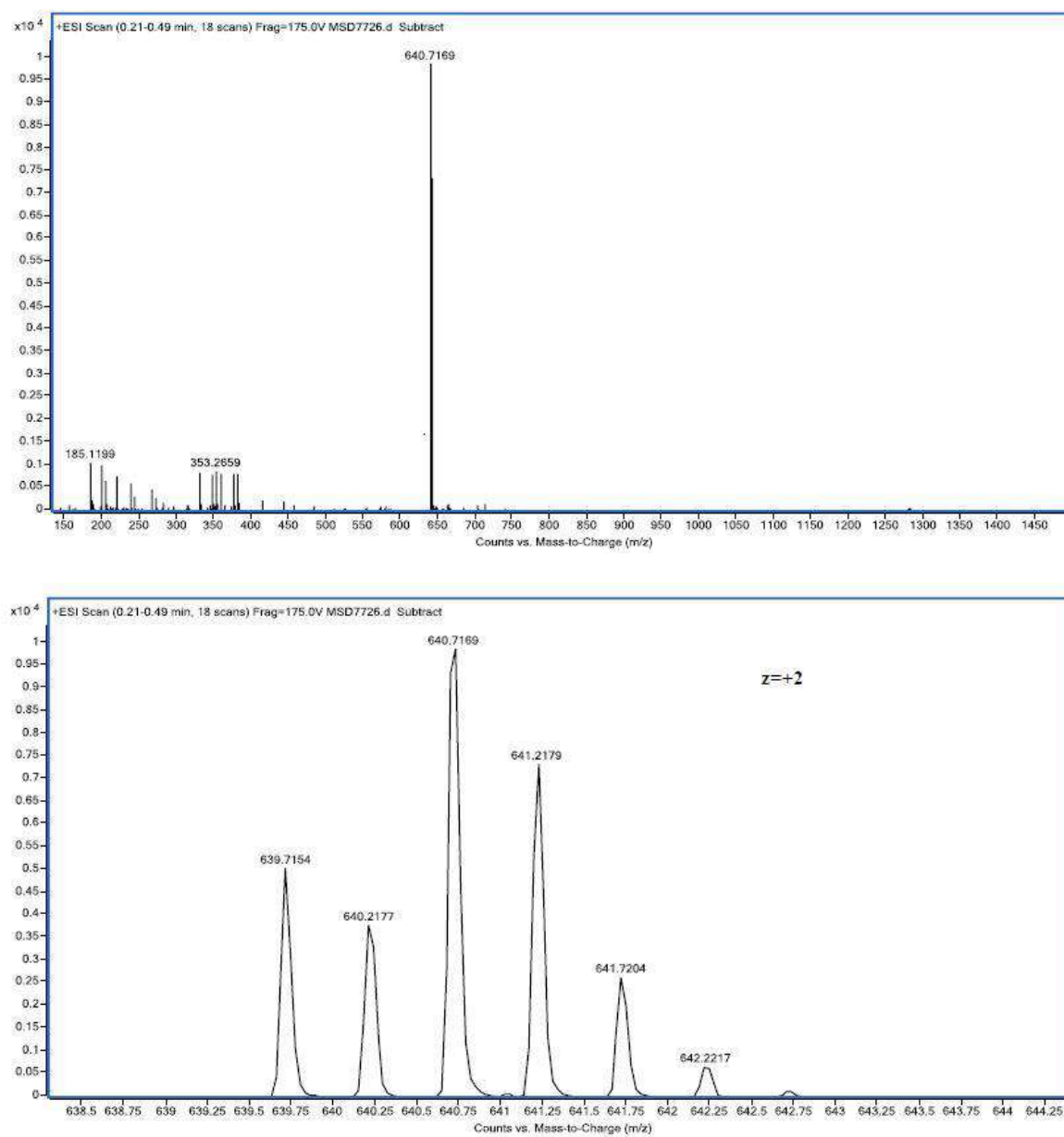


Figure S30. HR ESI-MS spectrum of compound 3b

Ir(III)-COUPY conjugate 3c

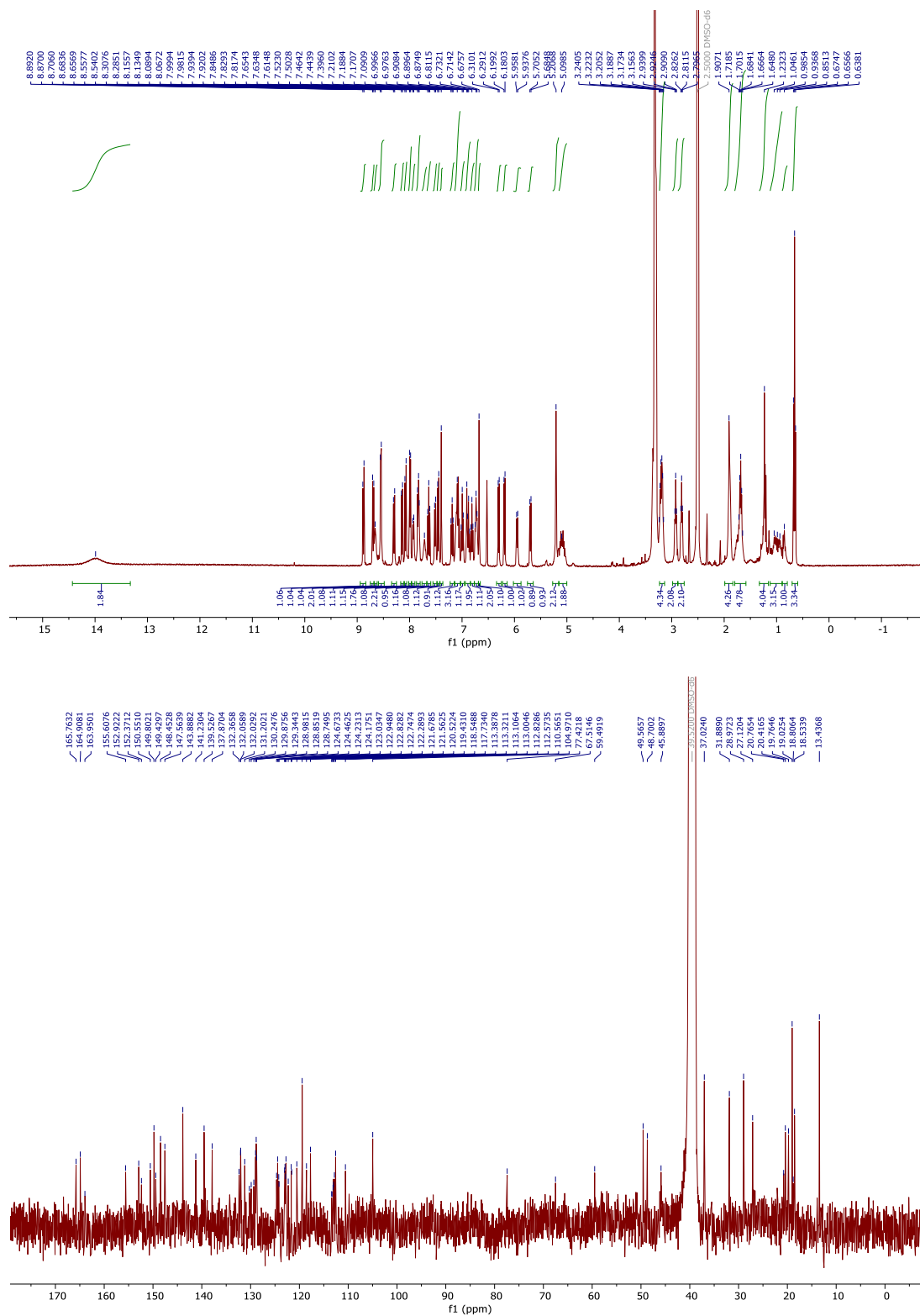


Figure S31. ¹H and ¹³C NMR spectra of compound **3c** in DMSO-*d*₆.

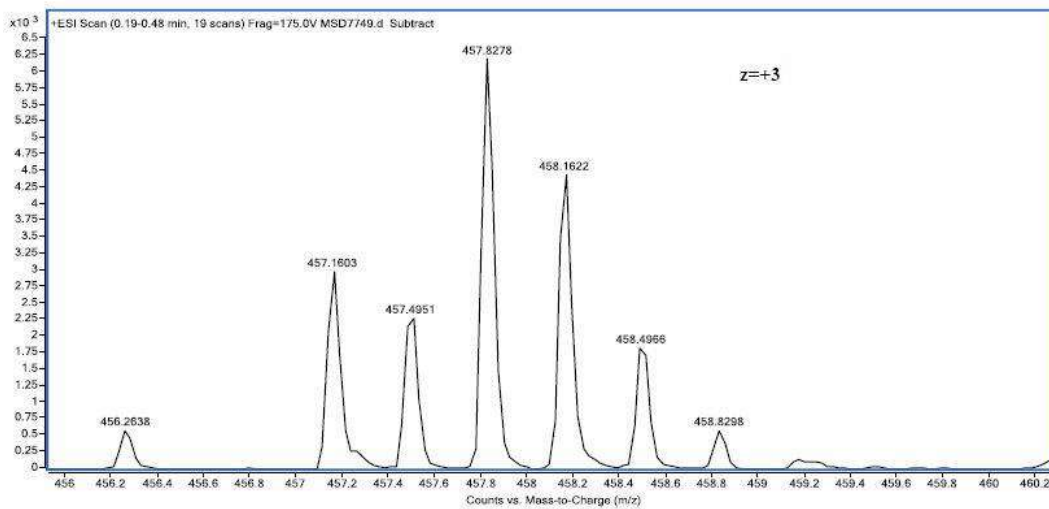
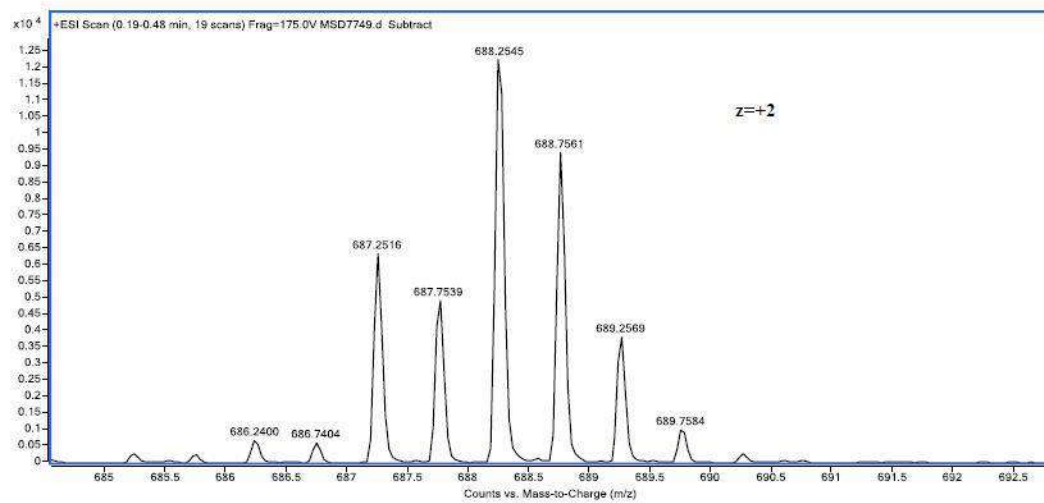
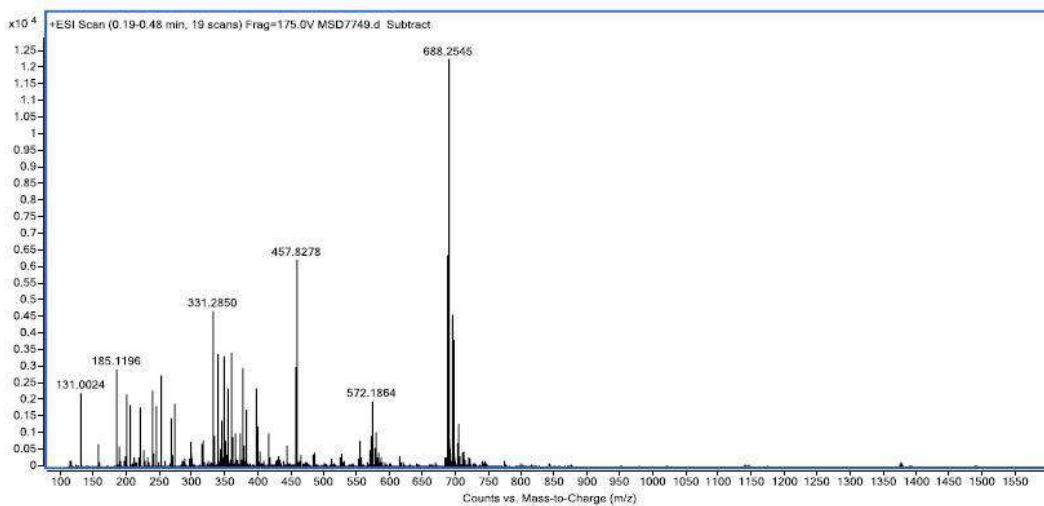


Figure S32. HR ESI-MS spectrum of compound **3c**

Ir(III)-COUPY conjugate 3d

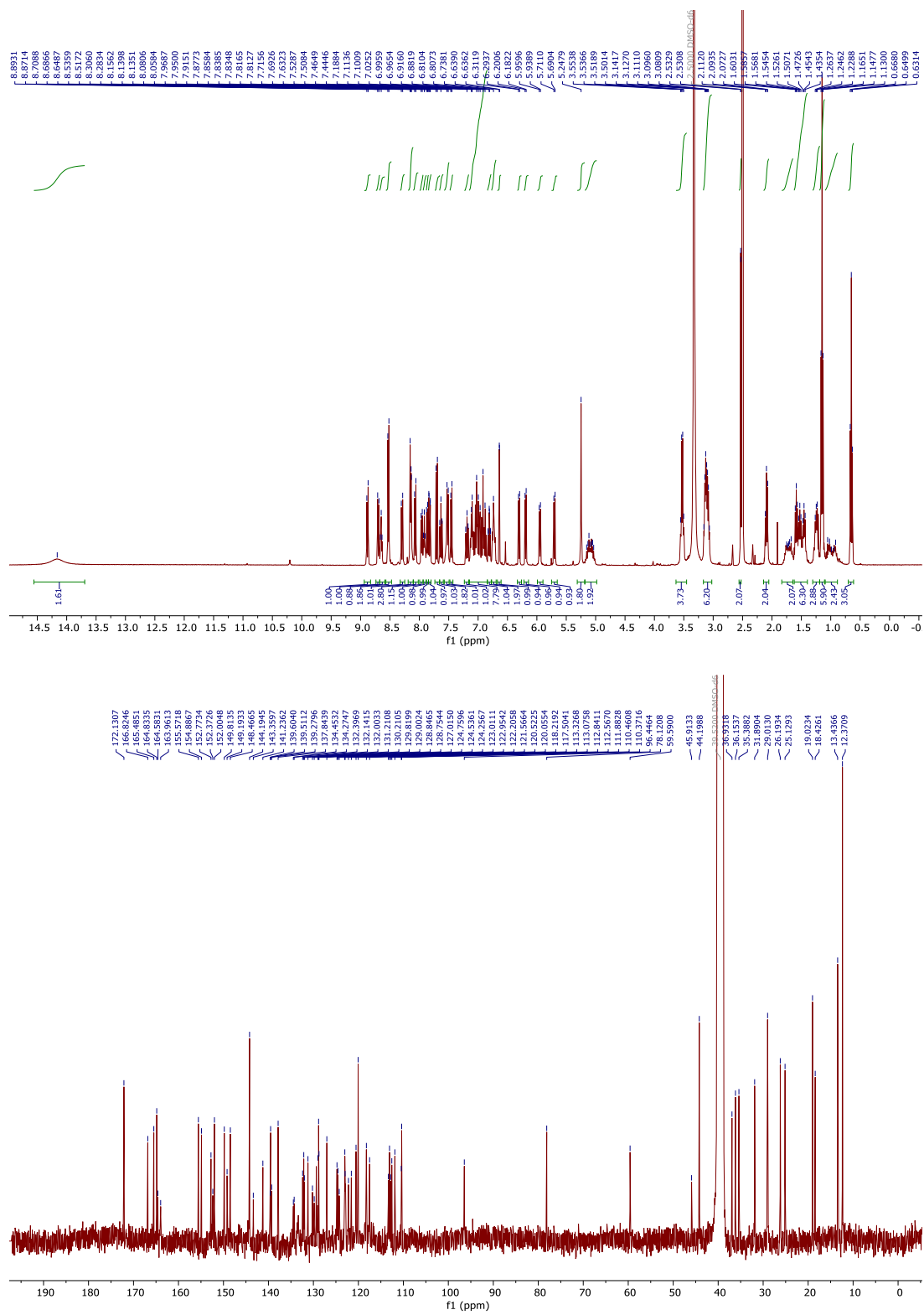


Figure S33. ¹H and ¹³C NMR spectra of compound 3d in DMSO-d₆.

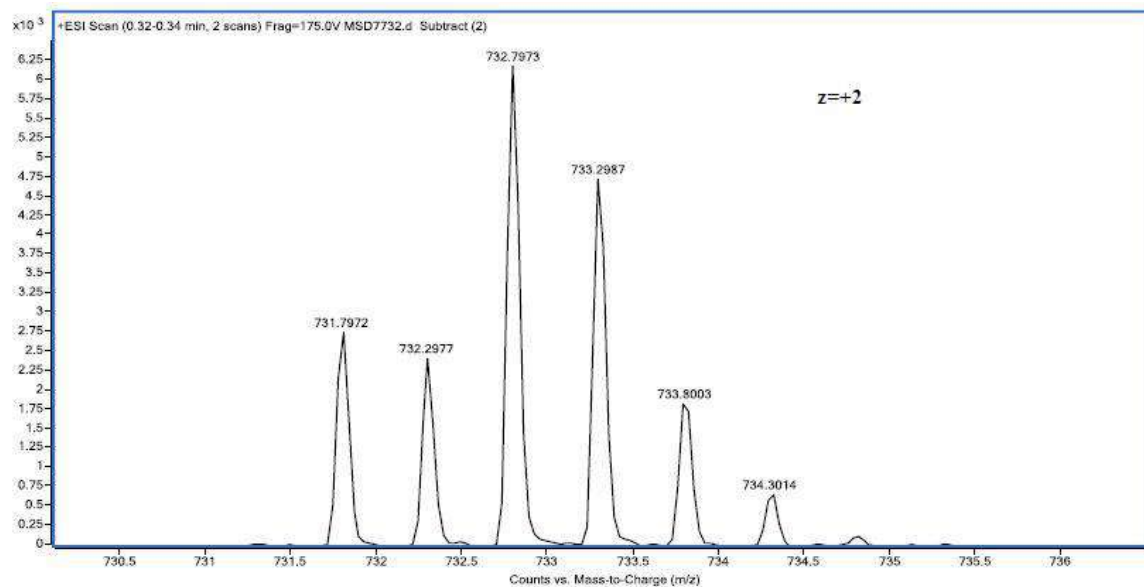
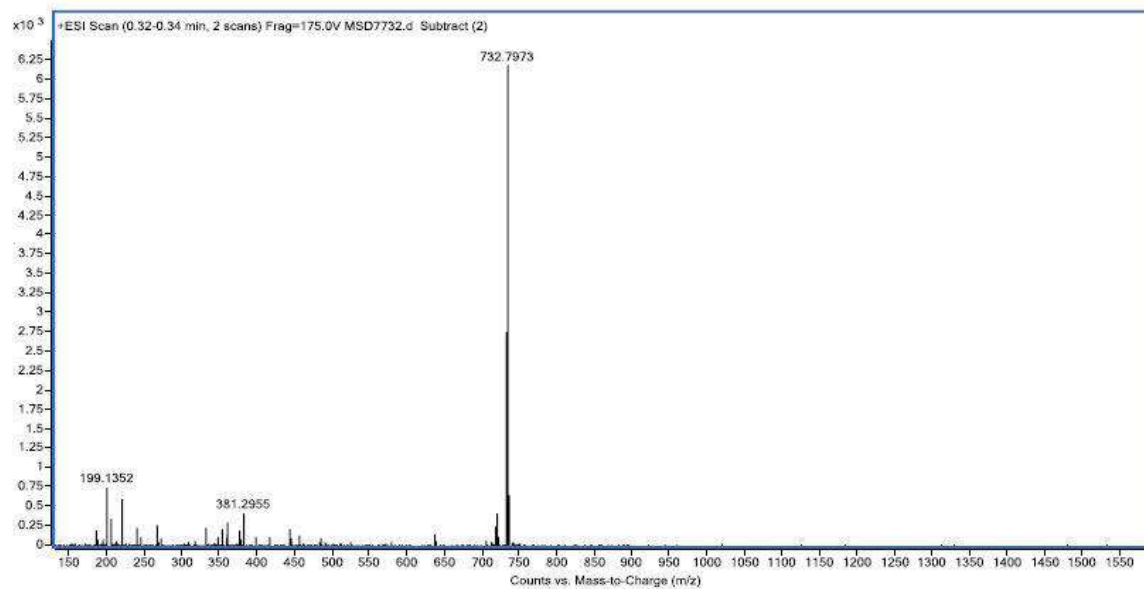


Figure S34. HR ESI-MS spectrum of compound **3d**

Ir(III)-COUPY conjugate 3e

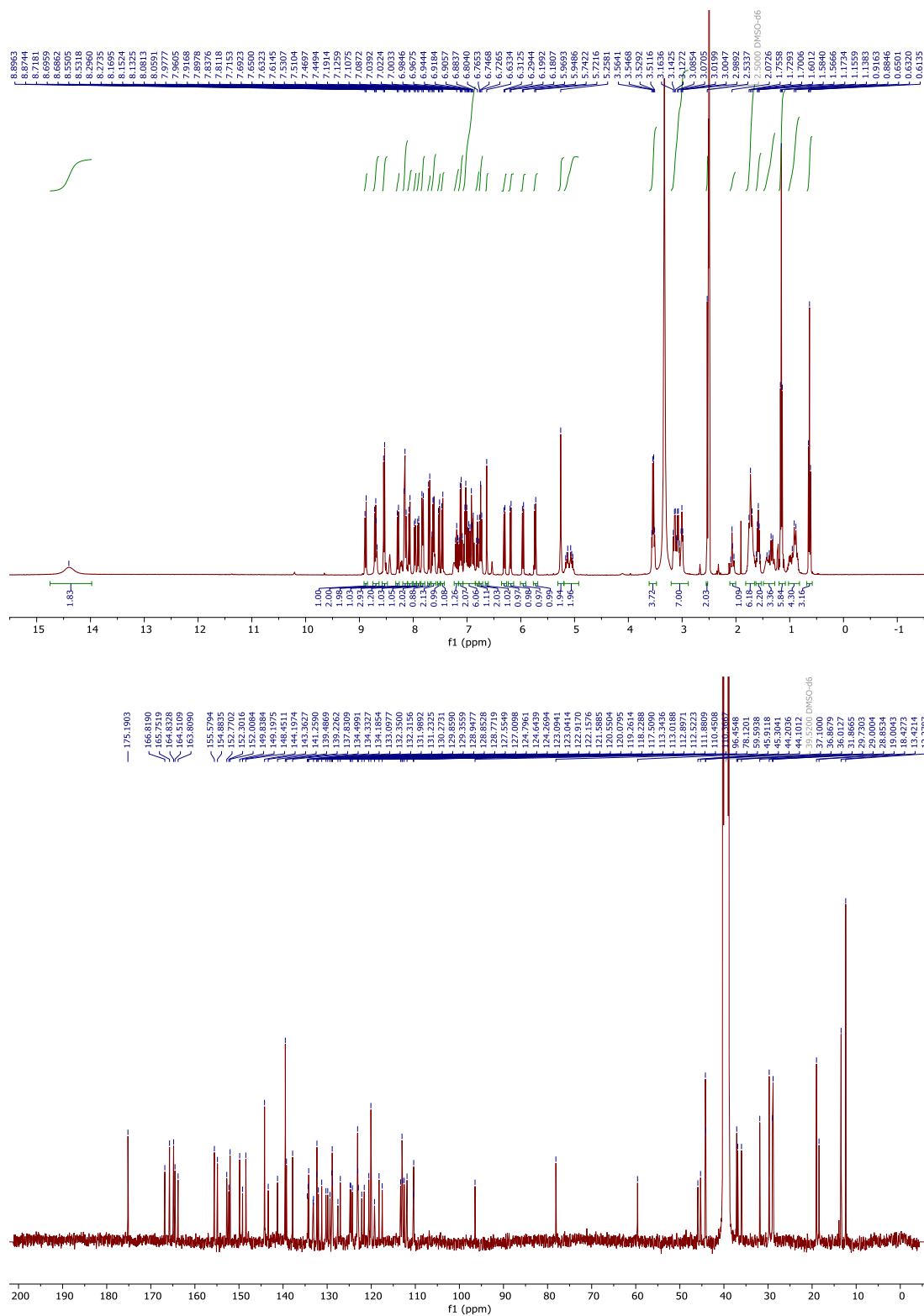


Figure S35. ¹H and ¹³C NMR spectra of compound **3e** in DMSO-*d*₆.

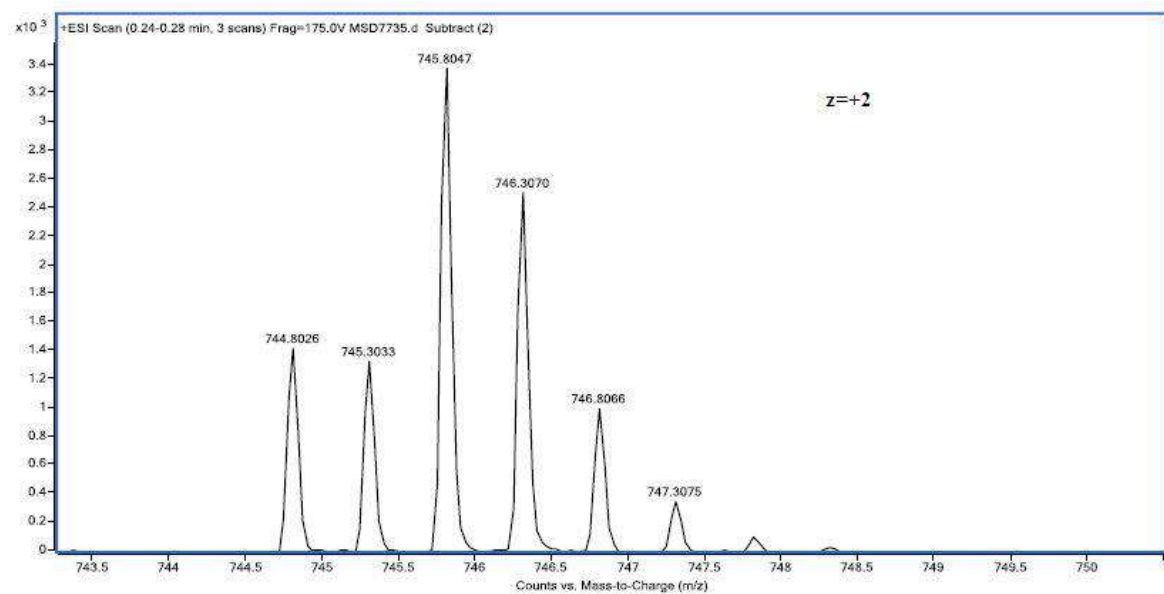
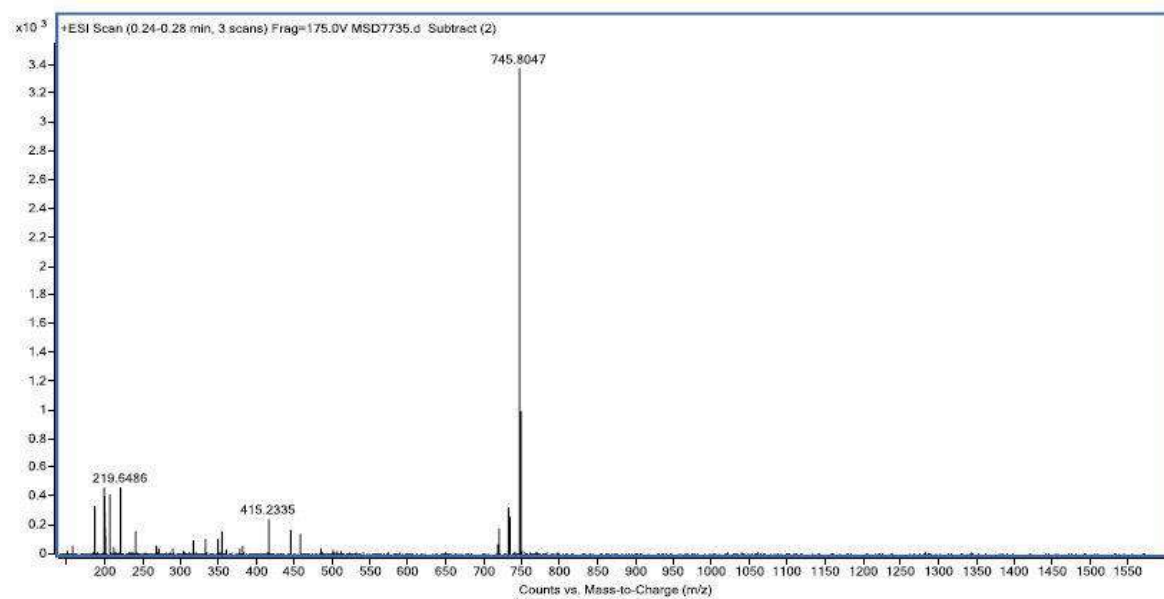


Figure S36. HR ESI-MS spectrum of compound 3e

10. Chapter IIc. Non-published results

Development of a new photosensitizer based on the conjugation of a NIR-emitting COUPY dye to a cyclometalated Ru(II) polypyridyl complex.

Development of a new photosensitizer based on the conjugation of a NIR-emitting COUPY dye to a cyclometalated Ru(II) polypyridyl complex.

INTRODUCTION

As stated in **Sections 3.1.2** and **3.2.1** of the general Introduction of the thesis, the excellent photophysical and biological properties of Ru(II) polypyridyl complexes have recently attracted the attention of researchers working in the Medicinal Inorganic Chemistry field.¹ Since Dwyer *et al.* demonstrated the antibacterial activity of a series of Ru(II) polypyridyl complexes in 1952, a large number of bioactive Ru complexes have been described in the literature for therapeutic and diagnostic applications, placing the focus on the cancer field.² Remarkably, McFarland and coworkers reported the first Ru(II)-based photosensitizer, a Ru(II) polypyridyl complex, named TLD1433, to enter human clinical trials for the treatment of non-muscle invasive bladder cancer (NMIBC) with PDT.^{3,4}

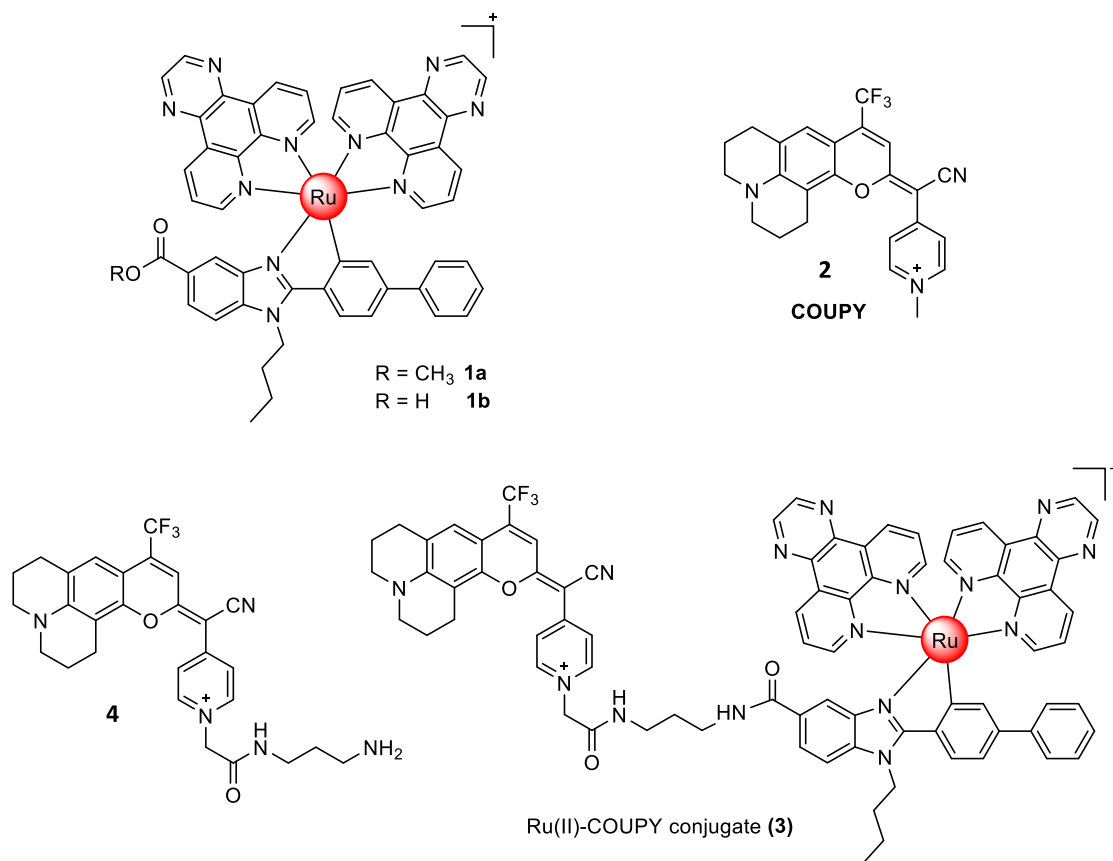
In general, the cytotoxicity of Ru(II) polypyridyl complexes is related to their exceptional reactivity, ability to bind DNA and redox chemistry.^{5,6} In addition, the nature of the polypyridyl ligands determines some important chemical properties, including aqueous solubility and lipophilicity. For example, Chao *et al.* reported a cyclometalated Ru(II) complex, [Ru(bpy)(phpy)(dppz)]⁺, with high DNA binding affinity due to the incorporation of highly conjugated heteroaromatic coordinating ligands, and the presence of a Ru-C covalent bond significantly increased the stability and lipophilicity.⁷

Likewise, the photophysical properties of Ru(II) polypyridyl complexes (e.g. photostability, luminescent lifetimes and absorption and emission maxima) can be also tuned by modifying the coordinating ligands. The development of Ru(II) polypyridyl complexes exhibiting suitable photophysical and photochemical properties, including high luminescent quantum yields, long emission lifetimes, large Stokes shifts and high oxygen singlet quantum yields, offers a good opportunity to use them as photosensitizers for anticancer photodynamic therapy (PDT).^{1,8-11}

Based on the results reported in Publications C and D that demonstrated that COUPY fluorophores are promising candidates for developing novel fluorescent PDT agents when conjugated to cyclometalated Ir(III) complexes,¹² here we explored the conjugation of a NIR-emitting COUPY dye to a cyclometalated Ru(II) polypyridyl complex of the type $[\text{Ru}(\text{C}^{\wedge}\text{N})(\text{N}^{\wedge}\text{N})_2][\text{PF}_6]$ previously reported by Ruiz and collaborators, which contains two dipyrido[3,2-d:20,30-f]quinoxaline (dpq) $\text{N}^{\wedge}\text{N}$ ligands and a methyl 1-butyl-2-arylbenzimidazolecarboxylate ligand (**1a**, **Scheme 1**). This Ru(II) polypyridyl complex was found a great green light-activatable PS with phototherapeutic indexes (PIs) up to higher than 700 under hypoxia conditions (2% O_2) in HeLa cancer cells. In addition, the main photogenerated species by the Ru(II) complex under hypoxia were H_2O_2 and $\text{O}_2^{\cdot-}$.¹³ On the other hand, with the aim of further red-shifting absorption and emission of the coumarin scaffold and, consequently, of the new Ru(II)-COUPY conjugate in comparison with previous Ir(III)-COUPY conjugates, we decided to increase the push-pull character of the fluorophore by modifying the substituents at the positions 4 and 7 of the coumarin skeleton. For this reason, we selected a julolidine-fused coumarin analogue containing a trifluoromethyl group (CF_3) at the 4-position (**2**, **Scheme 1**) to red-shift the absorption and emission maxima with respect the previous COUPY derivatives incorporated in Ir(III)-COUPY conjugates (Publications C and D). As previously indicated, the rigidification of the amino group at the 7-position and the incorporation of a strong EWG such as CF_3 at position 4 of the coumarin is known to have a strong impact on the photophysical properties of COUPY fluorophores.¹⁴

The synthesis of the Ru(II)-COUPY conjugate (**3**, **Scheme 1**) was carried out through the formation of an amide bond between the carboxylic group of Ru(II) complex **1b** and the amino group of a conjugatable version of COUPY **2** (compound **4**). Besides investigating the photophysical properties of the compounds, the ability of the new conjugate to produce singlet oxygen ($^1\text{O}_2$) and superoxide anion radical ($\text{O}_2^{\cdot-}$) were assessed. In addition, the cellular uptake of the Ru(II)-COUPY conjugate was studied in living HeLa cells by confocal microscopy and preliminary phototoxicity studies were carried out in the same cell line upon irradiation with red light.

This research project has been carried out in collaboration with the research group of Prof. José Ruiz from the University of Murcia, where the Ru(II) complex **1a** was synthesized by Dr. Francisco José Ballester and the biological evaluation was carried out by Enrique Ortega-Forte. The determination of singlet oxygen quantum yield of the new Ru(II)-COUPY conjugate as well as for the free coumarin has been carried out in collaboration with Mireia Jordà at the group of Prof. Santi Nonell from the Institut Químic de Sarrià. In addition, confocal microscopy studies were carried out under the supervision of Dr. Manel Bosch at the Advanced Optical Microscopy Unit of the University of Barcelona.

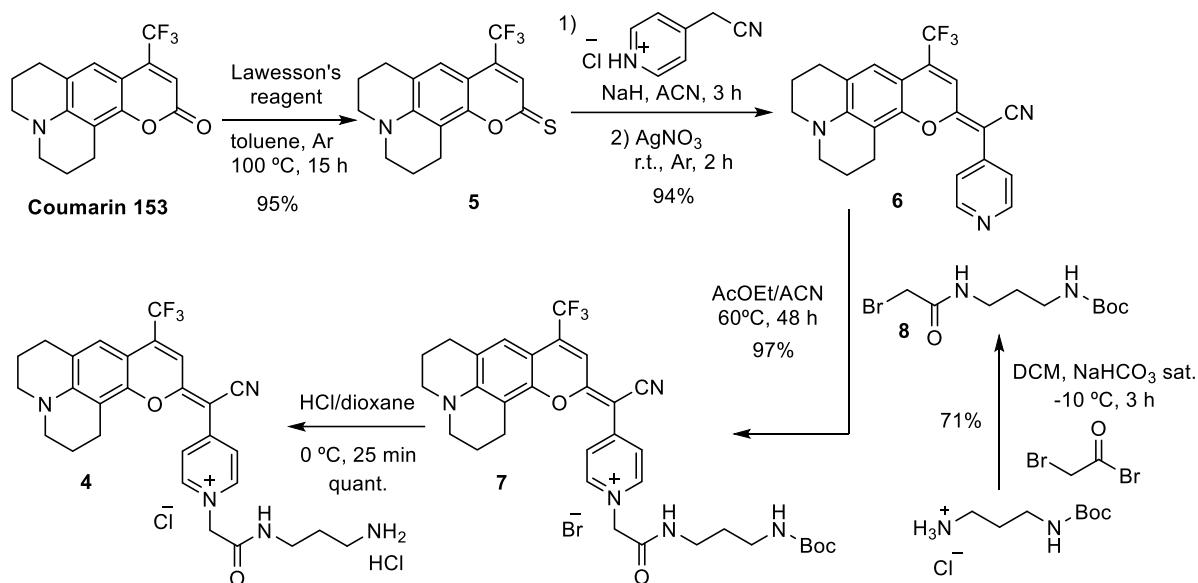


Scheme 1. Structures of the Ru(II) complexes **1a** and **1b**, COUPY coumarins **2** and **4**, and of the Ru(II)-COUPY conjugate **3** investigated in this work.

RESULTS AND DISCUSSION

Synthesis of conjugatable COUPY derivative 4

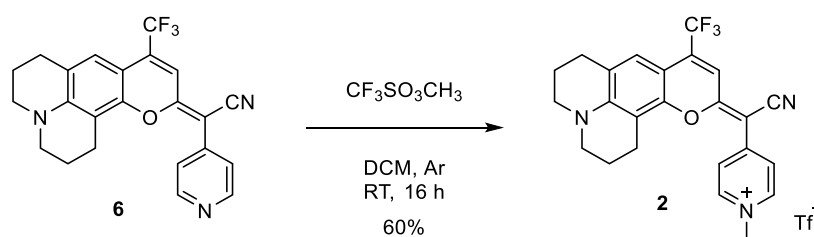
The required conjugatable COUPY dye **4** was synthesized from a commercially available coumarin precursor following our methodology described in publication D (**Scheme 2**).^{14,15} The synthesis route for COUPY **4** involved four steps starting with the reaction of Coumarin 153 with Lawesson's reagent (LW) to provide thiocoumarin **5**, which was condensed with 4-pyridylacetonitrile to give compound **6**. Coumarin **7** was obtained with excellent yield by *N*-alkylation of the pyridine heterocycle with the bromoacetamide derivative **8**, which had been previously synthesized by reaction of bromoacetyl bromide with *N*-Boc-1,3-diaminopropane. Finally, the Boc protecting group was removed under acidic conditions to give coumarin **4**. All of the compounds depicted in **Scheme 2** were purified by silica column chromatography and fully characterized by high-resolution mass spectrometry (HRMS) and ¹H and ¹³C NMR spectroscopy.



Scheme 2. Synthesis of COUPY derivative **4**.

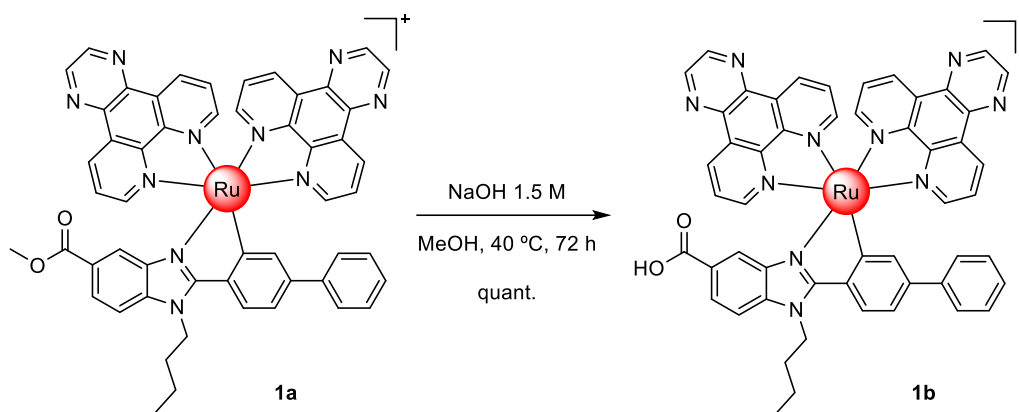
Synthesis of COUPY coumarin **2**

For the synthesis of the corresponding *N*-methylated COUPY dye **2** to be used as a control compound, coumarin **6** (**Scheme 3**) was reacted with methyl trifluoromethanesulfonate in DCM at room temperature yielding the expected compound as a dark blue solid with a 60% yield after column chromatography.



Scheme 3. Synthesis of control COUPY coumarin **2**.

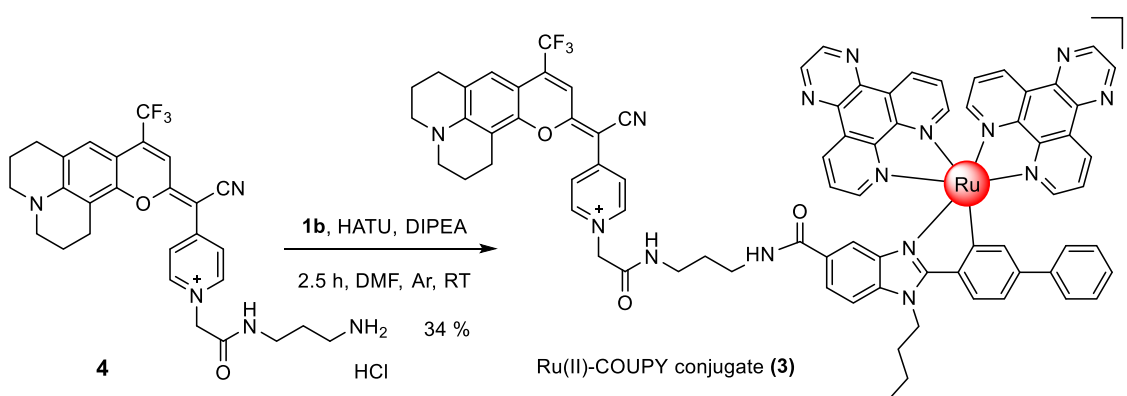
Synthesis of Ru(II) complex **1b**



Scheme 4. Hydrolysis of the ester group in Ru(II) complex **1a**.

The ester group of the Ru(II) complex **1a** was hydrolyzed under basic conditions at 40 °C for 72 h and protected from light. The crude was used without further purification since HPLC-MS analysis revealed that the hydrolysis of the ester group was quantitative.

Synthesis of Ru(II)-COUPY conjugate **3**



Scheme 5. Synthesis of Ru(II)-COUPY conjugate **3**.

The HATU-mediated conjugation between the amino-derivatized coumarin **4** and the Ru(II) complex **1b** afforded Ru(II)-COUPY conjugate **3** as a dark blue solid after column chromatography. However, it is worth nothing that several approaches had to be investigated for the purification of the conjugate since some stability problems were found. As shown in the HPLC chromatogram in **Figure 1**, the purification by silica gel column chromatography led to the partial decomposition of the compound, generating a fragment of the conjugate without the ruthenium moiety. On the other hand, the purification by reversed HPLC using 0.1% formic acid as an additive in the eluents (H₂O and ACN) was also found to provoke the decomposition of the conjugate because the exocyclic double carbon-carbon bond within the COUPY scaffold was broken (**Figure 2**). Fortunately, the use of neutral aluminum oxide as stationary phase allowed the isolation of the pure compound by column chromatography with a 34% yield (**Figure 3**).

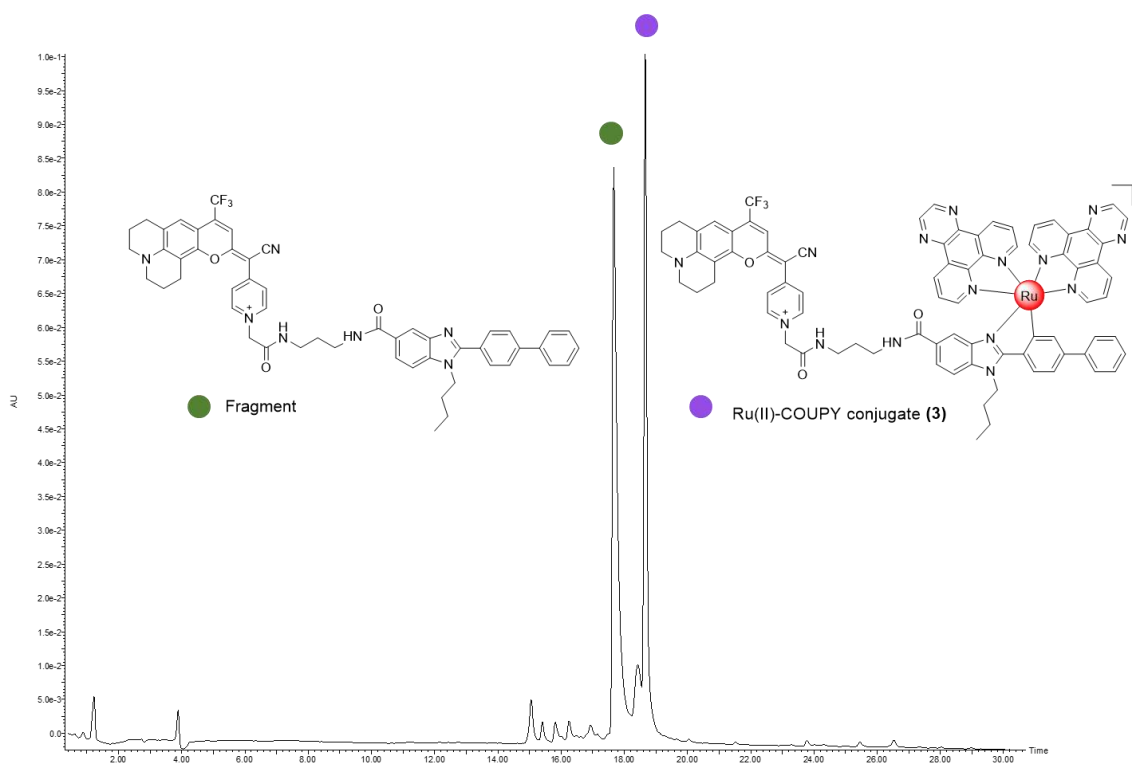


Figure 1. Reversed-phase HPLC traces for the analysis of Ru(II)-COUPY conjugate (**3**) after purification by silica column chromatography.

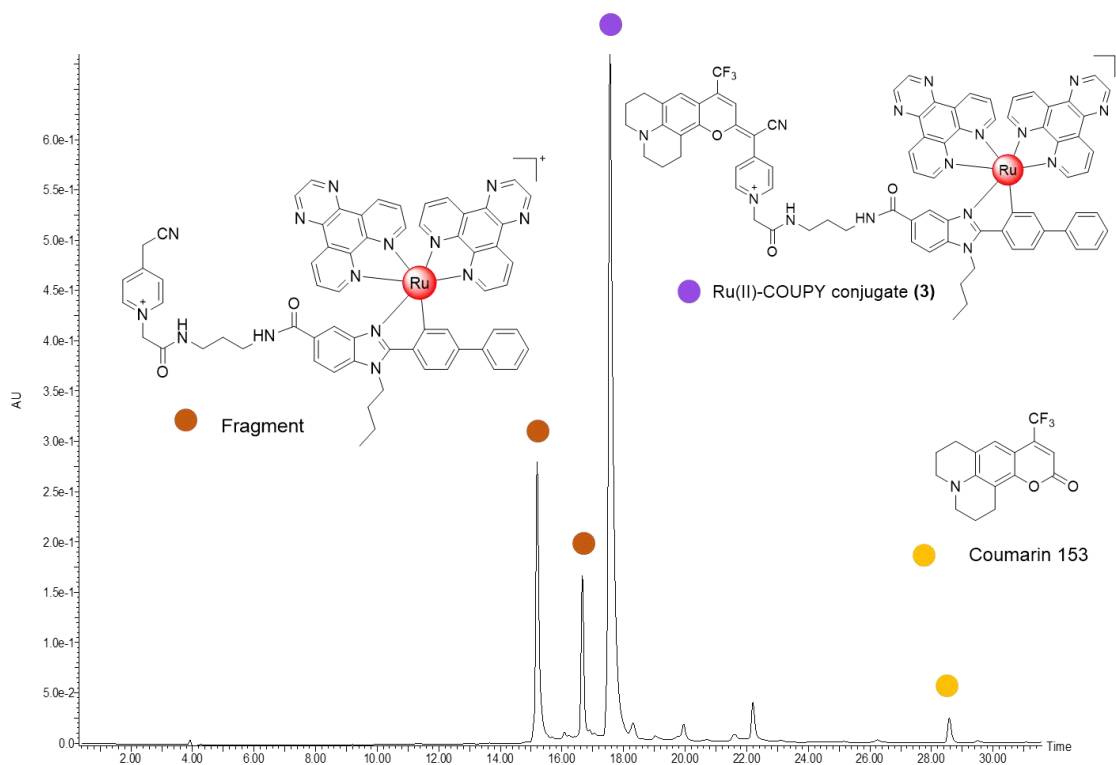


Figure 2. Reversed-phase HPLC traces for the analysis of Ru(II)-COUPY conjugate (**3**) after purification by reversed-phase HPLC (ACN/H₂O + 0.1% formic acid).

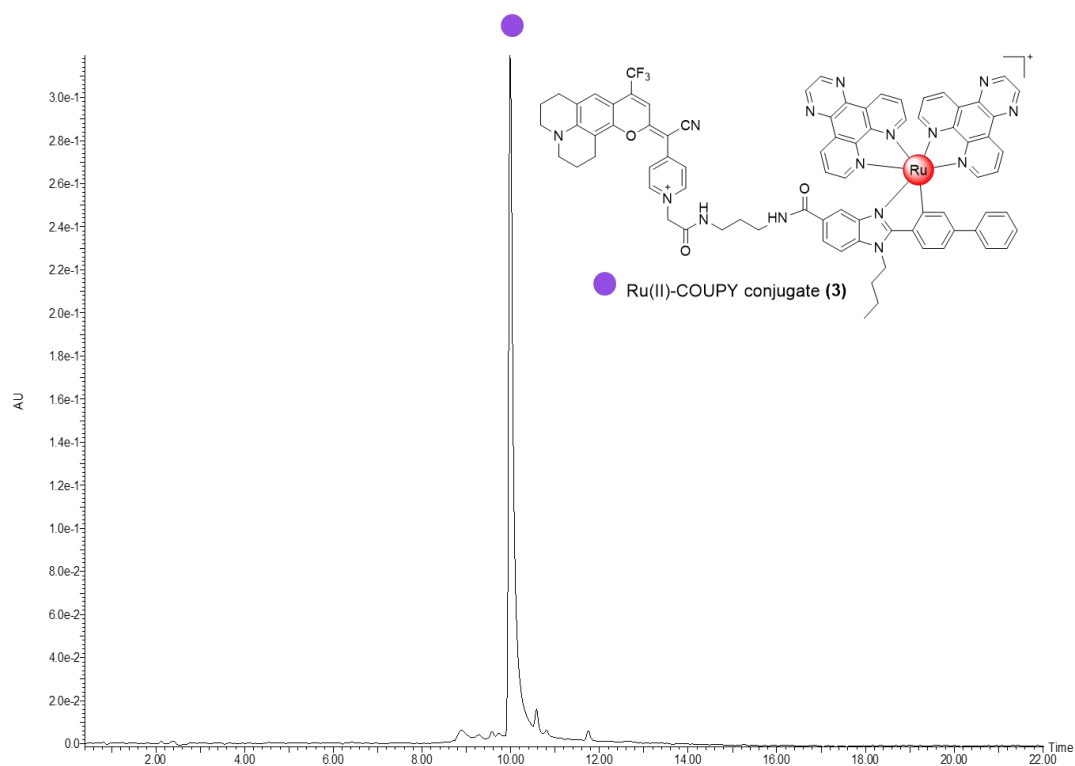


Figure 3. Reversed-phase HPLC traces of Ru(II)-COUPY conjugate (**3**) after purification by column chromatography using neutral aluminum oxide.

Photophysical characterization of the compounds

The photophysical properties (absorption and emission spectra, and fluorescence quantum yield (Φ_F)) of the new Ru(II)-COUPY conjugate **3** along with the Ru(II) complex **1a** and the COUPY coumarin **2** were studied in CH₃CN. The UV-vis absorption and emission spectra are shown in **Figure 4**, and their photophysical properties are summarized in **Table 1**.

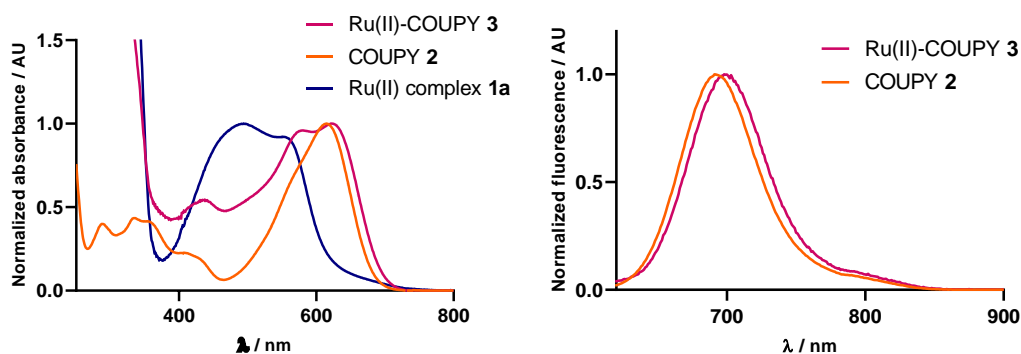


Figure 4. Comparison of the normalized absorption (left) and emission spectra (right) of the compounds in CH₃CN.

As shown in **Table 1**, the julolidine-fused coumarin analogue containing a trifluoromethyl group at the 4-position (**2**) exhibited an absorption and emission maxima in the far-red/NIR region of the electromagnetic spectrum (615 and 691 nm, respectively). An additional red-shift in the absorption (8 nm) and emission (7 nm) maxima occurred after conjugation to the Ru(II) complex. However, the fluorescent quantum yield of the Ru(II)-COUPY conjugate **3** was smaller than that of the parent COUPY dye **2**, which suggested the presence of competitive excited-state processes, thereby reproducing the behavior of Ir(III)-COUPY conjugates.

Table 1. Photophysical properties of the compounds **1a**, **2** and **3**.

Compound	λ_{\max} (nm)	λ_{em} (nm)	Stokes' shift (nm)	Φ_F	Solvent
Ru(II) complex 1a	258, 288, 321, 493, 561	356, 367 711	-	-	CH ₃ CN
COUPY 2	615	691	76	0.046	CH ₃ CN
Ru(II)-COUPY 3	623	698	75	0.007	CH ₃ CN

Generation of singlet oxygen (1O_2) and superoxide anion radical ($O_2^{\cdot-}$) upon visible light irradiation

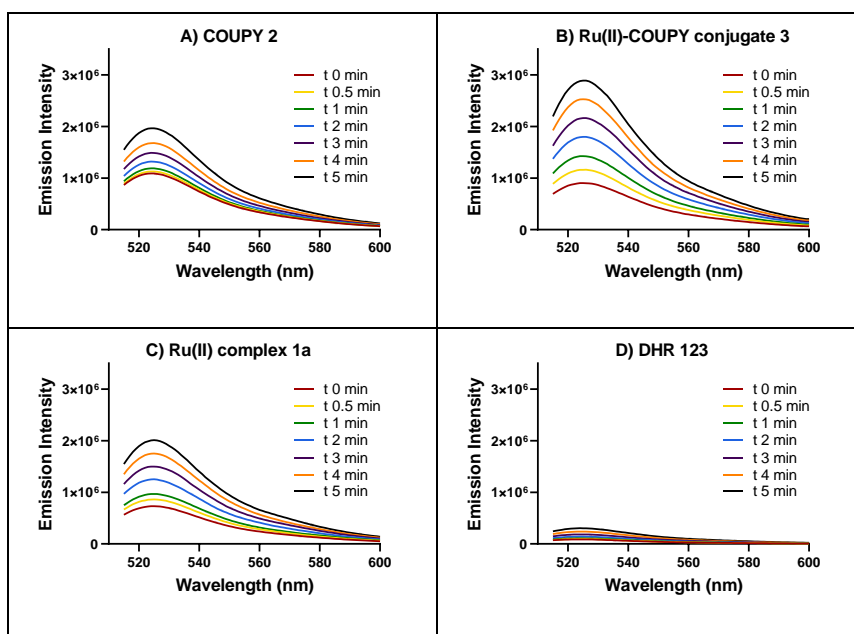
As previously reported by Ruiz's,¹³ the Ru(II) complex **1a** was found highly photoactive in HeLa and A2780cis cancer cells both in normoxia and in hypoxia conditions which was attributed to the generation of ROS. Under normoxia, the complex photogenerated mainly H_2O_2 and less markedly $\cdot OH$ in HeLa cells. However, under hypoxia the Ru(II) complex was also able to mainly photogenerate H_2O_2 , but also $O_2^{\cdot-}$. The production of ROS was also confirmed by a spectroscopic method since the Ru(II) complex was able to photocatalytically oxidize NADH in the presence of oxygen. Then, in order to determine the main ROS species involved in the oxidation, the irradiation of the complex with green light was undertaken in the presence of different selective ROS scavengers, being the reaction sensitive to the presence of sodium azide (1O_2 scavenger) and sodium pyruvate (H_2O_2 scavenger).

Based on these antecedents, the ability of the Ru(II)-COUPY conjugate **3** and of the two unconjugated moieties (COUPY **2** and Ru(II) complex **1a**) to produce 1O_2 and $O_2^{\cdot-}$ was evaluated spectroscopically. For 1O_2 phosphorescence measurements, a pulsed Nd:YAD laser working at a 1 or 10 KHz repetition rate was used for excitation at 355 nm or 532 nm. Then, the light emitted by the sample was filtered with a 1000-nm long-pass filter and later by a narrow bandpass filter at 1275 nm to isolate the NIR emission of singlet oxygen. Ru(II) complex **1a** did not produce significant 1O_2 in any evaluated solvent, reproducing the results previously obtained for this Ru(II) complex by Ruiz's group in living cells. On the other hand, similar to the previous COUPY derivatives evaluated in this Thesis, COUPY dye **2** did not generate 1O_2 in any solvent. However, unlike the Ir(III)-COUPY conjugates described in Publications C and D, the conjugation between the Ru(II) complex and the COUPY fluorophore did not have any impact on the 1O_2 quantum yield. Hence, we can conclude that the Ru(II)-COUPY conjugate **3** does not produce singlet oxygen in any evaluated solvent either by irradiation with UV or green light.

Table 2. Singlet oxygen quantum yields of compounds **1a**, **2** and **3**.

Compound	Solvent	Φ_{Δ} at 355 nm	Φ_{Δ} at 532 nm
Ru(II) complex 1a	PBS	≈ 0	< 0.01
	CH ₃ CN	0.07	0.09
	CH ₂ Cl ₂	0.07	0.08
COUPY 2	PBS	≈ 0	< 0.01
	CH ₃ CN	0.01	0.01
	CH ₂ Cl ₂	0.02	0.01
Ru(II)-COUPY 3	PBS	≈ 0	< 0.01
	CH ₃ CN	≈ 0	< 0.01
	CH ₂ Cl ₂	0.02	0.02

Having confirmed that the Ru(II)-COUPY conjugate **3** does not generate singlet oxygen, we investigated the ability of the compound **3** to produce $O_2^{\bullet-}$ by using a spectroscopic method based on dihydrorhodamine 123 (DHR123) probe: the non-fluorescent DHR123 can be oxidized by superoxide anion radical to form the fluorescent rhodamine 123 derivative.¹⁶ As shown in **Figure 5**, although the COUPY dye **2** alone and the Ru(II) complex **1a** produce $O_2^{\bullet-}$ after green light irradiation (505 nm), the conjugation between the fluorophore and the metal complex clearly led to an increase in the generation of this class of type I ROS. However, it is worth noting, that all of the compounds also generated $O_2^{\bullet-}$ in the dark, before irradiation, since the fluorescence intensity is higher at $t = 0$ than that obtained with DHR123 alone, used as a negative control.

**Figure 5.** Fluorescence spectra of DHR123 induced by irradiation with visible light (505 nm) for 5 min, in the presence of COUPY coumarin **2** (A), Ru(II)-COUPY conjugate **3** (B), Ru(II) complex **1a** (C), or without any compound (DHR 123 alone, D).

Biological studies

The cellular uptake of Ru(II)-COUPY conjugate **3** was studied in living HeLa cells by confocal microscopy by irradiation with a yellow ($\lambda_{\text{ex}} = 561 \text{ nm}$) and a red ($\lambda_{\text{ex}} = 633 \text{ nm}$) light laser. As shown in **Figure 6**, the compound was efficiently taken up by the cells since fluorescent vesicles were clearly observed in the cytoplasm in all of the examined cells by using both excitation lasers. Interestingly, the cell membrane was also stained.

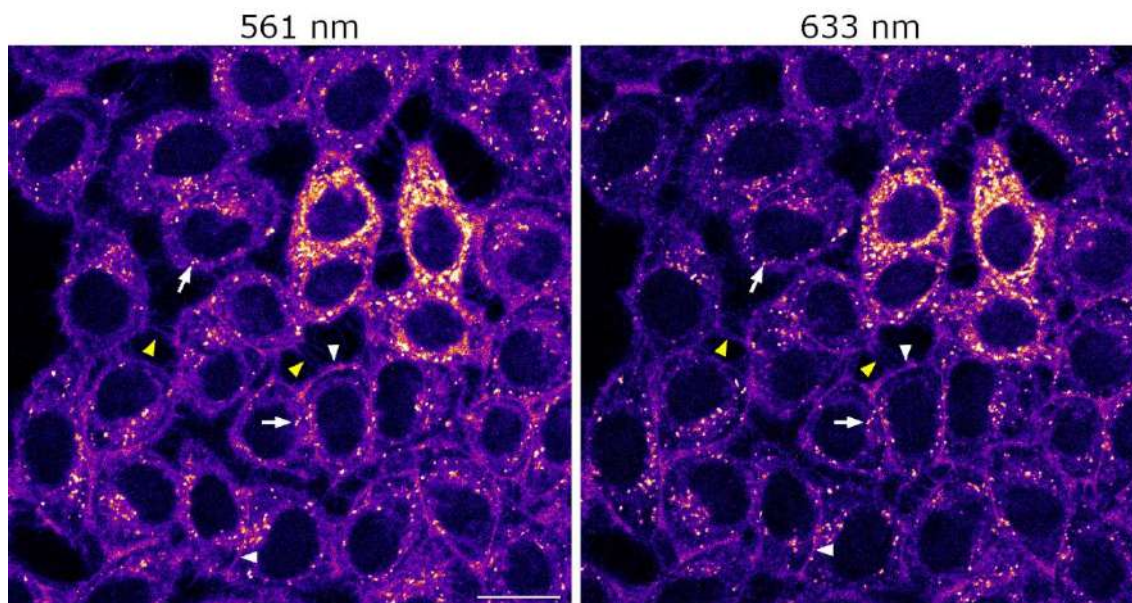


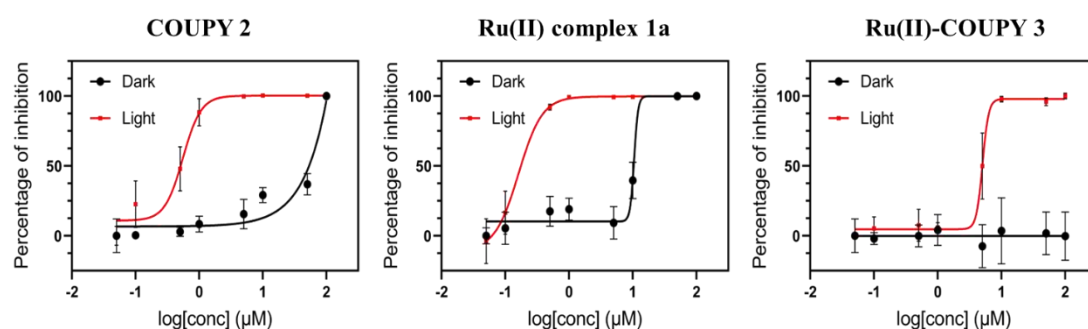
Figure 6. Cellular uptake of Ru(II)-COUPY **3** conjugate. Single confocal planes of HeLa cells incubated with **3** at $10 \mu\text{M}$ for 30 min at $37 \text{ }^\circ\text{C}$ after excitation at 561 nm (left) or at 633 nm (right). In both cases, emission was detected from 650 to 750 nm. White arrows point out vesicles, white arrowheads cell membrane, and yellow arrowheads stained filopodial protrusions. Scale bar: $20 \mu\text{m}$.

The *in vitro* antitumor activity of Ru(II)-COUPY conjugate **3** was evaluated in HeLa cells in normoxic conditions ($21\% \text{ O}_2$). Photocytotoxicity was assessed via irradiation with visible red-light (620 nm). The parent compounds (COUPY **2** and Ru(II) complex **1a**) were also evaluated to investigate the effect of conjugation. As shown in **Table 3**, the conjugation between the Ru(II) complex and the fluorophore resulted in a clear decrease in the dark cytotoxicity of the metaldrug ($\text{IC}_{50} = 7 \mu\text{M}$ for **1b** and $\text{IC}_{50} > 100 \mu\text{M}$ for **3**), which reproduces the tendency previously found with Ir(III)-COUPY conjugates (publications C and D). Very interestingly, red-light irradiation clearly improved the antitumor activity of the conjugate, leading to an IC_{50} value of $2.9 \mu\text{M}$ ($\text{PI} > 34.5$) upon irradiation with red light. Surprisingly, although COUPY **2** exhibited relatively low cytotoxicity in the dark ($\text{IC}_{50} = 61 \mu\text{M}$), red-light irradiation clearly improved its antitumor activity, leading to a IC_{50} value of $0.38 \mu\text{M}$ and an excellent PI value of 160.5.

Table 3. Cyto- and phototoxicity of the compounds towards HeLa cells.^a

	Dark	Light	PI ^b
	IC ₅₀ [μM]	IC ₅₀ [μM]	
Ru(II) complex 1a	7 ± 1	0.11 ± 0.03	63.6
COUPY 2	61 ± 4	0.38 ± 0.04	160.5
Ru(II)-COUPY 3	>100	2.9 ± 0.3	>34.5

^aCells were treated for 1.5 h (1 h incubation and 0.5 h irradiation at doses of 89 mW cm² of red light, followed by 48 h of incubation in a drug-free medium). ^bPI = phototoxic index, defined as the ratio of the toxic effect in dark and upon light irradiation; PI = [IC₅₀]_{dark}/[IC₅₀]_{620nm}

**Figure 7.** Dose-response curves based on cell inhibition for dark- and photo-cytotoxicity of indicated compounds in HeLa cells under dark or after red light irradiation.

EXPERIMENTAL SECTION

Synthesis and characterization

Synthesis of compound 5

Coumarin 153 (1 g, 3.23 mmol) and Lawesson's reagent (791 mg, 1.94 mmol) were dissolved in toluene (50 mL) and heated at 100 °C for 15 h. After evaporation under reduced pressure, the residue was purified by column chromatography (silica gel, 0-40% DCM in hexanes) to give a maroon solid (1.14 mg, 95%): TLC R_f (DCM) 0.9. ¹H NMR (400 MHz, CDCl₃) δ(ppm) 7.13 (1H, s), 7.11 (1H, s), 3.33 (4H, m), 2.98 (2H, t, *J* = 6.4 Hz), 2.78 (2H, t, *J* = 6.2 Hz), 1.99 (4H, m). ¹³C{¹H} NMR (101 Hz, CDCl₃) δ(ppm) 211.1, 147.3, 122.4, 121.3, 120.0, 106.8, 50.5, 50.1, 28.4, 20.9, 20.6; HRMS (ESI-TOF) *m/z* [M + H]⁺ calcd for C₁₆H₁₅F₃NOS 326.0821, found 326.0816.

Synthesis of compound 6

To a solution of 4-pyridylacetonitrile hydrochloride (380.2 mg, 2.46 mmol) and NaH (60% dispersion in mineral oil, 245.9 mg, 6.15 mmol) in dry ACN (100 mL) under an Ar atmosphere and protected from light, a solution of coumarin **5** (400 mg, 1.23 mmol) in dry ACN (20 mL) was added. After the mixture was stirred for 3 h at room temperature, silver nitrate (459.5 mg, 2.70 mmol) was added, and the reaction mixture was stirred at room temperature for 2 h under an Ar atmosphere and protected from light. The crude product was evaporated under reduced pressure and purified by column chromatography (silica gel, 0–1.2% MeOH in DCM) to give 471.4 mg of a red golden solid (yield 94%). TLC: R_f (10% MeOH in DCM) 0.33. ¹H NMR (400 MHz, DMSO-*d*₆) δ(ppm) 8.63 (2H, d, *J* = 6.2 Hz), 7.68 (2H, d, *J* = 6.2 Hz), 6.96 (1H, s), 6.87 (1H, s), 3.30 (4H, m), 2.79 (2H, t, *J* = 6.4 Hz), 2.73 (2H, t, *J* = 6.2 Hz), 1.90 (4H, m). ¹³C{¹H} NMR (101 Hz, DMSO-*d*₆) δ(ppm) 160.3, 150.4, 150.0, 149.8, 146.5, 139.0, 122.5, 121.2, 121.0, 119.4, 118.4, 109.4, 106.5, 101.8, 85.6, 49.4, 48.6, 27.0, 20.7, 20.5, 19.8. HRMS (ESI-TOF) *m/z* [M + H]⁺ calcd for C₂₃H₁₉F₃N₃O 410.1475, found 410.1475.

Synthesis of compound 8

Bromoacetyl bromide (331 μL, 3.80 mmol) was added to a cooled down solution (-10 °C) of *N*-Boc-1,3-diaminopropane hydrochloride (400 mg, 1.90 mmol) in DCM/NaHCO₃ sat. 1:1 (60 mL). The mixture was stirred at room temperature for 3 h. The DCM was evaporated under reduced pressure and the aqueous phase was extracted with AcOEt (2 × 100 mL). The organic phase was washed with aqueous solutions of sat. NaHCO₃ (2 × 50 mL), HCl 5% (2 × 50 mL) and brine (2 × 50 mL). The combined organic fractions were dried over anhydrous Na₂SO₄, filtered, and evaporated under reduced pressure. The crude product was purified by column chromatography (silica gel, 0-60% AcOEt in hexanes) to give 420.6 mg of white solid (yield 71%). TLC: R_f (50% AcOEt in hexanes) 0.53. ¹H NMR (400 MHz, CDCl₃) δ(ppm) 7.08 (1H, br s), 4.85 (1H, br s), 3.86 (2H, s), 3.34 (2H, q, *J* = 6.3 Hz), 3.18 (2H, q, *J* = 6.3 Hz), 1.66 (2H, quint, *J* = 6.3 Hz), 1.44 (9H, s). ¹³C{¹H} NMR (101 Hz, CDCl₃) δ(ppm) 166.1, 156.8, 79.6, 37.2, 36.9, 30.1, 29.3, 28.5. HRMS (ESI-TOF) *m/z* [M + Na]⁺ calcd for C₁₀H₁₉BrN₂NaO₃ 317.0471, found 317.0472.

Synthesis of compound 7

Compound **8** (180.2 mg, 0.61 mmol) was added to a solution of coumarin **6** (100 mg, 0.24 mmol) in AcOEt/ACN 1:1 (50 mL). The mixture was stirred for 48 h at 60 °C protected from light. The crude product was evaporated under reduced pressure and purified by column chromatography (silica gel, 0–10% MeOH in DCM) to give 156 mg of a blue solid (yield, 97%). TLC: Rf (10% MeOH in DCM) 0.43. ¹H NMR (400 MHz, DMSO-*d*₆) δ(ppm) 8.75 (2H, d, *J* = 6.6 Hz), 8.56 (1H, br s), 8.18 (2H, d, *J* = 6.6 Hz), 7.16 (1H, s), 6.99 (1H, s), 6.82 (1H, s), 5.28 (2H, s), 3.40 (4H, m), 3.13 (2H, q, *J* = 6.6 Hz), 2.95 (4H, m), 2.81 (2H, m), 1.92 (4H, m), 1.57 (2H, quint, *J* = 6.9 Hz), 1.37 (9H, s). ¹³C{¹H} NMR (101 Hz, DMSO-*d*₆) δ(ppm). 164.9, 164.5, 155.6, 151.0, 148.2, 147.8, 145.0, 122.2, 121.4, 117.6, 107.6, 107.5, 106.1, 103.6, 82.9, 77.5, 60.1, 49.7, 48.8, 37.5, 36.9, 29.3, 28.2, 27.1, 20.8, 20.2, 19.6. HRMS (ESI-TOF) *m/z* [M]⁺ calcd for C₃₃H₃₇F₃N₅O₄ 624.2792, found 624.2793.

Synthesis of compound 4

A cooled down solution of hydrochloric acid in dioxane (4 M, 17 mL) was added to coumarin **7** (33.3 mg, 0.047 mmol). The reaction mixture was stirred for 25 min at room temperature under an Ar atmosphere and protected from light. After removal of the solvent, several co-evaporations from acetonitrile were carried out. The crude product was used without further purification in the next step since HPLC-MS analysis revealed that the removal of the Boc group was quantitative. Analytical HPLC (10 to 70% B in 30 min, formic acid additive): Rt = 14.25 min. LRMS (ESI-TOF) *m/z*: [M]⁺ Calcd for C₂₈H₂₉F₃N₅O₂ 524.23, found 524.18.

Synthesis of compound 2

Methyl trifluoromethanesulfonate (17 μL, 0.15 mmol) was added to a solution of coumarin **6** (20 mg, 0.049 mmol) in DCM (20 mL) under an argon atmosphere. The mixture was stirred overnight at room temperature and protected from light. The reaction mixture was evaporated under reduced pressure and purified by column chromatography (silica gel, 0–9% MeOH in DCM) to give 16.7 mg of a blue solid (yield 60%). TLC: Rf (10% MeOH in DCM) 0.36. ¹H NMR (400 MHz, DMSO-*d*₆) δ(ppm) 8.80 (2H, d, *J* = 7.0 Hz), 8.16 (2H, d, *J* = 7.0 Hz), 7.15 (1H, s), 6.97 (1H, s), 4.23 (3H, s), 3.40 (4H, m), 2.89 (2H, t, *J* = 6.3 Hz), 2.80 (2H, t, *J* = 6.0 Hz), 1.91 (4H, m). ¹³C{¹H} NMR (101 Hz, DMSO-*d*₆) δ(ppm) 164.5, 150.8, 147.6, 147.4, 144.5, 122.1, 121.9, 121.4, 119.1, 117.6, 107.6, 106.2, 103.4, 82.8, 49.7, 48.8, 46.6, 27.0, 20.8, 20.3, 19.6. HRMS (ESI-TOF) *m/z* [M]⁺ calcd for C₂₄H₂₁F₃N₃O 424.1631, found 424.1634.

Synthesis of compound 1b

A solution of Ru(II) complex **1a** (25.5 mg, 0.023 mmol) in MeOH (25 mL) was mixed with an aqueous solution of NaOH 1.5 M (75 mL). The mixture was stirred for 72 h at 40 °C and protected from light. After evaporation of the MeOH under reduced pressure, the aqueous phase was neutralized with an aqueous saturated solution of NH₄Cl (pH between 7-8). Then, the aqueous phase was extracted with DCM (3 x 15 mL) and the combined organic fractions were dried over anhydrous Na₂SO₄, filtered, and evaporated under reduced pressure. The crude product was used without further purification since HPLC-MS analysis revealed that the hydrolysis of the ester group was quantitative.

Synthesis of Ru(II)-COUPY conjugate 3

To a solution of Ru complex **1b** (17 mg, 15.7 μmol) and HATU (6.0 mg, 15.7 μmol) in anhydrous DMF (4 mL) under an Ar atmosphere, DIPEA (9 μL, 47.2 μmol) was added and the mixture stirred for 10 min under Ar at room temperature and protected from light. After addition of a solution of coumarin **4** (26.0 mg, 43.6 μmol) and DIPEA (14 μL, 78.7 μmol) in anhydrous DMF (3 mL), the reaction mixture was stirred for 2.5 h at room temperature under Ar and protected from light. After evaporation under reduced pressure, the crude was purified by column chromatography (aluminium oxide neutral, 0-2.5% MeOH in DCM) to give 8.2 mg of dark blue solid (yield: 34%). TLC: R_f (10% MeOH in DCM) 0.50. HRMS (ESI-TOF) *m/z* [M]²⁺ Calcd for C₈₀H₆₄F₃N₁₅O₃Ru 720.7151; Found 720.7153.

Biological studies

HeLa cells were cultured in 96-well plates at a density of 5·10³ cells/well in complete medium and incubated for 24 h at 310 K and 5% CO₂ in a humidified incubator. Cell medium was removed by suction and serial dilutions of tested compounds in cell culture media were added at final concentrations in the range of 0 to 100 μM in a final volume of 100 μL/well (% v/v DMSO below 0.4%). After 1 h incubation with the compounds, light irradiation treatments were applied using Red Well Plate illuminator photoreactor (Luzchem; Canada) fitted with LED lamps centred at 620 nm (final intensity 89 mW/cm²) for 0.5 h. Dark control analogues were directly kept in the dark for 1.5 h. Cells were then incubated in drug-free media for a 48 h recovery period. Cells were washed with saline PBS buffer and loaded with 50 μL of MTT solution (1 mg/mL) for additional 4 h, then removed and 50 μL DMSO was added to solubilize the purple formazan crystals formed in active cells. The absorbance was measured at 570 nm using a microplate reader (FLUOstar Omega) and the IC₅₀ values were calculated based on the inhibitory rate curves using the next the equation:

$$I = \frac{I_{max}}{1 + \left(\frac{IC_{50}}{C}\right)^n}$$

Where I represent the percentage inhibition of viability observed, I_{max} is the maximal inhibitory effect, IC_{50} is the concentration that inhibits 50% of maximal growth, C is the concentration of the treatment and n is the slope of the semi-logarithmic dose-response sigmoidal curves. The non-linear fitting was performed using SigmaPlot 14.0 software. Two independent experiments were performed with triplicate points per concentration level ($n=3$).

CONCLUSIONS AND OUTLOOK

Based on previous results that demonstrated that coumarin-based COUPY fluorophores are promising candidates for developing novel fluorescent PDT agents in combination with metal complexes, in this work we have synthesized a novel PS agent based on the conjugation of a highly phototoxic cyclometalated Ru(II) polypyridyl complex to a NIR-emitting COUPY fluorophore. The Ru(II)-COUPY conjugate **3** exhibited several interesting features for cancer phototherapy, including an excellent uptake in HeLa cells, good photocytotoxicity under red-light irradiation, and minimal dark cytotoxicity compared with the parent compounds, especially in the case of the Ru(II) complex. In addition, spectroscopic studies confirmed that the conjugate generate type I ROS ($O_2^{\cdot-}$) under green light irradiation (505 nm) but did not generate 1O_2 upon excitation at 355 nm and 532 nm. Overall, although this a preliminary study, such interesting properties demonstrate that conjugation between NIR-emitting COUPY fluorophores to Ru(II) polypyridyl complexes can be used as a new strategy to develop PDT agents that can be activated within the phototherapeutic window (e.g., with far-red and NIR light). To complete the evaluation of this promising Ru(II)-COUPY conjugate, we will need to assess its phototoxicity towards different cancer and normal cell lines under both normoxic and hypoxic conditions, as well as to investigate ROS generation inside the cells, either in the dark or after irradiation, and identify the specific cytotoxic ROS involved in cell death.

REFERENCES

- (1) Cloonan, S. M.; Elmes, R. B. P.; Erby, M.; Bright, S. A.; Poynton, F. E.; Nolan, D. E.; Quinn, S. J.; Gunnlaugsson, T.; Williams, D. C. Detailed Biological Profiling of a Photoactivated and Apoptosis Inducing Pdppz Ruthenium(II) Polypyridyl Complex in Cancer Cells. *J. Med. Chem.* **2015**, *58*, 4494–4505. <https://doi.org/10.1021/acs.jmedchem.5b00451>.
- (2) Lee, S. Y.; Kim, C. Y.; Nam, T. G. Ruthenium Complexes as Anticancer Agents: A Brief History and Perspectives. *Drug Des. Devel. Ther.* **2020**, *14*, 5375–5392. <https://doi.org/10.2147/DDDT.S275007>.
- (3) Monroe, S.; Colón, K. L.; Yin, H.; Roque, J.; Konda, P.; Gujar, S.; Thummel, R. P.; Lilge, L.; Cameron, C. G.; McFarland, S. A. Transition Metal Complexes and Photodynamic Therapy from a Tumor-Centered Approach: Challenges, Opportunities, and Highlights from the Development of TLD1433. *Chem. Rev.* **2019**, *119*, 797–828. <https://doi.org/10.1021/acs.chemrev.8b00211>.
- (4) McFarland, S. A.; Mandel, A.; Dumoulin-White, R.; Gasser, G. Metal-Based Photosensitizers for Photodynamic Therapy: The Future of Multimodal Oncology? *Curr. Opin. Chem. Biol.* **2020**, *56*, 23–27. <https://doi.org/10.1016/j.cbpa.2019.10.004>.
- (5) Johnstone, T. C.; Suntharalingam, K.; Lippard, S. J. The Next Generation of Platinum Drugs: Targeted Pt(II) Agents, Nanoparticle Delivery, and Pt(IV) Prodrugs. *Chem. Rev.* **2016**, *116*, 3436–3486. <https://doi.org/10.1021/acs.chemrev.5b00597>.
- (6) Zeng, L.; Gupta, P.; Chen, Y.; Wang, E.; Ji, L.; Chao, H.; Chen, Z. S. The Development of Anticancer Ruthenium(II) Complexes: From Single Molecule Compounds to Nanomaterials. *Chem. Soc. Rev.* **2017**, *46*, 5771–5804. <https://doi.org/10.1039/c7cs00195a>.
- (7) Huang, H.; Zhang, P.; Yu, B.; Chen, Y.; Wang, J.; Ji, L.; Chao, H. Targeting Nucleus DNA with a Cyclometalated Dipyrrophenazineruthenium(II) Complex. *J. Med. Chem.* **2014**, *57*, 8971–8983. <https://doi.org/10.1021/jm501095r>.
- (8) Chen, Y.; Guan, R.; Zhang, C.; Huang, J.; Ji, L.; Chao, H. Two-Photon Luminescent Metal Complexes for Bioimaging and Cancer Phototherapy. *Coord. Chem. Rev.* **2016**, *310*, 16–40. <https://doi.org/10.1016/j.ccr.2015.09.010>.

- (9) Wu, W.; Sun, J.; Cui, X.; Zhao, J. Observation of the Room Temperature Phosphorescence of Bodipy in Visible Light-Harvesting Ru(II) Polyimine Complexes and Application as Triplet Photosensitizers for Triplet-Triplet-Annihilation Upconversion and Photocatalytic Oxidation. *J. Mater. Chem. C* **2013**, *1*, 4577–4589. <https://doi.org/10.1039/c3tc30592a>.
- (10) Sainuddin, T.; McCain, J.; Pinto, M.; Yin, H.; Gibson, J.; Hetu, M.; McFarland, S. A. Organometallic Ru(II) Photosensitizers Derived from π -Expansive Cyclometalating Ligands: Surprising Theranostic PDT Effects. *Inorg. Chem.* **2016**, *55*, 83–95. <https://doi.org/10.1021/acs.inorgchem.5b01838>.
- (11) Lifshits, L. M.; Roque, J. A.; Konda, P.; Monro, S.; Cole, H. D.; von Dohlen, D.; Kim, S.; Deep, G.; Thummel, R. P.; Cameron, C. G.; Gujar, S.; McFarland, S. A. Near-Infrared Absorbing Ru(II) Complexes Act as Immunoprotective Photodynamic Therapy (PDT) Agents against Aggressive Melanoma. *Chem. Sci.* **2020**, *11*, 11740–11762. <https://doi.org/10.1039/d0sc03875j>.
- (12) Novohradsky, V.; Rovira, A.; Hally, C.; Galindo, A.; Viguera, G.; Gandioso, A.; Svitelova, M.; Bresolí-Obach, R.; Kostrhunova, H.; Markova, L.; Kasparikova, J.; Nonell, S.; Ruiz, J.; Brabec, V.; Marchán, V. Towards Novel Photodynamic Anticancer Agents Generating Superoxide Anion Radicals: A Cyclometalated Ir III Complex Conjugated to a Far-Red Emitting Coumarin. *Angew. Chem. Int. Ed.* **2019**, *131*, 6377–6381. <https://doi.org/10.1002/ange.201901268>.
- (13) Ballester, F. J.; Ortega, E.; Bautista, D.; Santana, M. D.; Ruiz, J. Ru(II) Photosensitizers Competent for Hypoxic Cancers via Green Light Activation. *Chem. Commun.* **2020**, *56*, 10301–10304. <https://doi.org/10.1039/d0cc02417a>.
- (14) Gandioso, A.; Bresolí-Obach, R.; Nin-Hill, A.; Bosch, M.; Palau, M.; Galindo, A.; Contreras, S.; Rovira, A.; Rovira, C.; Nonell, S.; Marchán, V. Redesigning the Coumarin Scaffold into Small Bright Fluorophores with Far-Red to Near-Infrared Emission and Large Stokes Shifts Useful for Cell Imaging. *J. Org. Chem.* **2018**, *83*, 1185–1195. <https://doi.org/10.1021/acs.joc.7b02660>.
- (15) Rovira, A.; Pujals, M.; Gandioso, A.; López-Corrales, M.; Bosch, M.; Marchán, V. Modulating Photostability and Mitochondria Selectivity in Far-Red/NIR Emitting Coumarin Fluorophores through Replacement of Pyridinium by Pyrimidinium. *J. Org. Chem.* **2020**, *85*, 6086–6097. <https://doi.org/10.1021/acs.joc.0c00570>.
- (16) Yu, L.; Xu, Y.; Pu, Z.; Kang, H.; Li, M.; Sessler, J. L.; Kim, J. S. Photocatalytic Superoxide Radical Generator That Induces Pyroptosis in Cancer Cells. *J. Am. Chem. Soc.* **2022**, *144*, 11326–11337. <https://doi.org/10.1021/jacs.2c03256>.

Conclusions

Conclusions

The purpose of this Thesis was (i) to explore how the photophysical properties and subcellular accumulation of COUPY fluorophores can be fine-tuned by modifying the pyridine heterocycle within the coumarin scaffold, as well as to investigate their potential applications for developing (ii) novel targeted fluorescent imaging agents by conjugation to a receptor-binding peptide, and (iii) novel PDT anticancer agents in combination with highly potent cyclometalated Ir(III) and Ru(II) complexes.

According to the previously proposed objectives and to the results presented throughout this Thesis, the main conclusions of this work are the following ones:

Chapter I:

- The synthesis of a series of new coumarin-based COUPY fluorophores in which the *para*-pyridine moiety was replaced with three different heterocycles (*ortho*-pyridine and *ortho,ortho*- or *ortho,para*-pyrimidine) was satisfactorily accomplished.
- Similarly to previously reported COUPY derivatives, the 2D NOESY spectra of the new dyes confirmed the presence of two interconverting rotamers around the exocyclic C=C bond in solution.
- Regarding the photophysical properties, all of the new COUPY fluorophores exhibited an intense absorption band in the visible region of the electromagnetic spectrum. The replacement of the *para*-pyridine moiety with *ortho*-pyridine or *ortho,ortho*-pyrimidine had a negative effect on the spectroscopic properties since both absorption and emission were blue-shifted, leading to weakly fluorescent compounds. On the contrary, the absorption and emission maxima of *ortho,para*-pyrimidine-containing fluorophores were red-shifted with respect to the parent compounds, being located in the far-red/NIR region. In addition, the newly synthesized fluorophores exhibited some other suitable properties for bioimaging applications such as large Stokes' shifts and high photostability.
- *Ortho,para*-pyrimidine-containing COUPY dyes exhibited excellent cell membrane permeability and a higher preference for mitochondria than the parent *para*-pyridine-containing compounds.
- Conjugatable derivatives of COUPY dyes bearing suitable functional groups (e.g., carboxylic acid, azide or alkyne) were satisfactorily synthesized through *N*-alkylation of the pyridine heterocycle.

- Octreotide peptide was efficiently labeled following a stepwise Fmoc/tBu solid-phase strategy either via the formation of an amide bond with the COUPY dye bearing a carboxylic acid group, or via Cu(I)-catalyzed azide-alkyne cycloaddition reaction by using the azide- or alkynyl-containing COUPY dyes.
- The photophysical properties of COUPY-octreotide conjugates were found to be similar to those of their parent coumarin dyes, with absorption in the yellow/red part of the visible spectrum, and emission in the far red to the NIR region. Remarkably, the fluorescence quantum yields of the conjugates in aqueous solution were higher than those of their parent unconjugated coumarins.
- Cellular uptake by confocal microscopy in SSTR2-overexpressing HeLa cells confirmed the internalization and accumulation of COUPY-octreotide conjugates in the cytoplasm. In addition, the results from cellular uptake experiments at low temperature suggested that the internalization of the conjugates was mediated by the receptor.
- The visualization ability of COUPY dyes when conjugated to octreotide was comparable to that of a commercially available rhodamine dye and much better than that of the corresponding 5(6)-carboxyfluorescein-containing conjugate.

Chapter II:

- A conjugatable derivative of a COUPY dye bearing a linker with a free amino group was synthesized through *N*-alkylation of the pyridine heterocycle.
- The synthesis of a novel PDT agent based on the conjugation of a far-red emitting COUPY dye and a cyclometalated Ir(III) anticancer complex through the formation of an amide bond was accomplished satisfactorily.
- The intensity of the red phosphorescence associated to the cyclometalated Ir(III) complex was decreased in the Ir(III)-COUPY conjugate, indicating the presence of competitive excited-state processes. Similarly, the typical strong fluorescence of the COUPY dye decreased markedly in the conjugate. The Ir(III)-COUPY conjugate was found to exhibit a higher $^1\text{O}_2$ quantum yield than the Ir(III) complex or the COUPY dye alone in all organic solvents investigated. In addition, it was found photostable up to light fluences larger than those typically used for cell imaging purposes.
- The Ir(III)-COUPY conjugate was efficiently taken up by HeLa cells, and showed a different staining pattern than that of the unconjugated COUPY dyes, since only fluorescent vesicles were observed in the cytoplasm.

- The conjugation between the COUPY dye and the Ir(III) complex resulted in a compound with decreased cytotoxicity in the dark compared with the metallodrug or the fluorophore alone. However, visible-light irradiation (either green or blue) clearly improved the antitumor activity of the conjugate leading to excellent phototoxicity indexes both in normoxic and hypoxic conditions. The Ir(III)-COUPY conjugate was found to generate superoxide anion radicals in living cells upon visible-light irradiation, which was related with its high phototoxicity.
- A series of conjugatable derivatives of COUPY dyes containing several modifications at the 7-position of the coumarin scaffold and bearing different linkers were synthesized and characterized.
- The synthesis of four new photosensitizers based on Ir(III)-COUPY conjugates was satisfactorily accomplished by linking the COUPY derivatives and the Ir(III) complex through an amide-bond formation.
- Regarding the photophysical properties of the new conjugates, the same bathochromic or hypsochromic shifts observed for the new COUPY derivatives were also found when conjugated to the Ir(III) complex in comparison with the original compounds. The new conjugates containing the same COUPY derivative as the original Ir(III)-COUPY conjugate but bearing different linkers showed similar photophysical properties.
- All of the new PSs, regardless of the coumarin derivative or the linker, led to similar levels of $O_2^{\bullet -}$ generation when irradiated with green light. In addition, similar 1O_2 quantum yields were found for all Ir(III)-COUPY conjugates in comparison with the original conjugate.
- Ir(III)-COUPY conjugates containing a far-red emitting coumarin were efficiently taken up by HeLa cells and exhibited the same pattern of staining as the original conjugate according to confocal microscopy studies.

- The anticancer activity of all the Ir(III)-COUPY conjugates was tested in several cancer cell lines in normoxic conditions (HeLa, A2780, A2780cis, A375 and SK-MEL-28), as well as in hypoxia in the case of the cisplatin-resistant A2780 cell line. As previously found with the parent Ir(III)-COUPY conjugate, all of them were found non-toxic in the dark regardless of the cancer cell line, but exhibited high phototoxicity upon green light irradiation, which was attributed to the photogeneration of ROS. The most potent green-light photoactivation was found in ovarian cancer cells, particularly in resistant A2780cis cells, where PI values were markedly higher for the conjugates containing the parent COUPY dye regardless of the type and length of the spacer, as well as for the one incorporating the julolidine-fused system at the 7-position of the coumarin scaffold. Remarkably, the conjugates containing the longer linkers exhibited excellent PI values under hypoxia, which were much higher than that of the parent Ir(III)-COUPY conjugate.
- A new COUPY derivative combining a strong EWG (CF₃) at the 4-position of the coumarin scaffold and the julolidine-fused skeleton at the 7-position was synthesized, with the aim of increasing the push-pull character of the fluorophore.
- The synthesis of a novel PDT agent based on the conjugation of the resulting NIR-emitting COUPY dye with a cyclometalated Ru(II) polypyridyl anticancer complex was accomplished satisfactorily.
- The Ru(II)-COUPY conjugate showed an excellent cell membrane permeability in HeLa cells. The higher red-shifted absorption of the conjugate owing to the new COUPY derivative allowed visualization upon excitation with a red light laser ($\lambda_{\text{ex}} = 633 \text{ nm}$) in confocal microscopy studies.
- Conjugation between the Ru(II) complex and the COUPY fluorophore resulted in a decrease of the dark cytotoxicity of the metallodrug in HeLa cells. In addition, red-light irradiation clearly improved the antitumor activity of the conjugate leading to high PI values. Hence, although further biological studies needs to be done, such preliminary *in vitro* experiments highlight the potential of the newly synthesized conjugate for PDT applications upon irradiation within the phototherapeutic window.

Summaries

Resúmenes de resultados y discusión

Resumen del capítulo I

Introducción y objetivos

La fluorescencia se ha convertido en una de las herramientas más potentes y extensamente empleadas en áreas relacionadas con las ciencias biomédicas para la **visualización no invasiva de sistemas y procesos biológicos**. Así pues, permite detectar un gran número de enfermedades que antes resultaban fatales y tratarlas en sus etapas iniciales como, por ejemplo, el cáncer. Dichas técnicas ópticas requieren de la disponibilidad de sondas moleculares con propiedades fotofísicas adecuadas diseñadas para detectar y rastrear procesos moleculares o biomarcadores de interés.¹

Se pueden destacar tres características de la fluorescencia que hacen que este fenómeno sea particularmente útil para el diagnóstico del cáncer. En primer lugar, la **extraordinaria sensibilidad** que ofrece la fluorescencia debido a la alta eficiencia con la que se puede detectar la luz. En segundo lugar, es relativamente fácil alcanzar una **buena resolución espacial** (de alrededor de 1 μm) en el rango de longitudes de onda de la luz visible con microscopios ópticos simples. Finalmente, la escala de tiempo de emisión de luz es rápida (nano-microsegundos), lo que permite **monitorizar en tiempo real eventos** que están cambiando rápidamente.²

En este contexto, es necesario disponer de moléculas con propiedades fluorescentes como, por ejemplo, **fluoróforos orgánicos**. En particular, son especialmente interesantes los fluoróforos i) que operan en la región que abarca desde el **rojo lejano al infrarrojo cercano** (NIR, por sus siglas en inglés) del espectro electromagnético, y ii) que se puedan conjugar a **vehículos transportadores**, para desarrollar sondas fluorescentes dirigidas a un receptor específico. Las aplicaciones más importantes de los fluoróforos dirigidos incluyen el diagnóstico no invasivo de tumores, la terapia dirigida y la cirugía guiada por fluorescencia (FGS, por sus siglas en inglés).³

En las últimas décadas, se han desarrollado fluoróforos basados en compuestos orgánicos que mayoritariamente operan desde la zona ultravioleta del espectro electromagnético hasta el rojo lejano. Dichos compuestos contienen sistemas conjugados y suelen ser emisivos debido a las transiciones $\pi - \pi^*$. En la **Figura 1** se muestran las estructuras básicas de algunos fluoróforos representativos que se utilizan en aplicaciones de bioimagen, principalmente basados en derivados de cumarina,⁴ BODIPY, fluoresceína, rodamina y cianina.⁵⁻⁸

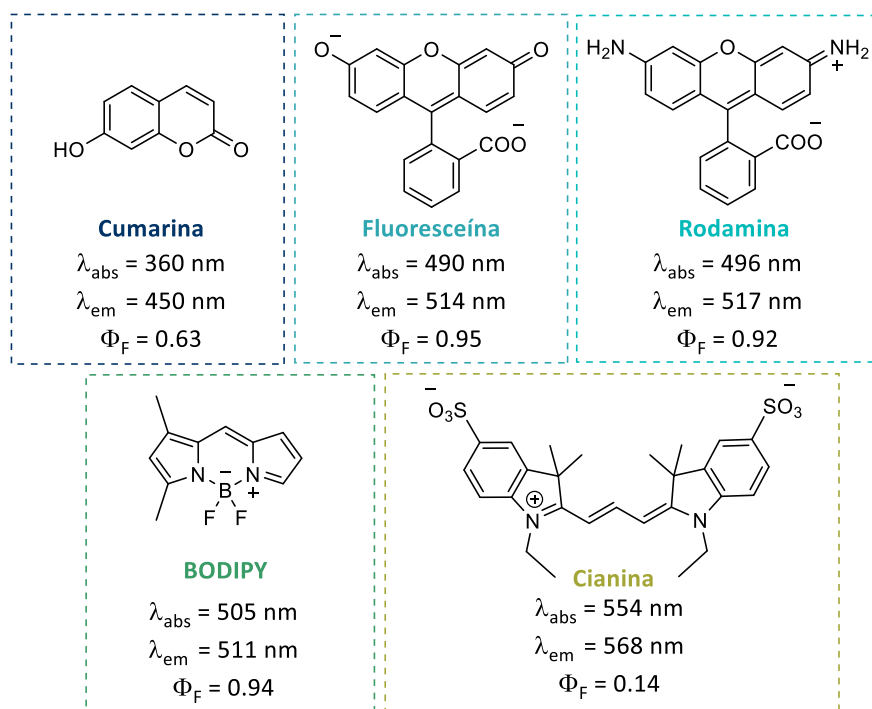
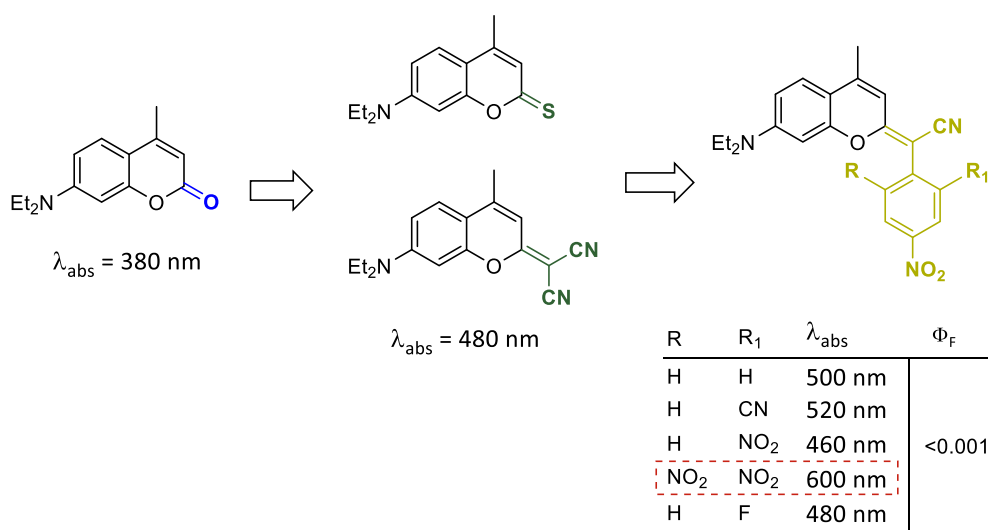


Figura 1. Ejemplos de moléculas orgánicas fluorescentes utilizadas en aplicaciones de bioimagen con operatividad a lo largo del espectro electromagnético.

El objetivo del desarrollo de nuevos fluoróforos orgánicos se centra en obtener propiedades fotofísicas óptimas, como i) **rendimientos cuánticos de fluorescencia altos**, ii) **buen brillo**, iii) **desplazamientos de Stokes grandes**, y iv) **fotoestabilidad**. Además, los fluoróforos que emiten a longitudes de onda más largas, en la región conocida como "**ventana fototerapéutica**" que va de 650 a 900 nm, son especialmente útiles debido a que dicha radiación presenta una mayor capacidad de penetración en los tejidos, mínima autofluorescencia y una menor dispersión de luz, así como provoca una baja o nula toxicidad en las células en comparación con radiaciones de longitudes de onda más cortas (ultravioleta y azul). Naturalmente, también se deben tener en cuenta otras propiedades a la hora de diseñar un fluoróforo orgánico como, por ejemplo, la **solubilidad en agua**, **tendencia a la agregación**, **citotoxicidad** y la **accesibilidad sintética**.⁹⁻¹¹

Teniendo en cuenta los requisitos anteriormente mencionados, en los últimos años se han dedicado grandes esfuerzos a la mejora de las propiedades fotofísicas y fisicoquímicas de la estructura de **cumarina**, principalmente a conseguir un desplazamiento hacia el rojo de las longitudes de onda de los máximos de absorción y emisión.¹² En dicho contexto, a pesar de no ser una de las modificaciones más estudiadas, algunos grupos de investigación se han centrado en la modificación de la lactona de la estructura de cumarina, especialmente de la **posición 2**. Así pues, dos de las modificaciones que han permitido un desplazamiento hacia el rojo son la tiónación del grupo carbonilo y la extensión de la conjugación a través de la posición 2 con un grupo dicianometileno (**Esquema 1**).¹³

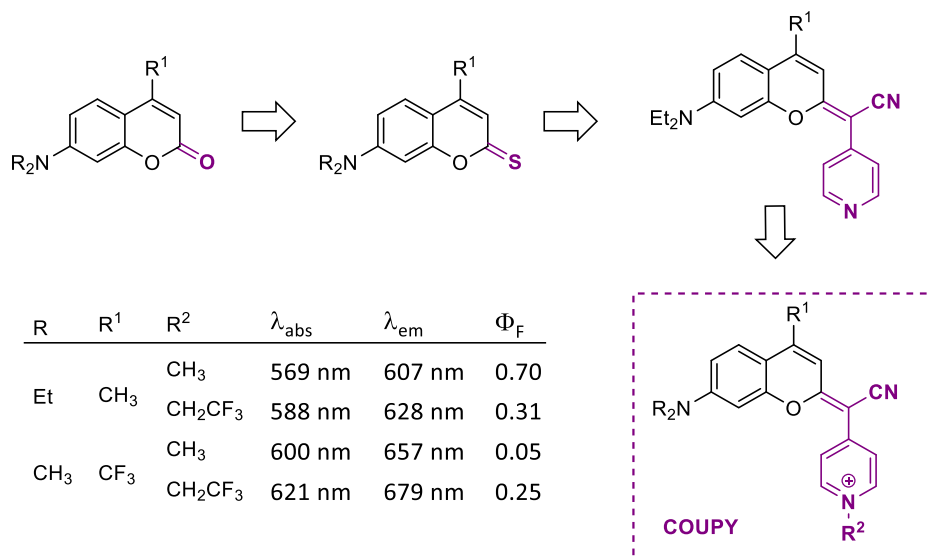
Anteriormente, en nuestro grupo de investigación se estudió la sustitución de un grupo nitrilo en los derivados de dicianocumarina por un anillo de benceno que contuviera grupos fuertemente atrayentes de electrones con el objetivo de aumentar el carácter ‘push-pull’ del fluoróforo.¹⁴ A pesar de lograr desplazar el máximo de absorción hasta 600 nm, la incorporación de dichos grupos, en particular de grupos nitro, tuvo un efecto negativo en la fluorescencia del cromóforo ($\Phi_F < 0.001$) (**Esquema 1**).



Esquema 1. Esquema de modificaciones realizadas en la posición 2 del esqueleto de cumarina con sus máximos de absorción en DCM.

Posteriormente, en nuestro grupo de investigación se sintetizaron nuevos derivados de cumarina en los que se reemplazó el grupo nitrilo de la dicianocumarina por un anillo de piridina (**Esquema 2**). Dicha modificación permitió aumentar la conjugación π y el carácter ‘push-pull’ del cromóforo, lo que resultó en un desplazamiento hacia el rojo en los espectros de absorción y emisión. La *N*-alquilación del heterociclo de piridina condujo al desarrollo de una **nueva familia de fluoróforos ‘push-pull’ basados en cumarina**, que denominamos **COUPY**.¹⁵

Las propiedades fotofísicas de los fluoróforos COUPY se pueden modular de forma selectiva mediante la combinación adecuada del grupo *N*-alquilante y del sustituyente en la posición 4 del esqueleto de cumarina. En general, los fluoróforos COUPY presentan propiedades fotofísicas muy adecuadas para aplicaciones en bioimagen, incluyendo emisión en la zona que abarca el rojo lejano y el infrarrojo cercano, desplazamientos de Stokes grandes, rendimientos cuánticos de fluorescencia altos y fotoestabilidad.



Esquema 2. Diseño de la nueva familia de fluoróforos, denominados COUPY, y sus datos fotofísicos en DCM.

Además de estas prometedoras propiedades fotofísicas, los fluoróforos COUPY presentan una excelente permeabilidad celular tanto a la membrana plasmática como a la membrana nuclear, lo que permite que puedan usarse en aplicaciones de bioimagen con células vivas a una concentración tan baja como 0.5 μM tras incubación durante cortos períodos de tiempo. Tal y como se muestra en la **Figura 2**, los fluoróforos COUPY tienden a acumular preferentemente en las mitocondrias y, en menor medida, en el nucléolo y en otros orgánulos como los lisosomas.

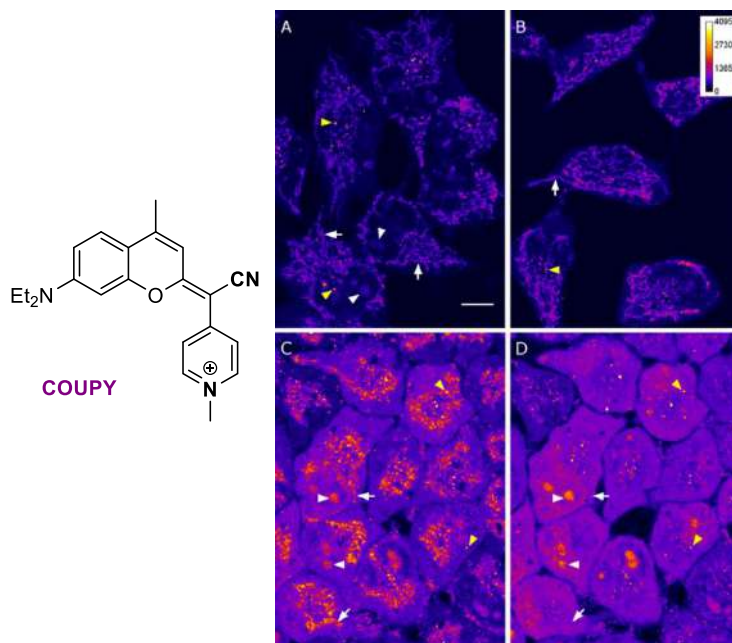
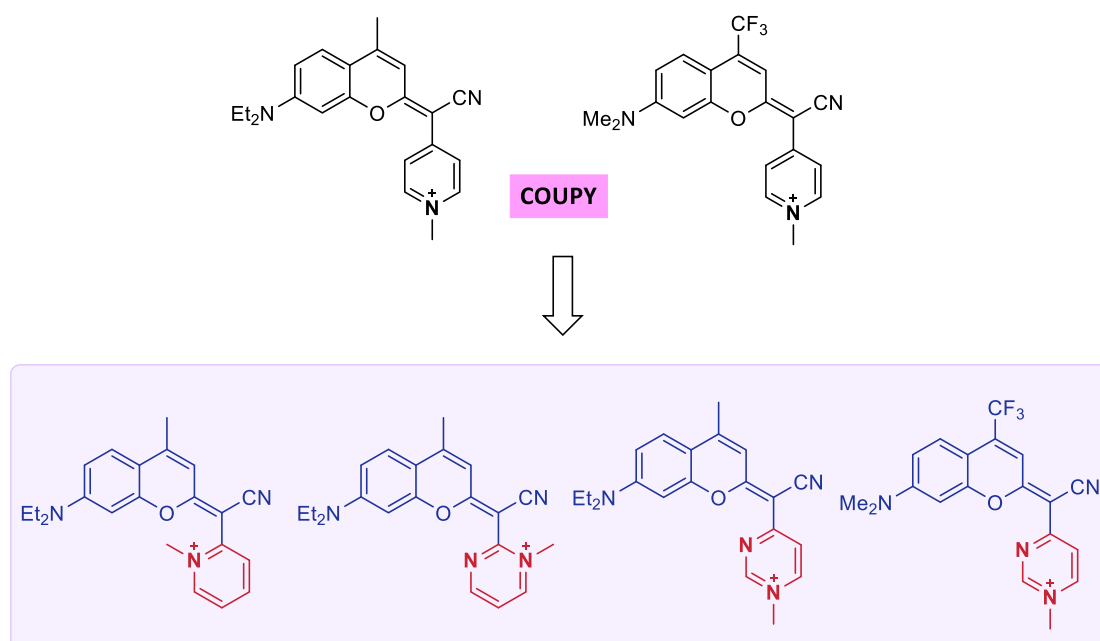


Figura 2. Imágenes de microscopía confocal de células HeLa incubadas con el fluoróforo COUPY indicado a diferentes concentraciones durante 20 min a 37 °C: (A) 0.5 μM , (B) 1 μM y (C y D) 2 μM . Las flechas blancas señalan mitocondrias, las puntas de flecha blancas nucleolos, y las puntas de flecha amarillas vesículas. Adaptado con el permiso de la referencia [15].

En base al descubrimiento de esta prometedora familia de fluoróforos basados en cumarina, en esta tesis doctoral nos hemos centrado en investigar cómo podría influir la modificación del anillo de piridina en las propiedades fotofísicas de los fluoróforos COUPY. En la primera publicación (**Apartado 6**), se describe la síntesis y caracterización de cuatro análogos de los fluoróforos originales COUPY en los que se ha reemplazado el grupo *p*-metilpiridinio por *o*-metilpiridinio o bien por dos pirimidinas metiladas (**Esquema 3**). Además, se ha estudiado su acumulación subcelular mediante microscopía confocal bajo la supervisión del Dr. Manel Bosch en la Unidad de Microscopía Óptica Avanzada de la Universidad de Barcelona.



Esquema 3. Estructura de los nuevos derivados COUPY descritos en la publicación A.

Por otra parte, teniendo en cuenta la necesidad de sintetizar fluoróforos dirigidos a ciertos receptores tumorales para una detección más específica del cáncer, en la segunda publicación (**Apartado 7**) se ha conjugado un fluoróforo COUPY a **octreotide**, un ciclooctapéptido aprobado por la FDA que muestra elevada afinidad y especificidad por el receptor de somatostatina, principalmente el subtipo 2 (SSTR2), que se encuentra sobreexpresado en la membrana de varios tipos de células tumorales (**Figura 3**). Para ello se han empleado metodologías de síntesis en fase sólida en combinación con química click.

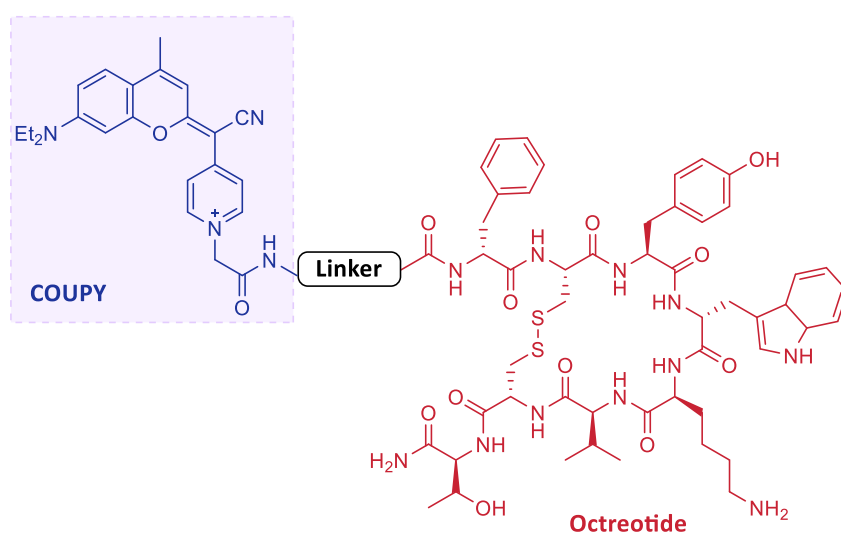


Figura 3. Estructura general de los conjugados COUPY-octreotide descritos en la publicación B.

Capítulo Ia

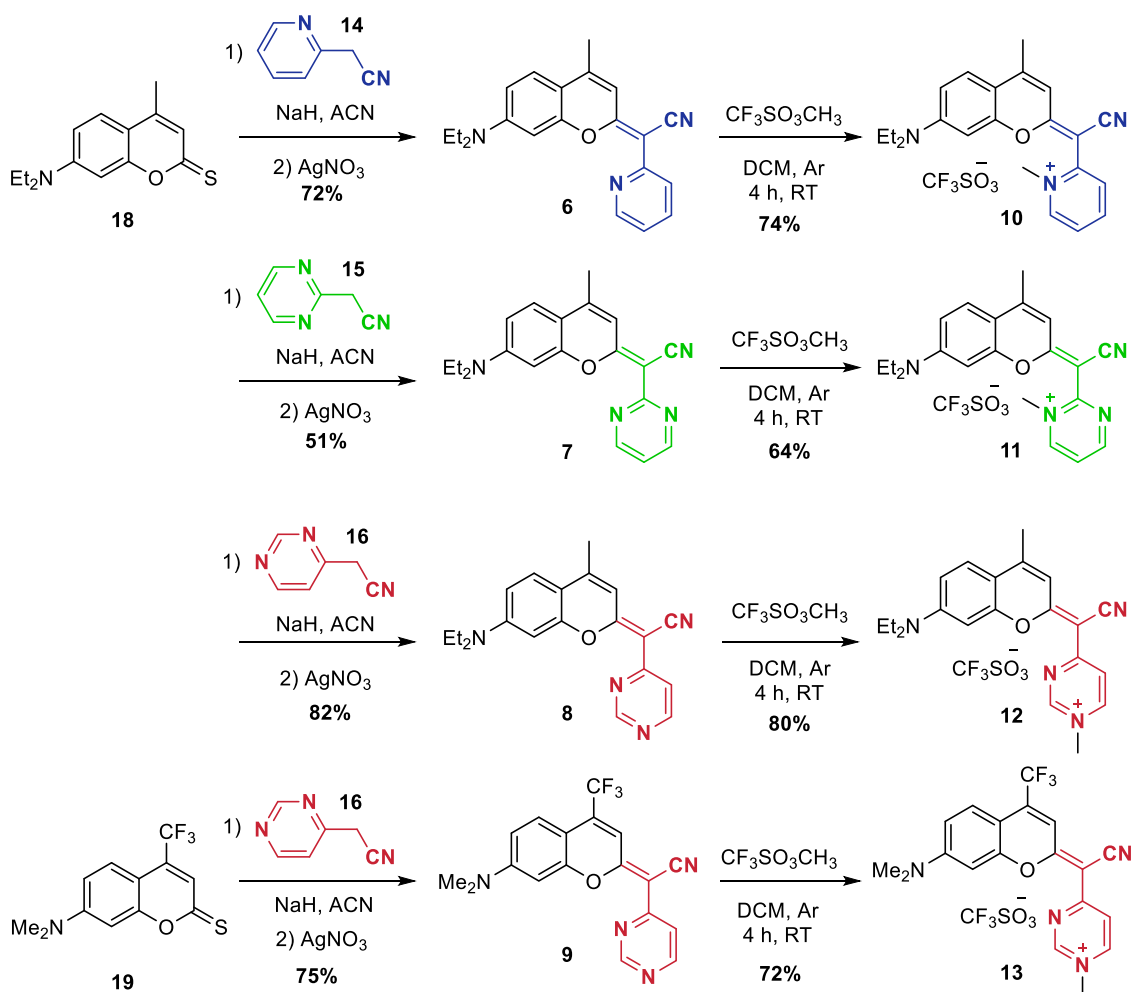
Publicación A: Rovira, A.; Pujals, M.; Gandioso, A.; López-Corrales, M.; Bosch, M.; Marchán, V. Modulating photostability and mitochondria selectivity in far-red/NIR emitting coumarin fluorophores through replacement of pyridinium by pyrimidinium. *J. Org. Chem.* **2020**, *85*, 6086-6097.

Nota: En el resumen se ha mantenido la numeración de los compuestos del artículo para facilitar su búsqueda.

Tal y como se ha indicado anteriormente, en este trabajo, nos centramos en investigar cómo la modificación del anillo de piridina en los fluoróforos COUPY influye tanto en sus propiedades fotofísicas como en su acumulación subcelular. Para ello, más concretamente, se sintetizaron 4 nuevos análogos en los que se reemplazaron el grupo *p*-metilpiridinio por diferentes heterociclos alquilados.

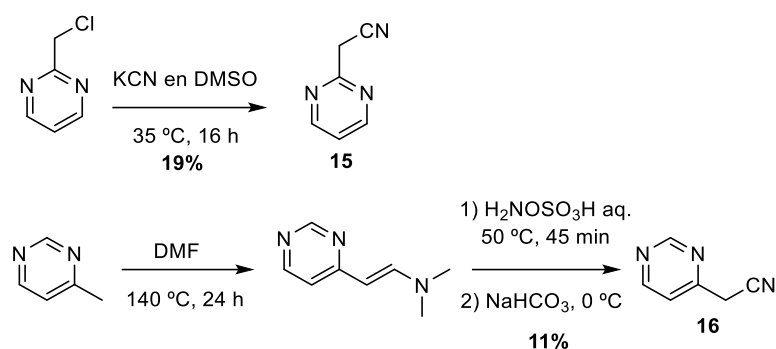
Diseño, síntesis y caracterización de los nuevos fluoróforos COUPY

Los fluoróforos COUPY **10-13** se sintetizaron siguiendo la metodología previamente descrita por nuestro grupo de investigación para la síntesis de este tipo de compuestos,¹⁵ la cual se basa en la condensación de un precursor de tiocumarina (**18** y **19** en este caso) con derivados de heteroarilacetonitrilo adecuados (**14-16**), seguido de la *N*-metilación de los anillos de piridina o pirimidina (**Esquema 4**).



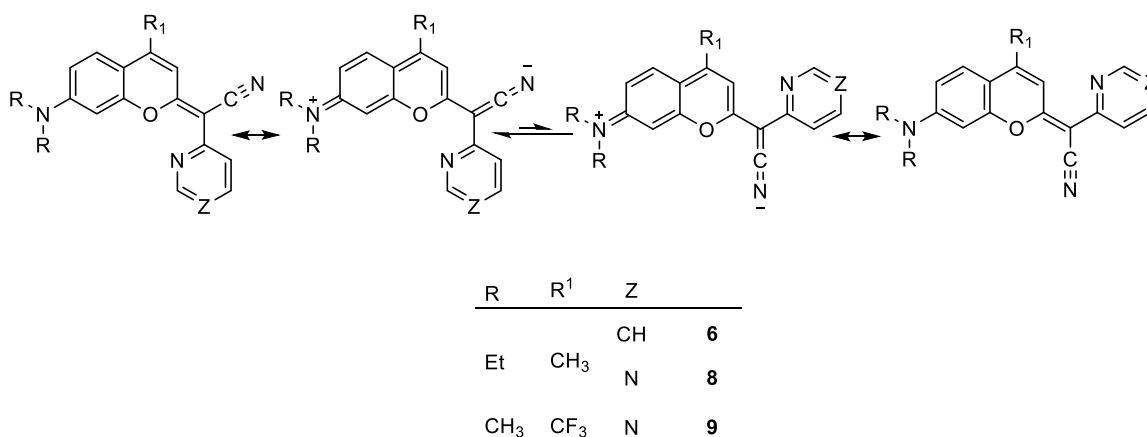
Esquema 4. Ruta sintética seguida para la preparación de los fluoróforos COUPY **10-13**.

En primer lugar, se sintetizaron los derivados de tiocumarina **18** y **19** mediante la reacción de las cumarinas comerciales que incorporan el grupo lactona con el reactivo de Lawesson. Seguidamente, se prepararon los derivados de pirimidina-acetonitrilo necesarios (**15-16**), tal y como se muestra en el **Esquema 5**, para su posterior condensación con la correspondiente tiocumarina. Así, la tiocumarina **18** se hizo reaccionar tanto con el derivado de piridina-acetonitrilo **14** como con los dos derivados de pirimidina-acetonitrilo **15** y **16** en presencia de hidruro de sodio seguido de un tratamiento con nitrato de plata, lo que condujo a la obtención de las cumarinas COUPY neutras **6-8** con unos rendimientos entre moderados y buenos (51-82%) tras purificación por cromatografía en columna. De una forma análoga, la cumarina **9** se obtuvo por condensación del derivado de pirimidina-acetonitrilo **16** con la tiocumarina **19**, con un rendimiento del 72%. Todos los compuestos se caracterizaron por espectrometría de masas de alta resolución en modo electrospray (HR ESI-MS) y por resonancia magnética nuclear (RMN) de ¹H, ¹⁹F y ¹³C.



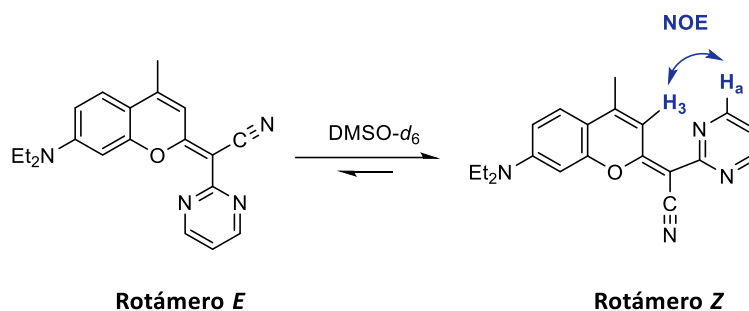
Esquema 5. Ruta sintética seguida para la preparación de los derivados pirimidina-acetonitrilo **15** y **16**.

Vale la pena mencionar que los experimentos NOESY ^1H - ^1H revelaron la presencia de dos especies en equilibrio en solución para algunos derivados COUPY como consecuencia de la rotación alrededor del doble enlace C=C exocíclico. Este mismo fenómeno se había observado previamente en los fluoróforos COUPY originales, y se atribuye a que el doble enlace exocíclico que une el esqueleto de la cumarina con los fragmentos heteroarilacetonitrilo presenta un cierto carácter de enlace sencillo fruto de la fuerte deslocalización electrónica, permitiendo así la rotación entorno a él y, por tanto, la aparición de los dos rotámeros *E* y *Z* (**Esquema 6**).



Esquema 6. Rotámetros *E* y *Z* de los precursores COUPY **6**, **8** y **9**.

Tal y como se muestra en las Figuras 1, S2, S4-S5 de la publicación A, los picos de correlación NOE permitieron determinar que en el caso de las cumarinas **6**, **8** y **9**, los dos rotámeros estaban presentes en una relación 60:40, siendo la especie mayoritaria el rotámero *E*. Caber decir que en el caso de los derivados COUPY que contienen piridina, el rotámero *E* también es la especie mayoritaria, pero en mayor proporción con respecto al rotámero *Z* (90:10). Sorprendentemente, para la cumarina **7** (**Esquema 7**), que contiene el heterociclo *orto,orto*-pirimidina, el rotámero *Z* fue la especie mayoritaria en solución siendo la relación *Z/E* 95:5 (véase Figura S3 en el artículo).



Esquema 7. Estructura de los rotámeros *E* y *Z* de la cumarina **7**. En el caso del rotámero *Z* se muestra la interacción NOE que permitió confirmar su estructura.

Una vez sintetizados y caracterizados los precursores **6-9**, se procedió a la síntesis de los fluoróforos *N*-metilados (**10-13**) mediante reacción con trifluorometansulfonato de metilo en DCM a temperatura ambiente durante 4 horas. Tal y como se esperaba, la metilación se produjo en el nitrógeno menos impedido estéricamente en los derivados de *orto,para*-pirimidina (**12** y **13**), tal y como se confirmó por RMN mediante la utilización de experimentos NOESY, y en todos los casos el rotámero *E* fue la principal especie en solución. Los cuatro nuevos derivados de cumarina fueron purificados por cromatografía en columna y se obtuvieron en forma sólidos de color naranja-rojizo (**10** y **11**), púrpura (**12**) y azul oscuro (**13**), con unos rendimientos entre el 64–80%.

Caracterización fotofísica de los fluoróforos COUPY

Una vez sintetizados los nuevos fluoróforos COUPY (**10-13**), se estudió como influía el hecho de reemplazar el fragmento de *para*-piridina en los fluoróforos originales (**4** y **5**) por los fragmentos *orto*-piridina, *orto,orto*-pirimidina y *orto,para*-pirimidina en las propiedades espectroscópicas y fotofísicas. Para ello, se registraron los espectros de absorción y emisión en 4 disolventes de diferente polaridad (PBS, EtOH, ACN y DCM). Tal y como se muestra en la **Figura 4** y en la **Tabla 1**, las propiedades fotofísicas de los nuevos fluoróforos COUPY **10-13** se compararon con las de los análogos sintetizados anteriormente en el grupo (**4** y **5**).

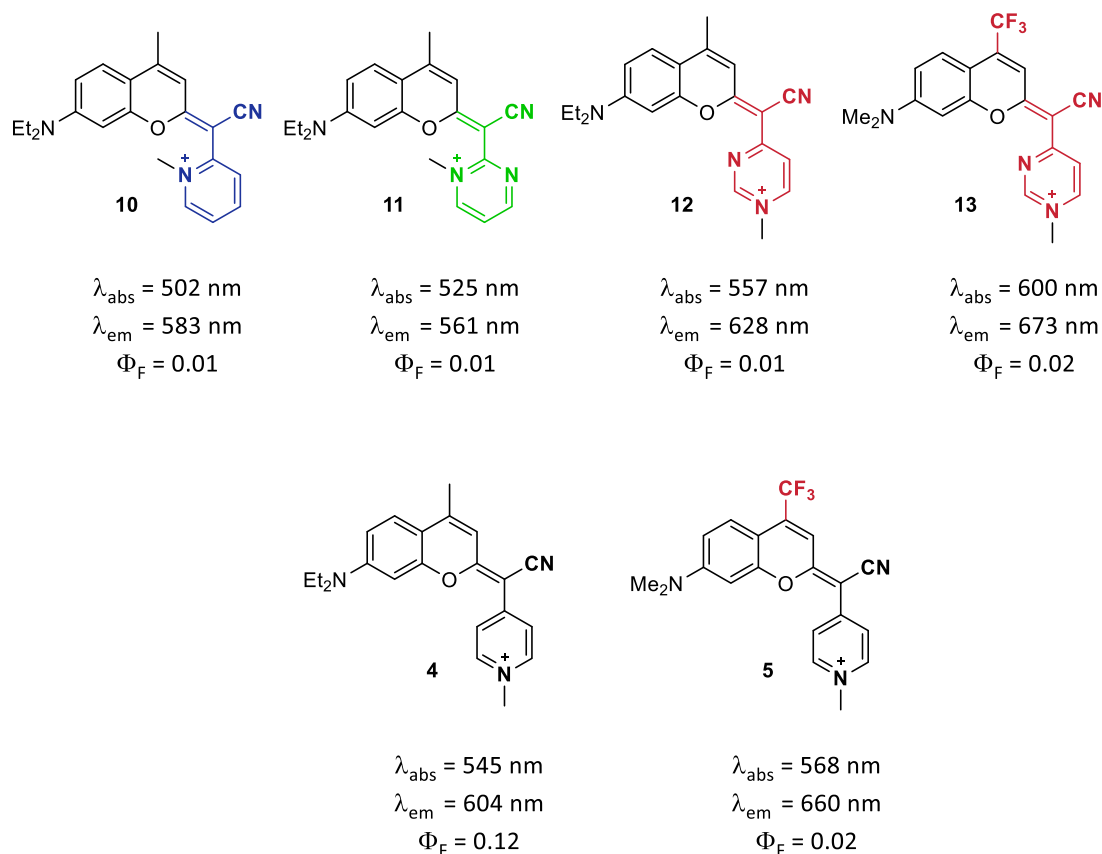


Figura 4. Estructura de los nuevos fluoróforos COUPY (**10-13**) y de los compuestos de referencia (**4-5**). Se indican los máximos de absorción y emisión y el rendimiento cuántico de fluorescencia en PBS.

Los resultados obtenidos en los estudios de caracterización espectroscópica y fotofísica de los nuevos fluoróforos (**10-13**) y de los fluoróforos de referencia (**4-5**) se resumen en la **Tabla 1**. Todos los nuevos derivados COUPY presentan una intensa banda de absorción en la región visible del espectro electromagnético. Ahora bien, sorprendentemente, los máximos de absorción de las cumarinas *orto*-piridina **10** y *orto,orto*-pirimidina **11** se desplazaron hacia el azul con respecto a la cumarina original **4** (por ejemplo, $\lambda_{\text{abs}} = 505 \text{ nm}$ para **10**, $\lambda_{\text{abs}} = 526 \text{ nm}$ para **11** y $\lambda_{\text{abs}} = 548 \text{ nm}$ para **4** en ACN). Por el contrario, se encontró un ligero desplazamiento hacia el rojo en el máximo de absorción de la cumarina *orto,para*-pirimidina **12** en comparación con la cumarina de referencia **4** (12 nm en PBS). Dicho desplazamiento hacia el rojo fue considerablemente mayor en el análogo 4-CF₃ (**13**), en comparación con el compuesto de referencia **5** (32 nm de diferencia en PBS). Tal y como se había observado previamente en los fluoróforos COUPY originales, los compuestos **10-13** también mostraron un solvatocromismo negativo ya que los máximos de absorción se desplazaron hacia el azul al aumentar la polaridad del disolvente.

Los máximos de emisión de las cumarinas **10** y **11** también se desplazaron hacia el azul en comparación con la cumarina de referencia **4** en todos los disolventes evaluados (por ejemplo, $\lambda_{em} = 589$ nm para **10**, $\lambda_{em} = 575$ nm para **11** y $\lambda_{em} = 609$ nm para **4** en ACN). Por el contrario, en el caso de los derivados de cumarina que contienen el fragmento *orto,para*-pirimidina **12** y **13**, los máximos de emisión se desplazaron hacia el rojo en comparación con las cumarinas de referencia **4** y **5**, respectivamente. En consecuencia, se encontró que los nuevos fluoróforos COUPY **12** y **13** mostraban emisión en la región del rojo lejano y el infrarrojo cercano, con máximos de emisión atractivos en medios polares, sobre todo para el derivado de cumarina que contiene el grupo 4-CF₃ ($\lambda_{em} = 673$ nm para **13** en PBS).

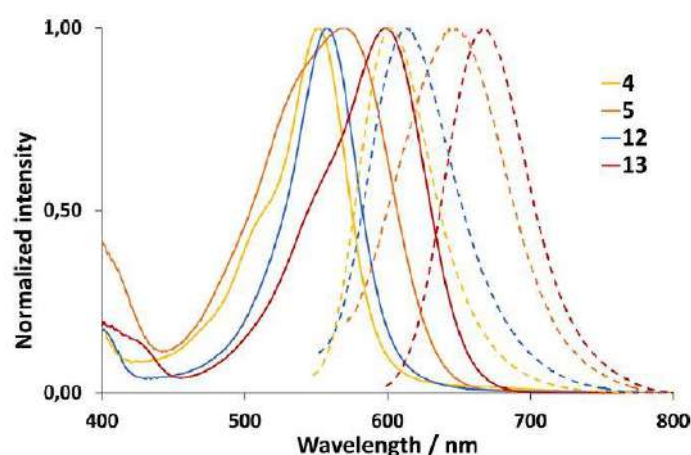


Figura 5. Comparación de los espectros normalizados de absorción (líneas continuas) y de fluorescencia (líneas discontinuas) de los fluoróforos COUPY (compuestos **4**, **5**, **12** y **13**) en EtOH. Adaptado con el permiso de la referencia [16].

Tal y como se muestra en la **Tabla 1**, los compuestos **10** y **11** presentaron una emisión de fluorescencia bajo en todos los disolventes investigados. Por el contrario, los rendimientos cuánticos de fluorescencia para la cumarina **13** fueron mucho más altos que los del compuesto original **5**, especialmente en disolventes menos polares (por ejemplo, 0.41 y 0.05 en DCM, respectivamente). Por otro lado, el rendimiento cuántico de fluorescencia para el compuesto **12**, que también contiene el fragmento *orto,para*-pirimidina, fue inferior al del compuesto de referencia **4** en disolventes apolares (por ejemplo, 0.11 y 0.70 en DCM, respectivamente). En cambio, en disolventes polares próticos ambos compuestos que contienen el fragmento *orto,para*-pirimidina exhibieron unos rendimientos cuánticos de fluorescencia moderados ($\Phi_F = 0.13$ para **12** y $\Phi_F = 0.08$ para **13** en EtOH).

Tabla 1. Propiedades fotofísicas de los compuestos **4**, **5** y **10-13** en diferentes disolventes.

Compuesto	Disolvente	λ_{\max} (nm)	λ_{em} (nm)	Desplazamientos de Stokes (nm)	Φ_{F}
4	PBS	545	604	59	0.12
	ACN	548	609	61	0.18
	DCM	569	607	38	0.70
10	PBS	502	583	81	0.01
	ACN	505	589	84	0.02
	DCM	543	594	51	0.20
11	PBS	525	561	36	0.01
	ACN	526	575	49	0.02
	DCM	551	565	14	0.02
12	PBS	557	628	71	0.01
	ACN	557	621	64	0.10
	DCM	575	618	43	0.11
5	PBS	568	660	92	0.02
	ACN	569	668	99	0.02
	DCM	600	657	57	0.05
13	PBS	600	673	73	0.02
	ACN	597	674	77	0.10
	DCM	624	663	39	0.41

Finalmente, se estudió la fotoestabilidad de las cumarinas COUPY más prometedoras (**12** y **13**) en tampón PBS bajo irradiación en luz verde, y se comparó con la de las cumarinas de referencia (**4** y **5**). Tal y como se muestra en la **Figura 6**, la sustitución de la piridina en la cumarina **4** por *orto,para*-pirimidina tuvo un efecto bastante positivo en la fotoestabilidad del fluoróforo resultante (**12**). Por el contrario, se encontró que la cumarina **13** era menos fotoestable que el compuesto de referencia **5** y la cumarina **12**, lo que indica que la sustitución del grupo CH₃ en la posición 4 por CF₃ en los fluoróforos COUPY que contienen *orto,para*-pirimidina no conduce a una mejora sustancial en la fotoestabilidad de los compuestos. Sin embargo, vale la pena señalar que los dos nuevos fluoróforos COUPY que contienen el fragmento *orto,para*-pirimidina (**12** y **13**), son fotoestables a la intensidad de la luz que se utiliza habitualmente en experimentos de bioimagen en células vivas.

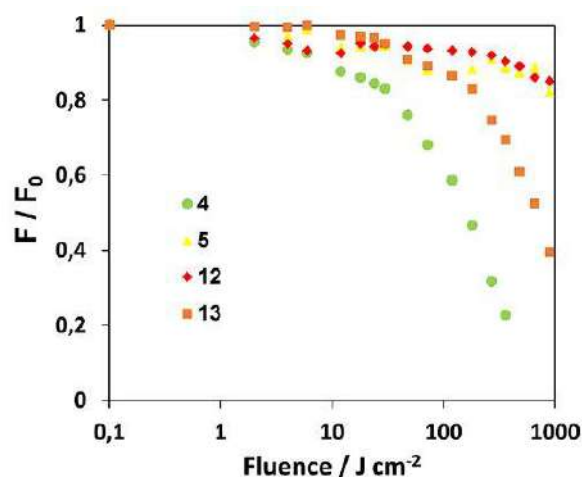


Figura 6. Comparación de la fotoestabilidad de los fluoróforos COUPY **4**, **5**, **12** y **13** en una solución tampón de PBS pH 7.4 (5 μ M) tras irradiación con luz verde (505 nm, 100 mW/cm²). Adaptado con el permiso de la referencia [16].

Estudios de internalización celular de los fluoróforos COUPY por microscopía confocal

Una vez determinadas las propiedades fotofísicas y la fotoestabilidad de las dos fluoróforos COUPY que contienen el fragmento *orto,para*-pirimidina (**12** y **13**), se evaluó su internalización en células HeLa mediante microscopía confocal a una concentración 2 μ M y tras 30 min de incubación, comparándose con la de los compuestos de referencia **4** y **5**. La irradiación se realizó con un láser de luz amarilla ($\lambda_{\text{ex}} = 561$ nm) en el caso de las cumarinas 4-CH₃ (**4** y **12**), mientras que el mayor desplazamiento hacia el rojo del máximo de absorción de las cumarinas 4-CF₃ (**5** y **13**) permitió el uso de un láser de luz roja ($\lambda_{\text{ex}} = 633$ nm). Tal y como se muestra en la **Figura 7**, todos los compuestos internalizaron de forma satisfactoria sin que se observara toxicidad alguna durante el transcurso de los experimentos.

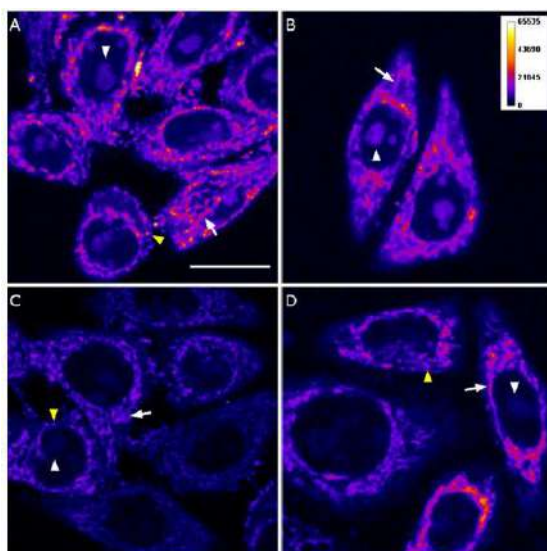


Figura 7. Internalización celular de los fluoróforos COUPY (A) **4**, (B) **5**, (C) **12**, y (D) **13**. Planos confocales de células HeLa incubadas con los compuestos (2 μ M, 30 min, 37 °C). Las flechas blancas señalan mitocondrias, las puntas de flecha blancas señalan nucléolos y las puntas de flecha amarilla señalan vesículas. Adaptado con el permiso de la referencia [16].

En general, el patrón general de marcaje, sin tener en cuenta las diferencias de intensidad de fluorescencia entre los diferentes orgánulos, de las cumarinas con el fragmento de pirimidina (**12** y **13**) es similar al de los fluoróforos de referencia que contienen piridina (**4** y **5**), acumulando en mitocondria, nucléolo y, en menor medida, en vesículas intracelulares, en su mayoría lisosomas. Posteriores experimentos de colocalización con dos marcadores específicos de mitocondria (MitoTracker Green FM, MTG) y lisosomas (LysoTracker Green FM, LTG) confirmaron la localización subcelular de los compuestos (**Figura 8**).

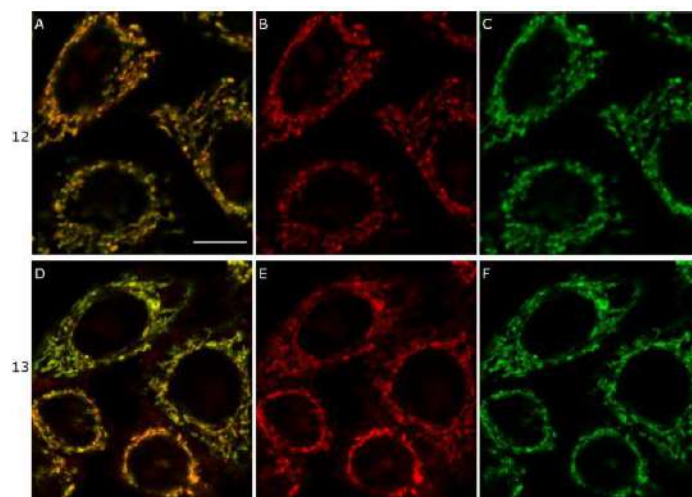


Figura 8. Estudios de colocalización de los compuestos COUPY **12** (arriba) y **13** (abajo) con MitoTracker Green FM. (A,D) Superposición de la señal de los dos compuestos (MTG y COUPY). (B, E) Señal de las cumarinas **12** y **13**, respectivamente. (C,F) Señal del MitoTracker Green FM. Adaptado con el permiso de la referencia [16].

Los coeficientes de Pearson y Manders (M1 y M2) se utilizaron para medir el grado de colocalización. Por un lado, los coeficientes de Pearson fueron 0.86 para **12** y 0.87 para **13**, confirmándose así una correlación clara entre la señal de cumarina y la del MTG (el rango del coeficiente de Pearson va desde -1 a +1, siendo +1 el indicador de una superposición perfecta). Dichos coeficientes fueron superiores a los obtenidos con las cumarinas de referencia (0.65 para **4** y 0.73 para **5**), indicando así una mejor correlación entre la señal de las cumarinas que incorporan el fragmento pirimidinio y la de MTG.

Por otro lado, los coeficientes de Manders (que van de 0 a 1, determinando la intensidad de un canal colocalizando con el otro) también confirmaron que los compuestos **12** y **13** colocalizaban principalmente en las mitocondrias. El grado de colocalización de **12** sobre MTG fue $M1 = 0.40$, mientras que el análisis de la colocalización de la señal de MTG sobre la de la cumarina **12** condujo a un valor de $M2 = 0.73$. Estos valores indican que hay más señal de MTG colocalizando con **12** que señal de **12** colocalizando con MTG. Para la cumarina de referencia **4** se obtuvieron valores ligeramente inferiores ($M1 = 0.28$ y $M2 = 0.68$). Aunque no tan pronunciado como en el caso de **12**, se obtuvieron resultados similares al comparar la cumarina **13** ($M1 = 0.19$ y $M2 = 0.86$) con el compuesto **5** ($M1 = 0.18$ and $M2 = 0.76$), lo que sugiere que las cumarinas con el fragmento *orto,para*-pirimidina (**12** y **13**) presentan una mayor preferencia por las mitocondrias que las cumarinas con el fragmento piridina (**4** y **5**).

Los experimentos de colocalización con LTG confirmaron que la mayor parte de la señal de fluorescencia observada en vesículas intracelulares estaba asociada con la acumulación en lisosomas (siendo el coeficiente de Pearson 0.52 para **12** y 0.49 para **13**). Por otro lado, se obtuvieron valores muy pequeños para los coeficientes de Manders para la colocalización de los compuestos sobre el LTG ($M_1 = 0.02$ para **12** y **13**) y de LTG sobre la señal de cumarina ($M_2 = 0.45$ para **12** y 0.62 para **13**), lo cual se podría atribuir a la menor abundancia de este orgánulo en las células en comparación con las mitocondrias.

Tal y como se muestra en la **Figura 9**, el hecho que el nucléolo se marcara de forma mucho menos intensa en el caso de las cumarinas **12** y **13**, confirmó que la sustitución del fragmento *para*-piridina por *orto,para*-pirimidina en los fluoróforos COUPY conduce a un aumento de la selectividad hacia mitocondria.

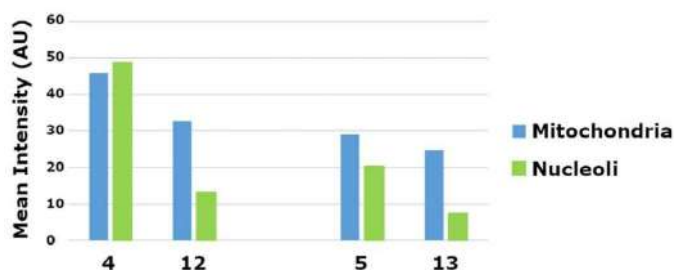


Figura 9. Medición de la intensidad de fluorescencia promedio en mitocondria y nucléolo para los fluoróforos COUPY **4**, **5**, **12** y **13**. Adaptado con el permiso de la referencia [16].

Finalmente, se estudió la fotoestabilidad de los fluoróforos COUPY **12** y **13** en células HeLa comparándose con la de las cumarinas originales **4** y **5**, mediante irradiación continua con el láser de 561 nm del microscopio confocal (**12** y **4**) o con el de 633 nm (**13** y **5**). Tal y como ya se había observado anteriormente en los estudios de fotoestabilidad con el LED de luz verde, la cumarina **12** presentó una mayor fotoestabilidad que su análogo **4**, mientras que la cumarina **13** se mostró algo menos fotoestable que la cumarina **5** (**Figura 10**). Sin embargo, cabe destacar que la intensidad del led utilizado en los experimentos de fotoestabilidad es mucho mayor que la que se utiliza habitualmente en experimentos de bioimagen con células vivas, confirmándose así una buena fotoestabilidad para los fluoróforos COUPY.

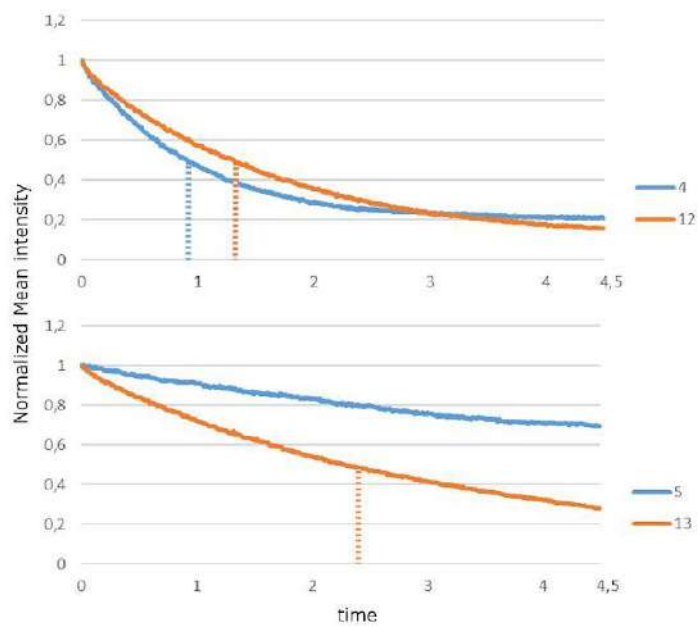


Figura 10. Fotoestabilidad de los fluoróforos COUPY **4**, **5**, **12** y **13** en células HeLa. Adaptado con el permiso de la referencia [16].

Capítulo Ib

Publicación B: Rovira, A.; Gandioso, A.; Goñalons, M.; Galindo, A.; Massaguer, A.; Bosch, M.; Marchán, V. Solid-phase approaches for labeling targeting peptides with far-red emitting coumarin fluorophores. *J. Org. Chem.* **2019**, *84*, 1808–1817.

Nota: En el resumen se ha mantenido la numeración de los compuestos del artículo para facilitar su búsqueda.

Gracias a su tamaño pequeño y a una fácil accesibilidad sintética, los fluoróforos COUPY son unos buenos candidatos para el marcaje de biomoléculas como, por ejemplo, péptidos. En este trabajo, se abordó la conjugación de una cumarina COUPY, con emisión en el rojo lejano, al péptido octreotide siguiendo tres estrategias de síntesis en fase sólida basadas en la formación de un enlace amida entre el péptido y el derivado de cumarina o bien en reacciones de cicloadición azida-alquino catalizadas por Cu(I), éstas últimas también conocidas como química click o CuAAC (por sus siglas en inglés). Como compuestos de referencia, también se sintetizaron dos conjugados que incorporasen como fluoróforo (i) la carboxifluoresceína, un fluoróforo comercial que se utiliza habitualmente para marcar péptidos y que es excitado con luz verde, o (ii) ATTO-Rho123, un derivado de rodamina comercial que se puede excitar con el mismo láser de luz amarilla que el fluoróforo COUPY.

A continuación, se estudiaron las propiedades fotofísicas de las cumarinas COUPY utilizadas y de los correspondientes conjugados con el péptido octreotide. Y, finalmente, se realizaron estudios de internalización del conjugado COUPY-octreotide en células HeLa mediante microscopia confocal comparándose con los resultados obtenidos con los dos conjugados de referencia (carboxifluoresceína-octreotide y ATTO-Rho123-octreotide).

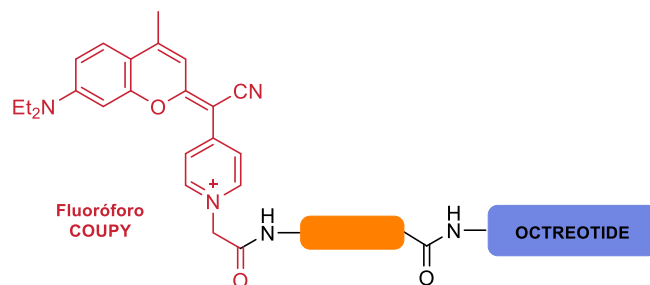


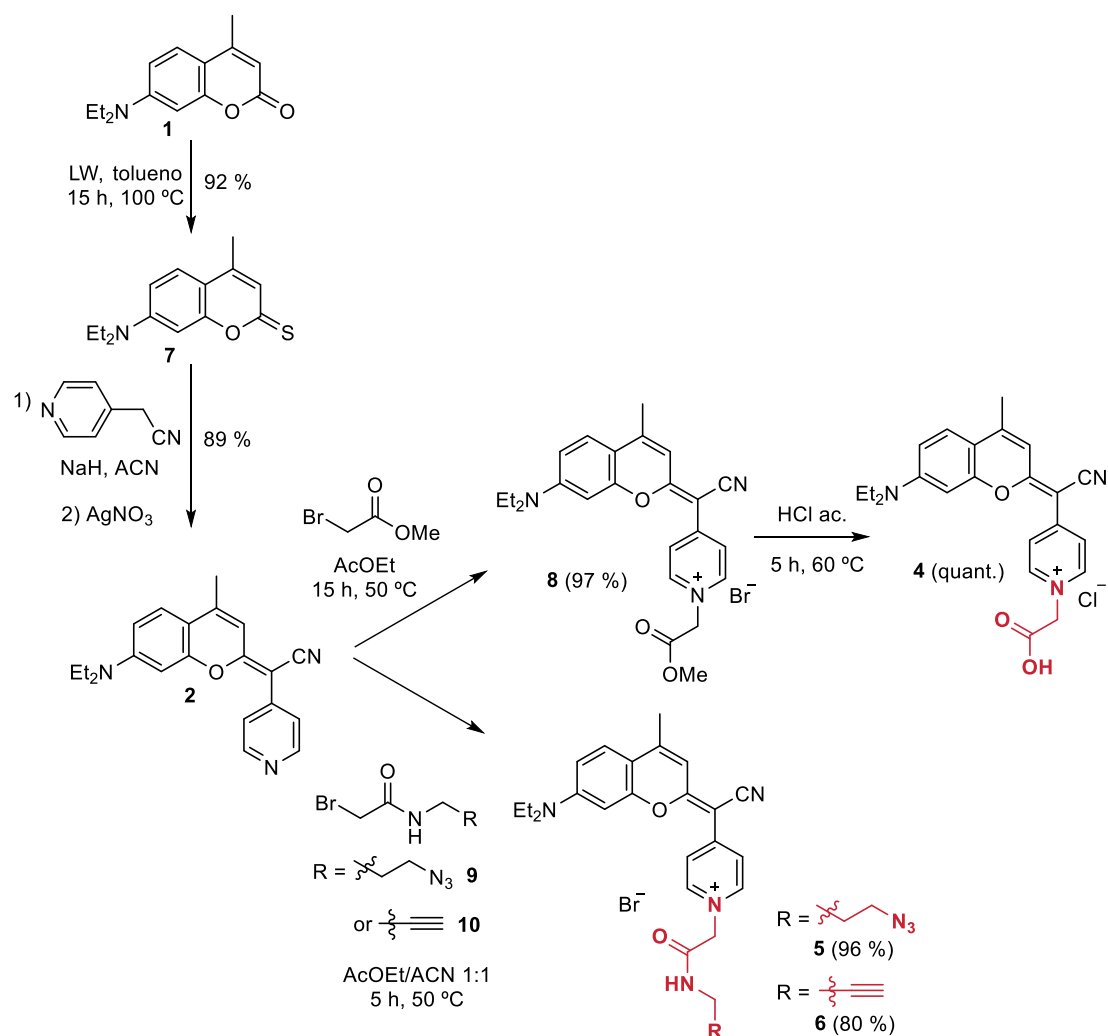
Figura 11. Esquema de la estructura del conjugado entre el fluoróforo COUPY y el péptido octreotide.

Síntesis y caracterización de los derivados COUPY conjugables

Tal y como se muestra en el **Esquema 8**, los derivados conjugables **4-6** se sintetizaron mediante alquilación del nitrógeno del anillo de piridina de la cumarina **2**, la cual se sintetizó siguiendo el procedimiento descrito anteriormente. Para ello, en primer lugar, se preparó la tiocumarina **7** por reacción de **1** con el reactivo de Lawesson. Seguidamente, la cumarina **2** se obtuvo mediante condensación de **7** con el fragmento 4-piridilacetónitrilo.

Por un lado, la cumarina **2** se alquiló con bromoacetato de metilo en AcOEt a 60 °C durante 4 h lo que condujo al intermedio **8** con un 97 % de rendimiento. Posteriormente, el grupo éster se hidrolizó con HCl acuoso a 60 °C durante 5 horas, obteniéndose la cumarina **4** con el ácido carboxílico libre que habría de permitir su unión al péptido a través de la formación de un enlace amida.

Por otro lado, los fluoróforos COUPY que contienen los grupos azida (**5**) o alquínilo (**6**) necesarios para llevar a cabo la reacción de CuAAC con el péptido que incorporase los grupos funcionales complementarios (alquínilo o azida, respectivamente), se sintetizaron por reacción de la cumarina **2** con un derivado de N-alquilbromoacetamida que contenía el grupo funcional adecuado (**9** o **10**, respectivamente) durante 5 h a 50 °C en una mezcla de AcOEt y ACN 1:1. Las cumarinas **5** y **6** se obtuvieron en forma de sólido de color azul oscuro tras purificación por cromatografía en columna y fueron caracterizados por HR ESI-MS y RMN de ^1H y ^{13}C .



Esquema 8. Síntesis de los fluoróforos COUPY conjugables (**4-6**).

De forma similar a lo observado con cumarinas COUPY sintetizadas anteriormente en el grupo, los espectros de NOESY (Figuras S2-S4 de la publicación B) revelaron que la especie mayoritaria en solución en todos los nuevos derivados de cumarina conjugables (**4-6**) era el rotámero *E* (**Figura 12**).

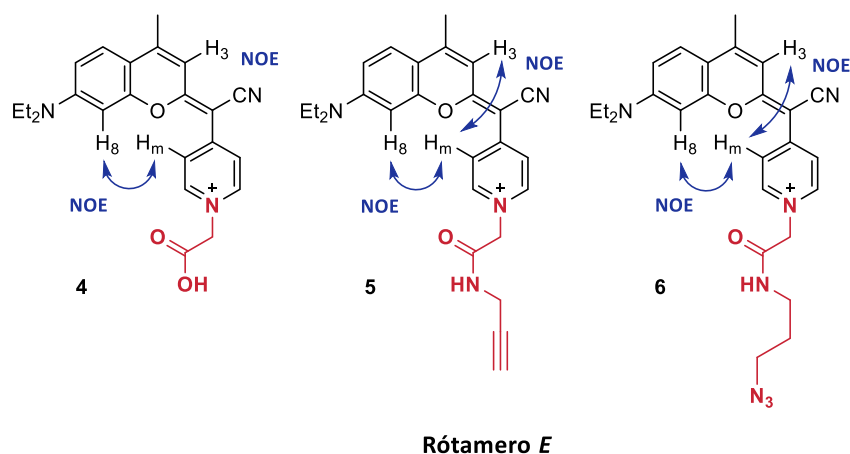


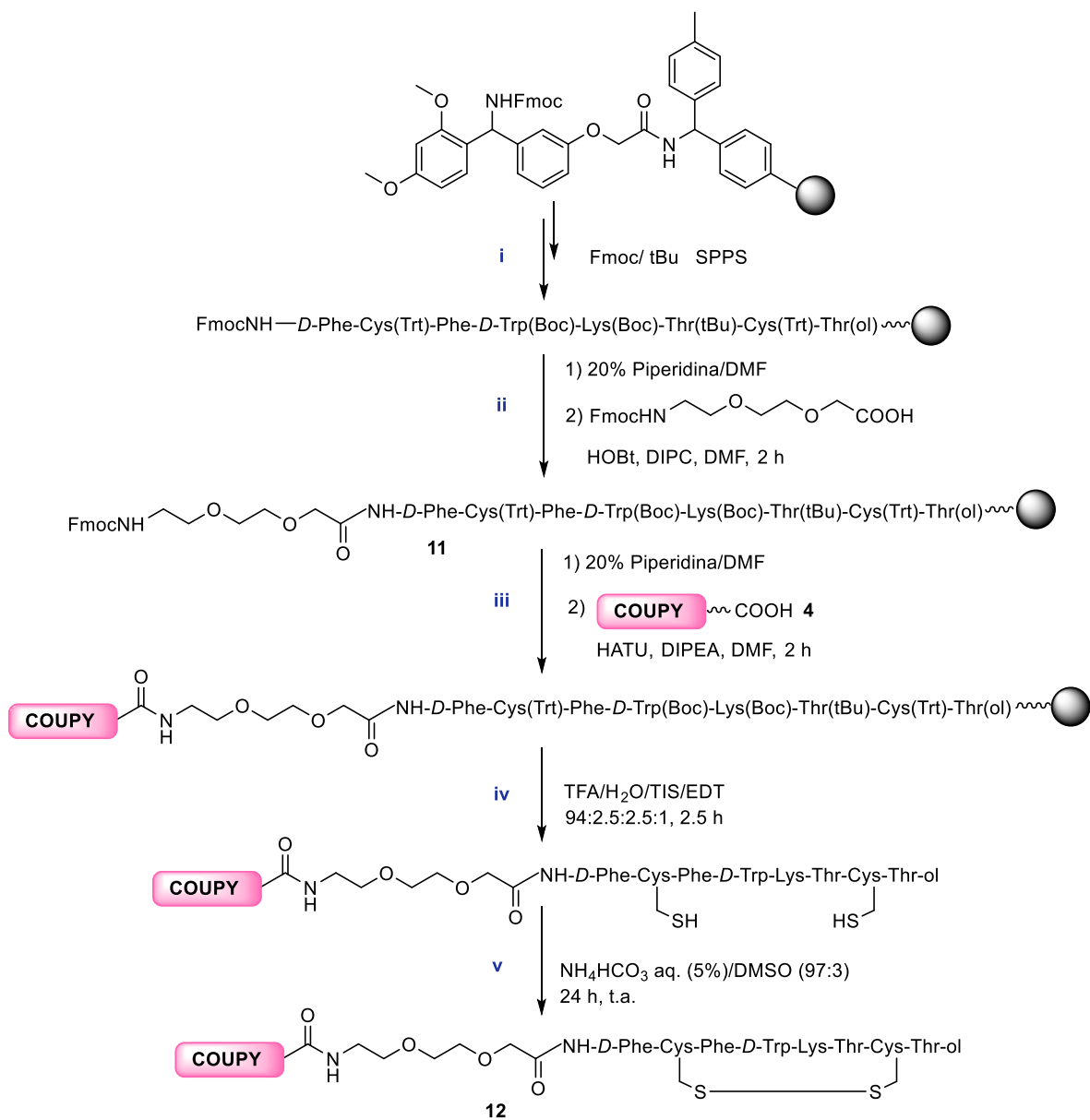
Figura 12. Estructura de los rotámeros *E* para las cumarinas **4-6** sobre las que se muestran algunas correlaciones NOE características.

Síntesis y caracterización de los conjugados COUPY-octreotide

La síntesis del péptido se llevó a cabo en fase sólida sobre una resina Rink amida siguiendo la estrategia Fmoc/tBu (**Esquema 9**). En primer lugar, se elongó la cadena peptídica con Fmoc-aminoácidos adecuadamente protegidos y utilizando como agentes acoplantes DIPC y HOAt en DMF anhidra (**Esquema 9**, i). Una vez ensamblada la cadena peptídica lineal, se acopló de forma similar un espaciador de polietilenglicol protegido también con el grupo Fmoc, obteniéndose la peptidil-resina **11** (**Esquema 9**, ii).

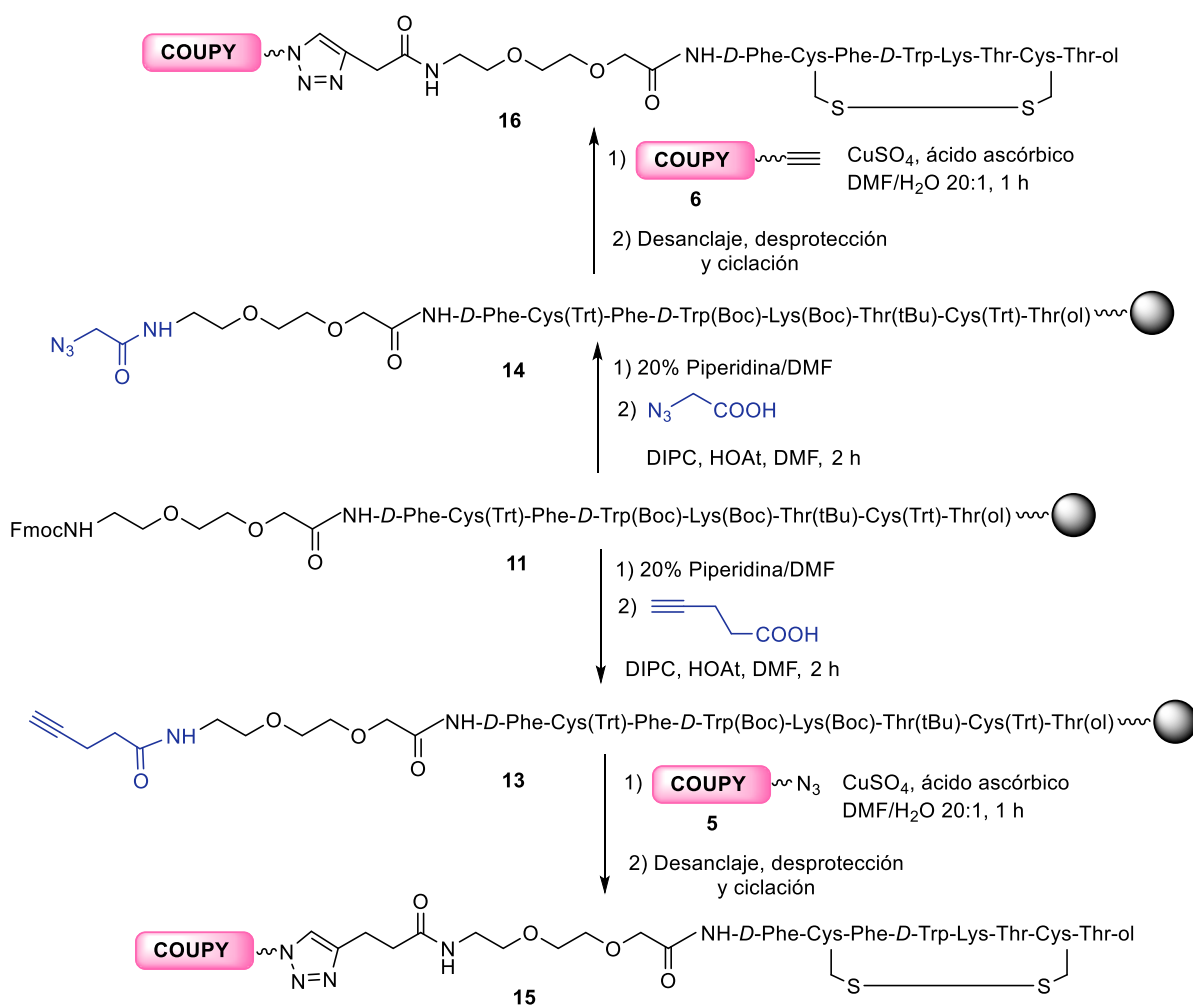
Seguidamente, tras la desprotección del grupo Fmoc del espaciador con 20 % de piperidina en DMF, se acopló la cumarina **4** utilizando HATU como agente acoplante y DIPEA en DMF anhidra, dejándose reaccionar durante 2 h y protegido de la luz (**Esquema 9**, iii). La desprotección y el desanclaje de la resina del conjugado COUPY-octreotide se realizó de forma simultánea mediante tratamiento con TFA en presencia de capturadores de carbocationes adecuados (TFA/H₂O/EDT/TIS 94:2.5:2.5:1), durante 2.5 h a temperatura ambiente y protegido de la luz (**Esquema 9**, iv). La mayor parte del TFA fue eliminado burbujeando la solución con N₂, y el residuo resultante se precipitó en éter frío. El producto se aisló mediante centrifugación, se disolvió en H₂O/ACN 9:1, y se liofilizó.

Finalmente, se procedió a la ciclación del péptido mediante la formación de un enlace disulfuro intramolecular entre los dos residuos de Cys, en una mezcla 97:3 (v/v) de una solución tampón de hidrogenocarbonato de amonio (5 %) a pH=7-8 y DMSO durante 24 horas a temperatura ambiente (**Esquema 9**, v). Una vez liofilizada la disolución, el conjugado **12** se purificó por HPLC en fase inversa, obteniéndose en forma de un sólido de color lila tras liofilización con un rendimiento global del 12%. El conjugado COUPY-octreotide fue caracterizado por HR ESI-MS y RMN de ¹H.



Esquema 9. Síntesis en fase sólida del conjugado COUPY-octreotide (**12**) mediante la formación de un enlace amida.

Por otro lado, una vez confirmada la compatibilidad de los fluoróforos COUPY con la síntesis de péptidos en fase sólida, se investigó si era posible marcar el péptido octreotide con los derivados de cumarina que contenían grupos azida (**5**) o alquínilo (**6**) mediante una reacción click catalizada por Cu(I) (**Esquema 10**). Para ello, en primer lugar, se incorporaron los grupos funcionales necesarios en el extremo *N*-terminal del péptido de la peptidil-resina **11** (tras eliminación del grupo Fmoc) mediante el acoplamiento de ácido 4-pentinoico o ácido 2-azidoacético, obteniéndose los péptidos alquínilo (**13**) y azida (**14**) anclados a la resina, respectivamente. Seguidamente, se investigó la **química click** en fase sólida haciendo reaccionar los péptidos protegidos anclados a resina **13** y **14** con la azido-cumarina (**5**) o la alquínil-cumarina (**6**), respectivamente, en presencia de CuSO₄ y ascorbato de sodio en una mezcla DMF/H₂O 20:1 durante 18 h. Tras la etapa de desprotección y desanclaje, el análisis por HPLC-MS reveló en ambos casos la formación del conjugado lineal COUPY-octreotide deseado sin que se detectaran productos secundarios. Finalmente, se llevaron a cabo las etapas de ciclación y purificación siguiendo el mismo procedimiento descrito anteriormente, lo que permitió obtener los conjugados COUPY-octreotide **15** y **16** en forma de sólidos de color rosa con unos rendimientos globales del 32 % (**15**) y del 13 % (**16**).



Esquema 10. Síntesis de los conjugados COUPY-octreotide **15** y **16** mediante CuAAC.

Es de destacar que aunque la mayoría de los procedimientos basados en química click descritos hasta el momento para el marcaje de péptidos requieren tiempos de reacción largos (12 - 48 h) e incluso irradiación de microondas, en nuestro caso obtuvimos una conversión casi cuantitativa tras 1 h de reacción a temperatura ambiente, independientemente de la estrategia click utilizada (COUPY-azida/péptido-alquínilo (conjugado **15**) o COUPY-alquínilo/péptido-azida (conjugado **16**)), tal y como se observó mediante análisis por HPLC-MS. En la **Figura 13** se muestra el seguimiento de la evolución de la reacción click entre la cumarina azida **5** y el péptido-alquínilo **13** a diferentes tiempos de reacción.

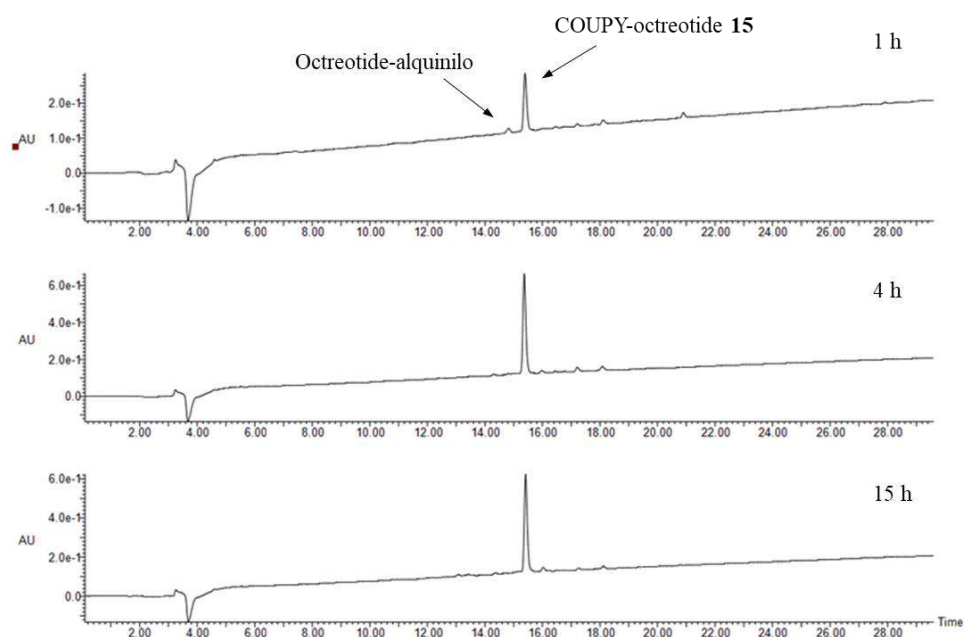


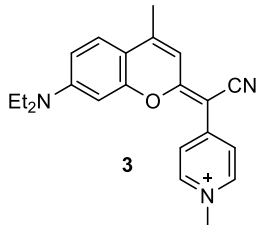
Figura 13. De arriba a abajo: cromatogramas correspondientes al análisis por HPLC-MS de los crudos de reacción entre la cumarina **5** y el peptidil-resina **13** a diferentes tiempos de reacción (1, 4 o 15 h), tras las etapas de desanclaje, desprotección y ciclación. Adaptado con el permiso de la referencia [17].

Caracterización fotofísica de los conjugados COUPY-octreotide

Las propiedades fotofísicas de los tres conjugados COUPY-octreotide (**12**, **15** y **16**) se determinaron en agua y se compararon con las de sus respectivos precursores de cumarina conjugables (**8**, **5** y **6**), así como con las de la cumarina de referencia **3** (Tabla 2). Todos los compuestos mostraron una banda de absorción intensa en la región amarilloraja del espectro del visible. Es de destacar que los máximos de absorción y de emisión para los derivados COUPY **5-6** y **8** están ligeramente desplazados hacia el rojo en comparación con la cumarina **3**, lo cual se atribuye al efecto electroatrayente de los grupos éster y amida incorporados en la estructura. Además, la conjugación al péptido octreotide supuso un mayor desplazamiento hacia el rojo tanto de los máximos de absorción como de los de emisión.

Finalmente, es destacable el hecho que los rendimientos cuánticos de fluorescencia de los nuevos derivados de cumarina (**5-6** y **8**) sean inferiores a los de la cumarina de referencia **3** (por ejemplo, $\Phi_F = 0.061$ para **6** y $\Phi_F = 0.15$ para **3** en H_2O). Sin embargo, se incrementaron de forma significativa una vez conjugados con el péptido (por ejemplo, $\Phi_F = 0.066$ para la cumarina **5** y $\Phi_F = 0.19$ para el conjugado **15** en H_2O).

Tabla 2. Propiedades fotofísicas de los fluoróforos COUPY (**3**, **5**, **6** y **8**) y de los conjugados COUPY-octreotide (**12**, **15-16**) en H₂O.

Compuesto	λ_{max} (nm)	λ_{em} (nm)	Desplazamiento de Stokes (nm)	Φ_{F}
 3	543	605	62	0.15
Cumarina 8	555	615	60	0.043
Cumarina 5	555	615	60	0.066
Cumarina 6	555	615	60	0.061
Conjugado 12	561	618	57	0.17
Conjugado 15	560	618	58	0.19
Conjugado 16	560	618	58	0.19

Estudios de internalización celular de los conjugados COUPY-octreotide mediante microscopia confocal

Finalmente, se estudió la internalización del conjugado COUPY-octreotide **12** por microscopía confocal en células HeLa, ya que sobreexpresan el receptor de somatostatina tipo 2, el cual reconoce selectivamente al péptido octreotide. Para ello, se incubó el conjugado **12** a una concentración 10 μM y se tomaron imágenes tras excitación con un láser de luz amarilla ($\lambda_{\text{ex}} = 561 \text{ nm}$). Tal y como se muestra en la **Figura 14**, se observaron vesículas fluorescentes, mayoritariamente endosomas, en el citoplasma de las células independientemente del tiempo de incubación (30 min o 1 h).

Como referencia, también se incubó en paralelo la cumarina **3**, observándose el típico patrón de los fluoróforos COUPY ya descrito anteriormente: acumulación en mitocondria y nucleolo. Dichas diferencias en el patrón de marcaje entre el conjugado y la cumarina sugirieron que la internalización del conjugado viene determinada únicamente por el péptido y no por el fluoróforo.

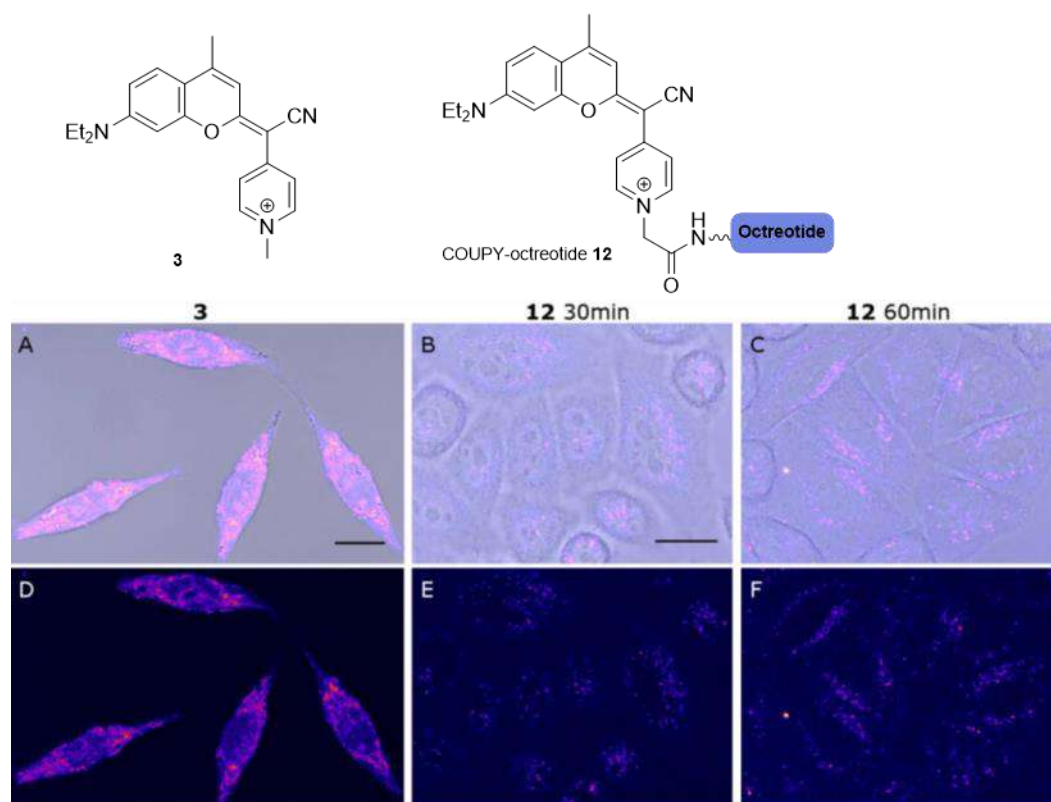


Figura 14. Comparación de la internalización celular de la cumarina de referencia **3** (A y D) y del conjugado COUPY-octreotide **12** a dos tiempos de incubación (B,C,E y F). Adaptado con el permiso de la referencia [17].

Con el objetivo de estudiar más a fondo el mecanismo de internalización del conjugado COUPY-octreotide, se incubaron células HeLa con el conjugado **12** a 4 °C durante 30 min. Tal y como se muestra en la **Figura 15**, en este caso no se observó marcaje en el interior de la célula a diferencia de lo que ocurre a 37 °C, lo cual indica que el conjugado **12** únicamente entra en las células a través de un mecanismo dependiente de energía. En cambio, el patrón de marcaje de la cumarina **3** no cambió a baja temperatura, sugiriendo que internaliza por difusión simple.

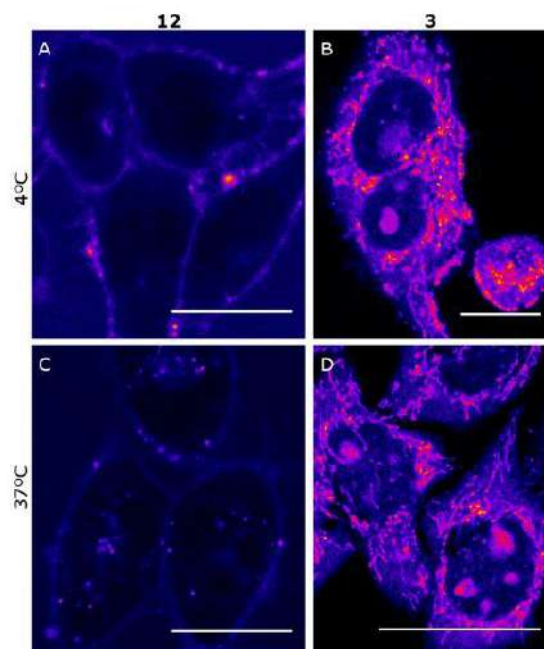


Figura 15. Comparación de la internalización celular del conjugado COUPY-octreotide **12** y del fluoróforo COUPY **3** a 4 °C y a 37 °C. Adaptado con el permiso de la referencia [17].

Para finalizar los estudios en células HeLa, se decidió comparar la eficiencia de visualización de los fluoróforos COUPY conjugados con el péptido octreotide con la de dos fluoróforos comerciales. Por un lado, se seleccionó un derivado de carboxifluoresceína ya que es uno de los fluoróforos más utilizados para marcar péptidos y que se excita a 488 nm. Por otro lado, se escogió un fluoróforo basado en rodamina, Atto-Rho12, que se puede excitar con el mismo láser de luz amarilla utilizado con el fluoróforo COUPY.

Tal y como se muestra en la **Figura 16**, en todos los conjugados se observó el mismo patrón de marcaje: vesículas en el citoplasma de las células. Es de destacar que los resultados obtenidos con el conjugado COUPY-octreotide **12** tras excitación con el láser de 561 nm son comparables a los obtenidos con el conjugado **17** que incorpora el fluoróforo basado en rodamina. Por el contrario, la cumarina conjugada al péptido permitió una mejor visualización que la proporcionada por el conjugado carboxifluoresceína-péptido (**18**), incluso a concentraciones mucho más bajas y, además, permitió una excitación a longitudes de onda más adecuadas (561 nm para **12** y 488 nm para **18**).

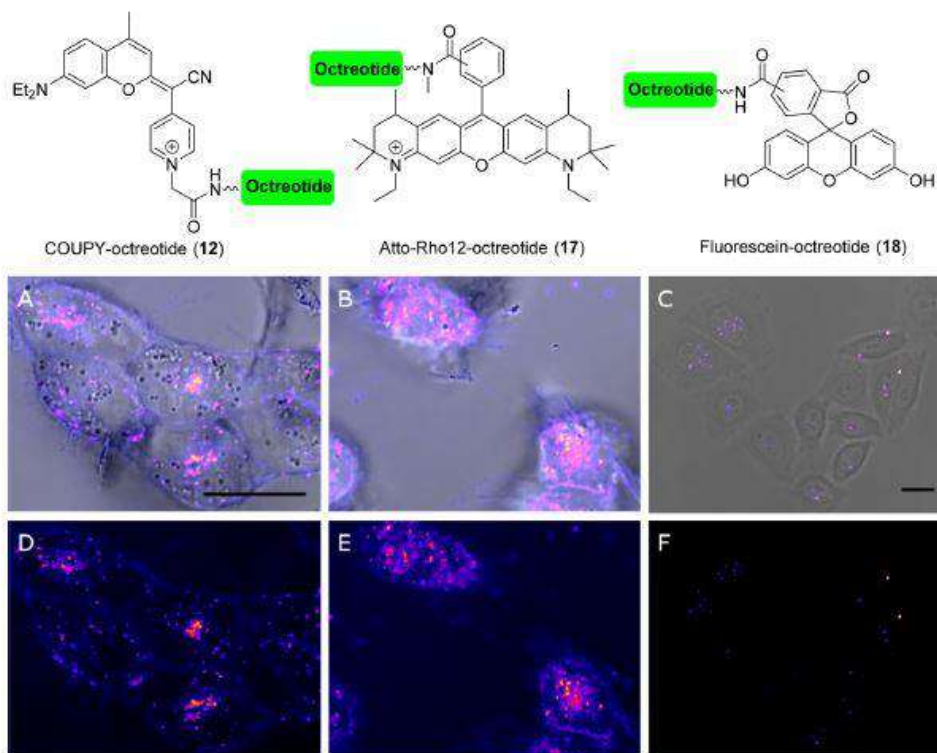


Figura 16. Comparación de la internalización celular de los conjugados del péptido octreotide con los fluoróforos COUPY (**12**), AttoRho12 (**17**) y carboxifluoresceína (**18**). Los conjugados **12** (A,D) y **17** (B,E) se incubaron a 10 μ M, mientras que el **18** (C,F) a 50 μ M durante 30 min a 37 °C. Adaptado con el permiso de la referencia [17].

Conclusiones

Por un lado, se han sintetizado nuevos fluoróforos basados en la familia de cumarinas COUPY desarrollada anteriormente en nuestro grupo de investigación. Concretamente, se ha reemplazado el fragmento *para*-piridinio por diferentes heterociclos (*orto*-piridinio y *orto,orto*- u *orto,para*-pirimidinio), con el objetivo de estudiar cómo se modifican las propiedades fotofísicas y la acumulación celular de los nuevos fluoróforos y así establecer relaciones entre estructura y propiedades fotofísicas. Los nuevos fluoróforos COUPY se sintetizaron a partir de compuestos comerciales en tan sólo tres etapas sintéticas que involucraron la preparación de los derivados de tiocumarina, su condensación con el correspondiente derivado de heteroarilacetonitrilo y, finalmente, la *N*-metilación de los heterociclos piridina o pirimidina.

En general, cabe destacar que las propiedades fotofísicas se vieron claramente influenciadas por dichas modificaciones. Así, la sustitución del grupo *para*-piridinio por *orto*-piridinio u *orto,orto*-pirimidinio en el fluoróforo COUPY tuvo un efecto negativo en las propiedades fotofísicas, ya que tanto los máximos de absorción como de emisión se desplazaron hacia el azul y, además, el rendimiento de emisión de fluorescencia también se redujo. Por el contrario, la incorporación del fragmento *orto,para*-pirimidinio en el esqueleto de cumarina COUPY permitió desplazar los máximos de absorción y de emisión hacia el rojo, sobre todo en disolventes polares.

Además, los estudios de internalización en células HeLa permitieron comprobar que los nuevos fluoróforos COUPY, al igual que los fluoróforos originales, presentaban una excelente permeabilidad celular y también una mayor preferencia por las mitocondrias. De esta manera, la incorporación del fragmento *orto,para*-pirimidinio en el esqueleto de cumarina permite obtener fluoróforos COUPY mucho más específicos de mitocondria.

Por otro lado, se han derivatizado satisfactoriamente los fluoróforos COUPY con grupos funcionales adecuados para su conjugación a péptidos u otras biomoléculas, ya sea mediante la formación de un enlace amida o bien mediante una reacción de cicloadición azida-alquino catalizada por Cu(I). Los derivados conjugables COUPY se sintetizaron en tan sólo 3 o 4 pasos a partir de compuestos comerciales. Además, dichos derivados se mostraron compatibles con la síntesis de péptidos en fase sólida basada en la estrategia Fmoc/tBu, permitiendo así un marcaje fácil y eficiente del péptido octreotide. Con respecto a la química click, es de destacar que se obtuvo una conversión casi cuantitativa a tiempos de reacción muy cortos (por ejemplo, 1 h) a temperatura ambiente utilizando CuSO₄ y ácido ascórbico.

Las propiedades fotofísicas de los conjugados COUPY-octreotide fueron similares a las de los correspondientes fluoróforos libres, presentando un máximo de absorción en la región del amarillo-rojo del espectro del visible y emisión en el rojo lejano. Los rendimientos cuánticos de fluorescencia de los conjugados COUPY-octreotide fueron superiores a los obtenidos con sus correspondientes cumarinas en agua.

Finalmente, se estudió la internalización de uno de los conjugados COUPY-octreotide (compuesto **12**) en células HeLa, ya que sobreexpresan el receptor de somatostatina tipo 2, el cual reconoce selectivamente al péptido octreotide. Mediante la realización de experimentos de microscopía confocal a 37 °C y a 4 °C, donde se observaron patrones de marcaje diferentes, pudimos concluir que la internalización del conjugado viene determinada básicamente por el péptido y no por el fluoróforo, sugiriendo un mecanismo dependiente de energía, a diferencia de lo que ocurre con los fluoróforos COUPY libres que internalizan a través de un simple mecanismo de difusión. Además, la visualización del fluoróforo COUPY conjugado al péptido octreotide fue comparable a la de un fluoróforo comercial basado en rodamina, Atto-Rho12, y mucho mejor que la obtenida con carboxifluoresceína, convirtiendo a los fluoróforos COUPY en candidatos prometedores para marcar biomoléculas para aplicaciones biológicas.

Resumen del capítulo II

Introducción y objetivos

Tal y como se presentó anteriormente en la **Sección 2.6** de la Introducción general de la tesis, la terapia fotodinámica (PDT, por sus siglas en inglés) es una técnica muy prometedora para el tratamiento no invasivo del cáncer, haciendo que el desarrollo de nuevos fotosensibilizadores con propiedades mejoradas se haya convertido en un tema de investigación relevante en los últimos años por sus aplicaciones en el campo de la medicina. La PDT involucra tres componentes esenciales que no son tóxicos por separado: un fotosensibilizador (PS, por sus siglas en inglés), luz y oxígeno. La combinación de los tres componentes desencadena la producción de especies de oxígeno altamente reactivas (ROS, por sus siglas en inglés) que acaban dañando a proteínas, ácidos nucleicos y orgánulos, y finalmente inducen la muerte celular.^{18,19}

En general, el tratamiento de la PDT (**Figura 17**) comienza con la administración intravenosa del fotosensibilizador a una dosis no tóxica. Dicho PS se puede distribuir de forma no selectiva en todo el organismo, o idealmente en un tejido diana concreto. Tras un periodo de incubación, el tumor es irradiado con luz de una longitud de onda adecuada con capacidad para inducir la generación de ROS. Cabe decir que la exposición a la luz no sólo se puede utilizar para provocar un efecto terapéutico, sino también para permitir la detección de tumores utilizando técnicas quirúrgicas guiadas por fluorescencia. El uso de la luz en una zona concreta ofrece la posibilidad de un tratamiento oncológico preciso y selectivo.^{20,21}

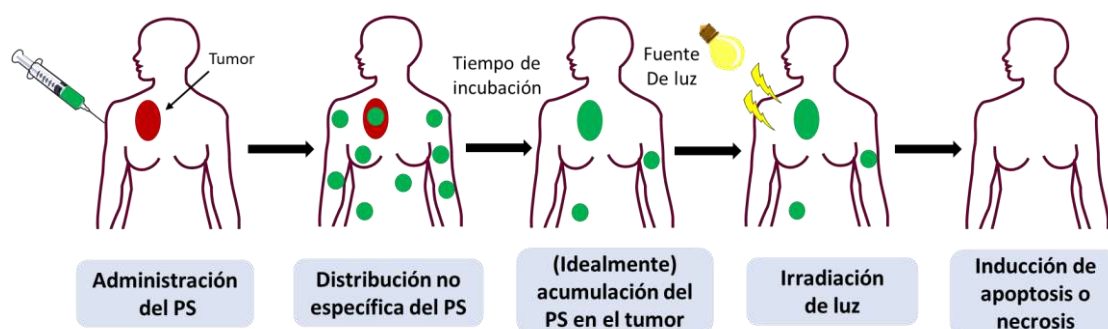
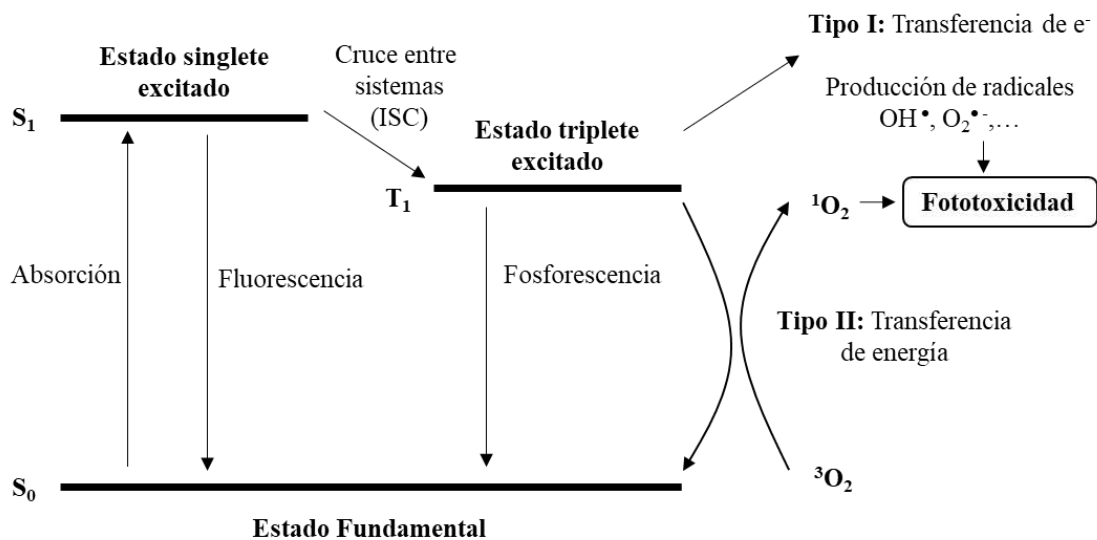


Figura 17. Representación esquemática del perfil del tratamiento de la PDT. Adaptado con el permiso de la referencia [20].

La selección del PS es crucial para una terapia fotodinámica efectiva. Idealmente, un PS debe estar basado en una molécula simple, robusta y que sea fácilmente sintetizable. El PS debe poder ser excitado en un rango de longitudes de onda óptimo, en general entre 650 y 800-900 nm. Tal y como se indicó anteriormente en la **Sección 2.2.2**, esta ventana fototerapéutica, que va del rojo lejano hasta el NIR, es la óptima para la PDT, ya que dicha radiación presenta una mayor capacidad de penetración en los tejidos biológicos y no general toxicidad por sí misma. Además, el agente PS no debe ser tóxico en la oscuridad y debe poder ser eliminado rápidamente de los tejidos sanos, minimizándose así la aparición de efectos secundarios no deseados.

En resumen, idealmente un fotosensibilizador debería cumplir varios requisitos incluyendo estabilidad química, solubilidad en agua, ausencia de citotoxicidad en la oscuridad, altos rendimientos cuánticos de generación de ROS, selectividad tumoral, eliminación rápida del paciente y absorción en la región del rojo lejano al infrarrojo cercano para una penetración más profunda en los tejidos.²¹

Como explicamos en la **Sección 2.6.3**, el mecanismo de acción fotofísico y fotoquímico de la PDT (**Esquema 11**) incluye varias etapas que se pueden ilustrar en un diagrama de Jablonski. En primer lugar, tras absorción de luz de longitud de onda adecuada, el PS alcanza un estado excitado singlete (S_1) cuya vida media se sitúa en el rango de los nanosegundos. A continuación, el estado excitado singlete S_1 puede volver rápidamente a su estado fundamental a través de la emisión de fluorescencia (o mediante procesos no radiativos), o bien estabilizarse en el estado triplete T_1 a través de un cruce entre sistemas no radiativo (ISC, por sus siglas en inglés). Gracias a una vida media mucho más larga del PS en el estado T_1 , alrededor de micro a milisegundos, puede participar en reacciones que son la base de la terapia fotodinámica. Así, el efecto PDT se basa en la transferencia de energía, electrones o protones del estado excitado T_1 del fotosensibilizador a otras moléculas, incluidos sustratos orgánicos u oxígeno molecular.^{18,21,22}



Esquema 11. Representación esquemática del mecanismo de acción de la PDT.

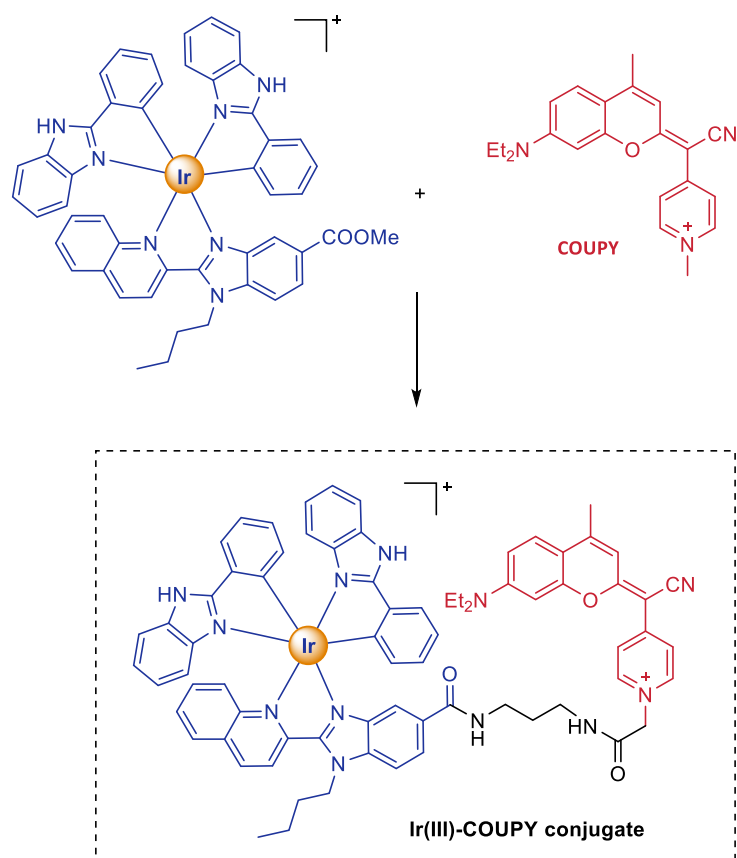
La transferencia de electrones o energía desde el estado excitado triplete del fotosensibilizador a otras moléculas promueve la generación de **ROS** altamente citotóxico a través de procesos de tipo I o tipo II. Las reacciones de **tipo I** requieren de una transferencia de electrones o protones entre el T_1 del PS y diferentes sustratos y que acaban generando iones radicales y radicales libres. Dichos radicales reaccionan con el oxígeno y generan productos oxigenados como los radicales anión superóxido ($O_2^{\bullet-}$) o los radicales hidroxilo (OH^\bullet). En el proceso **tipo II**, el estado excitado triplete del PS interactúa con el oxígeno molecular en estado fundamental (3O_2), lo que implica una transferencia de energía que lo transforma en una especie de oxígeno singlete altamente activa (1O_2). El oxígeno singlete puede reaccionar con diferentes biomoléculas lo que conduce a la muerte de las células cancerígenas. El mecanismo de tipo II es la vía principal de actuación de la mayoría de los PSs aprobados en la actualidad para uso clínico. Ahora bien, cabe decir que ambos mecanismos, tipo I y II, son capaces de provocar un daño biológico oxidativo de forma irreversible al tejido diana.^{18,21}

Por otro lado, es de destacar que el microambiente de los tumores sólidos presenta una baja concentración de oxígeno (**condiciones hipóxicas**), por lo que el mecanismo de PDT de tipo II resulta poco eficaz para el tratamiento de este tipo de tumores hipóxicos ya que es muy dependiente de la concentración de oxígeno molecular. En cambio, la PDT de tipo I presenta ventajas sobre la PDT de tipo II para el tratamiento de tumores hipóxicos debido a su menor dependencia de la concentración de oxígeno. Teniendo en cuenta las perspectivas prometedoras de la PDT de tipo I para el tratamiento de tumores hipóxicos, existe una necesidad creciente de desarrollar nuevos fotosensibilizadores que operen bajo mecanismos de tipo I.²²

El uso de **complejos de coordinación de metales de transición** como fotosensibilizadores para aplicaciones en PDT ha suscitado un gran interés en los últimos años. Esto es debido, entre otros factores, a que el tiempo de vida media del estado excitado triplete de los complejos metálicos es mayor que el de los PSs basados en fluoróforos orgánicos como consecuencia del efecto del átomo pesado, lo que le proporciona mayor tiempo para interactuar con el oxígeno molecular en estado fundamental. Entre los metales de transición más utilizados en PDT, los complejos basados en Ru(II) e Ir(III) son dos de los candidatos más prometedores debido a sus atractivas propiedades fotofísicas, como absorción en la región visible del espectro electromagnético, tiempos de vida media de luminiscencia relativamente largos, grandes desplazamientos de Stokes y una mayor fotoestabilidad en comparación con los PSs basados en fluoróforos orgánicos.²³⁻²⁶

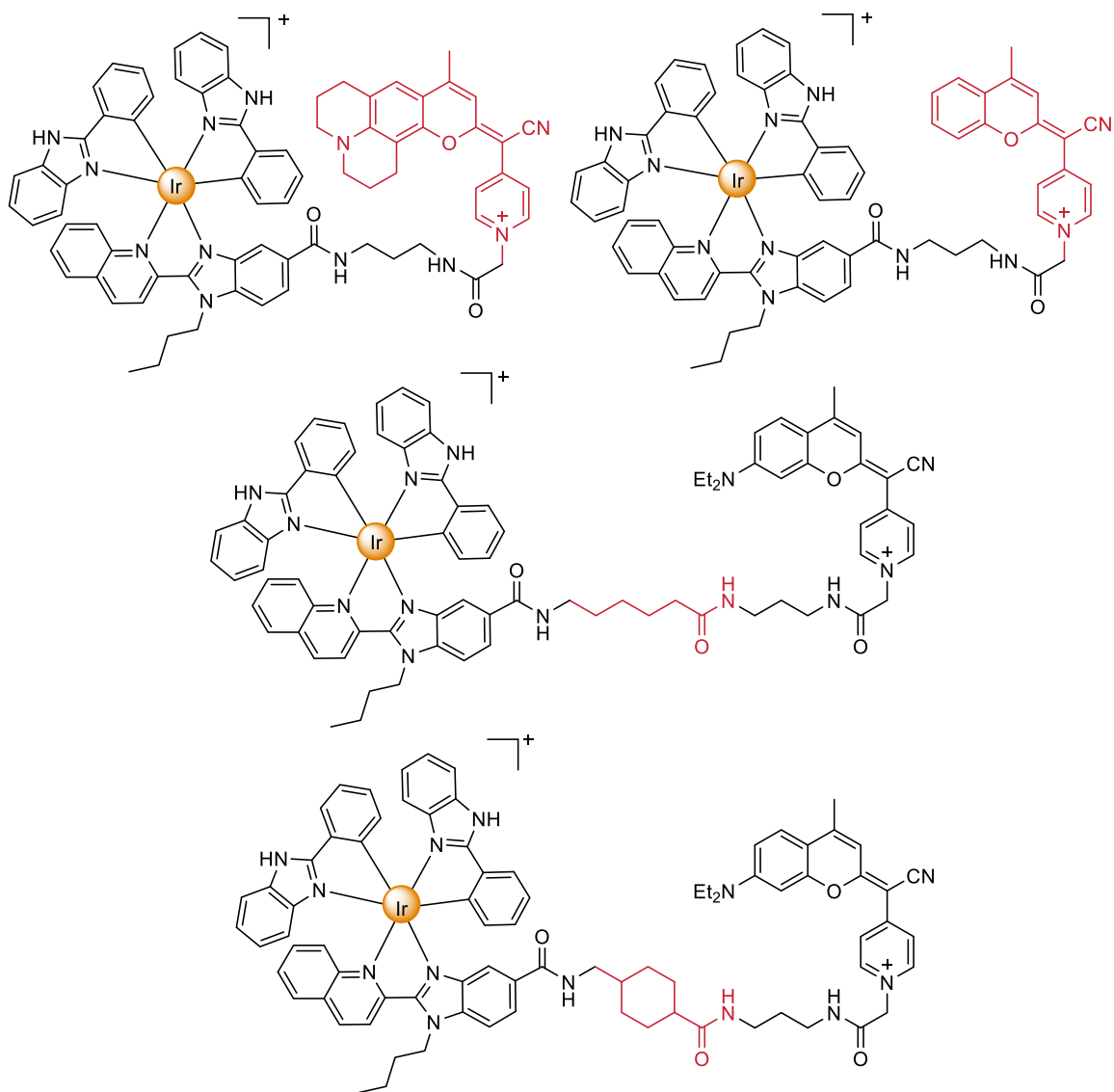
En este capítulo nos hemos centrado en el desarrollo de nuevos agentes fotosensibilizadores para la terapia fotodinámica basados en la conjugación de **fluoróforos orgánicos a complejos metálicos** con la idea de combinar en una sola molécula las propiedades anticancerígenas de los complejos de metales de transición y las propiedades fotofísicas de fluoróforos orgánicos de bajo peso molecular. Concretamente, se ha abordado la conjugación de **fluoróforos COUPY**, con emisión en la zona del rojo lejano y el infrarrojo cercano, a **complejos ciclometalados de Ir(III) y de Ru(II)**. Tal y como se ha comentado en la **Sección 2.4.2.5** y en el capítulo anterior, los fluoróforos COUPY presentan varias características que los hacen atractivos para aplicaciones de bioimagen como absorción y emisión en la ventana fototerapéutica, buen brillo, fotoestabilidad y grandes desplazamientos de Stokes. Además, como se ha comentado en la **Sección 2.6.6**, recientemente se ha demostrado que algunos fluoróforos COUPY también presentan buenas actividades anticancerígenas por sí solos tras irradiación con luz visible, tanto en condiciones de normoxia como de hipoxia, al tiempo que exhiben mínima toxicidad hacia células normales, lo que también les posiciona como candidatos prometedores a PSs para PDT.

En el primer artículo de este capítulo (publicación C), se describe la síntesis y caracterización fotofísica, fotoquímica y biológica de un fotosensibilizador basado en la conjugación de un complejo ciclometalado de Ir(III) a un fluoróforo COUPY (**Esquema 12**). Este proyecto de investigación se ha llevado a cabo en colaboración con el grupo de investigación del Prof. José Ruiz de la Universidad de Murcia, donde se sintetizó el complejo ciclometalado de Ir(III) por la Dra. Gloria Viguera, y el grupo del Prof. Santi Nonell del Institut Químic de Sarrià donde se llevaron a cabo los estudios de caracterización fotoquímica en colaboración con el Dr. Cormac Hally. Finalmente, la evaluación biológica fue realizada por el grupo del Prof. Viktor Brabec del Institute of Biophysics of the Czech Academy of Sciences.



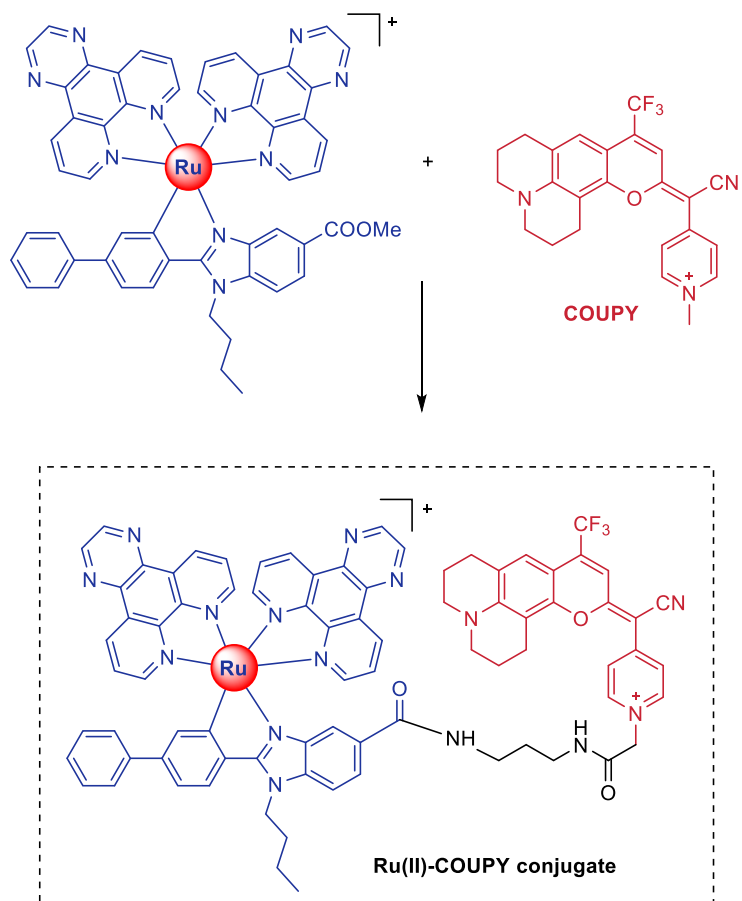
Esquema 12. Estructura del conjugado Ir(III)-COUPY.

En el segundo manuscrito pendiente de ser enviado para publicación (publicación D), se han sintetizado 4 nuevos conjugados entre el complejo ciclometalado de Ir(III) y fluoróforos COUPY con diferentes estructuras y propiedades fotofísicas con el objetivo de establecer relaciones estructura-actividad (SARS, por sus siglas en inglés). Para ello, también se han evaluado diferentes espaciadores entre el complejo metálico y la cumarina (**Esquema 13**). Se han realizado los estudios de internalización mediante microscopia confocal bajo la supervisión del Dr. Manel Bosch en la Unidad de Microscopia Óptica Avanzada de la Universidad de Barcelona. La caracterización fotofísica y fotoquímica de los nuevos conjugados Ir(III)-COUPY así como de las cumarinas libres se ha realizado en colaboración con el Dr. Cormac Hally y Mireia Jordà en el grupo del Prof. Santi Nonell del Institut Químic de Sarrià. Finalmente, la evaluación biológica ha sido realizada por Enrique Ortega-Forte en el grupo del Prof. José Ruiz de la Universidad de Murcia.



Esquema 13. Estructura de los 4 nuevos conjugados Ir(III)-COUPY.

Finalmente, en el apartado de resultados no publicados, se describe la síntesis y caracterización biológica de un nuevo fotosensibilizador basado en la conjugación de un complejo ciclometalado de Ru(II) tipo polipiridilo a un fluoróforo COUPY (**Esquema 14**). Este proyecto de investigación se ha llevado a cabo en colaboración con el grupo de investigación del Prof. José Ruiz de la Universidad de Murcia, donde se sintetizó el complejo ciclometalado de Ru(II) por el Dr. Francisco José Ballester y se realizó la evaluación biológica por Enrique Ortega-Forte. La determinación de la generación de oxígeno singlete para el conjugado Ru(II)-COUPY así como para la cumarina libre se ha realizado en colaboración con Mireia Jordà en el grupo del Prof. Santi Nonell del Institut Químic de Sarrià. Además, se ha estudiado su acumulación subcelular mediante microscopía confocal bajo la supervisión del Dr. Manel Bosch en la Unidad de Microscopía Óptica Avanzada de la Universidad de Barcelona.



Esquema 14. Estructura del conjugado Ru(II)-COUPY.

Capítulo IIa

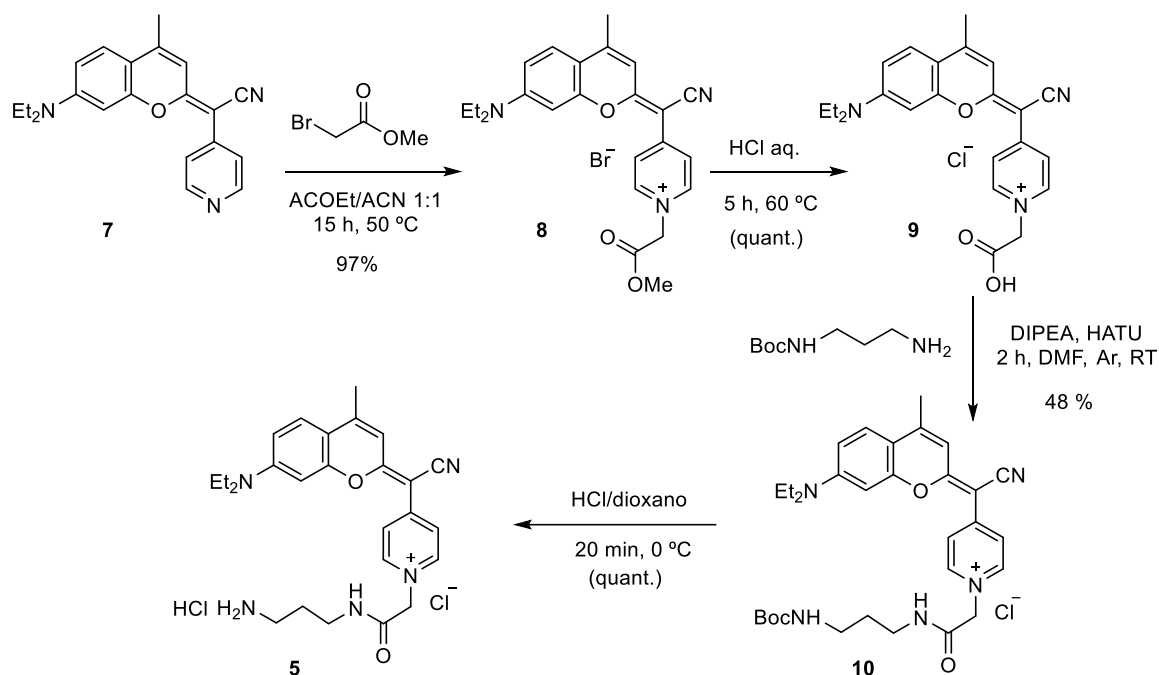
Publicación C: Novohradsky, V.; Rovira, A.; Hally, C.; Galindo, A.; Viguera, G.; Gandioso, G.; Svitelova, M.; Bresolí-Obach, R.; Kostrhunova, H.; Markova, L.; Kasparkova, J.; Nonell, S.; Ruiz, R.; Brabec, V.; Marchán, V. Towards novel photodynamic anticancer agents generating superoxide anion radicals: a cyclometalated Ir^{III} complex conjugated to a far-red emitting coumarin. *Angew. Chem. Int. Ed.* **2019**, *58*, 6311-6315.

Nota: En el resumen se ha mantenido la numeración de los compuestos del artículo para facilitar su búsqueda.

En este trabajo, se ha diseñado y sintetizado un nuevo agente fotosensibilizador basado en un conjugado entre un complejo ciclometalado de Ir(III) y un fluoróforo COUPY. Tras estudiar sus propiedades fotofísicas y fotoquímicas, se realizaron estudios de internalización y acumulación celular mediante microscopia confocal e ICP-MS, posteriormente, se determinó la fototoxicidad tanto del conjugado Ir(III)-COUPY como de los dos componentes por separado (complejo de Ir(III) y fluoróforo COUPY) tras irradiación con luz azul y verde. Finalmente, se investigó la generación de ROS dentro de las células tanto en la oscuridad como tras irradiación con luz visible.

Síntesis del fluoróforo COUPY conjugable

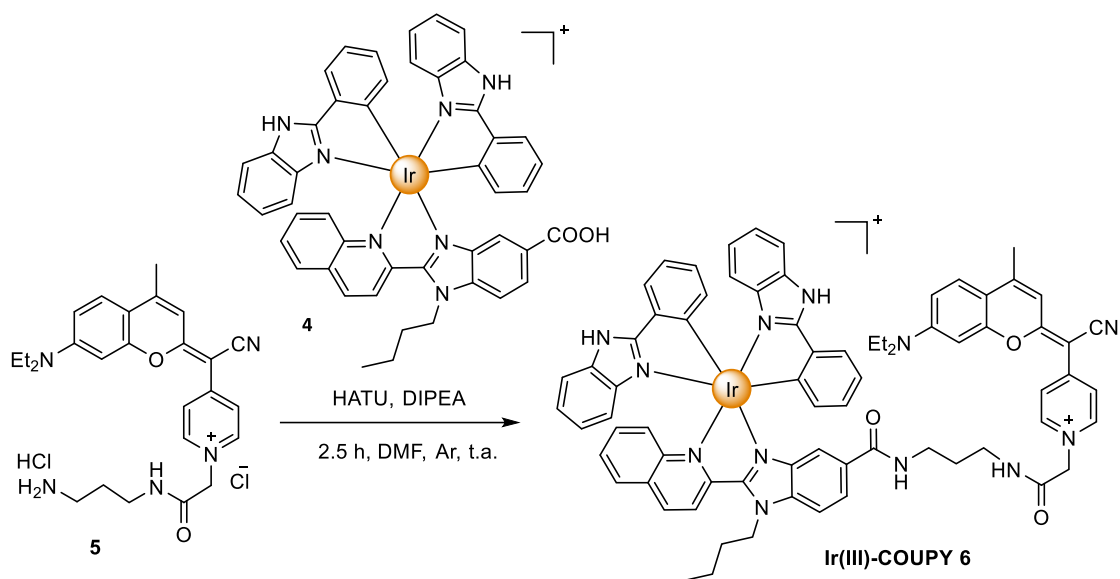
Tal y como se muestra en el **Esquema 15**, el derivado de cumarina **9** se sintetizó a partir del precursor de cumarina **7** en dos pasos lineales siguiendo los procedimientos descritos anteriormente en el capítulo I. A continuación, la cumarina **9** se hizo reaccionar con hidrocloreuro de *N*-Boc-1,3-propandiamina usando HATU como agente de acoplamiento en presencia de DIPEA durante 2 h a temperatura ambiente y protegido de la luz, obteniéndose el derivado de cumarina **10**. Finalmente, la eliminación del grupo protector Boc dio lugar al derivado de cumarina **5**, el cual contiene el grupo funcional amino necesario para el acoplamiento con el complejo metálico.



Esquema 15. Síntesis del derivado de cumarina **5**.

Síntesis y caracterización del conjugado Ir(III)-COUPY

La unión del complejo ciclotmetalado de Ir(III) al fluoróforo COUPY se llevó a cabo mediante la formación de un enlace amida entre el grupo carboxilo del complejo **4** y el grupo amino de la cumarina **5** (**Esquema 16**). Para ello, a una disolución del complejo **4** y HATU en DMF anhidra bajo atmosfera de argón, se añadió DIPEA y se dejó reaccionar durante 10 min a temperatura ambiente y protegido de la luz. A continuación, se añadió una solución de la cumarina **5** y DIPEA en DMF anhidra sobre la disolución del complejo metálico activado, y se dejó reaccionar durante 2.5 h a temperatura ambiente, bajo atmosfera de argón y protegido de la luz. Finalmente, el conjugado Ir(III)-COUPY **6** se purificó por cromatografía en columna de sílice, obteniéndose un sólido de color lila oscuro con un 30 % de rendimiento. El conjugado fue caracterizado por HR ESI-MS y RMN de ^1H y ^{13}C .



Esquema 16. Síntesis del conjugador Ir(III)-COUPY 6.

Cabe destacar que el conjugado, a diferencia del complejo metálico, se mostró completamente soluble en agua y, además, tal y como se muestra en la **Figura 18**, también se encontró que era estable en medio celular (DMEM-10% FBS).

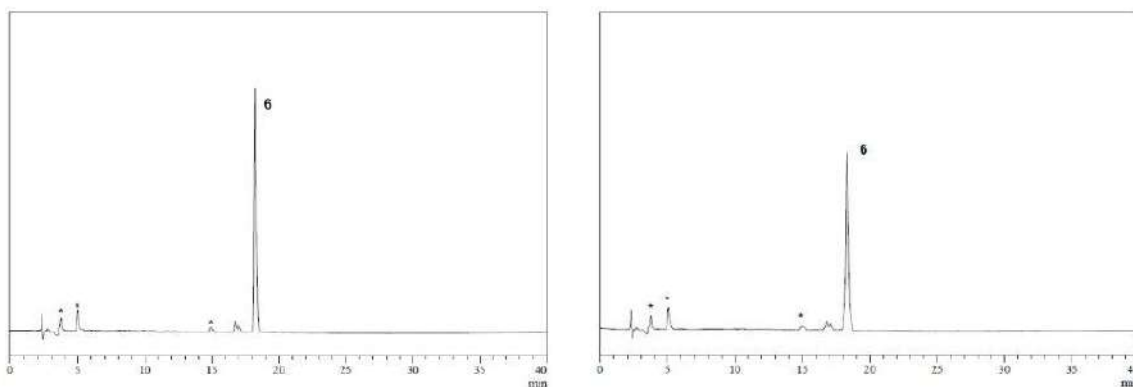


Figura 18. Análisis por HPLC de fase inversa del conjugado Ir(III)-COUPY (6) disuelto en DMEM-10 % FBS a t=0 (izquierda) y tras incubación a 37 °C durante 24 h (derecha). *picos del medio celular. Adaptado con el permiso de la referencia [27].

Caracterización fotofísica y fotoquímica del conjugado Ir(III)-COUPY **6**

Las propiedades fotofísicas del conjugado Ir(III)-COUPY **6** se estudiaron en cuatro disolventes de diferente polaridad (PBS, ACN, DCM y benceno), y se compararon con las de los correspondientes fragmentos por separado, el complejo de Ir(III) **3** que contiene el grupo funcional éster, y la cumarina de referencia **2**, con la piridina metilada (**Figura 19**). Se estudiaron los máximos de absorción (λ_{max}) y de emisión (λ_{em}), los desplazamientos de Stokes, los coeficientes de extinción molar (ϵ), el rendimiento cuántico de fluorescencia o fosforescencia ($\Phi_{\text{F}}/\Phi_{\text{P}}$), el tiempo de vida media de fluorescencia o fosforescencia ($\tau_{\text{F}}/\tau_{\text{P}}$) y el rendimiento de generación de oxígeno singlete (Φ_{Δ}). En la **Tabla 3** se muestran los valores en PBS y DCM para el conjugado **6**, el complejo de Ir(III) **3** y la cumarina **2**.

Respecto a los espectros de absorción y emisión de los compuestos, cabe señalar que el complejo de Ir(III) **3** mostró máximos de absorción alrededor de 305 nm y una fuerte fosforescencia en el rojo (λ_{em} 656-678 nm). La intensidad de la fosforescencia se observó que decrecía en el conjugado Ir(III)-COUPY **6** de una manera dependiente del disolvente, lo que sugirió la existencia de procesos competitivos en el estado excitado. Con respecto a la cumarina **2**, ésta mostró una fuerte fluorescencia ($\lambda_{\text{em}} = 599\text{-}609$ nm), cuya intensidad y tiempo de vida disminuyeron fuertemente en el conjugado, sugiriendo de nuevo la existencia de procesos competitivos en el estado excitado.

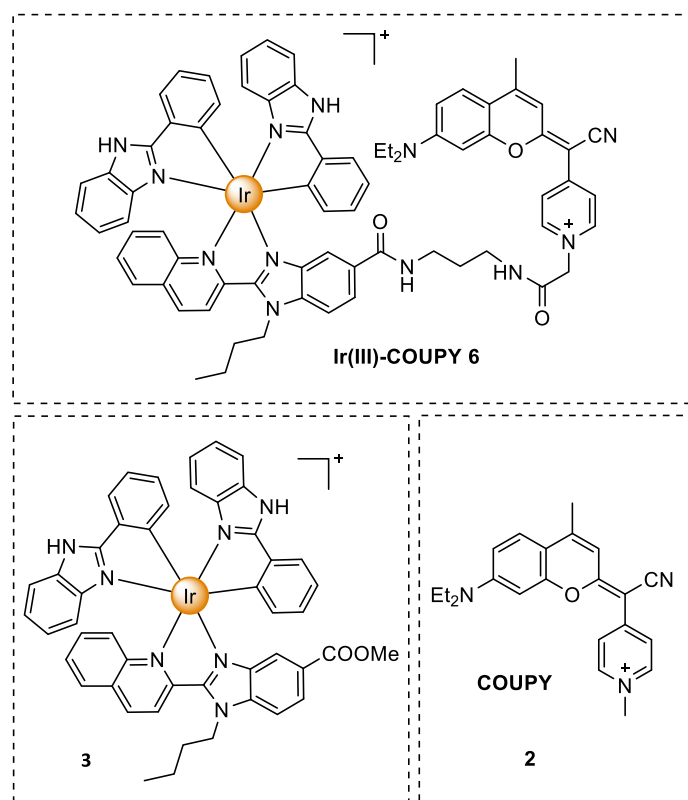


Figura 19. Estructuras de los compuestos cuyas propiedades fotofísicas y fotoquímicas fueron estudiadas.

Tabla 3. Propiedades fotofísicas de los compuestos **2**, **3** y **6** en PBS y DCM.

	Disol.	λ_{\max} (nm)	ϵ (mM ⁻¹ cm ⁻¹)	λ_{em} (nm)	Despl. Stokes (nm)	$\Phi_{\text{F}}/\Phi_{\text{F}}$	τ_{F}	τ_{P}	Φ_{Δ}
2	PBS	545	34	604	59	0.14	0.9	-	<0.01
	DCM	569	67	607	38	0.70	5.4	-	<0.01
3	PBS	305	40	656	351	>0.01	-	55 (95%) 281 (7%)	<0.01
	DCM	303	42	665	362	0.07	-	315	0.23
6	PBS	550	17	615	65	0.004	0.37 (73%) 3.3 (27%)	-	<0.01
	DCM	566	44	602	33	0.07	0.24	96 (70%) 234 (30%)	0.19

A continuación, se evaluó la capacidad de los compuestos de producir oxígeno singlete ($^1\text{O}_2$) en los diferentes disolventes. En presencia de oxígeno, el complejo de Ir(III) **3** generó $^1\text{O}_2$ en los tres disolventes orgánicos, pero no en PBS. Por otro lado, la cumarina **2** presentó valores muy bajos de rendimiento cuántico de generación de $^1\text{O}_2$ en todos los disolventes; sin embargo, estos valores aumentaron considerablemente en el conjugado Ir(III)-COUPY **6**, lo que sugiere una mejora en el cruce entre sistemas (ISC), probablemente inducido por el efecto del ion pesado de Ir(III), resultado por otra parte consistente con el acortamiento de su tiempo de vida media de fluorescencia. Aun así, cabe destacar que tampoco se detectó $^1\text{O}_2$ en PBS.

La fotoestabilidad del conjugado Ir(III)-COUPY **6** se estudió tras irradiación con luz verde y se comparó con la de tres compuestos de referencia: el fluoróforo COUPY **2**, rosa de bengala (RB) y meso-tetra(4-sulfonatofenil)porfirina (TPPS). Los estudios de fotoestabilidad se realizaron monitoreando la disminución de la fluorescencia de una disolución de los compuestos en PBS, a una concentración $5\ \mu\text{M}$, tras irradiación a $505\ \text{nm}$ con un LED de alta potencia ($100\ \text{mW}/\text{cm}^2$) a $37\ ^\circ\text{C}$. Tal y como se muestra en la **Figura 20**, el conjugado Ir(III)-COUPY se mostró algo más fotoestable que RB, el cual es un PS usado habitualmente para estudios en sistemas biológicos. Sin embargo, la porfirina TPPS resultó ser el compuesto más fotoestable de los cuatro, hecho esperable dada su conocida robustez. Aun así, el conjugado **6** demostró ser fotoestable a fluencias de luz más altas que las que se usan típicamente en aplicaciones de bioimagen.

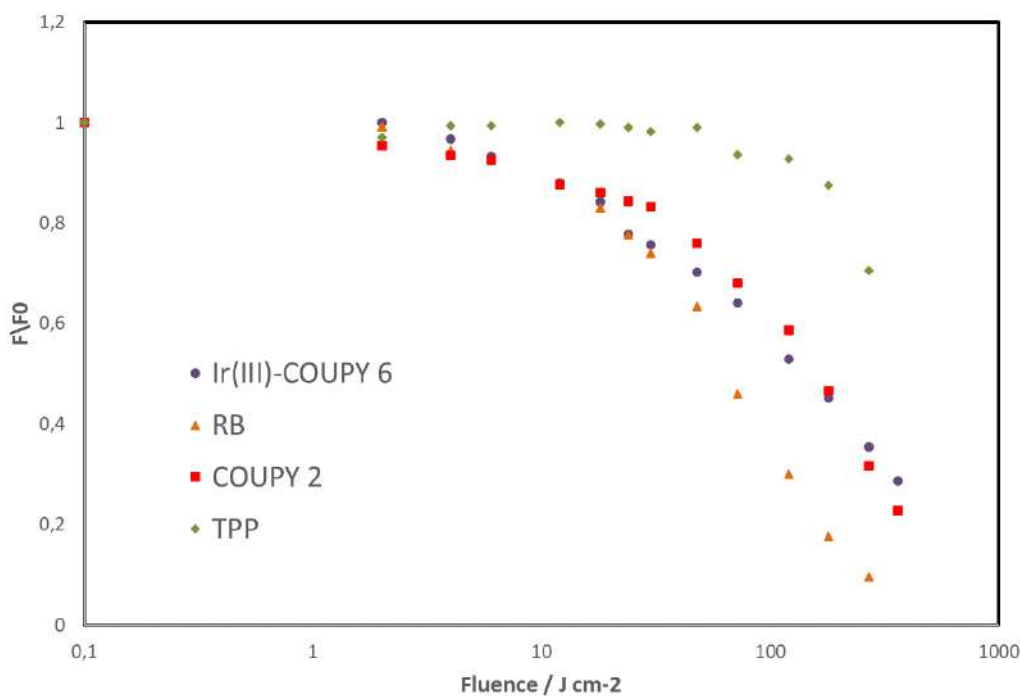


Figura 20. Comparación de la fotoestabilidad de los compuestos en PBS tras irradiación con luz verde. Adaptado con el permiso de la referencia [27].

Evaluación biológica del conjugado Ir(III)-COUPY

En primer lugar, se estudió la **internalización en células HeLa** del conjugado Ir(III)-COUPY **6** por microscopía confocal mediante irradiación con un láser de luz amarilla ($\lambda_{ex} = 561 \text{ nm}$). Como se muestra en la **Figura 21**, el conjugado internalizó de forma eficiente en las células, observándose vesículas fluorescentes en el citoplasma. En cambio, la cumarina **2**, tal y como se comentó en el capítulo anterior, mostró el patrón ya observado para este tipo de fluoróforos: mitocondrias y nucleolos.

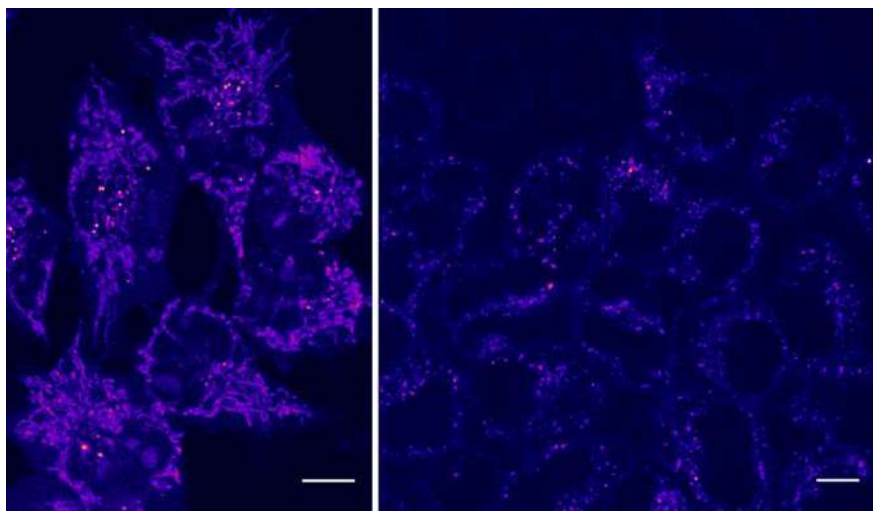


Figura 21. Experimentos de internalización mediante microscopía confocal en células HeLa del fluoróforo COUPY **2** (izquierda) y del conjugado Ir(III)-COUPY **6** (derecha). Adaptado con el permiso de la referencia [27].

También se cuantificó la acumulación celular de Ir mediante espectrometría de masas por plasma acoplado inductivamente (ICP-MS, por sus siglas en inglés) tras incubación de células HeLa con los compuestos de Ir. Como se muestra en la **Tabla 4**, la acumulación del conjugado **6** a 37 °C fue ligeramente superior a la del complejo de Ir(III) **3**, lo que indica que la conjugación con la cumarina tiene un efecto positivo tanto en la internalización como en la acumulación.

Tabla 4. Acumulación celular de Ir determinada por ICP-MS en células HeLa a 4 °C y 37 °C.

	ng Ir/10 ⁶ células		pmol Ir/10 ⁶ células	
	4 °C	37 °C	4 °C	37 °C
Complejo Ir(III) 3	1.3 ± 0.2	7.6 ± 0.4	6.5 ± 1.0	39.4 ± 2.2
Conjugado 6	11.6 ± 1.0	12.1 ± 0.7	60.4 ± 5.2	62.8 ± 3.4

Por otro lado, cabe destacar que la acumulación de conjugado **6** no se modificó cuando la incubación se realizó a 4 °C. En cambio, la cantidad de complejo de Ir(III) **3** acumulado disminuyó ligeramente a baja temperatura, sugiriendo un mecanismo de internalización celular dependiente de energía. En su conjunto, los experimentos de internalización celular sugieren que la vía de internalización del conjugado Ir(III)-COUPY **6** difiere de la de los dos fragmentos por separado, ya que éste no se acumula en orgánulos específicos, como mitocondrias o nucléolos, sino en el citoplasma, y entra en las células a través de un mecanismo de internalización no dependiente de energía.

Una vez comprobado que el conjugado Ir(III)-COUPY **6** es internalizado de forma eficiente en células Hela, se llevaron a cabo estudios de citotoxicidad en condiciones de normoxia e hipoxia, utilizando nuevamente la cumarina **2** y el complejo de Ir(III) **3** como compuestos de referencia. Es interesante destacar que a pesar de la mayor acumulación celular del conjugado **6** observada en los experimentos de ICP-MS, dicho compuesto no mostró toxicidad en la oscuridad lo que indica que la conjugación entre el complejo metálico y el fluoróforo COUPY dio como resultado una disminución de la citotoxicidad (**Tabla 5** **Tabla 5**).

Una vez determinada la citotoxicidad de los compuestos en la oscuridad, se estudió su fototoxicidad tras irradiar con luz azul o verde. Tal y como se muestra en la **Tabla 5**, la irradiación con luz visible mejoró claramente la actividad antitumoral del conjugado **6**, obteniéndose valores de IC₅₀ de 2.51 y 1.32 μM tras irradiación con luz verde y azul, respectivamente. Además, la baja citotoxicidad en la oscuridad del conjugado **6** condujo a unos excelentes índices de fototoxicidad (PI) tras la irradiación tanto con luz verde (85) como con azul (161). Es especialmente destacable el valor de PI del conjugado Ir(III)-COUPY **6** tras irradiar con luz verde si se compara con el del complejo de Ir(III) **3** libre (85 vs 2.9). Por otro lado, es importante destacar que la fototoxicidad de **6** fue similar tanto en condiciones normóxicas como en condiciones hipóxicas, lo que convierte al conjugado Ir(III)-COUPY en un potencial candidato para el tratamiento de tumores hipóxicos.

Tabla 5. Cito- y fototoxicidad de los compuestos en células HeLa.

		Oscuridad	Luz verde		Luz azul	
		IC ₅₀ [μ M]	IC ₅₀ [μ M]	PI	IC ₅₀ [μ M]	PI
COUPY 2	Normoxia	38.7 \pm 4.1	0.34 \pm 0.11	114	0.37 \pm 0.09	105
	Hipoxia	46.3 \pm 3.1	0.46 \pm 0.08	101	0.44 \pm 0.13	105
Complejo Ir(III) 3	Normoxia	95.2 \pm 6.4	32.7 \pm 4.9	2.9	2.02 \pm 0.24	47
	Hipoxia	101 \pm 10	31.5 \pm 3.3	3.2	2.52 \pm 0.19	40
Conjugado 6	Normoxia	213 \pm 14	2.51 \pm 0.32	85	1.32 \pm 0.09	161
	Hipoxia	119 \pm 6	2.77 \pm 0.20	79	1.43 \pm 0.11	153

Una vez confirmada la existencia de una estrecha relación entre la citotoxicidad de los compuestos y la irradiación con luz visible, el siguiente paso consistió en investigar la generación de ROS a nivel celular (**Figura 22**). Aunque los tres compuestos generaron un nivel basal de ROS intracelular en la oscuridad, es destacable el notable aumento en la producción de ROS en el caso del conjugado **6** tras irradiación con luz visible en comparación con los compuestos libres **2** y **3**, especialmente con luz azul.

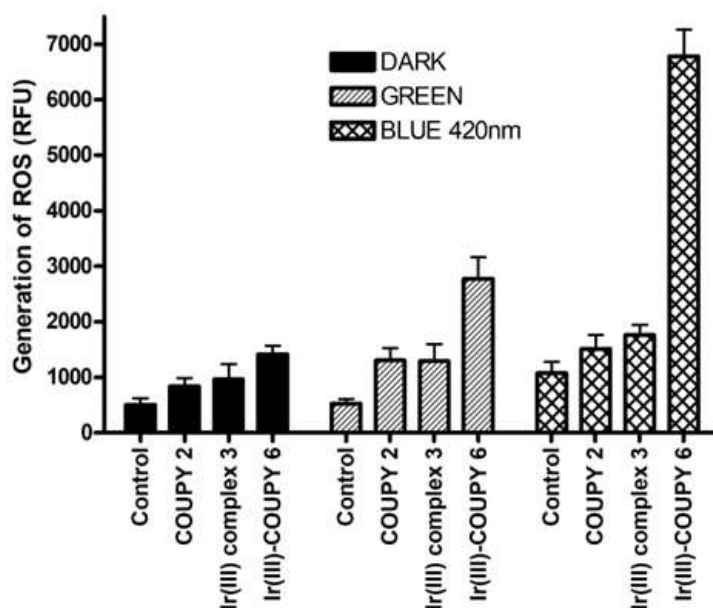


Figura 22. Cuantificación de ROS determinada por citometría de flujo en células HeLa. Las células se trataron con los compuestos a una concentración 10 μ M durante 1 h en la oscuridad seguido de 1 h de irradiación con luz verde o azul. Adaptado con el permiso de la referencia [27].

Una vez demostrada la capacidad del conjugado Ir(III)-COUPY **6** de generar ROS en el interior de las células tras irradiación con luz visible, nos centramos en identificar el tipo de especies reactivas de oxígeno producidas. Aunque tal y como se comentó en la **Sección 3.2.2** de la Introducción general de la tesis, los complejos ciclometalados de Ir(III) suelen producir preferentemente $^1\text{O}_2$ (PDT tipo II), también es conocida su capacidad de generar otro tipo de ROS a través de procesos fotoquímicos de tipo I (por ejemplo, H_2O_2 , OH^\bullet , $\text{O}_2^{\bullet-}$, etc.). Así pues, las células HeLa se trataron previamente con varios capturadores específicos de los diferentes tipos de ROS. Sorprendentemente, sólo el uso tirón fue capaz de prevenir la producción intracelular de ROS, lo que sugirió la generación de radicales anión superóxido ($\text{O}_2^{\bullet-}$) en las células tras irradiación con luz visible en presencia del conjugado Ir(III)-COUPY **6** (**Figura 23**).

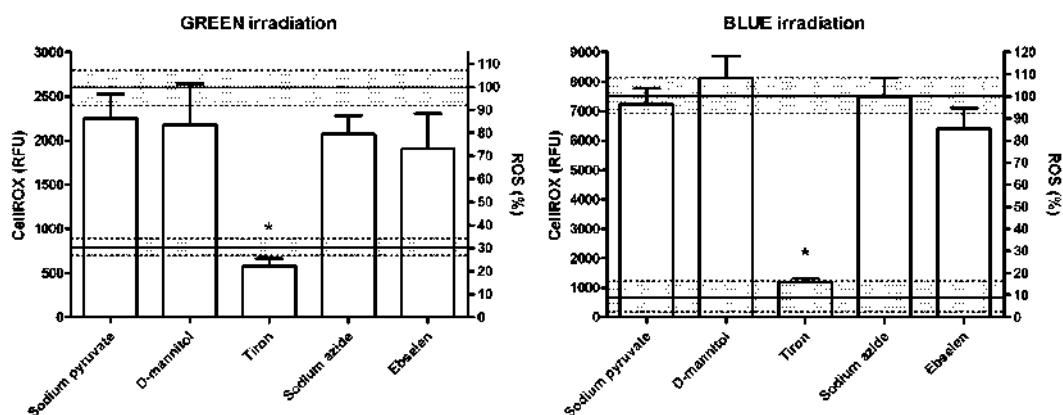


Figura 23. Cuantificación de ROS en células HeLa preincubadas con diferentes capturadores específicos de ROS tras tratamiento con el conjugado **6** (1 h en la oscuridad seguido de 1 h de irradiación). Adaptado con el permiso de la referencia [27].

Para confirmar la generación de $\text{O}_2^{\bullet-}$ en un medio no celular, se utilizó dihidrorrodamina 123 (DHR123), una sonda no fluorescente que emite fluorescencia verde tras reacción con $\text{O}_2^{\bullet-}$. Tal y como se muestra en la **Figura 24**, el conjugado **6** aumentó de forma notable la intensidad de fluorescencia de DHR123 tras irradiación con luz azul en comparación con el complejo de Ir(III) **3** y la cumarina COUPY **2**, lo que confirmó su capacidad de generar superóxido.

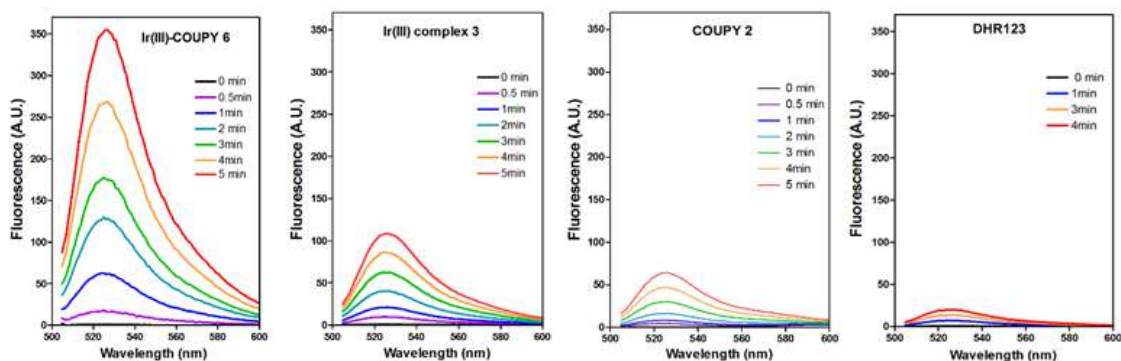


Figura 24. Espectros de fluorescencia de DHR123 inducidos por irradiación con luz azul (455 nm) en presencia de Ir(III)-COUPY **6** (primer panel), complejo de Ir(III) **3** (segundo panel), COUPY **2** (tercer panel) o sin compuesto (DHR123 sólo, cuarto panel). Adaptado con el permiso de la referencia [27].

Finalmente, para investigar la involucración de los radicales de anión superóxido en la muerte celular, se determinó la viabilidad de las células HeLa tras tratamiento con el conjugado **6** en las condiciones de irradiación, tanto en ausencia como en presencia de tirón. Como se muestra en la **Figura 25**, la fotocitotoxicidad de **6** desapareció por completo en las células pretratadas con el capturador de ROS, lo que confirmó el papel activo del $O_2^{\cdot-}$ en la muerte celular.

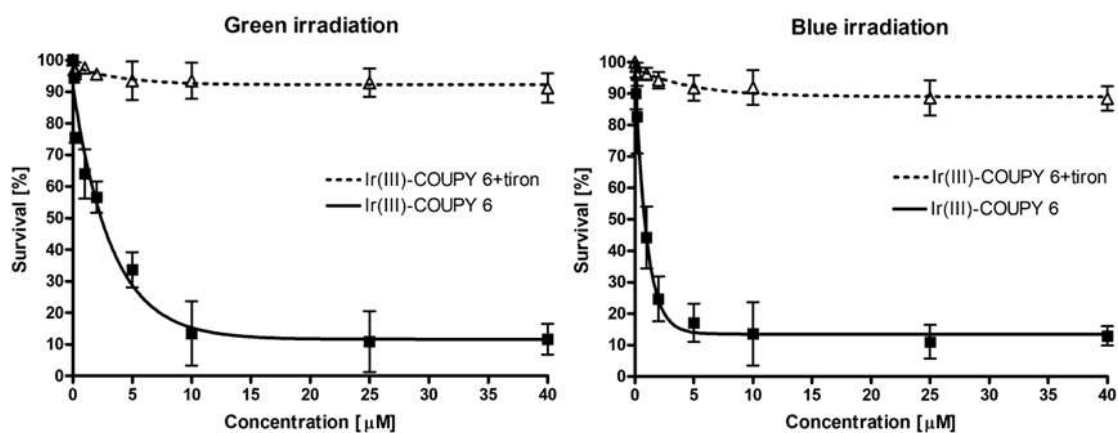


Figura 25. Impacto del capturador de radicales de anión superóxido en la viabilidad de las células HeLa en condiciones de irradiación. Adaptado con el permiso de la referencia [27].

Capítulo IIIb

Publicación D: Rovira, A.; Ortega-Forte, E.; Hally, C.; Jordà, M.; Viguera, G.; Bosch, M.; Nonell, S.; Ruiz, J.; Marchán, V. Exploring structure-activity relationships in photodynamic therapy anticancer agents based on Ir(III)-COUPY conjugates. *Manuscrito en preparación.*

Nota: En el resumen se ha mantenido la numeración de los compuestos del artículo para facilitar su búsqueda.

En base a los buenos resultados descritos en la publicación C donde describimos un nuevo tipo de fotosensibilizadores para PDT basados en la conjugación de una cumarina COUPY (**1a**) con emisión en el rojo lejano a un complejo ciclometalado de Ir(III) (**2a**), en este trabajo se ha abordado la síntesis de cuatro nuevos conjugados Ir(III)-COUPY con el objetivo de establecer relaciones estructura-actividad (SARs, por sus siglas en inglés). Principalmente, nos hemos centrado en investigar cómo las diferentes modificaciones en la estructura de los fluoróforos COUPY influyen en las propiedades fotofísicas, fotoquímicas y biológicas de los PSs resultantes.

Tal y como se muestra en la **Figura 26**, los nuevos conjugados Ir(III)-COUPY sintetizados en este trabajo (**3b-3d**) combinan el complejo ciclometalado de Ir(III) original (**2a**) y tres derivados COUPY (**1a-1c**) conectados a través de espaciadores flexibles o rígidos. La ausencia del grupo donador de electrones (EDG, por sus siglas en inglés) *N,N*-dietilamino en la posición 7 de la estructura de la cumarina (**1b**) podría proporcionar información sobre el papel de dicho grupo en la generación de ROS en el conjugado resultante Ir(III)-COUPY (**3b**). Además, se ha sintetizado un conjugado Ir(III)-COUPY (**3c**) que contiene un derivado de cumarina en el que el nitrógeno en la posición 7 forma parte de un sistema de anillos fusionados (**1c**) con el objetivo de estudiar su influencia en la transferencia de carga entre el centro metálico y el fragmento de cumarina.

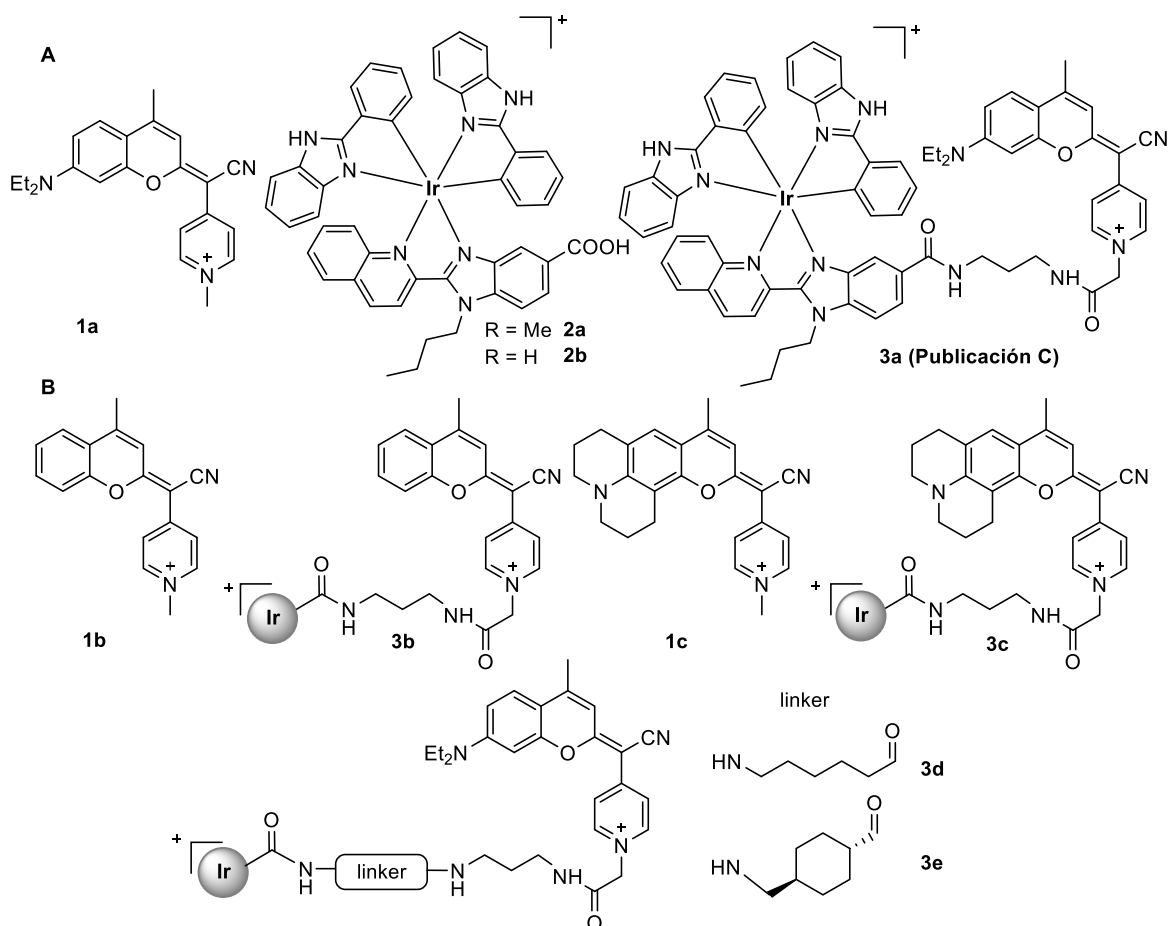
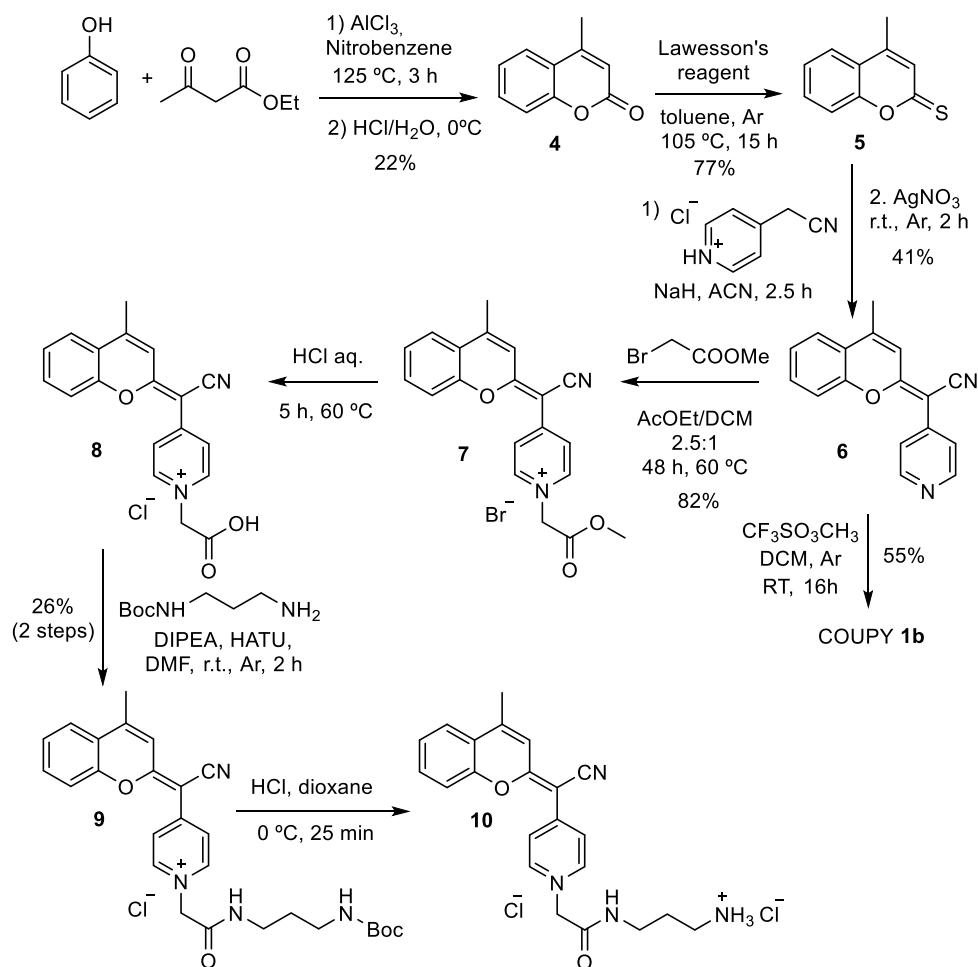


Figura 26. A) Estructura de los compuestos previamente evaluados en la publicación C: COUPY **1a**, complejo Ir(III) ciclometalado **2a** y el correspondiente conjugado Ir(III)-COUPY **3a**. B) Estructura de las nuevas cumarinas COUPY (**1b-1c**) y de los conjugados Ir(III)-COUPY (**3b-3e**) investigados en este trabajo.

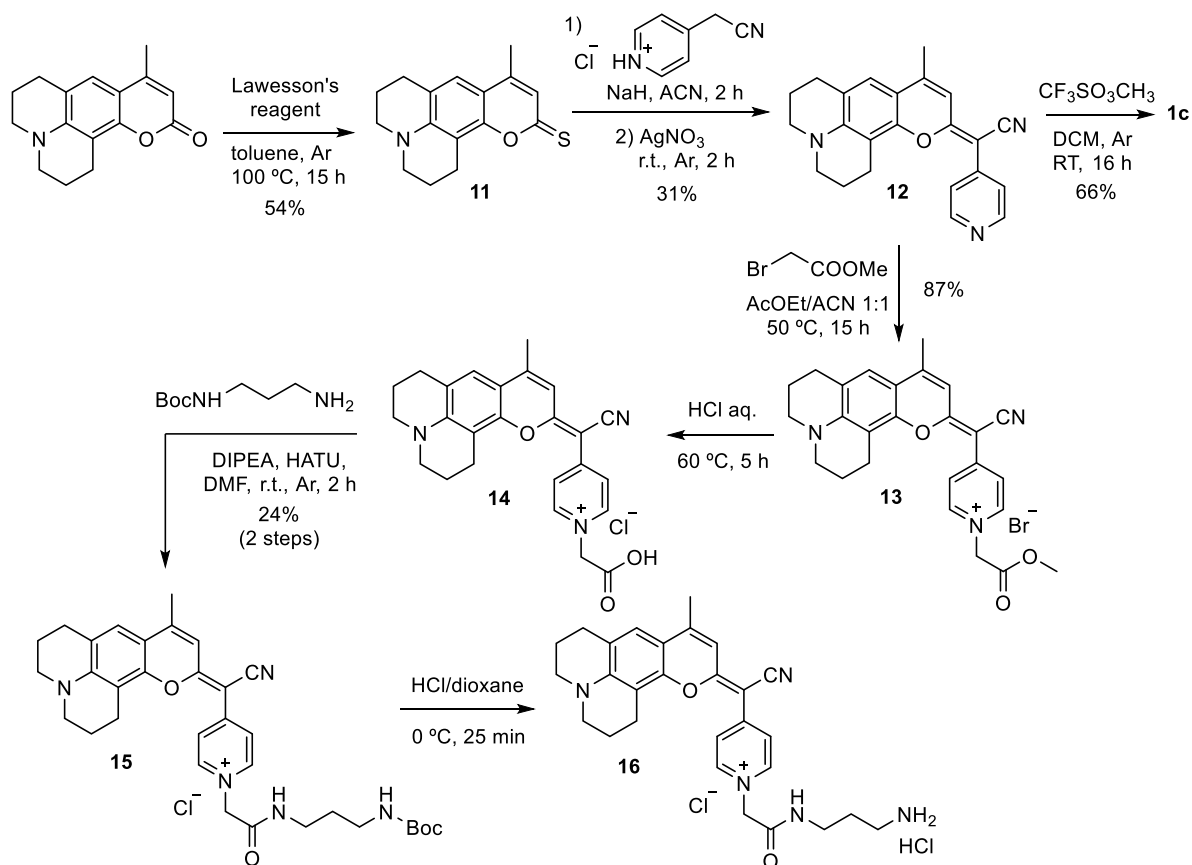
Síntesis de los fluoróforos COUPY conjugables

La ruta sintética seguida para la preparación del derivado COUPY **10** consta de siete pasos (**Esquema 17**) empezando por una condensación de Pechmann entre fenol y acetoacetato de etilo que proporcionó el esqueleto de cumarina sin el grupo EDG en la posición 7 (**4**). A continuación, la cumarina **4** se hizo reaccionar con el reactivo de Lawesson para obtener la tiocumarina **5**, que seguidamente se condensó con 4-piridilacetónitrilo para dar el compuesto **6**. El derivado éster de dicha cumarina (**7**) se obtuvo tras alquilación de **6** con bromoacetato de metilo. Tras una etapa de hidrólisis ácida, el grupo carboxilo de la cumarina **8** se hizo reaccionar con el hidrocloreto de N-Boc-1,3-propanodiamina utilizando HATU como agente acoplante en presencia de DIPEA para generar la cumarina **9**, cuyo grupo protector Boc se eliminó en condiciones ácidas para dar el derivado de cumarina **10**.



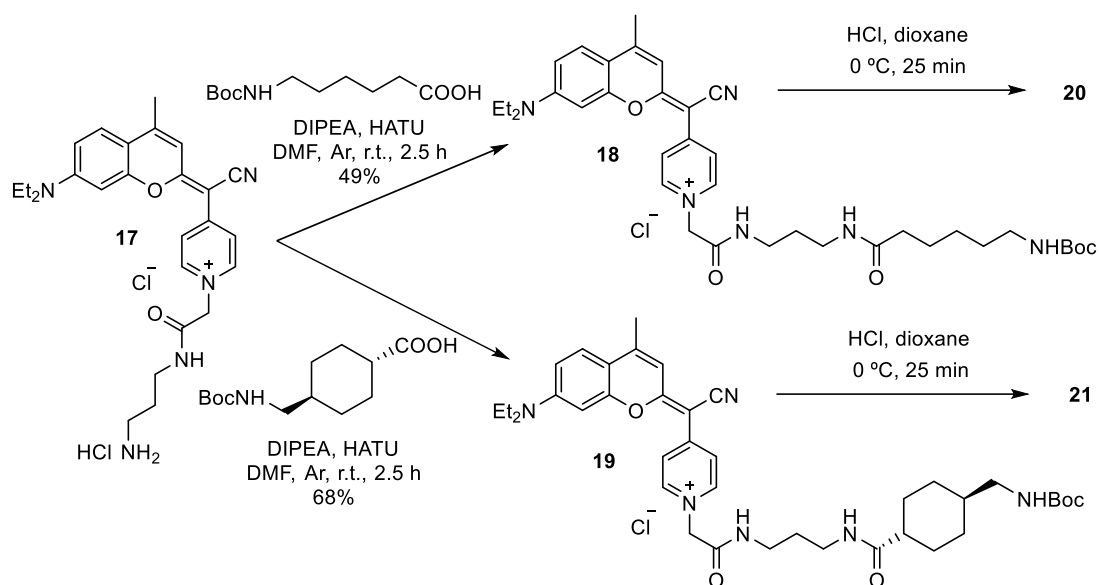
Esquema 17. Síntesis del derivado COUPY **10**.

Por otro lado, también se sintetizó un análogo de cumarina fusionado con julolidina con el objetivo de desplazar el máximo de absorción hacia al rojo con respecto a la 7-dialquilaminocumarina original. También queríamos evaluar si la rigidez del grupo amino tendría un impacto en las propiedades fotofísicas y fotoquímicas de los compuestos, ya que la rotación alrededor del enlace N-C no es posible debido a la fusión de los anillos de seis miembros con el anillo aromático. El derivado COUPY **16** se sintetizó a partir de un precursor de cumarina disponible comercialmente siguiendo un procedimiento similar al empleado para la preparación del derivado COUPY **10** (Esquema 18).



Esquema 18. Síntesis del derivado COUPY **16**.

Finalmente, con el objetivo de investigar el efecto de la distancia entre el fluoróforo COUPY y el complejo de Ir(III) en las propiedades fotofísicas y fotoquímicas de los compuestos y, en particular, en el conjugado original Ir(III)-COUPY **3a**, diseñamos dos análogos que incorporan un espaciador más largo entre ambos fragmentos. Como se muestra en el **Esquema 19**, para ello fue necesario sintetizar el derivado de cumarina **20** que incorpora un espaciador flexible, y el derivado **21** con un espaciador rígido, ambos escogidos para que los respectivos conjugados tengan el mismo número de átomos entre los dos fragmentos. La incorporación de ambos espaciadores se realizó a través de la formación de un enlace amida entre el grupo carboxilo de cada precursor protegido con Boc y el grupo amino libre de la cumarina. Finalmente, tras eliminación del grupo Boc en condiciones ácidas se obtuvieron los derivados COUPY **20** y **21**.



Esquema 19. Síntesis de los derivados COUPY **20** y **21**.

Síntesis de los conjugados Ir(III)-COUPY

Todos los conjugados Ir(III)-COUPY (**3b-3e**) se sintetizaron mediante la formación de un enlace amida entre el grupo carboxilo del complejo Ir(III) **2b** y el grupo amino libre de los derivados de cumarina conjugables (**10**, **16**, **20** y **21**), siguiendo el mismo procedimiento que el empleado para la preparación del conjugado original (Publicación C). Para ello, a una disolución del complejo **2b** y HATU en DMF anhidra bajo atmósfera de argón, se añadió DIPEA y se dejó reaccionar durante 10 min a temperatura ambiente y protegido de la luz. A continuación, se añadió una solución de los correspondientes derivados de cumarina conjugables (**10**, **16**, **20** y **21**) y DIPEA en DMF anhidra sobre la disolución del complejo metálico activado, y se dejó reaccionar durante 2.5 h a temperatura ambiente, bajo atmósfera de argón y protegido de la luz. Finalmente, los conjugados Ir(III)-COUPY se purificaron por cromatografía en columna de sílice, obteniéndose un sólido de color amarillo oscuro para **3b**, azul oscuro para **3c** y lila oscuro para **3d** y **3e**, con unos rendimientos que oscilaron entre 33 y 68 %. Los conjugados Ir(III)-COUPY se caracterizaron completamente por HR ESI-MS y RMN de ¹H y ¹³C.

Caracterización fotofísica y fotoquímica de los conjugados Ir(III)-COUPY

Las propiedades fotofísicas de los conjugados Ir(III)-COUPY (**3b-3e**) se estudiaron en tres disolventes de diferente polaridad (PBS, ACN y DCM), y se compararon con las del conjugado original **3a**, y con las de los correspondientes fragmentos por separado, tanto del complejo de Ir(III) **2a** que contiene el grupo funcional éster, como de las cumarinas de referencia **1a-1c**, con el anillo de piridina metilado (**Figura 26**). Se estudiaron los máximos de absorción (λ_{max}) y de emisión (λ_{em}), los desplazamientos de Stokes, los coeficientes de extinción molar (ϵ), el rendimiento cuántico de fluorescencia o fosforescencia ($\Phi_{\text{F}}/\Phi_{\text{P}}$), el tiempo de vida media de fluorescencia o fosforescencia ($\tau_{\text{F}}/\tau_{\text{P}}$) y el rendimiento de generación de oxígeno singlete (Φ_{Δ}). En la **Tabla 6** se muestran los valores en PBS y DCM para los conjugados **3a-3e**, el complejo de Ir(III) **2a** y las cumarinas **1a-1c**.

Tal y como se muestra en la **Tabla 6**, las modificaciones estructurales realizadas en el esqueleto de la cumarina tuvieron un fuerte impacto en las propiedades fotofísicas de los compuestos. Por un lado, la sustitución del grupo *N,N*-dialquilamino en la posición 7 de la cumarina por un análogo de cumarina fusionado con julolidina (**1c**), provocó un desplazamiento hacia el rojo en los máximos de absorción y de emisión (p.ej. $\lambda_{\text{abs}} = 548$ nm para la cumarina **1a** vs $\lambda_{\text{abs}} = 572$ nm para **1c**, en ACN). Por el contrario, la ausencia del grupo electrodonador en la cumarina **1b** tuvo un efecto negativo en las propiedades espectroscópicas del fluoróforo, ya que tanto los máximos de absorción como los de emisión se desplazaron fuertemente hacia el azul debido a la disminución del carácter “*push-pull*” del cromóforo (p.ej. $\lambda_{\text{abs}} = 548$ nm para **1a** vs $\lambda_{\text{abs}} = 446$ nm para **1b**, en ACN). Como era de esperar, el conjugado con el análogo de cumarina fusionado con julolidina (**3c**) también presentó los máximos de absorción y emisión desplazados hacia el rojo (25-30 nm dependiendo del disolvente), mientras que los conjugados **3d** y **3e** que contienen el espaciador flexible y rígido, respectivamente, mostraron máximos de absorción y emisión similares a los del conjugado original **3a** en todos los disolventes investigados, debido a que contienen la misma cumarina. Finalmente, los valores del rendimiento cuántico de fluorescencia también fueron similares para los tres conjugados, alrededor de 0,1 en DCM y ACN, y por debajo de 0.02 en PBS. Respecto al conjugado Ir(III)-COUPY **3b**, prácticamente no mostró fluorescencia en ningún disolvente, concordando así con el comportamiento de la cumarina **1b**.

Tabla 6. Propiedades fotofísicas de los compuestos **1a-1c**, **2a** y **3a-3e** en PBS y DCM.

	Disol.	λ_{\max} (nm)	ϵ (mM ⁻¹ cm ⁻¹)	λ_{em} (nm)	Despl. Stokes (nm)	$\Phi_{\text{F}}/\Phi_{\text{F}}$	τ_{F}	τ_{P}	Φ_{Δ}
1a	PBS	545	34	604	59	0.14	0.9	-	≈ 0
	DCM	569	67	607	38	0.70	5.4	-	<0.01
1b	PBS	443	23	486	43	0.002	3.37	-	≈ 0
	DCM	456	23	506	50	0.007	3.52	-	0.01
1c	PBS	557	38	629	72	0.031	0.031	-	≈ 0
	DCM	597	61	631	34	0.53	5.46	-	0.03
2a	PBS	305	40	656	351	>0.01	-	55 (93%) 281 (7%)	<0.01
	DCM	303	42	665	362	0.07	-	315	0.23
3a	PBS	550	17	615	65	0.004	0.37 (73%) 3.3 (27%)	-	<0.01
	DCM	566	44	602	36	0.07	0.25	121 (70%) 392 (30%)	0.37
3b	PBS	436	17	-	-	≈ 0	-	39 (52%) 211 (48%)	<0.01
	DCM	457	26	664	-	0.01	-	329	0.21
3c	PBS	575	13	610	35	0.003	1.4	317 (78%) 43 (22%)	<0.01
	DCM	592	26	629	37	0.17	2.66	69 (80%) 298 (20%)	0.20
3d	PBS	550	21	612	62	0.017	1.11	307 (72%) 1900(28%)	<0.01
	DCM	567	45	599	32	0.09	2.94	333 (89%) 59 (11%)	0.39
3e	PBS	541	20	618	77	0.006	1.03	315 (68%) 1913(32%)	<0.01
	DCM	566	40	600	34	0.08	0.55 (62%) 3.34 (38%)	377 (64%) 109(36%)	0.34

Seguidamente, nos centramos en investigar el impacto de las modificaciones estructurales en la generación de ROS por parte de los nuevos conjugados Ir(III)-COUPY. De la misma manera que ocurría en la cumarina original **1a**, ni **1b** ni **1c** generaron $^1\text{O}_2$. Curiosamente, todos los nuevos conjugados Ir(III)-COUPY generaron $^1\text{O}_2$ en DCM y ACN, pero no en PBS. Los conjugados **3d** y **3e**, con el mismo derivado de cumarina que el compuesto original (**3a**) mostraron rendimientos cuánticos de singlete oxígeno similares (aprox. 0.30-0.40 en DCM) independientemente del espaciador que une ambos fragmentos, mientras que los conjugados con los nuevos derivados de cumarina, **3b** y **3c**, exhibieron valores algo más bajos (aprox. 0.20 en DCM).

Teniendo en cuenta que una de las características principales del conjugado original Ir(III)-COUPY **3a** es la generación de radicales anión superóxido ($\text{O}_2^{\cdot-}$) en células vivas tras la irradiación con luz visible, investigamos la capacidad de los nuevos conjugados para producir este ROS de tipo I mediante el uso de un método espectroscópico basado en la sonda de dihidrorodamina 123 (DHR123). Como se muestra en la **Figura 27**, ninguno de los conjugados Ir(III)-COUPY produjo $\text{O}_2^{\cdot-}$ de forma significativa antes de la irradiación, resultado comparable al obtenido con la sonda DHR123 sola tras la irradiación, utilizada como control negativo. Sorprendentemente, tras irradiación con luz verde, todos los conjugados, incluido el que contiene el fluoróforo de cumarina sin el grupo amino en la posición 7, aumentaron claramente la intensidad de fluorescencia de DHR123 en mayor medida que el complejo Ir(III) **2a** y los derivados de COUPY **1a-1c**, confirmando así la generación de radicales anión superóxido.

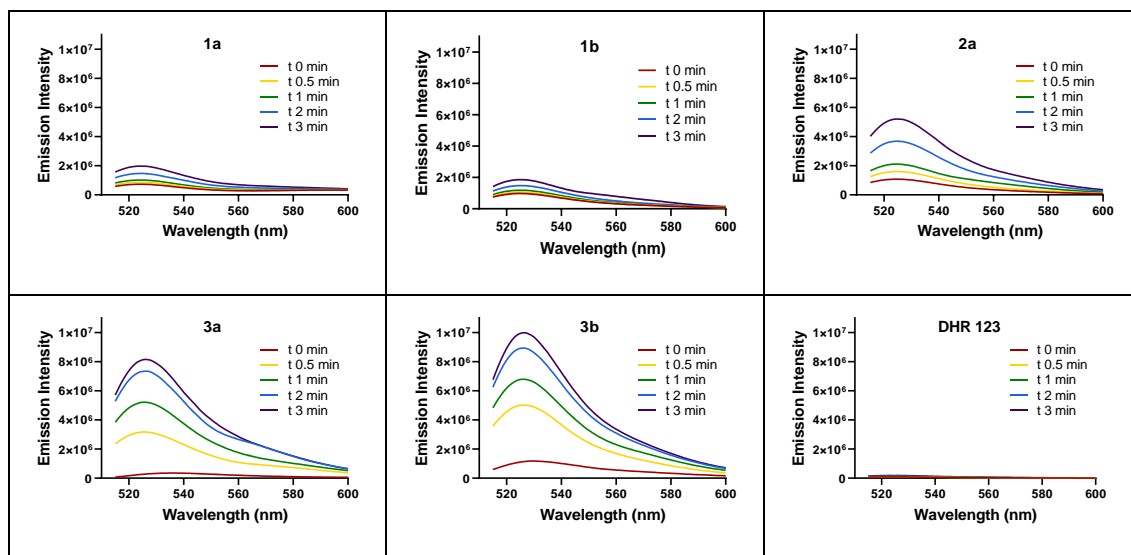


Figura 27. Espectros de fluorescencia de la sonda DHR123 inducidos por irradiación con luz visible (505 nm) en presencia de las cumarinas COUPY **1a** y **1b**, el complejo Ir(III) **2a**, los conjugados Ir(III)-COUPY **3a** y **3b**, o en ausencia de compuesto (DHR 123 sola).

Evaluación biológica de los conjugados Ir(III)-COUPY

En primer lugar, se cuantificó la acumulación celular de Ir mediante espectrometría de masas por plasma acoplado inductivamente (ICP-MS) tras incubación de células A2780cis con los compuestos de Ir. Como se muestra en la **Figura 28**, los niveles intracelulares de Ir oscilaron entre 185 ± 40 y 261 ± 25 ng/ 10^6 células para las células tratadas con los conjugados Ir(III)-COUPY **3a**, **3b**, **3e** y **3d**, siendo comparables a los resultados obtenidos con el complejo de Ir(III) **2a** (276 ± 12). Sorprendentemente, la cantidad de metal en las células tratadas con el conjugado **3c** fue considerablemente mayor (461 ± 74 ng Ir por millón de células), lo que indica que el sistema fusionado con julolidina **3c** conduce a una mejora en la internalización celular.

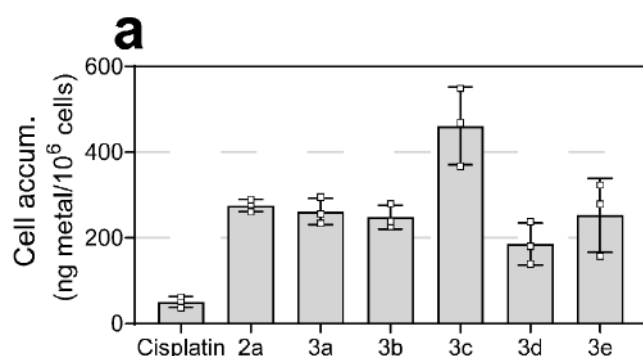


Figura 28. Acumulación celular de Ir determinada por ICP-MS en células A2780cis a 37 °C.

Por otro lado, también se estudió la internalización de los nuevos conjugados Ir(III)-COUPY en células HeLa mediante microscopia confocal irradiando con un láser de luz amarilla ($\lambda_{\text{ex}} = 561$ nm). Como se muestra en la **Figura 29**, todos los conjugados que contienen un derivado COUPY con emisión en el rojo lejano (**3c-3e**) internalizaron de forma eficiente en las células y mostraron el mismo patrón que el conjugado original **3a**, observándose vesículas fluorescentes en el citoplasma.

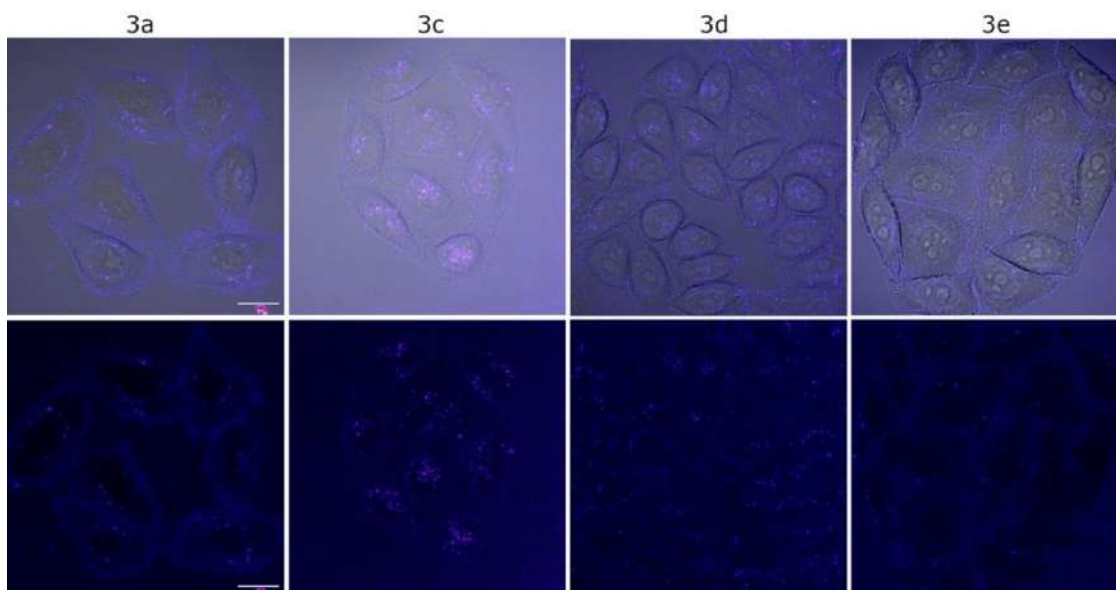


Figura 29. Experimentos de internalización mediante microscopía confocal en células HeLa de los conjugados Ir(III)-COUPY **3a-3e**.

Una vez comprobado que los nuevos conjugados Ir(III)-COUPY internalizaban de forma eficiente en células HeLa, se llevaron a cabo estudios de citotoxicidad en diversas líneas celulares y utilizando las cumarinas **1a-1c** y el complejo de Ir(III) **2a** como compuestos de referencia. La selección de líneas celulares incluyó dos líneas celulares de melanoma (A375 y SK-MEL-28), así como células cancerígenas con resistencia al fármaco clínico cisplatino. Para este último, se utilizaron células de cáncer de ovario sensibles y resistentes al cisplatino (A2780 y A2780cis), así como células HeLa, que también muestran un grado de quimiorresistencia al fármaco anticancerígeno de platino *in vitro*.

Tal y como se muestra en la **Tabla 7**, todos los compuestos, excepto la cumarina **1c**, no mostraron toxicidad alguna en la oscuridad. Por lo tanto, la incorporación del sistema fusionado con julolidina en el fluoróforo COUPY contribuye a en aumentar su citotoxicidad en la oscuridad. Ahora bien, cabe destacar que el conjugado formado por el complejo de Ir(III) y la cumarina **1c** no mostró citotoxicidad en la oscuridad.

Seguidamente se estudió la fototoxicidad de todos los compuestos mediante irradiación con luz verde (520 nm). En general, la irradiación con luz visible mejoró claramente la actividad anticancerígena de todos los conjugados en todas las líneas celulares de cáncer estudiadas, con valores IC₅₀ en el rango micromolar.

La cumarina **1b**, sin el grupo *N,N*-dialquilamino en la posición 7, no mostró actividad antitumoral tras la irradiación de luz en ninguna de las líneas celulares investigadas, probablemente debido a que su absorción se encuentra desplazada hacia el azul. Por el contrario, la cumarina COUPY original **1a** mostró una alta fototoxicidad, particularmente en las células de melanoma. El conjugado correspondiente (**3b**) mostró un ligero aumento en la actividad fototóxica en comparación con **1b**. Esto podría atribuirse al núcleo de Ir(III) del PS porque el complejo **2a** de Ir(III) presentó una actividad inhibidora moderada tras la irradiación. No obstante, la fotocitotoxicidad del conjugado **3b** fue menor que la del conjugado **3a** en todas las líneas de celulares (valores de IC₅₀ entre 3 y 78 µM en comparación con 0,7 y 18 µM). Para comprobar si la escasa fototoxicidad de **3b** se debía a su absorción desplazada hacia al azul, también se ensayó la fotoactivación con luz azul (465 nm). Como se presenta en la Tabla S4 del artículo, las células A2780cis incubadas con **3b** generaron valores de IC₅₀ muy similares a los obtenidos para **3a** después de la irradiación con luz azul (2,4 y 1,9 µM, respectivamente).

Por otro lado, la sustitución del grupo *N,N*-dialquilamino de la cumarina por un sistema fusionado con julolidina disminuyó la fototoxicidad del conjugado **3c** en células A375, SK-MEL-28 y HeLa en comparación con el conjugado **3a**. Sin embargo, el comportamiento de **3c** después de la irradiación con luz verde fue similar al de **3a** en las células cancerígenas A2780 y A2780cis, con valores IC₅₀ entre 0,7 y 2,1 µM.

La fotoactivación con luz verde más potente se encontró en células de cáncer de ovario, particularmente en células resistentes A2780cis, donde los valores de PI fueron notablemente más altos que para las otras líneas celulares (>143 para **3a**, >96 para **3c**, >90 para **3d** y >107.5 para **3e**).

Tabla 7. Cito- y fototoxicidad de los compuestos en células cancerosas de cuello uterino y ovario.

	HeLa			A2780			A2780cis		
	Oscur.	520 nm	PI	Oscur.	520 nm	PI	Oscur.	520 nm	PI
1a	>100	5.8 ± 0.4	>17.2	>100	5.2 ± 0.5	19.2	>100	2.1 ± 0.2	47.6
1b	>100	>100	1.0	>100	>100	1.0	>100	>100	1.0
1c	26 ± 4	1.1 ± 0.8	23.6	5.1 ± 0.9	0.09 ± 0.01	56.7	15 ± 2	0.15 ± 0.04	100.0
2a	>100	75 ± 6	>1.3	>100	4 ± n.d.	>25.0	>100	3.5 ± 0.4	28.6
3a	>100	8.6 ± 0.7	>11.6	>100	1.07 ± 0.07	>93.5	>100	0.7 ± 0.06	>142.9
3b	>100	18 ± 2	>5.6	>100	7.1 ± 0.1	>14.1	>100	61 ± 8	>1.6
3c	>100	45 ± 4	>2.2	>100	2.1 ± 0.2	>47.6	>100	1.04 ± 0.02	>96.2
3d	>100	2.0 ± 0.4	>50.0	>100	1.78 ± 0.07	>56.2	>100	1.1 ± 0.2	>90.9
3e	>100	9.3 ± 0.8	>10.8	>100	1.9 ± 0.2	>52.6	>100	0.93 ± 0.04	>107.5

En base a los buenos resultados obtenidos por los Ir(III)-COUPY en la línea A2780cis tras irradiación con luz verde, se evaluó su fototoxicidad en condiciones hipóxicas. En esta segunda prueba de fotocitotoxicidad, la citotoxicidad en la oscuridad se volvió a calcular usando concentraciones más altas dado que los compuestos se consideraron inactivos a 100 μ M. A excepción de la cumarina **1c**, no se pudieron determinar valores de IC₅₀ en la oscuridad, ni en normoxia ni en hipoxia, por debajo de 250 μ M. Como se muestra en la Tabla S3 del artículo, los valores más altos de PI en normoxia se lograron con **3a** (>357), seguido de los conjugados **3d** y **3e** (>227 y >269, respectivamente). Sin embargo, bajo condiciones de hipoxia, el efecto fotodinámico de **3a** disminuyó significativamente (PI > 66), mientras que **3d** y **3e** produjeron una fotocitotoxicidad más alta, con valores de PI >131 y >147, respectivamente. Por otro lado, el conjugado **3c**, que contiene el anillo de julolidina, mostró un valor de PI similar en normoxia (> 240), pero fue mucho menos fotoactivo en hipoxia (PI > 31). Finalmente, no se observó fototoxicidad significativa para **3b** tras la irradiación con luz verde ni en normoxia ni en hipoxia.

Una vez confirmada la existencia de una estrecha relación entre la citotoxicidad de los compuestos y la irradiación con luz visible, el siguiente paso consistió en investigar la generación de ROS en células A2780cis en condiciones de normoxia e hipoxia (**Figura 30**). Aunque todos los conjugados generaron un nivel basal de ROS intracelular en la oscuridad, es destacable el notable incremento en la producción de ROS en el caso de los conjugados que contienen un derivado de cumarina con un grupo EDG en la posición 7 (**3a**, **3c-3e**), tras irradiación con luz verde en comparación con los compuestos libres, tanto en condiciones de normoxia como en hipoxia. Por otro lado, en el caso del conjugado **3b**, que contiene la cumarina sin el grupo EDG en la posición 7, aunque no fue tan notorio como el resto de los conjugados, también aumentó la producción de ROS tras irradiación de luz visible, sobre todo en condiciones de hipoxia.

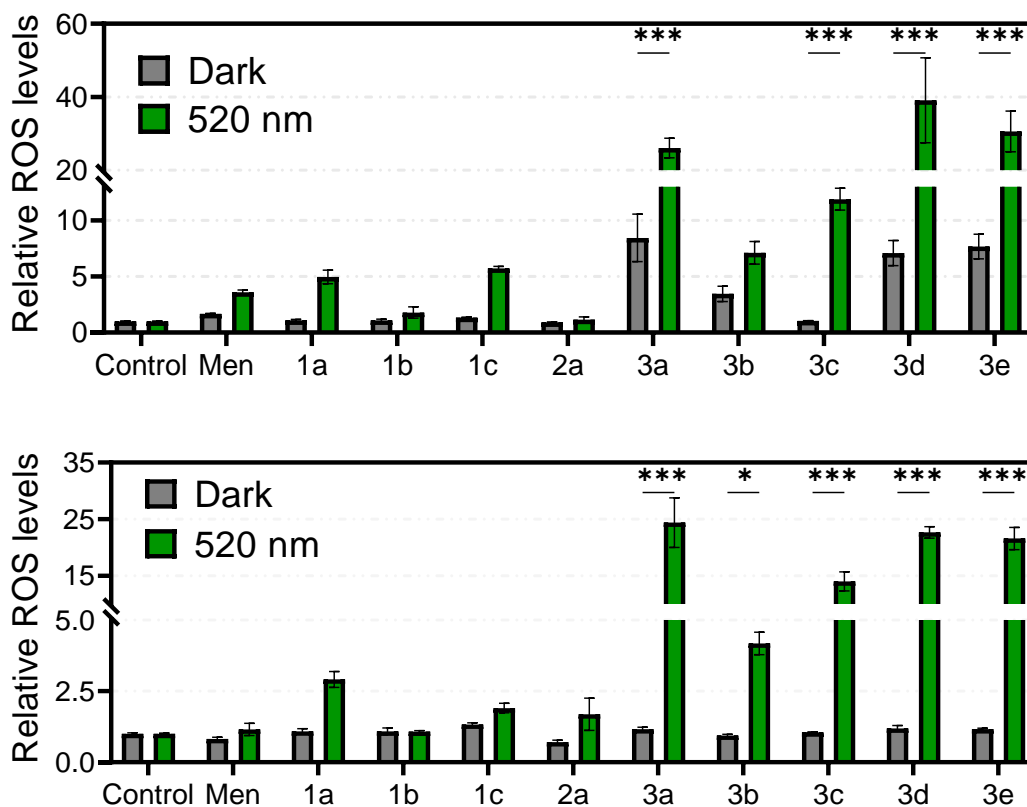


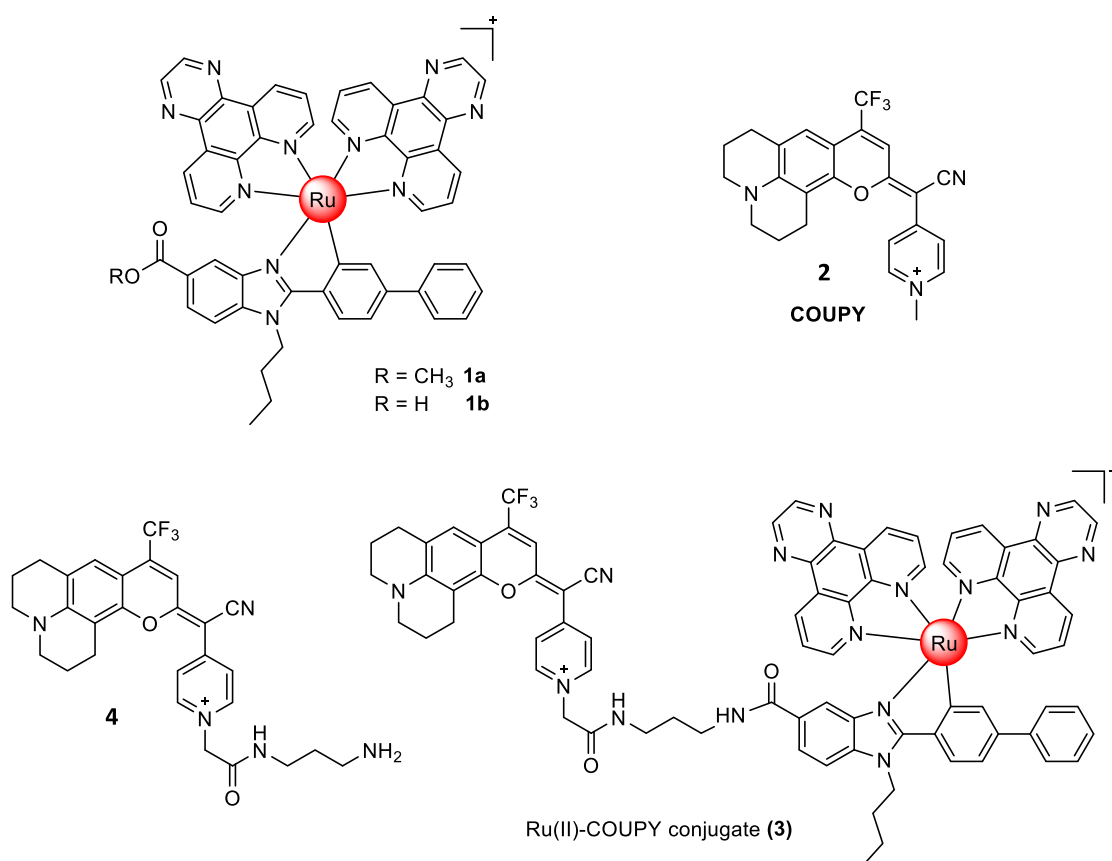
Figura 30. Niveles relativos de ROS en células A2780cis en condiciones de normoxia (arriba) e hipoxia (abajo).

Capítulo IIc

Resultados no publicados: A. Rovira *et al.* Development of a new photosensitizer based on the conjugation of a NIR-emitting COUPY dye to a cyclometalated Ru(II) polypyridyl complex.

Nota: En el resumen se ha mantenido la numeración de los compuestos del artículo para facilitar su búsqueda.

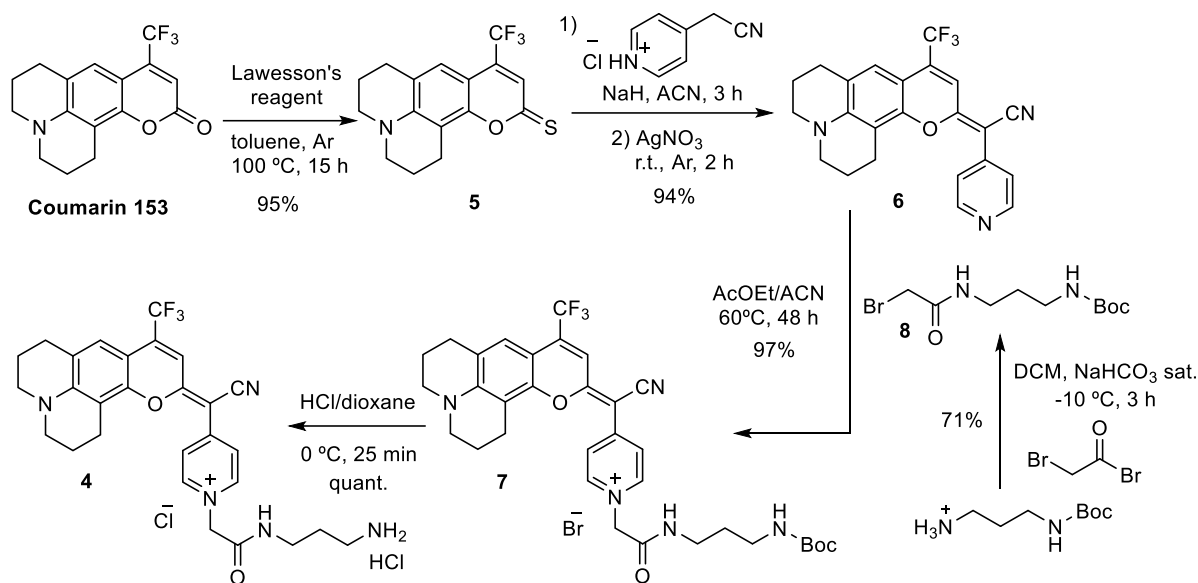
En este trabajo, se ha diseñado y sintetizado un nuevo agente fotosensibilizador basado en un conjugado entre un complejo ciclometalado de Ru(II) tipo polipiridilo (**1a**) y un fluoróforo COUPY que incorpora tanto un anillo de julolidina como un grupo CF_3 en la posición 4 del esqueleto de cumarina (**2**). Dicho fluoróforo presenta un máximo de absorción desplazado hacia el rojo lejano y emisión en el NIR. Además de realizar estudios de internalización celular mediante microscopia confocal, también se determinó la fototoxicidad tanto del conjugado Ru(II)-COUPY **3** como de los dos componentes por separado (complejo de Ru(II) y fluoróforo COUPY) tras irradiación con luz roja.



Esquema 20. Estructura de los complejos de Ru(II) **1a** y **1b**, de las cumarinas COUPY **2** y **4** y del conjugado Ru(II)-COUPY **3**.

Síntesis del fluoróforo COUPY conjugable 4

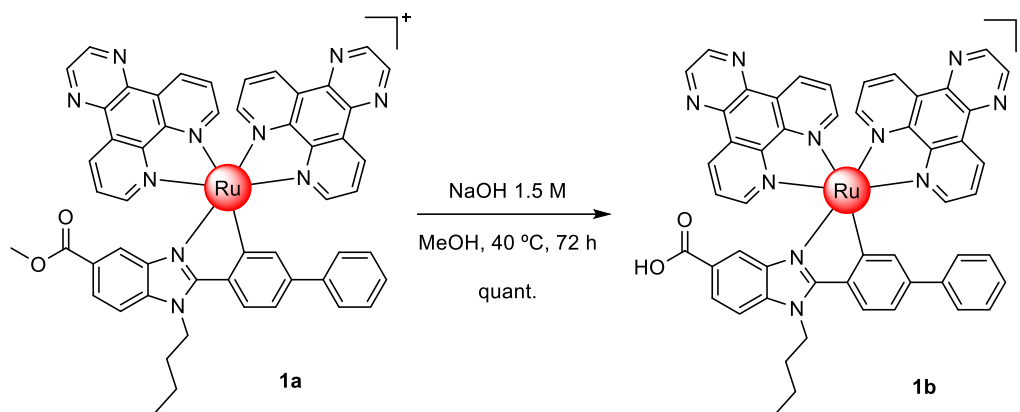
Tal y como se muestra en el **Esquema 21**, el derivado de cumarina **6** se sintetizó a partir de un precursor comercial (cumarina 153) en dos pasos lineales siguiendo los procedimientos descritos anteriormente en el capítulo I. A continuación, la cumarina **6** se hizo reaccionar con el espaciador **8** previamente sintetizado en un medio AcOEt/ACN durante 48 h a 60 °C y protegido de la luz, obteniéndose el derivado de cumarina **7**. Finalmente, la eliminación del grupo protector Boc mediante tratamiento ácido dio lugar al derivado de cumarina **4**, el cual contiene el grupo funcional amino necesario para el acoplamiento con el complejo metálico.



Esquema 21. Síntesis del derivado COUPY **4**.

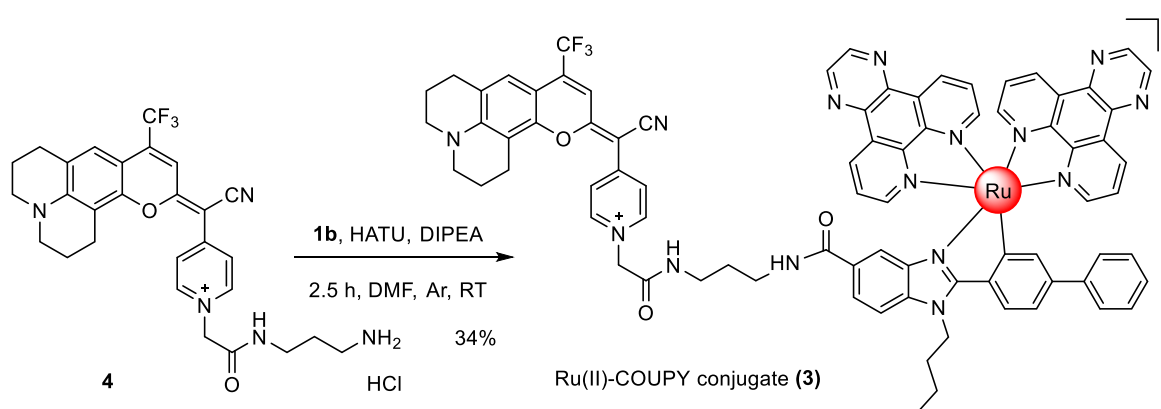
Síntesis y caracterización del conjugado Ru(II)-COUPY **3**

En primer lugar, fue necesario hidrolizar el grupo éster del complejo de Ru(II) **1a** en condiciones básicas a 40 °C durante 72 h y protegido de la luz con el objetivo de disponer del grupo carboxilo necesario para el acoplamiento con el derivado de cumarina **4** a través de un enlace amida (**Esquema 22**). El crudo obtenido se usó sin purificación adicional ya que el análisis HPLC-MS reveló que la hidrólisis del grupo éster fue cuantitativa.



Esquema 22. Hidrólisis del grupo éster del complejo de Ru(II) **1a**.

La unión del complejo ciclometalado de Ru(II) al fluoróforo COUPY se llevó a cabo mediante la formación de un enlace amida entre el grupo carboxilo del complejo **1b** y el grupo amino de la cumarina **4** (**Esquema 23**). Para ello, a una disolución del complejo **1b** y HATU en DMF anhidra bajo atmosfera de argón, se añadió DIPEA y se dejó reaccionar durante 10 min a temperatura ambiente y protegido de la luz. A continuación, se añadió una solución de la cumarina **4** y DIPEA en DMF anhidra sobre la disolución del complejo metálico activado, y se dejó reaccionar durante 2.5 h a temperatura ambiente, bajo atmosfera de argón y protegido de la luz. Finalmente, el conjugado Ru(II)-COUPY **3** se purificó por cromatografía en columna de alúmina neutra, obteniéndose un sólido de color azul oscuro con un rendimiento del 34%. El conjugado se caracterizó por HR ESI-MS.



Esquema 23. Síntesis del conjugador Ru(II)-COUPY **3**.

Para la purificación del conjugado se abordaron diferentes estrategias, pero sólo el uso de alúmina neutra proporcionó el compuesto deseado con un nivel de pureza óptimo. Como se muestra en los cromatogramas de HPLC, la purificación mediante cromatografía en columna de gel de sílice provocaba la descomposición de la molécula, generando un fragmento del conjugado sin el rutenio (**Figura 31**). Por otra parte, la purificación por HPLC de fase inversa, utilizando como fase móvil H₂O + 0.1% ácido fórmico y ACN + 0.1% ácido fórmico, también provocaba su descomposición, en este caso como consecuencia de la rotura del doble enlace exocíclico de la cumarina (**Figura 32**).

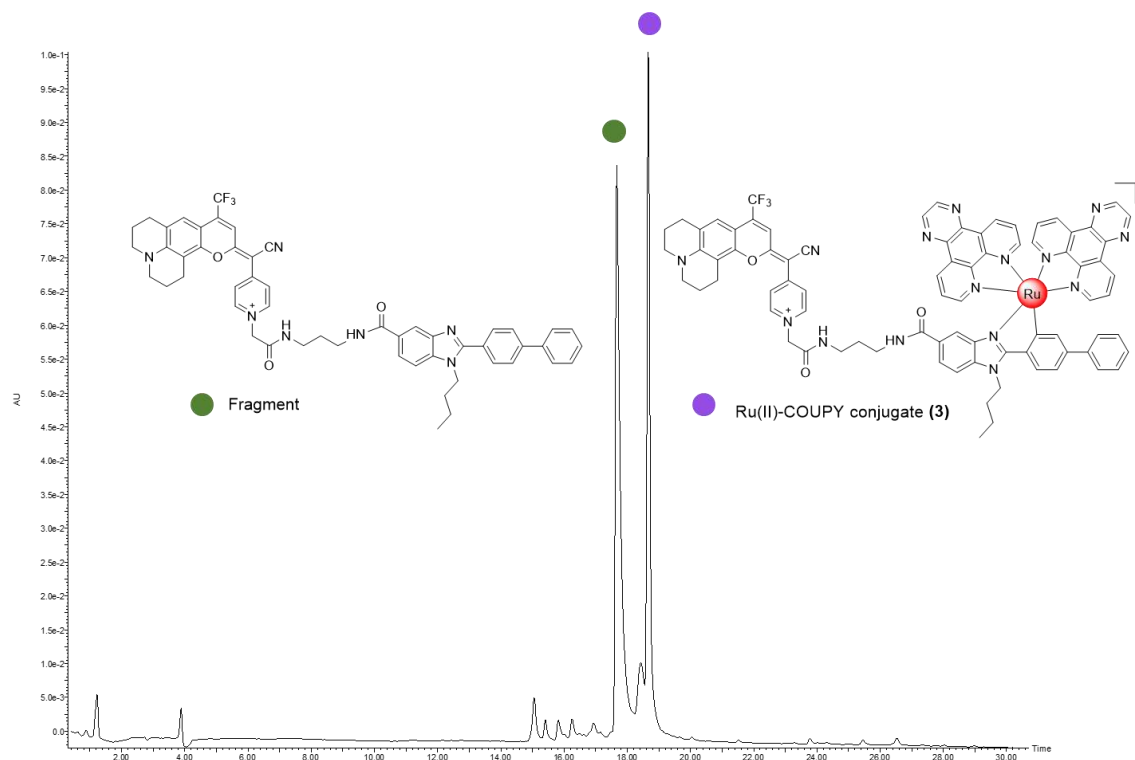


Figura 31. Análisis por HPLC de fase inversa del conjugado Ru(II)-COUPY purificado mediante cromatografía en columna de gel de sílice.

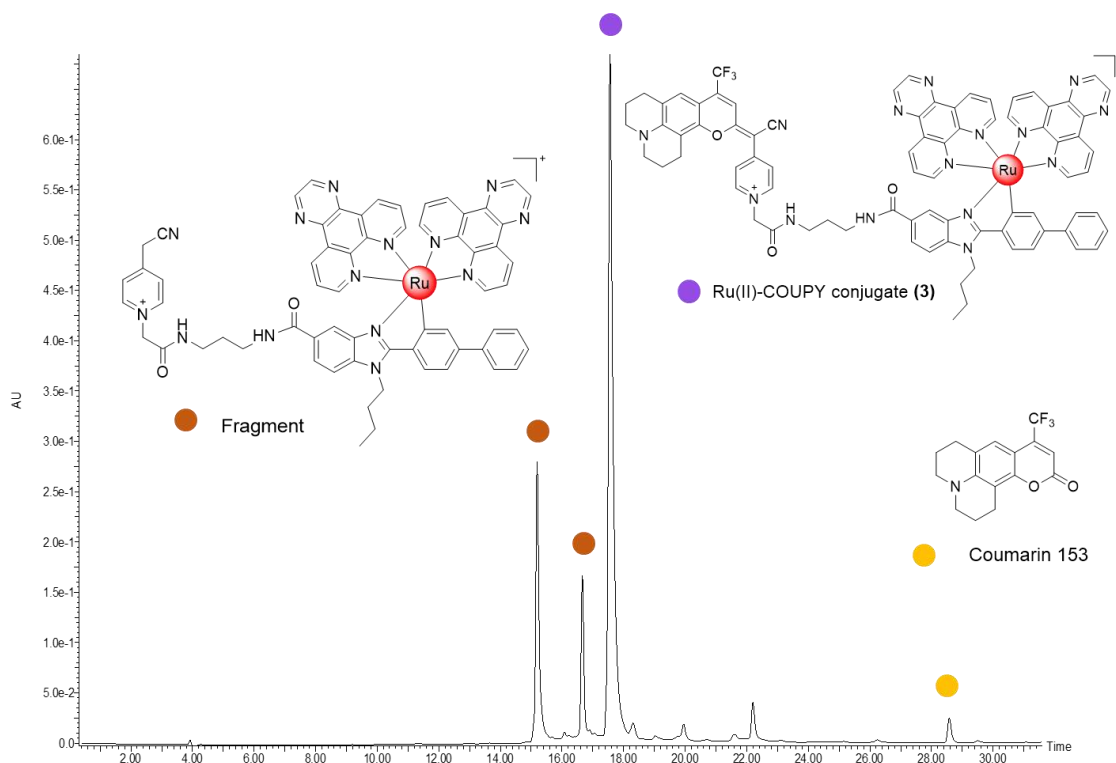


Figura 32. Análisis por HPLC de fase inversa del conjugado Ru(II)-COUPY purificado mediante HPLC.

Caracterización fotofísica de los compuestos

Las propiedades fotofísicas (espectros de absorción y emisión, y rendimiento cuántico de fluorescencia (Φ_F)) del nuevo conjugado Ru(II)-COUPY **3** junto con el complejo de Ru(II) **1a** y el fluoróforo COUPY **2** se estudiaron en CH_3CN . Los espectros de absorción y emisión se muestran en la **Figura 33**, y sus propiedades fotofísicas se resumen en la **Tabla 8**.

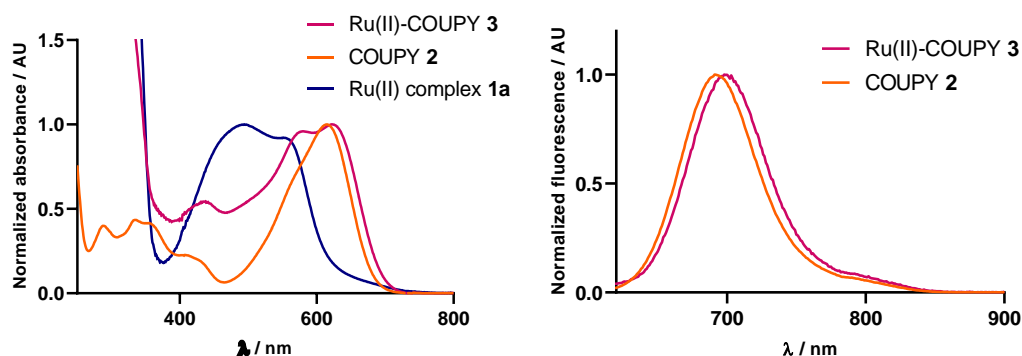


Figura 33. Comparación de los espectros normalizados de absorción (izquierda) y emisión (derecha) de los compuestos en CH_3CN .

Como se muestra en la **Tabla 8**, el derivado de cumarina (COUPY **2**) muestra unos máximos de absorción y emisión en la región del rojo lejano/NIR del espectro electromagnético (615 y 691 nm, respectivamente), lo que se atribuye tanto a la incorporación del grupo CF₃ en la posición 4 del esqueleto de cumarina como a la fusión del anillo de julolidina. Es destacable el hecho que se produzca un desplazamiento hacia el rojo adicional en los máximos de absorción (8 nm) y emisión (7 nm) como consecuencia de la conjugación con el complejo de Ru(II). Sin embargo, el rendimiento cuántico de fluorescencia del conjugado Ru(II)-COUPY **3** fue menor que el del fluoróforo COUPY **2**.

Tabla 8. Propiedades fotofísicas de los compuestos **1a**, **2** y **3**.

Compuesto	λ_{max} (nm)	λ_{em} (nm)	Desplazamiento de Stokes (nm)	Φ_{F}	Disolvente
Complejo de Ru(II) 1a	258, 288, 321, 493, 561	356, 367 711	-	-	CH ₃ CN
COUPY 2	615	691	76	0.046	CH ₃ CN
Ru(II)-COUPY 3	623	698	75	0.007	CH ₃ CN

Generación de oxígeno singlete (¹O₂) y radicales anión superóxido (O₂^{•-}) tras la irradiación con luz visible

El complejo de Ru(II) **1a**, descrito anteriormente por el grupo de investigación del profesor José Ruiz de la Universidad de Murcia, se había revelado muy fototóxico en células cancerígenas HeLa y A2780cis tanto en condiciones de normoxia como de hipoxia.²⁸ En condiciones de normoxia, dicho complejo fotogenera en células HeLa principalmente H₂O₂, y en menor medida •OH. Sin embargo, bajo hipoxia, el complejo Ru(II) también fue capaz de fotogenerar tanto H₂O₂ como O₂^{•-}.

En base a estos antecedentes, se evaluó espectroscópicamente la capacidad tanto del conjugado Ru(II)-COUPY **3** como del fluoróforo COUPY **2** y del complejo Ru(II) **1a** de inducir la generación de $^1\text{O}_2$ y $\text{O}_2^{\bullet-}$. El complejo Ru(II) **1a** no produjo $^1\text{O}_2$ en ninguno de los disolventes evaluados, reproduciéndose así los resultados obtenidos previamente para este complejo por el grupo del profesor Ruiz en células HeLa. Por otra parte, de forma similar a los derivados COUPY anteriormente evaluados en esta Tesis, COUPY **2** tampoco produjo $^1\text{O}_2$ en ningún disolvente. Sin embargo, a diferencia de lo ocurrido en el caso de los conjugados Ir(III)-COUPY descritos en las Publicaciones C y D, la conjugación entre el complejo de Ru(II) y el fluoróforo COUPY no aumentó el rendimiento cuántico de generación de $^1\text{O}_2$. Por tanto, se puede concluir que el conjugado de Ru(II)-COUPY **3** no produce oxígeno singlete en ningún disolvente evaluado (**Tabla 9**).

Tabla 9. Rendimientos cuánticos de oxígeno singlete.

Compuesto	Disolvente	Φ_{Δ} a 355 nm	Φ_{Δ} a 532 nm
Complejo de Ru(II) 1a	PBS	≈ 0	< 0.01
	CH ₃ CN	0.07	0.09
	CH ₂ Cl ₂	0.07	0.08
COUPY 2	PBS	≈ 0	< 0.01
	CH ₃ CN	0.01	0.01
	CH ₂ Cl ₂	0.02	0.01
Ru(II)-COUPY 3	PBS	≈ 0	< 0.01
	CH ₃ CN	≈ 0	< 0.01
	CH ₂ Cl ₂	0.02	0.02

Finalmente, teniendo en cuenta que una de las características principales de los conjugados descritos anteriormente en las Publicaciones C y D entre fluoróforos COUPY y un complejo de Ir(III) es la generación de radicales anión superóxido ($O_2^{\cdot-}$) tras irradiación con luz visible, investigamos la capacidad del conjugado Ru(II)-COUPY de producir este tipo de ROS mediante el uso de un método espectroscópico basado en la sonda de DHR123.²⁹ Como se muestra en la **Figura 34**, aunque el fluoróforo COUPY **2** y el complejo Ru(II) **1a** también producen $O_2^{\cdot-}$ tras irradiación con luz verde (505 nm), la conjugación entre ambos fragmentos condujo a un aumento en la generación de $O_2^{\cdot-}$. Vale la pena señalar que todos los compuestos generaron cierta cantidad de $O_2^{\cdot-}$ en la oscuridad ya que la intensidad de la fluorescencia es superior a $t = 0$ cuando se compara con los resultados obtenidos con la sonda de DHR123 por sí sola, utilizada como control negativo.

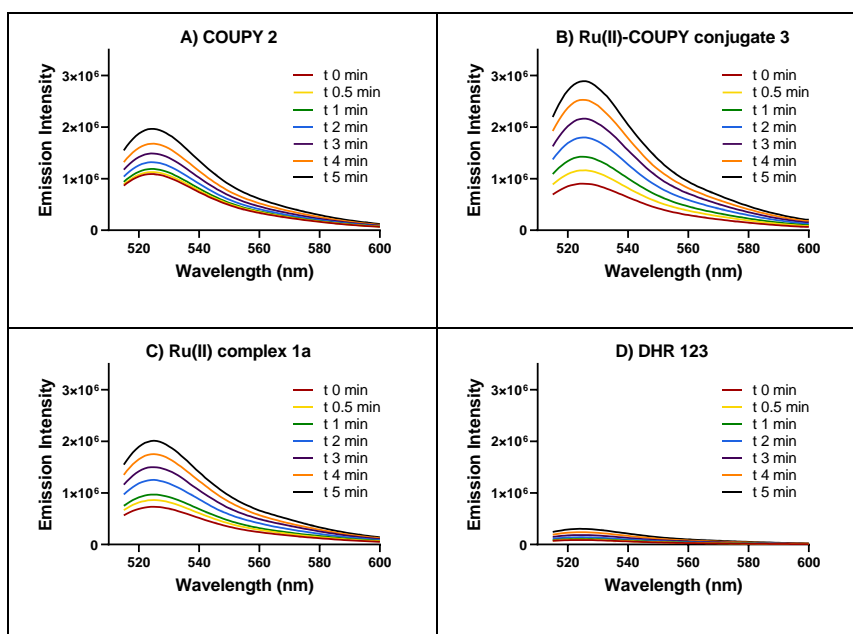


Figura 34. Espectros de fluorescencia de DHR123 inducidos tras irradiación con luz verde (505 nm) en presencia de (A) COUPY **2**, (B) Ru(II)-COUPY **3**, (C) complejo de Ru(II) **1a** o (D) sin compuesto (DHR123 sólo).

Evaluación biológica del conjugado Ru(II)-COUPY

En primer lugar, se estudió la internalización del conjugado Ru(II)-COUPY **3** en células HeLa mediante microscopía confocal tras irradiación con un láser de luz amarilla ($\lambda_{ex} = 561$ nm) o roja ($\lambda_{ex} = 633$ nm). Como se muestra en la **Figura 35**, el conjugado **3** internalizó de forma eficiente en las células, observándose vesículas fluorescentes en el citoplasma y, en menor medida, marcaje de la membrana celular a las dos longitudes de onda utilizadas.

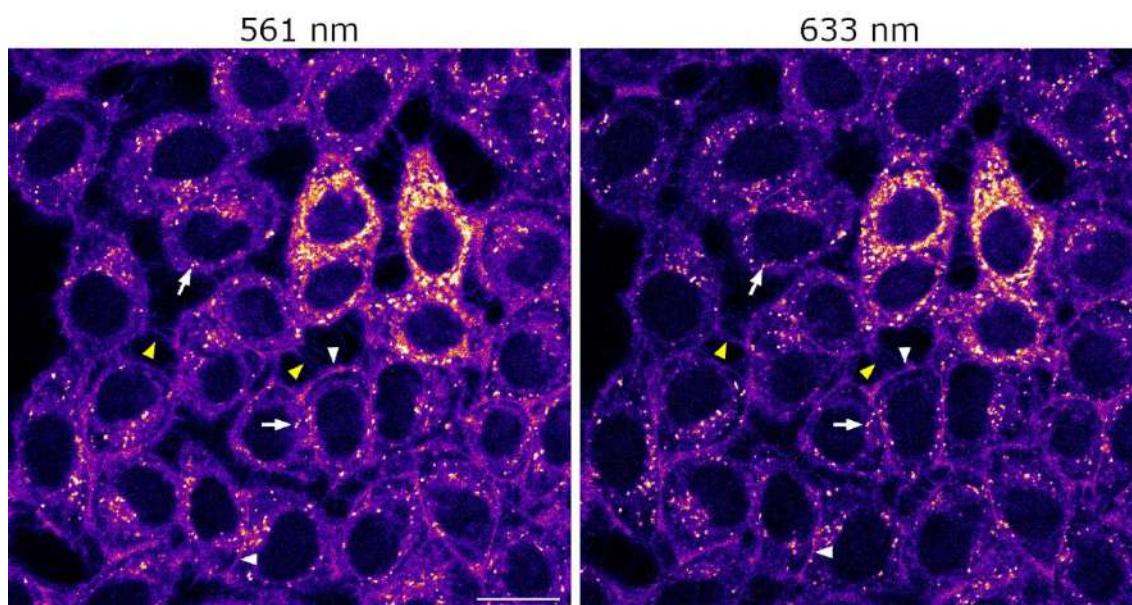


Figura 35. Experimentos de internalización mediante microscopía confocal en células HeLa del conjugado Ru(II)-COUPY **3** (10 μ M, 30 min, 37 $^{\circ}$ C). El conjugado **3** se excitó tanto con el láser de 561 nm (izquierda) como con el láser de 633 nm (derecha) y, en ambos casos, la emisión se detectó entre 650 y 750 nm. Las flechas blancas señalan vesículas, las puntas de flecha blancas la membrana celular y las puntas de flecha amarillas señalan las protuberancias filopodiales.

Seguidamente, se evaluó la citotoxicidad del conjugado de Ru(II)-COUPY en células HeLa, utilizando la cumarina **2** y el complejo de Ru(II) **1a** como compuestos de referencia. El conjugado **3** no mostró toxicidad en la oscuridad, a diferencia del complejo de Ru(II) **1a**, lo que indica que, al igual que en el caso de los conjugados Ir(III)-COUPY, la conjugación entre el complejo metálico y el fluoróforo COUPY conduce a una disminución de la citotoxicidad. Una vez determinada la citotoxicidad de los compuestos en la oscuridad, se estudió su fototoxicidad irradiando con luz roja. Tal y como se muestra en la **Tabla 10**, la irradiación con luz visible mejoró claramente la actividad antitumoral del conjugado **3**, obteniéndose un valor de IC_{50} de 2.9 μ M. Por otro lado, también son especialmente destacables los valores de IC_{50} y de PI del nuevo derivado de cumarina **2**, 0.38 μ M y 160.5, respectivamente.

Tabla 10. Cito- y fototoxicidad de los compuestos en células HeLa.

	Oscuridad	Luz roja	
	IC_{50} [μ M]	IC_{50} [μ M]	PI
Complejo Ru(II) 1a	7 ± 1	0.11 ± 0.03	63.6
COUPY 2	61 ± 4	0.38 ± 0.04	160.5
Conjugado Ru(II)-COUPY 3	>100	2.9 ± 0.3	>34.5

Conclusiones

Se han diseñado, sintetizado y caracterizado nuevos agentes fotosensibilizadores para la terapia fotodinámica anticancerígena basados en la conjugación de diferentes fluoróforos COUPY a complejos ciclometalados de Ir(III) y Ru(II). Así, en primer lugar, se llevó a cabo la síntesis y caracterización fotofísica, fotoquímica y biológica de un fotosensibilizador basado en un conjugado entre un complejo ciclometalado de Ir(III) y un fluoróforo COUPY con emisión en el rojo lejano. Dicho fotosensibilizador mostró características muy interesantes para la terapia fotodinámica, como son una excelente internalización celular, ausencia de citotoxicidad en la oscuridad y una elevada fototoxicidad tras irradiación con luz visible, tanto en normoxia como en hipoxia. Además, el conjugado Ir(III)-COUPY es capaz de generar radicales anión superóxido (ROS de tipo I) tras irradiación tanto con luz azul como con verde.

En base a estos buenos resultados, se llevó a cabo la síntesis de 4 nuevos fotosensibilizadores a través de la conjugación del complejo de Ir(III) original con diferentes derivados de fluoróforos COUPY, con el objetivo de establecer relaciones estructura-actividad (SARS, por sus siglas en inglés). Las modificaciones estructurales realizadas dentro del esqueleto de cumarina tuvieron un fuerte impacto en las propiedades fotofísicas tanto de los fluoróforos COUPY como de los conjugados. Además, se encontró que ninguno de los conjugados Ir(III)-COUPY mostró toxicidad en la oscuridad, independientemente de la línea celular evaluada, pero si exhibieron una elevada fototoxicidad tras irradiación con luz visible, lo que condujo a valores de PI relativamente altos. Por otro lado, se demostró mediante métodos espectroscópicos la generación fotoinducida de diferentes tipos de ROS (tipo II $^1\text{O}_2$ y tipo I $\text{O}_2^{\cdot-}$) para todos los conjugados Ir(III)-COUPY. Además, la generación de ROS también se confirmó en células cancerígenas A2780cis resistentes al cisplatino, tanto en normoxia como en hipoxia. Por este motivo, la buena fotoactividad en condiciones de normoxia e hipoxia unida a la ausencia de citotoxicidad en la oscuridad, así como unas excelentes propiedades fotofísicas, convierten a los conjugados Ir(III)-COUPY, los convierten en agentes fotosensibilizadores prometedores para la terapia fotodinámica, sobre todo para el tratamiento de tumores hipóxicos.

Finalmente, también se abordó la síntesis de un nuevo conjugado entre un fluoróforo COUPY, con emisión en el infrarrojo cercano, y un complejo ciclometalado de Ru(II) tipo polipiridilo con el objetivo de estudiar su potencial como agente fotosensibilizador en terapia fotodinámica. Los estudios biológicos preliminares sugieren que dicho compuesto presenta una excelente actividad tras irradiación con luz roja.

Referencias

- (1) Lakowicz, J. R. *Principles of Fluorescence Spectroscopy, 3rd Edition*, Joseph R. Lakowicz, Editor; **2006**. <https://doi.org/10.1007/978-0-387-46312-4>.
- (2) Baggaley, E.; Weinstein, J. A.; Williams, J. A. G. Lighting the Way to See inside the Live Cell with Luminescent Transition Metal Complexes. *Coord. Chem. Rev.* **2012**, *256*, 1762–1785. <https://doi.org/10.1016/j.ccr.2012.03.018>.
- (3) Zhang, K. Y.; Yu, Q.; Wei, H.; Liu, S.; Zhao, Q.; Huang, W. Long-Lived Emissive Probes for Time-Resolved Photoluminescence Bioimaging and Biosensing. *Chem. Rev.* **2018**, *118*, 1770–1839. <https://doi.org/10.1021/acs.chemrev.7b00425>.
- (4) Stefanachi, A.; Leonetti, F.; Pisani, L.; Catto, M.; Carotti, A. Coumarin: A Natural, Privileged and Versatile Scaffold for Bioactive Compounds. *Molecules* **2018**, *23*, 250–284. <https://doi.org/10.3390/molecules23020250>.
- (5) Zhang, R. R.; Schroeder, A. B.; Grudzinski, J. J.; Rosenthal, E. L.; Warram, J. M.; Pinchuk, A. N.; Eliceiri, K. W.; Kuo, J. S.; Weichert, J. P. Beyond the Margins: Real-Time Detection of Cancer Using Targeted Fluorophores. *Nat. Rev. Clin. Oncol.* **2017**, *14*, 347–364. <https://doi.org/10.1038/nrclinonc.2016.212>.
- (6) Lavis, L. D.; Raines, R. T. Bright Building Blocks for Chemical Biology. *ACS Chem. Biol.* **2014**, *9*, 855–866. <https://doi.org/10.1021/cb500078u>.
- (7) Jiao, Y.; Zhu, B.; Chen, J.; Duan, X. Fluorescent Sensing of Fluoride in Cellular System. *Theranostics* **2015**, *5*, 173–187. <https://doi.org/10.7150/thno.9860>.
- (8) Lavis, L. D.; Raines, R. T. Bright Ideas for Chemical Biology. *ACS Chem. Biol.* **2008**, *3*, 142–155. <https://doi.org/10.1021/cb700248m>.
- (9) Escobedo, J. O.; Rusin, O.; Lim, S.; Strongin, R. M. NIR Dyes for Bioimaging Applications. *Curr. Opin. Chem. Biol.* **2010**, *14*, 64–70. <https://doi.org/10.1016/j.cbpa.2009.10.022>.
- (10) Owens, E. A.; Henary, M.; el Fakhri, G.; Choi, H. S. Tissue-Specific Near-Infrared Fluorescence Imaging. *Acc. Chem. Res.* **2016**, *49*, 1731–1740. <https://doi.org/10.1021/acs.accounts.6b00239>.
- (11) Haque, A.; Faizi, M. S. H.; Rather, J. A.; Khan, M. S. Next Generation NIR Fluorophores for Tumor Imaging and Fluorescence-Guided Surgery: A Review. *Bioorg. Med. Chem.* **2017**, *25*, 2017–2034. <https://doi.org/10.1016/j.bmc.2017.02.061>.

- (12) Sharma, S. J.; Sekar, N. Deep-Red/NIR Emitting Coumarin Derivatives - Synthesis, Photophysical Properties, and Biological Applications. *Dyes Pigm.* **2022**, *202*, 110306. <https://doi.org/10.1016/j.dyepig.2022.110306>.
- (13) Fournier, L.; Aujard, I.; le Saux, T.; Maurin, S.; Beaupierre, S.; Baudin, J. B.; Jullien, L. Coumarinylmethyl Caging Groups with Redshifted Absorption. *Eur. J. Chem.* **2013**, *19*, 17494–17507. <https://doi.org/10.1002/chem.201302630>.
- (14) Gandioso, A.; Contreras, S.; Melnyk, I.; Oliva, J.; Nonell, S.; Velasco, D.; García-Amorós, J.; Marchán, V. Development of Green/Red-Absorbing Chromophores Based on a Coumarin Scaffold That Are Useful as Caging Groups. *J. Org. Chem.* **2017**, *82*, 5398–5408. <https://doi.org/10.1021/acs.joc.7b00788>.
- (15) Gandioso, A.; Bresolí-Obach, R.; Nin-Hill, A.; Bosch, M.; Palau, M.; Galindo, A.; Contreras, S.; Rovira, A.; Rovira, C.; Nonell, S.; Marchán, V. Redesigning the Coumarin Scaffold into Small Bright Fluorophores with Far-Red to Near-Infrared Emission and Large Stokes Shifts Useful for Cell Imaging. *J. Org. Chem.* **2018**, *83*, 1185–1195. <https://doi.org/10.1021/acs.joc.7b02660>.
- (16) Rovira, A.; Pujals, M.; Gandioso, A.; López-Corrales, M.; Bosch, M.; Marchán, V. Modulating Photostability and Mitochondria Selectivity in Far-Red/NIR Emitting Coumarin Fluorophores through Replacement of Pyridinium by Pyrimidinium. *J. Org. Chem.* **2020**, *85*, 6086–6097. <https://doi.org/10.1021/acs.joc.0c00570>.
- (17) Rovira, A.; Gandioso, A.; Goñalons, M.; Galindo, A.; Massaguer, A.; Bosch, M.; Marchán, V. Solid-Phase Approaches for Labeling Targeting Peptides with Far-Red Emitting Coumarin Fluorophores. *J. Org. Chem.* **2019**, *84*, 1808–1817. <https://doi.org/10.1021/acs.joc.8b02624>.
- (18) Pham, T. C.; Nguyen, V. N.; Choi, Y.; Lee, S.; Yoon, J. Recent Strategies to Develop Innovative Photosensitizers for Enhanced Photodynamic Therapy. *Chem. Rev.* **2021**, *121*, 13454–13619. <https://doi.org/10.1021/acs.chemrev.1c00381>.
- (19) Agostinis, P.; Berg, K.; Cengel, K. A.; Foster, T. H.; Girotti, A. W.; Gollnick, S. O.; Hahn, S. M.; Hamblin, M. R.; Juzeniene, A.; Kessel, D.; Korbelik, M.; Moan, J.; Mroz, P.; Nowis, D.; Piette, J.; Wilson, B. C.; Golab, J. Photodynamic Therapy of Cancer: An Update. *CA: Cancer J. Clin.* **2011**, *61*, 250–281. <https://doi.org/10.3322/caac.20114>.

- (20) Karges, J. Clinical Development of Metal Complexes as Photosensitizers for Photodynamic Therapy of Cancer. *Angew. Chem. Int. Ed.* **2022**, *61*, 1–9. <https://doi.org/10.1002/anie.202112236>.
- (21) Yano, S.; Hirohara, S.; Obata, M.; Hagiya, Y.; Ogura, S. ichiro; Ikeda, A.; Kataoka, H.; Tanaka, M.; Joh, T. Current States and Future Views in Photodynamic Therapy. *J. Photochem. Photobiol. C: Photochem. Rev.* **2011**, *12*, 46–67. <https://doi.org/10.1016/j.jphotochemrev.2011.06.001>.
- (22) Chen, D.; Xu, Q.; Wang, W.; Shao, J.; Huang, W.; Dong, X. Type I Photosensitizers Revitalizing Photodynamic Oncotherapy. *Small* **2021**, *17*, 1–21. <https://doi.org/10.1002/sml.202006742>.
- (23) Zhao, X.; Liu, J.; Fan, J.; Chao, H.; Peng, X. Recent Progress in Photosensitizers for Overcoming the Challenges of Photodynamic Therapy: From Molecular Design to Application. *Chem. Soc. Rev.* **2021**, *50*, 4185–4219. <https://doi.org/10.1039/d0cs00173b>.
- (24) Monroe, S.; Colón, K. L.; Yin, H.; Roque, J.; Konda, P.; Gujar, S.; Thummel, R. P.; Lilje, L.; Cameron, C. G.; McFarland, S. A. Transition Metal Complexes and Photodynamic Therapy from a Tumor-Centered Approach: Challenges, Opportunities, and Highlights from the Development of TLD1433. *Chem. Rev.* **2019**, *119*, 797–828. <https://doi.org/10.1021/acs.chemrev.8b00211>.
- (25) Li, J.; Chen, T. Transition Metal Complexes as Photosensitizers for Integrated Cancer Theranostic Applications. *Coord. Chem. Rev.* **2020**, *418*, 213355–213374. <https://doi.org/10.1016/j.ccr.2020.213355>.
- (26) McFarland, S. A.; Mandel, A.; Dumoulin-White, R.; Gasser, G. Metal-Based Photosensitizers for Photodynamic Therapy: The Future of Multimodal Oncology? *Curr. Opin. Chem. Biol.* **2020**, *56*, 23–27. <https://doi.org/10.1016/j.cbpa.2019.10.004>.
- (27) Novohradsky, V.; Rovira, A.; Hally, C.; Galindo, A.; Viguera, G.; Gandioso, A.; Svitelova, M.; Bresolí-Obach, R.; Kostřhunova, H.; Markova, L.; Kasparkova, J.; Nonell, S.; Ruiz, J.; Brabec, V.; Marchán, V. Towards Novel Photodynamic Anticancer Agents Generating Superoxide Anion Radicals: A Cyclometalated Ir III Complex Conjugated to a Far-Red Emitting Coumarin. *Angew. Chem.* **2019**, *131*, 6377–6381. <https://doi.org/10.1002/ange.201901268>.
- (28) Ballester, F. J.; Ortega, E.; Bautista, D.; Santana, M. D.; Ruiz, J. Ru(II) Photosensitizers Competent for Hypoxic Cancers via Green Light Activation. *Chem. Commun.* **2020**, *56*, 10301–10304. <https://doi.org/10.1039/d0cc02417a>.

- (29) Yu, L.; Xu, Y.; Pu, Z.; Kang, H.; Li, M.; Sessler, J. L.; Kim, J. S. Photocatalytic Superoxide Radical Generator That Induces Pyroptosis in Cancer Cells. *J. Am. Chem. Soc.* **2022**, *144*, 11326–11337. <https://doi.org/10.1021/jacs.2c03256>.

